Structure, Dynamics and Applications

# Alexander Soloviev and Roger Lukas

Atmospheric and Oceanographic Sciences Library

Springer

The Near-Surface Layer of the Ocean

## ATMOSPHERIC AND OCEANOGRAPHIC SCIENCES LIBRARY

VOLUME 31



*The titles published in this series are listed at the end of this volume.*

# Structure, Dynamics and Applications

by

Alexander Soloviev

*Oceanographic Center,*
*NOVA Southeastern University, Dania Beach,*
*FL, U.S.A.*

and

Roger Lukas

*Department of Oceanography,*
*University of Hawaii at Manoa, Honolulu,*
*HI, U.S.A.*

Springer

A C.I.P. Catalogue record for this book is available from the Library of Congress.

ISBN-10 1-4020-4052-0 (HB)
ISBN-13 978-1-4020-4052-8 (HB)
ISBN-10 1-4020-4053-9 (e-book)
ISBN-13 978-1-4020-4053-5 (e-book)

Published by Springer,
P.O. Box 17, 3300 AA Dordrecht, The Netherlands.

*www.springer.com*

*Printed on acid-free paper*



Printed in the Netherlands.

# Contents

# Preface

Until the 1980s, a tacit agreement among many physical oceanographers was that nothing deserving attention could be found in the upper few meters of the ocean. The lack of adequete knowledge about the near-surface layer of the ocean was mainly due to the fact that the widely used oceanographic instruments (such as bathythermographs, CTDs, current meters, etc.) were practically useless in the upper few meters of the ocean. Interest in the near-surface layer of the ocean rapidly increased along with the development of remote sensing techniques. The interpretation of ocean surface signals sensed from satellites demanded thorough knowledge of upper ocean processes and their connection to the ocean interior.

Despite its accessibility to the investigator, the near-surface layer of the ocean is not a simple subject of experimental study. Random, sometimes huge, vertical motions of the ocean surface due to surface waves are a serious complication for collecting quality data close to the ocean surface. The supposedly minor problem of avoiding disturbances from ships' wakes has frustrated several generations of oceanographers attempting to take reliable data from the upper few meters of the ocean. Important practical applications nevertheless demanded action, and as a result several pioneering works in the 1970s and 1980s laid the foundation for the new subject of oceanography – the near-surface layer of the ocean.

In 1988, K.N. Fedorov and A.I. Ginzburg published a monograph "The Near-Surface Layer of the Ocean", which summarized many of the new results but which was printed in limited numbers. In 1992 this book was translated into English. Since the publication of Fedorov's book, this area of research has dramatically advanced. Numerous exciting new experimental and theoretical results have been obtained. The idea of the importance of the ocean-atmosphere coupling on small scales found its practical realization in the TOGA COARE program which took place between 1992 and 1994. The concept of one-dimensional upper ocean dynamics has been enriched with the consideration of three-dimensional spatial structures. In particular, spatially coherent organized motions are attracting more attention.

Our book provides a comprehensive account of the structures and dynamics of the near-surface layer of the ocean under different environmental conditions. Fedorov's pioneering monograph attempted to achieve this objective, but it had unfortunate gaps and redundancies. Now it is possible to provide a more coherent presentation of this important subject.

In this book, detailed treatment is given to the following topics: molecular sublayers, turbulence and waves, buoyancy effects, fine thermohaline structure of the near-surface layer of the ocean, spatially

coherent organized motions having surface manifestations, and the high wind-speed regime. Although this selection of topics depends somewhat on the specific research interests of the authors, the monograph attempts to systematically develop its subjects from physical and thermodynamic principles. The accent on the analysis of the results from recent major air-sea interaction experiments (including the data collected by the authors) is our effort to ensure that the book comprises the most comprehensive and reliable sum of knowledge that has been obtained in this area of research. For the subjects that are related to the physics of the near-surface layer of the ocean but not covered in the book in sufficient detail (or not covered at all), the reader is referred to useful literature. Among these subjects are the biochemistry of surface films (*The Sea Surface and Global Change*, edited by P.S. Liss and R.A. Duce, 1997), surface wave dynamics (Donelan and Hui, 1990), atmospheric boundary-layer dynamics (Stull, 1988), mixed layer modeling (Kantha and Clayson, 2000), air-sea fluxes (Businger and Kraus, 1994; Csanady, 2001), and coupled ocean-atmosphere systems (Godfrey et al., 1998).

Chapter 1 introduces the reader to the main theme of the book—the near-surface layer of the ocean as an element of the ocean-atmosphere system. A general discussion of upper ocean dynamics and thermodynamics sets the stage for the content of Chapters 2–7. This discussion introduces the different processes that mix and restratify the upper ocean.

Very close to the air-sea interface, turbulent mixing is suppressed and molecular diffusion appears to dominate the vertical property transport. Viscous, thermal, and diffusive sublayers close to the ocean surface exist as characteristic features of the air-sea momentum, heat, and mass transport. Their dynamics, discussed in Chapter 2, can be quite complex due to the presence of surface waves, capillary effects, penetrating solar radiation, and rainfall.

Chapter 3 provides insight into dynamics of the upper ocean turbulent boundary layer. The turbulence regime is the key to understanding many other processes in the near-surface layer of the ocean. Because methodological issues of turbulence measurements near the ocean surface are still not resolved, we start Chapter 3 with analysis of the existing experimental approaches. (The measurement of wave-enhanced turbulence is a very important but specialized topic.) Analyses of turbulence observations reveal different (sometimes contradictory) points of view on the role of surface waves. Recent observations obtained under a wide range of environmental conditions allows us to explain and, in some cases, to reconcile different points of view.

The wave-induced turbulence does not depend directly on stratification effects, and it is therefore reasonable to analyze the stratification effects separately. The analysis of stratification effects on turbulence in Chapter 3 is

based on some analogy between the atmospheric and oceanic turbulent boundary layers. This analogy has been employed in the studies of Steve Thorpe and Michael Gregg. It may only be observed starting from the depth where wave-breaking turbulence is not important. A discussion of the surface mixed layer versus the Ekman layer concept will illustrate the depth to which momentum supplied by the wind penetrates relative to where the base of the mixed layer is found.

Chapter 4 is devoted to the fine thermohaline structure of the near-surface layer. We consider the penetrative solar radiation and the impacts of the distribution of radiant heating on the mixed layer dynamics. Stable stratification in the near-surface ocean due to diurnal warming or rainfall can reduce the turbulence friction, which results in intensification of near-surface currents. Unstable stratification leads to convective overturning, which increases turbulent friction locally. In addition, discrete convective elements—analogs of thermals in the atmosphere—penetrate into the stably stratified layer below and produce non-local transport. Experimental studies at the equator have produced striking examples of local and non-local effects on the dynamics of the diurnal mixed layer and thermocline. The last section of this chapter demonstrates how the local (diffusive) and non-local (convective) transport can be parameterized and incorporated into one- or three-dimensional models. This chapter contains a few effective examples of spatial near-surface structures. These examples should motivate the reader to study in detail the relatively lengthy Chapter 5.

Chapter 5 is devoted to the coherent structures within the near-surface layer of the ocean. Spatially-coherent organized motions have been recognized as an important part of turbulent boundary layer processes. In the presence of surface gravity waves, the Ekman boundary layer becomes unstable to helical motions (Langmuir cells). “Wind-rows” can often be seen from space due to spray patches and have already been used in advanced remote sensing algorithms to determine the direction of near-surface winds. Ramp-like structures are a common feature of boundary layer flows; they are, however, oriented perpendicular to the wind direction, while Langmuir cells are roughly aligned with wind. The Langmuir cells and ramp-like structures entrain bubbles and can be traced with side-scan sonars. Other types of quasi-periodical structures in the near-surface ocean, such as freshwater lenses produced by rainfalls and near-inertial oscillations induced by moving storms may have distinct signatures in the sea surface temperature field. Sharp frontal interfaces are an intriguing example of self-organization. These interfaces are supposedly related to the subduction process and are of different nature in mid- and low-latitudes. Internal waves, resonant interactions between surface and internal modes, and billows in the diurnal thermocline also produce signatures on the ocean surface under certain conditions.

Chapter 6 addresses high wind speed conditions, when breaking waves intermittently disrupt the air-sea interface producing a two-phase environment—air-bubbles in water and sea spray in air. These two-phase mixtures alter the distribution of buoyancy forces, which may affect the air-sea dynamics. The volume nature of the buoyancy forces further complicates the dynamics. Section 6.1 describes air-bubbles in the near-surface layer of the ocean. Section 6.2 has extensive references to the works on sea-spray production. Effects of sea spray as well as air bubbles on air-sea exchanges in a tropical cyclone are the subjects of Section 6.3.

Chapter 7, the final chapter of this monograph, describes current and potential applications of the near-surface results. Among these applications are remote sensing of the ocean, marine optics, marine chemistry and biology, ocean acoustics, and air-sea gas exchange. The last section of this chapter contains possible application of the near-surface results to ocean general circulation and climate modeling.

The upper ocean processes obtain another level of complexity in coastal zones due to several possible additional factors, including river (and other freshwater) discharge, wider range of air-humidity and air-sea temperature differences, typically short wave fetch (for offshore winds), wave shoaling, refraction, and breaking, surface and bottom boundary layers merging approaching the coast, anthropogenic surfactants and other contaminants (sewage, nutrients). Suspended sediments (due to river outflows and to wave action) alter optical properties and stratification. Though some of the related issues are discussed throughout the book, no attempt is made in this book to present the near-surface processes of coastal zones in a systematic way.

This book is mainly directed toward research scientists in physical and chemical oceanography, marine biology, remote sensing, ocean optics and acoustics. To broaden the potential audience, we have tried to make the book interesting and informative for people with different backgrounds. We also try to keep its style as close as possible to a textbook format to make it of value for graduate studies in oceanography and environmental sciences.

# Acknowledgments

Collaborations and discussions with Nikolai Vershinsky (P.P. Shirshov Institute of Oceanology), Vladimir Kudryavtsev (MGI), Peter Schlüssel (EUMETSAT), Julian McCreary (NSU and UH), Mark Donelan (UM), Kristina Katsaros (AOML/NOAA), Eugene Terray (WHOI), and Hiroshi Matsuura (JAMSTEC) helped to motivate writing this book.

We are grateful to Michael Gregg (APL/UW), Anatoly Arjannikov (Granit), Robert Weller (WHOI), Chris Fairall (ETL/NOAA), Robert Pinkel (SIO/UCSD), Peter Hacker (UH), Robert Weisberg (USF), Frank Bradley and Stuart Godfrey (CSIRO) for fruitful collaboration during TOGA COARE, when many results discussed in this book were obtained. Several topics that later formed the foundation for this book were presented during the 1980s at the Theoretical Seminar of the P. P. Shirshov Institute of Oceanology led by Prof. Grigory Barenblatt (now with UC Berkley). Selected parts of this book were presented at the WHOI GFD Summer School during 2002 and 2003 and at the UM Applied Marine Physics laboratory during 2000-2005. Follow up discussions provided important feedback.

Dean Richard Dodge of the NOVA Southeastern University Oceanographic Center, and university President Ray Ferrero, granted sabbatical leave to the lead author during which the bulk of this monograph was undertaken. Support from the Office of Naval Research, NOAA, and NSF are also gratefully acknowledged. The second author was generously supported by the University of Hawaii and by the National Science Foundation during the research leading up to this book, and during its production.

Technical help with the preparation of the manuscript by Nancy Paquin (UH), Kevin Kohler (NSU), Sharon DeCarlo (UH), Rebekah Walker (NSU) is gratefully acknowledged. Their important contributions and support were critical to the successful conclusion of this project.

Chapter 1

# INTRODUCTION

*General discussion of the principles and equations governing ocean-atmosphere interactions sets the stage for the main subject of this book.*

## 1.1 The Ocean Near-Surface Layer in the Ocean-Atmosphere System

The top 2-3 m of the ocean has the same heat capacity as the entire atmosphere above. Of the penetrating solar radiation, 50% is absorbed within the first 0.5 m of the ocean. Of the breaking surface wave kinetic energy, 50% dissipates within 20% of the significant wave height from the surface. These facts highlight the special role of the near-surface layer of the ocean in the ocean-atmosphere system.

Historically, standard oceanographic instruments (like CTDs, ADCPs, and most types of turbulence profilers) have not produced high quality measurements in the upper few meters of the ocean. As a result, important processes in the near-surface layer of the ocean, like the large diurnal warming event shown in *Figure 1-1*, were largely missed. The aim of this monograph is to cover this gap to provide the reader with a more complete picture of the upper ocean, which is of increasing importance for certain practical applications such as remote sensing, climate modeling, and determining the global carbon cycle.

We define the near-surface layer of the ocean as being immediately adjacent to the air-sea interface and dominantly influenced by the local fluxes of heat, moisture, momentum and gas from the atmosphere. It is impossible to give a universal definition of this layer in meters because the

mixing regime below the air-sea interface strongly depends on meteorological, radiation, and surface wave conditions. Instead in this monograph the near-surface layer of the ocean is considered as an integral part of the ocean-atmosphere system. There are in fact some processes that are unique to the upper few meters (*e.g.*, wave breaking) or even for the upper few millimeters (*e.g.*, molecular transport) of the ocean. Other processes may be confined to the upper few meters of the ocean under certain conditions (*e.g.*, large diurnal warming events) but for different environmental conditions will have depth scales of tens of meters. There are also processes that originate at the air-sea interface but extend to the overall depth of the upper ocean mixed layer (*e.g.*, Langmuir circulations and nighttime convection).

The variety of forcing factors, in combination with nonlinear feedbacks, result in different near-surface regimes. Fedorov and Ginzburg (1988) consider five regimes in the near-surface layer of the ocean:

1) Intensive wind-wave mixing (wind speed at 10 m height above the ocean surface $U_{10} >$ 8-10 m s$^{-1}$);
2) Intensive convection (nighttime, winter, or atmospheric cold fronts);
3) Langmuir circulations ($U_{10}$ from 3 to 10 m s$^{-1}$);
4) Intensive solar heating under low wind and calm weather conditions ($U_{10}$ from 0 to 3-5 m s$^{-1}$);
5) Near-surface freshening due to rain.

This classification is still valid in general and is useful for many practical applications. At this point, however, it requires comment.

The near-surface ocean under regime 1 is usually well mixed. However, surface molecular sublayers, which are not included in this classification, may develop even under conditions of intensive wind-wave mixing though only between wave breaking events (see Chapter 2).

The Langmuir circulations, which are considered as a separate regime (regime 3) by Fedorov and Ginzburg, is a type of spatially coherent organized motions in the upper ocean. There are also other types of organized structures in the upper ocean, that are not included in the Fedorov and Ginzburg classification but which are widely observed in the near-surface ocean (see Chapter 5). These are ramp-like structures, large-amplitude internal waves (developing on a shallow diurnal thermocline or rain-formed halocline), sharp frontal interfaces, and penetrative convection.

Now, it is becoming clear that conditions of very high wind speeds ($U_{10} >$ 25-30 m s$^{-1}$) should be considered as a separate near-surface regime. In these extreme conditions a two-phase environment with gradual transition from bubble-filled water to spray-filled air is formed (Chapter 6).

Before proceeding to the main subject of this book, the near-surface layer of the ocean, in Chapter 1 we provide a general discussion of the governing

equations and air-sea interaction processes. The organization of the material in the rest of Chapter 1 is as follows:

Section 1.2 formulates the equations of fluid dynamics that govern the ocean-atmosphere boundary layers. Most of the equations for the near-surface ocean and the calculated results in this book are derived from these basic equations. Surface heat, momentum, and freshwater fluxes provide boundary conditions for equations formulated in Section 1.2. These surface boundary conditions are discussed in Section 1.3.

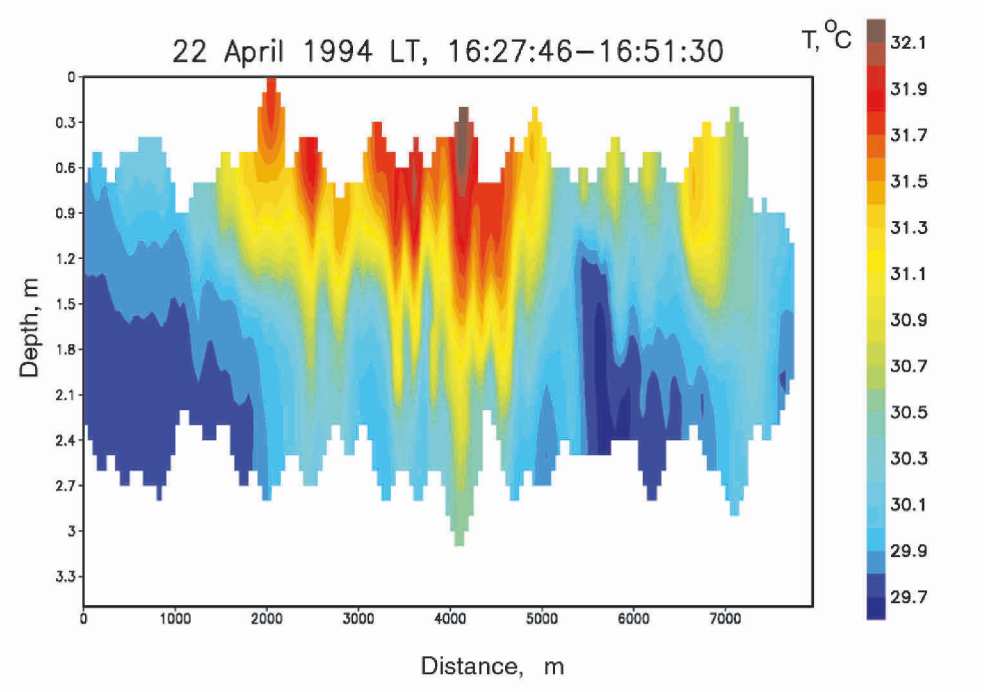


*Figure 1-1.* The temperature field in the upper 3 m of the ocean during a large diurnal event in the equatorial Pacific Ocean, from measurements by bow-mounted sensors (see Section 3.2.5). Temperature is given by the color bar on the right. Adapted from Soloviev and Lukas (1997a) by permission of Elsevier.

Section 1.4 considers solar radiation and its absorption in the near-surface layer of the ocean. The solar energy is the major forcing factor in the ocean-atmosphere system. For the upper few meters of the ocean, it should be treated as a body (volume) source of thermal energy. Formally, this term does not enter the surface boundary condition for heat flux. The rain contribution to the surface and volume heat fluxes is considered in Section 1.5.

Surface waves are the most important process distinguishing the near-surface layer of the ocean from its deeper layers. In Section 1.6, the elements

of surface wave theory directly relating to the dynamics of the near-surface layer of the ocean are introduced as solutions for the equations of fluid mechanics.

Matching the dynamics and thermodynamics of the ocean and atmosphere occurs in the planetary boundary layers (PBL), which are the subject of Section 1.7.

## 1.2 Basic Equations of Fluid Mechanics and Useful Approximations

### 1.2.1 Mathematical notation and governing equations

This book covers a variety of topics relating to different disciplines. Some reuse of symbols for different properties is therefore unavoidable. This is noted in the list of frequently used mathematical symbols given in Appendix. An attempt is made to avoid situations where a symbol with two different meanings would appear in the same equation or even in the same section. Symbols that appear only locally in the text typically are not included in the list of frequently used mathematical symbols.

The main equations that govern the oceanic and atmospheric boundary layers including the near-surface layer of the ocean have been formulated and discussed in many scientific publications. The full system of equations includes conservation laws for mass, momentum, heat, energy, salt or humidity plus the equation of state. The transport equation for an arbitrary passive tracer can be easily included.

From the developments of LeBlond and Mysak (1978) and Mellor (1996), the components of the *momentum equation* on a rotating sphere are as follows:

$$\rho\left(\frac{Du}{Dt} - fv + f_y w\right) = -\frac{\partial p}{\partial x} + \frac{\partial \tau_{xx}}{\partial x} + \frac{\partial \tau_{yx}}{\partial y} + \frac{\partial \tau_{zx}}{\partial z}, \tag{1.1}$$

$$\rho\left(\frac{Dv}{Dt} + fu\right) = -\frac{\partial p}{\partial y} + \frac{\partial \tau_{xy}}{\partial x} + \frac{\partial \tau_{yy}}{\partial y} + \frac{\partial \tau_{zy}}{\partial z}, \tag{1.2}$$

$$\rho\left(\frac{Dw}{Dt} - f_y u\right) = -\rho g - \frac{\partial p}{\partial z} + \frac{\partial \tau_{xz}}{\partial x} + \frac{\partial \tau_{yz}}{\partial y} + \frac{\partial \tau_{zz}}{\partial z} \tag{1.3}$$

where $\rho$ is the water density, and $\frac{D}{Dt} = u\frac{\partial}{\partial x} + v\frac{\partial}{\partial y} + w\frac{\partial}{\partial z} + \frac{\partial}{\partial t}$. The rectangular coordinate system has its origin at the sea surface, with $x$ directed eastward, $y$ directed northward, $z$ directed upward, and $u$, $v$, and $w$ represent the corresponding velocity components; $t$ is time; $f = 2\Omega\sin\varphi$ and $f_y = 2\Omega\cos\varphi$, where Ω is the magnitude of the Earth's rotation vector and φ is the latitude; $p$ is pressure; $g$ is the acceleration due to gravity. Symbol $\tau$ denotes different components of the *stress tensor*, due to viscosity (and to fluctuating velocities if $u$, $v$, and $w$ refer to ensemble mean quantities.)

In the Boussinesq approximation, which is applicable to many oceanic conditions, the density changes in equations (1.1)-(1.3) can be neglected except in the gravity term entering (1.3) where $\rho$ is multiplied by $g$. The Boussinesq approximation is not valid for acoustic applications and for two-phase environments like the surface wave breaker.

The system of equations (1.1)-(1.3) is complemented with the *continuity equation* for incompressible fluids,

$$\frac{\partial u}{\partial x} + \frac{\partial v}{\partial y} + \frac{\partial w}{\partial z} = 0\,. \tag{1.4}$$

In the general case of an isotropic *Newtonian fluid*, the different components of the viscous stress tensor depend linearly on strain components (Mellor, 1996):

$$\begin{bmatrix} \tau_{xx} & \tau_{yx} & \tau_{zx} \\ \tau_{xy} & \tau_{yy} & \tau_{zy} \\ \tau_{xz} & \tau_{yz} & \tau_{zz} \end{bmatrix} = \rho K_M \begin{bmatrix} 2\frac{\partial u}{\partial x} & \frac{\partial u}{\partial y} + \frac{\partial v}{\partial x} & \frac{\partial u}{\partial z} + \frac{\partial w}{\partial x} \\ \frac{\partial v}{\partial x} + \frac{\partial u}{\partial y} & 2\frac{\partial v}{\partial y} & \frac{\partial v}{\partial z} + \frac{\partial w}{\partial y} \\ \frac{\partial w}{\partial x} + \frac{\partial u}{\partial z} & \frac{\partial w}{\partial y} + \frac{\partial v}{\partial z} & 2\frac{\partial w}{\partial z} \end{bmatrix}, \tag{1.5}$$

where $\rho$ is the water density that under the Boussinesq approximation can be treated as a constant, and $K_M$ is the *kinematic viscosity*. (Newtonian fluids are fluids that have linear dependence of the stress tensor on strain components.)

### 1.2.2 Boundary-layer approximation

Adjacent to the air-sea interface there are boundary layers in both the atmosphere and the ocean. Their thickness is much less than their horizontal dimension, which leads to the so-called *boundary-layer approximation*. Under this approximation, the motion and continuity equations (1.1)-(1.4) are as follows (Mellor, 1996):

$$\frac{\partial u}{\partial t}+u\frac{\partial u}{\partial x}+v\frac{\partial u}{\partial y}+w\frac{\partial u}{\partial z}-fv=-\frac{1}{\rho}\frac{\partial p}{\partial x}+\frac{1}{\rho}\frac{\partial \tau_{zx}}{\partial z}, \tag{1.6}$$

$$\frac{\partial v}{\partial t}+u\frac{\partial v}{\partial x}+v\frac{\partial v}{\partial y}+w\frac{\partial v}{\partial z}+fu=-\frac{1}{\rho}\frac{\partial p}{\partial y}+\frac{1}{\rho}\frac{\partial \tau_{zy}}{\partial z}, \tag{1.7}$$

$$\frac{\partial p}{\partial z}=-\rho g, \tag{1.8}$$

$$\frac{\partial u}{\partial x}+\frac{\partial v}{\partial y}+\frac{\partial w}{\partial z}=0. \tag{1.9}$$

Under the boundary-layer approximation, the conservation equation for vertical momentum (1.3) reduces to the hydrostatic equation (1.8). This equation provides a substantial simplification of the governing system of equations because the vertical distribution of pressure can be determined from the density field, and it does not directly depend on the fluid motion.

The heat, salinity, and other material transport equations in the upper ocean under the boundary layer approximation are as follows:

$$\rho c_p\left(\frac{\partial \Theta}{\partial t}+u\frac{\partial \Theta}{\partial x}+v\frac{\partial \Theta}{\partial y}+w\frac{\partial \Theta}{\partial z}\right)=-\frac{\partial Q}{\partial z}+\frac{\partial I_R}{\partial z}-\frac{\partial Q_{rV}}{\partial z}, \tag{1.10}$$

$$\rho\left(\frac{\partial S}{\partial t}+u\frac{\partial S}{\partial x}+v\frac{\partial S}{\partial y}+w\frac{\partial S}{\partial z}\right)=-\frac{\partial J}{\partial z}-\frac{\partial J_{rV}}{\partial z}. \tag{1.11}$$

$$\frac{\partial C_i}{\partial t} + u\frac{\partial C_i}{\partial x} + v\frac{\partial C_i}{\partial y} + w\frac{\partial C_i}{\partial z} = -\frac{\partial G_i}{\partial z} - \frac{\partial G_{Vi}}{\partial z} - \sigma_* C_i \,, \tag{1.12}$$

where $c_p$ is the specific heat capacity, $\Theta$ is the *potential temperature*, $S$ is the salinity, and $C_i$ is the concentration of $i$-th component of tracer admixture; $Q$, $J$, and $G_i$ are the vertical fluxes of heat, salt, and $i$-th component of tracer, respectively. $I_R$ and $Q_{rv}$ are the volume heat sources due to absorption of solar radiation and decay of raindrops penetrating the sea surface; $J_{rV}$ is the volume source of freshwater due to the absorption of raindrops; $G_{Vi}$ is the volume source of material or gas (due to bubbles, biochemical reactions, etc.), and $\sigma_*$ is the dissolution rate. Parameterizations for $I_R$, $Q_{rV}$, and $J_{rV}$ are provided in Sections 1.4 and 1.5. Parameterizations for $G_{Vi}$ in application for gas transport are discussed in Section 7.5.

For most near-surface applications, $\Theta$ is practically equivalent to thermodynamic temperature, $T$; however, the difference between the potential and thermodynamic temperature becomes more important when a weakly stratified mixed layer is considered (Section 5.4).

The vertical heat flux is related to the gradient of temperature according to *Fourier's law*:

$$Q = -c_p \rho K_T \frac{\partial \Theta}{\partial z} \,, \tag{1.13}$$

where $K_T$ is the coefficient of thermal diffusivity. The vertical salt and scalar tracer fluxes are related to gradients of salinity and concentration according to *Fick's law:*

$$J = -\rho K_S \frac{\partial S}{\partial z} \,, \tag{1.14}$$

$$G_i = -K_{Ci} \frac{\partial C_i}{\partial z} \,, \tag{1.15}$$

where $K_S$ and $K_{Ci}$ are the diffusion coefficients for salt and an arbitrary scalar tracer, respectively.

### 1.2.3 Low Rossby number approximation

Further simplification of equations (1.6)-(1.7) is possible under the low *Rossby number*,

$$Ro = u_l / (lf) << 1, \tag{1.16}$$

where $u_l$ is the typical velocity scale, $l$ is the length scale characteristic of horizontal variation of properties in the ocean, and $f$ is the Coriolis parameter. Under the boundary layer and low Rossby number approximations, the advective terms in equations (1.6)-(1.7) vanish reducing these equations to:

$$\frac{\partial u}{\partial t} - fv = -\frac{1}{\rho}\frac{\partial p}{\partial x} + \frac{1}{\rho}\frac{\partial \tau_{zx}}{\partial z}, \tag{1.17}$$

$$\frac{\partial v}{\partial t} + fu = -\frac{1}{\rho}\frac{\partial p}{\partial y} + \frac{1}{\rho}\frac{\partial \tau_{zy}}{\partial z}. \tag{1.18}$$

Equations (1.10)-(1.12) for the heat, salinity, and other substances are unaffected by the low Rossby number approximation since the Coriolis term does not enter into those scalar equations.

### 1.2.4 Turbulence and turbulent kinetic energy budget

In the ocean, the diffusion processes are usually associated with turbulence. Turbulence can occur because of local (shear or convective) flow instability or may be transported from a nonlocal source by advection, convection, or turbulent velocity and pressure fluctuations. An important source of turbulence in the upper ocean is surface wave breaking (Chapter 3).

The criterion for shear instability commonly used in hydrodynamics is the Reynolds number,

$$\mathrm{Re} = u_l l / \nu \tag{1.19}$$

where $u_l$ is the velocity scale, $\nu$ is the molecular coefficient of kinematic viscosity ($\nu = 1.1 \cdot 10^{-6}$ m$^2$s$^{-1}$ at $T$ = 20°C and $S$ = 35 psu), and $l$ is the

characteristic length scale. The transition from a laminar to turbulent flow usually occurs at $\mathrm{Re}_{cr} \sim 10^3$.

Convective instability of the flow results from unstable temperature or salinity stratification. A relevant nondimensional criterion for thermal convection is the *Rayleigh number*,

$$Ra = -\alpha_T g \Delta T h^3 / (\kappa_T \nu), \tag{1.20}$$

where $g$ is the acceleration of gravity, $\alpha_T$ is the thermal expansion coefficient of seawater ($\alpha_T = -2.6 \cdot 10^{-4}$ °C$^{-1}$ at $T$ = 20°C and $S$ = 35 psu), $\Delta T$ is the vertical temperature difference between the top and bottom of the convecting layer, $h$ is the layer thickness, and $\kappa_T$ is the molecular coefficient of thermal diffusivity ($\kappa_T = 1.3 \cdot 10^{-7}$ m$^2$ s$^{-1}$ at $T$ = 20°C and $S$ = 35 psu). The term, $\alpha_T \Delta T = \Delta\rho/\rho$, represents the fractional density difference between the top and bottom of the convective layer. The transition from laminar to turbulent convection is usually observed in the ocean for critical Rayleigh number $Ra_{cr} \sim 5 \times 10^4$ (Turner, 1973).

The Reynolds number associated with ocean currents are very large, on the order of $10^7$, and these currents are generally turbulent. Rayleigh numbers in the ocean are also very large (typically greater than $10^{14}$ for a temperature difference of 0.1°C over 10 m), so convection is usually turbulent. However, for strong stable stratification $Ra$ may drop below $Ra_{cr}$. In the near-surface ocean such cases can occur under extreme conditions of calm weather and strong insolation or precipitation (Chapter 4).

Although originally derived for laminar flows, parameterization laws (1.5) and (1.13)-(1.15) are applicable for characterizing the turbulent transport of momentum and scalar properties like temperature, salinity, or gas. In the case of a turbulent flow, coefficients $K_M$, $K_T$, $K_S$, and $K_C$ represent the turbulent eddy transport. The conservation equations for momentum, heat, salt, and passive tracers expressed in terms of turbulent eddy coefficients appear exactly in the same form as their laminar analogs (1.1)-(1.3) and (1.10)-(1.12). In a developed turbulent flow (*i.e.*, at large Reynolds numbers), $K_M$, $K_T$, $K_S$, and $K_C$ are approximately equal (unlike the corresponding molecular diffusivities).

Turbulent eddy coefficients depend on the flow, geometry, and stratification. In the simplest form, the turbulent eddy coefficient for momentum is parameterized based on Prandtl's mixing length hypothesis $K_M \sim l u_l$ and Kolmogorov's hypothesis $u_l \sim \sqrt{b}$, where $l$ is the mixing length, and $b$ is the turbulent kinetic energy (TKE). More sophisticated semi-empirical closure schemes are considered in Chapters 3 and 5.

The individual components of the turbulent kinetic energy (TKE) budget are given in the form derived by Garwood (1977):

$$\frac{1}{2}\frac{\partial\overline{u'^2}}{\partial t} = -\overline{u'w'}\frac{\partial u}{\partial z} - \frac{\partial}{\partial z}\left(\frac{\overline{w'u'^2}}{2}\right) + \overline{\frac{p'}{\rho}\frac{\partial u'}{\partial x}} + f\overline{u'v'} - f_y\overline{u'w'} - \frac{\varepsilon}{3}, \qquad (1.21)$$

$$\frac{1}{2}\frac{\partial\overline{v'^2}}{\partial t} = -\overline{v'w'}\frac{\partial v}{\partial z} - \frac{\partial}{\partial z}\left(\frac{\overline{w'v'^2}}{2}\right) + \overline{\frac{p'}{\rho}\frac{\partial v'}{\partial y}} - f\overline{u'v'} - \frac{\varepsilon}{3}, \qquad (1.22)$$

$$\frac{1}{2}\frac{\partial\overline{w'^2}}{\partial t} = -\frac{g}{\rho}\overline{\rho'w'} - \frac{\partial}{\partial z}\left(\frac{\overline{w'^3}}{2} + \overline{\frac{w'p'}{\rho}}\right) + \overline{\frac{p'}{\rho}\frac{\partial w'}{\partial x}} + f_y\overline{u'w'} - \frac{\varepsilon}{3}, \qquad (1.23)$$

where $\rho'$ is the density fluctuation, $\varepsilon$ is the viscous dissipation and primes denote the fluctuating components. Garwood and Gallacher (1985) studied the usually neglected horizontal Coriolis term ($f_y\overline{u'w'}$) in the turbulent kinetic energy budget. In this term, the Reynolds stress interacts with the northward component of planetary rotation to exchange turbulent kinetic energy between horizontal and vertical components. In fact, the sum of equations (1.21)-(1.23) does not contain the horizontal Coriolis term:

$$\frac{\partial b}{\partial t} = \tau_{xz}\frac{\partial u}{\partial z} + \tau_{yz}\frac{\partial v}{\partial z} - \frac{g}{\rho}\overline{w'\rho'} - \frac{\partial E}{\partial z} - \varepsilon, \qquad (1.24)$$

where $b = \overline{\left(u'^2 + v'^2 + w'^2\right)}/2$ and $b' = \left(u'^2 + v'^2 + w'^2\right)/2$ are the turbulent kinetic energy (TKE) and its fluctuation, respectively; $E = \overline{w'\left(b' + p'/\rho\right)}$ is the vertical flux of TKE; $\tau_{xz} = -\rho\overline{u'w'}$ and $\tau_{yz} = -\rho\overline{v'w'}$ are the components of the Reynolds stress. The term associated with buoyancy forces ($g\overline{w'\rho'}/\rho$) can be expressed in terms of the turbulent heat ($Q = c_p\rho\overline{\Theta'w'}$), salt ($J = \rho\overline{S'w'}$), and tracer concentration ($G_i = \overline{w'C_i'}$) fluxes as follows: $\frac{g}{\rho}\overline{\rho'w'} = \frac{\alpha_T g Q}{c_p\rho} + \frac{\beta_S g J}{\rho} + g\sum_i\frac{\left(\rho_i - \rho\right)G_i}{\rho}$, where $\alpha_T$ is the thermal

expansion coefficient of seawater, $\beta_S$ is the coefficient of saline contraction, and $\rho_i$ is the density of *i*-th tracer.

## 1.3 Boundary Conditions

In order to compute changes in the ocean-atmosphere system, it is necessary to know the appropriate conditions to apply at boundaries. Volume sources must also be specified. In this section we consider the surface boundary conditions for the momentum, heat, and mass balance equations. The boundary condition for the turbulent kinetic energy equation is considered in Section 1.6.6. The volume sources due to solar radiation and penetrating raindrops are discussed in Sections 1.4 and 1.5 respectively.

Under sufficiently high winds, the phase boundary between air and water is locally disturbed by wave breaking events producing a two-phase zone (air bubbles in water and sea spray in air) of a finite thickness. The quantitative characterization of the boundary conditions under very high wind-speed conditions is still a challenge (see Chapter 6).

### 1.3.1 Types of surface boundary conditions

For the air-sea interface, boundary conditions are usually formulated in terms of velocity, temperature, and concentration or in terms of momentum, heat, and mass (gas) fluxes. In many practical situations, the detailed structure of the air-sea interface is difficult to resolve, in particular, due to the presence of molecular sublayers (see Chapter 2). As a result, a formulation of boundary conditions in terms of fluxes is often more suitable.

The surface boundary conditions for momentum balance equations (1.17) and (1.18) expressed in terms of fluxes are as follows:

$$\tau_{x0} = \tau_{xz}\big|_{z\to -0} \text{ and } \tau_{y0} = \tau_{yz}\big|_{z\to -0}, \tag{1.25}$$

where $\tau_{x0}$ and $\tau_{y0}$ are the east- and northward components of the surface wind stress, and $z \to -0$ denotes the one-sided limit from the water side. (Strictly speaking the wave- or rain-induced component of the wind stress should be treated as a volume source of momentum in the near-surface layer of the ocean, which, however, requires the addition of the volume source term into the equation for momentum balance.)

The surface boundary condition for the heat transport equation (1.10) in water is as follows:

$$Q_0 = Q\big|_{z\to -0} = Q_T + Q_E + I_L + Q_{rs}\,, \tag{1.26}$$

where $Q_0$ is the net surface heat flux; $Q_T$ and $Q_E$ are the sensible and latent heat fluxes respectively; $I_L$ is the net longwave radiative flux; $Q_{rs}$ is the surface component of the rain-induced heat flux (see Section 1.5.4). Solar radiation does not enter the surface boundary condition because it is treated as a volume source of heat.

The surface boundary condition for the salinity transport equation (1.11) is associated with freshwater fluxes at the air-sea interface. A vertical balance of freshwater flux across the ocean surface is as follows (Mellor, 1996):

$$E - P + m_0 \cdot \left(1 - S_0\right) = 0\,, \tag{1.27}$$

where $S_0$ is the sea surface salinity; $E$ is the evaporation rate, which is related to the latent heat flux as

$$Q_E = LE\,, \tag{1.28}$$

$L$ is the specific heat of vaporization for water; $P$ is the precipitation rate, and $m_0$ is the flux of seawater to the sea surface in units of volume of water per unit area per unit time. The factor $\left(1 - S_0\right)$ accounts for the exclusion of salt from seawater. The salt flux at the waterside of the air-sea interface in units of mass of water per unit area per unit time is

$$J_0 = J\big|_{z\to -0} = \rho S_0 m_0\,. \tag{1.29}$$

Combining (1.27) and (1.29) leads to the following boundary condition on the salt flux at the ocean surface:

$$J_0 = -\left(E - P\right)S_0 / \left(1 - S_0\right) \approx -\left(E - P\right)S_0 = -\left(Q_E / L - P\right)S_0\,. \tag{1.30}$$

Note that $S_0 \approx 35$ psu = 0.035; therefore, factor $(1 - S_0)$ is replaced with unity in (1.30).

The salinity increases towards the ocean surface when evaporation exceeds precipitation ($E > P$) or decreases when precipitation exceeds evaporation ($E < P$) because of freshwater flux subtracted from or added to the surface water, respectively. Vertical salinity gradients developing in the near-surface layer of the ocean due to surface forcing are considered in

Chapter 2 of this monograph in relation to the microlayer and in Chapter 4 in relation to diurnal warming and precipitation effects.

Due to generation and subsequent evaporation of spray droplets, salt crystals are transported into the atmosphere (see Chapter 6); however, no significant mass of salt actually crosses the air-sea interface. Although this amount of salt is unimportant from a salt balance point of view, the salt crystals left behind by evaporating spray play a role in the radiation balance and in cloud microphysics as condensation nuclei.

Fluxes of momentum, heat, and moisture at the air-sea interface can be estimated from covariance and inertial-dissipation measurements in the atmospheric boundary layer. However, such direct flux measurements are a rather complicated experimental task, which is only performed during specialized field campaigns. For many practical purposes, the fluxes at the air-sea interface can be linked to the properties of the bulk of the atmosphere and ocean and the properties of the interface.

The balance of forces that act upon the air-sea interface constitutes the dynamic boundary condition in the potential theory of surface waves. This boundary condition is discussed in Section 1.6.1.

### 1.3.2 Bulk-flux formulation

The turbulent flux of property $x$ is parameterized in bulk-flux algorithms as follows (Smith et al., 1996; Fairall et al., 2003):

$$\overline{w'\chi'} = c_\chi^{1/2} c_D^{1/2} U_a \Delta\chi = C_\chi U_a \Delta\chi \,, \tag{1.31}$$

where $w$ is the vertical component of the wind velocity vector, $\chi$ can represent components of wind velocity vector, temperature, specific humidity, or the mixing ratio of atmospheric gases (the prime sign denotes a fluctuation); $c_\chi$ is the bulk transfer coefficient for property $\chi$, $C_\chi = c_\chi^{1/2} c_D^{1/2}$ is the total transfer coefficient (symbol $D$ is reserved for wind speed).

The mean wind speed relative to the ocean surface $U_a$ is composed of a mean vector part ($u$ and $v$ components) and a *gustiness* component ($U_g$) in the following way:

$$U_a = \left(u^2 + v^2 + {U_g}^2\right)^{1/2} \tag{1.32}$$

The air-sea difference in the mean value of $\chi$ is defined as follows:

$$\Delta\chi = \chi_{sea} - \chi\left(z\right) \tag{1.33}$$

Both $U_a$ and $\Delta\chi$ are referenced to the specified height, $z$, of the mean quantities above the mean ocean surface (usually $z$ = 10 m).

The bulk-flux formulation for the magnitude of wind stress $\tau_0 = \left(\tau_{x0}^2 + \tau_{y0}^2\right)^{1/2}$ following from (1.25) and (1.31) is as follows

$$\tau_0 = C_D \rho_a U_{10}{}^2 , \tag{1.34}$$

where $C_D$ is the drag coefficient, $\rho_a$ is the density of air, $U_{10}$ is the wind speed at 10 m height ($z$ = 10 m). Sensible, $Q_{T,}$ and latent, $Q_{E,}$ heat flux are estimated from the following bulk formulations:

$$Q_T = c_{pa} \rho_a C_T U_{10} \left(T_0 - T_a\right) \tag{1.35}$$

$$Q_E = L \rho_a C_E U_{10} \left(q_0 - q_a\right) \tag{1.36}$$

where $c_{pa}$ is the specific heat capacity of air at constant pressure, $C_T$ is the bulk transfer coefficient for sensible heat, $C_E$ is the bulk transfer coefficient for latent heat, $T_0$ is the sea surface temperature (SST), $T_a$ is the air temperature at 10 m, $q_0$ is the saturation specific humidity of air at sea surface temperature, and $q_a$ is the specific humidity of air at 10 m.

For order of magnitude estimates, $C_D \sim 1.1 \times 10^{-3}$ for $U_{10}$ = 5 m s$^{-1}$, while for wind speeds within the range, 6 m s$^{-1}$ < $U_{10}$ < 22 m s$^{-1}$, Smith (1988) suggested a linear relationship

$$C_D \approx 1 \times 10^{-3} \cdot \left(0.61 + 0.063 U_{10}\right) \tag{1.37}$$

Smith (1988) also proposed empirical formulae for the sensible and latent heat transfer coefficients:

$$C_T = \begin{cases} 0.83 \times 10^{-3} \text{ for stable conditions} \\ 1.10 \times 10^{-3} \text{ for unstable conditions} \end{cases} \tag{1.38}$$

and

$$C_E = 1.5 \times 10^{-3} , \tag{1.39}$$

which are in reasonably good agreement with data in the above wind speed range.

Advanced bulk flux algorithms are based on the Monin-Oboukhov similarity theory (see Section 1.7.2), representing the fluxes in terms of mean quantities. While there are many algorithms available today, we will restrict our discussion to the COARE 3.0 bulk flux algorithm (Fairall et al., 2003).

The transfer coefficients depend on the Monin-Oboukhov stability parameter $\zeta = |z| / L_O$:

$$c_\chi^{1/2}(\zeta) = c_{\chi 0}^{1/2} / \left[1 - c_{\chi 0}^{1/2} \kappa^{-1} \psi_\chi(\zeta)\right] \tag{1.40}$$

where $z$ is the height of measurements, $L_O$ is the Oboukhov buoyancy length scale, $c_{\chi 0}^{1/2} = \kappa / \ln(z / z_{0\chi})$ is the transfer coefficient under neutral stratification ($\zeta = 0$), $\psi_\chi$ is an universal function of stability parameter $\zeta$, $\kappa$ is the von Karman constant (commonly used value $\kappa = 0.4$), and $z_{0\chi}$ is the *surface roughness length* for property $\chi$ under neutral stratification in the atmospheric boundary layer. The stability parameter is given by the formula of Zilitinkevich (1966):

$$\varsigma = \frac{-\kappa g |z|}{T} \frac{\left(\overline{w'\Theta'} + 0.61 T \overline{w'q'}\right)}{\left(-\overline{w'u'}\right)^{3/2}}, \tag{1.41}$$

where $g$ is the acceleration of gravity, and $T$ is the absolute temperature in K.

It is convenient to define a velocity scaling parameter $u_{*a} = \left(-\overline{w'u'}\right)^{1/2}$, which is known as the *friction velocity* (in the atmosphere, in this case) and respective scaling parameters for temperature $\Theta_{*a} = -\overline{w'\Theta'} / u_{*a}$, and humidity $q_* = -w'q' / u_{*a}$. Here $\overline{w'u'}$ denotes the streamwise component of the vertical momentum flux. The kinematic fluxes in (1.41) can then be replaced with $u_{*a}$, $\Theta_{*a}$, $q_*$ obtained by iteration within the bulk algorithm.

The bulk model formulated in (1.31), (1.40), and (1.41) has to be completed with representations (parameterizations) of the roughness length (or, equivalently, the transfer coefficients) and the profile stability functions ($\psi_\chi$). The roughness length can be parameterized with Charnock's (1955) velocity roughness formula plus a smooth flow limit expression from Smith (1988):

$$z_{0a} = a_C u_{*a}{}^2 / g + 0.11 \nu_a / u_{*a} \tag{1.42}$$

where $\alpha_C$ =0.011 for the COARE algorithm, and $\nu_\alpha$ is the kinematic molecular viscosity of the air.

The profile stability functions near neutral stratification conditions $\psi_\chi$ are known from accurate measurements over land, in particular, from the Kansas experiment (see Section 1.7.2). These functions have been extended theoretically for highly convective conditions (Fairall et al., 1996). For highly stable conditions, the Kansas functions predict zero fluxes. Later, Beljaars and Holstlag (1991) found finite, but highly intermittent, values for fluxes in very stable conditions and corrected the Kansas functions for the stable stratification limit. Adopting the stability functions with improved convective and stable limits eliminates occasional pathological results obtained with earlier versions of the COARE algorithm.

The addition of gustiness provides finite scalar fluxes as the wind speed approaches zero. In the COARE algorithm the gustiness is introduced using the convective velocity scale, $w_*$,

$$U_g = \beta_c w_* = \beta_c \left( \frac{g}{T} \overline{w' \Theta_v{}'} z_c \right)^{1/3}, \tag{1.43}$$

where $z_c$ is the depth of the convective boundary layer; $\Theta_v$ is the virtual potential temperature, which is analogous to the potential temperature that removes the adiabatic temperature variations caused by changes in the ambient pressure of an air parcel but also accounts for humidity effects (Stull, 1988), and $\beta_c$ is an empirical coefficient ( $\beta_c \approx 1.25$ ).

*Figure 1-2* shows the comparison between measured and modeled (COARE bulk flux algorithm) velocity transfer coefficients as a function of wind speed. Typically, measurements or model output provide input atmospheric variables ($U_a$, $T$, $q$) to a bulk flux algorithm at reference height $z$ and the surface properties (current vector, temperature). The surface value for specific humidity is computed from the sea surface temperature and the vapor pressure of seawater. Strictly speaking (1.31) requires the true interface temperature, $T_0$, and salinity, $S_0$, but usually only the temperature and salinity at some depth are available. The vapor pressure of seawater is 0.98 times the vapor pressure of pure water (Kraus and Businger, 1994). The dependence of the vapor pressure on the typical salinity changes in the near-surface layer is negligible (except during heavy rainfalls when $S_0$ may drop for as much as a few psu, see Chapters 2 and 4). When it is not raining, the salinity diffusion sublayer implies that the true salinity is only a few tenths psu higher than the bulk water salinity near the surface.

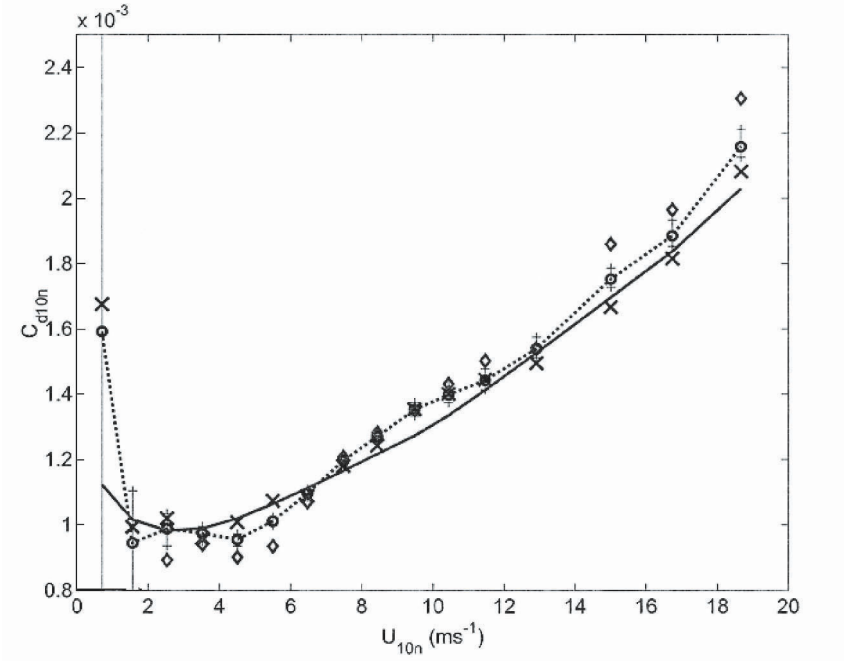


*Figure 1-2*. Median 10 m neutral velocity transfer coefficient as a function of 10 m neutral wind. Error bars indicate the statistical uncertainty (one sigma) of the median based on the distribution within the mean wind speed bin. Results of different experimental techniques are also shown: O is the combined covariance and inertia-dissipation values, X is the inertia-dissipation values only, and ◊ is the covariance values only. Reproduced from Fairall et al. (2003) by permission of American Meteorological Society.

In *Figure 1-3*, a scatter plot of streamwise covariance stress measurements is shown together with the COARE bulk-flux algorithm prediction. Negative values are part of the normal distribution of individual measurements. Grachev and Fairall (2001) found that at very low winds there is a tendency for the streamwise component to average to a negative value; this could be interpreted as the return of momentum to the atmosphere by waves. Though the COARE 3.0 algorithm incorporates a dependence of the bulk coefficient on the wave age, the bulk algorithm does not deal with negative momentum fluxes. This effect represents a difficulty in bulk-flux parameterizations.

The near-surface temperature gradients due to the cool skin (see Chapter 2) and diurnal warming may have some effect on the bulk-flux parameterization. The cool skin results in an interface temperature that is several tenths $^{o}$C cooler than the bulk water near the surface. During light wind and sunny conditions, the upper few meters of the ocean may also warm by 1-3$^{o}$C (see Chapter 4). In order to address these physics, the COARE algorithm incorporates sub-models that represent the millimeter-

scale cool skin near the interface and the diurnal warm layer in the upper few meters of the ocean, which estimate $T_0$ from $T_w$.

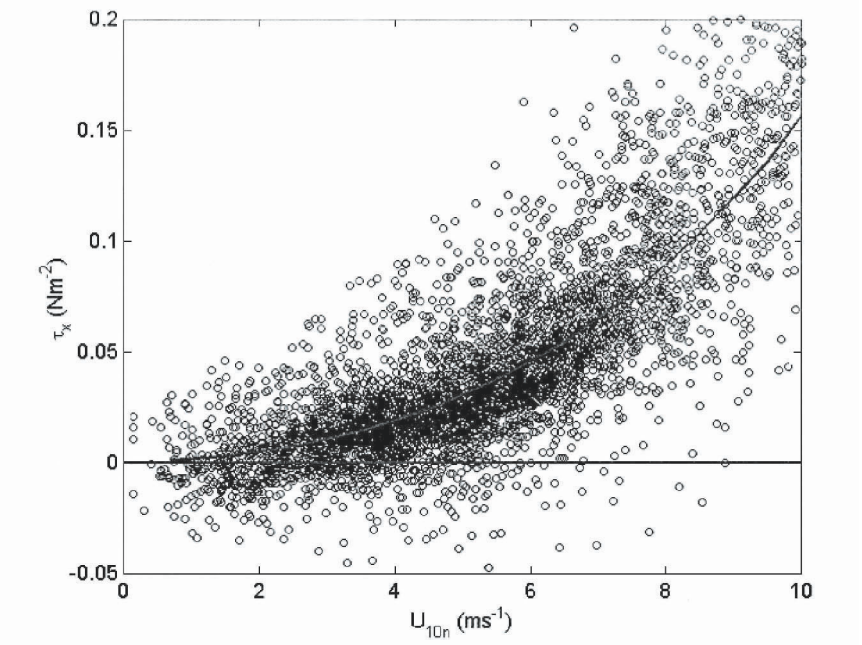


*Figure 1-3*. Covariance measurements of the streamwise momentum flux ($\tau_x$) as a function of 10 m neutral wind speed. The individual points are nominal 1-hour averages. The solid curve is the COARE 3.0 bulk flux algorithm. Reproduced from Fairall et al. (2003) by permission of American Meteorological Society.

The bulk coefficients $C_D$, $C_T$, $C_E$, and, especially $K_\mu$, are poorly known for very high wind speeds. The COARE bulk flux algorithm has been validated for wind speed ranging from 0 to 20 m s$^{-1}$. There are some indications that under very high wind speed conditions, starting from 35 or 40 m s$^{-1}$, the bulk coefficients may no longer be increasing with wind speed (Section 6.4.3).

The effects of sea spray, which are important under high wind speed conditions, have yet to be satisfactorily quantified. Sea spray enhances evaporation, influences atmospheric stratification and also transports momentum. Sea spray effects have been included in a heuristic bulk flux algorithm (Andreas, 2004) which, however, is not based on any data.

Since many trace gases of practical importance ($CO_2$, $O_2$, etc.) are almost infinitely soluble in air, the main difference in gas concentration is on the waterside of the air-sea interface (Bolin, 1960). The bulk-flux formulation for air-sea gas exchange is therefore somewhat different from (1.31):

$$G_0 = G\big|_{z\to -0} = K_\mu \Delta C\,, \tag{1.44}$$

where $\Delta C$ is the effective air-sea gas concentration difference, and $K_\mu$ is the gas transfer (piston) velocity. Expressed in terms of the gas partial pressure in water ($p_w$) and in air ($p_a$), and gas solubility $S_\mu$, formula (1.44) reads as follows:

$$G_0 = K_\mu S_\mu (p_w - p_a) . \qquad (1.45).$$

Strictly speaking, partial pressure in equation (1.45) should be replaced with gas fugacity (DOE, 1994). The fugacity of an ideal gas is simply its partial pressure. In terms of fugacity, the thermodynamic relationships for real (non-ideal) gases coincide with those established for ideal gases. An example of non-ideal gas is $CO_2$. For typical oceanic conditions, the difference between the $CO_2$ partial pressure and $CO_2$ fugacity is, however, only about 1 μatm, which is about 0.3% of the $CO_2$ fugacity in seawater.

The air-sea gas transfer velocity $K_\mu$ is determined by the properties of the turbulent boundary layer and sea surface (Section 7.5.1), while simplified parameterization formulas imply that $K_\mu$ is a function of wind speed only. A complicating issue is the bubble-mediated gas transport because it is a volume source, which depends on bubble dynamics (see Chapter 7). Representation of the volume source term $G_V$ in equation (1.12) involves such issues as gas solubility, bubble-mediated transport, and, in many cases, bio- and photochemical reactions in the sea surface microlayer.

### 1.3.3 Long-wave radiation

In many instances, the longwave radiation emitted from the sea surface (longwave exitance) is nearly balanced by the downward longwave radiation (longwave irradiance) emitted primarily from moisture in the atmosphere. It is possible, however, for the difference to be significant. To compute longwave exitance it is assumed that the ocean radiates as a gray body. This implies that the longwave exitance is proportional to the fourth power of the absolute sea surface temperature when expressed in degrees Kelvin (K).

The net long wave radiation flux is parameterized as follows:

$$I_L = \varepsilon_w \sigma T_0^4 - \varepsilon_w E_a , \qquad (1.46)$$

where $\sigma = 5.67 \times 10^{-8} W \cdot m^{-2} K^{-4}$ is the Stefan-Boltzmann constant, $T_0$ is the sea surface temperature, $\varepsilon_w \approx 0.97$ is the infrared emissivity of water (fraction of black-body radiation), and $E_a$ is the long wave irradiance from the sky that can be measured with an Eppley Precision Infrared Radiometer or calculated with an existing algorithm (see Katsaros (1990) for a review).

Ideally, the temperature difference across the millimeter-thick cool skin should be accounted for. Yet the temperature profile in the top few millimeters of the ocean is extremely difficult to measure. In many locations of the ocean the temperature in the upper few mm differs from the temperature at 0.5 m or more below the surface by less than 0.5 K. In some places and times, the difference can be as much as 4-5 K, making a correction to the bulk temperature necessary in order to closely approximate the skin temperature (Fairall et al., 1996).

## 1.4 Solar Radiation

### 1.4.1 Definitions

Radiation in the atmosphere and ocean can be described in terms of *radiance*, which is the radiant energy per unit time arriving from a specific direction and passing through a unit area perpendicular to that direction. *Irradiance,* or *downwelling irradiance*, is defined as the radiant energy that passes through a unit horizontal area per unit time coming from all directions (Kraus and Businger, 1994):

$$I_d = \int_{\phi=0}^{2\pi} \int_{\theta=0}^{\pi/2} L(z,\theta,\phi)\cos\theta\sin\theta d\theta d\phi\,, \tag{1.47}$$

where $L(z,\theta,\phi)$ is the radiance in the direction defined by the zenith angle $\theta$ and azimuth angle $\phi$, and z is the depth. Zenith angle $\theta$ is defined so that the direction pointing vertically downwards corresponds to zenith angle of zero. *Exitance* $I_u$, or upwelling irradiance, which is the irradiance from below the unit horizontal area, is defined by a similar integral but with the zenith angle limits corresponding to the hemisphere below the unit area:

$$I_u = \int_{\phi=0}^{2\pi} \int_{\theta=\pi/2}^{\pi} L(z,\theta,\phi)\cos\theta\sin\theta d\theta d\phi \tag{1.48}$$

Certain applications considered in Chapter 7 require introduction of spectral irradiances and radiances. Following IOCCG (2000), the *spectral irradiance*, or the *spectral downwelling irradiance*, is defined as

$$E_d(\lambda,z) = \int_{\phi=0}^{2\pi} \int_{\theta=0}^{\pi/2} L(\lambda,z,\theta,\phi)\cos\theta\sin\theta\, d\theta d\phi \tag{1.49}$$

where $L(\theta,\phi,\lambda,z)$ is now the *spectral radiance* and λ is the wavelength. Likewise, the *spectral exitance*, or the *spectral upwelling irradiance*, is defined here as follows:

$$E_u(\lambda,z) = \int_{\phi=0}^{2\pi} \int_{\theta=\pi/2}^{\pi} L(\lambda,z,\theta,\phi)\cos\theta\sin\theta\, d\theta d\phi, \tag{1.50}$$

The radiation budget at the sea surface consists of shortwave and long-wave components. Shortwave solar radiation is one of the most important components of the air-sea energy budget, accounting for almost all of the heat transferred into the ocean. Penetrating solar radiation and its variability in space and time are important for both the physics and biology of the ocean surface layer. Biologically, the *photosynthetically available radiation* (PAR) portion of the solar irradiance spectrum (usually from 400 to 700 nm) regulates marine primary productivity and therefore the evolution of aquatic ecosystems.

About one half of the penetrating solar radiation is absorbed within the upper half a meter of the ocean, while the longwave radiation is absorbed in or emitted from the top several μm of the ocean. Global circulation models of the ocean often consider the incident shortwave solar irradiance as a heat flux applied directly to the ocean surface. For studying the near-surface layer of the ocean, however, the solar radiation is more appropriately treated as a volume source of energy (see equation (1.10)), which requires detailed knowledge of solar energy absorption as a function of depth. At the same time, the net longwave irradiance in most practical applications is considered as a source of energy applied to the ocean surface and thus entering boundary condition (1.26).

Currently, models to predict upper ocean properties, such as temperature and primary productivity, use either shipboard measurements or climatological irradiance levels as input. *In situ* measurements, generally confined to process studies, are sparse while regional and seasonal averages produced from meteorological data collected aboard ships of opportunity are limited in both accuracy and coverage. Radiation fields from combined satellite data promise dramatic improvement in providing surface boundary conditions on global scales for upper ocean models.

### 1.4.2 Solar constant and insolation

The radiation from the Sun received at the top of the Earth's atmosphere on a surface oriented perpendicular to the Sun's rays (at the mean Earth-Sun distance), integrated over all wavelengths (hence total solar irradiance, is called the *solar constant*. It has been shown that the solar constant varies on

time scales from minutes to decades (*Figure 1-4*). The largest variations of up to a few tenths of a percent occurs on time scales from days to several months and are related to the photospheric features of solar activity. Decreases in the irradiance occur during the appearance of sunspots; increases due to bright faculae. The long-term modulation of the solar constant is associated with the well-known 11-year solar activity cycle and with less studied longer-term changes (Foukal, 2003).

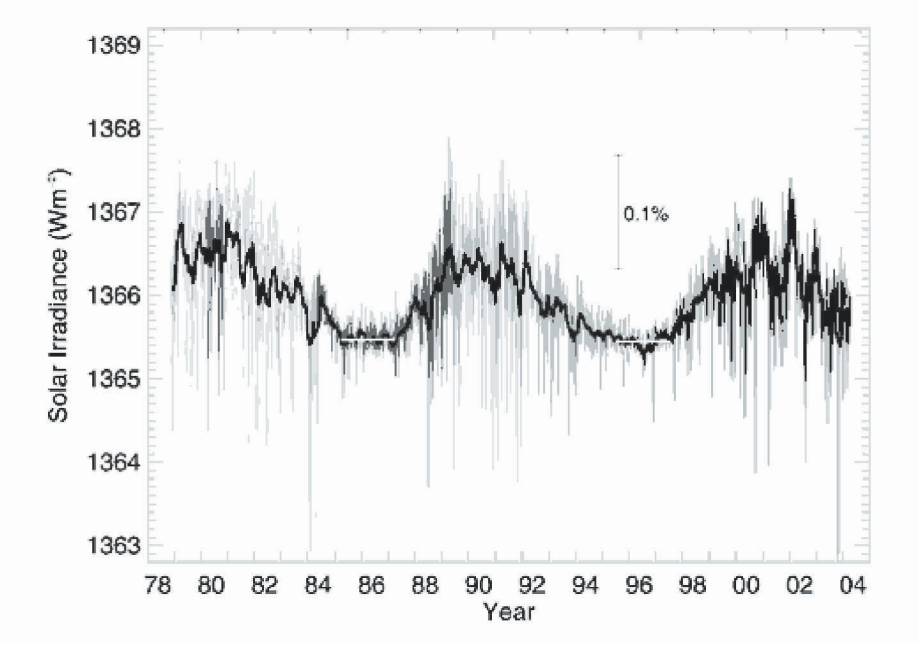


*Figure 1-4.* Composite total solar irradiance at the top of the Earth's atmosphere (solar constant) monitored since 1978 with satellites. (After Fröhlich, 2000.)

The total (spectrally integrated) downwelling solar energy at the ocean surface, $I_\Sigma$, which is also called the surface solar irradiance or *insolation*, substantially depends on the latitude, season, time of day, and optical properties of the earth's atmosphere. While satellites accurately measure the solar constant, the surface solar irradiance is much more difficult to assess. Passing through the earth's atmosphere, the sunlight is absorbed and scattered. Absorption in the atmosphere occurs mainly in the ultraviolet and infrared bands and is weak in the visible band. The ultraviolet part of the solar radiation spectrum is absorbed essentially by ozone. The ozone absorption limits the solar irradiance at sea level to wavelengths greater than 0.29 μm. The infrared part of the solar spectrum is absorbed by $CO_2$ and even more strongly by water vapor.

Molecular scattering by gases in the atmosphere closely follows a *Raleigh law*, obeying a $\lambda^{-4.09}$ relationship, which mainly results from the anisotropy of the air molecules involved in the scattering. The solid particles suspended in the atmosphere scatter the light close to a $\lambda^{-1}$ relationship, while the water droplets in clouds and fog scatter the light with no wavelength dependence. The water droplets, nevertheless, absorb strongly in the infrared part of the solar spectrum.

For the analysis of the solar radiation as a volume source of energy in the near-surface layer of the ocean, it is important to know the surface solar irradiance and its spectral distribution. The magnitude of the solar energy reaching sea level is essentially a function of cloudiness and the thickness of the section of atmosphere penetrated (*i.e.*, of the latitude, month of year, and time of day–the sun's elevation). We first consider the case of clear skies and, then, the more complex problem of skies partially or totally covered by clouds.

### 1.4.3 Insolation under clear skies

The surface solar irradiance $I_{CLR}$ under a clear sky is proportional to $\cos\theta$, where $\theta$ is the zenith angle. This leads to the following formula (Lumb, 1964):

$$I_{CLR} = m_a I_0 \cos\theta, \tag{1.51}$$

where $I_o$ is the solar constant, and $m_a$ is a factor determined by the optical properties of the atmosphere.

The zenith angle is dependent upon geographical latitude $\varphi$, solar declination angle $\delta$, and time of day in the following way:

$$\theta = \cos^{-1}\left[\sin\varphi\sin\delta + \cos\varphi\cos\delta\cos\left(180^o \times \left(t - t_0\right)/t_0\right)\right], \tag{1.52}$$

where time of day $t$ is given in *solar time* as the hour of the day from midnight, and $t_0$= 12 hr. Solar declination angle $\delta$ is defined as a measure of how many degrees North (positive) or South (negative) of the equator the sun is when viewed from the center of the Earth. The solar declination angle,

$$\delta = \varphi_\gamma \cos\left[2\pi\left(t_d - t_\gamma\right)/d_y\right], \tag{1.53}$$

varies from +23.5$^o$ (North) in June to -23.5$^o$ (South) in December. Here: $\varphi_\gamma = 23.45^{0.}$ is the latitude of the Tropic of Cancer; $d$ is the year day,

$t_\gamma = 173$ is the day of the summer solstice, and $d_y = 365.25$ is the average number of days per year.

Factor $m_a$ depends strongly on atmospheric variables. Numerous formulae have been proposed to estimate this factor. Lumb (1964) found from an interpolation of the stationary weather ship data (52°30'N, 20°W) that under virtually clear skies, $m_a \approx a_L + b_L \cos\theta$, where $a_L$ = 0.61 and $b_L$ = 0.2.

More sophisticated algorithms for $m_a$ have since been developed. A relatively simple yet accurate analytical formula to compute surface irradiance and PAR at the ocean surface under clear skies was proposed by Frouin et al. (1989). Their formula represents a parameterization of the more complex radiative transfer model of Tanre et al. (1979) and requires inputs of date, solar zenith angle, visibility, aerosol type, and the vertically integrated concentrations of ozone and water vapor. When compared to the Tanre et al. (1979) model, the Frouin et al. (1989) formulation is accurate to 1-2% for solar zenith angles below 75°.

### 1.4.4 Insolation under cloudy skies

Bishop and Rossow (1991) developed a computationally effective scheme for computing the surface solar irradiance during cloudy conditions. The fast algorithm for surface solar irradiance (FAST) utilizes the solar zenith angle ($\theta$), atmospheric water vapor profile ($H_2O$) and ozone column abundance ($O_3$), the cloud fraction and optical thickness, the visible surface reflectance ($R_S$), the surface type (land, water, coast, ice), and the surface pressure. The main algorithm components are depicted in *Figure 1-5*.

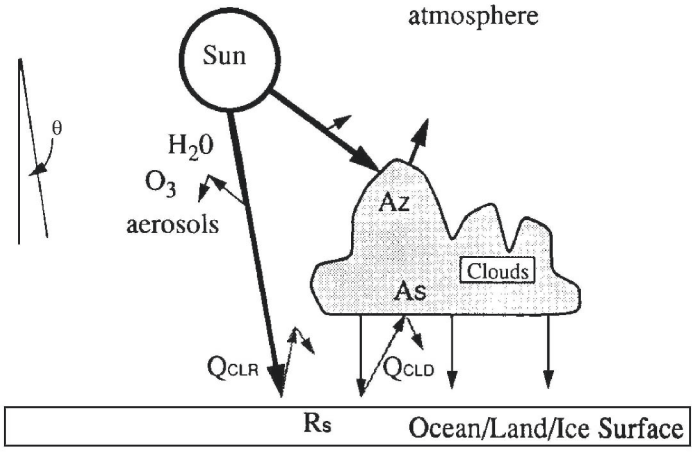


*Figure 1-5*. Schematic representation of the components of the fast scheme for surface solar irradiance. Adapted from Bishop and Rossow (1991) by permission of American Geophysical Union.

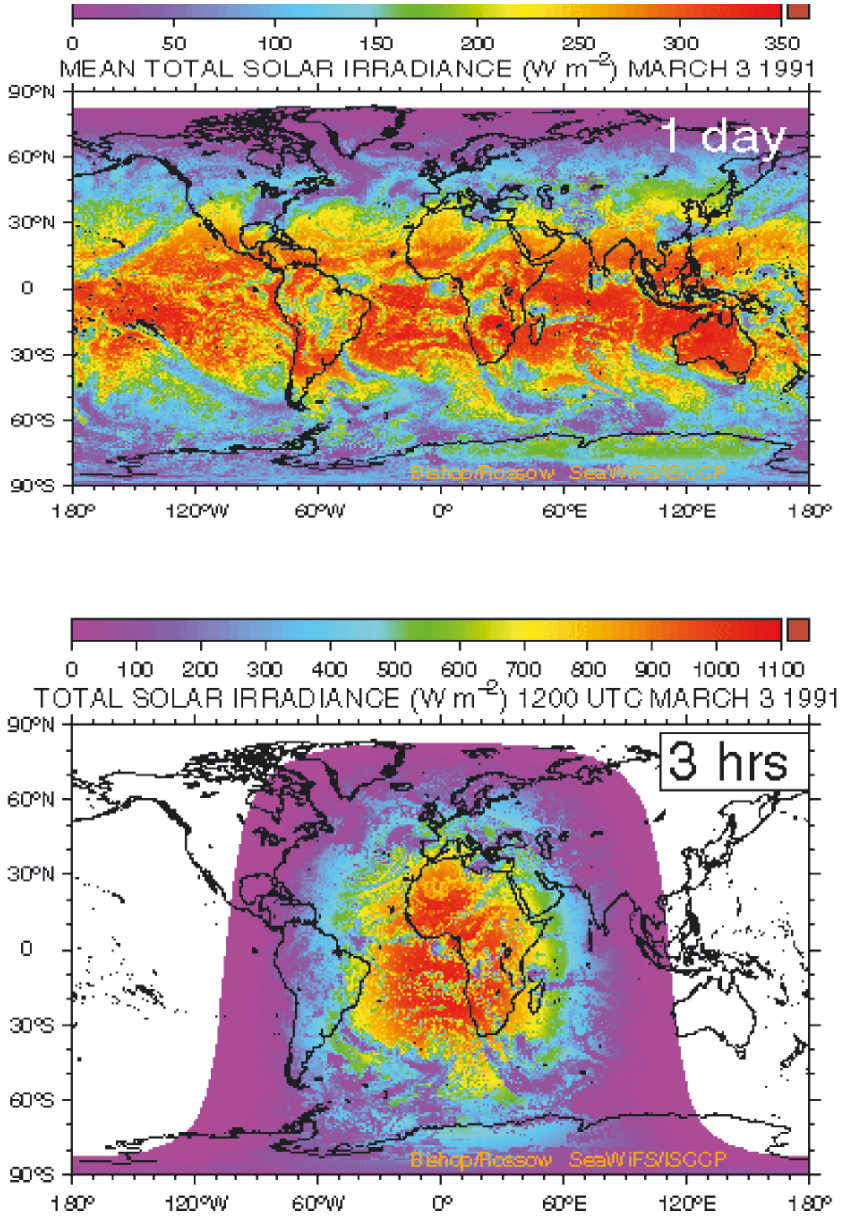


*Figure 1-6*. Example: surface solar irradiance at 3 hourly and daily resolutions from ISCCP (After Bishop et al., 2000. © 2000 NASA.)

The cloudy sky component of the calculation, $Q_{CLD}$, begins with the direct solar energy flux to the cloud top ($Q_{DIR}$), which is $Q_{CLR}$ evaluated with zero surface reflectance and zero cloud fraction. A fraction of that flux is

reflected back to space using a solar zenith angle dependent on cloud albedo $A_Z$. The remaining transmitted fraction exiting the cloud base, not absorbed by the surface (determined by surface reflectance, $R_S$), is reflected upward and is reflected downwards again from the cloud base (determined by spherical cloud albedo, $A_S$).

The International Satellite Cloud Climatology Project (ISCCP) produced global surface solar irradiance fields for several years (beginning in July 1983) using data from a number of satellites. Data were temporally resolved every 3 hours and spatially resolved at $0.5^o \times 0.5^o$ latitude and longitude. The major input data set for the ISCCP contained information about clouds, the atmosphere and the ocean surface at nominal 30 km resolution (4-8 km pixel size, randomly sub-sampled at 30 km resolution) collected every 3 hours from around the globe (Bishop et al., 1997). These data were then used to produce a 0.5 by 0.5 degree gridded product. The ISCCP data were available eight times per day for most of the globe (*Figure 1-6*) but gaps in the dataset were present over regions observed less frequently by polar orbiters rather than geostationary satellites. Validation of this remote sensing approach to collecting radiation data has been done by Waliser et al. (1999) by comparisons between buoy-observed, satellite-derived, and modeled surface shortwave flux over the subtropical North Atlantic for data collected during the Subduction Experiment.

### 1.4.5 Albedo of the sea surface

*Albedo* is the ratio of the amount of electromagnetic radiation reflected by the surface of a body to the amount incident upon it, commonly expressed as a percentage. The albedo of the sea surface is defined as follows (Ivanoff, 1977):

$$A = I_u / I_d = \left(I_r + I_b\right) / I_d \,, \tag{1.54}$$

where $I_d$ is the surface solar irradiance, $I_r$ the solar irradiance reflected from the sea surface, and $I_b$ is that part which is upward back-scattered from below the sea surface. Introducing the reflectance coefficient of the sea surface,

$$R_s = I_r / I_d, \tag{1.55}$$

the definition of albedo (1.54) can be rewritten as follows:

$$A = R_s + I_b / I_d \,, \tag{1.56}$$

while the flux absorbed by the sea is equal to

$$I_d - (I_r + I_b) = I_d (1 - A) \tag{1.57}$$

*Fresnel's formula* can be used for an idealized plane sea surface to calculate the reflectance coefficient, $R_s$, which is independent of absorption and scattering properties of the waters. Curve 1 in *Figure 1-7* corresponds to the idealized case of direct incident solar rays and flat ocean surface; curve 2 includes scattered solar radiation as well (cloudy sky). The reflectance coefficient typically lies in the range of 5 to 7 % for a plane sea surface and an overcast sky, but can exceed 30 % when the sun is low on the horizon of a clear sky.

Cox and Munk (1956) and Saunders (1967a) studied reflectance calculations in more complicated situations including rough seas and low solar elevation. Their results are also shown in *Figure 1-7* (curve 3). Note that the solar elevation $\xi$ and solar zenith angle $\theta$ are related by: $\xi = 90^o - \theta$.

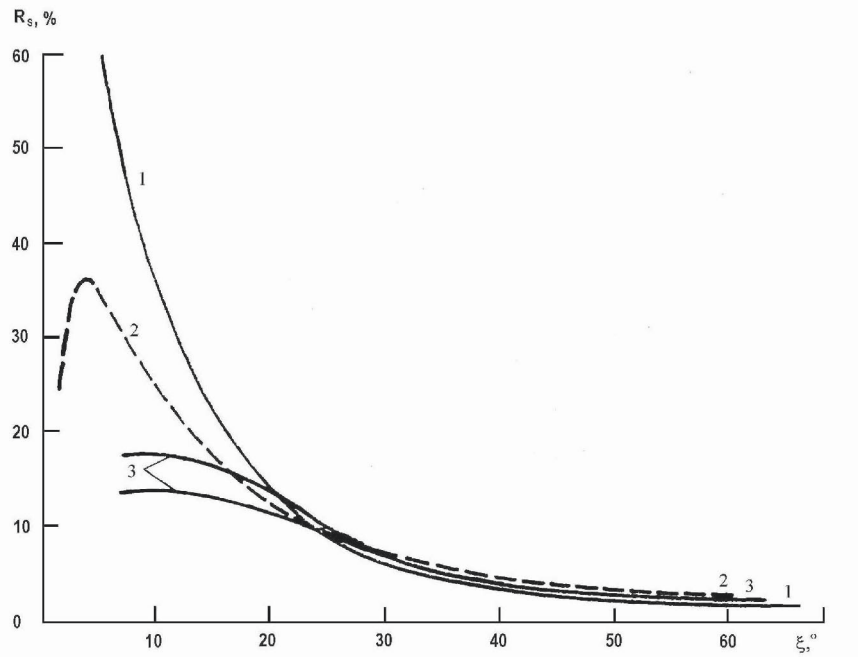


*Figure 1-7*. Reflectance coefficient ($R_s$ in our notation) as a function of the solar elevation $\xi$. Here: curve 1 is the idealized case of direct incident solar rays and flat ocean surface; curve 2 the case of total (direct and scattered) solar rays and flat ocean surface; curves 3 the case of direct solar rays and rough seas. Curves 3 are calculated from the Cox and Munk (1956) data for two different assumptions regarding multiple reflections at low sun elevations. (After Ivanoff, 1977.) Copyright owner could not be found.

For rough seas, the angle of incidence of direct solar rays varies with the slope of the waves. Difficulty again arises when the sun is low on the horizon, giving rise to shadow zones and multiple reflections. For solar elevation greater than about 25° surface roughness slightly increases the ocean surface reflectance. For lower angles, surface roughness results in a sharp reduction of the reflectance (*Figure 1-7*).

The formula for albedo (1.56) contains the ratio of upward to downward irradiance, $I_u/I_d$. Its magnitude and spectral distribution vary considerably as the absorption and scattering properties of the water change. In extremely clear water the spectral ratio of the upward to downward irradiance can reach 10% for $\lambda$ = 0.4 μm wavelength, while in strongly scattering water this ratio can also reach 10% for $\lambda$ between 0.55 to 0.56 μm. Ratio $I_b/I_d$ (remember that $I_u$ and $I_d$ are the integrals over all wavelengths) has a maximum of only 2% (when the water is very clear or strongly scattering) though it does not exceed 0.5% in typical situations. The upwelling light from the sea determines ocean color, which contains useful information about the upper ocean waters. The ocean color can be remotely sensed from satellites (see Section 7.1.6).

Experimental values of the albedo are very close to those shown above for the reflectance. Under clear skies, when solar elevations $\xi$ exceed 20° - 25°, the sea state plays a relatively minor role, the albedo of the sea can be roughly estimated from the Laevastu (1960) formula:

$$A = 300/\xi, \tag{1.58}$$

where $\xi$ is in degrees, and $A$ is in %.
For angles $25^\circ < \xi < 50^\circ$, empirical formula

$$A = 250/\xi \tag{1.59}$$

is more accurate than (1.58).

Payne (1972) parameterized sea surface albedo values from field data as a function of atmospheric transmittance (defined as the ratio of downward irradiance incident at the sea surface to irradiance at the top of the atmosphere) and solar zenith angle. Subsequent field study of Katsaros et al. (1985) and simulation with a radiation model by Ohlmann et al. (2000a) demonstrated good agreement with the Payne et al. (1972) parameterization for solar elevation angles $\xi > 25^\circ$.

For solar elevations $\xi < 25^\circ$, the values obtained by different authors, however, differ greatly as a result of the strong influence of the sea state. This presents a serious problem when calculating the rate of solar energy absorption by the ocean in latitudes higher than 50° or 60°. For these

latitudes, according to Payne (1972), mean values of albedo can be as high as 44%, while Budyko (1963) suggested values that do not exceed 23%.

The radiative models considered above treat radiative transfer in the atmosphere and ocean separately, often by regarding one medium as a boundary condition for the other. Coupled atmosphere-ocean radiative transfer models treat absorption and scattering by layers for both the atmosphere and the ocean explicitly and consistently. Such models are capable of more accurately calculating radiative flux and albedo over the ocean surface based on the optical properties of the atmosphere and ocean (Jin et al., 2002). The key input parameters in the Jin et al. (2002) model are aerosol optical depth, surface wind speed, and total precipitation water from *in situ* measurements. According to the results of the field test shown in *Figure 1-8*, the mean model-observation differences for the ocean surface albedo are generally less than 1%. Sensitivity tests conducted by Jin et al. (2002) indicate that the incorporation of scattering effects by air bubbles and/or suspended material into the algorithms has the potential to further reduce the model-observation differences in the ocean surface albedo.

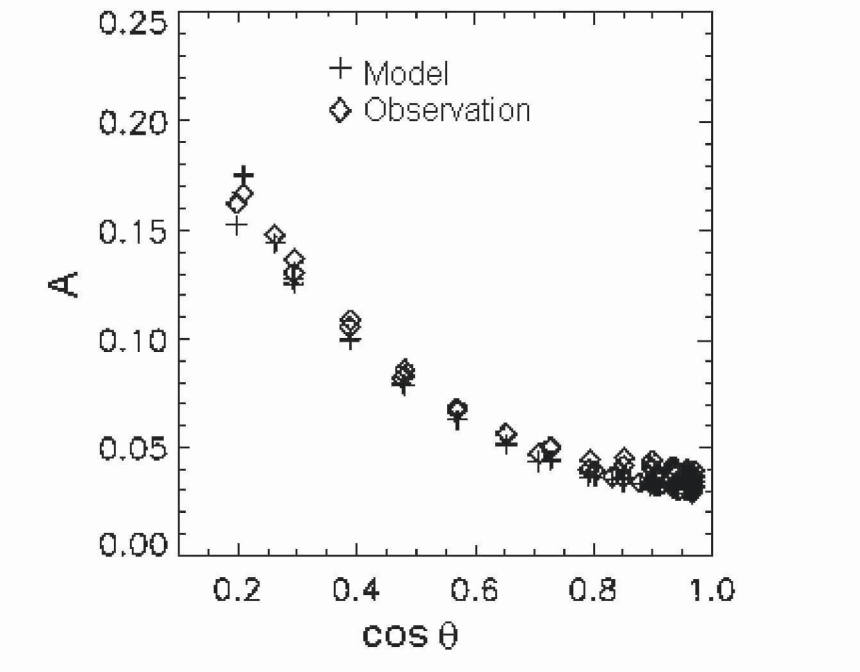


*Figure 1-8*. Model-observation comparison for the sea surface albedo $A$ as a function of solar zenith angle $\theta$ at a site 25 km east of Virginia in the Atlantic Ocean for 3 months from June to August 2000. The mean difference between model and observations is 0.44%; standard deviation is 0.34%. Adapted from Jin et al. (2002) by permission of American Meteorological Society.

### 1.4.6 Attenuation of solar radiation in the ocean

Similar to moist air, the attenuation of solar radiation in seawater involves both absorption and scattering. The absorption consists mainly of a conversion from radiant energy to heat, with some of the absorbed radiant energy being involved in chemical reactions such as photosynthesis. In reality, the portion of solar energy penetrating into the oceans and involved in photosynthesis is usually only of order 0.1%. The scattering of solar radiation consists of changes in the direction of photons without losing energy. This process increases the path length of photons between the sea surface and the depth under consideration. As a result, scattering leads to increased absorption and an additional energy loss.

An optical property that is often used in models of light penetration is the diffusive attenuation coefficient for downwelling irradiance, or $K_d$, which defines the rate of decrease of downwelling irradiance with depth:

$$K_d(\lambda) = -\frac{1}{E_d(\lambda, z)} \frac{dE_d(\lambda, z)}{dz}, \tag{1.60}$$

It is one of the important geophysical variables that can in principle be derived from ocean-color data (see Section 7.1.6).

Following the classification of Preisendorfer (1976), the diffusive attenuation coefficient defined with (1.60) is an *apparent optical property*, because it can be modified both by the nature and quantity of substances present in the medium and by the zenith-angular structure of the incident light field. At the same time *inherent optical properties*, according to Preisendorfer's classification, are the properties that are independent of variations in the angular distribution of the incident light field, and solely depend on the type and concentration of substances present in the medium.

The attenuation coefficient (including both absorption and scattering) is defined for the idealized conditions of collimated, monochromatic flux incident normally on the water, and traversing an infinitesimally thin layer of the water. Absorption is caused by the water itself, by dissolved salts, organic substances in solutions and by suspended matter. The absorption coefficient for pure water increases rapidly towards long wavelengths and exceeds 2.3 $m^{-1}$ for wavelengths greater than 0.8 μm. The absorption coefficient value in the ultraviolet is less well known than for the visible spectrum.

Scattering is partially due to molecules of water and substances in solution, but mainly results from suspended matter. Scattering becomes less important compared to absorption as absorption increases towards longer

wavelengths, eventually becoming negligible at wavelengths greater than 0.7-0.8 μm.

Investigation of the progressive attenuation of daylight with depth must simultaneously take into account the inherent properties of the water (absorbing and scattering) and the angular and the spectral distributions of light incident on the sea surface. Numerous experimental and theoretical studies have been carried out with these aims especially in relation to the remote sensing of the ocean color (see Section 7.1.6). Here, we will limit the following discussion to an analysis of the solar energy absorption as a function of depth, for this is the term entering the equation for heat conservation.

*Table 1-1*. Absorption of solar radiation in the top 1 m below the water surface.

| Depth, m | Absorbed part of total solar radiation, % | |
|---|---|---|
| | Bethoux (1968) | Pruvost (1972) |
| 0.01 | 17 | 13 |
| 0.1 | 35 | 31 |
| 0.2 | 41 | 41 |
| 0.5 | ~50 | - |
| 1 | - | 56.5-65 |

The attenuation of solar radiation with depth appears to follow a more or less exponential form depending on the wavelength or spectral band. Absorption of solar radiation in the top meter of the ocean (integrated over wavelength), according to measurements of Bethoux (1968) and calculations of Pruvost (1972), is given in *Table 1-1*. This data indicates that solar radiation is absorbed very unevenly in the upper ocean.

The absorption and scattering of light for wavelengths exceeding 0.7-0.8 μm mainly determine the transmission of solar radiation within the upper meter of the ocean. Chlorophyll, organic substances, or suspended matter do not affect the inherent optical properties of the oceanic water for these wavelengths. According to the radiative transfer model of Ohlmann et al (2000a) a tenfold increase in chlorophyll concentration results in less than 1% change in solar transmission for the upper ten centimeters of the ocean (*Figure 1-9*).

For depths greater than 1 m, with a greater portion of the irradiance in the visible spectral region (i.e., for less than 0.7-0.8 μm wavelength), the dependence of solar irradiance on the inherent optical properties of the water is more evident. Respectively, Jerlov (1976) proposed an optical classification of oceanic surface waters by distinguishing three major water types: I, II, and III and later adding two intermediate types: IA and IB and

coastal turbidity types: 1, 3, 5, 7, 9. (In the open ocean chlorophyll concentration mainly determines inherent optical properties of for $\lambda < 0.7 \mu m$).

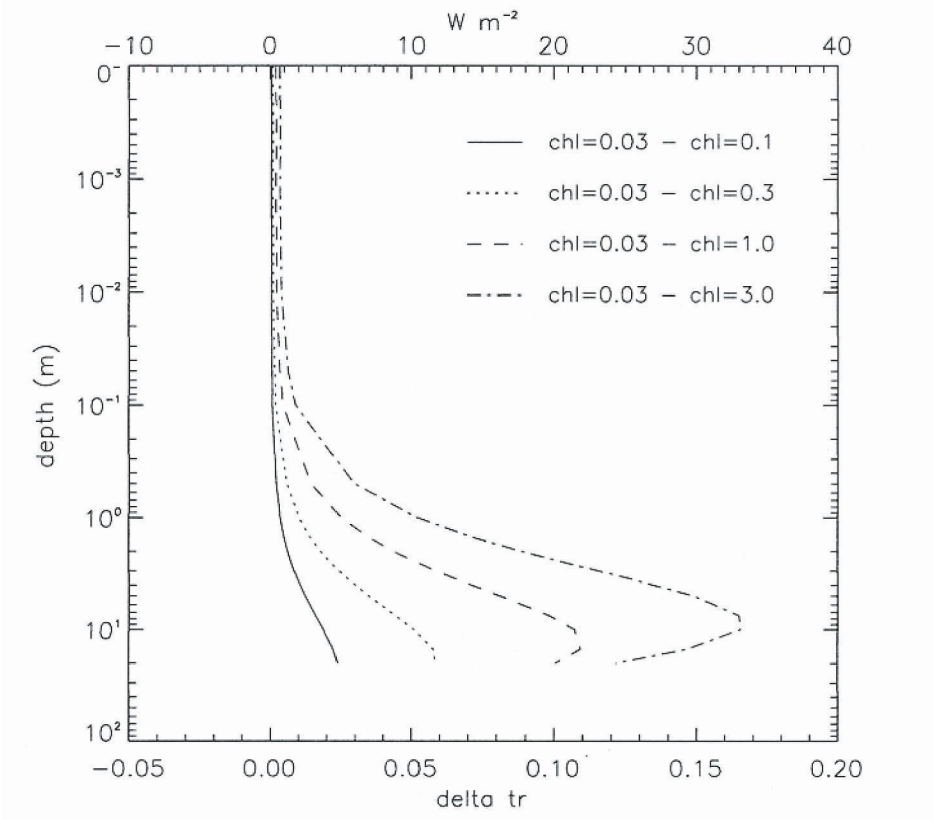


*Figure 1-9*. Solar transmission differences between the base case (chl = 0.03 mg $m^{-3}$, $\theta = 0°$, clear skies) and cases of increased chlorophyll concentration (chl = 0.1, 0.3, 1.0, 3.0 mg $m^{-3}$). Reproduced from Ohlmann et al. (2000a) by permission of American Meteorological Society.

The absorption of solar radiation in the ocean can be expressed in the following way:

$$I_R(z) = (1 - A) I_\Sigma f_R(z), \tag{1.61}$$

where $I_\Sigma$ is the surface solar irradiance (spectrally integrated), and function $f_R(z)$ characterizes the absorption of solar radiation with depth. Paulson and Simpson (1981) parameterized $f_R$ s a sum of nine exponentials:

$$f_R(z) = \sum_{i=1}^{9} a_i \exp(\alpha_i z), \tag{1.62}$$

where $a_i$ are the weights corresponding to the spectrally distributed absorption coefficients $\alpha_i$. The absorption coefficients in this parameterization were determined for pure water only based on measurements of Schmidt (1908). The more recent determination of the absorption coefficients in clear water by Pope and Fry (1997) produced similar results.

*Table 1-2*. Irradiance absorption coefficients $\alpha_i$ and spectral weighting coefficients $a_i$ according to Paulson and Simpson (1981) and the modification of coefficient $\alpha_1$ proposed by Soloviev and Schlüssel (1996), based on Jerlov's water-type classification.

| Wavelength (μm) | | | i | | $a_i$ | | | $\alpha_i$ ($m^{-1}$) | | |
|---|---|---|---|---|---|---|---|---|---|---|
| 0.2 - 0.6 | | | 1 | | 0.2370 | | | $2.874 \times 10^{-2}$ | | |
| 0.6 - 0.9 | | | 2 | | 0.3600 | | | $4.405 \times 10^{-1}$ | | |
| 0.9 - 1.2 | | | 3 | | 0.1790 | | | $3.175 \times 10^{1}$ | | |
| 1.2 - 1.5 | | | 4 | | 0.0870 | | | $1.825 \times 10^{2}$ | | |
| 1.5 – 1.8 | | | 5 | | 0.0800 | | | $1.201 \times 10^{3}$ | | |
| 1.8 – 2.1 | | | 6 | | 0.0246 | | | $7.937 \times 10^{3}$ | | |
| 2.1 – 2.4 | | | 7 | | 0.0250 | | | $3.195 \times 10^{3}$ | | |
| 2.4 – 2.7 | | | 8 | | 0.0070 | | | $1.279 \times 10^{4}$ | | |
| 2.7 – 3.0 | | | 9 | | 0.0004 | | | $6.944 \times 10^{4}$ | | |
| Water type | I | IA | IB | II | III | 1 | 3 | 5 | 7 | 9 |
| $\alpha_1$ ($m^{-1}$) | 0.066 | 0.076 | 0.088 | 0.132 | 0.382 | 0.49 | 0.70 | 1.00 | 1.09 | 1.60 |

To extend the calculations to real ocean water, Soloviev and Schlüssel (1996) proposed a small modification of the Paulson and Simpson (1981) parameterization. For wavelengths smaller than 0.6 μm, the absorption is strongly modified by phytoplankton, suspended inorganic matter, and yellow substance (Jerlov, 1976). These substances are not important at longer wavelengths because of a strong decrease of their absorption coefficients with wavelength. Therefore, taking Jerlov (1976) into account, Soloviev and Schlüssel (1996) replaced the absorption coefficient for the spectral band 0.2 to 0.6 μm by average values calculated from narrow-band spectral values for different types of water representing varying oceanic (types I, IA, IB, II, and III) and coastal turbidity (types 1, 3, 5, 7, 9). Furthermore, they excluded the spectral range below 0.31 μm because of the strong absorption by atmospheric ozone. The absorption coefficients from Soloviev and Schlüssel (1996) are listed in *Table 1-2*. Verevochkin and Startsev (2005)

have proposed to separate the spectral band 0.2 to 0.6 μm into two subranges, which provides a better approximation of the solar radiation absorption for the different types of oceanic water. This improvement, however, has only marginal effect for the upper meters of the ocean.

Formulation (1.61)-(1.62) provides a convenient description for the volume source $\partial I_R / \partial z$ in equation (1.10). Dependence of the incident solar radiation in the infrared range on the water vapor content (Ivanoff, 1977) may, however, affect values of the weight coefficients $a_3$ - $a_9$ in *Table 1-2*.

## 1.5 Rain Forcing

### 1.5.1 Dynamics of rain drops at the air-sea interface

Raindrops falling on to the sea surface behave differently depending on their size and impact velocity and they represent both a surface and a volume source of freshwater (Schlüssel et al., 1997). Drops of rain typically reach the sea surface at their terminal velocities, the vertical velocity when the gravitational force equals the drag force. Small droplets with a low impact velocity cannot break the surface and thereby accumulate freshwater on top of the sea surface. Heavier drops with higher vertical velocities can coalesce into the sea surface with little or no splashing and generate a vortex ring that penetrates downward into the ocean (Katsaros and Buettner, 1969; Rodrigues and Mesler, 1988; Hsiao et al., 1988). Alternatively, they repel or splash with the formation of a Rayleigh jet (which is the jet-like column of fluid at the sea surface). The occurrence of the Rayleigh jet depends on the Weber number

$$We = w_i \left( \rho_r D / \sigma_s \right)^{1/2}, \tag{1.63}$$

where $D$ is the drop diameter, $w_i$ is the impact (terminal) velocity, $\rho_r$ the density of the drop, and $\sigma_s$ the surface tension.

For small Weber numbers the drop entering the ocean directly penetrates downward without any prominent splash or jet production. For larger Weber numbers a jet is produced and the vortex formation is deferred until a secondary drop breaking off the tip of the jet column makes its way into the ocean. There is a critical Weber number $We_{cr}$ at which the transition from the direct coalescence to the production of a jet and/or splash takes place; according to Hsiao et al. (1988), $We_{cr} \approx 8$. Rodriguez and Mesler (1988) found that the submergence of large primary drops into the water is rather low due to their high impact velocities, in contrast to secondary ones that

break off the Rayleigh-jet column and enter the ocean at lower velocities allowing them to penetrate to deeper levels.

Remarkably, the formation of vortex rings is associated with drop oscillations. The best coalescence of an oscillating drop with the ocean occurs when the drop is spherical and changing from an oblate to a prolate spheroid at the moment of contact with the surface (Chapman and Critchlow, 1967).

Natural rain is an ensemble of raindrops. The penetration depth of primary and secondary drops depends not only on the behavior of single events, as mostly analyzed in laboratory studies, but is also governed by the interaction of raindrops with the vortex rings and surface waves generated by them. For natural rain, Maxworthy (1972) concluded that the depth $z_p$ reached by the vortex rings is proportional to the initial drop radius $r_0$. The constant of proportionality is large ($a_1 = z_p / r_0 \approx 300$) for single drops but decreases to $a \approx 100$ for a drop ensemble (Manton, 1973).

The kinetic energy of a falling drop entering the ocean is large compared with the potential energy reached at $z_p$; respectively, the buoyancy effects on the penetration depth can be ignored. The freshwater flux due to rain decreases the near-surface salinity and, thereby, further (though only slightly) reduces the buoyancy effect on the submerging drops.

### 1.5.2 Surface flux of freshwater due to rain

The total volume of the rainwater is

$$V_0 = V_u \int_0^\infty \frac{4}{3}\pi r_0^3 n(r_0)\, dr_0, \tag{1.64}$$

where $V_u = 1\,\mathrm{m}^3$ is the unit volume included by Schlüssel et al. (1997) for dimensional correctness of the equation, and $n(r_0)$ is the raindrop distribution expressed in the number of drops per (volume) unit of air per equivalent drop radius. The dimension of $n(r_0)$ is $\mathrm{m}^{-3}\mathrm{m}^{-1}$, and is commonly described by the Marshall-Palmer distribution (Marshall and Palmer, 1948)

$$n(r_0) = \frac{dN}{dr_0} = n_0 \exp(-2\Lambda r_0), \tag{1.65}$$

where $n_0 = 8\times10^6$ $\mathrm{m^{-3}m^{-1}}$ and $\Lambda = 4.1\times10^3\left(3.6\times10^6 P\right)^{-0.21}$ (in $\mathrm{m^{-1}}$) are parameters describing the distribution, $P$ is the rain rate (in m $\mathrm{s^{-1}}$), and $N$ is the particle density (in $\mathrm{m^{-3}}$).

Natural rain can exhibit more complicated drop size distributions (Ulbrich, 1983). In particular, (1.65) does not capture "instantaneous" raindrop size distributions. Remote sensing of reflectivity and attenuation with the dual-wavelength radar technique, or the reflectivities at horizontal and vertical polarization with the polarimetric radar, opens new opportunities in the measurement of rain parameters (Zhang et al., 2003). At this point the use of the Marshall-Palmer dependence is "justified" only by the fact that the rainrate has nearly always been the only rain parameter measured.

From (1.64) and (1.65), the total volume of rainwater is

$$V_0 = V_u \frac{4}{3}\pi n_0 \int_0^\infty r_0^3 \exp\left(-2\Lambda r_0\right) dr_0 = V_u \frac{\pi n_0}{2\Lambda^4}. \tag{1.66}$$

Surface tension prevents drops with smaller than critical radius $r_c$ from entering the water body, since they do not have sufficient energy to overcome the surface tension. These drops stay on the sea surface and lead to a surface flux rather than a volume flux. The critical radius below which raindrops do not penetrate the ocean surface has been observed to be $r_c$ = 0.4 mm by Oguz and Prosperetti (1991) and about $r_c$ = 0.75 mm by Green and Houk (1979). The latter result was obtained in a laboratory experiment at rather low impact velocities, however.

The volume of freshwater that does not submerge but stays at the surface is determined as follows:

$$V_s = V_u \int_0^{r_c} \frac{4}{3}\pi n_0 r_0^3 \exp\left(-2\Lambda r_0\right) dr_0 = V_0 \frac{8\Lambda^4}{3} \int_0^{r_c} r_0^3 \exp\left(-2\Lambda r_0\right) dr_0 . \tag{1.67}$$

Schlüssel et al. (1997) obtained the following solution to (1.67):

$$V_s = V_0 \left[1 - \left(1 + 2\Lambda r_c + \frac{4\Lambda^2 r_c^2}{2} + \frac{8\Lambda^3 r_c^3}{6}\right)\exp\left(-2\Lambda r_c\right)\right]. \tag{1.68}$$

The volume of freshwater due to rain submerging into the ocean is:

$$V_p = V_0 - V_s = V_0\left(1 + 2\Lambda r_c + 2\Lambda^2 r_c^2 + \frac{4}{3}\Lambda^3 r_c^3\right)\exp\left(-2\Lambda r_c\right). \qquad (1.69)$$

*Figure 1-10* shows dependence (1.69) for two critical radii

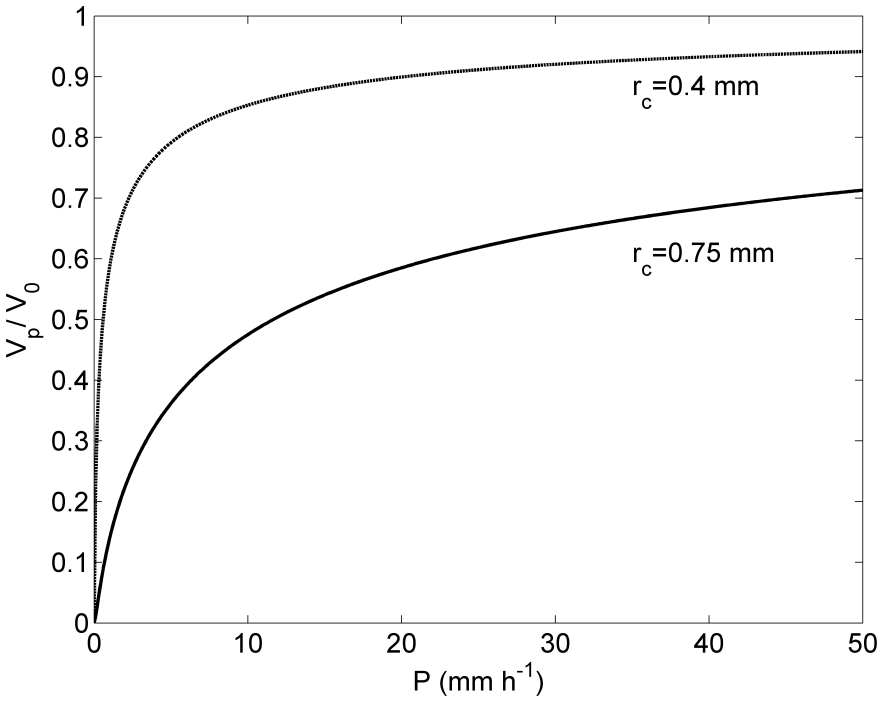


*Figure 1-10.* Volume fraction of rain that submerges into the ocean as function of rainrate for critical radii of $r_c$ = 0.4 mm and $r_c$ = 0.75 mm.

### 1.5.3 Volume source of freshwater due to rain

Following Schlüssel et al. (1997), we assume that the volume of a drop decays exponentially with depth, which results in the following parametric dependence:

$$V_r(z) = V_0 \exp\left(\frac{z}{ar_0}\right), \quad z < 0, \qquad (1.70)$$

where is $V_0$ the initial volume of the drop. Respectively, the drop radius $r$ changes with depth as follows:

$$r^3(z) = r_0^3 \exp\left(\frac{z}{ar_0}\right) \text{ or } r(z) = r_0 \exp\left(\frac{z}{3ar_0}\right). \tag{1.71}$$

The drop-size distribution at depth $z$ changes according to

$$n_z(r) = \frac{\partial N}{\partial r} = \frac{\partial N}{\partial r_0}\frac{\partial r_0}{\partial r}, \tag{1.72}$$

which, with (1.71) and (1.65), leads to

$$n_z(r) = n_0 \exp\left(-2\Lambda r_0 + \frac{z}{3ar_0}\right) \Big/ \left(1 - \frac{z}{3ar_0}\right). \tag{1.73}$$

The freshwater volume at depth $z$ is given by integral

$$V(z) = V_u \int_{r_c}^{\infty} \frac{4}{3}\pi r^3 n_z(r)\, dr. \tag{1.74}$$

Substituting (1.71) and

$$dr = \exp\left(\frac{z}{3ar_0}\right)\left(1 - \frac{z}{3ar_0}\right) dr_0 \tag{1.75}$$

into (1.74) results in the following integral:

$$V(z) = \frac{8\Lambda^4}{3} V_0 \int_{r_c}^{\infty} r_0^3 \exp\left(\frac{z}{ar_0} - 2\Lambda r_0\right) dr_0, \tag{1.76}$$

which is equivalent to

$$V(z) = \frac{8\Lambda^4}{3} V_0 \left[\int_0^{\infty} r_0^3 \exp\left(\frac{z}{ar_0} - 2\Lambda r_0\right) dr_0 - \int_0^{r_c} r_0^3 \exp\left(\frac{z}{ar_0} - 2\Lambda r_0\right) dr_0\right]. \tag{1.77}$$

With the first integral on the right side of (1.77) expressed via the MacDonald function (or modified Bessel function) $K_4$ (see Gradshtein and Ryzhik, 2000), the source function for penetrating rain in the near-surface

layer of the ocean due to penetrating raindrops can be represented as follows:

$$V(z) = V_0 f_V(z), \tag{1.78}$$

where

$$f_V(z) = \frac{4}{3}\frac{\Lambda^2 z^2}{a_r^{\,2}} K_4\left(\sqrt{-\frac{8\Lambda z}{a_r}}\right) - \frac{8\Lambda^4}{3}\int_0^{r_c} r_0^3 \exp\left(\frac{z}{a_r r_0} - 2\Lambda r_0\right) dr_0 . \tag{1.79}$$

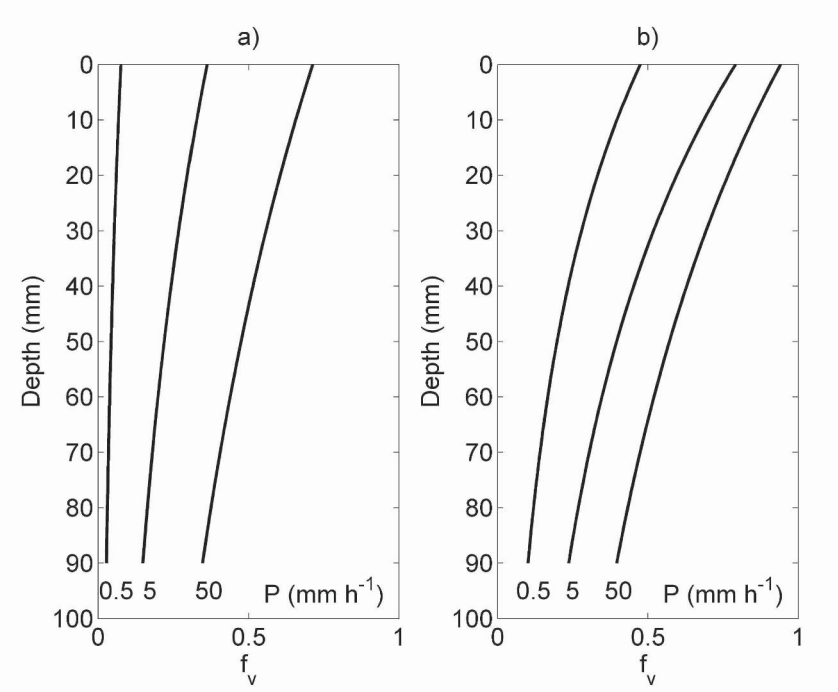


*Figure 1-11*. Decay function of the freshwater volume in the upper ocean due to rain $f_v$ for two critical droplet radii: (a) $r_c$ = 0.75 mm and (b) $r_c$ = 0.4 mm. The rainrate $P$ is given below each curve.

*Figure 1-11* shows dependence (1.79) as a function of depth for a number of rainrates and for two critical radii, $r_c$ = 0.75 mm and $r_c$ = 0.4 mm. The ratio between penetration depth and drop radius is taken as $a_1 = z_p / r_0 = 100$.

### 1.5.4 Rain-induced heat flux

Since the surface volume flux density is the surface rainrate, $P = d^2V_0 / dA_s dt$ , the heat flux related to rain is defined as follows:

$$Q_{rV} = \frac{d^2V_r}{dA_s dt} c_{pr}\rho_r \left(T_w - T_r\right), \tag{1.80}$$

where $A_s$ is the area, and $t$ is the time, $c_{pr}$ is the specific heat, and $\rho_r$ is the density of rain water, $T_r$ is the raindrop temperature, $T_w$ is the temperature of the upper ocean (which is a function of depth in the general case).

The heat flux density produced by drops not submerging into the ocean is then determined from (1.68), and (1.80) as follows:

$$\begin{aligned} &Q_{rs} = Pc_{pr}\rho_r \left(T_0 - T_r\right)\left[1 - f_V\left(0\right)\right] = \\ &Pc_{pr}\rho_r \left(T_0 - T_r\right)\left[1 - \left(1 + 2\Lambda r_c + \frac{4\Lambda^2 r_c^2}{2} + \frac{8\Lambda^3 r_c^3}{6}\right)\exp\left(-2\Lambda r_c\right)\right] \end{aligned} \tag{1.81}$$

where $T_0$ is the sea surface temperature. This surface heat flux enters boundary condition (1.26).

The heat flux related to the freshwater volume flux following from (1.78) and (1.80) is:

$$Q_{rV}\left(z\right) = Pc_{pr}\rho_r \left(T_w - T_r\right) f_V\left(z\right), \tag{1.82}$$

where decay function $f_V\left(z\right)$ is determined by (1.79). Formula (1.82) provides a parameterization for the volume source due to rain, $\partial Q_{rv} / \partial z$ , entering equation (1.10).

### 1.5.5 Surface stress due to rain

Wind accelerates the raindrops horizontally as they fall. The horizontal momentum acquired by the drops on their way from clouds to the ocean surface is released in the near-surface layer of the ocean producing tangential stress. Caldwell and Elliott (1971) parameterized this additional stress in the following way (ignoring the effect of raindrops penetrating the sea surface):

$$\tau_r = \gamma\rho_r U_{10} P \tag{1.83}$$

where $U_{10}$ is the wind speed at 10 m, and $\gamma$ is an empirically determined factor that varies between 0.8 and 0.9 in most cases except for situations where only very small drops are involved, and $P$ is the rain rate given by the volume rate of water accumulation per unit surface area.

For heavy rainfall, raindrops may provide an appreciable contribution to the momentum flux at the air-sea interface. In addition to raindrops, the contribution of sea-spray droplets to the momentum flux may become significant for hurricane force winds (Chapter 6).

Similar to (1.82), the rain-induced momentum flux can be decomposed into the surface $\tau_{rs}$ and volume $\tau_{rv}$ components as follows:

$$\tau_{rv} = \gamma \rho_r U_{10} P f_V(z), \tag{1.84}$$

and

$$\tau_{rs} = \gamma \rho_r U_{10} P\left[1 - f_V(0)\right] = \gamma \rho_r U_{10} P\left[1 - \left(1 + 2\Lambda r_c + \frac{4\Lambda^2 r_c^2}{2} + \frac{8\Lambda^3 r_c^3}{6}\right)\exp\left(-2\Lambda r_c\right)\right] \tag{1.85}$$

## 1.6 Surface Waves

The theory of surface gravity waves is one of the oldest areas of hydrodynamics. In particular, wave motion was one of the first subjects to which classical potential theory was applied. There is extensive literature covering various aspects of this phenomenon (cf. Phillips, 1977 and LeBlond and Mysak, 1977 for review). The aim of this section is to describe the main properties of surface waves important for understanding the near-surface processes.

### 1.6.1 Potential approximation

Surface gravity wave motion is a large Rossby number problem. According to (1.16), for typical wave orbital velocity $u_l$=1 m s$^{-1}$, wavelength $\lambda$ = 100 m, and Coriolis parameter $f$ = 10$^{-4}$ s$^{-1}$, the Rossby number estimate is $Ro = 10^2 >> 1$. Vertical velocity components are comparable to the horizontal velocity components, invalidating the boundary layer approximation (1.6)-(1.9).

In the application to surface waves, the equations of hydrodynamics (1.1)-(1.3), and (1.4) can be written as follows:

$$\frac{\partial u}{\partial t}+u\frac{\partial u}{\partial x}+w\frac{\partial u}{\partial z}=-\frac{1}{\rho}\frac{\partial p}{\partial x}, \tag{1.86}$$

$$\frac{\partial w}{\partial t}+u\frac{\partial w}{\partial x}+w\frac{\partial w}{\partial z}=-\frac{1}{\rho}\frac{\partial \rho}{\partial z}-g, \tag{1.87}$$

$$\frac{\partial u}{\partial x}+\frac{\partial w}{\partial z}=0. \tag{1.88}$$

The presence of advective and acceleration terms on the left side of (1.87) means that the flow is not hydrostatically constrained.

In addition to large Rossby number approximation (neglecting Coriolis terms), flow in equations (1.86)-(1.87) is specified as two-dimensional, since short ocean waves are nearly two-dimensional and the *x*, *z* coordinate system can be aligned to correspond to the direction of propagation. Therefore, all derivatives with respect to *y* and the velocity component *v* are zero. The density is constant and viscous terms are neglected (ocean waves dissipate weakly).

Differentiating (1.86) with respect to *z*, and (1.87) with respect to *x*, and finally subtracting the second result from the first one eliminates the pressure. This results in

$$\frac{D\omega_y}{Dt}=0, \tag{1.89}$$

where $\omega_y=\frac{\partial u}{\partial z}-\frac{\partial w}{\partial x}$ is the vorticity component in the *x*, *z* plane. If at some initial time all the velocity fields are zero, $\omega_y$ is initially zero and according to (1.89)

$$\omega_y=\frac{\partial u}{\partial z}-\frac{\partial w}{\partial x}=0 \tag{1.90}$$

for all time thereafter. Therefore, equations (1.86) and (1.87) can be replaced by the much simpler equation (1.90). Together with equation(1.88), we have two equations with two unknowns, *u* and *w*. It is then possible to reduce these to one equation for a potential function

$$u = \frac{\partial \phi}{\partial x}, \quad w = \frac{\partial \phi}{\partial z}, \tag{1.91}$$

satisfying (1.90).

When dealing with a free surface boundary condition, use of the potential function is more convenient. By stipulating (1.91) and inserting the expression into (1.88) we obtain Laplace's equation

$$\frac{\partial^2 \phi}{\partial x^2} + \frac{\partial^2 \phi}{\partial z^2} = 0 . \tag{1.92}$$

Equation (1.92) is useful if solving for flows bounded by solid surfaces. For example, if $n$ is a local coordinate normal to the solid surface and the velocity normal to the solid surface is zero, $\partial \phi / \partial n$ will also be equal to zero. Since the bottom is a solid surface and we have excluded viscous terms, $\omega = \partial \phi / \partial z = 0$ at the bottom.

Since the free surface is exposed to the atmosphere, the dynamic free-surface condition is imposed by the requirement that the difference of pressure on two sides of the interface,

$$\Delta p = p - p_0 , \tag{1.93}$$

is balanced by the effect of surface tension. For constant atmospheric pressure $p_0$, the boundary condition at $z = \eta$ is then derived from (1.86)-(1.87) in the form of Bernoulli's equation (see, for example, Debnath, 1994):

$$\begin{aligned} &\phi_t (x,\eta,t) + \frac{1}{2}\left[ \phi_x (x,\eta,t)^2 + \phi_z (x,\eta,t)^2 \right] + \\ &g\eta(x,t) = \frac{\sigma_s}{\rho} \eta_{xx} (x,t) \end{aligned} \tag{1.94}$$

where $\sigma_s$ is the surface tension ($\sigma_s \approx 7 \times 10^{-2}$ N m$^{-1}$ for seawater).

Note that for compactness, a subscript notation has been adopted here such that, for example, $\phi_x \equiv \partial \phi / \partial x$. Equation (1.92) then becomes

$$\phi_{xx} + \phi_{zz} = 0 . \tag{1.95}$$

Equation (1.94) is the *dynamic boundary condition*; it relates the surface elevation to the velocity field through the velocity potential $\phi$. A second surface boundary condition is the *kinematic boundary condition*:

$$\phi_z(x,\eta,t) = \phi_x(x,\eta,t)\eta_t(x,t) + \eta_t(x,t). \tag{1.96}$$

At the bottom, $z = -h_b$, the kinematic bottom boundary condition is as follows:

$$\phi_z(x,-h_b,t) = 0. \tag{1.97}$$

Equations (1.94) to (1.97) complete the formulation for irrotational gravity waves, except for stipulating initial and lateral boundary conditions.

### 1.6.2 Linear waves

Equations for the linear problem are difficult to solve since surface boundary conditions given by (1.94) and (1.96) are nonlinear. In classical wave theory, the amplitude is assumed to be small when compared to the wavelength. Boundary conditions (1.94) and (1.96) are replaced with their linear approximations as follows:

$$\phi(x,0,t) + g\eta(x,t) = \sigma_s \rho^{-1} \eta_{xx}, \tag{1.98}$$

$$\phi_z(x,0,t) = \eta_t(x,t). \tag{1.99}$$

For an elementary solution of this system in the form of plane harmonic waves,

$$\eta = a\cos\left(\vec{k}\cdot\vec{x} - \omega t\right), \tag{1.100}$$

the velocity potential is as follows

$$\phi = \frac{\omega a \cosh k\left(z + h_b\right)}{k \sinh kh_b} \sin\left(\vec{k}\cdot\vec{x} - \omega t\right). \tag{1.101}$$

The frequency $\omega$ and modulus $k$ of the two-dimensional wavenumber vector are related to each other via the dispersion relationship

$$\omega(k) = \left[\left(gk + \sigma_s k^3/\rho\right)\tanh kh_b\right]^{1/2}. \tag{1.102}$$

For deep-water waves, $kh_b >> 1$, and expression (1.101) reduces to

$$\phi = k^{-1} a\omega \exp(kz) \sin\left(\vec{k} \cdot \vec{x} - \omega t\right), \tag{1.103}$$

with dispersion relationship

$$\omega(k) = \left(gk + \sigma_s k^3 / \rho\right)^{1/2}. \tag{1.104}$$

For very short surface waves, where $\sigma_s k^2 >> \rho g$, gravity becomes negligible compared to surface tension; waves of this type are known as *capillary waves*. On the other hand, when $\sigma_s k^2 << \rho g$, surface tension is negligible and the dynamics are dominated by gravity.

The phase speed of deep-water waves following from dispersion relationship (1.104) is as follows

$$c = \omega / k = \left(g / k + \sigma_s k / \rho\right). \tag{1.105}$$

Analysis of (1.105) shows that the phase speed has a minimum $c = c_m = \left(4g\sigma_s / \rho\right)^{1/4} \approx 0.23$ m s$^{-1}$ at $k = k_m = \left(g\rho / \sigma_s\right)^{1/2} \approx 360$ m$^{-1}$ where gravity and surface tension are equally important. The phase speed of gravity waves ($k << k_m$) increases with wavelength $\lambda = 2\pi / k$ or with decreasing wavenumber *k*. The phase speed of capillary waves ($k >> k_m$) decreases with wavelength λ or with decreasing wavenumber *k*.

### 1.6.3 Nonlinear waves

A solution for the nonlinear system (1.94)-(1.97) is the plane steady nonlinear wave in the form $\eta(\vec{x}, t) = \eta(x - ct)$ propagating along axis *x* with a constant speed *c*. Stokes (1880) showed that the surface wave elevation of a plane wave train in deep water can be expanded in powers of a small parameter ε = *ak* << 1. The third order result is as follows:

$$\eta = a\cos\theta + \frac{1}{2}ka^2\cos 2\theta + \frac{3}{8}k^2a^3\cos 3\theta + \ldots, \tag{1.106}$$

where the phase $\theta = kx - \omega t$ and

$$\omega^2 = gk\left(1 + a^2k^2 + \frac{5}{4}a^4k^4 + ...\right). \qquad (1.107)$$

Equation (1.106) is the Fourier series for the wave displacement $\eta$. As illustrated in *Figure 1-12*b, the wave profile described by solution (1.106) is no longer sinusoidal. It has a flattened trough and a peaked crest. In finite amplitude waves, fluid particles no longer trace closed orbits, but undergo a slow drift in the direction of wave propagation; this is the so-called *Stokes drift*.

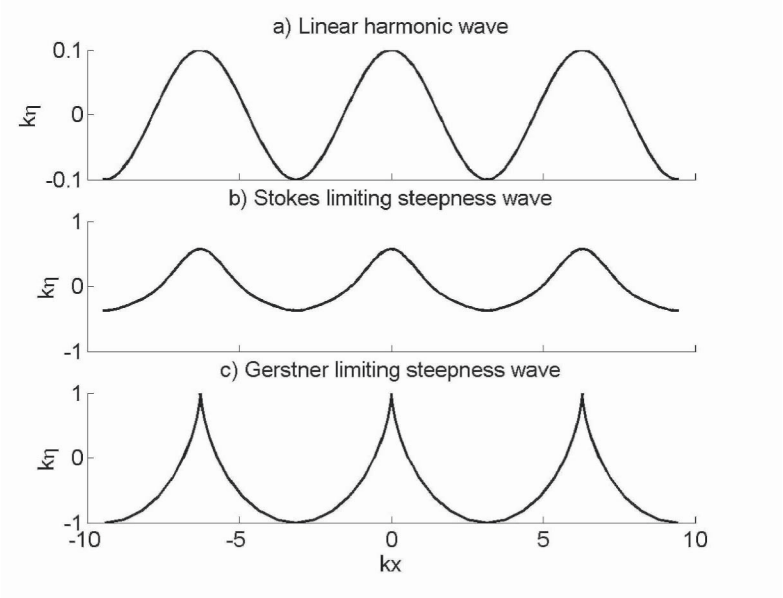


*Figure 1-12*. The surface elevation profile of linear (a) and nonlinear (b, c) waves.

As originally described by Stokes (1880), the maximum possible wave amplitude is $a_{\max} = 0.07\lambda$, at which point the crest becomes a $120^o$ angle. Attempt at generating waves of larger amplitude results in instability at the wave crest.

The system of equations (1.94)-(1.97) considered above describes a potential (*i.e.*, a non-rotational) approximation of the surface gravity wave theory. Gerstner (1802), however, found an exact solution of the equations of hydrodynamics (1.86)-(1.88) in Lagrangian coordinates in the form of steady, plane vorticity waves of finite amplitude on the free surface of an infinitely deep ideal fluid. According to his solution, illustrated in *Figure 1-12*c, coordinates $(x, z)$ of the fluid particle (in the absence of waves located at $(x_1, z_1)$) are the following function of time:

$$x = x_1 - a \exp kz_1 \sin\left[k\left(x_1 - ct\right)\right], \tag{1.108}$$

$$z = z_1 + a \exp kz_1 \cos\left[k\left(x_1 - ct\right)\right], \tag{1.109}$$

where $k$ is the wavenumber, $c = (g/k)^{1/2}$; and $a$ is the wave amplitude at $z_1 = 0$. This is a closed orbit trajectory with the rotation in opposite direction to the particle path (LeMehaute, 1976).

### 1.6.4 Wave breaking

If the ratio of wave amplitude to wavelength increases (due to wind work, for example), the waves are gradually deformed, become unstable, and eventually break, forming a whitecap. Wave breaking and the subsequent formation of whitecaps, bubbles, and spray droplets are complicated hydrodynamic processes. The full problem involves the wave dynamics before breaking, the transition of the one-phase medium to a two-phase mixture (bubbles in water and water droplets in air), and the hydrodynamics of the two-phase mixture. Improved knowledge of the wave breaking is vital for a better understanding of air-sea interactions from micro- to global scales (Melville, 1996).

The study of wave instabilities goes back to the classical works of Stokes (1880) and Michell (1893). Stokes suggested that wave-breaking inception occurs when the wave profile reaches the limiting wave steepness, and the water speed at the crest is equal to the phase speed of the wave. Theory suggests that the limiting steepness is achieved when the crest angle attains $120^o$, and $a_{max}/\lambda = 0.07$. However, observations show that waves usually break before achieving the limiting Stokes form. One possible reason is that a limiting wave, with a $120^o$ angle at the crest, has less energy than in a lower, symmetric wave with a smooth crest (Longuet-Higgins and Fox, 1978). Another reason is that the vorticity at the crest of the wave induced by the generating wind stress reduces the limit on wave steepness (Debnath, 1994). As a result, deep-sea wind waves with steepness larger than 0.10 are rarely encountered. Vorticity of the opposite sign theoretically increases the limiting wave steepness. This can be observed when the wave travels opposite to the wind direction. According to the closed-orbit Gestner theory, the maximum limiting steepness is 0.31, while the vorticity at the crest tends to infinity. Wave breaking is a complicated nonlinear phenomenon with wide variations in type and conditions. A general rotational wave theory including the mass transport due to wind action has yet to be finalized. An experimental demonstration of the limiting form of the wave appears to be

difficult, even though considerable empirical studies on the breaking process are available.

Mason (1952) distinguished two types of breaking waves, *spilling* and *plunging* breakers, applying to most situations in the open ocean. The transition from one kind to another is gradual, so such classification is more qualitative than quantitative. Galvin (1972) extended this empirical classification by introducing also *collapsing* and *surging* breakers, which are typical for shoreline.

In the open ocean, when the wave height reaches its maximum value, breaking first appears as foam and bubbles on the crests of the steepest waves. This is a spilling breaker according to the Galvin (1972) classification. It is usually accompanied by a relatively small amount of kinetic energy dissipation, and the wave crest for this type of breaker is almost symmetric.

When the front face of the wave becomes steep, the crest curls over the front face and falls into the base of the wave producing a large splash. This plunging breaker type is not unusual for wave breaking on beaches but much less frequent for deepwater waves.

In general, the problem of surface wave instability in deep water is a three-dimensional one. McLean et al. (1981) found two types of three-dimensional instability of finite-amplitude surface waves. Su (1982) later reported experimental evidence of these types of instabilities.

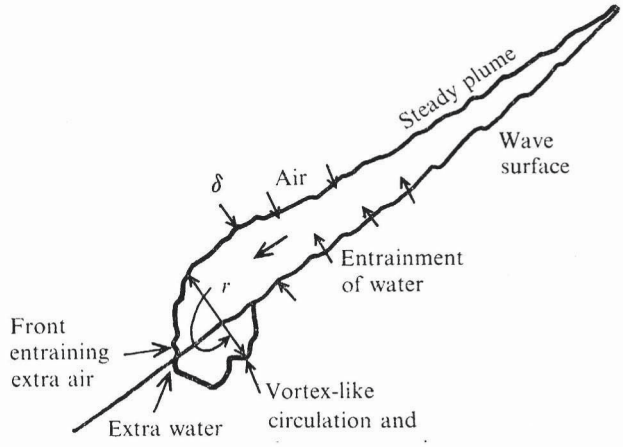


*Figure 1-13*. Schematic representation of the Longuet-Higgins and Turner (1974) model of advancing spilling breaker. The wave is moving from right to left and has a whitecap on its forward face. Here $\delta$ is the thickness of the whitecap. Reproduced with the permission of Cambridge University Press.

Spilling breakers are typical for deepwater (open ocean) conditions. A characteristic property of a spilling breaker is that, as it breaks gently at the

crest, it traps enough air bubbles for the resulting air-water mixture to be significantly lighter than the water below it. This density difference inhibits mixing with the face of the wave, so that the whitecap rides on top of the sloping sea surface. Accordingly, Longuet-Higgins and Turner (1974) proposed treating a spilling breaker as a turbulent gravity current riding down the forward slope of a wave in the same way a turbulent gravity current rides down a solid slopping boundary (*Figure 1-13*). As the flow continues, the turbulence leads to the entrainment of water from the wave surface below. This results in further incorporation of air, especially near the front of the whitecap, maintaining the density difference.

In the Longuet-Higgins and Turner (1974) model, the mean thickness of the whitecap $\delta$ increases proportionally to distance $s$ from the wave crest, while the whitecap accelerates down the slope. For maintaining the stationary state of the wave breaker corresponding to the limiting Stokes wave with a 120$^o$ angle at the crest ($\theta = 30^o$), $\rho$' should be at least 8% less than $\rho$.

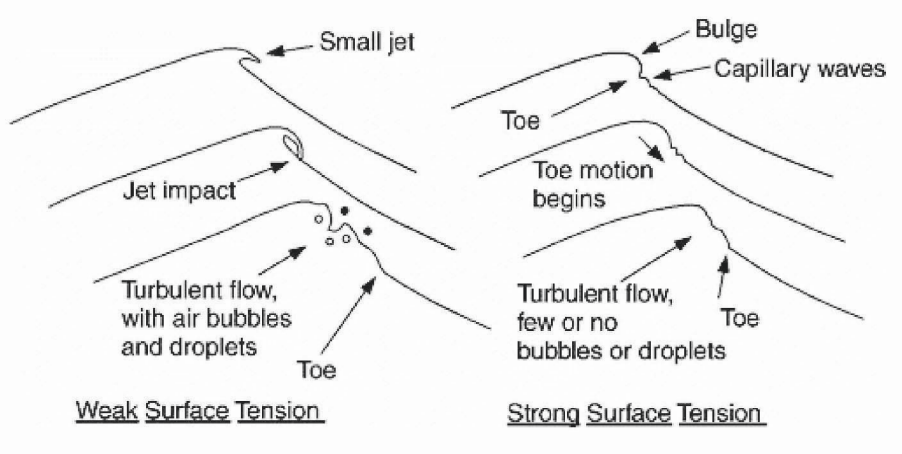


*Figure 1-14*. Schematic showing three phases of spilling breaking for weak and strong surface tension effects. Reprinted from Duncan (2001) with permission by Annual Reviews www. Annualreviews.org

The behavior of the spilling breaker depends on wavelength. For long waves, the wave breaking processes results in the appearance of a turbulent patch of fluid on the forward slope of the wave (as schematically shown in *Figure 1-13*). For short waves ($\lambda < 10$ cm), the wave breaking process is greatly influenced by surface tension; the turbulent bore is replaced with a capillary wave train that can break down without overturning of the water surface (see sketch *Figure 1-14*). This process resembles the microscale wave breaking that is described in Section 2.2.2 in relation to the sea surface microlayer.

### 1.6.5 Statistical description of surface waves

The detailed configuration of the ocean surface generally varies irregularly in time and space due to a broad spectrum of surface waves. Ocean waves can therefore be treated as a random process and analyzed with statistical methods. A stationary, random surface elevation $\eta(\vec{x},t)$ can be represented in terms of a Fourier-Stieltjes integral,

$$\eta(\vec{x},t) = \int_{\vec{k}}\int_{\omega} dZ_{\eta}(k,\omega)\exp\left[i\left(\vec{k}\cdot\vec{x}-\omega t\right)\right], \tag{1.110}$$

where the integration is over all time and wavenumber space. Fourier-Stieltjes coefficients are defined as follows:

$$dZ_{\eta}\left(\vec{k},\omega\right)dZ_{\eta}^{*}\left(\vec{k}',\omega'\right) = \begin{cases} 0 \text{ at } \vec{k},\omega \neq \vec{k}',\omega' \\ \Upsilon\left(\vec{k},\omega\right)d\vec{k}d\omega \text{ at } \vec{k}=\vec{k}',\ \omega=\omega' \end{cases} \tag{1.111}$$

where $\Upsilon\left(\vec{k},\omega\right)$ is the surface wave spectrum.

The wavenumber spectrum is obtained by integrating all frequencies:

$$\Psi\left(\vec{k}\right) = \int_{-\infty}^{\infty}\Upsilon\left(\vec{k},\omega\right)d\omega, \tag{1.112}$$

and the frequency spectrum by integrating all wavenumbers:

$$\Phi(\omega) = \int_{-\infty}^{\infty}\Upsilon\left(\vec{k},\omega\right)d\vec{k}. \tag{1.113}$$

It is possible to show that for a stationary wave field, $\Phi(\omega)$ is real and is symmetrical with respect to ω = 0. Often only positive frequencies are therefore considered, so that

$$\Phi(\omega) = 2\int_{0}^{\infty}\Upsilon\left(\vec{k},\omega\right)d\vec{k}. \tag{1.114}$$

The root mean square elevation

$$H_{rms} = \sqrt{\langle \eta^2 \rangle} \tag{1.115}$$

is related to the frequency spectrum as follows

$$\langle \eta^2 \rangle = \int_0^\infty \Phi(\omega) d\omega \,. \tag{1.116}$$

Significant wave height $H_S$ is defined as the mean of the highest one third of the waves. In the absence of swell, it is related to $H_{rms}$ by

$$H_S = 4 H_{rms} \,. \tag{1.117}$$

The sea is fully developed when the waves have grown to their maximum amplitude for a given wind speed. This implies that the shore is far away (*i.e.*, the sea is not fetch-limited) and the wind has been blowing for a long time so that the wave spectrum has become saturated and no more energy can be added.

In a fully developed sea the factors that are expected to be important for describing the surface wave spectrum are the wave frequency $\omega$, wind speed $U_a$, and acceleration of gravity $g$ (Kitaigorodskii, 1962). Standard dimensional analysis leads to the following dependence:

$$\Phi(\omega) g^3 / U_a^5 = \phi_1 (U_a \omega / g) \,, \tag{1.118}$$

where $\phi_1$, is a universal function. Pierson and Moskowitz (1964) plotted several field spectra for saturated conditions according to scaling (1.118) and proposed an interpolation formula,

$$\frac{\Phi(\omega) g^3}{U_{20}^5} = 4.05 \times 10^{-3} \left( \frac{U_{20} \omega}{g} \right)^{-5} \exp\left[ -0.74 \left( \frac{U_{20} \omega}{g} \right)^{-4} \right] \tag{1.119}$$

where $U_{20}$ is the wind speed at 20 m height. The latter became known as the *Pierson-Moskowitz spectrum*.

Two useful relations following from (1.119) are:

$$g H_S / U_{20}^2 \simeq 0.2 \,, \text{ and} \tag{1.120}$$

$$U_{20} \omega_p / g \simeq 0.88 \,, \tag{1.121}$$

where $\omega_p$ is the frequency of spectral peak.

For a saturated wavenumber spectrum, in the analysis leading to equation (1.118) frequency $\omega$ is replaced with wavenumber vector $\vec{k}$, which results in the following dependencies (Phillips, 1977):

$$\Psi\left(\vec{k}\right) = \Psi\left(\vartheta, k\right) = k^{-4}\phi_2\left(\vartheta, ku_*^2 / g\right), \tag{1.122}$$

$$\Psi_a\left(k\right) = k^{-3}\phi_3\left(ku_*^2 / g\right), \tag{1.123}$$

where $\phi_2$, *and* $\phi_3$ are universal functions, $\vartheta$ is the wave direction, and $u_*$ is the friction velocity. The wavenumber modulus spectrum, $\Psi_a$, is defined as follows:

$$\Psi_a\left(k\right) = \int_{-\pi}^{\pi} \Psi\left(\vartheta, k\right) k d\vartheta \tag{1.124}$$

The high frequency and high wavenumber tails of the surface wave spectra have been a subject of substantial interest. The small-scale waves that control these parts of the spectra determine the momentum exchange between the atmosphere and the ocean. These waves have other practical significance in air-sea heat and gas exchange, and are also important in remote sensing (Chapter 7). As to the low frequency and low wavenumber spectrum, it is not completely clear if the equilibration of the surface wave spectrum can be achieved at all (Balk and Zakharov, 1998).

### 1.6.6 Kinetic energy flux to waves from wind

The energy transfer from the wind to the wave field is the driving force for wave breaking, which is the main factor in wave energy dissipation (Komen et al., 1994). Direct measurement of the kinetic energy flux from wind to waves is a difficult task. Alternatively, the flux of kinetic energy to waves from wind can be determined as the integral of the growth rate, $\beta_w$, over the wave spectrum, where $\beta_w$ is the *e*-folding scale for the temporal growth of wave energy in the absence of nonlinear interactions and dissipation (Terray et al., 1996). Then,

$$F_0 = g\iint \frac{\partial \Phi_\eta}{\partial t} d\omega\, d\vartheta = g\iint \beta_w \Phi_\eta d\omega\, d\vartheta, \tag{1.125}$$

where $\Phi_\eta(\omega,\vartheta)$ is the frequency-direction spectrum of the surface waves. A formulation due to Donelan and Pierson (1987) relates $\beta_w$ at each frequency to the wind speed as

$$\frac{\beta_w}{\omega} = 0.194\frac{\rho_a}{\rho}\left(\frac{U_{\pi/k}\cos\vartheta}{c(k)}-1\right)\left|\frac{U_{\pi/k}\cos\vartheta}{c(k)}-1\right|, \tag{1.126}$$

where $U_{\pi/k}$ is the wind speed at the height of one half wavelength ($\lambda/2=\pi/k$), which is taken as the relevant forcing parameter for a component of wavenumber, $k$, and phase speed, $c(k)$.

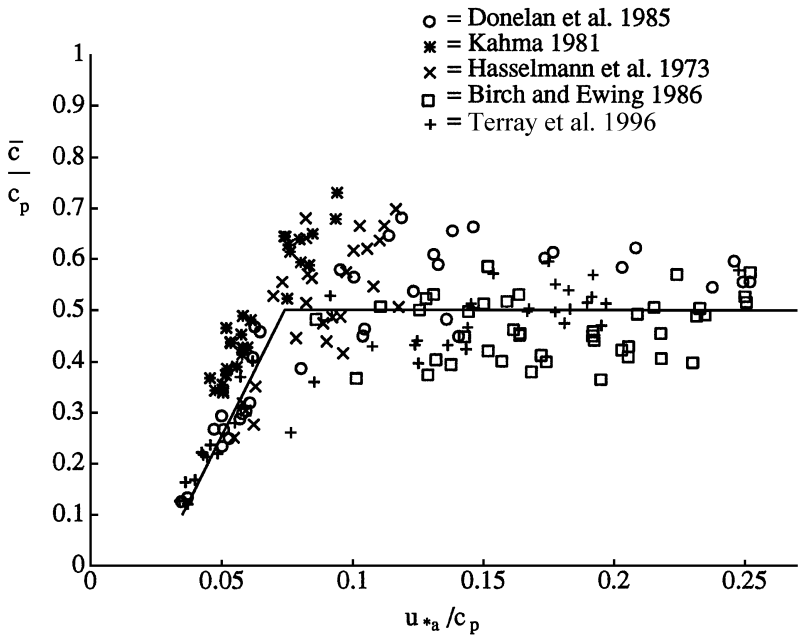


*Figure 1-15*. The ratio of the effective phase speed to the phase speed of the wind wave spectral peak, $\bar{c}/c_p$, versus inverse wave age, $u_{*a}/c_p$. Reproduced from Terray et al. (1996) with the permission of American Meteorological Society.

Terray et al. (1996) introduced an effective phase speed, $\bar{c}$, related to wind input by parameterizing $F_0$ in terms of this speed and the wind stress $\tau_0$ as:

$$F_0 = \bar{c}\tau_0/\rho \approx \bar{c}u_*^2, \tag{1.127}$$

which is based on an assumption that the entire wind stress is transferred to waves. The ratio $\bar{c}/c_p$ as a function of $u_{*a}/c_p$ is shown in *Figure 1-15*. Here $c_p$ is the phase speed at the spectral peak of wind waves, and $u_*$ is the friction velocity in the upper ocean boundary layer defined as $u_* = (\tau_0/\rho)^{1/2}$.

Terray et al. (1996) assumed that the waves are "young" (short fetched or developing waves) when their age $A_w = c_p/u_{*a} < 13$. The "old" waves (developed seas) were defined by an opposite inequality, $A_w > 13$. For waves at very early stages of development, $\bar{c}$ approaches the peak wave velocity, while for developed seas it is of the order of the friction velocity in the air, $u_{*a}$.

For developed seas, $\bar{c}/u_{*a}$ can be approximated by a constant; equation (1.127) thus reduces to

$$F_0 \approx \alpha_w u_*^3, \tag{1.128}$$

where $\alpha_w \approx 100$ is a dimensionless constant. For young waves ($A_w > 13$), $\alpha_w$ can't be a constant. Kantha and Clayson (2004) proposed the following approximate formula, which is intended to account for wave age:

$$F_0 \approx 4.053 \cdot u_*^3 (0.037 A_w^2 - 3.615/A_w), \tag{1.129}$$

Appreciable kinetic energy can be transferred to the water by rain droplets. When a droplet impacts water, its kinetic energy is transferred to the surface layer of the ocean along with its mass. This process is discussed in more detail in Chapter 2 in relation to the freshwater skin of the ocean.

## 1.7 Planetary Boundary Layers

The time and length scales of global oceanic and atmospheric processes are considerably different for reasons related to disparity in the density of the two media. These differences are bridged in the atmospheric and oceanic planetary boundary layers that develop adjacent to the air-sea interface. These boundary layers are subject to strong turbulence, and the turbulent exchange coefficients are much higher within boundary layers than outside of these regions. Ekman and Monin and Oboukhov developed one-dimensional framework for understanding planetary boundary layers

### 1.7.1 Ekman boundary layer

The theory of the planetary boundary layer formulated by Ekman (1905) provides a convenient framework for the analysis of the Earth's rotation effects. Here we present this theory in a manner close to that of Stull (1988) and Mellor (1996).

The Ekman theory considers a steady, barotropic flow. Retaining the turbulent stress terms but not the tendency terms, we rewrite equations of motion (1.17) and (1.18) (low Rossby number approximation) as

$$-fv = -\frac{1}{\rho}\frac{\partial p}{\partial x} + \frac{1}{\rho}\frac{\partial \tau_{zx}}{\partial z}, \quad fu = -\frac{1}{\rho}\frac{\partial p}{\partial y} + \frac{1}{\rho}\frac{\partial \tau_{zy}}{\partial z}, \tag{1.130}$$

Since the flow is barotropic, $\partial p/\partial x$ and $\partial p/\partial y$ are constant in the vertical.

It is customary to define geostrophic velocities, $u_g$ and $v_g$ from the equations:

$$-fv_g = -\frac{1}{\rho}\frac{\partial p}{\partial x}, \quad fu_g = -\frac{1}{\rho}\frac{\partial p}{\partial y}. \tag{1.131}$$

(The geostrophic velocity is a fictitious velocity, for which the Coriolis acceleration exactly balances the horizontal pressure force.) A combination of (1.130) and (1.131) leads to:

$$-fv = -fv_g + \frac{1}{\rho}\frac{\partial \tau_{zx}}{\partial z}, \quad fu = fu_g + \frac{1}{\rho}\frac{\partial \tau_{zy}}{\partial z} \tag{1.132}$$

Above the atmospheric or below the oceanic planetary boundary layer, $\tau_{zx}$ and $\tau_{zx}$, and their vertical gradients vanish so that $u = u_g$ and $v = v_g$.

Momentum fluxes in (1.132) can be expressed via velocity gradients as follows:

$$\frac{\tau_{zx}}{\rho} = K_M \frac{\partial u}{\partial z}, \quad \frac{\tau_{zy}}{\rho} = K_M \frac{\partial v}{\partial z}, \tag{1.133}$$

where $K_M$ is the turbulent momentum exchange coefficient or eddy viscosity. Thus, (1.132) may be written as:

$$\frac{\partial}{\partial z}\left(K_M \frac{\partial u}{\partial z}\right) + fv = fv_g, \quad \frac{\partial}{\partial z}\left(K_M \frac{\partial v}{\partial z}\right) - fu = -fu_g . \tag{1.134}$$

The classical Ekman theory assumes that $K_M$ does not vary with $z$, which is a strong constraint.

The boundary conditions for the atmospheric boundary layer:

$$u = v = 0 \text{ at } z = 0, \tag{1.135}$$

and

$$u \approx u_g \text{ and } v = 0 \text{ as } z \to \infty . \tag{1.136}$$

Condition (1.136) means (without loss of generality) that the geostrophic wind vector $\vec{G}$ is directed along the $x$-axis. In this case the magnitude of the geostrophic wind,

$$G = \left(u_g^2 + v_g^2\right)^{1/2} = u_g . \tag{1.137}$$

When the atmospheric boundary layer is in contact with a moving ocean surface, the atmospheric surface velocity is not exactly zero as stated in (1.135). It is, however, generally small relative to atmospheric geostrophic velocities, so (1.135) can be taken as a fairly good approximation. As stated in equation (1.136), as $z$ increases indefinitely, the velocity will approach the geostrophic velocity, although it is only necessary to state that the velocity is bounded as $z \to \infty$.

Solutions to equations (1.134) with boundary conditions (1.135) and (1.136) are

$$u = G\left[1 - e^{-\gamma_E z} cos\left(\gamma_E z\right)\right], \tag{1.138}$$

$$v = Ge^{-\gamma_E z} \sin\left(\gamma_E z\right), \tag{1.139}$$

where $\gamma_E = \left(2K_m / f\right)^{1/2}$. The velocity vectors described by solution (1.138) (1.139) are shown in *Figure 1-16*a as a function of height. The tip of the vectors traces out a spiral, which is known as the *Ekman spiral*.

For constant $K_M$, the geostrophic wind vector is aligned 45$^o$ (counter) clockwise from the surface stress vector in the northern (southern)

hemisphere. (Because $K_M$ generally is not constant with respect to $z$ in the turbulent boundary layer, the angle can be different.) The surface wind stress, which is caused by the drag of the surface wind against the surface, is in the same direction as the surface wind vector. Because, in this model, $K_M$ does not depend on height, (1.133) with (1.138) and (1.139) at $z = 0$ result in

$$\tau_0 = \left(\tau_{0x}^2 + \tau_{0y}^2\right)^{1/2} = \rho_a G\left(K_m f\right)^{1/2}. \tag{1.140}$$

The Ekman layer depth is often defined as $h_E = \pi / \gamma_E$, which is the lowest height at which the wind is parallel to the geostrophic flow (*Figure 1-16*). The eddy coefficient in Ekman theory is parameterized as $K_M = c_E \kappa u_{*a} h_E$, where $c_E \approx 0.1$, $\kappa$ is the von Karman constant ($\kappa \simeq 0.4$), $u_{*a}$ is the friction velocity from the airside of the interface defined as $u_{*a} = \left(\tau_o / \rho_a\right)^{1/2}$. The Ekman layer depth is then

$$h_E = 2 c_E \kappa \pi^2 u_{*a} / f \approx 0.8 u_{*a} / f \,. \tag{1.141}$$

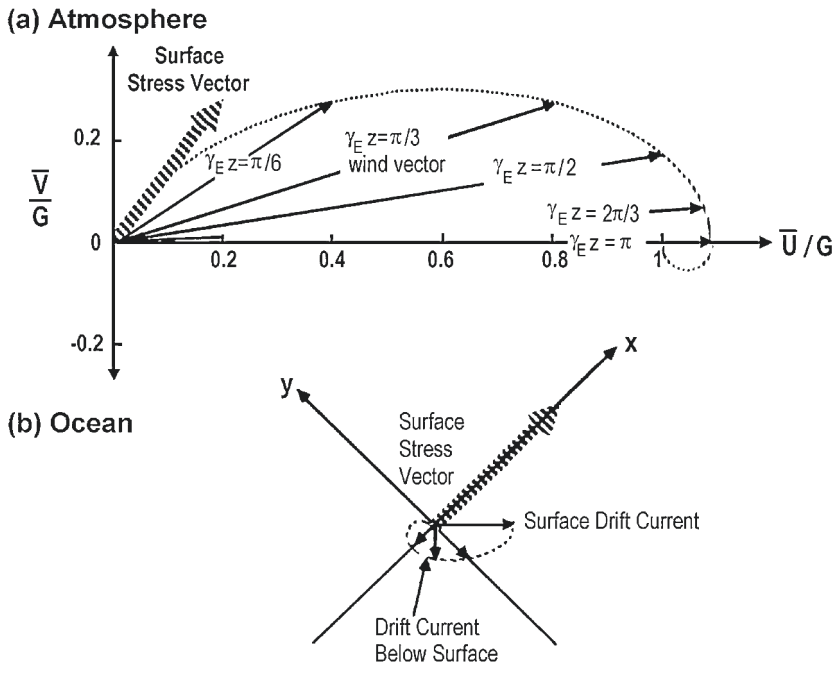


*Figure 1-16*. Ekman spiral hodograph for (a) wind and (b) current vectors (After Businger, 1982.)

The analysis of the velocity structure of the ocean surface boundary layer, or Ekman layer, is similar to the atmospheric layer (except for the boundary conditions). The surface boundary layer is also called the surface mixed layer, because temperature and salinity are often well mixed. equations (1.134) apply equally well to the ocean mixed layer, and definitions (1.131) are also applicable.

For the analysis of the ocean surface boundary layer, we choose a coordinate system with the *x*-axis aligned with the surface stress and with *z* being positive upwards. Change of variables, $u - u_g \to u$ and $v - v_g \to v$, transforms (1.134) into:

$$\frac{\partial}{\partial z}\left( K_m \frac{\partial u}{\partial z} \right) + fv = 0, \quad \frac{\partial}{\partial z}\left( K_m \frac{\partial v}{\partial z} \right) - fu = 0 . \tag{1.142}$$

The boundary conditions for the oceanic side of the interface differ from those for the atmosphere side. First, shear stress is imposed on the sea surface by the wind, so that in the oceanic coordinate system:

$$K_m \left( \frac{\partial u}{\partial z} \right)_{z \to -0} = u_*^2 \quad \text{and} \quad K_m \left( \frac{\partial v}{\partial z} \right)_{z \to -0} = 0 , \tag{1.143}$$

whereas, in deeper water, the velocity asymptotes to zero:

$$u \to 0 \text{ and } v \to 0 \text{ as } z \to -\infty . \tag{1.144}$$

In equations (1.142) and (1.143), $K_m$ and $u_*$ refer to their ocean values (where the surface stress, $\tau_0$, has been expressed via atmospheric and oceanic friction velocities as follows):

$$\tau_0 = \rho_a u_{*a}^2 = \rho u_*^2 \tag{1.145}$$

Solutions to (1.142) with boundary conditions (1.143)-(1.144) are as follows:

$$u = u_*^2 \left( K_m f \right)^{-1/2} \left[ e^{\gamma_E z} \cos\left( -\gamma_E z + \pi/4 \right) \right], \tag{1.146}$$

$$v = -u_*^2 \left( K_m f \right)^{-1/2} \left[ e^{\gamma_E z} \sin\left( -\gamma_E z + \pi/4 \right) \right]. \tag{1.147}$$

Equations (1.146) and (1.147) describe the Ekman spiral in the upper ocean, which is shown in *Figure 1-16*b.

Atmospheric pressure systems drive the atmospheric geostrophic velocities that determine the surface wind surface stress. Across the air-sea interface the horizontal stress vector is continuous. The sea surface velocity $\vec{U}_0$ deviates 45° to the right from the wind stress vector $\vec{\tau}_0$ (in the Northern Hemisphere) but, remarkably, retains the same direction as the geostrophic wind. It is possible to show (see for instance Kraus and Businger, 1994) that

$$\overrightarrow{U_0} = \left(\nu_a / \nu\right)^{1.2} \vec{G}\rho_a / \rho \approx 0.005\vec{G}\,, \tag{1.148}$$

where $\nu_a$ and $\nu$ are the viscosities of air and water, respectively.

Observations of wind driven currents in the ocean have shown that the surface current direction does deviate from the surface wind direction. However, the observed deviations are less than the 45° deviation predicted by Ekman theory. Moreover, the spiral pattern usually is more slab-like than the theoretical Ekman spiral (Price et al., 1987). The main reason is that the vertical mixing coefficient in the ocean changes up to several orders of magnitude depending on depth and stratification, while Ekman theory treats it as a constant.

### 1.7.2 Monin-Oboukhov similarity theory

The Monin-Oboukhov similarity theory is intended to account for the effects of stratification in the planetary boundary layer. This theory is based on the following approximations:

1) Horizontal homogeneity,
2) Stationary state,
3) Constant stress and heat flux.

In the atmospheric boundary layer, the vertical gradients of horizontal wind velocity *u*, potential temperature $\Theta$, and the dissipation rate of the turbulent kinetic energy $\varepsilon$ may then be represented as universal functions of the stability parameter $\zeta = |z| / L_O$ (Monin and Yaglom, 1971; Fairall et al., 1980):

$$\left(\kappa z / u_{*a}\right)\partial u / \partial z = \phi_M\left(\zeta\right), \tag{1.149}$$

$$\left(\kappa z / T_{*a}\right)\partial \Theta / \partial z = \phi_T\left(\zeta\right), \tag{1.150}$$

$$\kappa|z|\varepsilon/{u_{*a}}^3=\phi_\varepsilon(\zeta), \tag{1.151}$$

where $T_{*a}=-\overline{w'\Theta'}/(\kappa u_{*a})$, $u_{*a}$ is the friction velocity (in air), $\varepsilon$ is the dissipation rate of turbulent kinetic energy, stability parameter $\zeta$ is defined in (1.41) and $u$ and $w$ are the horizontal and vertical components of wind velocity vector, respectively. The stability parameter is negative when the atmosphere is statically unstable and positive when it is statically stable. In order to make this criterion applicable to both atmosphere and ocean, in the definition of the stability parameter we have replaced $z$ with $|z|$.

For intermediate depths, the constant stress and heat flux assumptions (that the Monin-Oboukhov theory is based on) strictly speaking are no longer valid (also because of volume sources). The Monin-Oboukhov theory, however, often holds even in the case of vertically variable fluxes. An approach to modifying the Oboukhov length scale $L_O$ in order to account for the presence of volume sources is considered in Chapter 4.

A commonly used approximation for the universal functions $\phi_M$ and $\phi_T$, based on the Kansas experiment is as follows (Kraus and Businger, 1994):

$$\phi_M\approx\begin{cases}1+\beta\zeta & \text{for } 0\le\zeta\\ (1-\alpha\zeta)^{-1/4} & \text{for } -0.20\le\zeta<0\\ (1.26-8.38\zeta)^{-1/3} & \text{for } \zeta<-0.20\end{cases}, \tag{1.152}$$

$$\phi_T\approx\begin{cases}1+\beta\zeta & \text{for } 0\le\zeta\\ (1-\alpha\zeta)^{-1/2} & \text{for } -1.0\le\zeta<0\\ (-28.26-98.96\zeta)^{-1/3} & \text{for } \zeta<-1.0\end{cases} \tag{1.153}$$

where $\beta$ = 5, and $\alpha$ = 16. For the dissipation rate of turbulent kinetic energy (TKE), Wyngaard et al. (1971) proposed:

$$\phi_\varepsilon(\zeta)=\begin{cases}\left(1+0.5|\zeta|^{2/3}\right)^{3/2}, & \text{for } \zeta<0\\ \left(1+2.5|\zeta|^{2/3}\right)^{3/2}, & \text{for } \zeta\ge0\end{cases} \tag{1.154}$$

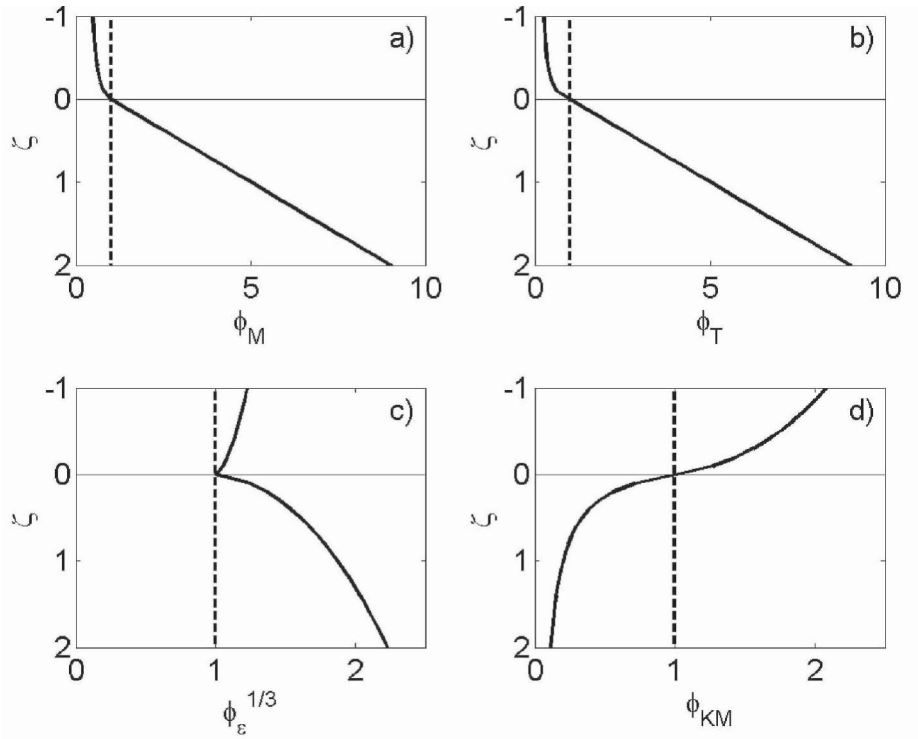


*Figure 1-17*. Universal functions for dimensionless (a) shear $\phi_M = (\kappa |z| / u_{*a}) \partial u / \partial z$, (b) potential temperature gradient $\phi_T = (\kappa |z| / \rho_{*a}) \partial \Theta / \partial z$, (c) dissipation rate of the turbulent kinetic energy $\phi_\varepsilon = \kappa |z| \varepsilon / u_{*a}^3$, and (d) turbulent eddy coefficient $\phi_{KM} = K_M / (\kappa u_{*a} |z|)$ expressed as a function of stability parameter $\zeta$. The vertical dashed lines represent the logarithmic-layer regime.

The mixing coefficients for momentum and temperature are defined as $K_M = -\overline{u'w'} / \partial u / \partial z$ and $K_T = -\overline{w'\Theta'} / \partial \Theta / \partial z$, respectively, and can be defined via the universal functions as follows:

$$\phi_{KM} = \phi_M^{-1}, \ \phi_{KT} = \phi_T^{-1}, \tag{1.155}$$

where

$$\phi_K = K_M / (\kappa u_{*a} z), \ \phi_{KT} = K_T / (\kappa T_{*a} z). \tag{1.156}$$

Several universal functions from the Monin-Oboukhov theory are shown in *Figure 1-17*. There are three asymptotic regimes in this theory:

1) Logarithmic layer, where stratification is negligible ($\zeta = 0$),
2) Free convection ($\zeta \to -\infty$), and
3) Marginal stability ($\zeta \to \infty$).

Vertical dashed lines in *Figure 1-17* indicate the logarithmic layer regime. The regime of marginal stability is characterized by linear profiles of nondimensional shear $\phi_M$ and temperature gradient $\phi_T$, which is observed starting for sufficiently large positive $\zeta$. The asymptotic regimes are discussed in more detail in Section 3.4.

The Monin-Oboukhov similarity theory has provided an important conceptual framework for understanding the dynamics of planetary boundary layers. The constant stress layer assumption, which is the main assumption of this theory, is however valid only within approximately 10% of the total thickness of the planetary boundary layer. The Monin-Oboukhov similarity theory was originally developed for the atmospheric boundary layer. Its application to the upper ocean boundary layer has some specific issues, which are discussed in Chapter 3

### 1.7.3 Surface mixed layer

The planetary boundary layers are subject to strong turbulence, and the turbulent exchange coefficients are much higher within boundary layers than outside of these regions. The surface mixed layer is a generic feature of the upper ocean. Vertical profiles of temperature, salinity and other scalar quantities show nearly constant values adjacent to the surface due to continuous or episodic, but frequent, mixing. Wind-induced shear and waves are important sources of turbulent mixing in the upper ocean. In addition, thermal convection, in the form of loss of heat through long-wave radiation flux and evaporative cooling cause turbulent mixing.

The model of an Ekman layer shows surface stress is carried away from the boundary layer and toward the interior of the ocean. The Ekman equations assume a dominant balance between the frictional force and the Coriolis force while approximating the equations of motion. The velocity vector then decays in amplitude by spiraling down away from the ocean's surface toward the interior. The Monin-Oboukhov theory assumes that the dominant balance is between the frictional force and buoyancy force. It helps to explain how buoyancy fluxes due to diurnal warming, precipitation, or horizontal advection suppress turbulence in the upper ocean. The Ekman and Monin and Oboukhov theories represent a one-dimensional framework for understanding planetary boundary layers, which may however be a substantial oversimplification in certain cases (see Chapter 5).

The daily averaged depth of the mixed layer changes with season being relatively shallow during the spring and summer and deeper during the fall

and winter. Wind plays a large role in the development of the mixed layer because of the vertical shear resulting from wind-induced surface currents. Seasonal wind variations can account somewhat for seasonal mixed layer depth since winds are stronger in the winter and weaker in the summer. In addition, heating and cooling influence mixed layer depth. Stronger heating during the summer leads to greater stratification, stability, and lower potential energy. On the other hand, cooling destabilizes the water column in the winter, allowing mixing to occur even in the absence of winds. For this reason winds and surface heat fluxes combine to affect formation and seasonal variation of the mixed layer.

In addition to seasonal differences, latitudinal and hemispheric trends are present in mixed layer depth. Seasonal variation in mixed layer depth generally increases poleward. This is a result of increased winds and cooling towards higher latitudes. Mixed layers are generally deeper in the Southern Hemisphere than in the Northern hemisphere, especially during the summer (Soloviev and Klinger, 2001). This may reflect the fact that winds are generally stronger in the Southern Hemisphere and there is a greater input of heat in the Northern Hemisphere summer.

There are also significant differences in mixed layer depth between oceans. During the winter, the high latitude North Atlantic develops very deep (>1000 m) mixed layers. The winter deepening is not nearly as intensive in the North Pacific. There is net evaporation and hence higher salinity in the North Atlantic, which may lead to a greater destabilization of the water column, accounting for the difference.

The mixed layer of the ocean is an important part of the global climate system. It effectively exchanges momentum, energy, and greenhouse gases with the atmosphere. Turbulent transport in the mixed layer also controls the supply of nutrients to the upper, sunlit layers, greatly affecting the phytoplankton grows and, consequently, the overall biological productivity of the ocean.

### 1.7.4 Barrier layer

The depth of the surface mixed layer was traditionally determined as the depth over which the temperature is uniform. However, in the presence of strong freshwater sources (rainfalls, ice melting, river runoff) there is often a halocline within the isothermal layer, which results in a change in density. Lukas and Lindstrom (1991) refer to the layer between the tops of the halocline and the thermocline as the *barrier layer* because of its impact on the heat budget of the upper ocean. An example of the barrier layer from the Indian Ocean is shown in *Figure 1-18*. The temperature within the barrier

layer is nearly identical to the mixed layer temperature, while the salinity is larger than in the mixed layer.

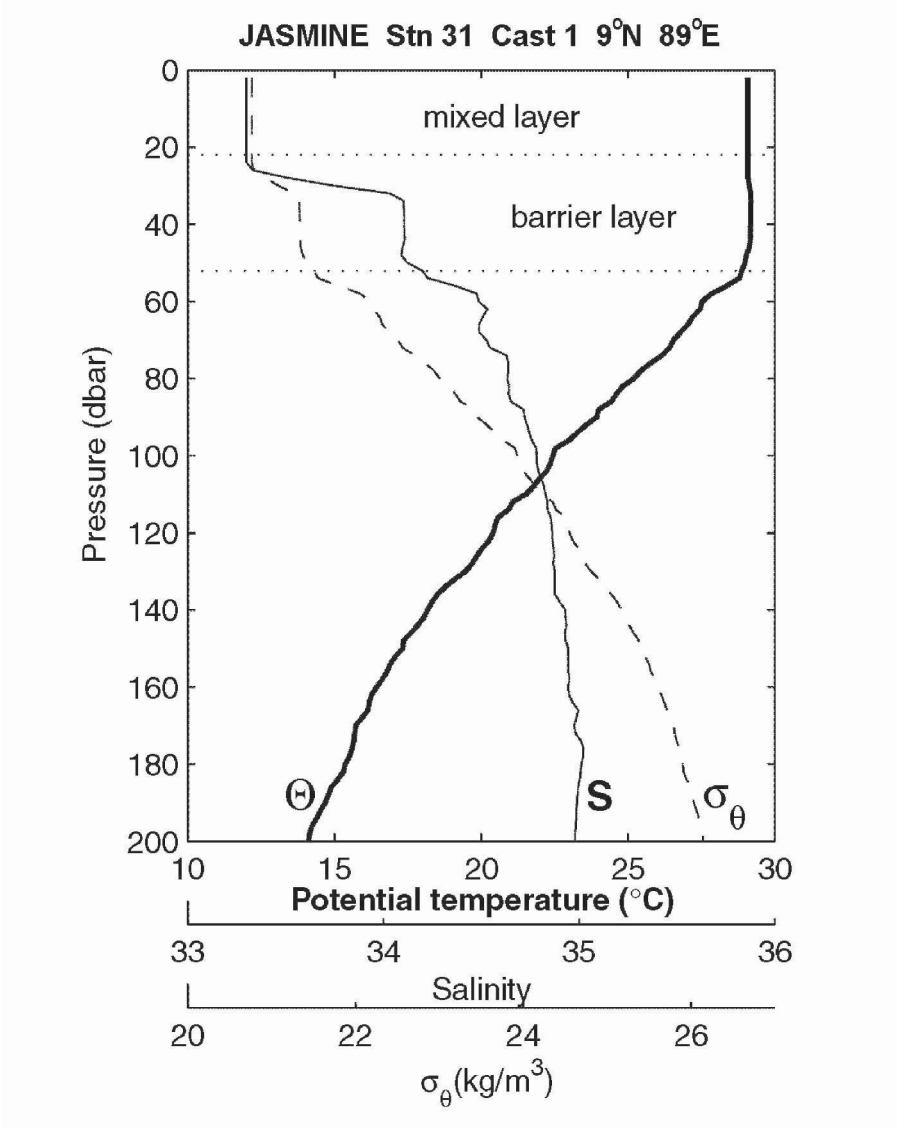


*Figure 1-18*. An example of the vertical profiles of potential temperature θ, salinity *S*, and potential density $\sigma_\theta$ in the upper 200 m layer of the Indian ocean (After Lukas et al., 2001).

The barrier layer is likely to be observed in regions of low winds and high precipitation favoring the development of a thin fresh surface layer. Such regions are typically in the western equatorial Pacific Ocean, and the eastern Indian Ocean due to strong precipitation. Freshwater input from

rivers is an additional source of freshwater in the eastern Indian Ocean. The barrier layer can also be important in dynamics of coastal regions with river run-off (like the Bay of Bengal) and in the marginal polar seas under conditions of ice melting.

The existence of the barrier layer plays a key role in the onset of *El Niño*, through a complex process that involves ocean vertical mixing, sea surface temperature, wind stress, freshwater flux, and large-scale ocean-atmosphere dynamics (Lukas and Lindstrom, 1991; Webster and Lukas, 1992; Vialard and Delecluse, 1998; Maes et al., 2002). The barrier layer favors the maintenance and displacement of the western Pacific warm pool into the central Pacific by isolating the mixed layer from entrainment cooling at depth and by confining the momentum of westerly wind events to a shallow mixed layer.

Chapter 2

# SEA SURFACE MICROLAYER

*The top few millimeters of the ocean surface, where properties are most altered relative to deeper water, are often referred to as the sea surface microlayer.*

The microlayer is involved in the heat and momentum transfer between the ocean and atmosphere and plays a vital role in the uptake of greenhouse gases by the ocean. A striking variety of physical, biological, chemical, and photochemical interactions and feedbacks occur in the ocean surface microlayer. There is a widely held presumption that the microlayer is a highly efficient and selective micro-reactor, effectively concentrating and transforming materials brought to the interface from the atmosphere and oceans by physical processes (Liss and Duce, 1997). These processes are very intriguing and potentially of great importance for remote sensing of sea surface temperature and salinity, climate change, and many other practical applications still waiting their time to come.

Direct measurement of the sea surface microlayer is still a challenge. As a result, surprisingly little experimental information exists on the structure of sea surface microlayers. The majority of microlayer results have been obtained from laboratory studies.

The physics of the sea surface microlayer is related to fundamental properties of turbulent boundary layers. While in the bulk of the water turbulence largely controls the transport, molecular diffusion take over the transfer of momentum, heat and mass from the upper ocean to the sea surface because the vertical component of turbulent velocity is suppressed close to the surface. Surface organic and inorganic films formed as a result of complex interplay between biological, chemical, and physical processes

can interfere with air-sea interaction (for instance, via capillary-gravity waves) and affect the properties of molecular sublayers.

Around breaking waves, the sea surface is not well defined–it includes the surface of bubbles and the outside of spray droplets, and the overhang of plunging waves. The height values of the sea surface can be multiply defined. In this case, the sea surface can be defined only in the topological sense and the concept of microlayer needs to be extended.

As a first approximation, the thickness of the viscous, thermal, and diffusion molecular sublayer at the ocean surface can be associated with the internal (Kolmogorov's) length scale of turbulence,

$$\eta_\nu = \left(\nu^3 / \varepsilon\right)^{1/4}, \tag{2.1}$$

where $\nu$ is the molecular kinematic viscosity, and $\varepsilon$ is the dissipation rate of the turbulent kinetic energy. Similar length scales also exist for thermal and diffusive turbulent processes,

$$\eta_T = \mathrm{Pr}^{-1/2}\left(\nu^3 / \varepsilon\right)^{1/4} \tag{2.2}$$

and

$$\eta_D = Sc^{-1/2}\left(\nu^3 / \varepsilon\right)^{1/4} \tag{2.3}$$

where $\mathrm{Pr} = \nu / \kappa_T$ is the Prandtl number ($\mathrm{Pr} = 7.1$ for water at 20°C), $Sc = \nu / \mu$ is the Schmidt number (Sc~$10^3$), $\kappa_T$ is the molecular coefficient of kinematic thermal diffusivity, and $\mu$ is the molecular coefficient of kinematic salinity or gas diffusivity.

An instructive schematic diagram is shown in *Figure 2-1*. The logarithmic scale ranges from the diameter of a molecule to the maximum depth of the world ocean emphasizing the top millimeter of the ocean. Molecular sublayers extend from the surface to typical depths of about 1500 μm (viscous sublayer), 500 μm (thermal sublayer), and 50 μm (diffusion sublayer). There are also organic films on the sea surface.

These are of course only nominal values. The thickness of molecular sublayers depends substantially on the air-sea interaction regime. In fact, the structure of the molecular sublayers are quite complex. It depends on wind stress acting on the sea surface, on shortwave radiation absorbed in the upper millimeters of the ocean, on heat, salt, freshwater, and gas fluxes crossing

these sublayers, on gravity and capillary waves and surface films. We will consider many of these factors in detail throughout this chapter.

Section 2.1 describes the phenomenology of the viscous, thermal, and diffusion sublayers at the waterside of the air-sea interface. Intimately linked to the physical processes are the complex chemical, photochemical, and biological metamorphoses that take place in the ocean microlayer. The physics of the microlayer, and even the regime of air-sea exchanges, depend on the organics and chemical composition of surface films, and, to some extent, on the sea surface microlayer ecosystem.

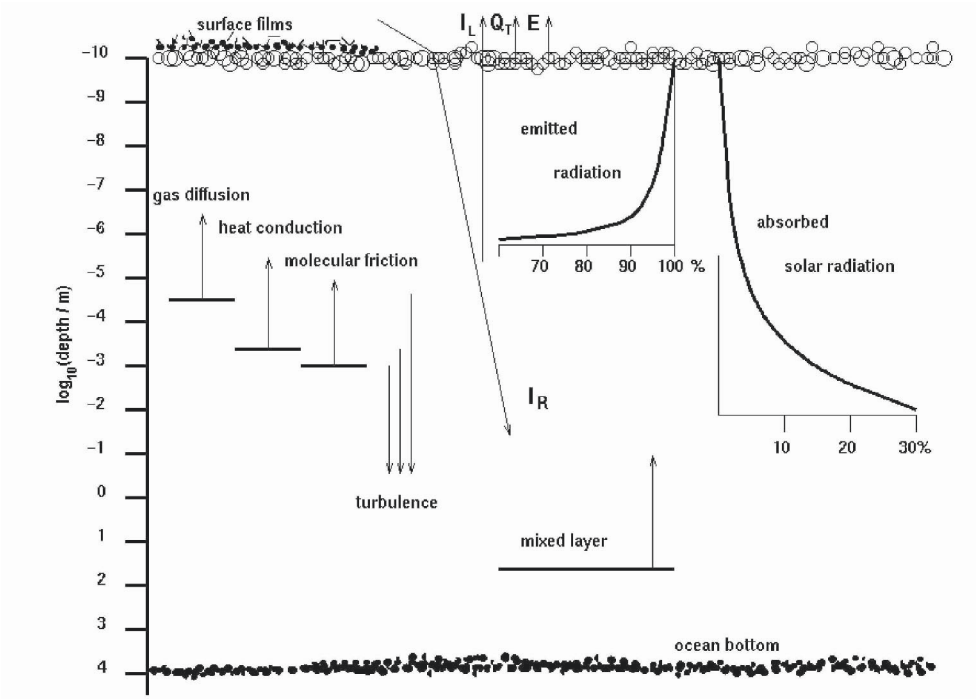


*Figure 2-1.* Schematic representation of the vertical structure of physical processes related to the sea surface microlayer (Courtesy of Peter Schlüssel, private communication).

The physics of the microlayer is discussed in detail in Section 2.2. Renewal and boundary layer models of the aqueous molecular sublayers are introduced in Section 2.3. The renewal model results in a coupled set of parameterizations describing the surface wind drift current, cool skin, and interfacial gas transfer velocity. In Section 2.4, we discuss the effect of solar radiation absorption on molecular sublayers. Section 2.5 is devoted to the effect of precipitation on the microlayer.

## 2.1 Phenomenology

### 2.1.1 Viscous sublayer

Viscous sublayers develop on both sides of the air-sea interface. To our knowledge, direct measurements of the viscous sublayer either from the oceanic or atmospheric side of the air-sea interface have never been made under real oceanic conditions. Information about the aqueous viscous sublayer of the ocean has been mainly obtained from theoretical considerations (for instance, Csanady, 1978) or laboratory studies (McLeish and Putland, 1975; Wu, 1975; and others).

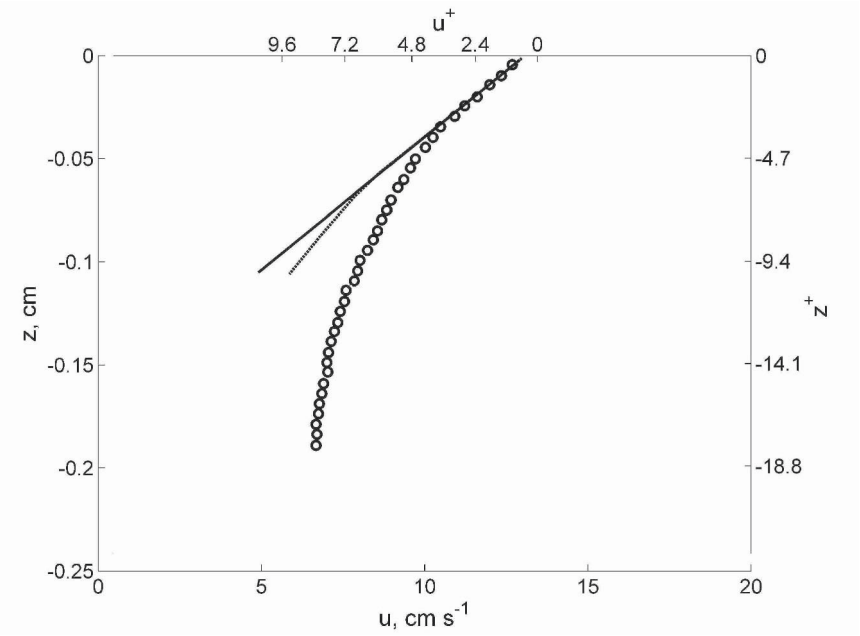


*Figure 2-2*. Velocity profile below a free water surface measured in a laboratory tank (circles). The continuous straight line fits the near-surface slope, and the curved dashed line follows the mean profile at a solid boundary. The solid boundary dependence is derived from nondimensional values by Kline et al. (1967). The nondimensional coordinates are as follows: $z^+ = zu_*/\nu$ and $u^+ = (u_0 - u)/u_*$, $u_*$ is the friction velocity in water, $\nu$ is the molecular kinematic viscosity of water, $u$ is the downwind water velocity, and $u_0$ is the downwind water velocity at the surface. Reproduced from McLeish and Putland (1975) by permission of American Meteorological Society.

*Figure 2-2* shows the velocity profile below the water surface measured for a 0.07 N m$^{-2}$ wind stress in the laboratory experiment of McLeish and Putland (1975). The slope of the near-surface velocity profile is fit with a straight line. The linear vertical profile of velocity is a distinctive feature of the viscous sublayer. The departure of the velocity profile from its linear fit

can therefore serve as an indicator of the viscous sublayer depth. It is remarkable that in dimensionless coordinates the thickness of the viscous sublayer near the free surface is approximately half of what it would be near a rigid wall. This is explained by the fact that only the vertical component of turbulent fluctuation is effectively suppressed near the free surface; as a result, turbulent eddies can penetrate closer to a free boundary than to a wall.

### 2.1.2 Thermal sublayer (cool skin)

The sea surface temperature may differ from the temperature of the underlying mixed layer due to the presence of the aqueous thermal molecular sublayer. This sublayer is also referred to as the *cool skin* of the ocean (Saunders, 1967b).

Above the interface, there is a millimeter-thick atmospheric boundary layer, where the vertical transport is also dominated by the molecular diffusion. The main temperature difference across the air-sea interface is observed in the atmospheric rather than oceanic molecular sublayer (Volkov and Soloviev, 1986).

*Figure 2-3* gives an example of the temperature profile in the upper 10 m of the ocean obtained with a *free-rising profiler* (Soloviev, 1992). For this measurement, the profiler was equipped with a high-resolution temperature probe (5 μm diameter wire sensing element). The shunting of the micro-wire probe by seawater is small due to the fact that its internal resistance was only 7 Ohms, while the area of the micro-wire surface for this thin wire is extremely small (Azizyan et al., 1984).

The vertical temperature profile shown in *Figure 2-3* was taken during nighttime. The upper part of the profile reveals an abrupt temperature change in the upper few millimeters due to the cool skin. This abrupt temperature change near the surface is associated with the cool skin of the ocean. The temperature difference across the cool skin in the example shown in *Figure 2-3* is $\Delta T = T_0 - T_b \approx$ -0.3°C, where $T_0$ is the sea surface temperature, and $T_b$ is the temperature of the bulk (diurnal mixed layer) water. The temperature gradient below 2 meters represents the remnants of the diurnal thermocline formed during the previous, daylight hours.

The temperature difference across the cool skin depends on the local regime of air-sea interaction and thus varies in space and time. Historically, much effort has been devoted to the cool skin parameterization. Saunders (1967b) initially parameterized the averaged temperature difference across the cool skin of the ocean $\overline{\Delta T}$ by ascribing a constant value to the nondimensional coefficient, $\lambda_S = c_p \rho u_* \overline{\Delta T} / (\mathrm{Pr} Q_0)$. Grassl (1976) found that $\lambda_S$ varied with wind speed. The parameter $\lambda_S$ increased from 0 for calm weather conditions to approximately 5 at moderate wind speeds.

Kudryavtsev and Soloviev (1985) explained this dependence of $\lambda_S$ on wind speed by the transition from convection to a wind-wave regime.

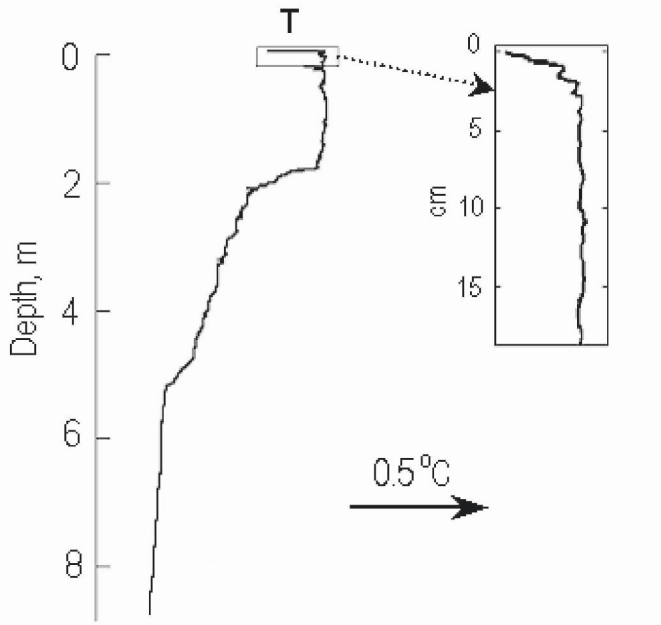


*Figure 2-3*. An "instantaneous" vertical profile of temperature in the upper ocean taken under low wind speed conditions. (After Soloviev, 1992.)

The typical temperature difference across the cool skin of the ocean is from -0.2 to -0.3°C increasing approximately two times under calm weather conditions (Horrocks et al., 2003). Under strong insolation and/or air temperature exceeding water temperature, the interfacial layer can become slightly warmer than the underlying water.

Collecting high-quality measurements of the cool skin in the open ocean is still a challenge, requiring very specialized techniques. In the oceanographic literature, there are only a few reports of direct profile measurements in the cool skin in the open ocean (Mammen and von Bosse, 1990; Soloviev, 1992; Ward and Minnett, 2001). At the same time, infrared measurement techniques have been under intensive development (Saunders, 1967b; McAlister and McLeish, 1969; Hasse, 1971; Grassl, 1976; Paulson and Simpson, 1981; Schlüssel et al., 1990 and others). As a result, most of the open ocean data on the cool skin come from infrared SST measurements. A problem of interpretation of the infrared SST measurements is that the longwave radiation reflected from clouds produces strong disturbance of the SST measurement. In order to address this problem, Grassl (1976) constructed an infrared radiometer moving the beam between the sea surface

and a seawater bath, which substantially reduced the error due to the signal reflected from clouds. TOGA COARE exploited an advanced version of Grassl's method: From 30 January to 24 February 1993, measurements were taken from the R/V *Vickers* in the western equatorial Pacific Ocean (156°E, 2°S). The skin temperature measured with this setup was accurate to 0.05°C.

Fiedler and Bakan (1997) and Minnett et al. (2001) have developed a multi-channel infrared interferometer, which does not require a reference seawater bath. This approach can provide large high quality datasets of the cool skin of the ocean.

For calculating the temperature difference across the cool skin from the infrared SST measurement it is also necessary to know the bulk water temperature below the cool skin. Unfortunately, measurements with sensors towed behind or near the ship are disturbed by the ship's wake, which may introduce substantial errors. The alternative approach is to derive the bulk water temperature from a ship's thermosalinograph, which takes in water from 3 to 5 m depth; although, a shallow diurnal or rain-formed thermocline may result in a vertical temperature gradient between the depth of the thermosalinograph intake and the cool skin layer. An appropriate temperature correction can be calculated with a diurnal mixed layer model forced with the air-sea momentum, heat, and precipitation fluxes, assuming these are available. This correction, however, may introduce outliers by itself due to errors of the model and atmospheric forcing data.

### 2.1.3 Diffusion sublayer

The near-surface molecular diffusion sublayer is a crucial element in air-sea gas exchange. The resistance to air-sea gas transfer for water-side limited gases is mainly due to the diffusion sublayer in water, which is of the order of 50 μm thick (Bolin,1960).

The diffusion sublayer associated with salinity transport has approximately the same thickness as the gas diffusion sublayer (Fedorov and Ginzburg, 1979). Under evaporative conditions, the sea surface salinity is higher than in the bulk of water, while during rainy conditions, a *freshwater skin* of the ocean is formed (Schlüssel et al., 1997).

There are no direct observations of the diffusion molecular sublayer in the open ocean because of the complexity of the microscale measurements near the moving air-sea interface. Some parameters of the aqueous diffusion sublayer can be evaluated from data on the gas transfer velocity if practically all gas concentration difference is in the ocean rather than the atmospheric diffusion sublayer. In particular, the thickness of the diffusion sublayer is defined as follows:

$$\delta_\mu = \mu \Delta C / G_0 \tag{2.4}$$

where μ is the kinematic molecular diffusion coefficient of gas, $G_0$ is the flux of property $C$ at the air-sea interface, $\Delta C = C_w - C_0$ is the is the ensemble averaged air-sea gas concentration difference in property $C$ across the diffusion sublayer, $C_0$ and $C_b$ are the averaged concentrations of property $C$ at the water surface and in the bulk (mixed layer) water respectively. Taking into account (1.50) we obtain the following relationship connecting the gas exchange coefficient and the thickness of the diffusion sublayer:

$$\delta_\mu = \mu / K_\mu . \tag{2.5}$$

### 2.1.4 Sea surface microlayer ecosystem

The sea surface is a highly productive, metabolically active interface (Hardy et al., 1997). Due to extreme conditions at the air-sea interface, the sea surface is believed to be the place where life on the Planet originated (a competing theory is that of extraterrestrial origin for life on the Earth).

Phytoplankton in the water column produces an abundance of particulate and dissolved organic material, some of which is transported to the surface either passively by buoyancy or actively by upwelling, turbulence, and bubble transport. The natural and anthropogenic compounds deposited from the atmosphere often accumulate on the ocean surface in relatively high concentrations compared to those in the water column. The abundance of organic matter at the sea surface provides a substrate for the growth of the surface-dwelling organisms, the marine *neuston*, which inhabits the sea surface microlayer (Zaytsev, 1997).

Neuston realm is a vast habitat. The distinctive physical and chemical characteristics of the sea surface can explain a highly diverse and abundant assemblage of species in the microlayer. Organisms from most major divisions of the plant and animal kingdoms either live or reproduce or feed in the surface layers (Zaitsev, 1971). Many of these species are of commercial and ecological importance. The microneuston, which may be involved in biogeochemical cycling, and neustonic eggs and larvae of commercially important fish and shellfish, are of particular interest.

*Figure 2-4* shows Hardy's (1982) conceptual model of the sea surface microlayer ecosystem. Permanent inhabitants of the surface layer often reach much higher densities than similar organisms found in subsurface waters. There are also numerous temporary inhabitants of the neuston. These are particularly the eggs and larvae of a great number of fish and invertebrate species. The latter utilize the surface during a portion of their embryonic and larval development. Some neuston can remain in the microlayer until

turbulence created by breaking waves at winds exceeding 10-15 m $s^{-1}$ disperses them (Zaitsev, 1971).

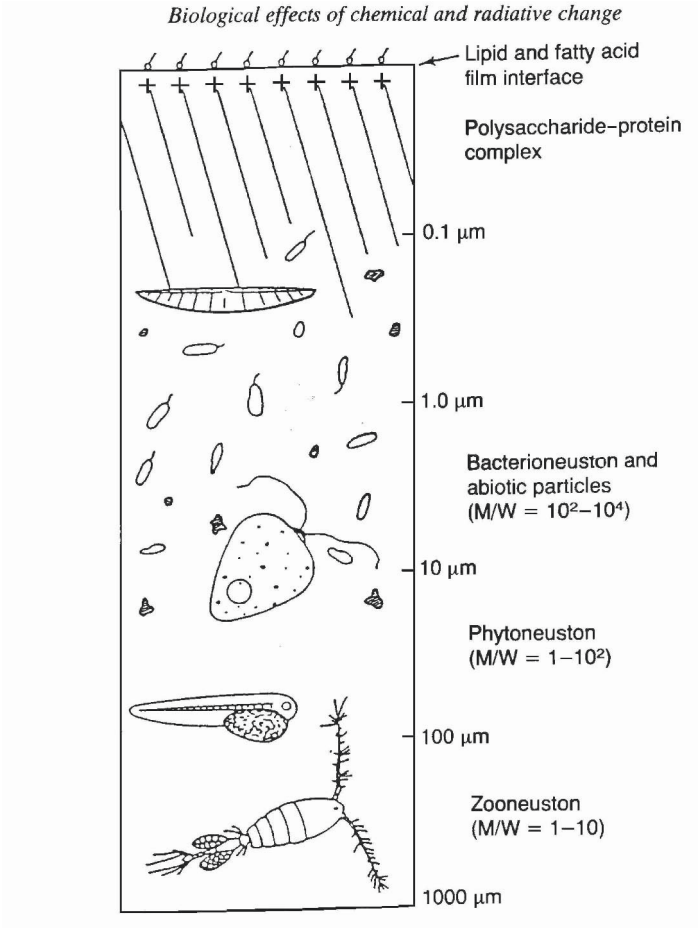


*Figure 2-4*. Conceptual model of the sea surface microlayer ecosystem. M/W = typical microlayer to water concentration ratios based on a number of studies. Reproduced from Hardy (1982) by permission of Elsevier from Progr. Oceanogr. V 11 © 1982.

### 2.1.5 Surfactants and surface films

Following Liss and Duce (1997), here we use the following terminology: A film refers to surfactant-influenced surface and a *slick* refers to a visibly surfactant-influenced surface.

Sea surface films are derived from multiple, sea and land based sources, including bulk seawater dissolved organic matter, terrestrial sources (natural and anthropogenic), and from petroleum seeps and spills (Liss et al., 1997). Surface films dissipate due to loss of material at the surface, including

microbial degradation, chemical and photo chemical processes, and loss due to absorption and adsorption onto particulates.

Under favorable physical conditions, the concentration of dissolved organic matter is sufficient to produce surface enrichments of organic matter even in oligotrophic waters, where biological productivity is low. Lifecycles of neuston organisms and phytoplankton blooms also lead to the production of the surface-active substances.

The source contribution primarily controls the chemical composition of surface films. A variety of biological, chemical and physical processes may, nevertheless, change composition, concentration, and spatial structure of the surface films and thus modify physical properties of the air-sea interface. Turbulence and diffusion, scavenging and transport by bubbles and buoyant particles effectively spread surfactants over broad areas of the ocean surface. At the same time, flow convergences associated with organized structures, upwelling events, and internal waves have tendency to localize surface-active materials on various spatial scales, ranging from a few meters to kilometers (Bock and Frew, 1993; Liss and Duce, 1997).

## 2.2 Physics of Aqueous Molecular Sublayers

The surface microlayer is subject to disturbances from near-surface turbulence (wave breaking, shear, convection, rising bubbles, spray hitting the sea surface, raindrops etc.) Breaking waves that entrain air and thereby produce whitecaps are the most intense and obvious manifestation of the turbulent disturbance. Waves may also break without entraining air and producing whitecapping. This phenomenon is associated with the free-surface boundary condition and is called *microscale* wave breaking (Banner and Phillips, 1974) or *rollers* (Csanady, 1990). Surface films on the ocean significantly complicate the physics of the microlayer due to the involvement of chemical and biological processes.

### 2.2.1 Convective and shear instability

Convection and wind-induced shear are important factors in the physics of aqueous molecular sublayers. The molecular sublayers are not stationary and continuous but intermittent in time and space. The boundary layer processes in the near-surface layer of the ocean are altered by the presence of the free surface (see Chapter 3).

Surface cooling and/or salinity increase due to evaporation initiate convection in the upper layer of the ocean. Convection as a type of hydrodynamic process has a tendency to self-organization and therefore exhibits features of organization (Section 5.8). The absorption of solar radiation or rainfall inhibits the convective instability.

With no solar radiation and precipitation effects, convective instability of a thermal molecular sublayer occurs at low wind speeds. Under moderate and high wind speeds, the molecular sublayers are controlled by the wind stress and surface waves.

Laboratory experimentation involving visualization techniques helps to understand the physics of molecular sublayers. *Figure 2-5*a shows infrared images of the water surface under convective conditions. The mean temperature is subtracted in the images. White represents temperatures above the mean, and black represents temperatures below the mean. The full range of shades corresponds to 2°C. The spatial and temporal structures observed in the surface temperature field are obviously linked to the near-surface turbulence. The thin cool sheets (black on infrared images) are the convergences, while the wide areas of warm water (white) are divergences. These processes are indicative of surface renewal events. Note a pronounced change in the surface structures from light winds to moderate winds (*Figure 2-7*b).

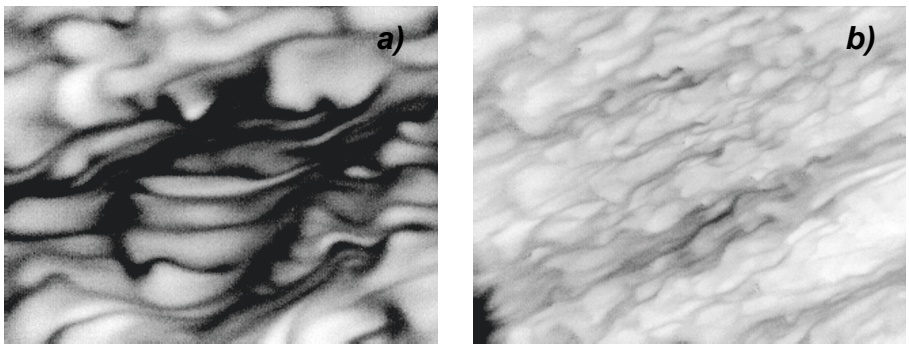


*Figure 2-5*. Infrared images of the surface taken in the RSMAS Air-Sea Interaction Saltwater Tank Facility for: (a) light and (b) moderate winds with an imposed air-water temperature difference of 10°C. The water is warmer than the air and light areas are warmer water. (Courtesy of Prof. Mark Donelan, private communication.)

In a laboratory experiment, Syalor et al. (2002) studied the cross-correlation between surface temperature and the vertical component of subsurface velocity in the regime of free convection and found practically zero time lag between the surface and subsurface events. In the Syalor et al. (2002) experiment, the event occurring at the surface would require a delay on the order of 20 s to reach 2 cm depth via turbulent transport. Spangenberg and Rowland (1961), Katsaros et al. (1977), and Volino and Smith (1999) previously reported falling sheet structures during evaporative convection penetrating to several cm depth and migrating significant horizontal distances across the surface before disappearing. As structures pass over the measurement location, a sudden change in velocity and temperature

resembling bursting event should almost simultaneously be observed at the surface and at 2 cm.

Observations in the open ocean appear to be consistent with the idea of periodic water renewal in near-surface molecular sublayers. *Figure 2-6*a shows a temperature profile in the upper 10 m obtained with a free-rising profiler under conditions of nighttime convective cooling and low wind speed. The upper part of the temperature profile marked by a rectangle *B* in *Figure 2-6*a is shown in more detail in *Figure 2-6*b. The simultaneous conductivity profile is also shown. The upper 2 mm of the conductivity profile are removed because of the disturbance to the conductivity measurement in the vicinity of the air-water interface.

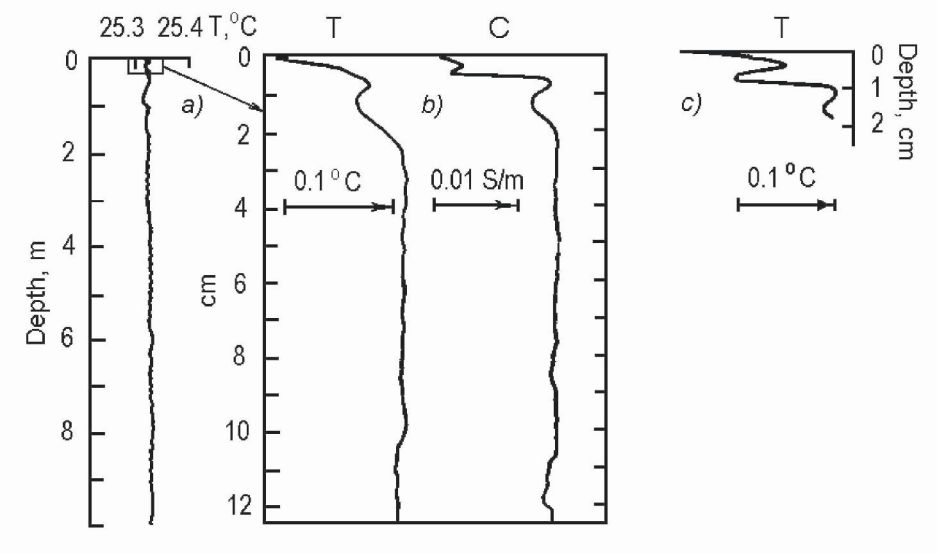


*Figure 2-6*. (a, b) Vertical structure of the near-surface layer of the ocean from measurements with a free-rising profiler in the equatorial Atlantic made at night (02:57 LT) under conditions of low wind speed ($U_{10}$ = 3 m $s^{-1}$) and intense cooling of the ocean surface ($Q_0$ = 170 W $m^{-2}$) in comparison (c) with the data from laboratory experiment of Ginzburg et al. (1977). Here: *T* is the temperature, and *C* is the conductivity of seawater. (After Soloviev and Vershinsky, 1982.) Reprinted with permission of Elsevier from *Deep-Sea Res.* 29, 1437-1449. © 1982.

In the upper few cm the temperature (and conductivity) profile is characterized by inversion, which is presumably caused by convection. According to Katsaros et al. (1977), the temperature inversions in the upper few cm can be due to passage of discrete convective elements (thermals). *Figure 2-6*c shows a temperature profile obtained near the water surface in a laboratory experiment conducted by Ginzburg et al. (1977) in the free convection regime.

The conductivity sensor in this experiment had higher spatial resolution (better than 1 mm in vertical direction) than the temperature sensor and

therefore revealed more detail (*Figure 2-6*b). According to estimates by Soloviev and Vershinsky (1982), in the nighttime convective mixing regime (no precipitation or insolation) the conductivity profiles in the near-surface layer of the ocean mainly depend on the temperature rather than salinity variations. Frictional scales of the turbulent temperature and salinity fluctuations are

$$T_* = \frac{Q_0}{c_p \rho \kappa u_*} \text{ and } S_* = \frac{Q_E S_0}{\rho \kappa u_* L}, \tag{2.6}$$

respectively, $S_0$ is the average surface salinity, $L$ is the latent heat of vaporization, $Q_E$ is the latent heat flux, $c_p$ is the specific heat capacity of water, and κ is the von Karman constant.

For inhomogeneities exceeding the Kolmogorov internal length scale of turbulence (2.2), the ratio of the temperature and salinity scales expressed in terms of the equivalent conductivity changes is as follows:

$$\frac{\Delta C_T}{\Delta C_S} = \frac{\gamma_T T_*}{\gamma_S S_*} = \frac{\gamma_T}{\gamma_S} \frac{L Q_0}{c_p S_0 Q_E} \approx 25, \tag{2.7}$$

where $\gamma_T = \left(\partial C / \partial T\right)_{S,p}$, and $\gamma_S = \left(\partial C / \partial S\right)_{T,p}$. The estimates of the Kolmogorov length scale for temperature (2.2) and salinity (2.3) are $\eta_T \approx 0.7$ mm and $\eta_D \approx 0.07$ mm respectively. These estimates are made for the conditions of experiments reported by Soloviev and Vershinsky (1982) under an assumption that the turbulence is driven by convective instability. Since the shear and surface wave instability can only add to the turbulence dissipation level, these are the upper bound estimates of $\eta_T$ and $\eta_D$. According to (2.7), the contribution of temperature to the conductivity changes during nighttime convection well exceeds that of salinity. The high-resolution conductivity profiles can therefore be interpreted in terms of temperature.

*Figure 2-7* shows a series of conductivity profiles in the depth range from 2 mm to 20 cm obtained during nighttime. The time interval between successive profiler was from 5 to 9 minutes; the ship drifted for tens of meters.

For the conditions of this experiment, an estimate for the flux Rayleigh number defined according to Foster (1971) is $Ra_f = \alpha_T g Q_0 h^4 / (\kappa_T{}^2 \nu) \approx 10^{12}$, where $h$ is the mixed layer depth (equal to 50 m in this estimate). Free convection at very large Rayleigh numbers is intermittent in space and time (Turner, 1973). Howard (1966) formulated a phenomenological theory of the

convection at large Rayleigh numbers that represented turbulent convection as the following cyclic process: The thermal boundary layer forms by diffusion, grows until it is thick enough to develop convective instability, and is destroyed by convection, which in turn dies down once the boundary layer is destroyed. Then the cycle begins again.

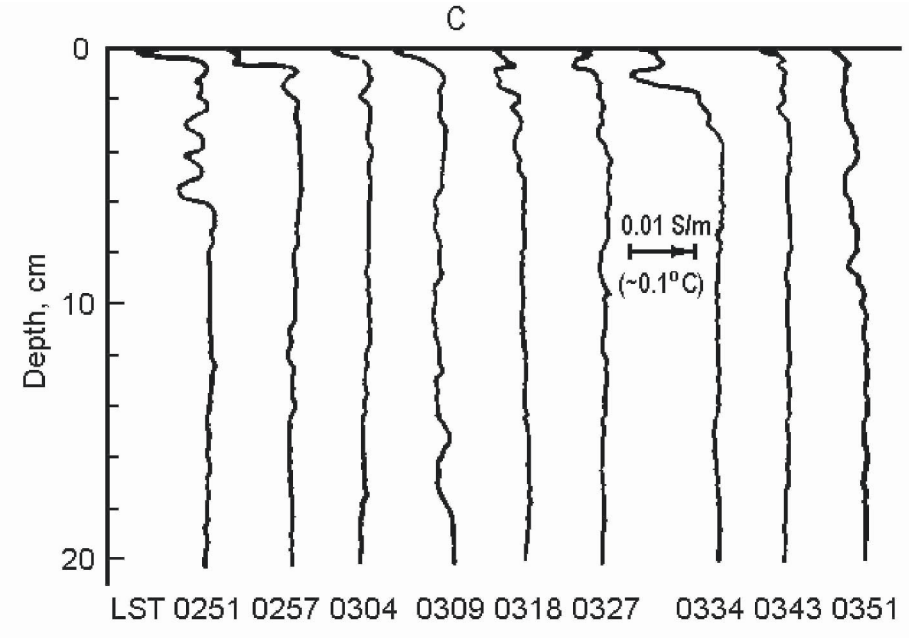


*Figure 2-7*. Vertical profiles of conductivity observed during night under convectively unstable conditions near the surface according to measurements in the equatorial Atlantic. The time of observation is marked (LST) under each profile. Wind speed $U_{10}$ = 3 m $s^{-1}$, net surface heat flux $Q_0$ = 170 W $m^2$. The scale of conductivity is shown in the equivalent temperature units under the assumption of constant salinity. (After Soloviev and Vershinsky, 1982.) Reprinted with permission of Elsevier from *Deep-Sea Res.* 29, 1437-1449 © 1982.

The convective period at the ocean surface is of the order of tens of seconds only; the horizontal length scale of the convective cells is about 1 cm (Foster, 1971). The vertical profiles shown in *Figure 2-7* are consistent with Howard's theory in general. Since the profiling time interval greatly exceeded the intermittency period of the convection, in interpreting the results shown in *Figure 2-7* it is necessary to assume that there is no correlation between any two successive temperature profiles in this series of measurements. Following Howard's (1966) phenomenology, the profiles obtained at 02:51, 02:57, 03:18, 03:27, and 03:34 LST can be interpreted as the stage of destruction of the cold surface sublayer by a discrete convective element (thermal). The profiles obtained at 03:04, 03:09, 03:43, and 03:51 LST can be related to the stage of dissipation of the thermal and beginning

of the next cycle by the formation of the unstably stratified thermal sublayer due to the molecular heat diffusion.

The observations shown in *Figure 2-6* and *Figure 2-7* provide an insight into the renewal process near the surface in convectively unstable conditions. In particular, the data is consistent with the concept of intermittent convection in the near-surface layer, which has found its application for the modeling of the aqueous molecular sublayers.

### 2.2.2 Microscale wave breaking

Microscale wave breaking has been the subject of several theoretical, laboratory, and modeling studies. Laboratory wind-wave studies of Okuda (1982) and Ebuchi et al. (1987) revealed a high-vorticity region near the crests of gravity waves with capillary ripples generated ahead of the crests. Longuet-Higgins (1992) identified the origin of vorticity within this surface roller as accompanying parasitic capillaries, which themselves generate fluid rotation (i.e., vorticity) via the surface tension effect (Yeh, 1992; 1995). Rollers (Longuet-Higgins, 1992), breaking wavelets (Csanady, 1990), steep wind waves accompanied by a high-vorticity layer near the crest (Okuda, 1982), and microscale breaking (Banner and Phillips, 1974) appear to be descriptions of the same phenomena.

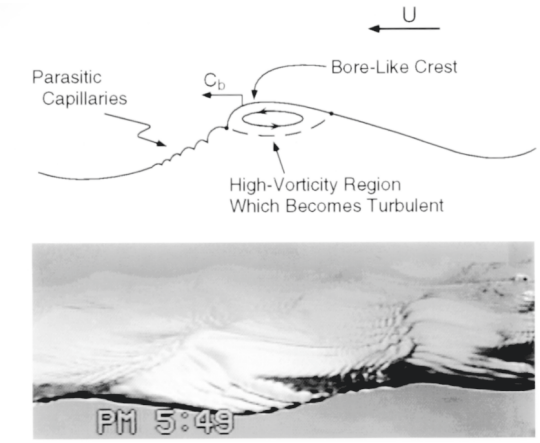


*Figure 2-8*. The characteristic feature of a microscale breaking wave is the bore-like crest with parasitic capillary waves riding along the forward face. Here: $U$ is the wind speed and $C_b$ is the crest speed of the breaking wavelet (After Longuet-Higgins, 1992). Bottom: photograph of a breaking wavelet with a wavelength of roughly 0.1 m (adapted from Jessup et al., 1997).

Microscale breaking waves are typically 0.1-1 m in length and a few centimeters in amplitude. The schematic diagram and the photo from a laboratory experiment shown in *Figure 2-8* illustrate the typical features of

microscale wave breaking. Note the bore-like structure at the crest accompanied by parasitic capillary waves distributed along the forward face. Microscale wave breaking is far more widespread than whitecapping. Absence of air entrainment makes the microscale breaking difficult to identify visually. The microscale wave breaking, however, produces the convergence of flow that leads to intense renewal of surface water. The process of surface renewal substantially determines properties of the aqueous molecular sublayers under moderate wind speed conditions (Csanady, 1990).

The widespread occurrence of microscale wave breaking suggests that its cumulative effect on the fluxes of heat and gas across the air-sea interface is significant (Csanady, 1990; Banner and Peregrine, 1993; Soloviev and Schlüssel, 1994; Donelan, 1995; Melville, 1996).

### 2.2.3 Wave breaking and whitecapping

The aqueous molecular sublayers at the air-sea interface are associated with the action of the tangential wind stress on the sea surface. The tangential component represents only a part of the total wind stress that is transferred from the atmosphere to the ocean. Under high wind speeds, a significant portion of the momentum is transferred to surface waves. Surface waves periodically break destroying the aqueous viscous sublayer as well as the thermal and diffusion sublayers. The molecular sublayers regenerate between wave breaking events.

The ratio of the tangential wind stress $\tau_t$ controlling the aqueous viscous sublayer to the total air-sea momentum flux $\tau_0$ is as follows (Soloviev and Schlüssel 1996):

$$\tau_t = \tau_0 \left(1 + Ke / Ke_{cr}\right)^{-1}, \tag{2.8}$$

where

$$Ke = u_*^3 / \left(g\nu\right). \tag{2.9}$$

is the *Keulegan number*, which is a fundamental parameter in the dynamics of free interfaces (Csanady, 1990). At low Keulegan numbers, $Ke << Ke_{cr}$ interfacial instabilities are suppressed by molecular viscosity.

Formula (2.8) reflects the transformation of a substantial part of the surface wind stress to form drag and whitecapping at high wind speeds (valid for stationary conditions only). *Figure 2-9* illustrates this dependence for $Ke_{cr}$ = 0.18 in comparison with the data from the Banner and Peirson (1998) laboratory experiment. The theoretical curve is in reasonably good agreement with the experimental data taking into account that the estimate,

$Ke_{cr}$ = 0.18, had been independently derived by Soloviev and Schlüssel (1994) from the wind speed conditions for which energy containing surface waves first start breaking.

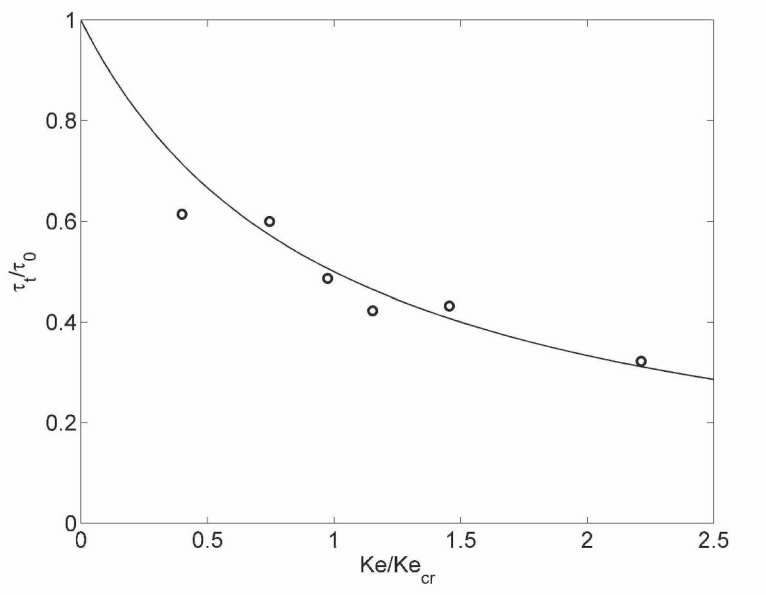


*Figure 2-9*. Transformation of the surface wind stress to form drag and whitecapping for high wind speeds. The line is equation (2.8); the circles represent the experiment of Banner and Peirson (1998). Adapted from Soloviev and Schlüssel (2002) by permission of American Geophysical Union.

### 2.2.4 Capillary wave effects

The presence of capillary waves on the sea surface is a characteristic feature of air-sea interaction. In particular, parasitic capillaries accompany microscale wave breaking, which is one of the principle mechanisms controlling the molecular sublayers, as discussed in the previous section. The overall knowledge about the role of capillary waves in air-sea molecular sublayers and exchanges is still far from a satisfactory level.

Csanady's (1990) theoretical analysis suggests that the capillary waves by themselves do not contribute substantially to the convergence in the aqueous molecular sublayer. For the molecular sublayers the surface within capillary waves still appears to be smooth from the waterside, unless there are substantial divergences occurring in parts of the wavelets, for instance as produced by the rollers on top of short gravity waves

Wu (1996) refers to laboratory measurements reporting a rapid increase in the gas transfer velocity coinciding with the onset of capillary waves on the water surface (Kanwisher, 1963; Broecker et al., 1978). After a critical discussion of the laboratory findings, Wu (1996) proposed the idea of a

sudden change of the gas transfer velocity due to the direct influence of the steep capillary waves on the aqueous molecular sublayer.

Soloviev and Schlüssel (1998) proposed an alternate explanation of the Wu (1996) results: The change of surface roughness due to capillary waves could directly influence the flow on the airside of the interface, thus modifying the wind stress. The sudden change could be merely a reaction to enhanced roughness modifying the wind field rather than a direct impact of the ripples on the aqueous molecular sublayer. The change of roughness could result in a sudden increase of the friction velocity and hence in the intensification of the air-water gas exchange. Another interpretation of the Wu (1996) results points to the connection between microscale wave breaking (rollers) and the parasitic capillaries (Soloviev and Schlüssel 1998). The rollers, if present in the Wu (1996) experiment, would result in a significant effect on the air-sea exchange. In any case, this is a rather indirect influence of capillary waves on the diffusion sublayer.

There is nevertheless evidence of a direct impact of the capillary waves on air-sea exchange. Saylor and Handler (1997) experimented in a small laboratory tank with capillary waves from 2.62 to 3.62 mm wavelength (which corresponds to 400 to 200 Hz frequencies) and found an almost two orders of magnitude increase in the interfacial gas transport rate as the wave slope was increased from zero to 0.2 m $m^{-1}$. In this work, small vertical vibration of the tank generated capillary waves via the Faraday instability. The Saylor and Handler (1997) experiment provides remarkable evidence that capillary waves can greatly increase fluxes across the air-water interface. Applicability of these results to the real ocean, however, is not completely clear since the Faraday waves differ from the parasitic capillaries observed in a wind/wave tank or on the open ocean surface. In natural conditions, the capillary waves of these frequencies (from 200 to 400 Hz) dissipate quickly and may only cover a very small percentage of the sea surface, while in the tank waves excited via the Faraday instability completely covered the water surface.

As seen on the ocean surface, capillary waves indeed appear suddenly when the wind speed exceeds some threshold level. The wind speed has not only a mean but also a variance that makes the sea surface patchy with respect to the coverage with capillary waves (the so-called “cats paws”). As the wind speed increases, the area covered by ripples gradually increases so that the surface averaged over a larger area should demonstrate a smooth transition from no capillary waves to full coverage without an obvious “jump”. This is relevant to the mean gas transfer (i.e., averaged over some space and time intervals). The sudden increase should only be observed on a small scale that might be relevant to fluctuations but not to the mean exchange.

The sudden increase in gas transfer has been observed mainly (if not exclusively) in laboratory studies (see for instance Fedorov and Ginzburg,

1988). The natural variance of the wind speed, and the implied variance of the surface patches covered with capillaries, does not occur in the laboratory airflow. This is an important difference between the tank airflow and the open-ocean wind pattern; it is basically because timescales of wind velocity fluctuations in the laboratory and in the field conditions are very different (Soloviev and Schlüssel, 1998).

Finally, as summarized by Cox (2001), several processes may be at work:

1) Convergence/divergence of orbital motions in waves disturbs the boundary layer at the interface where fluxes are controlled by molecular diffusion.

2) The decay of capillary wave trains accompanying rollers delivers horizontal momentum to the water in patches corresponding to the locations of the wave trains. This patchy driving force can induce turbulent motions of a size corresponding to the length of the wave train.

3) Short gravity waves and capillaries dramatically increase the momentum transferred to the ocean via increased sea surface roughness, thus enhancing near-surface mixing.

In addition, the properties of capillary waves depend considerably on the presence of surfactants and surface films.

### 2.2.5 Chemical and photochemical reactions in the sea surface microlayer

Complex chemical, photochemical, and biological metamorphoses take place in the ocean microlayer. Photochemical and chemical reactions rapidly developing within the microlayer could produce a variety of feedbacks to the biological and physical processes (Plane et al., 1997). For example, elevated levels of highly reactive intermediate products produced in the microlayer could represent a ‘reaction barrier’ to the transport of gases and some chemicals across the air-sea interface. Certain photochemical reactions destroy or produce surfactants modifying surface films; altered surface waves from the gravity-capillary band then affect gas exchange rates. Many other reactions occur within the microlayer, in particular those increasing or reducing the surface concentrations of certain gases relative to their bulk water concentrations, as well as those influencing the types and the distributions of microlayer materials ejected to the atmosphere during bubble bursts and delivered to the deep ocean by coalescent particles.

### 2.2.6 Biological and anthropogenic influences

In this book, we mainly focus on the physics of aqueous molecular sublayers. The physics, chemistry and biology of the sea surface,

nevertheless, are closely related. For example, phytoplankton in the water column produces particulate organic matter and a variety of biogenic chemicals and gases, which then rise to the surface where they enter the microlayer (Hardy et al., 1997). This organic matter modifies surface films, which affects the gravity-capillary waves and, thus, the air-sea gas exchange on the global scale.

Increasing pollution of the ocean threatens marine neuston and represents one of the significant factors accelerating global ecological changes. Anthropogenic enrichment of the sea surface impacts natural biochemical processes in the ocean microlayer affecting the air-sea $CO_2$ exchange with possible consequences for global climate (Hardy et al, 1997).

On the other hand, iron (the element which limits primary biological productivity) is supplied to the ocean via the surface microlayer. The increase of productivity due to an increased iron supply stimulates the ocean's "biological pump" increasing the $CO_2$ uptake by the ocean and potentially reducing the global warming (Wu et al., 2003).

The mechanical influence of disturbances produced by the swimming motion of small zooneuston organisms perhaps may also contribute to the microlayer structure at some level (Gladyshev, 1997). Flying fish, birds, and ships disturb the microlayer significantly, though only locally.

### 2.2.7 Effects of surface films

Surface films are an important part of the surface microlayer. Air-sea exchanges depend on film properties, especially under low wind speed conditions. The presence of surface films on the ocean is one of the factors leading to uncertainty in the existing air-sea exchange parameterizations.

The effects of surface films are dependent on surfactant type, concentration, and wind-wave regime. Breaking waves and near-surface flow convergences substantially erode the surface films above wind speeds of 5 - 6 m $s^{-1}$. Surface films are also fragmented by rain.

Surface films can affect air-sea exchanges through static and dynamic mechanisms (Liss, 1983). The static mechanism results from the physical barrier provided by the film; it requires the presence of organized (condensed, solid) surfactant films that can easily be reproduced in the laboratory but hardly survive typical oceanic conditions of wind and waves. The surfactant films or slicks with high surface concentrations of organic material occupy only a small fraction of the global ocean surface. The dominant point of view among ocean chemists is that surfactant concentrations are quite low in the open ocean. The static mechanism thereby is not of primary importance for typical open ocean conditions (Liss and Duce, 1997). The dynamic mechanism is more important in the ocean, because it can be effective even with relatively low surfactant concentrations.

The dynamic mechanism relates to the viscoelastic properties of surface films (Frew, 1997). Non-zero viscoelasticity modifies the surface boundary conditions, which affects hydrodynamic processes at the air-sea interface. *Figure 2-10* shows infrared images of clean and surfactant covered water surfaces obtained in convectively unstable conditions. The spatial scale of the convective structures dramatically changes when surfactant is present on the water surface compared to a clean surface. The surfactant film inhibits very fine structures and emphasizes larger-scale motions, some of which can be vortical.

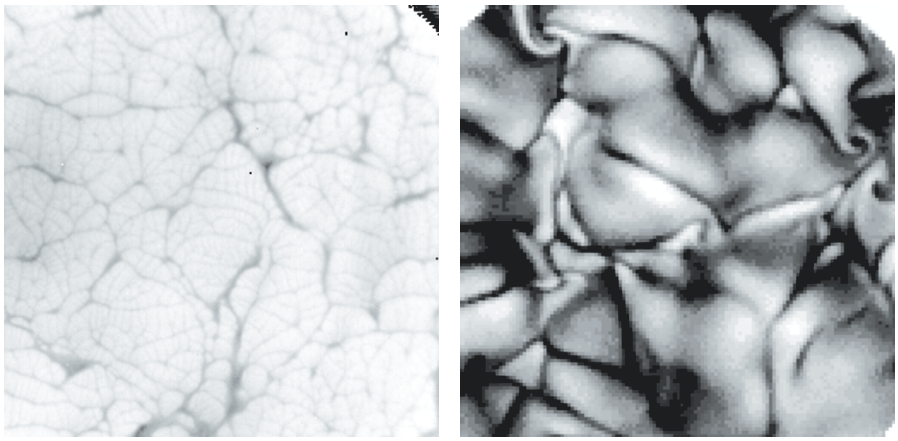

*Figure 2-10*. Infrared images of sea temperature under convective conditions for clean (left subplot) and surfactant covered (right subplot) surface for a heat flux of 407 W $m^{-2}$. The mean temperature is subtracted in the images so that white represents temperatures above the mean and black represents temperatures below the mean. The dynamic range of the image is approximately 1 K. Reused with permission from K.A. Flack, J. R. Saylor, and G. B. Smith, *Phys. Fluids* 13, 3338-3345. © 2001 AIP.

Surface films suppress the dependence of surface tension on temperature. The temperature dependence leads to circulations driven by horizontal temperature gradients, referred to as the Maragoni effect (Katsaros, 1980). Horizontal temperature gradients are produced by adjacent but phase lagged surface renewals. Calculations of the Maragoni effect for typical temperature gradients produced by the surface renewals show that under low wind speed conditions the renewal time would be reduced by orders of magnitude in the case of totally film-free water surfaces. This is not observed in the ocean because under natural conditions the sea surface is always covered by surface active agents that diminish the temperature dependence of the surface tension to negligible values. Although the rain fragments surface films, there are observations suggesting that even in the case of intense rain the surface films are not completely removed (Baier et al., 1974).

Dynamic effects are also due to the surface tension itself, which modifies the length and velocity scales of near-surface turbulence, inhibits wave

growth (especially capillaries), and enhances wave energy dissipation. Laboratory and field measurements show that the surface tension can be reduced by up to 60% due to surface films (Baier, 1972; Huhnerfuss, 1977).

Removal of surface films by convection, rain, near-surface shear, and breaking waves affects hydrodynamic processes at the air-sea interface, especially the capillary wave field, which substantially determines the surface roughness and thus air-sea exchanges. This process has a dual effect on the gravity-capillary wave field: It damps waves due to increased turbulence, and it enhances waves due to fragmentation and dissipation of surface films.

The lack of in situ measurements of the viscoelastic properties of films under various ocean regimes and particularly under different forcing conditions, limits the direct estimates of the global surface film effects on air-sea exchange. There are, however, indications that this uncertainty can be largely reduced if the mean square wave slope due to capillary-gravity waves is used rather than wind speed (Frew, 1997). Glazman and Greysuku (1993) demonstrated the correlation between the surface wind stress and the sea surface roughness associated with capillary-gravity waves detected by backscattering from altimeters. This means that surface films may have less effect on the air-sea exchange parameterizations that are derived in terms of the mean square wave slope or friction velocity rather than in terms of the wind speed.

## 2.3 Modeling Molecular Sublayers during Nighttime Conditions

Conceptual models of the aqueous molecular sublayers can be divided into two classes: surface renewal models and boundary layer models. In renewal models, the properties of molecular sublayers depend on the surface *renewal time*. The renewal time is then related to the environmental parameters causing hydrodynamic instabilities that control the properties of molecular sublayers. Boundary-layer models are based on the quasi-stationary representation of boundary-layer processes. Below we describe these modeling approaches in detail.

### 2.3.1 Dimensional analysis

Dimensional considerations can provide initial insight into the dynamics of aqueous molecular sublayers. Here, we ignore the bubble and droplet production in whitecaps and hence account for only interfacial (direct) heat, mass, and momentum transport. In the case of stationary meteorological and wave conditions, the following set of functional dependences can be formulated:

$$\overline{\Delta u} = function\left(u_*, q_0, \alpha_T, g, \nu, \kappa_T, h\right) \tag{2.10}$$

$$\overline{\Delta T} = function\left(u_*, q_0, \alpha_T, g, \nu, \kappa_T, h\right) \tag{2.11}$$

$$K_\mu = function\left(u_*, q_0, \alpha_T, g, \nu, \mu, \kappa_T, h\right) \tag{2.12}$$

where $\Delta u = u_0 - u_b$ is the velocity difference across the aqueous viscous sublayer, $u_b$ the magnitude of the bulk (mixed layer) horizontal velocity, $u_0$ is the magnitude of the sea surface velocity; $\Delta T = T_0 - T_b$ is the temperature difference across the cool skin, $T_0$ is the sea surface temperature, and $T_b$ is the temperature of the bulk (mixed layer); $K_\mu$ is the gas transfer velocity defined by equation (1.50); $q_0 = Q_0 / \left(c_p \rho\right) = \left(Q_T + Q_E + I_L\right) / \left(c_p \rho\right)$ is the scaled net heat flux at the sea surface, $Q_T$ is the sensible heat flux, $I_L$ is the net longwave irradiance, $Q_E$ is the latent heat flux; $\alpha_T$ is the coefficient of thermal expansion of water, $g$ is acceleration due to gravity, $\nu$ is the kinematic molecular viscosity, $\kappa_T$ is the thermal molecular conductivity, $\mu$ is the coefficient of molecular gas diffusion; and $h$ is the depth of the upper ocean mixed layer.

Since the transport across molecular sublayers is intermittent, functional dependences in (2.10)-(2.12) are formulated for ensemble-averaged parameters. These relationships take into account the influence of thermally driven convection, wind-induced turbulence, and surface gravity waves on molecular sublayers. The effects of precipitation and solar radiation are ignored here but considered elsewhere in this chapter.

Choosing the friction velocity ($u_*$) instead of wind speed reduces the uncertainty caused by surface films (see discussion at the end of the previous section). The functional connection between the sea surface roughness associated with capillary-gravity waves and the wind stress ($\tau_0 = \rho u_*^2$) also simplifies the application of observational and theoretical results to remote sensing applications. Unfortunately, the replacement of wind speed with friction velocity does not solve the problem of surface films completely, because the experimental friction velocities are often determined from wind speed measurements and a bulk flux algorithm, normally ignoring any surface film effects.

A standard dimensional analysis of functional dependences (2.10)-(2.12) leads to the following dimensionless relations,

$$\Delta\overline{u} / u_* = f_u\left(Rf_0, Ke, \mathrm{Pr}, Ra_f\right), \tag{2.13}$$

$$\Delta\overline{T} / T_* = f_T\left(Rf_0, Ke, \mathrm{Pr}, Ra_f\right), \tag{2.14}$$

$$K_\mu / u_* = f_C\left(Rf_0, Ke, \mathrm{Pr}, Sc, Ra_f\right), \tag{2.15}$$

where $T_* = q_0 / u_*$; $f_u$, $f_T$, and $f_C$ are non-dimensional functions of their non-dimensional arguments: $\mathrm{Pr} = \nu / \kappa_T$ is the Prandtl number, $Sc = \nu / \mu$, $Ra_f = -\alpha_T g q_0 h^4 / \left(\nu \kappa_T{}^2\right)$, $Rf_0 = \alpha_T g q_0 \nu / u_*^4$ and $Ke = u_*^3 / \left(g\nu\right)$ (we will identify the last two numbers a little bit later.)

In the upper ocean the Raleigh number $Ra_h$ is usually very large. It is well known that in a fully developed turbulent flow, parameters of a molecular boundary layer no longer explicitly depend upon the external scale of the flow. It has been customary in such cases to hypothesize self-similarity for the $Ra_h$ number; this dimensionless number respectively drops out of the number of determining parameters. Dimensionless relationships (2.13)-(2.15) reduce to

$$\Delta\overline{u} / u_* = F_u\left(Rf_0, Ke, \mathrm{Pr}\right), \tag{2.16}$$

$$\Delta\overline{T} / T_* = F_T\left(Rf_0, Ke, \mathrm{Pr}\right), \tag{2.17}$$

$$K_\mu / u_* = F_C\left(Rf_0, Ke, \mathrm{Pr}, Sc\right), \tag{2.18}$$

where $F_u$, $F_T$, and $F_C$ are the universal functions of non-dimensional arguments $Rf_0$, $Ke$, Pr, and $Sc$ (in case of the gas transfer velocity).

Parameters *Sc* and Pr entering (2.16)-(2.18) are the Schmidt and Prandtl numbers respectively, which are well known from classical boundary layer problems. Two other dimensionless numbers, $Rf_0$ and *Ke*, are less known but substantially determine the physics of the aqueous molecular sublayers at the air-sea interface.

Parameter $Rf_0$ proposed by Kudryavtsev and Soloviev (1985) determines the transition from convective to shear instability of aqueous molecular sublayers. From the definition of the flux Richardson number in the near-

surface layer of the ocean $Rf = \alpha_T g q_0 \rho / \left( \tau_{xz} \partial u / \partial z + \tau_{yz} \partial v / \partial z \right)$ and from the expression for the momentum flux within the viscous sublayer $\tau_{xz} = \tau_{x0} = \rho \nu \partial u / \partial z$ and $\tau_{yz} = \tau_{y0} = \rho \nu \partial v / \partial z$ (also using relation $\tau_0 = \rho u_*^2 = \left( \tau_{x0}^2 + \tau_{y0}^2 \right)^{1/2}$), the following expression for the flux Richardson number in the viscous sublayer follows:

$$Rf \Big|_{-z<\delta_\nu} = \alpha_T g q_0 \nu / u_*^4 = Rf_0 , \tag{2.19}$$

where $\delta_\nu$ is the thickness of the viscous sublayer. Since $Rf_0$ appears to be the surface asymptote of *Rf*, Kudrayvtsev and Soloviev (1985) named this parameter the *surface Richardson number*. For convectively unstable conditions $Rf_0$ is negative because $\alpha_T q_0 < 0$.

Parameter *Ke* determines the transition from micro-scale breaking to whitecapping at the air-sea interface. Csanady (1990) named this parameter the *Keulegan number*. As emphasized in Section 2.2.3, it is a fundamental parameter in the dynamics of free interfaces.

Specification of dependences (2.16)-(2.18) is possible within the framework of physical models.

### 2.3.2 Renewal model

The renewal concept follows from the idea of intermittent transport of properties across molecular sublayers. Kim et al. (1971) found that the turbulent momentum transport and production in a wall layer take place intermittently in time and space through small-scale bursting motions.

The renewal model developed by Liu and Businger (1975) capitalized on the Kim et al. (1971) result and considered intermittent transport of properties across molecular sublayers. Liu and Businger (1975) developed a method for calculation of average temperature profiles in molecular sublayers by assuming that the sublayers undergo cyclic growth and subsequent destruction. Kudryavtsev and Soloviev (1985) parameterized the transition from free to forced convection in the cool skin using the surface Richardson number $Rf_0$ as the determining parameter. Soloviev and Schlüssel (1994) incorporated a Keulegan number (*Ke*) dependence for high wind speed conditions and developed a coupled parameterization for the temperature difference across the cool skin of the ocean and the air-sea gas transfer velocity.

Further developing the surface renewal model, let us consider a fluid element adjacent to the sea surface. Initially, it has a uniform velocity $u_w$, temperature $T_w$, and concentration of a scalar property $C_w$ equal to the

corresponding bulk-water values. As the fluid element is exposed to the interface, the appropriate molecular diffusion laws (1.6), (1.10), and (1.12) govern the velocity ($\Delta u$) and temperature ($\Delta T$) differences, and the interfacial gas flux ($G_o$). Under assumption of horizontal homogeneity, no insolation and no rain, one-dimensional molecular diffusion laws are as follows:

$$\frac{\partial u}{\partial t} = \frac{\partial}{\partial z}\left( \nu \frac{\partial u}{\partial z} \right), \tag{2.20}$$

$$\frac{\partial T}{\partial t} = \frac{\partial}{\partial z}\left( \kappa_T \frac{\partial T}{\partial z} \right), \tag{2.21}$$

$$\frac{\partial C}{\partial t} = \frac{\partial}{\partial z}\left( \mu \frac{\partial C}{\partial z} \right). \tag{2.22}$$

The classic error-function integral solutions of equations (2.20)-(2.22) result in the following dependences:

$$\Delta u\left(t\right) = 2\pi^{-1/2}\left(t/\nu\right)^{1/2} \tau_t / \rho\,, \tag{2.23}$$

$$\Delta T\left(t\right) = -2\pi^{-1/2}\left(t/\kappa_T\right)^{1/2} q_0\,, \tag{2.24}$$

$$G_0\left(t\right) = \pi^{-1/2}\left(t/\mu\right)^{-1/2} \Delta C\,, \tag{2.25}$$

where $\Delta u\left(t\right) = u_0\left(t\right) - u_w$, $\Delta T\left(t\right) = T_0\left(t\right) - T_w$, $t$ is the elapsed time, vertical coordinate $z$ is related to the instantaneous position of the sea surface (uncertain during wave breaking events), and $\pi$ =3.14. Note that in (2.23)-(2.24) the evolutions of the velocity and temperature differences are considered under conditions of constant tangential stress $\tau_t$ and scaled heat flux $q_0$ respectively, while in (2.25) the gas flux evolution is considered under conditions of constant gas concentration difference across the diffusion sublayer, $\Delta C = C_w - C_0$, which is assumed to be close to effective air-sea concentration difference.

Wind-induced surface current constitutes only a tiny part of the total velocity difference between air and sea (about 2%). The condition of constant momentum flux rather than constant velocity difference is therefore appropriate in (2.23). Waves are a volume source of momentum in the near-surface layer of the ocean; formally, they do not enter the surface boundary condition for velocity. We nevertheless neglect here the second order effect relating to the modification of the gravity-capillary waves and, thereby, the surface roughness and momentum fluxes by surface drift current. This secondary effect, however, may become of primary importance under conditions of very high wind speed (see Chapter 6).

The dependence of the net longwave irradiance $I_L$ and latent heat flux $Q_E$ on the temperature difference due to the cool skin is typically within several % (Paulson and Simpson, 1981). Only $Q_T$ may depend appreciably on the cool skin presence. Usually $|I_L + Q_E| >> |Q_T|$, which means that the net surface flux, $q_0$, does not depend strongly on the cool skin presence. As a result, the condition of constant heat flux is justified for deriving dependence (2.24). Solar radiation is a volume source of heat for the near-surface layer of the ocean and does not enter the surface boundary condition.

The condition of constant concentration difference accepted in (2.25) follows from the assumption that the aqueous diffusion sublayer provides the main resistance to the gas transfer and thereby contains the main gas concentration difference across the air-sea interface.

The average velocity and temperature difference across the aqueous viscous and thermal sublayers and the average surface gas flux at the air-sea interface can be defined as follows:

$$\overline{\Delta u} = \int_0^\infty p(t) t^{-1} \left( \int_0^t \Delta u(t') dt' \right) dt \tag{2.26}$$

$$\overline{\Delta T} = \int_0^\infty p(t) t^{-1} \left( \int_0^t \Delta T(t') dt' \right) dt \tag{2.27}$$

$$\overline{G_0} = \int_0^\infty p(t) t^{-1} \left( \int_0^t G_0(t') dt' \right) dt \tag{2.28}$$

where $p(t)$ is the probability density for time periods, $t$, of bursting motions in the molecular sublayers. This is the probability of local destruction of the molecular sublayers in a time interval $(t, t + dt)$, where $t$ is the elapsed time since the previous destruction.

Experiments of Rao et al. (1971) on the structure of the boundary-layer turbulence indicate that the time between bursts is distributed according to a lognormal law. The probability density for such a process is given by

$$p(t) = \pi^{-1/2} (\sigma t)^{-1} \exp\left[ -(\ln t - m)^2 / \sigma^2 \right], \; t > 0. \tag{2.29}$$

where $m$ is the mean value and $\sigma^2$ is the variance for the logarithm of the random variable $t$. Garbe et al. (2002) found the lognormal distribution (2.29) as being in good agreement with the histogram of time intervals between two successive renewal events derived from infrared images in a laboratory tank (*Figure 2-11*).

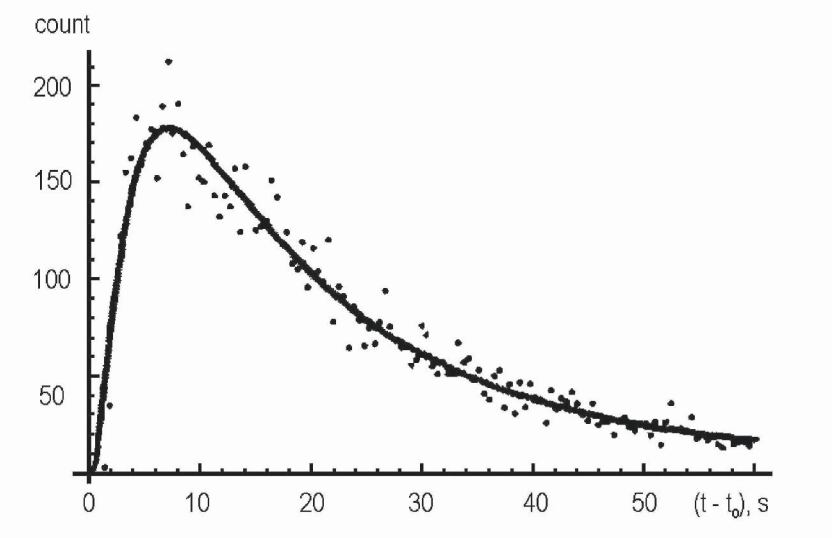


*Figure 2-11*. Lognormal distribution (2.29) fitted to the histogram of the time between two consecutive surface renewal events $t$ - $t_0$ for a wind speed of 2 m s$^{-1}$. Reproduced from Garbe et al. (2002) by permission of American Geophysical Union.

Inserting (2.29) into relationships (2.26)-(2.28), we obtain:

$$\overline{\Delta u} = \left(4\pi^{-1/2}/3\right) \exp\left(-\sigma^2/16\right) \left(t_* / \nu\right)^{1/2} \tau_t, \tag{2.30}$$

$$\overline{\Delta T} = -\left(4\pi^{-1/2}/3\right) \exp\left(-\sigma^2/16\right) \left(t_* / \kappa_T\right)^{1/2} q_0, \tag{2.31}$$

$$K_\mu = 2\pi^{-1/2} \exp\left(3\sigma^2/16\right)\left(t_*/\mu\right)^{-1/2}, \tag{2.32}$$

where $K_\mu$ is the gas transfer velocity (the piston velocity) defined by equation (1.44), and $t_* = \exp\left(m + \sigma^2/4\right)$ is the average time between bursts, which has been referred to as the renewal time. Since the bursting events have significant energy, we assume that they affect the viscous, thermal, and diffusion molecular sublayers in the same manner, and the quantity $\sigma^2$ in (2.30)-(2.32) is the same.

Following Soloviev and Schlüssel (1994), we consider three wind speed regimes:

1) Calm and low wind speed conditions. The cyclic injection of fluid from the molecular sublayers is of convective nature. The time period of the convective bursts is defined by Foster (1971b) as follows:

$$t_c = a_c\left(-\nu/\alpha_T g q_0\right)^{1/2}, \tag{2.33}$$

where $a_c$ is a dimensionless constant.

2) Intermediate wind speed conditions. According to Csanady (1990) the most intense surface renewal on a wind-blown surface is caused by viscous surface-stress variations associated with rollers on breaking wavelets. The time period of these variations is defined as

$$t_r = a_r \nu / u_*^2, \tag{2.34}$$

where $a_r$ is a dimensionless constant.

3) High wind speed conditions. Surface waves take most of the wind stress and the development of rollers is less probable. The surface renewal due to waves breaking and whitecapping dominates. For fully developed wind waves the time scale of the surface renewal depends on the parameters $u_*$ and $g$. A dimensional analysis leads to the following relation:

$$t_w = a_w u_*^2 / g, \tag{2.35}$$

where $a_w$ is a dimensionless constant.

The surface Richardson number ($Rf_0$) controls the transition from free convection (regime 1) to rollers (regime 2) at the air-sea interface, while the Keulegan number ($Ke$) controls the transition from rollers (regime 2) to

wave breaking (regime 3). Combining (2.33), (2.34), and (2.35) the renewal (or exposure) time can then be expressed as follows:

$$t_* = \begin{cases} a_c \left[ \nu / \left( -\alpha_T g q_0 \right) \right]^{1/2} \text{at } 0 \le u_* \le \left( \alpha_T g q_0 \nu / Rf_{cr} \right)^{1/4} \\ a_r \nu / u_*^2 \quad \text{at } \left( \alpha_T g q_0 \nu / Rf_{cr} \right)^{1/4} \le u_* \le \left( Ke_{cr} \nu g \right)^{1/3} \\ a_w u_* / g \qquad\qquad \text{at } u_* \ge \left( Ke_{cr} \nu g \right)^{1/3} \end{cases} \tag{2.36}$$

where $Rf_{cr}$ and $Ke_{cr}$ are the critical values of the surface Richardson number and the Keulegan number, respectively. In dimensionless form, formula (2.36) is as follows:

$$t_* / \left( a_r \nu / u_*^2 \right) = \begin{cases} \left( Rf_0 / Rf_{cr} \right)^{-1/2} \qquad \text{at } Rf_0 / Rf_{cr} \ge 1 \\ 1 \quad \text{at } Rf_0 / Rf_{cr} \le 1 \text{ and } Ke / Ke_{cr} \le 1 \\ Ke / Ke_{cr} \qquad\qquad \text{at } Ke / Ke_{cr} \ge 1 \end{cases} \tag{2.37}$$

where $Rf_{cr} = -\left( a_c / a_r \right)^2$ and $Ke_{cr} = a_r / a_w$.

Formula (2.37) can be approximated in the following way:

$$t_* / \left( a_r \nu / u_*^2 \right) \simeq \left( 1 + Rf_0 / Rf_{cr} \right)^{-1/2} \left( 1 + Ke / Ke_{cr} \right), \tag{2.38}$$

which is a sufficiently accurate and convenient analytical expression. An interpretation of the *Ke*-number dependence in (2.38) is that under high wind-speed conditions the tangential stress $\tau_t$ relates to the total wind stress $\tau_0$ according to (2.8).

Inserting the renewal time (2.38) into (2.30)-(2.32) and taking into account (2.8) and the definition of the friction velocity $u_* = \left( \tau_0 / \rho \right)^{1/2}$ leads to the following coupled set of parametric relationships

$$\overline{\Delta u} / u_* = \Lambda_0 \left( 1 + Rf_0 / Rf_{cr} \right)^{-1/4} \tag{2.39}$$

$$\overline{\Delta T} / T_* = -\Lambda_0 \, \mathrm{Pr}^{1/2} \left( 1 + Rf_0 / Rf_{cr} \right)^{-1/4} \left( 1 + Ke / Ke_{cr} \right)^{1/2} \tag{2.40}$$

$$K_\mu / u_* = A_0 \Lambda_0^{-1} Sc^{-1/2} \left(1 + Rf_0 / Rf_{cr}\right)^{1/4} \left(1 + Ke / Ke_{cr}\right)^{-1/2} \tag{2.41}$$

where $T_* = q_0 / u_*$, $\mathrm{Pr} = \nu / k$, and $Sc = \nu / \mu$. The dimensionless coefficients $A_0$ and $\Lambda_0$ are expressed through the parameter of lognormal distribution (2.29) as follows

$$A_0 = \left(8\pi^{-1} / 3\right) \exp\left(\sigma^2 / 8\right), \tag{2.42}$$

$$\Lambda_0 = \left(4\pi^{-1/2} / 3\right) \exp\left(-\sigma^2 / 16\right) a_r^{1/2}. \tag{2.43}$$

The calculation of $A_0$ with $\sigma$ determined from the Garbe et al. (2002) laboratory experiment is presented in *Table 2-1*.

For low wind speed conditions, $Rf_0 \to -\infty$ and $Ke \to 0$; equations (2.39) -(2.41) have the following asymptotes:

$$\overline{\Delta u} \approx \Lambda_0 u_* \left(\frac{Rf_0}{Rf_{cr}}\right)^{-1/4} = \Lambda_0 u_*^2 \left(\frac{Rf_{cr}}{\alpha_T g q_0 \nu}\right)^{1/4}, \tag{2.44}$$

$$\Delta T \approx -\Lambda_0 \,\mathrm{Pr}^{1/2} \left(\frac{Rf_0}{Rf_{cr}}\right)^{-1/4} \frac{q_0}{u_*} = -\Lambda_0 \,\mathrm{Pr}^{1/2} \left(\frac{Rf_{cr}}{\alpha_T g \nu q_0}\right)^{1/4} q_0, \tag{2.45}$$

$$K_\mu \approx A_0 \Lambda_0^{-1} Sc^{-1/2} u_* \left(\frac{Rf_0}{Rf_{cr}}\right)^{1/4} = A_0 \Lambda_0^{-1} Sc^{-1/2} \left(\frac{\alpha_T g \nu q_0}{Rf_{cr}}\right)^{1/4}. \tag{2.46}$$

A low wind speed asymptote for the velocity difference across the aqueous viscous sublayer at the air-sea interface similar to (2.44) could not be found in the literature. At the same time, formula (2.45) is similar to that of Katsaros et al. (1977),

$$\overline{\Delta T} = a_0^{-3/4} \left(\frac{\nu}{-\alpha_T g \kappa_T{}^2}\right)^{1/4} q_0^{3/4}, \tag{2.47}$$

obtained for calm weather conditions; the appropriate nondimensional coefficients are interrelated by

$$a_0 = \Lambda_0^{-4/3} \left(-Rf_{cr}\right)^{-1/3} . \tag{2.48}$$

Soloviev and Schlüssel (1994) previously derived the asymptotic formula (2.46) for the gas transfer velocity.

*Table 2-1*. Parameter $\sigma$ in (2.29) from the results of Garbe et al. (2002) and the computation of coefficient $A_0$ from equation (2.42).

| Wind speed, m s$^{-1}$ | 2.0 | 4.2 | 8.0 |
|---|---|---|---|
| $\sigma$ | 1.39 | 0.8 | 0.7 |
| $A_0$ | 1.08 | 0.92 | 0.89 |

For moderate wind speed conditions, which is an intermediate asymptotic $\left|Rf_0\right| << \left|Rf_{cr}\right|$ and $Ke << Ke_{cr}$, parameterizations (2.39)-(2.41) reduce to

$$\overline{\Delta u} = \Lambda_0 u_* , \tag{2.49}$$

$$\overline{\Delta T} \approx -\Lambda_0 \,\mathrm{Pr}^{1/2}\, T_* = -\Lambda_0 \,\mathrm{Pr}^{1/2}\, q_0 / u_* , \tag{2.50}$$

$$K_\mu = A_0 \Lambda_0^{-1} Sc^{-1/2} u_* . \tag{2.51}$$

There is presumably no direct analog of (2.49) in the literature. Formula (2.50) has an analog previously derived by Saunders (1967b)

$$\overline{\Delta T} = -\lambda_S \,\mathrm{Pr}\, q_0 / u_* , \tag{2.52}$$

while the formula similar to (2.51),

$$K_\mu = \gamma_0 Sc^{-1/2} u_* , \tag{2.53}$$

can be found in several previous publications on air-sea gas exchange. The dimensionless coefficients entering (2.50) and (2.52) are interrelated by $\lambda_S = \Lambda_0 \,\mathrm{Pr}^{-1/2}$ and $\gamma_0 = A_0 \Lambda_0^{-1}$.

For high wind speed conditions, equations (2.39)-(2.41) have asymptotes $|Rf_0| << |Rf_{cr}|$ and $Ke >> Ke_{cr}$, which lead to:

$$\overline{\Delta u} = \Lambda_0 u_*, \tag{2.54}$$

$$\overline{\Delta T} \approx -\Lambda_0 \,\mathrm{Pr}^{1/2}\, T_* \left(Ke / Ke_{cr}\right)^{1/2} = -\Lambda_0 \,\mathrm{Pr}^{1/2} \left(\nu g Ke_{cr}\right)^{-1/2} q_0 u_*^{1/2}, \tag{2.55}$$

$$K_\mu \approx A_0 \Lambda_0^{-1} Sc^{-1/2} u_* \left(Ke / Ke_{cr}\right)^{-1/2} = A_0 \Lambda_0^{-1} Sc^{-1/2} \left(\nu g Ke_{cr}\right)^{1/2} u_*^{-1/2}, \tag{2.56}$$

Same as for (2.49), no direct analog to (2.54) could be found in literature. Parameterization for the velocity difference across the aqueous viscous sublayer is closely related to the problem of determining the wind drift coefficient; related issues are considered elsewhere in this section. High wind-speed parameterizations for the temperature difference across the cool skin and the gas transfer velocity (2.55) and (2.56) were previously derived by Soloviev and Schlüssel (1994).

Active breaking events (whitecaps) occupy a relatively small area of the sea surface. In the process of wave breaking, molecular sublayers are destroyed, however they are restored in between wave breaking events. In accordance with (2.8), a reduced fraction of the momentum flux transfers to tangential stress at higher wind speeds. As a result, the velocity difference is maintained proportional to the friction velocity (2.54). The temperature difference across the cool skin slightly increases with wind speed (2.55), while the interfacial gas transfer velocity slightly decreases. Equations (2.54) -(2.56), however, do not include two important effects associated with wave breaking: 1) The residual turbulence after wave breaking maintains for several wave periods, affecting the molecular sublayers; 2) Bubble production in whitecaps can substantially affect the air-sea gas exchange. The effect of the residual wave-breaking turbulence on the interfacial gas transport (as well as the inclusion of the bubble-mediated gas transport) is discussed in Chapter 7 of this book.

Bubble-mediated heat transport is apparently negligible in comparison with the direct flux at the ocean-air interface, due to the low heat capacity of air inside the bubbles. In contrast, droplet and spray production by breaking waves is an important mechanism of the air-ocean heat and mass transport at wind speeds greater than about 15-17 m $s^{-1}$ (Chapter 6).

Substituting (2.48) into (2.39)-(2.41), we obtain a coupled set of parameterizations:

$$\Delta\overline{u}/u_* = \Lambda_0\left(1 - a_0{}^3\Lambda_0^4 Rf_0\right)^{-1/4} \tag{2.57}$$

$$\Delta\overline{T}/T_* = -\Lambda_0\,\mathrm{Pr}^{1/2}\left(1 - a_0{}^3\Lambda_0^4 Rf_0\right)^{-1/4}\left(1 + Ke/Ke_{cr}\right)^{1/2} \tag{2.58}$$

$$K_\mu/u_* = A_0\Lambda_0^{-1}Sc^{-1/2}\left(1 - a_0{}^3\Lambda_0^3 Rf_0\right)^{1/4}\left(1 + Ke/Ke_{cr}\right)^{-1/2} \tag{2.59}$$

Replacing the surface cooling $Q_0 = Q_E + Q_T + I_L$ with the *virtual cooling*, which includes the buoyancy effects of salinity due to evaporation

$$Q_v = Q_E + Q_T + I_L + \frac{S_0\beta_S c_p}{\alpha_T L}Q_E\,, \tag{2.60}$$

the expression for the surface Richardson number transforms in the following way:

$$Rf_0 = \frac{\alpha_T g\nu}{c_p\rho u_*^4}\left(Q_E + Q_T + I_L + \frac{\beta_S S_0 c_p}{\alpha_T L}Q_E\right). \tag{2.61}$$

Coefficients $\Lambda_0$, $a_0$, $Ke_{cr}$, and $A_0$ are now to be determined from the comparison with experimental data.

From the comparison with Grassl's (1976) data, which represented a relatively small number of field observations, Kudrayvtsev and Soloviev (1985) derived tentative estimates of the two constants $\Lambda_0 \approx 13.3$ and $Rf_{cr} \approx -1.5\cdot 10^{-4}$, treating them as independent constants. From relationship (2.48) it then follows that $a_0 \approx 0.6$, which is much bigger than the commonly accepted estimate $a_0 = 0.25$ (Fedorov and Ginzburg, 1988). Since the publication of the Kudryavtsev and Soloviev (1985) work, new laboratory data sets on the surface wind drift current using particle image velocimetry and infrared imaging have been obtained, which allow us to specify more accurately numerical constant $\Lambda_0$.

Formulation (2.57)-(2.59) including constants $\Lambda_0$ and $a_0$ is more convenient than formulation (2.39)-(2.41) including constants $\Lambda_0$ and $Rf_{cr}$, because it is believed that, in contrast to $Rf_{cr}$, the numerical value of $a_0$ can be determined with an acceptable accuracy from laboratory experiments. It is also remarkable that according to (2.57) the dimensionless ratio $\overline{\Delta u}/u_*$ does not depend on the Keulegan number, which means that constant $\Lambda_0$ can be estimated from the experimental data on the surface wind drift current.

According to (2.49) and (2.54) for intermediate and high wind speed conditions $\Lambda_0 = \overline{\Delta u} / u_*$,

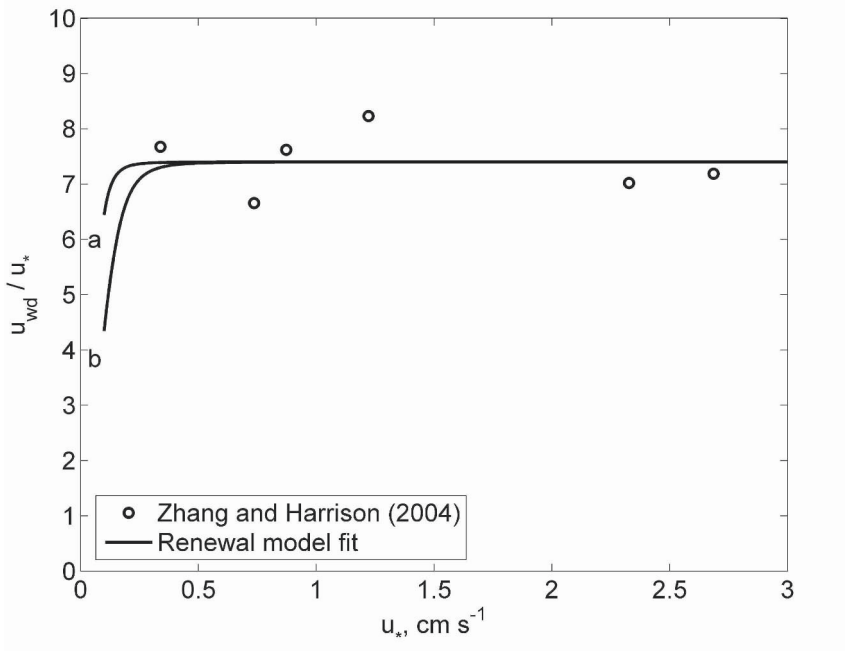


*Figure 2-12.* Non-dimensional wind-induced surface current in the laboratory tank for different wind friction velocities and in comparison with the renewal model (2.57) at $a = 0.25$ and $\Lambda_0 = 7.4$, calculated for two surface cooling rates: (a) $Q_0 = 20$ W m$^{-2}$, and (b) $Q_0 = 200$ W m$^{-2}$.

The ratio, $\overline{\Delta u} / u_*$, is closely related to the *wind drift coefficient*, $u_0 / U_{10}$, where $u_0$ is the averaged current velocity at the sea surface (relative to the background ocean current), and $U_{10}$ is the wind speed at 10 m height. The current velocity at the sea surface includes the Stokes drift as well, which provides a relatively small (between 5 and 20%) contribution to the wind-drift coefficient however. The difference between the current velocity at the sea surface $u_0$ and the Stokes surface drift $u_S$ is the wind-induced surface drift:

$$u_{wd} = u_0 - u_S \,. \tag{2.62}$$

The ratio between the wind-induced surface drift $u_{wd}$ and the water friction velocity $u_*$ as measured by Wu (1975) varied between 11 and 20.

Wu (1975) concluded that $\langle u_{wd}/u_* \rangle \approx 17.0$ and has no obvious systematic dependence upon friction velocity. Phillips and Banner (1974) laboratory experiment indicated that $\langle u_{wd}/u_* \rangle \approx 16.1$.

Values of $u_{wd}/u_*$ derived from particle image velocimetry and from infrared imaging also demonstrate no obvious dependence on the friction velocity but consistently indicate smaller surface drift currents than those derived from drifter measurements (Zhang and Harrison, 2004). The wind-induced velocities derived from the infrared images are shown in *Figure 2-12*. Averaging over all friction velocities results in $\langle u_{wd}/u_* \rangle \approx 7.4$. Based on these laboratory results we accept an estimate $\Lambda_0 \approx 7.4$. This is in fact an upper estimate, because it does not take into account the existence of relatively small current velocity difference across the turbulent layer (*i.e.*, below the viscous sublayer).

A fit of parameterization (2.57) to the results of the Zhang and Harrison (2004) is shown in *Figure 2-12*. In (2.57), the term $\left(1 - a_0{}^3 \Lambda_0^4 R f_0\right)^{-1/4}$ relating to buoyancy effects is of importance under low wind speed conditions. *Figure 2-12* therefore shows parameterization (2.39) for two values of the net surface heat flux $Q_0$.

A tentative estimate of $Ke_{cr} \approx 0.18$ was derived by Soloviev and Schlüssel (1994) from indirect data–the critical wind speed, $U_{10} \approx 10$ m s$^{-1}$, at which, according to the visual Beaufort scale, long-wave breaking sets in. Later, Zhao and Toba (2001) proposed a parameter $R_B = u_{*a}{}^2/\left(\nu_a \omega_p\right)$ with a critical value of $R_B = 10^3$ for the onset of wind-wave breaking. Parameter $R_B$ can be rewritten as

$$R_B = A_w u_{*a}^3/\left(g\nu_a\right) \tag{2.63}$$

where $A_w$ is the wave age defined as $A_w = g/\left(\omega_p u_{*a}\right)$.

$$Ke = \frac{u_*^3}{g\nu} = \frac{u_{*a}^3 \beta}{g\nu_a}\frac{\nu_a}{\nu}\left(\frac{\rho_a}{\rho}\right)^{3/2}\frac{1}{A_w} = R_B \frac{\nu_a}{\nu}\left(\frac{\rho_a}{\rho}\right)^{3/2}\frac{1}{A_w} \tag{2.64}$$

From (2.64), it follows that critical value $R_B = 10^3$ corresponds to $Ke_{cr} = 0.18$ at wave age $A_w = 3.25$.

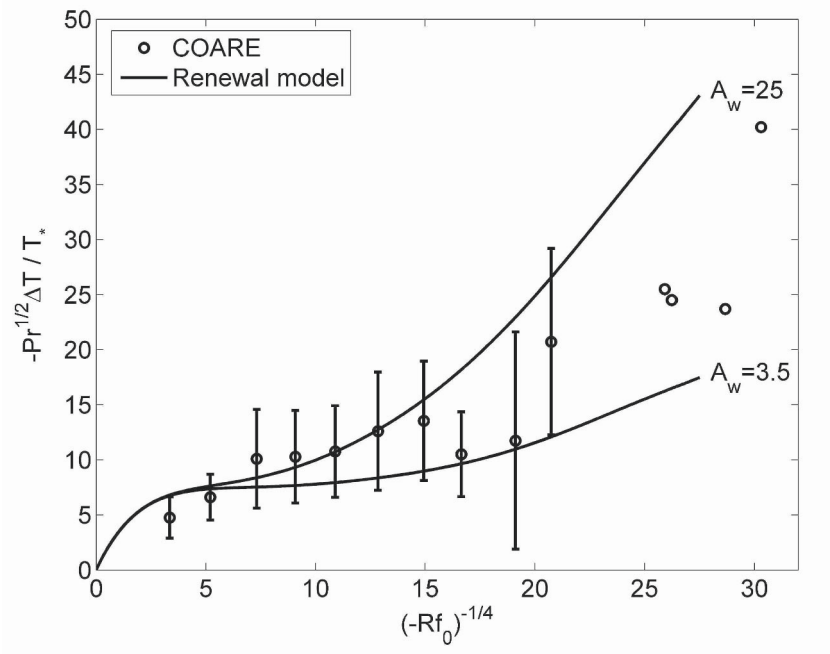


*Figure 2-13*. Nighttime variation of $-\mathrm{Pr}^{1/2}\Delta T/T_*$ with $\left(-Rf_0\right)^{-1/4}$: each circle represents the mean over an interval $\Delta\left(-Rf_0\right)^{-1/4} = 2$, the vertical bars cover the 95% confidence intervals; the circles with no error bars represent single points at high values of $\left(-Rf_0\right)^{-1/4}$. The continuous lines are parameterization (2.58) at $a_0 = 0.25$, $\Lambda_0 = 7.4$ for young ( $A_w = 3.5$ ) and old ( $A_w = 25$ ) seas.

During COARE Hartmut Grassl collected substantial statistics on the temperature difference across the cool skin in the western equatorial Pacific. *Figure 2-13* shows parameterization (2.58) plotted for $a_0 = 0.25$, $\Lambda_0 \approx 7.4$, and two different values of wave age $A_w$ in comparison with the COARE data set.

According to *Table 2-1*, constant $A_0$ entering the gas-exchange parameterization is close to unity, varying within $\pm 10\%$ as a function of wind speed. For simplicity, we take $A_0 = 1$.

*Figure 2-14* compares open ocean data on the gas transfer velocity with parameterization (2.59). The data from *GasEx-01* are direct (eddy-correlation) measurements (Hare et al., 2004). The bubble-mediated contribution to the gas transfer velocity $K_\mu$ for $CO_2$ is expected to be relatively small in the range of wind speeds for which the data were collected because $CO_2$ is a highly soluble gas. The data are from indirect (dual-tracer) measurements (Wanninkhof et al., 1999), relatively low-soluble

gases. For the low solubility gas, the effects of bubbles can be significant. In *Figure 2-14* only the data from the *GasEx-98* dual-tracer measurement obtained below the wave-breaking threshold are therefore shown. Further consideration of the gas transfer parameterization problem including the bubble-mediated transport is offered in Chapter 7.

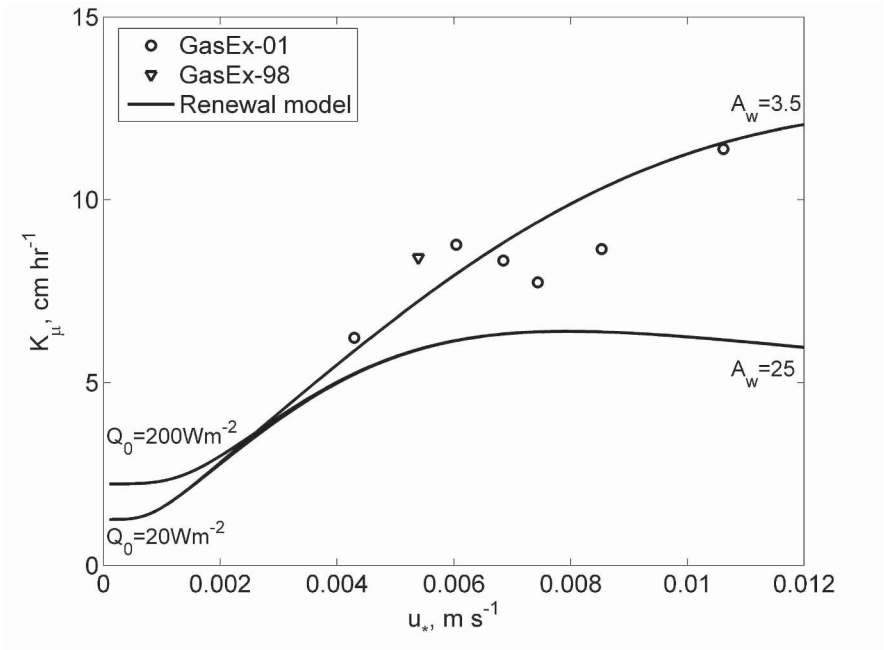


*Figure 2-14*. Comparison of the gas transfer velocity obtained in the open ocean with parameterization (2.59) for $a_0 = 0.23$, $\Lambda_0 = 7.4$, and $A_\mu = 1$, calculated for two surface cooling rates ($Q_0 = 20$ W m$^{-2}$ and $Q_0 = 200$ W m$^{-2}$) and for young ($A_w = 3.5$) and old ($A_w = 25$) seas.

The comparisons in *Figures 2-12, 2-13,* and *2.14* imply that during nighttime the layer below the microlayer is well mixed (which may not be true under certain conditions).

### 2.3.3 Boundary-layer model

Though boundary-layer models operate with the averaged turbulent characteristics such as the dissipation rate ε (for instance, defining the viscous sublayer depth as proportional to Kolmogorov's internal scale of turbulence, $\eta_v = \left(\nu / \varepsilon^3\right)^{1/4}$), these models are consistent with the concept of intermittency of molecular sublayers in time and space through small-scale bursting motions (Kim et al., 1971).

Initial development of the boundary-layer model for molecular sublayers is usually attributed to Saunders (1967b) who, based on the wall layer analogy, derived a formula for the temperature difference across the cool skin in the form (2.52). Boundary layer modeling has also been applied to the free convection problem for a cooling sea surface. A theoretical formula for convective heat transfer over a horizontal plate,

$$Nu = a_0 Ra^{1/3} \tag{2.65}$$

in application to the thermal molecular sublayer below the air-water interface leads to the Katsaros et al. (1977) formula for the temperature difference across the aqueous thermal sublayer (cool skin) (2.47). The Nusselt and Rayleigh numbers are defined as,

$$Nu = \frac{q_0}{\kappa_T \left( \overline{\Delta T} / h \right)}, \tag{2.66}$$

$$Ra = \frac{\alpha_T g \overline{\Delta T} h^3}{\kappa_T \nu}, \tag{2.67}$$

and $a_0$ is a dimensionless constant. When the exponent on the Rayleigh number is 1/3, the equality (2.65) becomes independent of depth resulting in the Katsaros et al. (1977) equation (2.47).

Since both shear and convection contribute to the energy dissipation, the boundary-layer model describes the transition from free to forced convection in pretty much the same way as the renewal model. In particular, the same dimensionless number $Rf_0$ controls this transition. Correspondingly, Fairall et al. (1996) modified the Saunders (1967b) parameterization (2.52) as follows:

$$\overline{\Delta T} = -\frac{\lambda_S \, \mathrm{Pr} \, q_0}{u_*} \left[ 1 + \left( a_0{}^3 \lambda_S^4 Rf_0 \, \mathrm{Pr}^2 \right)^{3/4} \right]^{-1/3} \tag{2.68}$$

where $Rf_0 = \alpha_T g Q_v \nu / \left( c_p \rho u_*{}^4 \right)$ is the surface Richardson number introduced by Kudryavtsev and Soloviev (1985) from modeling surface renewals, and $Q_v$ is the virtual cooling given by (2.60). The model remains bounded as $u_* \to 0$ (asymptotically approaching Katsaros' formula (2.47) for free convection), which is an improvement over the original Saunders (1967b) formula (2.52).

Taking into account that $\Lambda_0 = \lambda_S \mathrm{Pr}^{1/2}$, boundary-layer parameterization (2.68) practically coincides with parameterization (2.58) for low and moderate wind speed conditions. Similar to the renewal model, the boundary layer type model can be extended to high-wind speed conditions including wave breaking and whitecapping. Such an extension is considered in Chapter 7 for the example of air-sea gas transfer modeling.

## 2.4 Effect of Penetrating Solar Radiation

### 2.4.1 Model equations

The impact of penetrating solar radiation on the dynamics of molecular sublayers can be quantified in a consistent way with a renewal model (Soloviev and Schlüssel, 1996). Note that the term "cool skin" might not be completely appropriate during daytime hours since in extreme situations the solar warming may reverse the sign of the temperature gradient in the thermal molecular sublayer.

Following the same approach as in Section 2.3.2, consider a fluid element adjacent to the sea surface that participates in the process of cyclic renewal of the surface water in the presence of both surface cooling and the volume absorption of solar radiation. Initially, the fluid element has a uniform temperature equal to the bulk-water value. As it is exposed to the interface, the molecular diffusion law governs the evolution of the temperature difference across the thermal sublayer:

$$\frac{\partial T}{\partial t} = \frac{\partial}{\partial z}\left( \kappa_T \frac{\partial T}{\partial z} \right) + \frac{\partial q_R}{\partial z} . \tag{2.69}$$

where $q_R = I_R / \left( c_p \rho \right)$ is the volume source due absorption of solar radiation in water.

The boundary condition on the waterside of the air-sea interface is

$$-\kappa_T \frac{\partial T}{\partial z}\Big|_{z \to -0} = q_0 , \tag{2.70}$$

and the initial condition is formulated as follows:

$$T\left( z, 0 \right) = T_w . \tag{2.71}$$

where $q_0 = Q_0 / \left( c_p \rho \right) = \left( Q_T + Q_E + I_L \right) / \left( c_p \rho \right)$, and $T_w$ is the bulk water temperature. $Q_E$ and $I_L$ do not depend strongly on the presence of the temperature difference across the cool skin (Paulson and Simpson, 1981). The sensible heat flux $Q_T$ can appreciably depend on the temperature difference across the cool skin; the magnitude of $Q_T$ is, however, usually much less that that of $Q_E$ or $I_L$. The total heat flux $Q_0$ is thereby assumed to be constant during the time period between successive surface renewals.

Equation (2.69) is a linear equation in partial derivatives with a volume source, and the superposition principle can be applied with initial and boundary conditions (2.70) and (2.71). This is a mixed problem with boundary conditions of the second type. Introducing a new variable $\Delta T \left( z,t \right) = T \left( z,t \right) - T_w$ the solution can be represented as follows (Vladimirov, 1976):

$$\Delta T \left( z,t \right) = \Delta T_c \left( z,t \right) + \Delta T_R \left( z,t \right) \tag{2.72}$$

where

$$\Delta T_c \left( z,t \right) = -q_0 \left( \kappa_T \pi \right)^{-1/2} \int_0^t \left( t - t' \right)^{-1/2} \exp \left\{ -\frac{z^2}{4\kappa_T \left( t - t' \right)} \right\} dt' \tag{2.73}$$

and

$$\Delta T_R \left( z,t \right) = \int_0^t \int_{-\infty}^0 \hat{f} \left( \eta \right) \left[ 4\kappa_T \pi \left( t - t' \right) \right]^{-1/2} \exp \left\{ -\frac{\left( z - \eta \right)^2}{4\kappa_T \left( t - t' \right)} \right\} d\eta dt' \tag{2.74}$$

with $f \left( z \right) = \partial q_R / \partial z$. The circumflex denotes an even extension of the function to $z > 0$ so that

$$\hat{f} \left( z \right) = \hat{f} \left( -z \right). \tag{2.75}$$

The quantities $\Delta T_c$ and $\Delta T_R$ are interpreted as the near-surface temperature differences due to surface cooling and due to absorption of solar radiation, respectively. Integration of (2.73) results in the following expression for the temperature difference developing due to surface cooling and molecular heat diffusion:

$$\Delta T_c\left(z,t\right)=-2q_0\left(t/\kappa_T\right)^{1/2}\left[\pi^{-1/2}\exp\left(-\xi^2\right)-\xi erfc\left(\xi\right)\right], \tag{2.76}$$

where $\xi=z\left(4\kappa_T t\right)^{-1/2}$. Expression (2.74) for the temperature difference due to absorption of solar radiation can be rewritten in the following way:

$$\begin{aligned}\Delta T_R\left(z,t\right)=&\int_0^t\int_{-\infty}^0\hat{f}\left(\eta\right)\left[4\kappa_T\pi\left(t-t'\right)\right]^{-1/2}\exp\left\{-\frac{\left(z-\eta\right)^2}{4\kappa_T\left(t-t'\right)}\right\}d\eta dt'+\\&\int_0^t\int_{-\infty}^0\hat{f}\left(-\eta\right)\left[4\kappa_T\pi\left(t-t'\right)\right]^{-1/2}\exp\left\{-\frac{\left(z+\eta\right)^2}{4\kappa_T\left(t-t'\right)}\right\}d\eta dt'\end{aligned} \tag{2.77}$$

Since $\hat{f}\left(\eta\right)=\hat{f}\left(-\eta\right)$ for $\eta<0$ and $\hat{f}\left(\eta\right)\equiv f\left(\eta\right)$ for $\eta\geq 0$, (2.77) can be transformed as follows:

$$\begin{aligned}\Delta T_R\left(z,t\right)=&\int_0^t\int_{-\infty}^0 f\left(\eta\right)\left[4\kappa_T\pi\left(t-t'\right)\right]^{-1/2}\exp\left\{-\frac{\left(z-\eta\right)^2}{4\kappa_T\left(t-t'\right)}\right\}d\eta dt'+\\&\int_0^t\int_{-\infty}^0 f\left(\eta\right)\left[4\kappa_T\pi\left(t-t'\right)\right]^{-1/2}\exp\left\{-\frac{\left(z+\eta\right)^2}{4\kappa_T\left(t-t'\right)}\right\}d\eta dt'\end{aligned} \tag{2.78}$$

Substitution of the expression for the absorption of solar radiation in the form given by equation (1.62):

$$f\left(\eta\right)=q_{R0}\sum_1^9 a_i\alpha_i\exp\left(\alpha_i\eta\right) \tag{2.79}$$

into (2.78) results in the following formula:

$$\Delta T_R\left(z,t\right)=q_{R0}\sum_1^9 a_i\alpha_i\left[I_1\left(z,t;i\right)+I_2\left(z,t;i\right)\right], \tag{2.80}$$

where

$$I_1(z,t;i)=\int_0^t\int_{-\infty}^0 \exp(-\alpha_i\eta)\exp\left\{-\frac{(z-\eta)^2}{4\kappa_T(t-t')}\right\}\times \left[4\kappa_T\pi(t-t')\right]^{-1/2} d\eta dt', \tag{2.81}$$

$$I_2(z,t;i)=\int_0^t\int_{-\infty}^0 \exp(-\alpha_i\eta)\exp\left\{-\frac{(z+\eta)^2}{4\kappa_T(t-t')}\right\}\times \left[4\kappa_T\pi(t-t')\right]^{-1/2} d\eta dt', \tag{2.82}$$

and $q_{R0}$ is the scaled solar irradiance just below the sea surface mathematically defined as $q_{R0}=(c_p\rho)^{-1} I_R(z)|_{z\to -0}=(c_p\rho)^{-1}(1-A)I_\Sigma$.

Change of variables in (2.81) and (2.82) $\theta=t-t'$, $u=(z-\eta)(4\kappa_T\theta)^{-1/2}-\alpha_i(\kappa_T\theta)^{1/2}$, and $u'=(z+\eta)(4\kappa_T\theta)^{-1/2}+\alpha_i(\kappa_T\theta)$ leads to:

$$\Delta T_R(z,t)=q_{R0}\sum_{i=1}^{9}a_i\alpha_i\int_0^t\left\{\exp(\kappa_T\alpha_i^2\theta-\alpha_i z)\left[1+erf\left(\frac{z}{(4\kappa_T\theta)^{1/2}}-\alpha_i(\kappa_T\theta)^{1/2}\right)\right]+\exp(\kappa_T\alpha_i^2\theta+\alpha_i z)\left[1-erf\left(\frac{z}{(4\kappa_T\theta)^{1/2}}+\alpha_i(\kappa_T\theta)^{1/2}\right)\right]\right\}d\theta. \tag{2.83}$$

Equation (2.83) is integrated to obtain:

$$\Delta T_R(z,t)=\frac{1}{2}q_{R0}\kappa_T^{-1}\sum_{i=1}^{9}a_i\alpha_i\left\{\exp(-\alpha_i z+\delta_i^2)\left[1+erf(\xi-\delta_i)\right]+\exp(\alpha_i z+\delta_i^2)\left[1-erf(\xi+\delta_i)\right]-2\exp(-\alpha_i z)+4\delta_i\left[\pi^{-1/2}\exp(-\xi^2)-\xi+\xi erf(\xi)\right]\right\} \tag{2.84}$$

where $\xi=z(4\kappa_T t)^{-1/2}$ and $\delta_i=\alpha_i(\kappa_T t)^{1/2}$ are non-dimensional depth and time, respectively.

According to (2.76) and (2.84), the near-surface temperature difference between the renewal events evolves in the following way:

$$\Delta T(0,t) = \Delta T_c(0,t) + \Delta T_R(0,t) = -2q_{R0}\left(\frac{t}{\kappa_T \pi}\right)^{1/2} + q_{R0}\kappa_T^{-1}\sum_{i=1}^{9} a_i \alpha_i^{-1}\left\{\exp\left(\delta_i^2\right)\left[1 - erf\left(\delta_i^2\right)\right] - 1\right\} + 2q_R(0)\left(\frac{t}{\kappa_T \pi}\right)^{1/2} \tag{2.85}$$

The average temperature difference across the thermal molecular sublayer of the ocean is defined as follows:

$$\Delta \overline{T} = \int_0^{\infty} p(t)\Delta T_w(0,t)\,dt \tag{2.86}$$

where

$$\Delta T_m(0,t) = \frac{1}{t}\int_0^t \Delta T(0,t')\,dt', \tag{2.87}$$

and $p(t)$ is the probability density. From (2.85) and (2.87), the following expression can be obtained:

$$\Delta T_m(0,t) = -\frac{4}{3}q_0\left(\frac{t}{\kappa_T \pi}\right)^{1/2} + \frac{q_{R0}}{\kappa_T}\sum_{i=1}^{9} a_i \alpha_i^{-1}\left(\delta_l^{-2}\left\{\exp\left(\delta_l^2\right)\left[1 - erf\left(\delta_l^2\right)\right] - 1\right\} + 2\pi^{-1/2}\delta_l - 1\right) + \frac{4}{3}q_{R0}\left(\frac{t}{\kappa_T \pi}\right)^{1/2} \tag{2.88}$$

With the Rao et al. (1971) probability density function (2.29), expression (2.86) can be rewritten in the following way:

$$\Delta \overline{T} = \pi^{-1/2}\sigma^{-1}\int_{-\infty}^{+\infty} \exp\left[-\frac{\left(t_{\ln} - m\right)^2}{\sigma^2}\right]\Delta T_m\left(0, \exp\left(t_{\ln}\right)\right)dt_{\ln}, \tag{2.89}$$

where $t_{\ln} = \ln t$, $m = \ln t_* - \sigma^2/4$, $t_*$ is the mean time between bursting events (renewal time); $m$ and $\sigma^2$ are the mean value and the variance of the

logarithm of the random variable $t$. Transformation to the logarithmic variable $t_{\ln}$ is required to estimate integral (2.89) numerically.

### 2.4.2 Renewal time

It follows from (2.38) that the renewal time can be expressed in the following way:

$$t_* = \frac{9\pi\nu}{16u_*^2}\exp\left(\sigma^2/8\right)\Lambda_0^2\left(1-a_0{}^3\Lambda_0^4 Rf_0\right)^{-1/2}\left(1+Ke/Ke_{cr}\right). \qquad (2.90)$$

The introduction of a coefficient $A_0 = \frac{8}{3}\pi^{-1}\exp\left(\sigma^2/8\right)$, which appears in the parameterization of the air-sea gas transfer velocity, leads to the following expression for the renewal time:

$$t_* = \frac{27A_0\nu\pi^2}{128u_*^2}\Lambda_0^2\left(1-a_0{}^3\Lambda_0^4 Rf_0\right)^{-1/2}\left(1+Ke/Ke_{cr}\right). \qquad (2.91)$$

The expression for renewal time (2.91) is applicable only for nighttime conditions, when the surface flux is negative and, therefore $Rf_0 < 0$. During daytime, solar heating can affect the renewal time by inhibiting convective instability of the near-surface layer of the ocean. Moreover, in some regions of the ocean evaporation may be replaced by condensation of vapor at the ocean surface; the latent heat flux reverses its sign, and $Rf_0$ may become positive. In the next section, the definition of the surface Richardson number is extended for conditions of solar heating and condensation of vapor at the ocean surface.

### 2.4.3 Convective instability of the cool skin during daytime

Under calm weather $Rf << -a_0{}^{-3}\Lambda_0^{-4}$, and the renewal time is determined by convective instability. The positive buoyancy flux due to absorption of solar radiation may modify dynamics of the near-surface layer of the ocean. Woods (1980a) proposed the following Rayleigh-number criterion characterizing the influence of solar radiation absorption on thermally driven convection in the upper ocean:

$$Ra(z) = \frac{z^4\alpha_T g q_{R0}\left[f_R(D) - f_R(z)\right]}{\nu\kappa_T{}^2}, \qquad (2.92)$$

where $f_R(z)$ is the solar radiation absorption function (defined in Section 1.4.6), $q_{R0}$ is the solar irradiance just below the sea surface, and $D$ is the *compensation depth* defined from the following relationship:

$$q_0 = q_{R0}\left[1 - f_R(D)\right]. \tag{2.93}$$

The maximum of $Ra(z)$ is determined by

$$dRa(z)/dz = 0 \tag{2.94}$$

With (2.92) and (2.93), condition (2.94) reduces to

$$4\left[f_R(z) - 1 + q_0/q_{R0}\right] + z df_R(z)/dz = 0, \tag{2.95}$$

which is used to determine the value, $z = z_{\max}$ (being somewhere between 0.7 $D$ and 0.9 $D$) so that $Ra_{\max} = Ra(z_{\max})$. The absorption of solar radiation in water inhibits the thermally driven convection in the near-surface layer of the ocean when

$$Ra_{\max} = -\frac{z_{\max}^4 \alpha_T g\left[-q_0 + q_{R0} - q_{R0} f_R(z_{\max})\right]}{\nu \kappa_T{}^2} < Ra_{cr} = 1700 \tag{2.96}$$

Under low and calm wind-speed conditions the absorption of solar radiation may therefore dramatically increase the renewal time especially near midday. Such an extreme effect supposedly takes place in lakes and rivers under low wind speed conditions and a strong insolation. In the open ocean, however, additional convective instability is caused by the increase of sea surface salinity due to evaporation. The effect of absorption of solar radiation and of the additional buoyancy flux due to evaporation from the ocean surface can be included into the renewal time parameterization (2.91) by extending the definition of the surface Richardson number (2.61) in the following way:

$$Rf_0 = \frac{\alpha_T g \nu}{c_p \rho u_*^4} \begin{cases} \left(Q_E + Q_T + I_L + \left(\beta_S S_0 c_p Q_E\right)/\alpha_T L\right) & \text{for } Ra_{\max} \geq Ra_{cr} \\ \left(\beta_S S_0 c_p Q_E\right)/\alpha_T L & \text{for } Ra_{\max} < Ra_{cr} \end{cases} \tag{2.97}$$

In order to extend the parameterization to cases with positive latent heat flux (condensation), $Rf_0$ should be reset equal to zero if it becomes positive according to expression (2.97).

### 2.4.4 Model calculations

Penetrating solar radiation is specified according to (1.61)-(1.62). There are also material coefficients to be set in the model as functions of temperature and salinity; they are $\nu, \kappa_T, \alpha_T, L, c_p$, and $\rho$. As a first approximation, the influence of sea surface temperature and salinity variability on the material coefficients is ignored, while the dimensionless product $\beta_T S_0$ is fixed at 0.026.

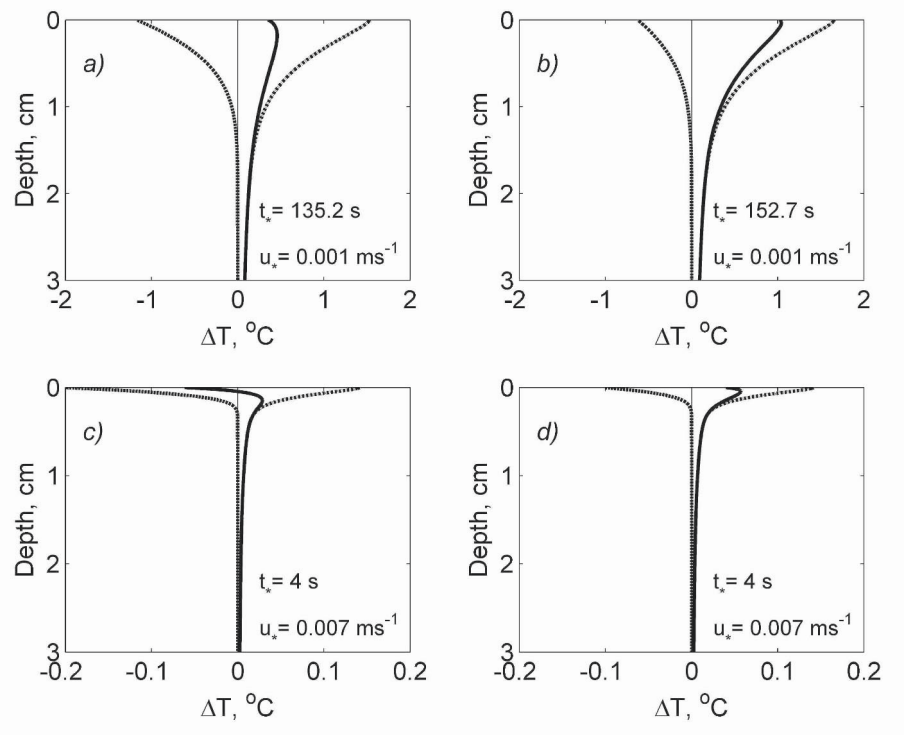


*Figure 2-15*. Instantaneous vertical temperature profiles in the upper 3 cm of the ocean at the end of the time period between renewal events. The contribution of the solar heating (dash-dotted), surface cooling (dashed), and the combined effect (contiguous) are calculated from a renewal model for (a, c) $Q_0$ = 140 W m$^{-2}$, $Q_E$ = 70 W m$^{-2}$ and (b, d) $Q_0$ = 70 W m$^{-2}$, $Q_E$ = 35 W m$^{-2}$. The top row (a, b) corresponds to free and the bottom row (c, d) to forced convection regimes. Solar irradiance just below the sea surface $I_{R0}$ = 1000 W m$^{-2}$, water temperature $T_0$ = 29$^o$C, and salinity $S_0$= 36 psu are the same in all cases. Note the different temperature scale between the top and bottom pairs of diagrams.

In *Figure 2-15*, vertical profiles of $\Delta T_c$, $\Delta T_R$, and $\Delta T$ within the upper 4 cm of the ocean have been calculated for three wind-speed and two heat-flux regimes from equations (2.76), (2.84), and (2.72), respectively. Shown in *Figure 2-15* are the instantaneous profiles developed after a surface renewal event at the end of the renewal time period (*i.e.*, at $t = t_*$). The renewal time is determined from formula (2.90) with the surface Richardson number defined by equation (2.97).

As expected the low wind speed regime shows the greatest temperature deviations extending to depths of several centimeters (*Figure 2-15* a, b). The model calculations are consistent with the instantaneous temperature profiles in the open ocean that have been observed with the free-rising profiler (see *Figure 2-3* and Section 2.2.1)

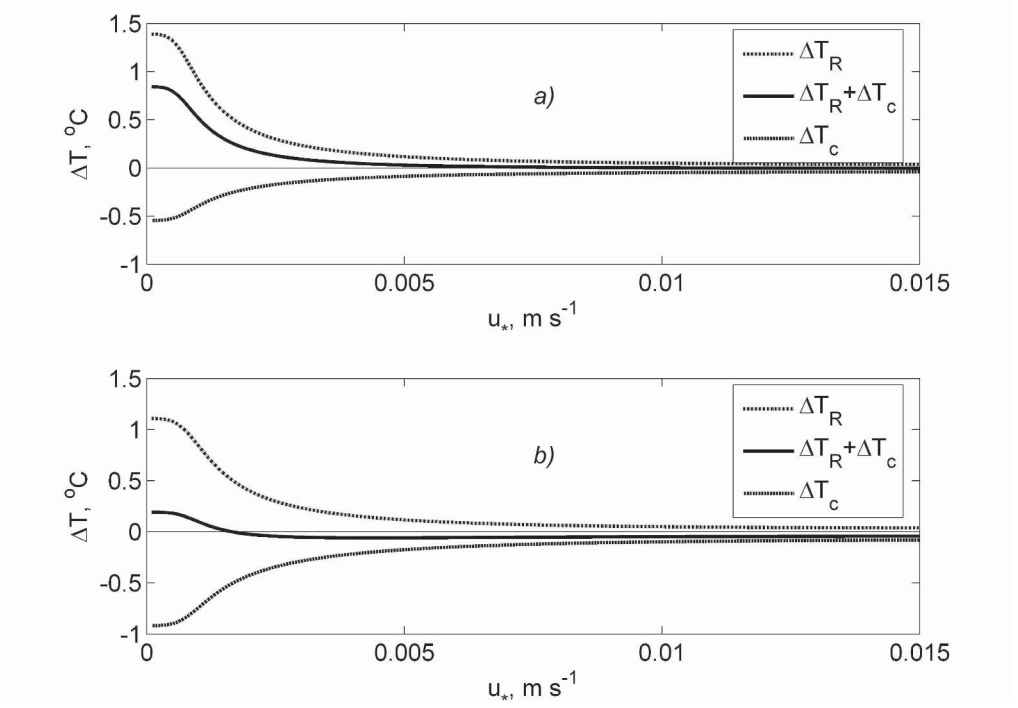


*Figure 2-16*. Temperature difference across the cool skin due to solar heating $\Delta T_R$, surface cooling $\Delta T_c$, and the combined effect, $\Delta T_R + \Delta T_c$, as a function of friction velocity $u_*$ calculated from parameterization (2.89) for (a) $Q_0$ = 70 W m$^{-2}$, $Q_E$ = 35 W m$^{-2}$, and (b) $Q_0$ = 140 W m$^{-2}$, $Q_E$ = 70 W m$^{-2}$. The solar irradiance just below the ocean surface is $I_{R0}$ = 1000 W m$^{-2}$, water temperature $T_0$ = 29°C, and salinity $S_0$= 36 psu are the same for both cases.

In contrast, the profiles generated by the model for higher friction velocities (*Figure 2-15* c, d) are affected by surface cooling and heating only

very close to the interface. The combined effect, $\Delta T(z)$, shows a maximum in a small range of depths between 50 and 150 $\mu$m. Above this maximum, surface cooling prevails at high wind speeds, while for the values of energy fluxes chosen here, the net effect at low wind speed is a surface warming.

Calculations with different water types from *Table 1.2* do not show the temperature differences larger than 0.02 °C. The absorption and scattering of light in near infrared band mainly determine the transmission of solar radiation within the upper few millimeters of the ocean. Dependence on the water type is small for this wavelength range.

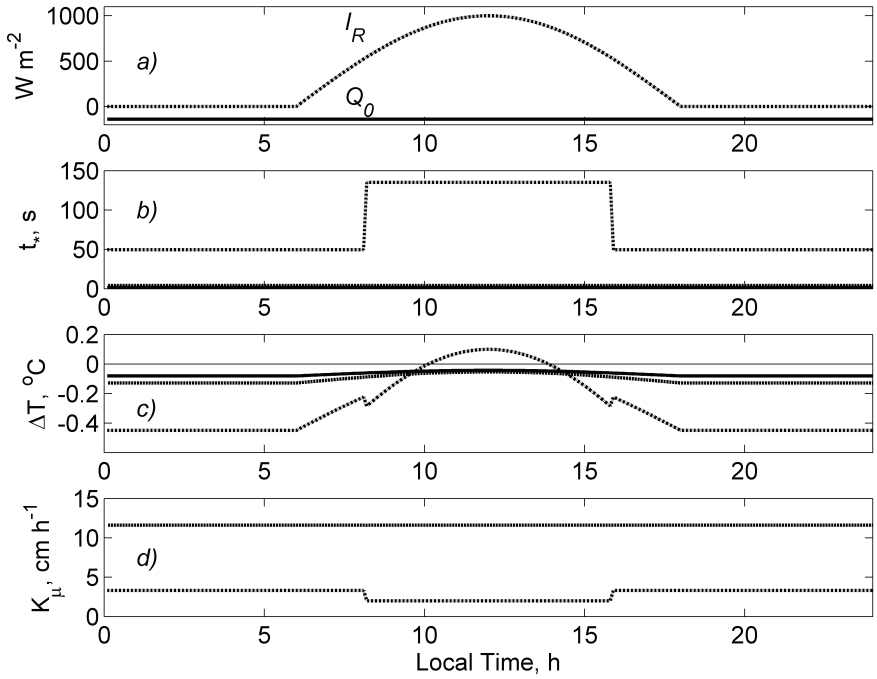


*Figure 2-17*. Evolution of temperature difference across the cool skin and of the direct air-sea gas transfer coefficient during 24 hrs at three different friction velocities: (a) idealized diurnal cycle of the surface solar irradiance and the net surface heat flux; (b) renewal time; (c) temperature difference across the cool skin; (d) Direct air-sea gas transfer coefficient for a Schmidt number Sc = 430 ($CO_2$ at 29°C and 35 psu). In (b), (c), and (d) the dash-dotted, dashed and contiguous lines correspond to the condition of free convection ($u_* = 0.001$ m s$^{-1}$), forced convection ($u_* = 0.007$ m s$^{-1}$), and intensive surface waves breaking ($u_* = 0.015$ m s$^{-1}$), respectively.

Observation of SST by infrared radiometer averages over relatively large areas and shows an integrated contribution of the surface renewal process at different stages. *Figure 2-16* shows the averaged temperature difference across the aqueous thermal molecular sublayer $\Delta T$, as well as its components

$\Delta T_c$ and $\Delta T_R$, as a function of $u_*$. The main effect of solar radiation on the cool skin is observed at low wind speeds. *Figure 2-17* shows the diurnal evolution of the temperature difference across the aqueous thermal molecular sublayer and the direct (interfacial) air-sea gas transfer velocity under idealized insolation conditions. For low wind speeds, suppression of free convection due to the absorption of solar radiation has a strong effect on the gas transfer at the ocean-air interface. This is because the surface renewal time "jumps" at some threshold level of insolation. For the temperature difference across the aqueous thermal molecular sublayer, this effect is not as big as for the gas exchange because of the partial compensation of surface cooling by solar heating.

### 2.4.5 Comparison with cool-skin field data

Sea surface temperature measurements in the western equatorial Pacific made by Hartmut Grassl from the R/V *Vickers* during TOGA COARE from 30 January to 26 February 1993 near 156°E, 2°S have provided the data set that is particularly useful in validating parameterizations for the temperature difference across the cool skin. The sea surface temperature data were taken with infrared radiometer. The bulk water temperature was measured with a standard shipboard thermosalinograph pumping water from 3 m depth. At night, the temperature differences in the upper 3 m were usually very small (a few hundredths of a degree at most). During daytime the difference between sea surface temperature and water temperature taken at 3 m depth could be affected by the presence of shallow diurnal thermocline as schematically shown in *Figure 2-18*. In addition, precipitation effects result in a stable salinity stratification (the near-surface rain-formed halocline), which is usually accompanied by temperature gradients. The likely presence of fine thermohaline structure in the upper few meters of the ocean under low wind speed conditions is one of the limitations of the cool-skin model validation. (More details about the fine thermohaline structure of the near-surface layer of the ocean can be found in Chapter 4.)

As a first approximation, the temperature difference across the diurnal thermocline ($\Delta T_d$) can be accounted for with a model of the diurnal mixed layer and thermocline. We make use of two types of models for the diurnal mixed layer and thermocline. The first model is that of Price et al. (1986), hereafter referred to as PWP. The second model is that of Stull and Kraus (1987), hereafter referred as SK. The SK model is the so-called transilient (nonlocal) model, which represents the turbulent transport by a cascade of eddies. The absorption of solar radiation is simulated with 9 spectral components for water type IB (see Chapter 1, *Table 1.2*), which prevails in the TOGA COARE domain.

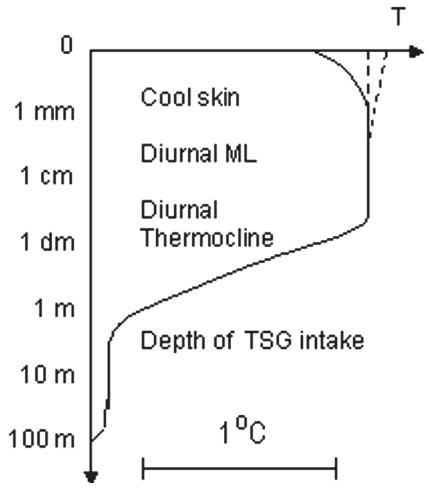


*Figure 2-18*. Schematic representation of the vertical temperature profile during a large diurnal warming event. Typical depth and temperature scales are shown (but may vary greatly).

*Figure 2-19* compares parameterization (2.89), hereafter referred to as $SS_m$, with the TOGA COARE data. Since the field measurements include both the thermal molecular sublayer and diurnal thermocline, a diurnal mixed layer model has been included, either PWP or SK (only the PWP model results are shown in *Figure 2-19*c). Both mixed layer model calculations include the surface heat and radiation fluxes, wind stress and rainfall rates as measured from the R/V *Vickers*. (Technical details relating to mixed layer modeling in this case can be found in Soloviev and Schlüssel, 1996). *Figure 2-19*d suggests that there is a phase shift between the PWP model prediction and field data under conditions of evening deepening. This is related to the slow, diffusive response of the PWP model during deepening of the diurnal thermocline. The SK model reproduces the SST evolution with no phase delay; it, however, results in a larger bias than the PWP model.

*Table 2-2* compares several parameterizations and models of the cool skin with the TOGA COARE data set. The Paulson and Simpson (1981) parameterization (labeled PS), the Soloviev and Schlüssel (1996) parameterization (labeled SS) as well as the Hasse (1971) model (labeled H) are designed to calculate $\Delta\overline{T}$ during day and night. The parameterization specified by Schlüssel et al. (1990) is labeled S; it has the night- and daytime components. Models H and S implicitly include the effect of the diurnal thermocline ($\Delta T_d$); PS, SS, and $SS_m$ are designed to parameterize the temperature difference $\Delta\overline{T}$ across the thermal molecular sublayer (cool skin) only.

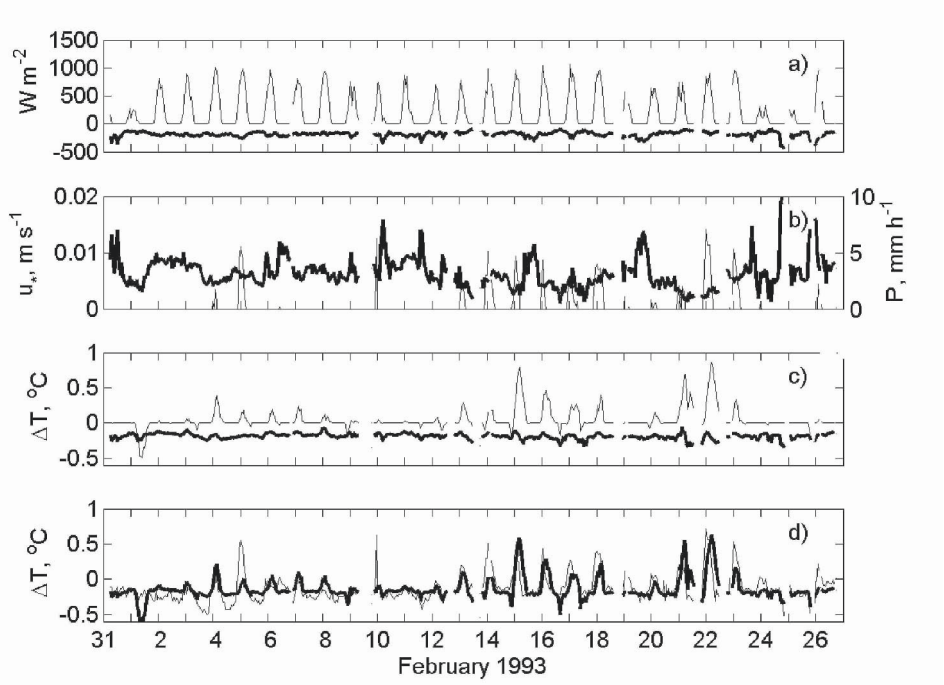


*Figure 2-19*. Comparison of parameterization $SS_m$ with measurements during TOGA COARE. (a) Hourly means of the surface solar irradiance $I_{R0}$ (thin line) and net surface heat flux $Q_0$ (bold line), (b) hourly means of friction velocity $u_*$ (bold line) and rain rate $P$ (thin line), (c) calculated temperature difference across the cool skin (parameterization $SS_m$, bold line) and across the diurnal thermocline with the PWP model, thin line), (d) hourly means of the difference between bulk and skin temperature as observed during COARE (thin line), parameterized by $SS_m$ plus PWP model (bold line). (Adapted from Soloviev and Schlüssel, 1996.)

The SS cool skin parameterization combined with the PWP model produces a bias of –0.03°C and standard deviation of 0.17°C. The SS parameterization combined with a nonlocal model of the diurnal thermocline SK gives a slightly better standard deviation (0.15°C) but larger bias (-0.08°C). The $SS_m$ cool skin parameterization, which represents the SS parameterization with updated constants ($a_0 = 0.23$, $\Lambda_0 \approx 10$, and $Ke_{cr} \approx 0.18$), produces a bias of -0.02°C and standard deviation of 0.17°C.

Model S (including both cool skin and diurnal thermocline parameterizations) and the PS+PWP model produced comparable results. Traditional parameterization H exhibits larger bias and standard deviation. The H parameterization is, however, based entirely on data from a field experiment in the Northeast Atlantic Ocean and is not necessarily valid in other parts of the world ocean.

*Table 2-2* Comparison of different parameterizations and models for the temperature difference, $\Delta T$, between the sea surface and 4 m depth (ship's thermosalinograph intake), with measurements made by Hartmut Grassl during TOGA COARE. The cool skin models are labeled as follows: H (Hasse, 1971), S (Schlüssel et al., 1990), PS (Paulson and Simpson, 1981), SS (Soloviev and Schlüssel, 1996), and $SS_m$ (Soloviev and Schlüssel, 1996 with updated empirical constants); the diurnal thermocline models, PWP (Price et al., 1986), and SK (Stull and Kraus, 1987). All temperature differences are in $^oC$.

| Cool-Skin Model | Diurnal Mixed Layer and Thermocline Model | Night | | Day | | Day and Night | |
|---|---|---|---|---|---|---|---|
| | | Bias | Std. Dev. | Bias | Std. Dev. | Bias | Std. Dev. |
| **H** | Included | 0.32 | 0.27 | 0.28 | 0.23 | **0.30** | 0.25 |
| S | Included | 0.14 | 0.10 | -0.02 | 0.19 | 0.05 | 0.15 |
| PS | PWP | 0.06 | 0.13 | 0.14 | 0.20 | 0.10 | 0.17 |
| SS | PWP | 0.01 | 0.13 | 0.06 | 0.20 | 0.03 | 0.17 |
| **$SS_m$** | PWP | 0.02 | 0.12 | 0.05 | 0.20 | **0.02** | 0.17 |
| SS | SK | 0.06 | 0.11 | 0.10 | 0.18 | 0.08 | 0.15 |

Though parameterization $SS_m$, combined with the PWP model follows the main features of the field data (*Figure 2-19*) and outperforms the other models brought to the analysis, in some situations, especially under low wind speed conditions, the difference between the model and data exceeds $0.5^{\circ}C$. As mentioned above, numerical models of the diurnal mixed layer and thermocline are not yet perfect, in particular under low wind speed conditions. Improvement of the mixing parameterization is one of the closely related issues (see Chapter 7).

Note that the SS cool skin model uses the Soloviev and Schlüssel (1996) version of the renewal model. New field data instigated a modification of the empirical coefficients entering this model, as described in Section 2.3.2. Quantitative comparison of the revised model with the COARE data set presented has been presented in *Figure 2-19*.

Both mixed layer models, SK and PWP, account for the rain-formed stratification in the near-surface layer. None of the cool skin models mentioned in this section, however, accounts for the rain-related effects that are the subject of the next sections.

## 2.5 Cool and Freshwater Skin of the Ocean during Rainfall

Rain falling into the sea modifies the aqueous molecular sublayers through a variety of different effects. These effects include additional momentum flux and stabilizing buoyancy flux from air to sea, additional sensible heat flux of the rain, modification of physical water constants

because of temperature and salinity changes, increase of the surface roughness, damping of short gravity waves, excitation of capillary waves at higher wave frequencies, and the surface mixing by droplets.

During rainfall the raindrops penetrate to tens of centimeters directly affecting the near-surface salinity. Rain falling on the sea surface also establishes a haline diffusive molecular sublayer with a salinity gradient. Schlüssel et al. (1997) refer to this layer as the *freshwater skin* of the ocean. The freshwater skin is only about 50 μm thick. The salinity difference developing in the haline diffusive molecular sublayer can to some extent affect the interpretation of the radar and radiometric observations of the sea surface at low microwave frequencies. The dielectric constant of water depends on the sea surface salinity at centimeter wavelengths (Lagerloef et al., 1995). The dielectric constant change may cause interpretation problems when remotely measuring wind speed or sea surface temperatures at these frequencies. The dielectric constant dependence on salinity may also be used for remote sensing of the sea surface salinity. Though the depth of the haline molecular sublayer is much less then the penetration depth of the electromagnetic radiation at these wavelengths, the exponential decay of the radiation energy entering the ocean can, however, make it sensitive to salinity changes in the skin layer.

An important effect is the dependence of gas solubility on salinity. For instance, a 1% decrease of the seawater salinity results in a 0.5% increase of the $CO_2$ solubility and 0.1% increase of the $O_2$ solubility (Stephen and Stephen, 1964; Riley and Skirrow, 1965).

In view of the different effects that can be expected from rainfall on the surface molecular sublayer, Schlüssel et al. (1997) provide a comprehensive description of the modifications of this layer of the ocean due to precipitation. According to these authors, the impact of precipitation on the thermal and diffusive molecular sublayers of the ocean includes the following processes:

1) The freshwater flux due to rain produces a buoyancy flux in the near-surface layer of the ocean, which tends to suppress convection (Ostapoff et al., 1973).
2) Raindrops temperatures are usually lower than the sea surface temperature (Katsaros, 1976). The precipitation falling into the ocean results in an interfacial sensible heat flux $Q_{rs}$ caused by small drops that do not penetrate into the ocean and in a volume heat flux $Q_{rV}$ due to drops submerging into the ocean and gradually mixing with depth.
3) Changes in the temperature and salinity due to rain mentioned in the previous two points modify physical constants of sea surface water (Katsaros and Buettner, 1969). In particular, the kinematic viscosity

increases with decreasing temperature and decreases with decreasing salinity.

4) Rainfall can enhance the surface roughness as much as two orders of magnitude by generation of impact craters, Rayleigh jets, splash drops, and small waves (Houk and Green, 1976).
5) Raindrops falling into the ocean fragment and partly remove surface films (Green and Houk, 1979).
6) Raindrops penetrating through the surface disturb wave motions and damp the short gravity waves by reducing the amplitudes at which they break (Yakimov, 1959; Manton, 1973; Tsimplis and Thorpe, 1989; Méhauté and Khangaonkar, 1990; Poon et al., 1992). As a result, small-scale wave breaking intensifies and the surface-renewal time period decreases.
7) Raindrops impact the sea surface and submerge into the ocean, generating additional surface renewals.
8) Raindrops obtain horizontal momentum from the airflow at cloud levels. These raindrops subsequently pass this momentum to the atmospheric boundary layer and to the sea surface, adding to the wind stress that acts on the surface (Caldwell and Elliot, 1971). All the momentum of the drop is transferred to the ocean, as opposed to only a small fraction of air momentum.
9) The freshwater skin coexisting with the cool skin is subject to irreversible thermodynamic processes due to significant local temperature and salinity gradients (Doney, 1995).

Schlüssel et al. (1997) made an attempt to quantify the various effects of rain on the aqueous molecular sublayers. The irreversible thermodynamics processes in the presence of the cool skin and freshwater skin, however, have not yet been quantified.

### 2.5.1 Effects of rain on the cool skin

Following again the same approach as in Section 2.3.2, consider a fluid element adjacent to the sea surface that participates in the process of cyclic renewal of the surface water in the presence of rain. Initially, the fluid element has a uniform temperature equal to the bulk-water value $T_w$. As it is exposed to the interface, the molecular diffusion law governs the evolution of the temperature difference across the thermal sublayer:

In the framework of the surface renewal theory described in Section 2.3.2 the temperature change between subsequent renewal events in the thermal molecular sublayer of the ocean including a volume source is described by the molecular diffusion equation similar to (2.69) but, instead of solar radiation term, including the volume source of heat due to rain:

$$\frac{\partial T}{\partial t} = \frac{\partial}{\partial z}\left(\kappa_T \frac{\partial T}{\partial z}\right) - P\left(T_0 - T_r\right)\frac{\partial f_V}{\partial z}, \tag{2.98}$$

where $f_V$ the volume source function defined according to (1.79), $T_r$ the raindrop temperature. We ignore here the difference between specific heats and densities of seawater and rainwater.

The surface boundary condition is defined by rain-induced surface heat flux (1.82):

$$-\kappa_T \frac{\partial T}{\partial z} = \frac{Q_{rs}}{c_p \rho} = P\left(T_0 - T_r\right)\left[1 - f_V\left(0\right)\right]. \tag{2.99}$$

Instead of the volume heat source due to the absorption of solar radiation, equation (2.98) includes the volume source of heat due to raindrops mixing with their environment. In order to reduce the problem of the rain effect to the already considered problem of the solar radiation effect on the cool skin, Schlüssel et al. (1997) approximated the volume source function in (2.98) by a sum of exponentials (similar to the solar radiation absorption function):

$$\partial f_V\left(z\right)/\partial z \simeq \sum_{i=1}^{N_r} \varsigma_l \exp\left(\psi_l \Lambda z / a_r\right), \tag{2.100}$$

where $\varsigma_l$ and $\psi_l$ are coefficients obtained by a nonlinear least squares fit. The requirements, $\varsigma_l > 0$ and $\psi_l > 0$, resulted in $N_r$=14 terms for a good fit. The numerical values of these coefficients for $r_c$ = 0.40 mm and $r_c$ = 0.75 mm can be found in the original publication of Schlüssel et al. (1997).

The solution to a linear problem (2.98)-(2.99) with a homogeneous vertical temperature profile as the initial condition is obtained in the same way as for equation (2.98) (for details, see Section 2.4.1). The temperature difference between the sea surface temperature $\Delta T_r\left(0,t\right)$ and the bulk water temperature is then as follows:

$$\Delta T_r\left(0,t\right) = \Delta T_{rs}\left(0,t\right) + \Delta T_{rv}\left(0,t\right) \tag{2.101}$$

where

$$\Delta T_{rs}\left(0,t\right)=P\left(T_r-T_w\right)2\sqrt{\frac{t}{\kappa_T\pi}}\left(1+2\Lambda r_c+\frac{4\Lambda^2 r_c^2}{2}+\frac{8\Lambda^3 r_c^3}{6}\right)\exp\left(-2\Lambda r_c\right),$$

$$\Delta T_{rV}\left(0,t\right)=P\left(T_r-T_w\right)\frac{1}{\kappa_T}\sum_{l=1}^{L}\frac{\varsigma_l a_r}{\Lambda\psi_l}\left[\exp\left(\delta_l^2\right)\left[erf\left(\delta_l\right)-1\right]+1-\pi^{-1/2}\delta_l\right],$$

$\xi=z/\sqrt{4\kappa_T t}$, and $\delta_l=\psi_l\Lambda\sqrt{kt}/a_r$. The first term on the right side of (2.101) is related to the surface flux of rainwater, while the second term is related to the volume source of rainwater.

In accordance with the renewal concept, this temperature difference should be averaged over time by weighting with probability density $p\left(t\right)$ of the surface renewals:

$$\overline{\Delta T}=\int_0^\infty p\left(t\right)\Delta T_{wr}\left(0,t\right)dt \tag{2.102}$$

where

$$\Delta T_{wr}\left(0,t\right)=\frac{1}{t}\int_0^t\Delta T_r\left(0,t'\right)dt' \tag{2.103}$$

With (2.101), the solution to (2.103) is

$$\begin{aligned}&\Delta T_{wr}\left(0,t\right)=P\left(T_r-T_w\right)\times\\&\left\{\frac{4}{3}\sqrt{\frac{t}{\kappa_T\pi}}\left(1+2\Lambda r_c+\frac{4\Lambda^2 r_c^2}{2}+\frac{8\Lambda^3 r_c^3}{6}\right)\exp\left(-2\Lambda r_0\right)-\right.\\&\frac{1}{\kappa_T}\sum_{l=1}^{L}\frac{\varsigma_l a_r}{\Lambda\psi_l}\left(\delta_l^{-2}\left\{\exp\left(\delta_l^2\right)\left[1-erf\left(\delta_l^2\right)\right]-1\right\}+2\pi^{-1/2}\delta_l-1\right)-\\&\left.\sum_{l=1}^{L}\frac{4}{3}\varsigma_l\sqrt{\frac{t}{\pi\kappa_T}}\right\},\end{aligned} \tag{2.104}$$

which is used together with (2.102) and the log-normal probability density function of the surface renewals similar to (2.88)-(2.89); this allows the numerical integration that gives the modification of the cool skin caused by the sensible heat flux related to the rain.

### 2.5.2 Freshwater skin of the ocean

Besides the modification of the cool skin, rainfall creates a freshwater skin on the top of the ocean where a salinity flux takes place via molecular diffusion (Schlüssel et al., 1997). Under no-rain conditions, evaporation at the sea surface increases salinity, which tends to destabilize the near-surface water enhancing the renewal process at the surface. However, when rain starts, the part of the rain that does not submerge into the ocean can compensate for the evaporation effect and create a stably stratified freshwater skin. This is analogous to the conversion of the cool skin into its antipode, the warm skin, which sometimes occurs under conditions of strong insolation. Consequently, this freshwater effect on diffusion can be described by the diffusion equation in analogy to equation (2.98) that was derived for the thermal sublayer:

$$\frac{\partial S}{\partial t} = \frac{\partial}{\partial z}\left( \mu \frac{\partial S}{\partial z} \right) - PS \frac{\partial f_V}{\partial z}, \tag{2.105}$$

where $\mu$ is the coefficient of molecular salinity diffusion and $f_V$ is the volume source function due to rain submerging into the ocean.

The surface boundary condition for salinity flux due to rain that is to be included in the boundary condition for the diffusion equation (2.105) is as follows:

$$-\mu \frac{\partial S}{\partial z} = J_{rs} = S_0 P\left[ 1 - f_V\left(0\right) \right]. \tag{2.106}$$

Assuming that

$$\Delta S << S_w, \tag{2.107}$$

the salinity $S$ and its surface value $S_{0,}$ entering equations (2.105) and (2.106) respectively, are both replaced with the bulk water salinity $S_b$. The solution to the linear problem (2.105)-(2.107) is then obtained in the same way as in Section 2.4.1 (as well as in the previous section, Section 2.5.1):

$$\Delta S_r\left(0,t\right) = \Delta S_{rs}\left(0,t\right) + \Delta S_{rv}\left(0,t\right), \tag{2.108}$$

where

$$\Delta S_{rs}\left(0,t\right)=-PS_0 2\sqrt{\frac{t}{\kappa_T\pi}}\left(1+2\Lambda r_c+\frac{4\Lambda^2 r_c^2}{2}+\frac{8\Lambda^3 r_c^3}{6}\right)\exp\left(-2\Lambda r_c\right),\ \text{and}$$

$$\Delta S_{rV}\left(0,t\right)=-PS_0\frac{1}{\kappa_T}\sum_{l=1}^{L}\frac{\varsigma_l a_r}{\Lambda\psi_l}\left[\exp\left(\delta_l^2\right)\left[erf\left(\delta_l\right)-1\right]+1-\pi^{-1/2}\delta_l\right].$$

The first term on the right side of (2.108) is related to the surface flux of rainwater, while the second term is related to the volume source of rainwater.

The salinity difference should be averaged over time by weighting with probability density $p\left(t\right)$ of the surface renewals:

$$\overline{\Delta S}=\int_0^\infty p\left(t\right)\Delta S_{mr}\left(0,t\right)dt \tag{2.109}$$

where

$$\begin{aligned}&\Delta S_{mr}\left(0,t\right)=-PS_0\times\\&\left\{\frac{4}{3}\sqrt{\frac{t}{\kappa_T\pi}}\left(1+2\Lambda r_c+\frac{4\Lambda^2 r_c^2}{2}+\frac{8\Lambda^3 r_c^3}{6}\right)\exp\left(-2\Lambda r_0\right)-\right.\\&\frac{1}{\kappa_T}\sum_{l=1}^{L}\frac{\varsigma_l a_r}{\Lambda\psi_l}\left(\delta_l^{-2}\left\{\exp\left(\delta_l^2\right)\left[1-erf\left(\delta_l^2\right)\right]-1\right\}+2\pi^{-1/2}\delta_l-1\right)-\\&\left.\sum_{l=1}^{L}\frac{4}{3}\varsigma_l\sqrt{\frac{t}{\pi\kappa_T}}\right\},\end{aligned} \tag{2.110}$$

Solutions (2.110) holds for the linear case only under an assumption that $S\approx S_w$ (*i.e.*, $\Delta S<<S_w$) and physical properties of seawater do not change substantially because of the salinity dependence. The properties that could be affected by the rain-caused changes in sea surface salinity are the thermal expansion coefficient, kinematic viscosity, density, specific heat, and latent heat of vaporization. The large salinity differences arising from substantial freshwater influx and relatively long renewal times would require a nonlinear solution to (2.105)-(2.106). However, as shown in the next section, under moderate and heavy rain conditions the renewal time is restricted to

very small values while in light rain the drop of surface salinity remains relatively small so that the solution for the nonlinear case may not be required in most cases.

### 2.5.3 Surface renewals due to rain mixing

Small raindrops do not produce an impact crater on the sea surface, while large drops do, disturbing the aqueous molecular sublayer. The area covered by each impact crater is subject to a surface renewal event since the impact crater is deeper than the conductive layer and represents a "catastrophic" event for the molecular sublayer (Engel, 1966). (Note that spray droplets from breaking waves also have to be considered in this regard.)

Rodriguez and Mesler (1988) studied drops falling from low heights into pools of liquid; they found that the impact crater radius $r_k$ exceeds about two to three times the corresponding drop radius $r_0$. Drops falling from higher altitudes generate even bigger craters, with radii up to $r_k \approx 4r_0$ (Prosperetti and Oguz, 1993). Dimensional analysis conducted by these authors suggests that the radius of the impact crater can be represented by a formula

$$r_k = r_0 \left( \frac{8}{3} Fr \right)^{1/4} \approx \varphi_c r_0 Fr^{1/4}, \tag{2.111}$$

where $Fr = w_t^2 / g r_0$ is the Froude number, $g$ is the acceleration of gravity, $w_t$ is the terminal velocity of raindrops, and $\varphi_c = (8/3)^{1/4} \approx 1.278$ is a dimensionless constant. Relationship (2.111) has been supported by observations of Pumphrey and Elmore (1990). Comparison with data from Engel (1966) suggests a somewhat smaller constant of about $\varphi_c = 1.05$. This discrepancy is nevertheless relatively small compared to other uncertainties relating to rain-induced mixing (*e.g.*, the size distribution of droplets).

The terminal velocity of raindrops falling on the ocean surface can be estimated from an empirical formula given by Best (1950):

$$w_t = w_\upsilon \left[ 1 - \exp\left( -\left( r_0 / r_\upsilon \right)^\upsilon \right) \right], \tag{2.112}$$

where $w_\upsilon = 9.43$ m s$^{-1}$, $r_\upsilon = 1.77 \times 10^{-3}$ m, and $\upsilon = 1.147$. For radii $0.3 \times 10^{-3}$ m $< r_0 < 6 \times 10^{-3}$ m, representing the majority of the raindrops, (2.112) is approximated within 0.1 m s$^{-1}$ accuracy by

$$w_t = w_\upsilon \left[ b_1 - b_2 \exp\left( -r_0 / r_\upsilon \right) \right] \tag{2.113}$$

where $b_1 = 1.0528$ and $b_2 = 1.07733$. Substituting $w_t$ from (2.113) into (2.111) transforms formula (2.111) into a functional dependence of the impact crater radius solely on the raindrop radius:

$$r_k = \varphi_c r_0 \left( \frac{w_\upsilon^2 \left[ b_1 - b_2 \exp\left(-r_0 / r_\upsilon\right) \right]^2}{g r_0} \right)^{1/4} . \tag{2.114}$$

The area that is subject to renewal due to the raindrop impact is equal to the impact crater area. The number of drops of size $r_0 \pm dr_0$ that reach the surface per unit time and unit area is $n(r_0) w_t(r_0) dr_0$, where $n(r_0)$ is the drop size distribution in the atmosphere near the water surface. Respectively, Craeye and Schlüssel (1998) represented the crater flux density (*i.e.*, the production rate of crater area per unit area and unit time) as follows:

$$F_k = \int_{r_c}^{\infty} \pi r_k (r_0)^2 n(r_0) w_t(r_0) dr_0 . \tag{2.115}$$

Representing the distribution of the rain above the sea surface by the Marshall-Palmer drop size spectrum (1.65) and substituting relationships (2.113) into equation (2.115), and (2.114) into (2.115) results in the following formula:

$$F_k = \int_{r_c}^{\infty} \pi r_0^2 \varphi_c^{\,2} \left( \frac{w_\upsilon^2 \left[ b_1 - b_2 \exp\left(-r_0 / r_\upsilon\right) \right]^2}{g r_0} \right)^{1/2} \times \tag{2.116}$$
$$n(r_0) w_\upsilon \left[ b_1 - b_2 \exp\left(-r_0 / r_\upsilon\right) \right] dr_0 .$$

The renewal time is then defined as the inverse of the impact-flux density $F_k$,

$$t_{*r} = 1 / F_k \tag{2.117}$$

The calculation of the integral on the right side of (2.116) and substituting the result into (2.117) leads to

$$t_{*r} = \frac{g^{1/2}}{\pi n_0 \varphi_c^{\,2} w_\upsilon^2}\Big[ b_1^2 \left(2\Lambda\right)^{-5/2} \Gamma\left(5/2, 2\Lambda r_c\right) - 2b_1 b_2 \left(2\Lambda + r_\upsilon^{-1}\right)^{-5/2} \Gamma\left(5/2, 2\Lambda r_c + r_c r_\upsilon^{-1}\right) + b_2^2 \left(2\Lambda + 2r_\upsilon^{-1}\right)^{-5/3} \Gamma\left(5/2, 2\Lambda r_c + r_c r_\upsilon^{-1}\right)\Big], \quad (2.118)$$

where $\Gamma$ is the incomplete gamma function.

*Figure 2-20* shows the surface renewal time $t_{*r}$ as a function of rainrate *P*. The rainfall strongly influences the renewal time even for low rainrates. For $P > 2$ mm h$^{-1}$, the rain-induced surface disruptions dominate the renewal process including the surface renewals caused by breaking wavelets or long breaking waves. In calm situations even light rainfall easily surpasses the effect of free convection on the renewal time.

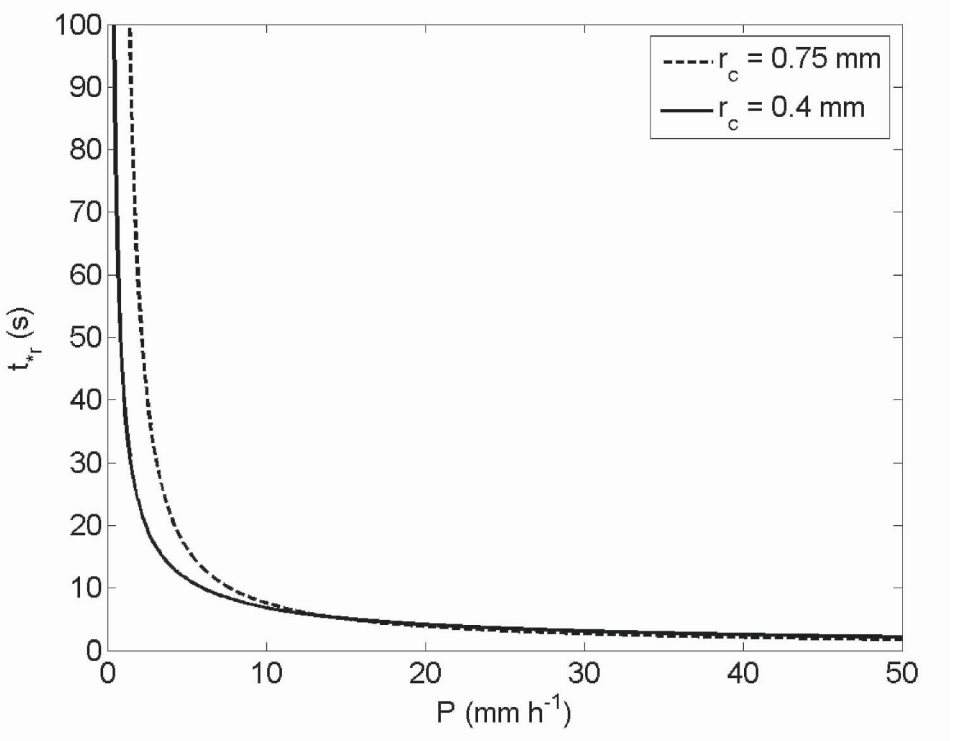


*Figure 2-20*. Surface renewal time due to rain calculated from (2.118) as a function of rainrate for two critical radii $r_c$.

*Figure 2-21*a shows the skin cooling due to rainfall for renewal times determined by the rain as a function of rainrate. The variation of the volume

flux of heat with rainrate is compensated by the rain-induced mixing, leaving an almost constant, but small temperature difference that depends on the difference between surface and rain temperatures only (the latter is here held constant at 5°C). The effect of surface heat flux, however, does increase with rainrate. Nevertheless, at rainrates below 50 mm $h^{-1}$ the temperature difference across the cool skin does not exceed $\Delta T = -0.08\,^{o}\mathrm{C}$ for the given surface versus rain temperature difference.

*Figure 2-21*b shows the freshwater skin due to rainfall for renewal times determined by the rain. The maximum salinity difference across the diffusion sublayer does not exceed $\Delta S$ = 5 psu for rain rates up to 50 mm $hr^{-1}$. It is, nevertheless, a dramatic salinity change compared to the range of typical salinity variations in the ocean. The drop in the surface salinity due to rain is mainly due to the surface component of the freshwater flux; the contribution of submerging raindrops appears to be small.

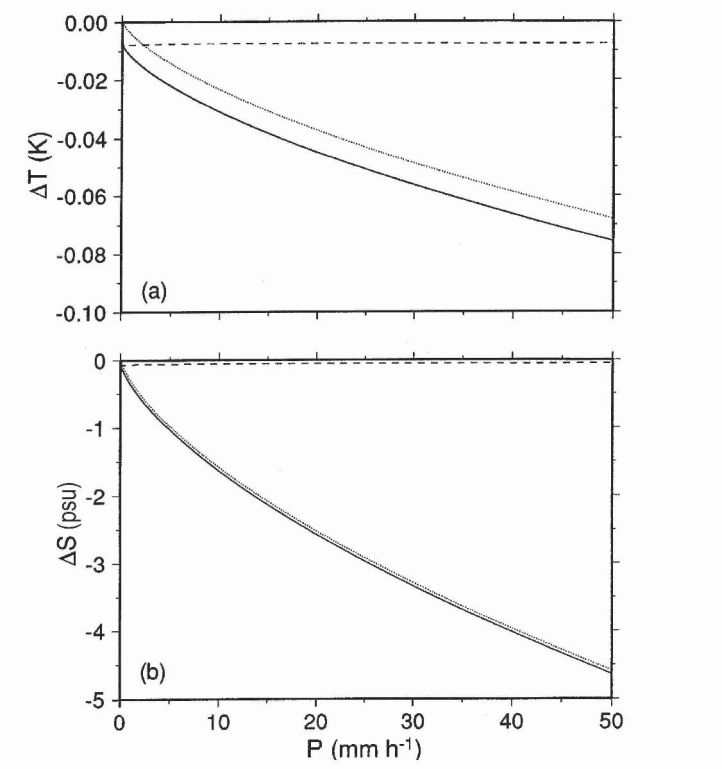


*Figure 2-21*. Skin cooling by rainfall with a typical rain drop temperature of 5°C below the sea surface temperature (a) and freshwater skin due to rainfall at bulk salinity of $S_w$ = 35 psu (b), both as a function of rainrate with respect to renewal times determined by the rainfall; the total effects are shown by the solid line, the effects due to drops penetrating into the ocean by the dashed lines and that due to surface heat flux by the dotted lines. Reproduced from Schlüssel et al. (1997) with permission from Springer Science and Business Media.

The combined renewal time can be derived by considering renewal events caused by skin friction and kinetic energy fluxes and rain-induced renewals as independent processes. Hence, within a given time period, the number of total renewals equals the sum of renewals due to rain $t_{*r}$ and renewals due to momentum and energy fluxes $t_{*f}$ The combined renewal time is then given by formula suggested in Schlüssel et al. (1997):

$$1/t_* = 1/t_{*f} + 1/t_{*r} \tag{2.119}$$

### 2.5.4 Buoyancy effects in molecular sublayer due to rain

At the sea surface from the waterside ($z \to -0$) the vertical flux of buoyancy is as follows:

$$B_0 = -\frac{g}{\rho}\overline{(w'\rho')}\Big|_{z\to -0} = \\ -\frac{\alpha_T g}{c_p \rho}\left(Q_E + Q_T + Q_L + Q_{rs}\right) - \beta_S S_0 g \frac{Q_E}{\rho L} - \beta_S g Q_{rs}. \tag{2.120}$$

The buoyancy flux due to rain stabilizes the upper ocean, which affects the dynamics of molecular sublayers. The description of this effect is included through a modification of the surface Richardson number $Rf_0$

$$Rf_0 = -\nu B_0 / u_*^4, \tag{2.121}$$

where $B_0$ is defined in (2.120).

Expression (2.121) accounts for surface fluxes only; volume absorption of solar radiation or raindrops submerging into the ocean complicates the analysis. In the general case, the approach described in Section 2.4.3 can be applied: $B_0$ is set to zero when the maximum Rayleigh number is less than the critical value for negative values of $Rf_0$; positive values of $Rf_0$ are always set to zero. Estimates, however, show that even for very low rainrates the buoyancy flux due to freshwater input is stronger than the counterparts due to the thermal convection and evaporative surface salinity increase. Under low wind speed and rainy conditions $Rf_0$ easily becomes zero, leading to very high values of $t_{*f}$. Below a certain rainrate ($\sim 0.1$ mm h$^{-1}$) the buoyancy effect inhibits the additional mixing due to rain; while, the additional mixing due to rain prevails at larger rainrates.

The analysis of *Figure 2-21* also suggests that the contribution of the volume freshwater flux into the diffusion molecular sublayer (freshwater skin) is relatively small compared to that of the surface freshwater flux. The contribution of the volume source into the freshwater skin is negligible in most cases.

### 2.5.5 Rain effects on sea surface roughness

Disruptions of the sea surface produced by rain increase the sea surface roughness. The Rayleigh-jet columns, together with the raindrops on their tops and the wavelets radiated from the drop impact zones, are roughness elements that can increase the surface roughness beyond the wind-induced roughness. The roughness elements produced by the rain do not propagate as the wind-induced waves do and therefore resemble fixed obstacles such as roughness elements on land surfaces.

The molecular sublayers of the surface ocean are mainly controlled by the tangential shear stress. The flow above the surface is aerodynamically smooth as long as the height of the roughness elements is smaller than $5\nu/u_*$, where $\nu$ is the kinematic viscosity and $u_*$ is the friction velocity of the air (Schlichting, 1979). In the aerodynamically smooth flow the momentum is passed to the ocean by skin friction only. If the roughness elements are greater than $70\nu/u_*$, the flow is aerodynamically rough, and the momentum transfer is affected by the form drag. *Figure 2-22*a shows the smooth and rough regimes as a function of friction velocity. There is a transition zone between these regimes, where both skin and form drag are important. The Rayleigh-jet that extends a centimeter or more into the air (Siscoe and Levin, 1971) therefore affects form drag, except for situations with very low friction velocities when the thickness of the viscous sublayer increases without bound.

Engel (1966) proposed a formula for the maximum height of the waves directly adjacent to the impact craters generated by drop impacts:

$$h_{w,\max} = \alpha_0 \left( \left[ \alpha_1 \frac{r_0^3 \rho_r w_t^2}{g\rho} + \alpha_2 \frac{{\sigma_s}^2}{g^2 \rho^2} \right]^{1/2} - \alpha_3 \frac{\sigma_s}{g\rho} \right)^{1/2} \tag{2.122}$$

where $\sigma_s$ is the surface tension of the sea surface, $\alpha_0 = 33.33$, $\alpha_1 = 1.2 \times 10^8$, $\alpha_2 = 3.1149 \times 10^{10}$, and $\alpha_3 = 1.7649 \times 10^5$. *Figure 2-22*a shows dependence of $h_{w,\max}$ on the drop radius (2.122) with the terminal velocity parameterized according to (2.112), the flow is smooth no matter what the drop size is for very small friction velocities owing to the unbounded

increase of the viscous sublayer thickness. With increasing friction velocities, drops with radii greater than about 1 mm lead to waves that cause a rather rough flow, while waves produced by smaller drops do not disturb the flow smoothness.

Smooth surface waves contribute to the surface roughness in a different way compare to random roughness elements. According to Motzfeld's (1937) experiment in a wind tunnel, the drag coefficient at a height of 0.2 m over surface waves is about seven times smaller than that over a surface with rough elements of the same size. Schlüssel et al. (1997) estimated that under the assumption of a logarithmic wind profile this implies a reduction of the roughness length of the rain-induced wavelets by a factor of 0.4 when compared to the roughness length of random rough elements of the same height. This effect leads to some increase in the wave height above which the flow becomes rough shown by the curve labeled $h_{w,red}(r_0)$ in *Figure 2-22*a. Taking into account the Marshall-Palmer drop-size distribution (1.71) an upper limit of the mean height of the wavelets is estimated from the formula,

$$\overline{h}_{w,red}(P) = \int_{r_c}^{\infty} h_{w,red} n_0 \exp(2\Lambda r_0)\, dr_0 \Big/ \left( \int_{r_c}^{\infty} n_0 \exp(2\Lambda r_0)\, dr_0 \right) \tag{2.123}$$

Formula (2.123) implies that the rain-induced waves do not decay and uniformly cover the sea surface. Equation (2.123) has been resolved substituting (2.113) into (2.122) and subsequently approximating

$$h_{w,red} = \beta_0 + \beta_1 r_0^{3/4} \left(1 - \beta_2 \exp\left(-r_0 / r_\upsilon\right)\right), \tag{2.124}$$

where $\beta_0 = 0.0129$ mm, $\beta_1 = 1.60686\ \text{mm}^{1/4}$, and $\beta_2 = 1.0978$. The resulting relationship is;

$$\begin{aligned} \overline{h}_{w,red}(R) = \beta_0 + \Big\{ & \beta_1 (2\upsilon)^{-7/4} \Gamma(7/4, 2\Lambda r_c) + \\ & \beta_2 \left(r_\upsilon^{-1} + 2\Lambda\right)^{-7/4} \Gamma\left(7/4, \left(r_\upsilon^{-1} + 2\Lambda\right) r_c\right) \Big\} 2\Lambda \exp(2\Lambda r_c). \end{aligned} \tag{2.125}$$

*Figure 2-22*b shows the roughness length calculated for the rain-induced wavelets using a coarse estimate given by Lettau (1969) as $z_{0r} \approx 0.058 \overline{h}_{w,red}^{1.19}$. For comparison purposes, the roughness length $z_{0C}$ of the wind-induced surface roughness under neutral conditions according to Charnock's (1955) formula is also given on this composite plot. The above estimate for the rain-induced roughness length is the maximum possible value, requiring an

optimal drop impact and a surface uniformly covered with rain-induced wavelets. Wave interactions, which have been neglected here, likely result in greater wave heights.

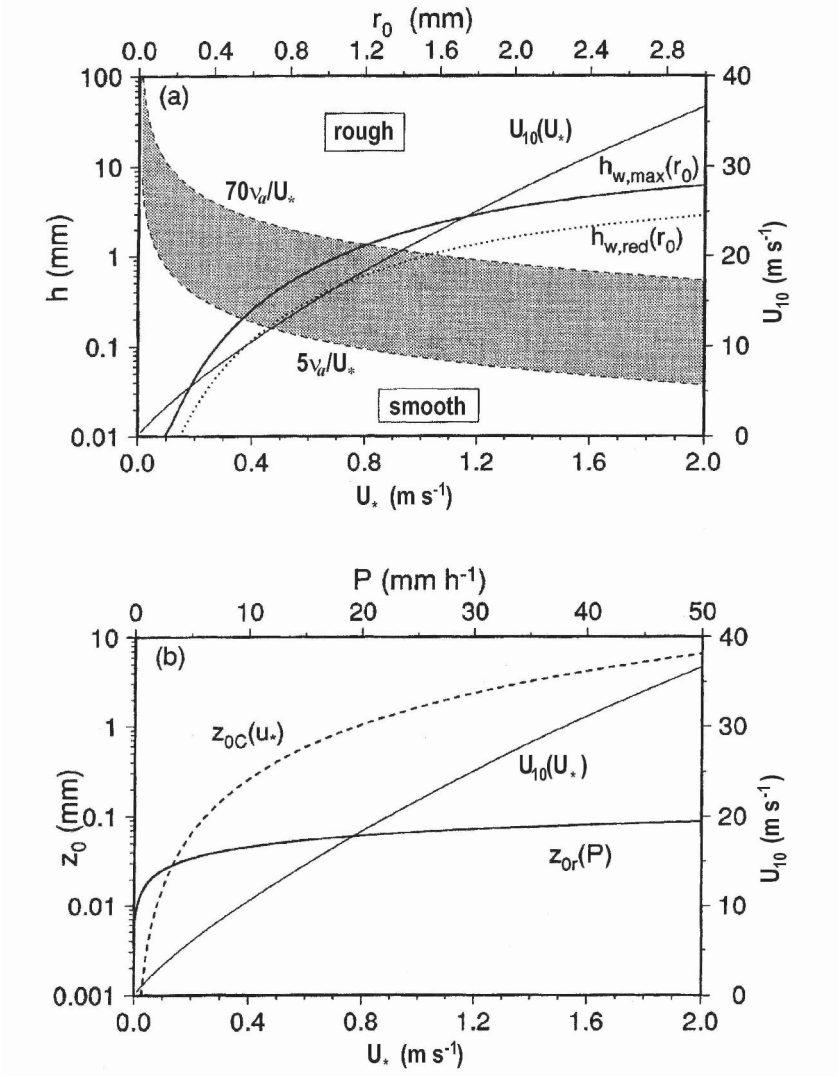


*Figure 2-22*. (a) Separation of aerodynamically smooth and rough domains (dashed cures) with the transition region indicated by the hashed area, maximum ($h_{w,\ max}(r_0)$, solid) and reduced ($h_{w,\ red}(r_0)$, dotted) heights of the rain-induced wavelets depending on drop radius $r_0$ and the relation between wind speed $u_{10}$ and friction velocity of the air $u_*$ (thin solid); (b) roughness length $z_0$ of wind-roughed surface (dashed) and rain-induced wavelets (solid) as a function of friction velocity of air $u_*$ and rainrate P, respectively, as well as the relation between wind speed and friction velocity (thin solid). Note: axes on opposite sides are not independent. (After Schlüssel et al., 1997.)

The rain-induced roughness increases strongly with rainrates up to about 2 mm $h^{-1}$, while at higher rainrates $z_{0r}$ increases only slightly (*Figure 2-22*b). Only for air friction velocity less than approximately 0.15 m $s^{-1}$, can the rain-induced waves appreciably contribute to the surface roughness. Charnock's (1995) formula employed for the calculation of $z_{0C}$ in *Figure 2-22*b, however, does not work under low wind speed conditions. In fact, due to viscous effects, the surface roughness under low wind stresses increases with decreasing wind.

*Figure 2-22* exhibits considerable differences in the rain-induced roughness lengths compared to those from laboratory studies by Houk and Green (1976). This is because of a more realistic raindrop spectrum employed by Schlüssel et al. (1997), which also covers many small, sub-millimeter drops while in the laboratory the effect of large drops (several mm in diameter) had been mainly investigated. The large drops in fact cover a very small portion of the natural spectrum of raindrops (Pruppacher and Klett, 1987).

The rain-induced stress leads, together with the wind stress, to increased surface wind-drift currents. This effect coexists with the attenuation of short gravity waves by enhanced turbulence in the upper ocean during rainfall (Tsimplis and Thorpe, 1988). The rain-induced wind-drift currents also reduce the amplitude threshold at which short gravity waves break (Philips and Banner, 1974).

From investigations in a wind-wave tank, Poon et al. (1992) found that gravity waves in the frequency range between 2 and 5 Hz decay during rainfall. At the same time, the spectral density of wave slopes in the frequency domain between 10 and 100 Hz drastically increases. The latter effect is due to rain-induced waves; however, it is pronounced only under low wind speed conditions. Results of experiments in a wind-wave tank by Yang et al. (1997) are consistent with the Poon et al. (1992) findings but provided some more details to the rain effects on fine structure of wind waves.

Due to damping of short gravity waves, a substantial part of the momentum transferred to the ocean by form drag under non-precipitating situations is instead transferred by skin friction during rainfall. This results in decrease of the surface renewal time, which is concurrent with the damping of short gravity waves.

### 2.5.6 Flux of kinetic energy carried by rain

According to Tsimplis (1992), the flux of kinetic energy carried by rain with a uniform drop size distribution is:

$$F_k = \frac{1}{2}\rho P w_t^2 . \tag{2.126}$$

In order to include the effect of natural drop size distributions, Craeye and Schlüssel (1998) introduced the spectral rainrate falling on the sea surface

$$\frac{dP}{dr_0} = \frac{4}{3}\pi r_0^3 n(r_0) w_t \tag{2.127}$$

which leads to a kinetic energy flux of

$$F_k = \frac{2}{3}\pi\rho \int_{r_c}^{\infty} r_0^3 n(r_0) w_t^3 dr_0 . \tag{2.128}$$

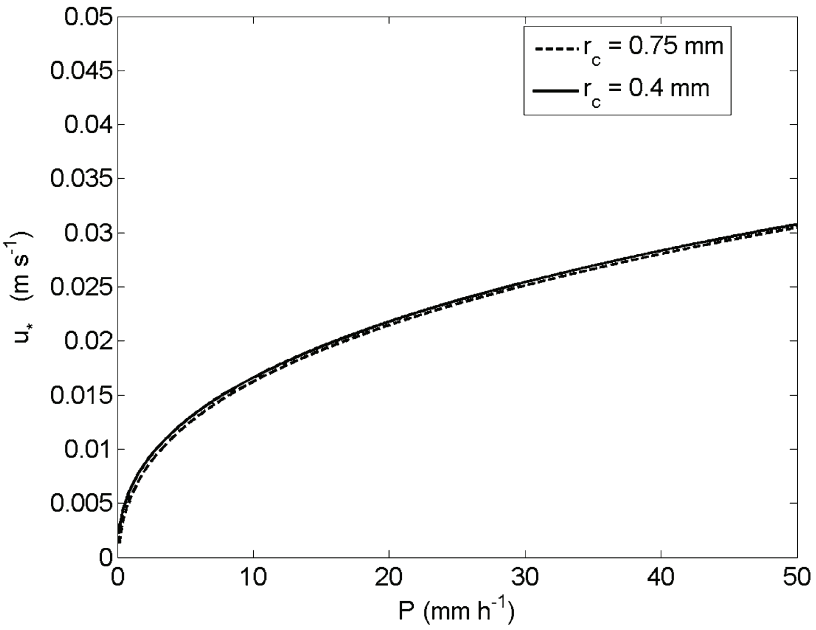


*Figure 2-23*. Friction velocity in the upper ocean attributed to the flux of kinetic energy carried by rain as function of rainrate for two values of critical radii $r_c$ calculated from (2.131).

For rain with a drop size distribution (1.65) and terminal velocities described by (2.113) the kinetic energy flux is then determined by

$$F_k = \frac{2}{3}\pi\rho n_0 \int_{r_c}^{\infty} r_0^3 \left[ b_1^3 \exp\left(-2\Lambda r_0\right) - 3b_1^2 b_2 \exp\left(-\left(2\Lambda + r_\upsilon^{-1}\right) r_0\right) + 3b_1 b_2^2 \exp\left(-\left(2\Lambda + 2v r_\upsilon^{-1}\right) r_0\right) - b_2^3 \exp\left(-\left(2\Lambda + 3r_\upsilon^{-1}\right) r_0\right)\right], \tag{2.129}$$

where only drops entering the ocean ( $r_0 > r_c$ ) are considered. The solution is

$$F_k = \frac{2}{3}\pi\rho n_0 w_\upsilon{}^3 \left[ \frac{b_1^3}{\left(2\Lambda\right)^4}\Gamma\left(4, 2\Lambda r_c\right) - \frac{3b_1^2 b_2}{\left(2\Lambda + r_\upsilon^{-1}\right)^4}\Gamma\left(4, 2\Lambda + \frac{r_c}{r_\upsilon}\right) + \frac{3b_1 b_2^2}{\left(2\Lambda + 2r_\upsilon^{-1}\right)^4}\Gamma\left(4, 2\Lambda r_c + \frac{2r}{r_\upsilon}\right) - \frac{b_2^3}{\left(2\Lambda + 3r_\upsilon^{-1}\right)^4}\Gamma\left(4, 2\Lambda r_c + \frac{3r_c}{r_\upsilon}\right)\right] \tag{2.130}$$

The equivalent friction velocity scale in the upper ocean is

$$u_{*r} = \left(F_k / \rho\right)^{1/3} \tag{2.131}$$

*Figure 2-23* shows the friction velocities corresponding to the flux of kinetic energy carried by the rain as a function of rainrate for two critical radii $r_c$. The friction velocity in water $u_*$ reaches 3 cm s$^{-1}$ at $P$ = 50 mm h$^{-1}$.

### 2.5.7 Combined effect

The enhancement of the near-surface mixing by rain is estimated by accounting for the area impacted by the raindrops of given rain rate and size distribution. It turns out that the interval between rain-induced surface renewal events can be far shorter than for wind-generated renewal events, which strongly reduces the temperature difference across the cool skin. However, for small rain rates this can be counteracted by the density stratification caused by the freshwater input. Subsequently, the extra momentum carried by the rain to the surface is accounted for, and the creation of additional surface roughness by rain-induced waves is estimated. The enhanced surface stress causes increased wind-drift currents, which, according to laboratory observations, can reduce the amplitude threshold for short gravity waves to break. This effect is parameterized as a function of rain rate. The rain-induced changes of physical properties of seawater become important at low wind speeds, while the effect of surface film fragmentation and removal by rain is believed to be negligible in affecting the molecular sublayer (Schlüssel et al., 1997).

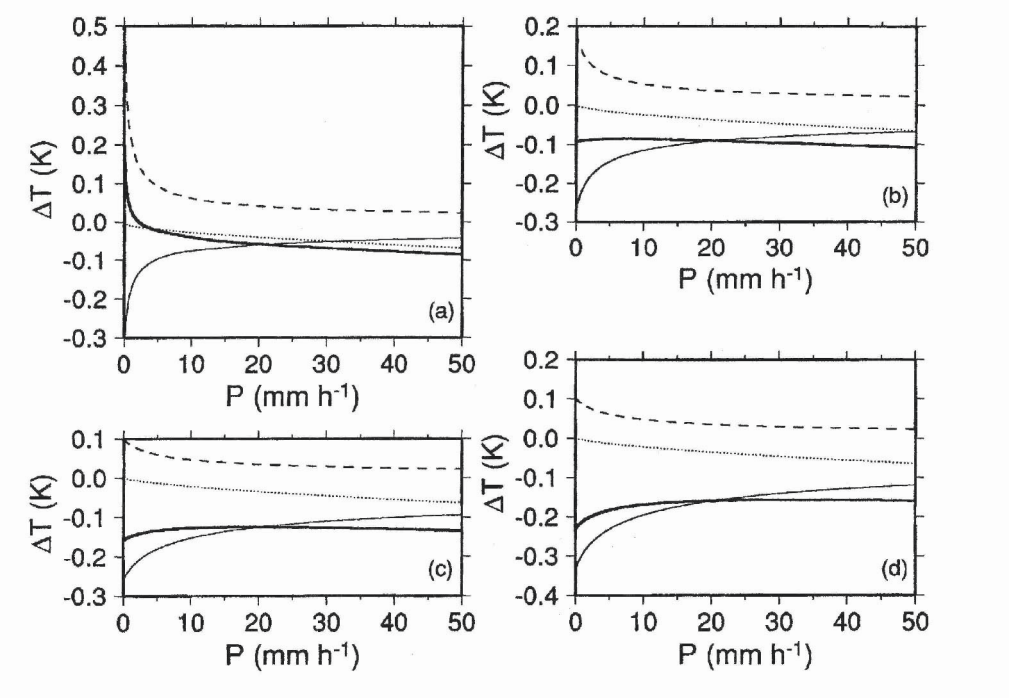


*Figure 2-24*. Temperature differences across the thermal molecular sublayer as a function of rainrate for (a) $U_{10}$ = 1 m s$^{-1}$, (b) $U_{10}$ = 5 m s$^{-1}$, (c) $U_{10}$ = 10 m s$^{-1}$, and (d) $U_{10}$ = 15 m s$^{-1}$. The curves correspond to differences due to cooling by turbulent and long wave fluxes (thin solid line), warming due to the absorption of solar radiation (dashed line), rain-induced cooling (dotted line) and the combined effect (thick solid line). (After Schlüssel et al., 1997.)

Schlüssel et al. (1997) incorporated all of the effects described above in a surface renewal model in order to study the combined effect of the processes involved in the physics of the aqueous molecular sublayers at the ocean surface. *Figure 2-24* shows temperature differences for wind speeds of $U_{10}$ = 1, 5, 10, 15 m s$^{-1}$ for an air-sea temperature difference of 1°C, a dew point difference of 6 K, a net long wave radiative flux of 70 W m$^{-2}$, and a solar irradiance of 1000 W m$^{-2}$. (Note that fixing the radiative fluxes as done here is unrealistic, but is done to illustrate the physics. As wind and rainrate increase, clouds will change, certainly affecting both shortwave and longwave components.) The turbulent heat fluxes are calculated from the TOGA COARE bulk flux algorithm version 2.5b (Fairall et al., 1996). For the situations simulated, the corresponding latent and sensible heat fluxes are $Q_E$ = 33, 107, 186, 252 W m$^{-2}$ and $Q_T$ = 2, 7, 11, 14 W m$^{-2}$. The rain temperature is assumed equal to the wet-bulb temperature calculated from the psychometric equation; its value is $T_r$ = 20.6°C when compared to the surface temperature of $T_0$ = 25°C.

*Figure 2-24* suggests that the most pronounced effect is due to additional mixing caused by the rain. This is observed at low rainrates where the rather high temperature differences prevailing in the non-precipitating situations quickly drop to low values when the rainrate increases to few mm $h^{-1}$. However, with further rainrate increase the strong decrease of the temperature differences weakens. It is remarkable that the temperature differences do not vanish even for precipitation rates of 50 mm $h^{-1}$. The additional skin cooling by the rain increases with rainrate though it does not exceed -0.1 K. At low wind speeds and very low rainrates the combined effect of solar warming and cooling by the turbulent and long wave fluxes results in a warm skin. At higher wind speeds the combined effect shows a minimum skin cooling at a distinct rainrate, which depends on the actual friction velocity. Further increasing rainrates lead to a slightly enhanced cooling due to the rain-induced heat flux (*Figure 2-24*b-d).

### 2.5.8 Comparison with data

The surface renewal model including the precipitation component described above has been tested by Schlüssel et al. (1997) with the COARE data taken from the R/V *Vickers* in January-February 1993 near 156°E, 2°S and from the R/V *Wecoma* near 156°E, between 2°S and 5°N. The frequent convective rain in the western equatorial Pacific shows strong variability with rainrates ranging from less than 0.1 to more than 100 mm $h^{-1}$; this tests the parameterization under a great variety of situations.

The R/V *Vickers* surface fluxes in the Schlüssel et al. (1997) comparison were identical to those shown in *Figure 2-19*. The calculated temperature differences across the cool skin that were caused by surface and volume cooling due to the rain showed values generally below 0.05°C; only one case with heavy precipitation exceeding 100 mm $h^{-1}$ gave a cooling by more than 0.1°C. There were just a few cases with strong daytime precipitation; during these rare periods the solar warming of the skin was about halved, according to the model. During nighttime the net effect of rain on the cool skin was rather small. Apart from several cases with strong rain when the cool skin was reduced by rain-induced mixing to values below 0.1°C, the effects of mixing and additional cooling partly cancelled each other during this observation in the western equatorial Pacific Ocean.

Similar to the analysis shown in *Figure 2-19*, a quantitative comparison of the parameterization with measurements of the skin versus bulk temperature difference from the R/V *Vickers* required that the temperature difference between the bulk sampling depth (*i.e.*, the depth of the thermosalinograph intake) and the surface microlayer was accounted for. This temperature difference was calculated with the mixed-layer model of Price et al. (1986) (PWP).

The overall agreement of the cool skin parameterization including rain is slightly better when compared to the results presented in *Figure 2-19*. While the RMS error remains unchanged (0.17°C), the small bias of 0.03°C to 0.02°C found earlier (*Table 2-2*) has now vanished completely. This is also true for the night and daytime data considered separately. In view of the skin measurement errors and the relatively small amount of data (total sample size of hourly means is 578), the result of this comparison is rather an indication that the inclusion of the rain parameterization in the surface renewal model is useful.

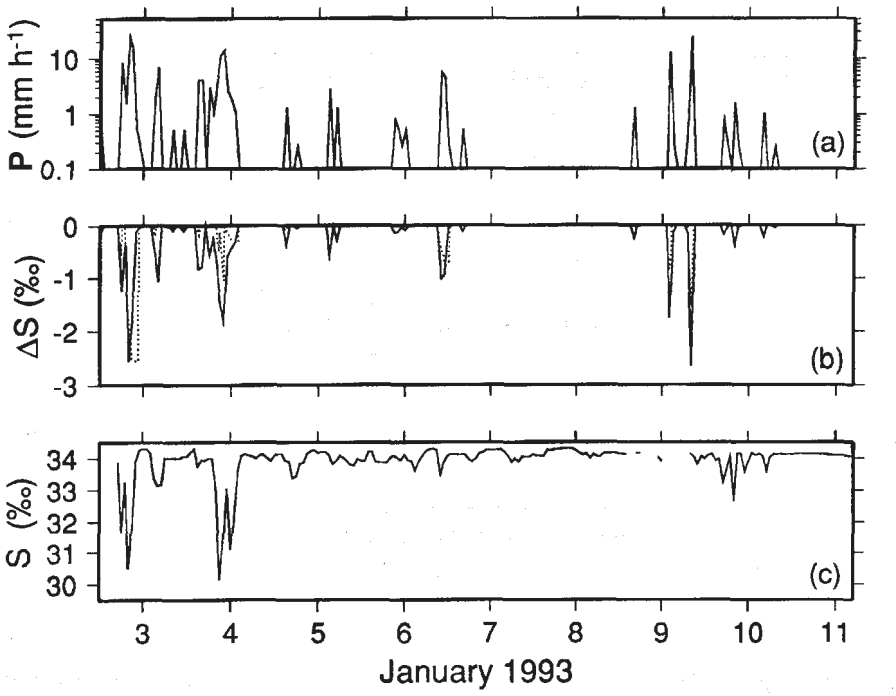


*Figure 2-25*. Parameterization of the freshwater skin during raining episodes of COARE; (a) hourly mean rain rates, (b) calculated hourly mean salinity difference across the haline molecular layer (solid) and across the upper part of the mixed layer (dotted), (c) hourly mean salinity of water collected from the upper 2–3 cm of the ocean; the labels of the time axis identify the end of the days in UT. (After Schlüssel et al., 1997.)

Paulson and Lagerloef (1993) performed a pilot study of the near-surface salinity under rainy conditions in the tropical Pacific Ocean near 156°E and between 2°S and 5°N. From the R/V *Wecoma* during COARE leg 2, they collected surface water from the upper 2 to 3 cm of the ocean with a scoop and hose. The temperature and salinity of the water was measured with a thermosalinograph. The salinity measurements were accompanied by detailed measurements of surface meteorological parameters including

rainrates and downwelling short- and long-wave radiation. Schlüssel et al. (1997) averaged these data sets over hourly intervals and used them with the surface renewal model to estimate the parameters of the freshwater skin of the ocean.

*Figure 2-25* shows time series of the rainrate, the salinity difference across the freshwater skin and the salinity measured at the surface for a rainy time period in January 1993. The direct comparison of the model and field data is not feasible because the model calculation is for the freshwater skin (the upper few tens of micrometers of the ocean only) while the measured salinities include surface water from the upper few centimeters.

Schlüssel et al. (1997) assumed that the freshwater skin layer must account for the greater part of the observed salinity changes because even heavy rainfall ($\approx 60\,\mathrm{mm\ h^{-1}}$) alters the salinity in the upper mixed layer by less than 1 psu (Kantha and Clayson, 1994). Because the wind speeds during this experiment were rather low, the salinity changes in the mixed layer can be expected to be slightly higher. Calculations with the model of Price et al. (1986) show maximum differences exceeding 2 psu over the top half meter on 3 January that are of the same magnitude as the difference across the freshwater skin. The observed salinity changes on this day are up to 4 psu (some of this signal may, however, be associated with nonlocal rain).

For other rainfall events during this time series the observed salinity differences in the mixed layer are generally smaller than those across the skin. A full explanation of the salinity deficits measured can only be given by considering the combined differences across the skin and mixed layers, which has not yet been done.

### 2.5.9 Discussion

Of the various processes that can modify the molecular layers during rainfall, the most important appear to be the rain-induced mixing that leads to enhanced surface renewals and the additional surface and volume cooling by raindrops with temperatures below the sea surface temperature. Simulations with the renewal model have shown that the additional surface cooling by rain could exceed $1^{o}$C, if the rain did not affect the surface renewal time. Nevertheless, the additional mixing and the implied increase in renewal frequencies limit the effect to less than $0.1^{o}$C when the rainwater is 5 K cooler than the sea surface. The more impressive effect is the creation of a haline molecular diffusion layer during rainfall—a freshwater skin of the ocean—that exhibits salinity differences greater than 4 psu during strong rains.

Since laboratory studies overemphasized large drops that are a small fraction of the natural raindrop spectrum, the calculations of the rain-induced surface roughness for a realistic drop size spectrum shows that this effect has been overestimated in the past (Houk and Green, 1976). The wind-induced

surface roughness is more important than that caused by rain except during low wind speed conditions.

The application of the cool skin parameterization, including the rain component, to the field measurements taken during COARE, shows some additional surface cooling that is still generally less than 0.1$^{o}$C. The cooling and mixing effects of the rainfall on the molecular sublayer partly compensate each other so that the net effect on the temperature difference almost vanishes. Nevertheless, the measured bulk versus skin temperature difference across the cool skin shows a reduction of systematic deviations of parameterized from measured differences when the rain effects are included. The errors in the measured parameters and parameterization of the turbulent surface fluxes that enter the surface renewal and mixed layer models, however, prevent a statistically significant improvement between the measured and parameterized cool skin. The salinity changes during rainfall observed in the upper 2 to 3 cm of the ocean can only be explained when the salinity difference across the haline molecular diffusion layer is included.

Studies of rain impacts on the sea surface have been limited to a single rain drop-size distribution, namely the Marshall-Palmer distribution. While this limitation is due to the fact that it is a distribution based on the rainrate as the only available rain parameter (which is really not a justification), the effects induced by a more precise drop-size distribution should be assessed. Further work is necessary to analyze the effect of high-latitude types of precipitation on the molecular boundary layers. For example, snowfall certainly leads to enhanced surface cooling without much volume flux, while hail falling on the sea surface penetrates deeper into the ocean than rain but subsequently pops back to the surface. Precipitation in the form of hail particles results in more complicated surface and volume fluxes because of a prolonged decay time compared to rain or snow.

Chapter 3

# NEAR-SURFACE TURBULENCE

*Physical processes that determine the character and magnitude of turbulence in the the upper ocean are surveyed and the reader is exposed to the challenges of studying near-surface turbulence.*

The main sources of turbulence in the near-surface layer of the ocean are breaking surface waves, shear, and convection. Upper ocean turbulence resulting from shear and convective instabilities may be substantially influenced by the diurnal cycle of solar radiation and by precipitation events. The shear that develops at the bottom of a shallow diurnal or rain-formed mixed layer can greatly increase the turbulence generation (though on relatively small scales) and thus the dissipation rate of turbulence. Below the mixed layer (*i.e.*, in the pycnocline), turbulence decays due to the stabilizing effect of buoyancy forces. The dramatic effect of stratification is observed under low wind speed conditions, when the turbulence regime depends strongly on near-surface stratification, while the strong stratification is also the result of reduced turbulent mixing.

The near-surface thermohaline stratification is eliminated quickly when wave breaking starts. It is therefore reasonable to analyze the thermohaline stratification effects separately, but we cannot do this for bubble-related stratification. Bubbles from breaking waves alter density stratification. The bubble volume fraction (void fraction) is high in spilling breakers; the resulting increased stability affects near-surface dynamics. Conversely, the bubble size distribution appears to depend on turbulence parameters. Beyond the near-surface zone stirred by breaking waves, the average void fraction is too small to influence the flow dynamics but may serve as a tracer for detection of turbulence and coherent structures.

The analysis of turbulence observations reveals different, often contradictory, aspects of the role of surface waves. Since methodological issues of turbulence measurements in the near-surface layer of the ocean still greatly affect the study of wave-enhanced turbulence; one of the sections in this chapter (Section 3.2) is devoted to the analysis of the challenges of observing the near-surface turbulence.

In this chapter, we consider only local and essentially one-dimensional models of near-surface turbulence; this is the so-called "small eddy" theory. We consider the role of large eddies (Langmuir circulations, billows, ramp-like structures) in Chapter 5 when discussing coherent structures in the near-surface layer.

## 3.1 Free-Surface Turbulent Boundary Layer

An important feature of the upper ocean turbulent boundary layer is that it develops near a free surface. In the near-surface layer affected by waves and wave-breaking turbulence, the properties of the boundary layer may differ substantially from the classic wall layer. In contrast to a rigid wall, the tangential component of the velocity field at the free surface is not zero. Velocity components in all directions disappear at the wall due to no-slip conditions, while the free surface restricts motion in the normal direction only.

### 3.1.1 Wave-following coordinate system

An important factor for interpreting near-surface data is the choice of coordinate system. In a fixed coordinate system it is practically impossible to study near-surface layers with thickness less than the maximum surface wave height. In fact, any observational point between the wave trough and crest will be alternately in water and in air.

The influence of surface waves on the near surface flow can be provisionally divided into reversible (kinematic) and irreversible deformations. The former are due to linear (irrotational) components of surface waves, while the latter are caused by nonlinear (rotational) components of surface waves and by turbulence. Examples of irrotational waves are swell and long wind waves. Nonlinearity increases as wavelength decreases. An extreme effect of wave nonlinearity is wave breaking.

A reasonable approach is to interpret the near-surface layer of the ocean in a coordinate system linked to the ocean surface. Csanady (1984) suggested that "...depth should be expressed in the coordinate system connected with the surface produced by the nearly irrotational component of

the wave field." This allows one to analyze the near-surface processes between wave troughs and crests.

The amplitude of wave oscillations decreases as $\exp(kz)$ with depth, where $k$ is the wavenumber and $z$ is the vertical coordinate (conventionally directed upward). Csanady's (1984) coordinate system can, therefore, only be used close to the air-sea interface (*i.e.*, at $|z| << k^{-1}$). Soloviev (1992) proposed an extension of the Csanady (1984) approach by introducing a Lagrangian coordinate system that accounts for the depth attenuation of the surface wave-induced perturbation. This co-ordinate system is described by the following transformation:

$$x' = x\,;\; y' = y\,;\; z' = z + \eta(z,t)\,, \tag{3.1}$$

where $x$ and $y$ are the horizontal axes, $z$ is the vertical coordinate fixed to the still water level of the ocean. Wave displacement, $\eta$, is given as a Fourier-Stieltjes integral (Iyanaga and Kawada, 1980),

$$\eta(x,y,z,t) = \iint \exp(-k|z|)\exp[i(\vec{k}\cdot\vec{l} - \omega t)]dZ(\vec{k},\omega)\,, \tag{3.2}$$

where $dZ(\vec{k},\omega)$ is the Fourier-Stieltjes amplitude introduced in such a way that $\left\langle dZ(\vec{k},\omega)dZ(\vec{k},\omega)^*\right\rangle = \Phi_\eta(\vec{k},\omega)d\vec{k}d\omega$, $\Phi_\eta(\vec{k},\omega)$ is the surface wave spectrum, $\vec{k}$ is the wavenumber vector with components $(k_x, k_y)$, and $\vec{l}$ is the vector with components $(x, y)$.

An important property of transformation (3.1)-(3.2) is that kinematic effects of waves on the near-surface flow in this Lagrangian coordinate system are largely eliminated. Transformation (3.1)-(3.2) projects the surface layer disturbed by the linear potential waves into a flat near-wall layer. Turbulence properties of this near-wall layer may differ from the classical wall layer because of slip boundary conditions. Nevertheless, it is sometimes convenient to compare the near-surface turbulence to well-known properties of the turbulent boundary layer near a wall.

### 3.1.2 Wall layer analogy

A classic wall layer consists of an inner and outer part. Following Nowell (1983), the inner part of the wall layer is defined as $0 < |z| \le 0.2h$; the outer part, as $0.2h \le |z| \le h$ (where $z$ is the distance to wall and $h$ is the depth of the mixed layer of the thickness of the turbulent boundary layer). Some

authors define the inner part of the wall layer as $0 < |z| \le 0.1h$; the outer part is then defined as $0.1h \le |z| \le h$, respectively.

In the inner boundary layer, the current velocity profile, $u(z)$, depends on boundary conditions (surface stress and hydrodynamic surface roughness) and distance $|z|$. The properties of the inner boundary layer near a rigid wall are well known from classical works in hydrodynamics (Hinze, 1955, Monin and Yaglom, 1971; and others). In particular, a logarithmic layer may develop in the inner boundary layer. The velocity and dissipation rate profiles in the log layer are as follows

$$u(z) = \frac{u_*}{\kappa} \ln \frac{|z| + z_0}{z_0}, \tag{3.3}$$

$$\varepsilon = \frac{{u_*}^3}{\kappa\left(|z| + z_0\right)}, \tag{3.4}$$

where $u_* = \left(\tau_0 / \rho\right)^{1/2}$, $\tau_0$ is the surface stress, $\rho$ the density, $\kappa$ the von Karman constant, and $z_0$ is the surface roughness length scale.

In the outer boundary layer, $0.2h \le |z| \le h$, buoyancy and/or rotation effects are important. These factors limit the depth of the turbulent boundary layer. The lower boundary of the surface mixed layer is usually identified by a sharp change of temperature, salinity, and density with depth.

When buoyancy forces are weak, the Earth's rotation controls the depth of the upper ocean turbulent boundary layer and, thus, the depth of the surface mixed layer. The Ekman boundary layer is scaled with the length scale,

$$L_E = u_* / f, \tag{3.5}$$

where $f = 2\Omega \sin\varphi$ is the Coriolis parameter, $\Omega$ is the angular velocity of Earth's rotation, and $\varphi$ is the latitude.

The heat flux at the air-sea interface produces stratification, which affects near-surface turbulence via buoyancy forces. This process is scaled with the buoyancy (Oboukhov) length scale, which, in the absence of salinity fluxes, is as follows:

$$L_O = \frac{c_p \rho u_*^3}{\alpha_T g Q_0 \kappa}, \tag{3.6}$$

where $Q_0$ is the net heat flux at the ocean surface, $\alpha_T$ is the thermal expansion coefficient for water ($\alpha_T < 0$), $g$ is the acceleration of gravity, $c_p$ and $\rho$ are the specific heat and density of sea water respectively, and $\kappa$ is the von Karman constant. The depth at which buoyancy forces become important is proportional to the Oboukhov length scale. With a positive $L_O$, the near-surface turbulent boundary layer is stably stratified. Stable stratification inhibits turbulence, which leads to the restriction of the turbulent boundary layer thickness and thus of the surface mixed layer depth.

The turbulent near-surface flow is dominated by buoyancy forces when:

$$L_O / L_E = c_p \rho u_*^2 f / \left(\alpha_T g Q_0\right) << 1. \tag{3.7}$$

Hence, as the friction velocity decreases, the influence of buoyancy forces increases. In this limiting case, the surface mixed layer depth, $h$, is determined by buoyancy rather than rotation forces and $h \sim L_O$. A similar effect is observed when approaching the Equator, where the Coriolis parameter $f$ becomes zero.

Note that the quadratic dependence of the ratio $L_O/L_E$ on friction velocity in (3.7) means that above some critical level the buoyancy influence rapidly decreases with increasing wind speed. Stratification effects are considered in more detail in Section 3.4.

Lombardo and Gregg (1989) found the wall layer analogy to be useful for the analysis of dissipation rate profiles in the upper ocean under convectively unstable conditions. These observations were essentially below the layer affected by breaking waves. Thorpe (1985) was able to explain his observation of ramp-like structures in the upper ocean turbulent boundary layer based on the wall layer analogy. The wall layer analogy can also provide a reference level for the analysis of the turbulence dissipation in the wave-turbulent layer (see Section 3.3).

### 3.1.3 Deviations from the wall layer analogy in a free-surface layer

Important deviations from the wall layer analogy are associated with the slip condition at the air-sea interface (from the water side) and with the surface waves developing at the free ocean surface. The vortices with horizontal axes weaken when approaching the free surface; while vertically aligned vortices tend to attach to the free surface and are long-lived (Shen et

al., 1999). In near-surface flows with significant vorticity, there is a thin transitional layer inside which the values of the two horizontal vorticity components and the vertical derivative of the vertical vorticity component change from their bulk (isotropic) values to the much smaller values imposed by the zero-stress conditions at the free surface.

In the absence of surface stress but in the presence of internal sources of turbulence (for instance in the post wave-breaking interval or in a ship's wake), the surface layer developing near a free surface is a region of decreased kinetic energy dissipation and increased enstrophy dissipation (enstrophy is the total squared vorticity). When surface stress is imposed, the properties of the near surface turbulent eddies are still determined by the slip conditions at the free surface; as a result, the mean shear flow near a free surface is different from that near a rigid wall. In particular, the thickness of molecular sublayers at a free surface appears to be smaller than at a rigid wall.

According to the direct numeric simulation (DNS) by Shen et al. (1999), a vertically aligned vortex can attach to the ocean surface and experience significantly slower decay. The second order Stokes drift of the waves tilts and stretches such vortices in the horizontal direction presumably leading to the generation of Langmuir circulations (see Chapter 5). At low wind speeds, when wind waves cease, the wind-induced shear current could carry out the same function as the Stokes drift tilting and stretching the turbulent vortices. Remarkably, there are numerous reports of wind streaks on the ocean surface even before waves develop, which resemble miniature Langmuir circulations.

The Shen et al. (1999) concept of a free-surface turbulent boundary layer is essential for understanding free-surface turbulence. Important practical applications for this information include using surface sensing to deduce characteristics of the underlying flow (Swean et al., 1991; Handler et al., 1993). This concept has not yet been applied to situations with finite amplitude surface waves.

The presence of surface waves alters the hydrodynamics of near-surface flows. Borue et al. (1995) found that the interaction of surface waves and free-surface turbulence is weak. Their DNS, however, was confined to infinitesimally small waves. High-resolution simulation of finite-amplitude surface waves interacting with fully developed turbulence are not yet feasible. Large eddy simulation (LES) schemes may not work well for fully three-dimensional boundary layer flows because there is insufficient spectral separation between small and large eddies. In particular, LES does not seem to produce realistic results in the case of Langmuir circulations (see discussion in Section 5.7).

Elsewhere in this chapter, we consider $k$-$\varepsilon$ type models, which may perform better than LES in a three-dimensional boundary layer flow. The $k$-$\varepsilon$ models, however, depend on semi-empirical functions and coefficients; some of them may not be well known in the case of free-surface turbulent boundary layer.

There are also other deviations of the free-surface boundary layer from the wall layer analogy associated with surface waves. In particular, breaking waves distinguish the free-surface boundary layer from the wall layer. This is a very powerful source of turbulent energy. The process of wave breaking is associated with the entrainment of air and the production of bubbles. Conversely, bubbles have a significant effect on the turbulence dynamics in wave breakers.

In the case of near-surface stratification (low wind speed conditions), resonant interaction between two surface waves and an internal wave developing on a near-surface pycnocline may result in the energy transfer from surface to internal modes. Such interaction is obviously impossible near a rigid wall. Surface waves also modulate strain and shear (thus the gradient Richardson number), which may result in flow instability, turbulence, and microstructure when the Richardson number drops below its critical value.

### 3.1.4 Structure of the upper ocean turbulent boundary layer below breaking surface waves

Surface waves produce turbulence due to wave breaking and vortex instability. Wave breaking is a powerful mechanism producing significant energy flux to small-scale turbulence and momentum flux to the mean surface current. The local vorticity production due to vortex instability of the surface waves should also be taken into account in the balance of momentum and turbulent kinetic energy below breaking waves.

Mean shear flow is a principal source of small-scale turbulence in the ocean. In this respect, upper ocean turbulence should be similar to the classical shear turbulence when the mean shear energy production dominates. The effect of stratification on the near-surface mean shear flow can be substantial, especially for low winds. In contrast, under high wind speed conditions when waves break, the influence of stratification on the wave-turbulent layer is negligible (except when wind squalls are accompanied by strong rainfalls). This means that when waves start breaking there is a near-surface layer where the effect of the Coriolis and buoyancy forces can be neglected.

At no stratification effects, energy from the mean shear flow, wave motion and wave breaking contribute to the turbulent energy balance. The dominant source will control the turbulent kinetic energy and dissipation rate

creating sublayers where the energy takes different forms. Accordingly, Benilov and Ly (2002) suggested that the upper ocean turbulent boundary layer where stratification and rotation effects are negligible could be conveniently divided into three sublayers. These are

1) The wave-stirred layer: The turbulent kinetic energy (TKE) production by wave breaking significantly exceeds the mean shear effect, and the turbulent diffusion of the wave kinetic energy dominates in the range of depths where the wave motion continues to be vigorous;
2) The turbulent diffusion layer: Here the turbulent diffusion of TKE exceeds the wave (as well as the mean shear) effect in the TKE budget; and
3) The wall layer: The mean shear production of turbulent energy dominates. In terms of the classic horizontally homogeneous and steady turbulent boundary layer problem, this layer, in steady or quasi-steady cases, obeys wall-layer laws. As discussed in Section 3.1.2, a classic wall layer consists of an inner and outer part. In the inner part, a logarithmic velocity profile can develop; stratification and rotation effects are important in the outer part.

*Figure 3-1* illustrates the concept described above. In order to complete the Benilov and Ly (2002) dynamical scheme we have included an additional characteristic feature of the upper ocean turbulent boundary layer:

4) The aqueous viscous sublayer. Viscous sublayers develop at both the water- and air-side of the air-sea interface due to the suppression of the normal component of turbulent velocity fluctuations near the density interface. This sublayer is controlled by the tangential wind stress $\tau_t$ and is an important component of the sea surface microlayer (Section 2.2). Under low wind speed conditions, the aqueous viscous sublayer is also controlled by the buoyancy flux. Under high wind speed conditions, $\tau_t$ represents only a small fraction of the total momentum flux, $\tau_0$, from the atmosphere to the ocean. Breakers disrupt the viscous sublayer; however it recovers rapidly and is believed to exist between the wave breaking events even in high seas. The viscous sublayer is found within the upper few millimeters of the ocean; its thickness is proportional to the Kolmogorov internal scale of turbulence, $\eta_\nu$, defined in (2.1). Note that the viscous sublayer should be considered in the wave following coordinate system (3.1)-(3.2), because the sublayer thickness is much less than the wave height.

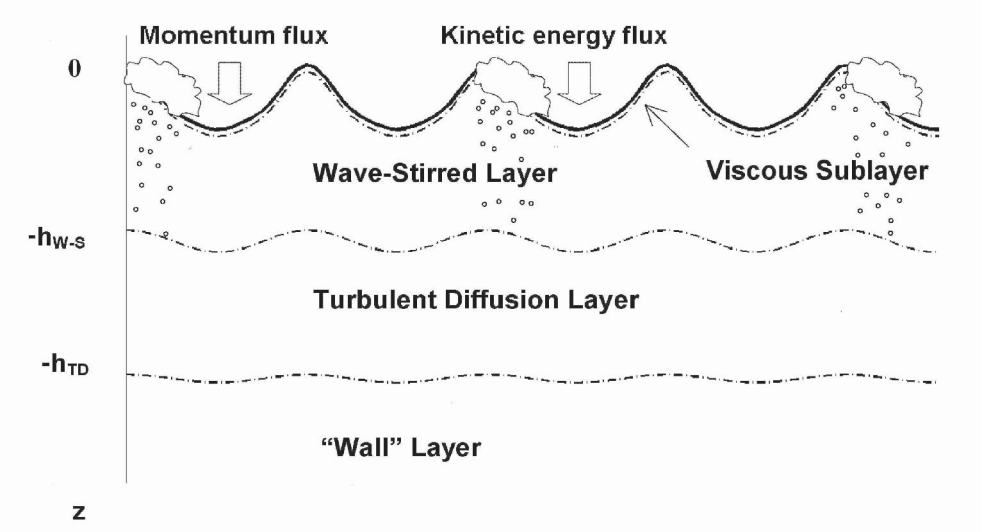


*Figure 3-1*. Diagram of the upper ocean turbulent boundary layer dynamic structures. Here $h_{W\text{-}S}$ is the wave-stirred layer depth, and $h_{TD}$ the turbulent diffusion layer depth.

A comprehensive theoretical model of upper ocean turbulence has yet to be developed. It should include the momentum and kinetic energy equations for the mean and fluctuating components of the turbulent flow, interactions between turbulence and surface waves, wave breaking and turbulent mixing length, quasi-organized (coherent) motions, viscous sublayers, and bubble dynamics. The boundary conditions should describe the fluxes of momentum and energy produced by wave breaking as well as from direct atmospheric action on the ocean surface. Several approaches to one-dimensional modeling of the turbulent processes in the near-surface layer of the ocean are presented in Sections 3.3-3.5.

## 3.2 Observation of Near-Surface Turbulence

### 3.2.1 Observational challenges

Breaking surface waves generate strong turbulence in the near-surface layer of the ocean. These same waves present serious challenges to turbulence measurements. Bubble clouds and random, sometimes huge, vertical motions of the ocean surface due to surface waves complicate collecting quality turbulence data close to the ocean surface.

The velocity scale of near-surface turbulent fluctuations is about 1 cm $s^{-1}$, while typical surface-wave orbital velocities are 1 m $s^{-1}$. The energy of wave orbital velocities is four orders of magnitude higher than that of the turbulence signal. In terms of the dissipation rate of TKE, $\varepsilon$, the wave

disturbance is six orders of magnitude greater than the useful signal. Such exceptionally strong disturbance from surface waves imposes special requirements on the measurement techniques and sensors for observations of near-surface turbulence. Buoy devices (Jones and Kenney, 1977), ship- or submarine-mounted instruments (Stewart and Grant, 1962; Volkov et al., 1989; Osborn et al., 1992; Soloviev and Lukas, 2003), free ascending profilers (Soloviev et al., 1988), tower-based instruments (Terray et al., 1996), and autonomous underwater vehicles (Thorpe et al., 2003a) have been utilized to obtain measurements in the upper few meters of the ocean.

Each approach offers different insights into near-surface physics and suffers from different limitations. For example, tower-based measurements yield temporal measurements. However, there is no clear separation in frequency space of the surface wave velocity field and that due to turbulence. The lack of a dependable mean speed prevents conversion to the spatial domain, which complicates correct estimation of the kinetic energy dissipation rate. Vertical profiling methods can provide such estimates if the vertical speed of the profiler is much greater than the surface wave orbital velocities. However, vertical profiling is inefficient for obtaining large sample sets of turbulence statistics in the near-surface region due to the change of the turbulent statistics as a function of depth. It might also be difficult to detect and adequately measure regions of large horizontal gradients by vertical profiling.

Among the key factors that can affect the quality and interpretation of measurements in the near surface layer from a vessel are surface wave perturbations, influence of the ship wake, variation of the sensor motion, impact of bubbles on conductivity (and hence salinity and density) measurements, and strong electrical currents coupled to the water near the vessel due the ship's electrical field. Sharp vertical gradients in the near-surface physics can also be a factor depending on the measurement approach.

Towed methods can efficiently generate large sample sets of dissipation estimates, but they are typically degraded by broadband motion contamination due to the non-stationary push/pull motion of these devices. The large area of influence of the ship's wake can also affect near-surface measurements. Ship's bow-, submarine-, or AUV-mounted devices can efficiently produce large sample sets, but offer unique challenges - such as the need to assess and minimize ship motion-induced effects and flow perturbations in the vicinity of the sensors due to interaction of the vehicle with the wave field.

Three principal questions associated with collecting turbulence data near the ocean surface are as follows:

1) What reference system should be used?
2) How can the flow disturbance from the vehicle carrying the sensor be reduced?

3) How can surface wave disturbances be eliminated from the signal?

### 3.2.2 Wave-following versus fixed coordinate system

Since the wave breaking energy substantially dissipates above the trough line, and the dissipation rate profile is a nonlinear function of depth, then the difference between fixed and wave-following measurements can be significant. For instance, in a fixed coordinate system it is practically impossible to study near-surface layers with a thickness less than the surface wave height. Any observational point between the maximum wave trough and crest will alternate between water and air. Therefore, in order to study turbulence close to the ocean surface, a wave following coordinate system should be used. Csanady (1984) suggested analyzing near-surface data in a coordinate system connected to the ocean surface; this system is, however, efficient only close to the ocean surface (within a few significant wave heights). It is easy to see that for depths where the surface wave motion diminishes, this coordinate system is irrelevant. The coordinate system proposed in Section 3.1.1 (equations (3.1)-(3.2)) resolves this difficulty.

The Craig and Banner (1994) and Benilov (2002) models of wave-enhanced turbulence that are discussed throughout this chapter are consistent with the coordinate system (3.1)-(3.2). The Terray et al. (1996) model, which was originally fitted to the data collected in a fixed coordinate system, would produce a different dissipation profile in the wave-following coordinate system.

The coordinate system (3.1)-(3.2) at a first glance seems to be infeasible. However, it can be easily implemented with a free-ascending instrument by a proper choice of its hydrodynamic characteristics (Section 3.2.4).

### 3.2.3 Disturbances from surface-waves

The orbital velocities of surface waves influence turbulence measurements by

a) Generating an additive fluctuation velocity signal, and
b) Modulating the relative speed (and direction) of the flow.

We should mention here that (a) is an additive (that is a linear) process while (b) is a nonlinear process, which resembles the process of frequency modulation in radio techniques (Dozenko, 1974). (Recall the difference between AM (amplitude modulated) and FM (frequency modulated) ranges in your automobile radio).

An additional complication is that the time scales of surface waves and near-surface boundary-layer turbulence substantially overlap.

Linear filtering has been widely used to separate waves from turbulence in mooring or tower-based velocity records (*e.g.*, Benilov and Filyushkin, 1970; Kitaigorodskii et al., 1983). This filtering procedure is capable of distinguishing turbulence from linear waves, which effectively addresses problem (a). Problem (b), however, is essentially nonlinear.

In the case of mooring and tower-based measurements, the orbital velocity fluctuation of surface waves usually exceeds the mean drift current. Taylor's frozen field approximation (3.8), which requires that the fluctuation of the flow is less than 10% of its mean speed, cannot be satisfied for these types of measurements; the standard techniques of turbulence analysis, therefore, are not applicable. To address problem (b) for tower-based observations, Kitaigorodskii et al. (1983) used the RMS fluctuation velocity in Taylor's hypothesis of frozen turbulence instead of the mean drift velocity. The error in calculations of the turbulence dissipation rates using these alternative techniques is unknown.

Linear filtering cannot remove nonlinear components of surface waves from the measured signal, however. This may have resulted in an overestimation of the turbulence dissipation rate calculated from tower measurements. Not yet mentioned are the flow reversals due to orbital velocities of surface waves that are typical for tower-based measurements. A turbulent patch produced by the sensor package or mounting structure can occasionally get into the sensing area and disturb measurements. All these circumstances sometimes make tower-based turbulence measurements difficult to interpret.

It is remarkable that spatial scales of turbulence and surface waves may differ greatly. Stewart and Grant (1962) and Soloviev et al. (1988) demonstrated that a fast moving sensor provides an effective separation between the turbulence and surface waves. As a result no statistical filtering is required to solve problem (a). Moreover, if the sensor moves fast enough when compared to the velocity scale of wave orbital motions, problem (b)—modulation of the relative speed (and direction) of the flow due to surface wave disturbances—can be solved as well (Drennan et al., 1996; Soloviev et al., 1999). The frequency spectrum $S_u(f)$ can then be transformed into the wavenumber domain using Taylor's (1938) frozen field hypothesis:

$$k_x = 2\pi f / U_0, \quad E_u(k_x) = S_u(f) U_0 / (2\pi) \tag{3.8}$$

where $f$ is the frequency in Hz, $U_0$ is the relative flow speed (towed or mean flow advection speed), and $k$ is the wavenumber in $m^{-1}$ (everywhere in this Chapter we use the radian wavenumber, $k = 2\pi / U_0$). Taylor's hypothesis is acceptable if the RMS variation of the flow does not exceed 10% of the mean flow speed.

### 3.2.4 Dynamics of a free-rising instrument in the near-surface layer of the ocean

The equation for the vertical motion of a freely ascending device (free-rising profiler) in the presence of long surface waves in a fixed coordinate system has the following form:

$$\left(m_d + m_a\right)\frac{dw}{dt} = \left(\rho V_d - m_d\right)g - C_d S_d \rho \left(w - w_w\right)^2, \tag{3.9}$$

where $m_d$ is the mass of the instrument, $m_a$ is the apparent additional mass, $w$ is the vertical velocity of the instrument center of mass, $V_d$ is the volume of the instrument, $\rho$ is the water density, $C_d$ is the drag coefficient, $g$ is the acceleration of gravity, $S_d$ is the cross-sectional area of the instrument, and $w_w$ is the vertical component of the velocity field induced by surface waves. Equation (3.9) is true for wavelengths $\lambda >> L_d$, where $L_d$ is the vertical size of the instrument.

The velocity sensor mounted on the device measures the relative vertical velocity $w_r = w - w_w$ Substituting new variable $w_r$ into equation (3.9) and expressing it in nondimensional form results in the following equation:

$$\frac{d}{dt}\left(w_r / w_0\right) = A_d\left[1 - \left(w_r / w_0\right)^2\right] - d_t\left(w_w / w_0\right), \tag{3.10}$$

where $A_d = g\left(\rho V_d - m_d\right)\left(m_d + m_a\right)^{-1} w_0^{-1}$, and $w_0$ is the nominal ascending speed of the profiler in still water obtained from the equation,

$$\left(\rho V_d - m_d\right)g = C_d S_d \rho w_0^2. \tag{3.11}$$

Solution to equation (3.10) in still water ( $w_w = 0$ ) with initial condition $w = 0$ at $t = 0$ is as follows:

$$w(t)/w_0 = \tanh\left(A_d t\right). \tag{3.12}$$

The instrument achieves 99% of the nominal ascending speed within the time interval,

$$t_0 = a\tanh(0.99)/A_d. \tag{3.13}$$

During this time interval the profiler passes the vertical distance,

$$d_0 = \int_0^{t_0} w(t)\,dt = w_0 \int_0^{t_0} \tanh(A_d t)dt = w_0 A_d^{-1} \ln\left|\cosh(A_d t_0)\right|. \qquad (3.14)$$

Substituting (3.12) and (3.13) into (3.14) gives:

$$d_0 \simeq 0.28 w_0 A_d^{-1}. \qquad (3.15)$$

According to *Table 3-1*, the free-rising profiler described in Soloviev et al. (1988) and Soloviev et al. (1995) achieved 99% of the nominal velocity after rising only 0.4 m and 0.3 m respectively.

*Table 3-1*. Dynamical parameters for two versions of the free-rising profiler described in (a) Soloviev et al. (1988) and (b) Soloviev et al. (1995).

| Instrument version | $m_d$ kg | $10^3 V_d$ $m^3$ | $w_0$ $m\ s^{-1}$ | $A_d$ $s^{-1}$ | $t_0$ s | $d_0$ m |
|---|---|---|---|---|---|---|
| *a* | 5 | 6.75 | 2.2 | 1.6 | 1.65 | 0.4 |
| *b* | 10.5 | 10.4 | 2.8 | 2.8 | 0.95 | 0.3 |

For small velocity disturbances $\left|w_r'\right| << w_0$, equation (3.10) in the presence of surface waves takes the following form:

$$\frac{dw_r'}{dt} + 2A_d w_r' = -\frac{dw_w}{dt}, \qquad (3.16)$$

where $w_r' = w_r - w_0$.

A random surface elevation $\eta(\vec{x},t)$ can be represented in terms of a Fourier-Stieltjes integral (3.2). The vertical component of the orbital velocity field is then expressed as follows

$$w_w(z,t) = \frac{\partial}{\partial t}\eta(z,t) = \int_{-\infty}^{\infty} (-i\omega)\exp(-i\omega t)\exp\left(-\omega^2 |z|/g\right) dZ_\eta(\omega), \qquad (3.17)$$

where $dZ_\eta(\omega)$ is the Fourier-Stieltjes amplitude introduced in such a way that $\left\langle dZ(\omega)dZ(\omega)^* \right\rangle = S_\eta(\omega)d\omega$, and $S_\eta(\omega)$ is the surface wave spectrum. For wavelength $\lambda$ much exceeding the characteristic size of the instrument $L$, wavenumber dependence in the Fourier-Stieltjes integral (3.2) can be ignored.

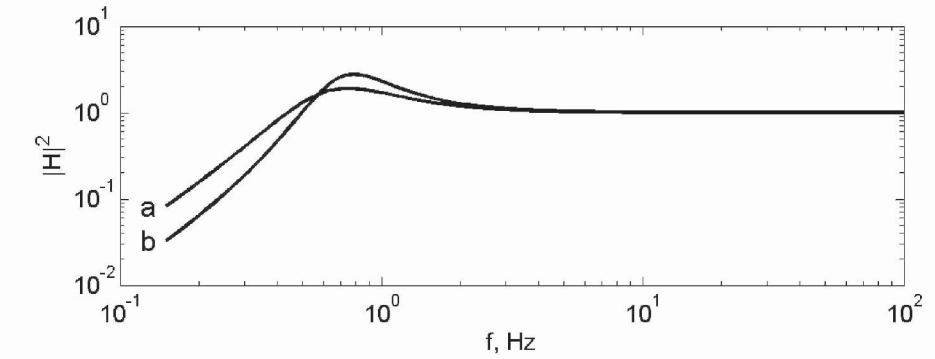


*Figure 3-2*. Squared modules of the transfer function calculated from equation (3.18) for two versions of the freely ascending profiler, (a) and (b), explained in *Table 3-1*.

The solution of linear equation (3.16) can be expressed in terms of the transfer function, $H(i\omega)$, and the frequency spectrum of surface waves, $S_\eta(\omega)$. Substituting the vertical component of orbital velocities in the form (3.17) into equation (3.16) results in the following formula:

$$\left|H(i\omega)\right|^2 = \frac{\omega^2 + w_0^2\omega^4/g^2}{\omega^2 + \left(2A_d - w_0\omega^2/g\right)^2}, \tag{3.18}$$

where $\omega = 2\pi f = 2\pi/T$, and $T$ is the wave period. The transfer function for two versions of the free-rising profiler is illustrated in *Figure 3-2*.

The interpretation of the results shown in *Figure 3-2* is that long surface waves entrain the profiler's body if its excess buoyancy-to-weight ratio is sufficiently large. For wave frequencies $f$ < 0.4 Hz the transfer function drops sharply, the free-ascending profiler is coupled with surface waves. This cut off frequency is determined by the ratio of profiler's excess buoyancy to its weight. The profiler does not follow waves with higher frequencies. Note also a small rise of the transfer function for $f$ = 0.7 Hz, which results from the exponential depth dependence of the orbital wave motion.

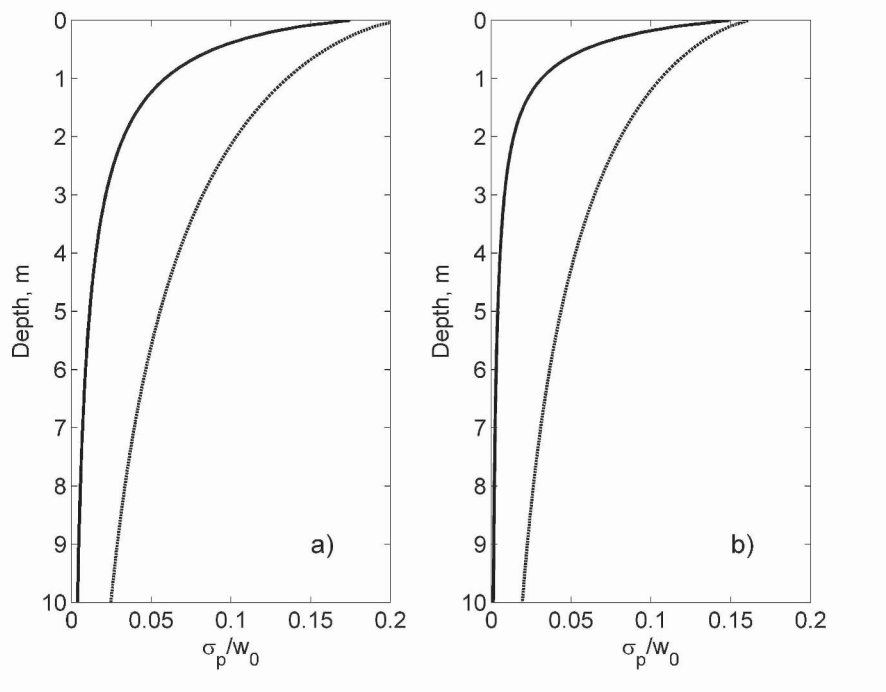


*Figure 3-3.* Relative RMS velocity disturbance from waves in the coordinate system moving with a freely ascending instruments, (a) and (b), explained in *Table 3-1* for 7 m $s^{-1}$ wind speed. Dashed curves in subplots (a) and (b) show the disturbance from waves for an instrument moving with a steady vertical velocity in a fixed coordinate system.

The RMS velocity disturbance in the coordinate system moving with the freely ascending instrument can be written in the following way:

$$\sigma_p^{\,2}(z) = \int_{-\infty}^{+\infty} \left|H(i\omega)\right|^2 S_\eta(\omega) \exp(-2\pi|z|) d\omega \tag{3.19}$$

Substituting $\left|H(i\omega)\right|^2$ in the form (3.18) and using a dispersion relation for linear surface waves $k = \omega^2 / g$, (3.19) is written as follows:

$$\sigma_p^{\,2}(z) = \left[ \int_{-\infty}^{+\infty} \frac{\left(\omega^2 + w_0^2 \omega^4 / g^2\right) \omega^2 \exp\left(-2\omega^2 |z| / g\right) S_\eta(\omega)}{\left(2A_d - w_0 \omega^2 / g\right)^2 + \omega^2} d\omega \right]. \tag{3.20}$$

*Figure 3-3* shows the relative velocity disturbance in the coordinate system of the moving profiler for two different weight-to-buoyancy ratios calculated with the Pierson and Moskowitz (1964) spectrum of surface

waves (1.119) for a 7 m $s^{-1}$ wind speed. Reduction of the RMS velocity disturbance due to the profiler's coupling with surface waves is significant; the depth range where Taylor's hypothesis of frozen turbulence is applicable ($\sigma_p/w_0 < 0.1$) substantially increases. For larger wind speeds, the profiler coupling with surface waves is even more efficient since the surface wave spectral peak shifts to lower frequencies.

### 3.2.5 A near-surface turbulence and microstructure sensor system

Original instrumentation and techniques were developed for near-surface turbulence and microstructure studies during *TOGA COARE* and *GasEx-98* (Soloviev et al., 1998; 1999). They were based on the following experimental approach:

1) Turbulence measurements are acquired with a fast-moving sensor;
2) Sensors with linear output are used; and
3) The analysis is made in a wave following coordinate system.

The system consisted of a free-rising profiler, the bow-mounted sensors, and the dropsonde. *Figure 3-4* schematically shows deployment of the devices on board the R/V *Moana Wave*. *Figure 3-5* includes a photograph of the free-rising profiler and the bow sensors. They are also described briefly below and details are found in Soloviev et al., (1995; 1998; 1999). Azizian et al. (1984) and Volkov and Soloviev (1986) described the dropsonde.

*a) Free-rising profiler*

An advantage of this method proposed by Vershinsky and Soloviev (1977) is the absence of a rigid mechanical connection with the ship's body. The measurement is done from below the surface, which assures minimal disturbance of natural conditions at the air-sea interface. This approach appears to be effective in measuring parameters of near-surface turbulence (Soloviev et al., 1988; 1998). The increased excess buoyancy to weight ratio of this free-ascending device reduces the influence of surface waves on turbulence measurements (see Section 3.2.4).

The profiler's body is a hydrodynamic cylinder with a semi-spherical front constructed from dense foam that is positively buoyant (*Figure 3-5*c). The tail section uses a weighted ring with stabilizers to assure vertical orientation during ascent and to increase the efficiency of water flow around the instrument. The electrical communication cable attaches at the tail section so as not to disturb the water being measured. The sensors protrude 15 cm out of the front of the instrument, which assures undisturbed water is sampled by the sensors (*Figure 3-5*d). A weighted delivery device is used to shuttle the profiler to its desired depth, 15-25 meters, where a pressure sensitive mechanism releases profiler for its ascent to the surface.

During TOGA COARE, a free-rising profiler connected with the "shuttle" (winged frame) was deployed from the stern of the R/V *Moana Wave* with help of a metal frame, which allowed the device to slide from the ship into the water (*Figure 3-5*c). After leaving the metal frame, the profiler fell into the water and slid outside the ship's wake a distance of about 15 to 35 meters as it sank (*Figure 3-4*). This distance depended on the drift of the ship and the intensity of near-surface currents. Normally at 20-m depth the pressure release mechanism released the profiler from the shuttle and the profiler turned to a vertical orientation. The profiler then ascended to the surface with a vertical velocity of 2 to 3 m $s^{-1}$, depending on the net buoyancy of the profiler. The rather large net buoyancy-to-weight ratio of the profiler provided nearly constant vertical speed with respect to the surrounding water mass (see Section 3.2.4). Studies of the temperature, salinity, and density profiles in the near-surface layer of the ocean with the free-rising profiler are described in Chapter 4.

*b) Bow probes*

Bow probes included the electrical conductivity, temperature and pressure (ECTP) probe and the electromagnetic velocity and acceleration (EMVA) probes (*Figure 3-5*a). The EMVA sensor, originally developed for use on submarines, had a hydrodynamic form and a low hydrodynamic noise level. This probe is a linear device for a wide flow-speed range (0 - 12.5 m/s); the spatial resolution is about 1 cm. According to laboratory tests, the electronic noise level of the velocity sensor in the frequency range 2 Hz - 400 Hz was equivalent to 0.8 mm $s^{-1}$. More details about the EMVA probe and the ECTP probes can be found in Soloviev et al. (1998; 1999).

A special metal frame was designed to install these probes on the bow of the vessel (*Figure 3-5*b and *Figure 3-6*). The mean depth of the sensors was about 1.7 m, which varied slightly during the cruise, depending on the levels of the ship's fuel and water tanks, and the ship speed.

The pressure wave in front of a moving ship can result in a rapid flow distortion (Fornwalt et al., 2002). From classical hydrodynamics it is known that the flow in front of a moving sphere is significantly disturbed within approximately 3 radii of the sphere (Van Dyke, 1982). To reduce disturbances by ship's hydrodynamics, a vessel with a sharp-angled hull should be used. At the level of the sensors, the angle of the hull of the R/V *Moana Wave* was +/-15$^{o}$ and the curvature radius of the bow tip was about 0.2 m. The pressure wave therefore concentrated within a distance of approximately 0.6 m ahead of the hull. The bow frame (*Figure 3-6*) positioned the sensor system at a distance of 2 m from the ship's hull, therefore, placing it outside the zone of most intense pressure disturbance.

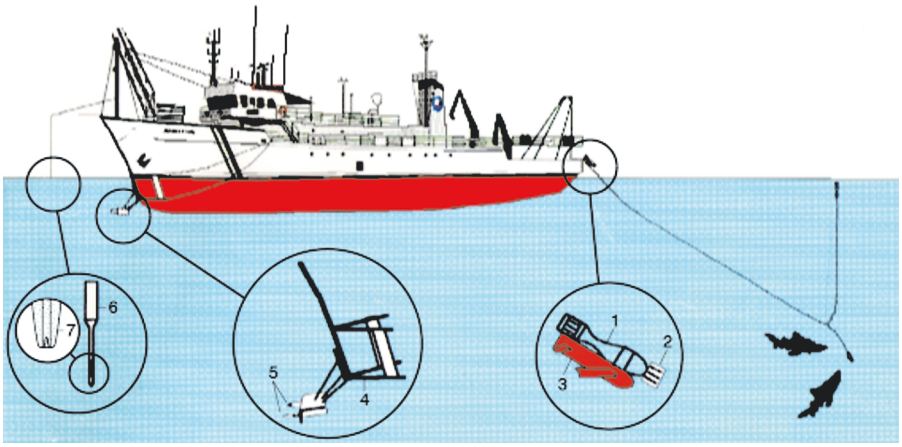


*Figure 3-4*. Schematic illustration of devices deployed for small-scale measurements near the ocean-air interface on the R/V *Moana Wave*. Here 1 - free-rising profiler coupled with carrier; 2- temperature, conductivity and fluctuation-velocity probes on free-rising profiler; 3 - carrier; 4 - bow frame; 5 - bow units (temperature, conductivity, pressure sensor; fluctuation-velocity, tilt sensor); 6 – dropsonde; 7 - temperature probe of micro-wire type.

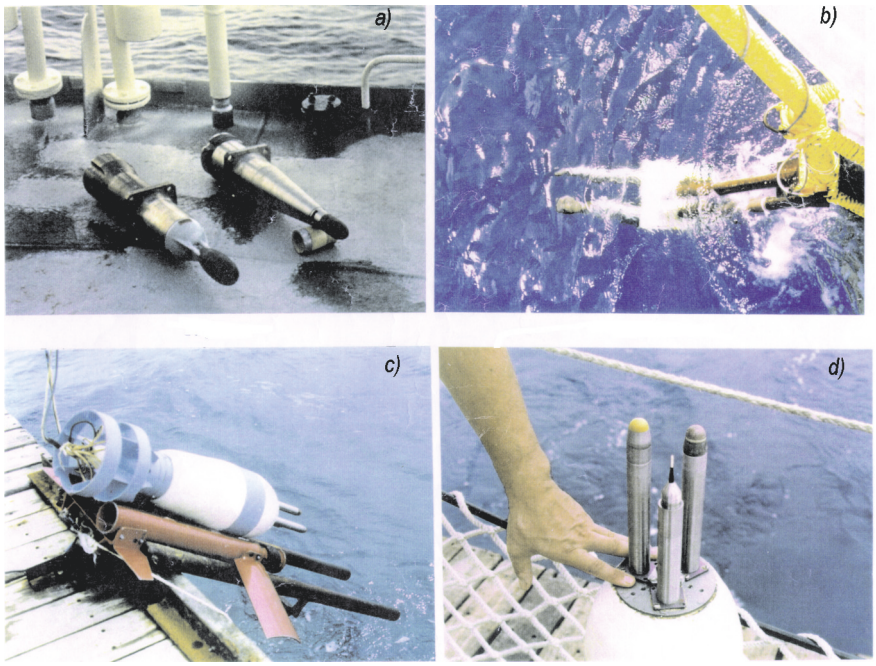


*Figure 3-5*. Photo of bow sensors (a and b) and free-rising profiler (c and d).

Ship pitching and surface waves (including those reflected from the ship's hull) induce fluctuations in the mean flow at the sensor location. A strong velocity fluctuation may result in flow reversal, which affects the turbulence measurements. Though the problem of flow reversals during measurements with bow-mounted sensors is not that severe as in the case of mooring or tower-based systems, it may increase the noise level of measurements under low ship speeds and/or large waves. To identify such cases, Soloviev et al. (1999) analyzed the sum $U_0 + V_x$, where $U_0$ is the ship speed, and $V_x$ is the longitudinal component of the bow velocity signal. (For the analysis of small-scale processes in this chapter we assume that the sensor moves in the $x$-direction.) Negative values of $U_0 + V_x$ are flow reversals; these recorded segments are removed from further analysis. Flow reversals were found mainly at low ship speeds ($U_0 < 2$ m s$^{-1}$). Most of the data were taken at $U_0 \approx 5$ m s$^{-1}$; the cases with $U_0 < 2$ m s$^{-1}$ have been removed from the analysis.

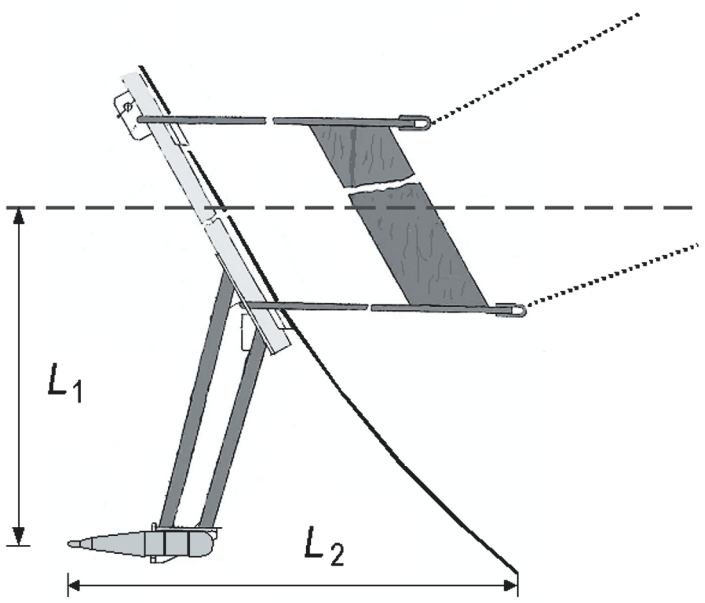


*Figure 3-6*. Schematic diagram showing the probe mounting on the bow of the R/V *Moana Wave*. Mean depth of the probe $L_1 \approx 1.7$ m, spacing from the ship's hull $L_2 \approx 2$ m. Adapted from Soloviev and Lukas (2003) with permission from Elsevier.

Due to surface waves and the ship pitching, the instantaneous depth of the sensors (defined here as the distance to the ocean surface) was continuously changing. The pressure signal was used to estimate the distance of the sensor to the ocean surface. To reduce dynamic pressure effects, the pressure sensor

was positioned in the tail part of the bow probe. An RMS uncertainty of <0.1 dbar (equivalent to less than 0.1 m) in pressure-to-depth conversion at a ship speed of 10-11 knots was estimated by Soloviev and Lukas (1996) using the pressure readings at the intersections of the water-air interface as detected by the conductivity sensor. The sensor depth variation profiled the vertical structure of the near-surface layer of the ocean.

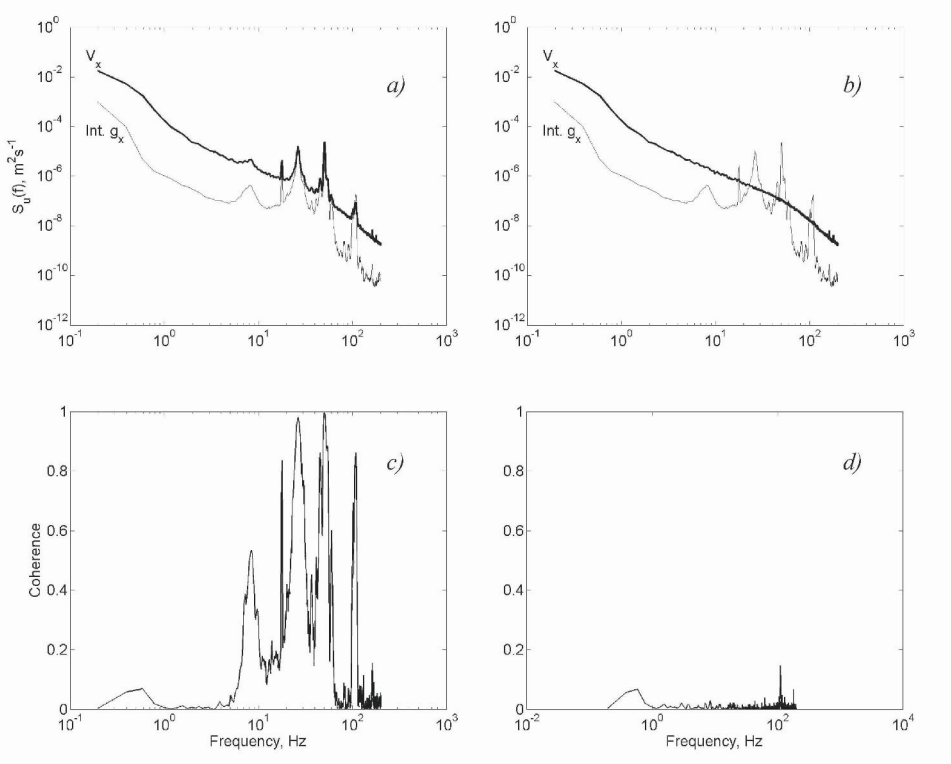


*Figure 3-7*. Spectra of longitudinal velocity $V_x$ and integrated longitudinal acceleration $g_x$ (a) before and (b) after the coherence noise reduction using the Wiener filter. The coherence function between these two signals (c) before and (d) after filtering reveals practically complete cancellation of the ship vibrations in the velocity signal. Reproduced from Soloviev and Lukas (2003) with permission from Elsevier.

The data were collected at a sampling rate of either 400 Hz or 40 Hz. Due to pitching of the vessel at times the sensors broke through the surface. The segments of signal corresponding to the probe surfacing or entering bubble clouds were removed from the analysis using the algorithm described in Soloviev et al. (1995). (A significant part of the turbulent kinetic energy in the near-surface layer dissipates within the actively breaking waves that produce bubble clouds. Removing the segments affected by bubbles may

unfortunately introduce a bias in the turbulence statistics close to the ocean surface.)

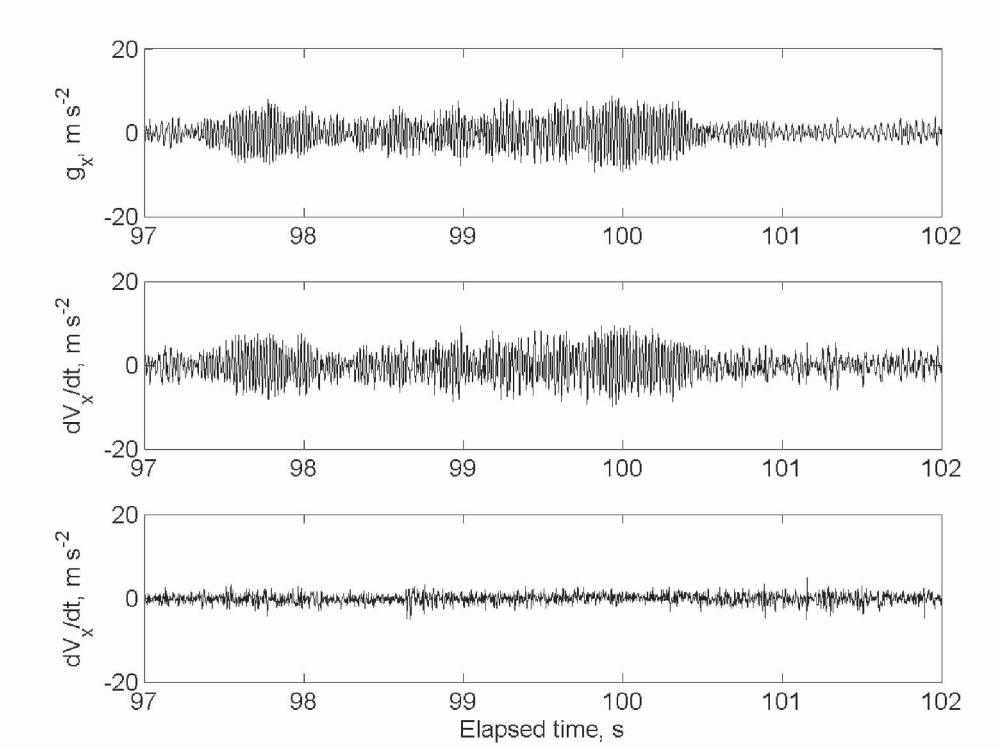


*Figure 3-8*. Illustration of the coherent noise cancellation techniques in the time domain. This is a 5-s segment from the 10-min record used for spectral calculations in the example shown in *Figure 3-7*. Here: (a) longitudinal component of acceleration, (b) time derivative of the original longitudinal velocity signal, and (c) time derivative of the longitudinal velocity signal after the coherent noise cancellation using a Wiener filter. The acceleration signal is shown in the same scale as that of the velocity derivative. Adapted from Soloviev and Lukas (2003) with permission from Elsevier.

*Figure 3-7* provides an example of the $V_x$-velocity spectrum calculated from a 10-min segment obtained at 5.5 m s$^{-1}$ ship speed and 4 m s$^{-1}$ wind speed. For spectral calculations, the measured velocity is "pre-whitened" by numerical differentiation in the time domain and then integrated in the frequency domain. The pre-whitening is a procedure aimed at reducing the "spectral leakage".

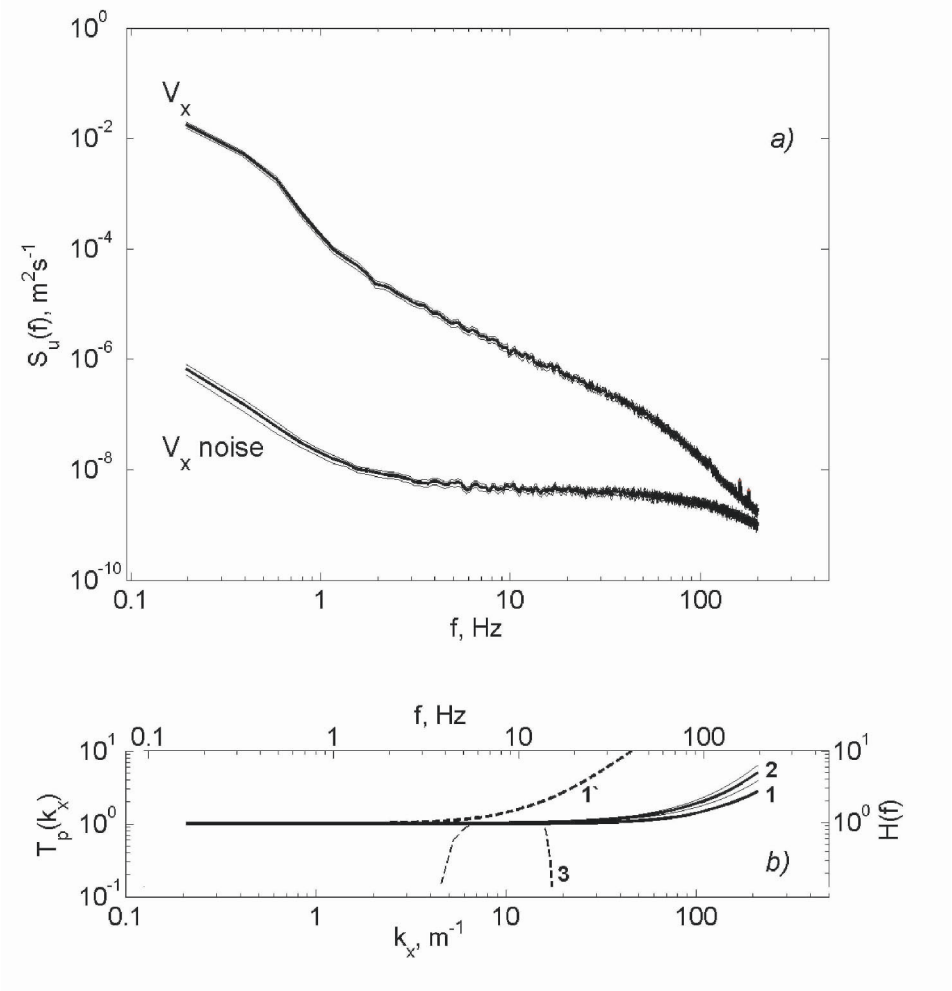


*Figure 3-9*. (a) Spectrum of the velocity signal *u* after processing with the Wiener filter in comparison with the spectrum of electronic noise measured in the laboratory tank. Thin lines represent 95% confidence intervals. (b) Line 1 is the correction for anti-alias filter for 400-Hz sampling rate, while line 1‘ is the correction for 40-Hz sampling rate; curve 2 is the correction for the spatial averaging of the sensor (thin lines indicate the error interval in determining the sensor’s transfer function in laboratory); curve 3 (dashes) shows the frequency range that is being used for calculation of dissipation rates from short velocity segments. Plate b contains both frequency and wavenumber axes. The wavenumber axis is calculated using the frozen field hypothesis (3.8) for $U_0 = 5.94$ m s$^{-1}$. Adapted from Soloviev and Lukas (2003) with permission from Elsevier.

For comparison, the spectrum of integrated acceleration is also shown in *Figure 3-7*a. The acceleration spectrum suggests that the vibration “contamination” occurs in narrow frequency bands. Further evidence of the nature and degree of the vibration contamination can be seen in the plot of

the coherence between the velocity and integrated acceleration, as shown in *Figure 3-7*c. The velocity contamination at frequencies less than 1 Hz is associated with the ship's motion and is outside of the band used for turbulence estimates. Above 8 Hz, there are varying degrees of contamination, with high coherence at 18, 25, 50 and 110 Hz. Removal of this vibration contamination by extrapolating the spectrum through known motion peaks or using a notch filter turns out to be relatively ineffective here because the resonant properties of the bow frame and ship depend on the position of the air-water interface with respect to the frame, which changes during the pitching period. Instead, we use the coherent noise cancellation technique, based on the Wiener filter, developed by Schoeberlein and Baker (1996) and tested with the TOGA COARE bow data in Soloviev et al. (1999).

One important aspect of implementing the Wiener filter is to insure that the reference correlation matrix is not singular and thus can be inverted. This can be a problem when using data that contains a strong low-frequency component, such as the ship's motion and the surface wave velocities at frequencies less than 1 Hz. To avoid this problem, the data are pre-whitened by numerical differentiation. To restore the velocity spectrum after the coherent noise cancellation, the signal is integrated.

*Figure 3-7*b shows the velocity spectrum after applying the coherent noise cancellation techniques using the Wiener filter with 60 weights; *Figure 3-7*d presents the residual coherence. Note that the 95% confidence intervals of the coherence encloses zero. This means that no statistically significant coherent contamination is left in the filtered signal. The effectiveness of the Wiener filter in the time domain is demonstrated in *Figure 3-8*.

In *Figure 3-9*, the spectrum of the velocity signal processed with the Wiener filter as described above is compared to the sensor electronics noise spectrum. The corresponding 95% confidence intervals are shown with thin lines. The confidence intervals for the spectral estimates calculated from 10-min velocity segments are very small because the number of degrees of freedom is large (234). The noise spectrum shown in *Figure 6*a was measured in a laboratory tank with motionless seawater during the post-cruise calibration. The RMS noise for the $u$ channel over the frequency range 2-200 Hz was 0.8 mm $s^{-1}$.

Since the electronic noise and the measured velocity signal are not correlated, the noise spectrum can be subtracted from the $u$ velocity spectrum. However, if the experimental spectrum is close to its noise level, this procedure may result in unrealistic negative spectral components at some frequencies. (Note that in *Figure 3-10* we subtract the noise spectrum from the velocity spectrum only for demonstration purposes.)

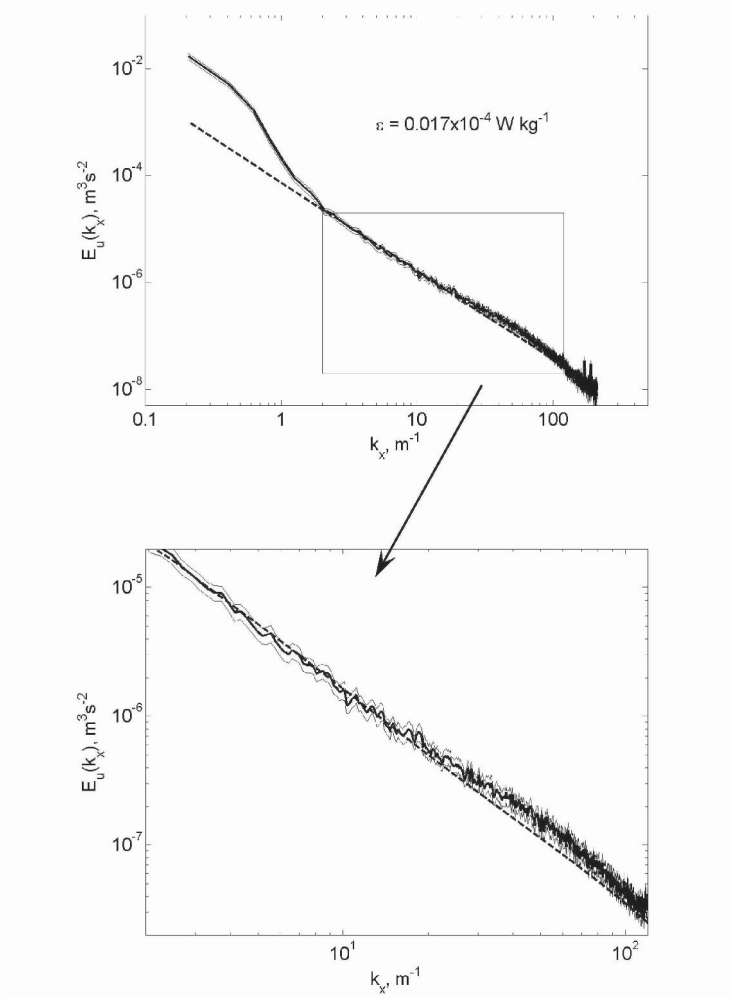


*Figure 3-10.* Theoretical spectrum of turbulence and its fit to the experimental spectrum using the Stewart and Grant (1962) techniques. Dashed line is the Nasmyth turbulence spectrum, bold line is the experimental velocity spectrum, and thin lines indicate 95% confidence limits. The segment marked by a rectangle is shown in more detail. Adapted from Soloviev and Lukas (2003) with permission from Elsevier.

According to Kolmogorov's hypothesis, at sufficiently high wave numbers, the statistical structure of turbulence has a universal form; the scaling parameters depend only upon ε, the dissipation rate of TKE, and upon ν, the kinematic viscosity. This hypothesis implies that at high wave numbers the turbulence is locally isotropic. The one-dimensional velocity spectrum in the *inertia-viscous subrange* that is taken by a sensor moving in the *x* direction is as follows (Stewart and Grant, 1962):

$$E_u(k_x) = \left(\varepsilon \nu^{-5}\right)^{1/4} F_u(k_x \eta_v) \tag{3.21}$$

where $E_u$ is the longitudinal (in the $x$ direction) velocity spectrum, $k_x$ is the wavenumber in the $x$ direction ($k_x = 2\pi f / U_0$ by Taylor's hypothesis (3.8)), $F_u$ is a universal function of its non-dimensional argument $k_x \eta_v$, and $\eta_v = \nu^{3/4} \varepsilon^{-1/4}$ is the Kolmogorov internal scale of turbulence. In the inertia interval ($k_x \eta_v << 1$), equation (3.21) reduces to $E_u(k_x) = \alpha_1 \varepsilon^{2/3} k_x^{-5/3}$, where dimensionless constant $\alpha_1 \approx 0.5$.

Several interpolation formulas of the universal function $F_u$ can be found in the literature on turbulence (Novikov, 1961; Hinze, 1975; Oakey, 1982; Moum et al., 1995). Here we will use the form of function $F_u$ as empirically determined by Nasmyth (1970; c.f. Oakey, 1982), which has been used in many studies of oceanic turbulence.

The theoretical spectrum of turbulence and its fit to a measured velocity spectrum using the Stewart and Grant (1962) techniques are shown in *Figure 3-10*. The measured spectrum is taken as a frequency spectrum; then, it is converted into the wavenumber spectrum using Taylor's hypothesis and transfer functions for anti-alias filter and spatial averaging (*Figure 3-9*b). The theoretical spectrum in *Figure 3-10* corresponds to $\varepsilon = 1.7 \times 10^{-6}$ W kg$^{-1}$.

The large deviation from the theoretical turbulence spectrum on the left (*Figure 3-10*, upper subplot) is due to the surface wave and ship pitching disturbances, which is consistent with the results of Stewart and Grant (1962). There is also a slight difference between the experimental and theoretical spectra in the wavenumber range from 20 m$^{-1}$ to 120 m$^{-1}$. This is presumably an effect of the rapid flow distortion produced by the pressure wave in front of the moving ship. Recently, Fornwalt et al. (2002) modeled this effect numerically and found that the rapid flow distortion results in the net production of TKE concentrated at relatively small scale, which thus affects the velocity spectrum primarily at high wave numbers. Note that the observed deviation might also be introduced by the correction factor for the probe spatial resolution that is known with only 20% accuracy (*Figure 3-9*b). Similar to the disturbance from surface waves, this deviation is not expected to affect the dissipation rate estimate made with the spectrum fitting techniques of Stewart and Grant (1962).

The uncertainty of the ε estimation due to spectral scatter is small in this example because confidence intervals are small. The spectral scatter, however, is not the only source of error in the dissipation rate estimation. Other errors are introduced by the uncertainty of the instrument towing speed and probe calibration. As we analyze only the data that satisfy Taylor's hypothesis of frozen turbulence, the fluctuation of the towing speed

does not exceed 10%. The calibration coefficient for the velocity probe is known with 5% accuracy. Not included are the errors associated with the assumption of isotropy that are implicit in (3.21), which alone may introduce a 50% error (Oakey and Elliott, 1982). The individual estimates of ε are therefore known within a factor of 2.

The dissipation rates calculated from the records longer than the ship's pitching period are in fact averages over the probe depth range. In the near-surface layer of the ocean (where the vertical profile of dissipation rate can be a nonlinear function of depth) this may result in additional errors in the calculation of ε. To address this problem, Soloviev and Lukas (2003) have developed an alternative technique: Dissipation rates are estimated from short segments and are sorted by depth.

Calculation of the dissipation rate from short segments consists of the following steps:

a) Each 10-min $u$ record is edited with the processing algorithm described in Soloviev et al. (1995) to remove the segments when the probes surface or enter bubble clouds. Continuous segments of 5 s or longer are identified and processed with a 60-weight Wiener filter to remove the vibration contamination.

b) Variance $\sigma_u^2 = \mathrm{var}(u')$ is calculated for 0.1 s long, 50% overlapping segments, where $u'$ is the velocity signal processed with the Wiener filter and band-passed with a Finite Impulse Response (FIR) filter. The transfer function of the band-pass filter is shown in *Figure 3-9*b. The 4 Hz to 16 Hz frequency band is selected to minimize the influence of surface waves and ship's pitching from one side and possible rapid flow distortion and the uncertainty in the probe's spatial resolution from the other side.

c) The theoretical variance, $\sigma_{ut}^2$, is defined as a function of the dissipation rate $\varepsilon$ as follows:

$$\sigma_{ut}^2(\varepsilon) = \int_0^\infty H_{hp}(f) H_{lp}(f) S(f;\varepsilon) df \,, \tag{3.22}$$

where $H_{hp}(f)$ is the transfer function of the band-pass FIR filter, and $H_{lp}(f)$ is the transfer function of the anti-alias filter; $S(f;\varepsilon) = 2\pi U_0^{-1} E_u(k_x;\varepsilon)'$, $E_u'(k_x;\varepsilon) = T_p(k_x) E_u(k_x;\varepsilon)$, $T_p(k_x)$ is the transfer function characterizing probe's spatial averaging, $E_u(k_x;\varepsilon)$ is calculated from (3.21) using the Nasmyth spectrum, and wavenumber $k_x = 2\pi U_0^{-1}$. The transfer functions, $H_{bp}(f)$, $H_{lp}(f)$, and $T_p(k_x)$ are shown in *Figure 3-9*b.

d) In order to estimate $\varepsilon$, the equation,

$$\sigma_u^{\,2} = \sigma_{ut}^{\,2}(\varepsilon) \tag{3.23}$$

is solved by an iteration method, where $\sigma_{ut}^{\,2}(\varepsilon)$ is determined using the discrete version of integral (3.22). The iteration process starts from a very small initial dissipation rate $\varepsilon = 1.2 \times 10^{-12}$ W kg$^{-1}$ and finishes at the value of $\varepsilon$ that satisfies Eq. (3.23) with 1% accuracy.

e) The dissipation rate estimates obtained from 0.1-s segments are then averaged within overlapping 10 cm depth bins over the 10-min record segments. In order to account for the intermittent nature of turbulence, the mean dissipation rate and the confidence intervals are calculated using formulas of Baker and Gibson (1987). These formulae assume a lognormal distribution of the turbulence dissipation rate.

Note that the fluctuation of the mean flow speed during a 0.1-s interval is much smaller than for a segment including the full pitching period. The reduction of the mean flow fluctuation facilitates the use of Taylor's hypothesis of frozen turbulence under conditions of high seas and strong pitching of the ship. *Figure 3-11*a, b demonstrates two examples of the averaged vertical profile of dissipation rate $\varepsilon$ obtained with this algorithm. The example shown in *Figure 3-11*b was taken under high wind and wave conditions. The confidence intervals in *Figure 3-11*b are bigger than in *Figure 3-11*a in part because a larger percentage of points were removed due to the probe surfacing or entering bubble clouds.

For further analysis, we use the dissipation rates calculated from short segments according to the method described above. The dissipation rates calculated for a month long COARE cruise are plotted in *Figure 3-12* as a function of wind speed. The cases when the ship speed was less than 2 m s$^{-1}$ or the ship course or speed varied more than 10% are excluded from these statistics. Note that the data in *Figure 3-12* are not sorted by depth.

The equivalent electronics noise level of the velocity sensor, $\varepsilon_n = 1.8 \times 10^{-10}$ W kg$^{-1}$, shown in *Figure 3-12* by a horizontal line is obtained by processing the laboratory noise record via steps a) through d). According to *Figure 3-12*, this noise level is much less than the dissipation rate that is typically observed in the near-surface layer of the ocean. No noise correction is therefore required.

To elucidate possible influence by surface waves on the dissipation rate estimation, we have calculated the wave kinetic energy in the wavenumber band that is used here for dissipation rate estimates. The theoretical variance is calculated using the Pierson and Moskowitz (1964) spectrum (multiplied by $\omega^2$, where $\omega = 2\pi f$), surface wave dispersion relationship $k = \omega^2 / g$,

the transfer function of the band-pass filter (shown in *Figure 3-9*b, curve 3), and the depth attenuation factor, $\exp(2kz)$. The theoretical variance is then processed via steps a) through d) to obtain an error estimate, $\varepsilon_r$. The relative error, $\varepsilon_r/\varepsilon$ exceeded 10% only in 0.2% of all cases collected during the EQ-3 cruise. These points are removed from the analysis, but this does not affect the dissipation rate profile averaged over the EQ-3 cruise in any significant way.

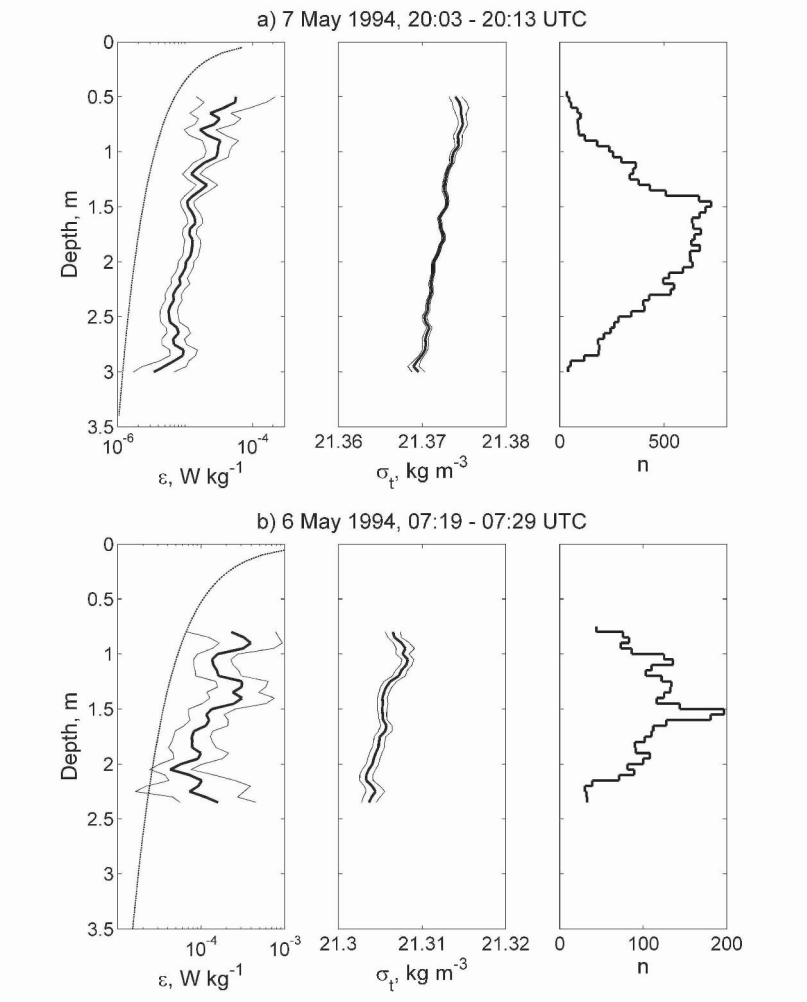


*Figure 3-11*. Vertical profiles of dissipation rate $\varepsilon$ and $\sigma_t$ density averaged within 5 cm depth bins over a 10 min bow record segment. Thin lines are 95% confidence intervals calculated using the method of Baker and Gibson (1987). Dashed line is the logarithmic layer prediction. Number of points $N$ in each depth bin is also shown. (a) Wind speed $U_{15}$ = 9.4 m s$^{-1}$, significant wave height $H_s$ = 1.8 m; (b) $U_{15}$ = 19 m s$^{-1}$ and $H_s$ = 3.3 m. Adapted from Soloviev and Lukas (2003) with permission from Elsevier.

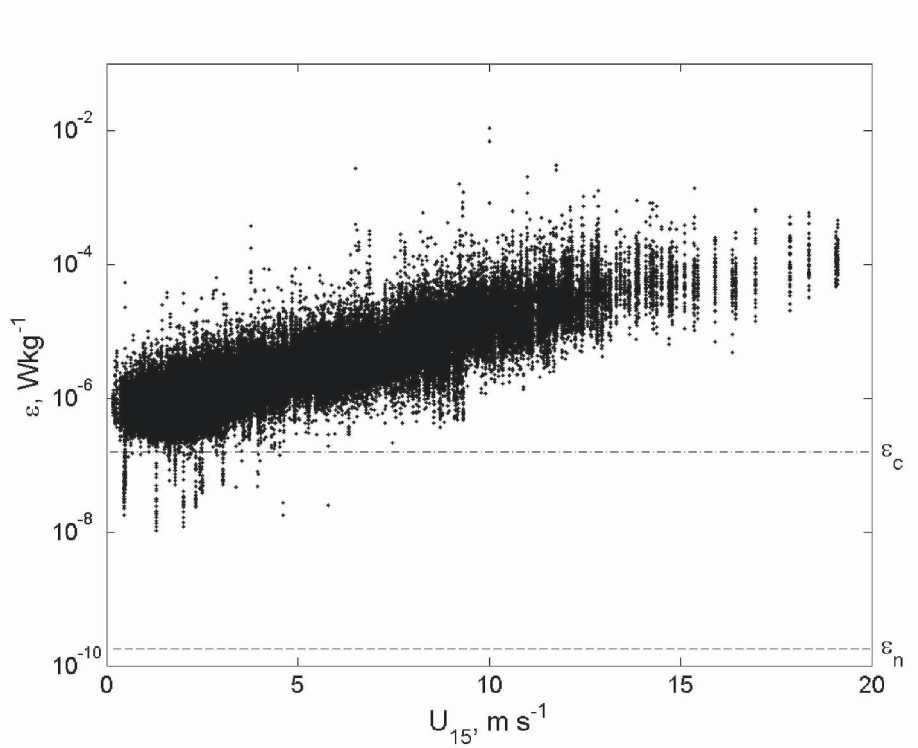


*Figure 3-12*. Estimated $\varepsilon$ from the bow sensors versus wind speed, $U_{15,}$ at 15 m height during the month-long COARE EQ-3 cruise of the R/V *Moana Wave*. Each point represents a 10-min average (no sorting by depth in this graph). The electronic noise of the sensor is indicated as a horizontal dashed line $\varepsilon_n = 1.8 \times 10^{-10}$ W kg$^{-1}$. Reproduced from Soloviev and Lukas (2003) with permission from Elsevier.

Both the ship's pitching and surface waves induce fluctuations of angle between the flow direction and the probe's longitudinal axis. At sufficiently large angles, the 40 mm diameter tip of the EM probe containing sensing electrodes may start shedding vortices, which are the source of additional hydrodynamic noise. In the example shown in *Figure 3-9*a, the ship speed $U_0$ = 5.9 m s$^{-1}$; disturbances with 40 mm wavelength translates into a frequency $f$ = 140 Hz. There are several, relatively small but persistent spectral peaks observed in the velocity spectrum at $f$ > 140 Hz (*Figure 3-9*a). These peaks are not observed in the noise spectrum taken in the laboratory (motionless water) and are supposedly due to the hydrodynamic noise of the sensor. The signal in the frequency range from 4 Hz to 16 Hz (that we use here for dissipation rate estimates) is not affected by the hydrodynamic noise.

## 3.3 Wave-Enhanced Turbulence

### 3.3.1 Dimensional analysis

One of the important parameters of turbulence is the dissipation rate of TKE, ε. Some conclusions about the vertical profile of ε in the near-surface layer of the ocean can be made from dimensional analysis.

For an equilibrium surface wave spectrum, ignoring buoyancy, Earth's rotation, and capillary wave effects, the following functional dependence can be hypothesized (Soloviev et al., 1988):

$$\varepsilon = function\left(u_*, |z|, g\right), \tag{3.24}$$

where $u_*$ is the friction velocity in the near-surface layer of the ocean, $g$ is the acceleration of gravity, and $z$ is the depth (expressed in a wave-following coordinate system (3.1) for instance). Standard dimensional analysis leads to the following dependence:

$$\varepsilon\kappa|z|/u_*^3 = \psi\left(g|z|/u_*^2\right), \tag{3.25}$$

where $\psi$ is a universal function of its nondimensional parameter $g|z|/u_*^2$. The asymptote of (3.25) at $z \to -\infty$ should be logarithmic layer law (3.4), which corresponds to $\psi \equiv 1$.

*Figure 3-13*a shows the data obtained by Soloviev et al. (1988) and Thorpe (2003a) under conditions of developed seas (wave age $A_w = c_p/u_{*a} > 13$). For turbulence measurements, Soloviev et al. (1988) used a free-rising profiler, while Thorpe et al. (2003a) employed an autonomous underwater vehicle (AUV). In order to minimize the influence of thermohaline stratification on the near-surface turbulence, only the data obtained under conditions of surface wave breaking ($U_{10} \geq 6$ m s$^{-1}$) are analyzed in *Figure 3-13*a.

Though the nondimensional variables $g|z|/u_*^2$ and $\varepsilon\kappa|z|/u_*^3$ provide a convenient reference system for the analysis of near-surface turbulence data, this scaling may not work well under conditions of developing seas. The latter conditions are typical for lakes and coastal regions with short fetch but are also often observed in the open ocean due to changing wind patterns. The wave breaking process and, hence, parameters of near-surface turbulence depend on the stage of surface wave development.

A simple way to account for the effect of surface wave age on the near-surface turbulence dissipation has been proposed by Terray et al. (1996). These authors hypothesized that the proper nondimensional variables for the

analysis of near-surface turbulence at different stages of surface wave development are $|z|/H_S$ and $\varepsilon\kappa z/F_0$, where $H_s$ is the significant wave height, and $F_0$ is the surface flux of TKE. Standard dimensional analysis then leads to the following formula:

$$\varepsilon H_S / F_0 = \psi_D \left( |z| / H_S \right), \tag{3.26}$$

where $\psi_D$ is a universal function of dimensionless depth $z/H_S$.

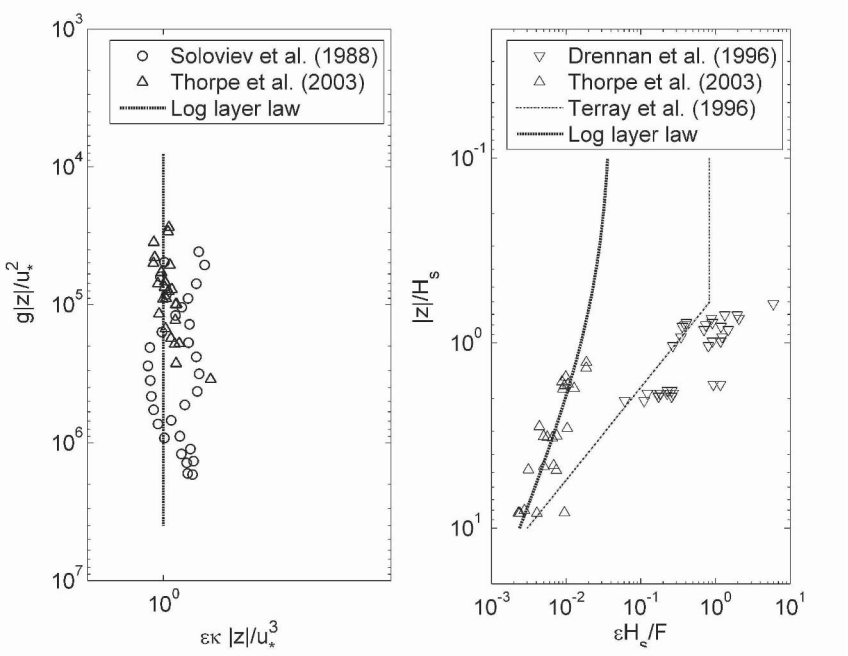


*Figure 3-13*. The vertical distribution of (a) nondimensional dissipation $\varepsilon\kappa|z|/u_*^3$ as a function of nondimensional depth $g|z|/u_*^2$ according to measurements of Soloviev et al. (1988) and Thorpe et al. (2003a); (b) data of Drennan et al. (1996) and Thorpe et al. (2003a) in dimensionless coordinates $\varepsilon H_S / F_0$ and $|z|/H_S$. The field data shown here are for developed seas. In order to reduce possible effects of stratification, only data obtained under wave breaking conditions ($U_{10} \geq 6$ m s$^{-1}$) are shown.

From the tower-based data collected in Lake Ontario under conditions of developing seas, Terray et al. (1996) proposed the following parameterization for the wave dissipation rate $\varepsilon_{wv}$ based on scaling (3.26):

$$\varepsilon_{wv} H_S / F_0 = \begin{cases} 0.3(|z|/H_S)^{-2} & \text{for } |z| > 0.6H_S \\ 0.83 & \text{for } |z| < 0.6H_S \end{cases}. \tag{3.27}$$

Parameterization (3.27) represents only the wave-breaking turbulence; the shear-generated turbulence must be treated separately.

*Figure 3-13*b demonstrates the dissipation data sets of Thorpe et al. (2003a) and Drennan et al. (1996), which were obtained under conditions of developed seas. The flux of the TKE from wind to waves was determined from the parameterization formula for developed wave spectrum (1.119). (The measurements of Soloviev et al. (1988) could not be scaled according to (3.26), because only visual estimates of surface wave heights were available.) One group of data (Thorpe et al., 2003a) is consistent with the log layer model (3.4); while the other (Drennan et al., 1996) appears to follow the Terray et al. (1996) parameterization (3.27). Since both datasets are for developed seas, the wave age is not expected to be a major factor in this difference. We attempt to reconcile these data sets in Section 3.3.4 with theoretical models of wave-enhanced turbulence of Craig and Banner (1994) and Benilov and Ly (2002).

### 3.3.2 Craig and Banner (1994) model of wave-enhanced turbulence

Craig and Banner (1994; hereafter CB94) proposed a one-dimensional model of wave-enhanced turbulence based on the level 2-1/2 Mellor and Yamada (1982) turbulence closure scheme. Surface wave effects are incorporated into this model via the TKE flux at the air-sea interface. A basic assumption of the CB94 model is that the random hydrodynamic fields of the upper layer are horizontally homogeneous. Thus, all statistical characteristics of the turbulence and surface waves are functions only of $z$ and $t$.

The momentum equations (1.17) and (1.18) for the mean flow driven by the wind represent a balance between the flow acceleration, Coriolis force, and viscous forces under low Rossby number approximation. These equations under the additional assumption of horizontal homogeneity and no mean horizontal pressure gradients are as follows:

$$\frac{\partial u}{\partial t} = -\frac{1}{\rho_0}\frac{\partial \tau_{zx}}{\partial z} + fv, \tag{3.28}$$

$$\frac{\partial v}{\partial t} = -\frac{1}{\rho_0}\frac{\partial \tau_{zy}}{\partial z} - fu\,, \tag{3.29}$$

in which $t$ is the time, $z$ is vertical coordinate measured positive upward, $f$ is the Coriolis parameter; $\tau_{zx} = -\rho K_M \partial_z u$, $\tau_{zy} = -\rho K_M \partial_z v$, and $K_M$ is the eddy viscosity for momentum transfer. In equation (3.29), $u(z,t)$ is the mean velocity component in the $x$ direction and $v(z,t)$ is the mean velocity component in the $y$-direction, normal to the mean wind stress. The vertical coordinate $z$ in CB94 is specified relative to the still water surface. The model, however, is compatible with the wave following coordinate system described by transformation (3.1)-(3.2).

The eddy viscosity $K_M$ is expressed according to the Kolmogorov-type hypothesis (Mellor and Yamada, 1982):

$$K_M = lqS_M\,, \tag{3.30}$$

where $l$ is the turbulent length scale, and $q$, the turbulent velocity scale, is formally introduced as $q = (2b)^{1/2}$, where $b$ is the turbulent kinetic energy. The dimensionless parameter $S_M$ in (3.30) is an empirical constant; for stratified conditions, however, it will depend on the Richardson number.

The equation for TKE is as follows:

$$\frac{\partial b}{\partial t} = \frac{\partial}{\partial z}\left( lqS_q \frac{\partial b}{\partial z}\right) + lqS_M\left[\left(\frac{\partial u}{\partial z}\right)^2 + \left(\frac{\partial v}{\partial z}\right)^2\right] - \varepsilon\,, \tag{3.31}$$

where $S_q$ and $S_M$ are empirical constants ( $S_M$ = 0.39, and $S_q$ = 0.2). Equation (3.31) follows from Eq. (1.24) given in Chapter 1 and parameterization for eddy viscosity (3.30). Buoyancy forces are ignored in CB94. The term on the left-hand side of (3.31) is the rate of change of the turbulent kinetic energy, the first term on the right-hand side describes the diffusion of the turbulent kinetic energy, and the second term on the right-hand side represents energy generation by shear. The final term is the dissipation due to turbulent motion, which is parameterized via another hypothesis by Kolmogorov,

$$\varepsilon = q^3/(Bl)\,, \tag{3.32}$$

where $B$ =16.6 is a dimensionless constant. The length scale in the CB94 model is approximated as a linear function of depth (distance from the surface):

$$l = \kappa\left(|z| + z_0\right). \tag{3.33}$$

where $\kappa$ = 0.4 is von Karman's constant, $|z|$ is the depth (expressed in coordinate system (3.1) for instance), and $z_0$ is the surface roughness parameter (from the water side).

Boundary conditions for the momentum equations (3.28) and (3.29) are respectively:

$$K_M \frac{\partial u}{\partial z} = {u_*}^2 \text{ and } K_M \frac{\partial v}{\partial z} = 0. \tag{3.34}$$

Boundary conditions (3.34) imply that the wind stress is along the *x*-axis.

The turbulent kinetic energy input due to waves is set as a surface boundary condition (1.128):

$$F_0 = lqS_q \frac{\partial b}{\partial z} = \alpha_w {u_*}^3, \tag{3.35}$$

where $a_w \approx 100$. This parameterization is relatively insensitive to the sea state for wave ages embracing wind seas from wave age $A_w = c_{pw}/u_{*a} > 13$ to fully developed situations, where $u_*$ is the friction velocity in the atmospheric boundary layer. For $A_w < 13$, $a_w$ is no longer constant and depends on the wave age.

Equation (3.35) is based on an assumption that wave-breaking turbulence is a surface source of turbulence. In fact, wave stirring penetrates to some finite depth. An approach that treats breaking surface waves as a volume source of TKE is described in Section 3.3.3.

Boundary conditions for the momentum components and TKE at $z \to -\infty$ are set in the following way:

$$K_M \frac{\partial u}{\partial z} = 0,\ K_M \frac{\partial v}{\partial z} = 0, \text{ and } lqS_q \frac{\partial b}{\partial z} = 0. \tag{3.36}$$

The interpretation of the CB94 model presented here is slightly simplified, because it involves an infinite-depth layer (*i.e.*, open ocean conditions).

Now consider the situation where the shear production of turbulent kinetic energy balances dissipation, which leads to the classic logarithmic boundary layer. The steady state solution for this asymptotic regime is obtained by neglecting terms with time derivative in (3.28), (3.29), and (3.31). The balance of two terms on the right-hand side of (3.31),

representing the shear turbulence production and the dissipation, the assumption of a constant stress layer, and the surface boundary conditions produce the relationship:

$$q = u_* \left( B / S_M \right)^{1/4}. \tag{3.37}$$

Substituting $q$ and $l$ in (3.32) with (3.33) and (3.37) respectively gives the classic formula (3.4) for the dissipation rate in the logarithmic layer:

$$\varepsilon_{sh} = \frac{u_*^3 \left( B / S_m \right)^{3/4}}{B\kappa \left( |z| + z_0 \right)} = \frac{u_*^3}{\kappa \left( |z| + z_0 \right)}. \tag{3.38}$$

Note that constants in the Mellor and Yamada (1982) closure scheme are chosen so that $S_M{}^3 B \equiv 1$ to ensure that for $|z| >> z_0$ the logarithmic layer asymptote (3.4) is achieved; the logarithmic layer (or constant stress layer) asymptote requires that the Coriolis terms in (3.28) and (3.29) are neglected.

For the asymptotic steady state regime, when TKE is produced at the surface according to (3.35) and the shear production term is eliminated from (3.31), the TKE equation represents a balance between the downward diffusion of energy injected at the surface and dissipation $\varepsilon_{wv}$. Thus (3.31) reduces to

$$S_q \kappa^2 B \frac{\partial}{\partial z} \left[ \left( |z| + z_0 \right) \frac{\partial q^3}{\partial z} \right] = 3 \frac{q^3}{\left( |z| + z_0 \right)}. \tag{3.39}$$

The solution to (3.39) is as follows:

$$q^3 = c_+ \left( |z| + z_0 \right)^n + c_- \left( |z| + z_0 \right)^{-n}, \tag{3.40}$$

where $n = [3/(S_q \kappa^2 B)]^{1/2} = 2.4$, and constants $c_+$ and $c_-$ are to be determined from (3.36) and the condition of turbulence decay at large depth: $b = 0$ at $z \to -\infty$. The $c_-$ term in (3.40) represents decay away from the surface while the $c_+$ term should be equal to zero to satisfy the boundary condition at $z \to -\infty$. The turbulence velocity scale is then described as follows:

$$q = c_-{}^{1/3} \left( |z| + z_0 \right)^{-n/3}, \tag{3.41}$$

and the asymptotic formula for dissipation rate due to wave breaking reads:

$$\varepsilon_{wv} = c_{-}\left(|z| + z_0\right)^{n-1} / \left(\kappa B\right) \tag{3.42}$$

The constant $c_{-}$ can be determined from boundary condition (3.35) to give

$$\varepsilon_{wv} = \alpha_w {u_*}^3 \sqrt{\frac{3B}{S_q}} \left( \frac{z_0}{|z| + z_0} \right)^n \tag{3.43}$$

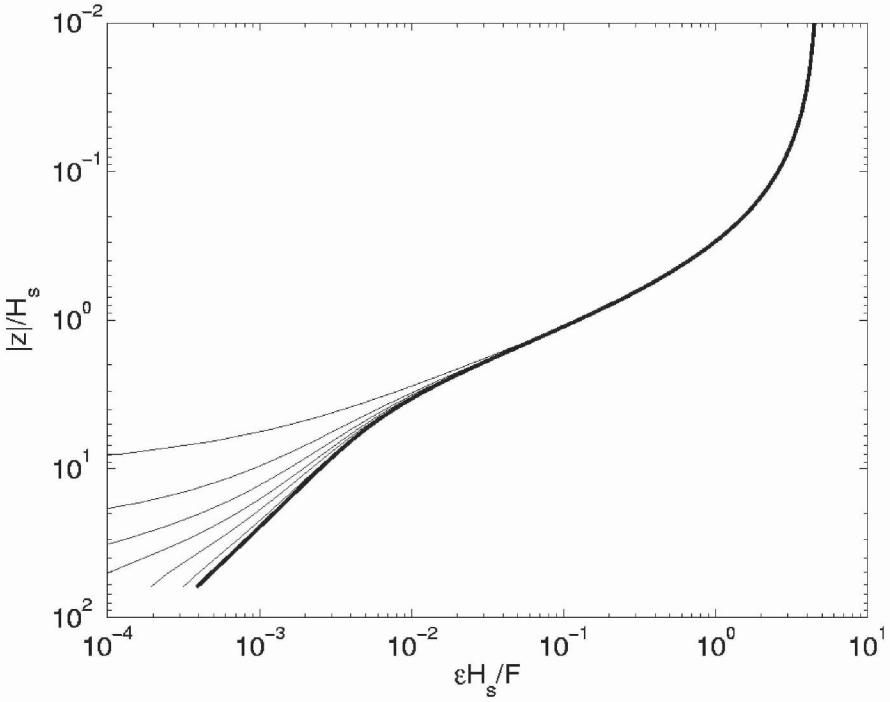


*Figure 3-14*. Numerical solution of the Craig and Banner (1994) model for a finite-depth layer $H$ = 100 m. First thin line is the solution for $t$ = 0.5 hr, bold line is the solution for $t$ = 10 hr. Time interval between lines is 95 min.

When both shear production and diffusion are present, the dissipation rate can be approximated as a sum of the two asymptotic terms, (3.38) and (3.43):

$$\varepsilon \approx \varepsilon_{sh} + \varepsilon_{wv} = \frac{{u_*}^3}{\kappa\left(|z| + z_0\right)}\left[1 + \alpha_w \sqrt{\frac{3}{BS_q}}\left(\frac{z_0}{|z| + z_0}\right)^n\right]. \qquad (3.44)$$

where $\sqrt{3/(BS_q)} \approx 0.95$.

Adjustment of the turbulence regime to local conditions is relatively fast (*Figure 3-14*); in many cases, it is possible to use the steady-state solution for the upper few meters of the ocean. *Figure 3-15* demonstrates the numerical steady-state solution of the CB94 model, its asymptotes and analytical approximation (3.44). According to *Figure 3-15*, formula (3.44) approximates the numerical solution very well (they are almost indistinguishable on the plot).

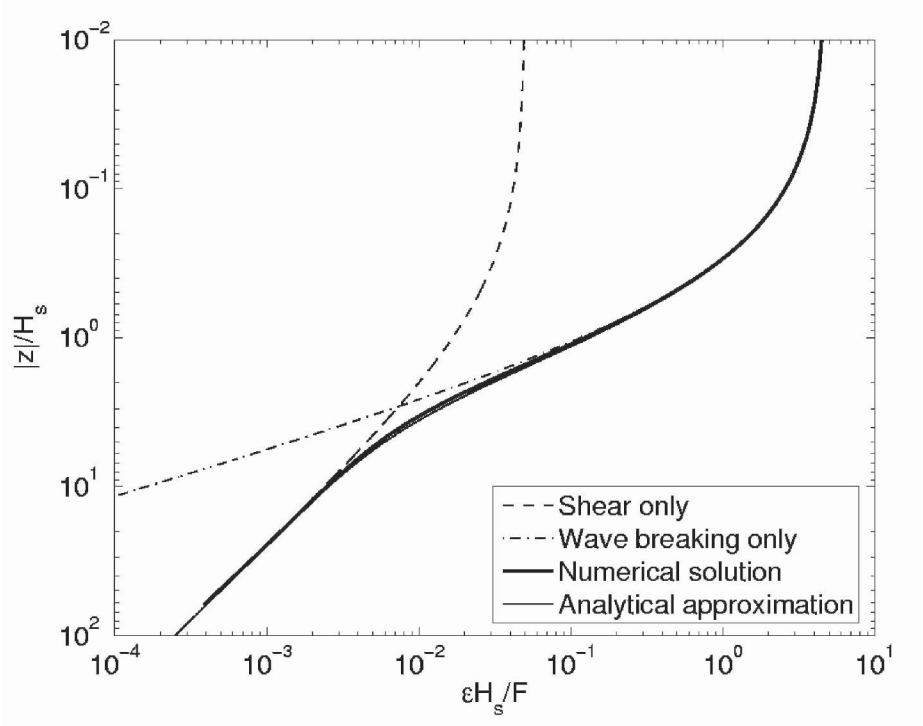


*Figure 3-15*. Steady state numerical solution of the Craig and Banner (1994) model and its analytical approximations (3.38), (3.43), and (3.44). Note that approximation (3.44) is difficult to distinguish in this figure because it is very close to the numerical solution. Reproduced from Soloviev and Lukas (2003) with permission from Elsevier.

In nondimensional coordinates $\tilde{\varepsilon} = \varepsilon\kappa\left(|z| + z_0\right)/u_*$ and $\tilde{z} = \left(|z| + z_0\right)/z_0$ formula (3.44) reduces to a compact form:

$$\tilde{\varepsilon} = 1 + \alpha_w \sqrt{\frac{3}{BS_q}} \tilde{z}^{-n} \approx 1 + 0.95 \alpha_w \tilde{z}^{-n} . \tag{3.45}$$

For developed waves ($A_w > 13$): $\alpha_w \approx 95$. For developing waves ($A_w < 13$), $\alpha_w$ is no longer a constant and depends on wave age $A_w = c_p / u_{*a}$.

The surface roughness from the waterside, $z_0$, is a critical but still poorly known parameter. It depends both on the physics of the turbulent boundary layer and on the properties of the free sea surface. Bye (1988) proposed a Charnock's (1955) type formula for $z_0$:

$$z_0 = a_C u_*^2 / g \tag{3.46}$$

with $a_C$ =1400. Terray et al. (1996) concluded that for wave breaking conditions dimensionless coefficient $a_C$ is much larger ($a_C$ ~150,000). A magnitude of $a_C$ higher than in Bye (1988) also follows from the modeling study of the near-surface circulation in Knight Inlet by Stacey (1999) who noted that it also depends on wave age.

Alternatively, Terray et al. (1996) parameterized surface roughness via significant wave height:

$$z_0 = c_T H_S , \tag{3.47}$$

where $c_T$ ~1. According to Pierson and Moskowitz (1964), for a fully developed (equilibrium) surface wave spectrum,

$$H_S = 4\sigma_\eta \approx 1.576 \times 10^5 u_*^2 / g . \tag{3.48}$$

Assuming that parameterizations (3.46) and (3.47) should converge for conditions of fully developed waves, that is,

$$z_0 = c_T H_S = a_C u_*^2 / g , \tag{3.49}$$

one can find that $c_T$ =1 corresponds to $a_C$ =157,600. The two orders of magnitude difference in $a_C$ between authors is an indication of the extent of the problem of parameterizing and modeling near surface turbulence.

Integration of the dissipation profile given by equation (3.43) from $z = 0$ to depth $h_{50}$ (where 50% of the wave energy dissipates) results in the following equation for $h_{50}$,

$$\int_{-h_{50}}^{0} \varepsilon dz = \alpha_w u_*^3 \left(3B/S_q\right)^{1/2} \int_{-h_{50}}^{0} \left[z_0/\left(z+z_0\right)\right]^n dz = 0.5\,\alpha_w u_*^3 \qquad (3.50)$$

The solution of this equation is

$$h_{50} = z_0\left(2^{1/n} - 1\right) \approx z_0/3\,. \qquad (3.51)$$

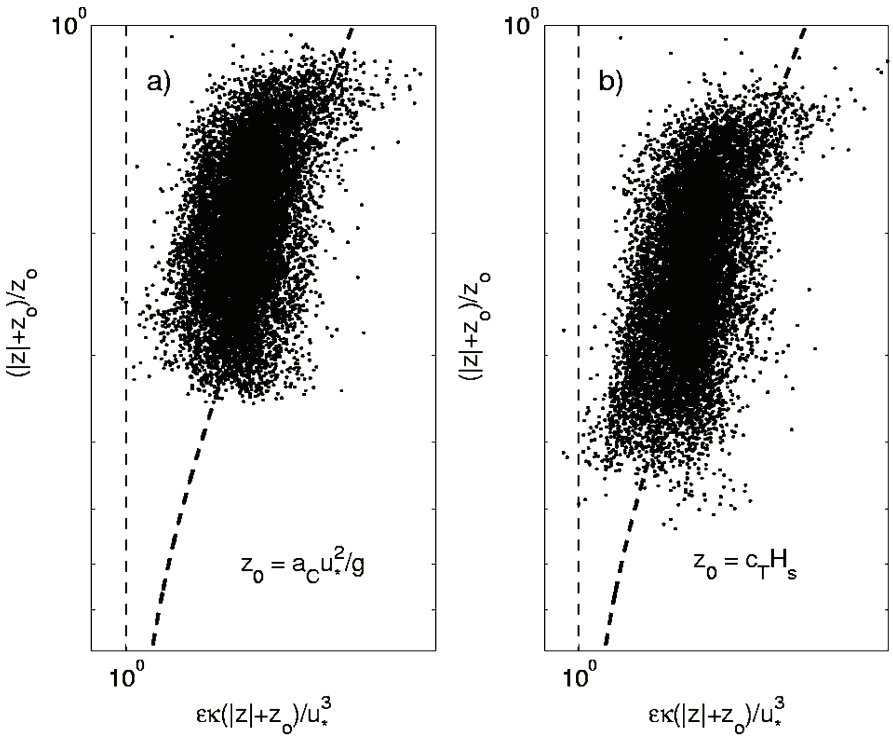


*Figure 3-16*. (a) Dissipation rates scaled according to (3.45) and the waterside surface roughness $z_0$ parameterized with (a) (3.46) and (b) (3.47). Points are the COARE EQ-3 bow data (10-min averages) taken under moderate wind speed conditions ($U_{15} > 9.5$ ms$^{-1}$). The vertical dashed line is the logarithmic layer model. The bold dashed curves are the Craig and Banner (1994) model of wave enhanced turbulence (3.45) at (a) $a_C = 9\text{x}10^4$ and (b) $c_T = 0.6$. Adapted from Soloviev and Lukas (2003) with permission from Elsevier.

This means that in the CB94 model, 50% of the wave-breaking energy dissipates within the layer $h_{50} = c_T H_S / 3$ (if parameterization (3.47) holds). Solution (3.51) is invariant with respect to constant $\alpha_w$. However, the vertical distribution of dissipation rate (3.44) does depend on $\alpha_w$ (in general $\alpha_w$ is a function of wave age).

In *Figure 3-16*, the COARE turbulence dissipation rates and the CB94 model (3.22) are plotted together in dimensionless coordinates $\varepsilon\kappa(|z| + z_0)/u_*^3$ and $(|z| + z_0)/z_0$, where $z_0$ is parameterized with formula (3.46) or (3.47). Dissipation rates $\varepsilon$ are 10-min averages of the dissipation rate calculated from 0.1 s segments with techniques described in Section 3.2.5. The wall layer prediction is shown by dashed vertical line $\tilde{\varepsilon} \equiv 1$.

According to the time averaged experimental results presented here, a dissipation rate 3 to 20 times larger than the logarithmic layer prediction is observed in the upper few meters of the ocean under moderate and high wind speed conditions. We interpret these increased turbulence levels as the effect of surface wave breaking.

The main cause of the scatter of dissipation rate estimates shown in *Figure 3-16* is believed to be turbulence intermittency, which is a fundamental property of turbulence (though complicated here by the intermittency of the wave-breaking events). Gurvich and Yaglom (1967) presented theoretical considerations based on Kolmogorov's idea of intermittent turbulence leading to the conclusion that the dissipation rate of TKE should have a lognormal distribution.

*Figure 3-17* illustrates the average COARE profiles of the dissipation rate from *Figure 3-16*. Averaging is done according to Baker and Gibson (1987); confidence intervals are shown with thin lines. The fit between the field data and model profiles shown in *Figure 3-17*a is obtained with $z_0$ parameterized according to (3.46) with $a_C = 9 \times 10^4$. Further tuning of constant $a_C$ does not improve the agreement between the experimental data and theory. The same experimental data and the same model are shown in *Figure 3-17*b for $z_0$ parameterized according to (3.47) with $c_T = 0.6$, close to that of Terray et al. (1996).

From equation (3.48) and equality (3.49), $c_T = 0.6$ corresponds to $a_C = 94{,}560$. This is consistent with $a_C = 90{,}000$ obtained from the fit of the CB94 model to the field data shown in *Figure 3-17*b.

Very close to the ocean surface, a substantial part of the data was removed from the analysis because of bubbles disturbing the measurements. The editing procedure thus might bias average dissipation rate estimates close to the ocean surface because bubble areas are associated with the most energetic wave breaking events. To determine the constant $c_T$, we therefore

used the deeper part of the experimental profile. (This constant would be smaller if we used the near-surface part of the profile.)

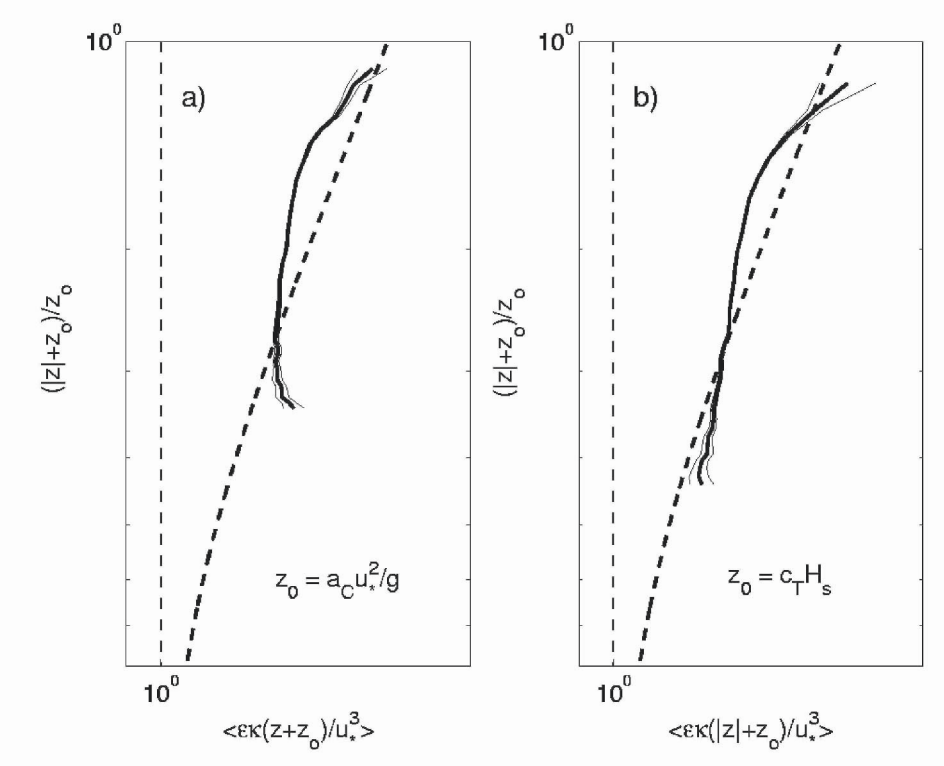


*Figure 3-17*. Average dimensionless dissipation rate profiles for the COARE EQ-3 cruise versus dimensionless depth at $U_{15} > 7$ ms$^{-1}$, for different parameterizations of the waterside surface roughness length: (a) formula (3.46) for $a_C = 90{,}000$, (b) formula (3.47) with $c_T = 0.6$. Thin lines represent the 95% confidence intervals. The vertical dashed line is the logarithmic layer model. The bold dashed curves are the Craig and Banner (1994) model (3.45). Adapted from Soloviev and Lukas (2003) with permission from Elsevier.

*Figure 3-18* shows the COARE data scaled according to the Terray et al. (1996) variables $|z|/H_s$ and $\varepsilon H_s/F_0$. The CB94 model (3.44) with $z_0$ parameterized according to (3.47) and with the turbulence flux of the kinetic energy expressed with (3.35) reads in dimensionless coordinates $\varepsilon H_S / F_0$ and $|z|/H_S$ as follows:

$$\varepsilon H_S / F_0 = \frac{\left[1 + \alpha_w \sqrt{3/(BS_q)} \left(1 + c_T{}^{-1} |z|/H_S\right)^{-2.4}\right]}{\kappa \left(c_T + |z|/H_S\right)}. \qquad (3.52)$$

The original Terray et al. (1996) model (3.27), the Craig and Banner (1994) model (3.44) with $c_0$ = 0.6, and the logarithmic layer model (3.4) are also shown.

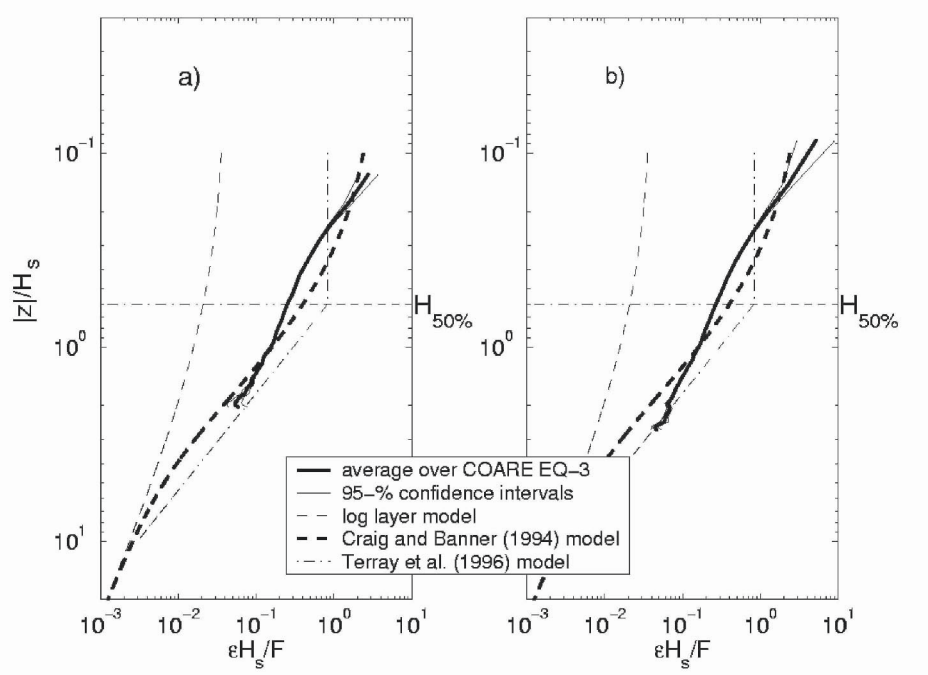


*Figure 3-18*. The normalized dissipation rate, $\varepsilon H_s/F_0$, versus dimensionless depth, $z/H_s$, for (a) wind speed range from 9.5 m s$^{-1}$ to 19.1 m s$^{-1}$ and (b) wind speed range from 7 m s$^{-1}$ to 19.1 m s$^{-1}$). The CB94 dependence is calculated with surface roughness from waterside parameterized as $z_0 = 0.6\ H_s$ .Reproduced from Soloviev and Lukas (2003) with permission from Elsevier.

The horizontal point-dashed line in*Figure 3-18* represents the depth of the layer, $H_{50} = 0.6H_s$, within which 50% of the wave energy dissipates according to the model of Terray et al. (1996) given by (3.27). Depth $h_{50}$, where 50% of the wave induced turbulence energy dissipates, is determined for the Craig and Banner (1994) model by $h_{50} = z_0/3$ (see (3.51)). With parameterization (3.47) for $c_T$= 0.6, this corresponds to

$$h_{50} \approx 0.2H_S\,, \tag{3.53}$$

which is 3 times smaller than $H_{50}$ from Terray et al. (1996). Equation (3.53) means that 50% of the wave breaking turbulence dissipates within only 20% of significant wave height.

According to *Figure 3-18*a, the near-surface dissipation rates are in a better agreement with the Craig and Banner model (3.52) using the Terray et

al. (1996) parameterization (3.47) than with the original Terray et al. (1996) model (3.27). Note that no tuning coefficients are available in the original Terray et al. (1996) model. Model (3.52) predicts lower values of dissipation than model (3.27) in the layer, $|z| > 0.4\ H_s$; above this layer, model (3.52) has larger dissipation rates than (3.27).

A possible reason for this difference is the use of the wave following versus fixed co-ordinate system. If the wave breaking energy substantially dissipates above the trough line, and the vertical dissipation rate profile is a nonlinear function of depth, then the difference between fixed and wave-following measurements can be significant. For instance, in a fixed coordinate system it is practically impossible to study near-surface layers with a thickness less than the surface wave height. In fact, any observational point between the wave trough and crest will alternate between water and air. Therefore, in order to study turbulence above the trough line, a wave-following coordinate system is required. We follow here Csanady's (1984) suggestion to analyze the near-surface data in the coordinate system connected to the ocean surface. The Craig and Banner (1994) model is consistent with the Csanady (1984) concept. The Terray et al. (1996) model, which is originally fit to tower-based data, would produce a different dissipation profile in the wave-following coordinate system.

Two other possible reasons for unresolved differences between (3.27) and (3.52) can be related to the fact that model (3.27) is substantially based on the fit to a tower-based data set. The standard Taylor hypothesis of a frozen field of turbulent eddies cannot be directly applied for the turbulence analysis of the tower-based measurements because the velocity fluctuation is not small relative to the mean flow. Also, nonlinear components of surface waves, which are not removed from the tower-based velocity records, might result in an overestimation of $\varepsilon$.

It should be noted that there is no reliable estimate of the average dissipation rate within the wave-turbulent layer $|z| < 0.6H_s$ in the literature. The constant dissipation rate that is set in (3.27) for $|z| < 0.6\ H_s$ is not based on any experimental data; it results from energy constraints. In Soloviev and Lukas (2003), the dissipation data were averaged in a wave-following co-ordinate system and were available starting from a depth $|z| = 0.1H_s$. These estimates of the dissipation rate in the layer stirred by breaking surface waves could, however, be biased because of extensive editing of the bubble-disturbed segments. This editing procedure might exclude the most energetic turbulence events associated with breaking waves from the statistics. The experimental dissipation profile systematically deviates from model (3.52) for $|z| < 0.6\ H_s$ (*Figure 3-18*a). In the layer $0.1\ H_s < |z| < 0.6\ H_s$, the integral dissipation rate, $\int \varepsilon(z) dz$, is about 5 times less than that predicted by model (3.52). This suggests that during these measurements about 80% of the wave energy dissipating in the layer stirred by breaking waves might be

unaccounted for because of bubble disturbances. Though we are using here the averaging technique of Baker and Gibson (1987) that accounts for the turbulence intermittency, it nevertheless may not completely compensate for editing bubble-disturbed segments. For the same reason, the confidence intervals might also be underestimated close to the ocean surface.

*Figure 3-18*b shows the same graphs but for the average dissipation rate profile for moderate and high wind speed conditions ($U_{15}$ = 7 m $s^{-1}$ - 19.2 m $s^{-1}$). The experimental profile in *Figure 3-18*b extends to deeper layers than in *Figure 3-18*a. The interpretation of *Figure 3-18*b is, however, hindered because of larger uncertainty in the significant wave height data than in *Figure 3-18*a. In the experiment of Soloviev and Lukas (2003) this uncertainty rapidly increases with the decrease of the wind speed.

The main features of the CB94 model can be summarized as follows:

1) Prandtl-type mixing length specification;

2) A turbulent kinetic energy equation representing a balance between parameterized versions of diffusion, dissipation and shear generation;

3) The Kolmogorov-type eddy viscosity (proportional to the mixing) length and the square root of turbulent kinetic energy;

4) Dimensionless constants ($\kappa$, $B$, $Sq$, $S_M$) are determined from fluid dynamics problems that are not related directly to wave enhanced turbulence.

5) A surface turbulent kinetic energy input, due to the waves, set proportional to the cube of the friction velocity.

We should make one final remark here about the CB94 model, which is based on the turbulence closure scheme of Mellor and Yamada (1982). There have been reports that this closure scheme does not work well in flows with negligible shear-production (Umlauf and Burchard, 2001). Though the flow in spilling wave breakers is not shear free because of intense air entrainment leading to the formation of a bore-like structure (Section 1.6.4), the length scale hypothesis (3.33) may not necessarily hold in this case. In the next section we consider the model of Benilov and Ly (2002), which intends to address this problem.

### 3.3.3 Benilov and Ly (2002) wave-turbulent model

The CB94 model treats breaking waves as a surface source for the turbulent kinetic energy. Benilov and Ly (2002; hereafter BL02) considered breaking waves as a volume source of energy. They incorporated wave kinetic energy $b_w$ into the turbulent kinetic energy budget equation (1.24) following ideas of Kitaigorodskii et al. (1983):

$$\frac{\partial b}{\partial t} = \mathrm{Pr}_b^{-1} \frac{\partial}{\partial z}\left[ \nu_T \left( \frac{\partial b}{\partial z} + \sigma_w \frac{\partial b_w}{\partial z} \right) \right] + \nu_T \left[ \left( \frac{\partial u}{\partial z} \right)^2 + \left( \frac{\partial v}{\partial z} \right)^2 \right] - \varepsilon \,, \qquad (3.54)$$

where $\mathrm{Pr}_b$ is the Prandtl number for the turbulent kinetic energy diffusion, $\sigma_w = \mathrm{Pr}_b/\mathrm{Pr}_\varepsilon$, $\mathrm{Pr}_\varepsilon$ is the turbulent Prandtl number for dissipation rate, $b_w = 1/2\left(u_w^2 + v_w^2 + w_w^2\right)$, $u_w, v_w, w_w$ are the velocity components of the potential velocity wave field, and the eddy viscosity in terms of $k$-$\varepsilon$ turbulence theory is as follows:

$$\nu_T = c_v b^2 / \varepsilon = l b^{1/2} \,, \qquad (3.55)$$

Parameterization (3.55) for eddy viscosity $\nu_T$ is derived from the same (Kolmogorov type) hypothesis as that for $K_M$ in the CB94 model. The numerical values of the corresponding empirical constants in BL02 are however somewhat different form CB94. We therefore reserved a separate symbol for eddy viscosity in this section.

A common estimate of the turbulent Prandtl number is $\mathrm{Pr}_b = 1$, and constant $c_v$ is the dimensionless empirical constant with typical numerical value $c_v = 0.09$ (Hoffmann, 1989). Equation (3.54) is similar to the regular form of the kinetic energy budget equation (3.31). There is, however, an important difference–the kinetic energy of potential waves $b_w$ appears to enter the turbulent kinetic energy budget in the form of the turbulent diffusion of the wave kinetic energy. Parameter $\sigma_w$ shows the relative wave kinetic energy that can be transferred by turbulence. According to Longuet-Higgins (1969) $\sigma_w << 1$. In the formulation of BL02, parameter $\sigma_w$ is an eigenvalue of the boundary layer problem.

In the BL02 model, the equation for length scale (3.33) is replaced with the equation for dissipation rate in the form of $k$-$\varepsilon$ turbulent theory with an extra term $\Pi_v$, which is the wave source of dissipation increase:

$$\frac{\partial \varepsilon}{\partial t} = \mathrm{Pr}_\varepsilon^{-1} \frac{\partial}{\partial z}\left( \nu_T \frac{\partial \varepsilon}{\partial z} \right) + c_1 c_v b \left[ \left( \frac{\partial u}{\partial z} \right)^2 + \left( \frac{\partial v}{\partial z} \right)^2 \right] + \Pi_v - c_2 \frac{\varepsilon^2}{b} \,, \qquad (3.56)$$

where $c_1$, $c_\nu$, and $c_2$ are the dimensionless constants.

As $b_w \to 0$, equation (3.54) reduces to the corresponding equation (3.31) in the CB94 model. As we mentioned above, the numerical constants in CB94 and BL02 appear to be somewhat different. The variability of all constants for the $k$-ε group models is discussed in Patel et al. (1984). In order

to preserve the integrity of the BL02 model we accept the same typical numerical values, $\mathrm{Pr}_\varepsilon = 1.3$, $c_1 = 1.44$, $c_v = 0.09$, $c_2 = 1.92$ as in the original BL02 model. The impact of the variability of constants on the BL02 model output has not yet been studied.

The term $\Pi_v$ in the equation for $\varepsilon$ describing the "production of dissipation" due to the wave kinetic energy $b_w$ is not known. From general considerations, it should vanish as $z \to -\infty$ because the wave motion degrades far enough from the ocean surface. The system of equations (3.54)-(3.56) has hence two unknown functions: the kinetic energy of potential waves, $b_w$, and the production of the dissipation rate by waves, $\Pi_v$.

An analytical expression for the vertical distribution of the wave kinetic energy, $b_w(z)$, can be obtained from the linear theory of waves. The wave kinetic energy via the spectrum of surface waves $S_\eta(w)$ is described by the formula:

$$b_w(z) = \tfrac{1}{2}\int_0^\infty S_\eta(\omega)\omega^2 \exp\left(-2\omega^2|z|/g\right)d\omega\,, \tag{3.57}$$

which follows from the formulation of the surface wave spectra via the Fourier-Stieltjes integral (see Chapter 1, Section 1.6.5).

For the spectrum of surface waves in the form (1.127), which is the Pierson-Moskowitz spectrum, Benilov and Ly (2002) derived the following formula:

$$b_w(z) = b_w(0)\left(1+\sqrt{|z|/L_*}\right)\exp\left(-\sqrt{|z|/L_*}\right), \tag{3.58}$$

where $b_w(0) = 0.5\beta_0\left(g/\omega_p\right)^2$, $L_* = g/\left(24\omega_p{}^2\right) = \sigma_\eta/\left(12\beta_0^{1/2}\right)$, $\beta_0 \approx 10^{-2}$, $\sigma_\eta^2$ is the variance of surface wave elevation, and $\omega_p$ is the frequency of the surface wave spectral peak.

Boundary conditions for the momentum balance equations, (3.28) and (3.29), remain the same as for the CB94 model (3.34). The boundary condition for the kinetic energy balance equation (3.54) is specified as the kinetic energy flux at $z = 0$:

$$F_0 = \mathrm{Pr}_b^{-1}\nu_T\frac{\partial}{\partial z}\left(b+\sigma_w b_w\right), \tag{3.59}$$

where the energy flux $F_0$ can be expressed either via the wave phase speed,

$$F_0 = \tfrac{1}{3}\gamma_1\beta_0\rho c_{pw}{}^3 \tag{3.60}$$

or via the friction velocity as in (3.35). Here $c_{pw} = g/\omega_p$ is the phase velocity of the wind waves spectral peak $\omega_p$.

The boundary condition for the dissipation rate $\varepsilon$ in equation (3.56) is specified as follows:

$$\varepsilon(0,t) = \varepsilon_0 . \tag{3.61}$$

As, $z \to -\infty$,

$$\frac{\partial b}{\partial z} = 0 ,\ \varepsilon = 0 ,\ \nu_T \frac{\partial u}{\partial z} = 0 , \text{ and } \nu_T \frac{\partial v}{\partial z} = 0 . \tag{3.62}$$

Following the vertical structure of the upper ocean turbulent boundary layer outlined in Section 3.1.4 (*Figure 3-1*), there are three intermediate asymptotic solutions:

1) The wave-stirred layer. This is a layer where the surface wave effect dominates and defines the dynamics of the turbulence. Hence, in the equation for the turbulent kinetic energy (3.54) the energy production by the mean shear can be neglected (perhaps, except the upper few millimeters where the viscous effects between wave-breaking events are of importance). The vertical diffusion of the turbulent kinetic energy is relatively small in this layer due to anticipated nearly uniform vertical distribution of TKE. Thus in the wave-stirred layer, $0 \le |z| \le H_{w-s}$:

$$\left|\frac{\partial b}{\partial z}\right| << \sigma_w \left|\frac{\partial b_w}{\partial z}\right| \text{ and } \nu_T \left[\left(\frac{\partial u}{\partial z}\right)^2 + \left(\frac{\partial v}{\partial z}\right)^2\right] << \varepsilon \tag{3.63}$$

The equation of TKE budget (3.54) in the steady case reduces as follows:

$$\sigma_w \,\mathrm{Pr}_b^{-1} \frac{d}{dz}\left[\nu_T \left(\frac{db_w}{dz}\right)\right] = \varepsilon \tag{3.64}$$

Rather than dealing with basically unknown function $\Pi_v$ in (3.56), the BL02 model defines the turbulence length scale for the wave-stirred layer from relationship,

$$\mathrm{Pr}_v^{-1}\,\nu_T\,\frac{db_w}{dz} = r_c b^{1/2} b_w\,, \tag{3.65}$$

and from accepting the hypothesis that the correlation coefficient $r_c$ = const. Substituting the Kolmogorov type relationship (3.55) into (3.65) results in the following equation:

$$l = \chi b_w \Big/ \frac{db_w}{dz} = 2\sigma_w^{-1}\,\mathrm{Pr}_b\, r L_* \left(1 + \sqrt{\frac{|z|}{L_*}}\right), \tag{3.66}$$

where $\chi$ is the dimensionless proportionality constant.

Equation (3.64) with relationships (3.55) and (3.66) has an exact solution in the form:

$$\varepsilon(z)/\varepsilon_0 = \left[\frac{3/2\left(1+\sqrt{|z|/L_*}\right)^{1/3}\exp\left(-\sqrt{|z|/L_*}\right)}{1+1/2\left[\left(1+\sqrt{|z|/L_*}\right)\exp\left(-\sqrt{|z|/L_*}\right)\right]^3}\right]^{3/2}, \tag{3.67}$$

where $L_* = H_s/\left(48\beta_0^{1/2}\right) \approx 0.21 H_S$ and

$$\varepsilon_0 = a_\varepsilon F_0 / H_S\,, \tag{3.68}$$

and $a_\varepsilon$ is a dimensionless coefficient.

2) <u>The turbulence diffusion layer</u>. This layer is a transition zone between the wave-stirred layer and the layer where the mean shear controls the turbulent regime,

$$H_{w-s} \le |z| \le H_{TD}\,. \tag{3.69}$$

In this layer, the wave stirring effect, however, becomes insignificant compared to the turbulent diffusion, that is,

$$\left|\frac{db}{dz}\right| >> \sigma_w \left|\frac{db_w}{dz}\right|. \tag{3.70}$$

The turbulent diffusion nevertheless still exceeds the mean shear contribution into the turbulent kinetic energy budget, which can be expressed by the following inequality:

$$\nu_T\left[\left(\frac{\partial u}{\partial z}\right)^2+\left(\frac{\partial v}{\partial z}\right)^2\right]<<\varepsilon\,. \tag{3.71}$$

The BL02 model finds the solution in this layer as an intermediate asymptotic, where the turbulent kinetic energy flux is balanced by the dissipation, and the dissipation production term $\Pi_v$ is assumed to be insignificant. Equations (3.54) and (3.56) then reduce to a set of two nonlinear ordinary equations:

$$\mathrm{Pr}_b^{-1}\frac{d}{dz}\left(\nu_T\frac{db}{dz}\right)=\varepsilon,\quad \nu_T=c_v\frac{b^2}{\varepsilon}=lb^{1/2}\,, \tag{3.72}$$

$$\mathrm{Pr}_\varepsilon^{-1}\frac{d}{dz}\left(\nu_T\frac{d\varepsilon}{dz}\right)=c_2\frac{\varepsilon^2}{b}\,. \tag{3.73}$$

The boundary condition for (3.72) and (3.73) is set at $z$ = -$H_{w\text{-}s}$ in the following way:

$$c_v\,\mathrm{Pr}_b\left(\frac{b^2}{\varepsilon}\frac{db}{dz}\right)\Bigg|_{z=-H_{w-s}}=q_{w-s},\quad \varepsilon\Big|_{z=-H_{w-s}}=\varepsilon_1\,, \tag{3.74}$$

where $q_{w-s}$ is the turbulent kinetic energy flux from the wave-stirred layer, and $\varepsilon_1$ is the dissipation rate at the lower boundary of the wave-stirred layer. As $|z|-H_{w-s}\to\infty$, the solutions for $b$ and $\varepsilon$ tend to zero since the asymptotic analysis assumes that the boundary conditions at the lower boundary of this layer does not influence the solution. This implies that the turbulence diffusion layer is sufficiently thick for the existence of the asymptotic behavior of the solution.

There is an ambiguity in the BL02 model in identifying the boundary between the wave-stirred and turbulence diffusion layer, $z=-H_{w-s}$, which is in fact the boundary between two asymptotic solutions. This ambiguity extends to the formulation of the TKE flux $q_{w-s}$ at $z=-H_{w-s}$.

We will use here continuity of the dissipation rate ε at $z = -H_{w-s}$ and the value of coefficient $a_\varepsilon$ in the formula for the surface dissipation rate of wave energy (3.68) preserving the total energy form wind to waves in the following way:

$$\int_{-\infty}^{-H_{w-s}} \varepsilon dz + \int_{-H_{w-s}}^{0} \varepsilon dz = F_0 . \tag{3.75}$$

Boundary conditions (3.74) are correspondingly specified as follows:

$$c_v \,\mathrm{Pr}_b \left( \frac{b^2}{\varepsilon} \frac{d_z b}{dz} \right) \Bigg|_{z=-H_{w-s}} = F_0 - \int_{-H_{w-s}}^{0} \varepsilon dz, \quad \varepsilon \Big|_{z=-H_{w-s}} = \varepsilon_1 \tag{3.76}$$

The exact solution of (3.72)-(3.73) for the dissipation rate in the turbulence diffusion layer is found in the form:

$$\varepsilon = \varepsilon_1 \left[ 1 + \left( |z| - H_{w-s} \right) / L_{*1} \right]^{-\upsilon_2} , \tag{3.77}$$

where $\varepsilon_1$ and $L_{*1}$ are linked by boundary conditions (3.76) as follows:

$$L_{*_1} = 3 q_{w-s} / \varepsilon_1 , \tag{3.78}$$

and parameter $\upsilon_2$ is set as $\upsilon_2 = 4$ based on the laboratory measurements of the turbulence decay behind an oscillating grid (Thompson and Turner, 1975).

3) The logarithmic layer. For this layer we accept the formula for constant stress layer,

$$\varepsilon_{sh} = u_*^3 / \left( \kappa |z| \right) . \tag{3.79}$$

This solution is simply added to the wave solution to obtain the following parameterization formula for the dissipation rate:

$$\varepsilon = \varepsilon_{sh} + \varepsilon_{wv} , \tag{3.80}$$

where $\varepsilon_{sh}$ is the shear-generated dissipation, and $\varepsilon_{wv}$ is the wave-induced dissipation. The latter is described for developed waves by equations (3.67)-(3.77), which are combined below into a single expression:

$$\varepsilon_{wv} = 3.78\frac{F_0}{H_S}\begin{cases}\left[\dfrac{3\left(1+\sqrt{\gamma\dfrac{|z|}{H_S}}\right)^{1/3}\exp\left(-\sqrt{\gamma\dfrac{|z|}{H_S}}\right)}{2+\left[\left(1+\sqrt{\gamma\dfrac{|z|}{H_S}}\right)\exp\left(-\sqrt{\gamma\dfrac{|z|}{H_S}}\right)\right]^3}\right]^{3/2} & \text{at } \dfrac{|z|}{H_S}\le 0.6 \\ 0.22\left[1+0.66\left(\dfrac{|z|}{H_S}-0.6\right)\right]^{-4} & \text{at } \dfrac{|z|}{H_S}>0.6\end{cases} \tag{3.81}$$

where $\gamma = 48\beta_0^{1/2}$.

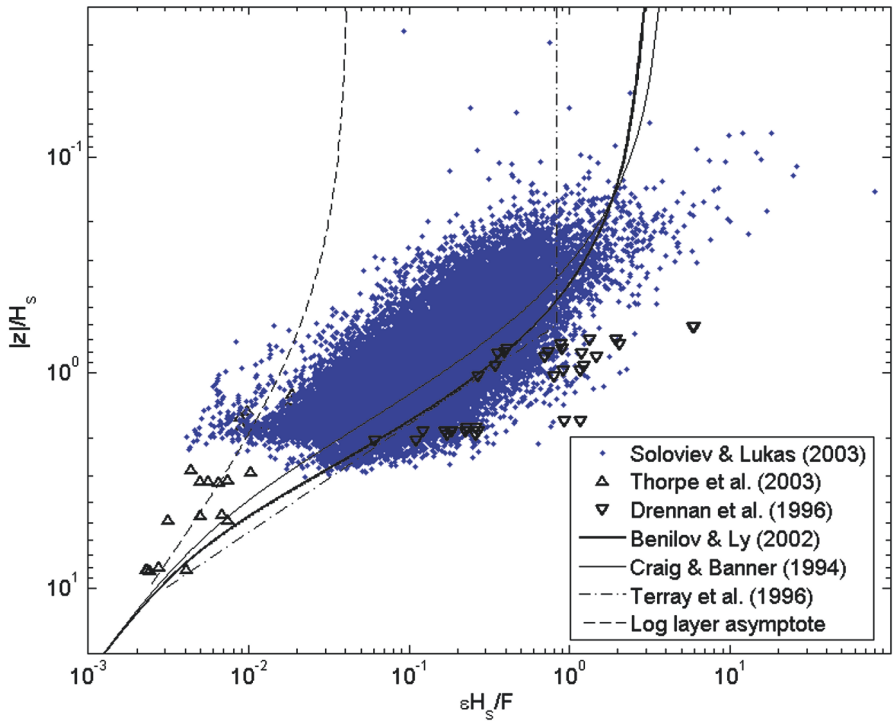


*Figure 3-19*. Normalized dissipation rate $\varepsilon H_s/F_0$ versus dimensionless depth $|z|/H_s$ according to field (open ocean) and theoretical results. Here: $\varepsilon$ is the dissipation rate of the turbulent kinetic energy, $F_0$ the flux of the kinetic energy from wind to waves, and $H_s$ the significant wave height. Wind speed range is from 7 m s$^{-1}$ to 19 m s$^{-1}$. The Craig and Banner (1994) model is calculated with surface roughness from waterside parameterized as $z_0 = 0.6\ H_s$; the Benilov and Ly (2002) model is for $H_{w\text{-}s}/H_s = 0.4$, where $H_{w\text{-}s}$ is the effective depth of the wave-stirred layer.

The Benilov and Ly (2002) model accounts for the transfer of kinetic energy from breaking waves to turbulence and the length scale is not constrained by formula (3.33). This model is therefore expected to perform well in the wave-stirred layer. Note that in the diffusive and logarithmic sublayers this model is practically identical to CB94.

An important feature of the Benilov and Ly (2002) model is that it does not require the $z_0$ to be specified (as in CB94 model). The surface roughness from waterside is no longer a model parameter in Benilov and Ly (2002). In the wave-stirred layer, the Benilov and Ly (2002) model, nevertheless, employs a simplified version of the dissipation rate budget equation, which unfortunately introduces a new adjustable parameter, which is the effective depth of the wave-stirred layer, $H_{w\text{-}s}/H_s$.

*Figure 3-19* summarizes the results of the recent field and theoretical studies of wave-enhanced turbulence. In order to minimize the influence of thermohaline stratification effects on near-surface turbulence characteristics, only the data obtained during high wind speeds are analyzed. The one-month long data set of Soloviev and Lukas (2003) was collected under various wind-wave conditions. The contribution of remotely forced swell to the significant wave height, $H_s$, could contribute some scatter in the nondimensional dissipation rate, $\varepsilon H_s/F_0$, and the nondimensional depth, $|z|/H_s$.

Solution (3.80) is shown in *Figure 3-19* in comparison with the field data. At $H_{w\text{-}s}/H_s$ = 0.4, parameterization formula (3.80) approximates reasonably well both Thorpe et al. (2003a) and Drennan et al (1996) data sets (in contrast to the analysis shown in *Figure 3-13*b); it is also consistent with the Soloviev and Lukas (1993) data.

### 3.3.4 Concluding remarks on wave-enhanced turbulence

One of the first observations of near-surface turbulence dissipation was made by Stewart and Grant (1962) with a velocity sensor (thermo-anemometer) mounted on the bow of a vessel. Their data indicated that wave-generated turbulence essentially dissipates above the trough line.

A similar conclusion was reached by Soloviev et al. (1988) based on the analysis of dissipation rate profiles obtained with a free-rising profiler and of the observations made by Arsenyev et al. (1975), Jones and Kenney (1977), Dillon et al. (1981), and Oakey and Elliott (1982). In nondimensional coordinates $g|z|/u_*^2$ and $\varepsilon\kappa|z|/u_*^3$, the dissipation rates were near or slightly exceeding (within a factor of 2-3) the logarithmic layer prediction. Soloviev et al. (1988) suggested that all of these data came mainly from below the layer of wave-enhanced turbulence. However, these analyzed data were confined to moderate and low wind speed conditions. Later, Greenan et al. (2001) and Thorpe et al. (2003a) obtained dissipation rate data sets under

high-wind speed conditions and developed seas (*Figure 3-19*) that appeared to confirm the conclusion of Stewart and Grant (1962) and Soloviev et al. (1988) that the main part of the wave-generated turbulence dissipates within a near-surface layer, whose depth is less than one significant wave height.

Tower-based turbulence measurements made in a lake by Kitaigorodskii et al. (1983) and Agrawal et al. (1992) under a wide range of wind speed conditions produced evidence in favor of a thicker layer of wave enhanced turbulence and higher turbulence levels. Terray et al. (1996) proposed a new scaling that accounted for the limited fetch in the lake observations and dramatically reduced the difference between the two groups of data. Some differences, however, could not be explained solely by difference in fetch and wave age and might be related to methodical issues. The interpretation of the above tower-based turbulence measurements is somewhat uncertain because the transfer from frequency to wavenumber domain is not well defined for oscillating flows.

For turbulence measurements, Soloviev et al. (1988) used a free-rising profiler, Greenan et al. (2001) employed a free-gliding instrument, and Thorpe et al. (2003a) utilized an autonomous underwater vehicle (AUV). All of those were moving instruments: It is apparently easier to satisfy Taylor's hypothesis of frozen turbulence with a moving instrument. All of those three instruments at some extent follow surface waves and, hence, have a tendency to provide the data in the Lagrangian wave following coordinate system (see Section 3.1.1). At the same time, the parameterization of Terray et al. (1996) is based on tower data that are collected and interpreted in a fixed coordinate system.

Energy budget considerations provide an estimate of the wavelength $\lambda_{dis}$ where the transition toward the dissipation regime occurs (Kitaigorodskii, 1991):

$$\lambda_{dis} = 2\pi E_0^{2/3}/(a_1 g) \tag{3.82}$$

where $E_0$ is the energy flux from the region of energy input through the non-dissipative region of the wave spectrum toward the dissipation subrange, and $a_1 \approx 1\times10^{-4}$ according to the most recent estimates of Gemmrich and Farmer (1999). Following Gemmrich et al. (1994), we equate this energy flux to the integral dissipation of surface wave energy due to wave breaking in the upper ocean, which in stationary conditions is equal to the flux of the TKE at the air-sea interface, $E_0 = F_0$. According to Pierson and Moskowitz (1964), for the saturated surface wave spectrum, the dominant wavelength $\lambda_p \approx 2\pi a_2 u_*^2 / g$, where $a_2 = 8.3\times10^{-5}$. From equations (3.35) and (3.82), it follows that $\lambda_{dis}/\lambda_p = \alpha_w{}^{2/3}/(a_1 a_2) \approx 0.26$. This means that breaking waves

are much shorter than the dominant wave. Moreover, in the open ocean about 98% of breaking waves are of spilling type, which do not penetrate deeply (Gemmrich and Farmer, 1999). About 2% of breaking events show deeper penetration. The deeper penetrating events, which are typical for plunging wave breakers, however, play a minor role in upper ocean dynamics (even under the condition of swell opposing wind waves, when the occurrence of deep penetrating events increases to 10% of the total number of breaking waves). The turbulent kinetic energy produced by spilling breakers is localized in a shallow layer (also due to intensive bubble entrainment–see Melville, 1994) and decays quickly with depth (Ly and Garwood, 2000; Benilov and Ly, 2002). This is consistent with results shown in *Figure 3-19*, indicating that the wave-breaking energy mostly dissipates within less than one significant wave height from the ocean surface.

The flux of the TKE at the air-sea interface $F_0$ is the principal component of the upper ocean parameterization schemes considered above. Although the direct (eddy correlation) measurement of $F_0$ is still a challenge, it can be estimated as the integral of the growth rate over the surface wave spectrum (see Section 1.6.6). Remote sensing techniques may provide an effective way for obtaining information about the frequency-direction spectrum of surface waves on global scale.

In our analysis of wave-enhanced turbulence we have ignored convection as a source of TKE in the near-surface layer of the ocean. According to Lombardo and Gregg (1989), the dissipation rate of TKE due to gravitational convection in the upper ocean

$$\varepsilon_c \approx -\alpha_T g Q_0 /(c_p \rho), \tag{3.83}$$

where $\alpha_T$ is the thermal expansion coefficient of seawater, $g$ the acceleration of gravity, and $Q_0$ is the net surface heat flux. For $Q_0 = 200$ W m$^{-2}$, we obtain $\varepsilon_c \approx 2\times10^{-7}$ W kg$^{-1}$, which is much less than typical dissipation rates observed in the upper few meters of the ocean under high wind speed conditions (*Figure 3-12*). Thus, gravitational convection is not a primary source of turbulence in this case. Addition of the salinity effect due to evaporation (see (3.96)) does not change the above estimate substantially.

The models of CB94, Terray et al. (1996), and BL02 do not consider bubbles. A model of wave-enhanced turbulence incorporating the buoyancy effect of bubbles, which has yet to be developed, could probably provide a better insight into the problem of turbulence closure.

## 3.4 Effects of Thermohaline Stratification

In this section we consider the effect of thermohaline stratification on the near-surface turbulence. Air bubbles produced as a result of wave breaking also create density stratification, which may affect near-surface turbulence. The role of bubbles will be considered in Section 6.1.

*Figure 3-20* shows the turbulence dissipation data obtained in stratified conditions, below the layer of wave-enhanced turbulence. The dissipation rate exhibits a three order of magnitude enhancement compared to the log layer prediction. This is a much stronger relative increase of the dissipation rate compared to what can be caused by surface wave breaking. This shows that the effect of stratification on the dissipation of turbulent energy in the near-surface layer of the ocean can be significant.

### 3.4.1 Formulation of the Monin-Oboukhov theory for the upper ocean

The effect of thermohaline stratification on the turbulent boundary layer can be characterized via the stability parameter, $\zeta = |z| / L_O$, where $|z|$ is the depth and $L_O$ is the Oboukhov length scale. The stability parameter is related to the Monin-Oboukhov similarity theory, which has been found useful in many studies of the atmospheric boundary layer (see Chapter 1).

Application of the Monin-Oboukhov theory to the upper ocean boundary layer, however, is not straightforward. The main problem is that the velocity scale in water is $\sqrt{\rho / \rho_a} \approx 30$ times smaller than that in air. For the identical length scale the kinematic mixing coefficient in water is about 30 times smaller than in the air. It therefore takes much more time for heat and momentum fluxes from the ocean surface to propagate to the same distance in the oceanic boundary layer compared to the atmospheric boundary layer. During this time interval surface heat fluxes may change significantly, especially due to the diurnal cycle of solar radiation. This can make the Oboukhov scale, which includes the surface fluxes, irrelevant.

Soloviev et al. (2001) suggested using an earlier version of the Monin-Oboukhov theory for upper ocean conditions, which was formulated in terms of the gradient Richardson number,

$$Ri = \frac{g \rho^{-1} \partial \rho / \partial z}{\left(\partial u / \partial z\right)^2 + \left(\partial v / \partial z\right)^2}, \tag{3.84}$$

where $\rho$ is the density, $z$ is the depth, $u$ and $v$ are the horizontal velocity components, and $g$ is the acceleration of gravity.

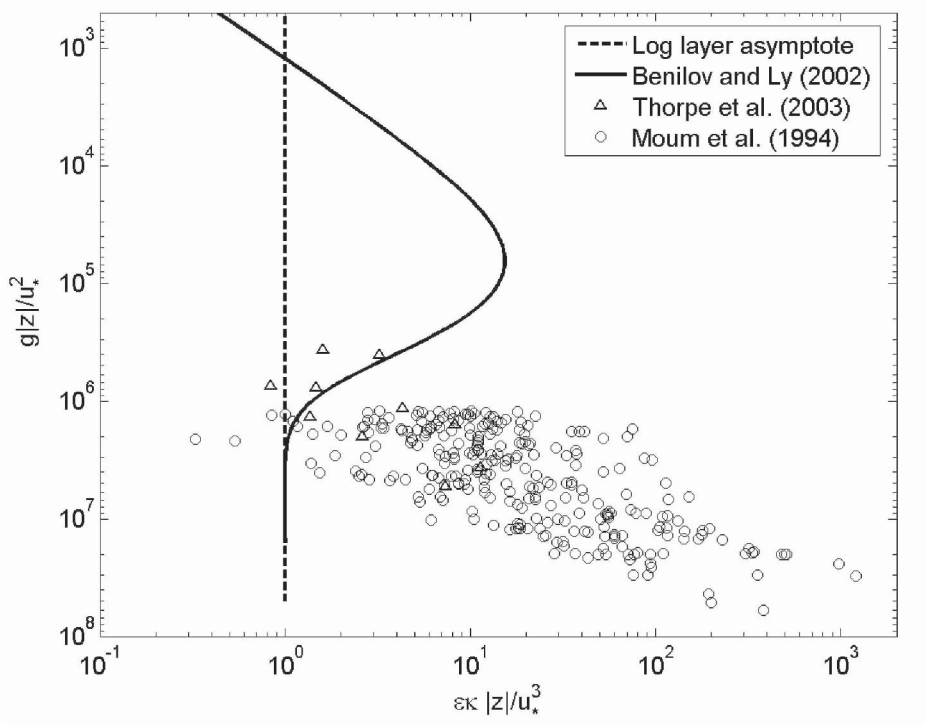


*Figure 3-20*. The effect of stratification on near-surface turbulence.

Although $\zeta$ and $Ri$ are both related to the stratified turbulent boundary layer, $\zeta$ is a function of the surface boundary conditions and $Ri$ is a function of the local density and velocity gradients. For a statistically steady and homogeneous turbulent boundary layer, parameters $\zeta$ and $Ri$ are related:

$$Ri(\zeta) = \zeta \phi_\rho(\zeta) \phi_m(\zeta)^{-2} = \begin{cases} \zeta & \text{for } 0 \geq \zeta \geq \zeta_m \\ \zeta / (1 + \beta\zeta) & \text{for } \zeta > 0 \end{cases}, \tag{3.85}$$

where $\beta$ is a dimensionless constant, and $\phi_\rho$ and $\phi_m$ are the universal functions for density and velocity respectively (see Chapter 1). According to (3.85), $Ri$ monotonically increases with $\zeta$, achieving an extreme as $\zeta \to \infty$:

$$Ri(\zeta)|_{\zeta\to\infty} = \beta^{-1} = Ri_{cr} \approx 0.25 \tag{3.86}$$

The Richardson number within the steady turbulent boundary layer is restricted from above to its critical value $Ri_{cr}$. If the Richardson number exceeds the critical value, this is an indication that this is an area outside of the surface turbulent boundary layer.

From (3.85), $\zeta$ can be expressed as a function of $Ri$:

$$\zeta = \begin{cases} Ri \text{ at } -0.20 \le Ri < 0 \\ Ri/\left(1 - Ri/Ri_{cr}\right) \text{ at } 0 \le Ri < Ri_{cr} \end{cases} \tag{3.87}$$

(The analytical relationship between $Ri$ and $z$ is bulky for $\varsigma < -0.20$; therefore it is not shown in (3.85) and (3.87).)

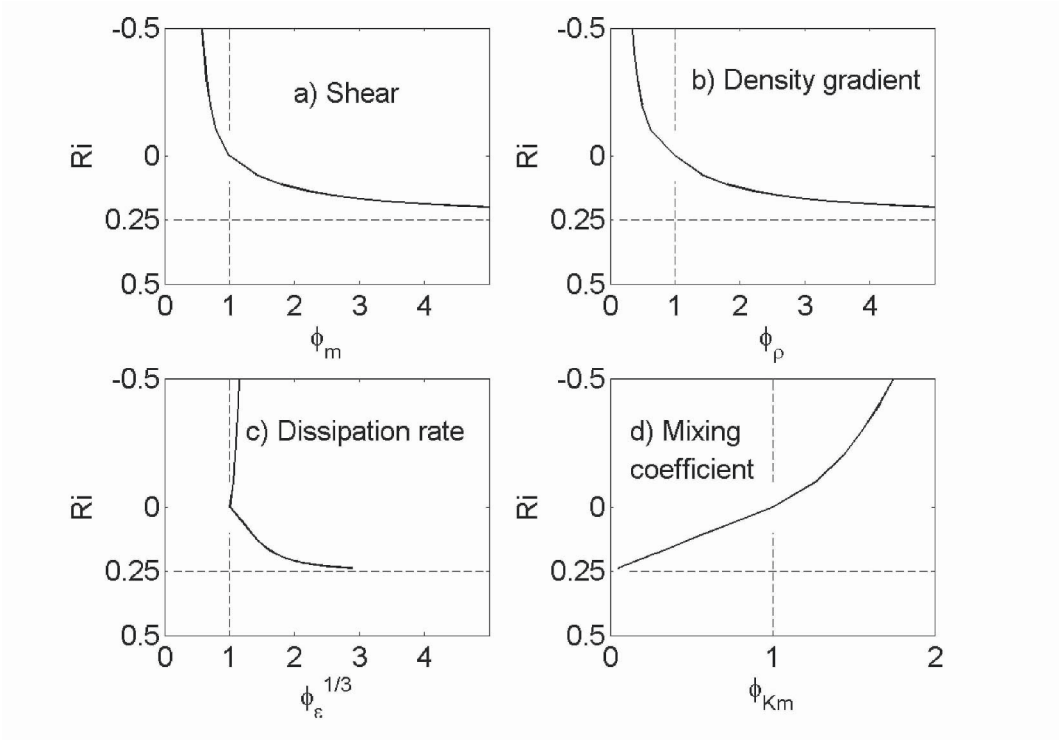


*Figure 3-21*. Universal functions for dimensionless (a) shear $\phi_m$, (b) density gradient $\phi_\rho$, (c) dissipation rate of the turbulent kinetic energy $\phi_\varepsilon$, and (d) turbulent eddy coefficient $\phi_{Km}$ expressed as a function of *Ri*. Reproduced from Soloviev et al. (2001) by permission of American Geophysical Union.

The universal functions for velocity $\phi_m(\zeta)$, density $\phi_s(\zeta)$, and dissipation rate $\phi_\varepsilon(\zeta)$ can then be expressed through *Ri* using formula (3.87). We do not

give here the corresponding analytical expressions, $\phi_m(Ri)$, $\phi_\rho(Ri,)$, and $\phi_\varepsilon(Ri)$ because of their bulkiness. They can be easily derived from (1.155), (1.156), and (1.157) by substituting $\zeta$ with $Ri$ according to relationship (3.87).

The coefficients of turbulent exchange for momentum and scalar properties in the boundary layer are defined as $K_M = -\overline{w'u'}/\partial u/\partial z$ and $K_s = -\overline{w'\rho'}/\partial\rho/\partial z$ respectively. Using the definition of the universal functions in the Monin-Oboukhov theory (see formulas (1.151)-(1.153) in Chapter 1), the mixing coefficients can be expressed as follows:

$$K_M = \kappa u_* |z|/\phi_m \tag{3.88}$$

$$K_\rho = \kappa \rho_* |z|/\phi_\rho \tag{3.89}$$

where $u_*^2 = \left(-\overline{w'u'}\right)|_{z=0}$ and $\rho_* = \left(\overline{w'\rho'}\right)\Big|_{z=0}/\left(\kappa u_*\right)$.

*Figure 3-21* shows boundary layer functions $\phi_m = \left(\kappa|z|/u_*\right)\partial u/\partial z$, $\phi_\rho = \left(\kappa|z|/\rho_*\right)\partial\rho/\partial z$, $\phi_\varepsilon = \varepsilon\kappa|z|/\left(-\overline{w'u'}\right)^{3/2}$, and $\phi_{Km} = K_M/\left(\kappa u_*|z|\right)$ plotted versus $Ri$. It is remarkable that the vertical shear and density gradients as well as the dissipation rate increases sharply when $Ri$ approaches its critical value, $Ri$ (corresponding to the mixed layer bottom), while the turbulent exchange coefficient vanishes as $Ri \to Ri_{cr}$.

The stratified turbulent boundary layer has the following three asymptotic regimes: 1) logarithmic layer (no stratification effects, *i.e.*, $Ri$ = 0), 2) free convection (unstable stratification and $u_* = 0$, *i.e.*, $Ri = -\infty$, and 3) marginal stability ( $Ri = Ri_{cr}$ ).

### 3.4.2 Asymptotic regimes

*a) Logarithmic layer*

With neutral stratification (*i.e.*, $Ri$=0) the buoyancy forces are not important, and $Ri$ falls out from the set of defining parameters in the Monin-Oboukhov similarity theory. As a result, functions $\phi_m$, $\phi_\rho$ $\phi_\varepsilon$, and $\phi_{Km}$ become constants. According to conventional normalization: $\phi_m(0) = \phi_\rho(0) = \phi_e(0) = \phi_{Km}(0) \equiv 1$. The shear and vertical gradient of a

scalar property in this layer for $|z| >> z_0$ are determined by well-known formulas:

$$\partial u / \partial z = u_* / \left(\kappa |z|\right), \tag{3.90}$$

$$\partial \rho / \partial z = \rho_* / \left(\kappa |z|\right). \tag{3.91}$$

The dissipation rate of TKE in the logarithmic layer

$$\varepsilon = u_*^{\,3} / \left(\kappa |z|\right), \tag{3.92}$$

while the mixing coefficient is

$$K_0 = \kappa u_* |z|. \tag{3.93}$$

The very near surface part of the oceanic turbulent boundary layer is subject to strong wave influence. The wave dissipation is essentially concentrated within a relatively thin near-surface layer of the ocean, equal to only about 20% of the significant wave height (Section 3.3.4). Csanady (1984) and Cheung and Street (1988) showed that the surface waves influence only the surface roughness parameter $z_0$ rather than the logarithmic velocity law.

*b) Free convection*

According to Beljaars (1994) the mixing coefficients for unstable stratification and zero wind stress can be expressed as follows:

$$K_M = \kappa w_* |z|, \tag{3.94}$$

where

$$w_* = a_p \left(hB_0\right)^{1/3} \tag{3.95}$$

is the Priestly (1959) convective velocity scale, $a_p$ is an empirical constant close to unity, $h$ is the mixed layer depth, and $B_0$ is the vertical buoyancy flux. A similar expression can be derived for $K_\rho$.

The dissipation rate of the TKE under free-convection conditions is

$$\varepsilon = -\alpha_T g Q_0 / \left(c_p \rho\right) + \beta_S S_0 g Q_E / \left(L\rho\right), \tag{3.96}$$

which differs from (3.83) by an additional term due to evaporation from the sea surface and the respective salinity increase. Here $S_0$ is the surface salinity, and $L$ is the latent heat of vaporization.

*c) Marginal stability*

The situation when $Ri$ is near its critical value is of special interest. In this case, the flow is in the so-called regime of marginal stability (Turner, 1973). This is a self-regulated state where the flow adjusts to the existing gross shear and stratification. It is characterized by essentially linear profiles of horizontal velocity and density (note that the linear profiles of density and velocity are the asymptotic limit of relations (1.152) and (1.153) as $\zeta \to \infty$. The regime of marginal stability has been observed in the atmospheric boundary layer over the ice in Antarctica, in the nocturnal atmospheric boundary layer, in the outer boundary layer of the gravity current (Turner, 1973), during dust storms in the atmosphere (Barenblatt and Golitsyn, 1974), and in the equatorial diurnal thermocline (Kudryavtsev and Soloviev, 1990).

The self-regulated layer effectively isolates the near-surface turbulent boundary layer from the water below. From (1.152), (3.87), and (3.88) it follows that for $0 < Ri < Ri_{cr}$,

$$K_M = K_0 \left(1 - Ri / Ri_{cr}\right), \tag{3.97}$$

where $K_0 = \kappa u_* \left|z\right|$ is the coefficient of turbulent mixing in the logarithmic boundary layer. According to (3.97) the turbulent boundary layer exchange vanishes when $Ri \to Ri_{cr}$. Actually, $K_M \left|_{Ri=Ri_{cr}} \neq 0\right.$ because there is always some background turbulence below the mixed layer (*i.e.*, for $Ri \geq Ri_{cr}$) caused by intermittent mixing events. However, $K_M \left|_{Ri=Ri_{cr}} << K_0\right.$.

### 3.4.3 Boundary layer scaling of the velocity and dissipation rate profiles

Though the gradient Richardson number $Ri$ appears to be a convenient parameter for study of the upper ocean turbulent boundary layer, its measurement *in situ* is complicated by velocity measurement errors. Within the turbulent boundary layer the observed shear is usually small (on the order of the measurement accuracy or even less), which results in an

enormous relative error for $Ri$. (Note that in definition (3.84) the shear enters into the denominator.) Velocity measurements involve both systematic and random errors. However, it is notable that acoustic Doppler current profiler (ADCP) techniques provide almost unbiased shear measurements (limited only by the effects described by Lien et al. (1994)), thus substantially reducing the systematic error. Ensemble averaging can significantly reduce the random error.

Shipboard ADCP instruments typically obtain measurements from the depth range 16 m - 300 m. The boundary layer laws can be tested with this technique only for relatively high wind speed conditions when the mixed layer depth exceeds 20 m.

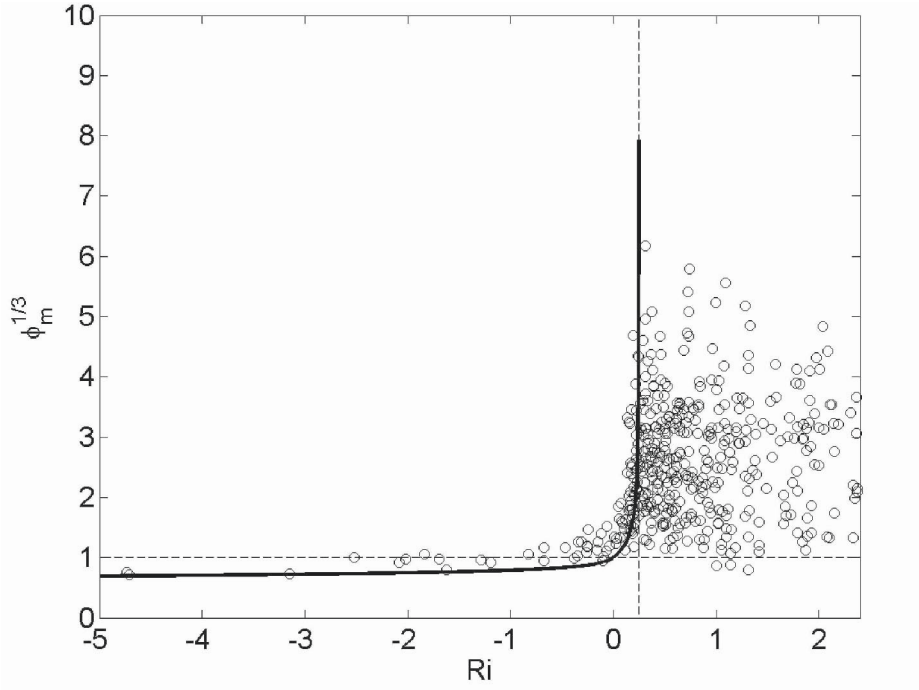


*Figure 3-22*. Dimensionless shear $\phi_m = \left(\kappa |z| / u_*\right) \partial u / \partial z$ as a function of Richardson number *Ri*. The bold line represents the turbulent boundary layer law from atmospheric measurements. Points are the observations from the depth range of 20-80 m for three R/V *Wecoma* surveys during TOGA COARE. Measurements taken under light winds ($u_*$ < 0.3 cm $s^{-1}$) are excluded. The vertical dashed line represents the critical value of the Richardson number, $Ri_{cr}$ = 1/4; while the horizontal dashed line corresponds to the logarithmic layer dependence. Reproduced from Soloviev et al. (2001) by permission of American Geophysical Union.

In *Figure 3-22*, observations of shear within the depth range of 20–80 m are plotted as a function of the Richardson number. The data were taken

from the repeated ship track observations of the R/V *Wecoma* during TOGA COARE. The Richardson number was calculated from the towed undulating CTD (SEASOAR) and ADCP gridded data (10 m in depth and ~3 km in horizontal distance) and the formula,

$$Ri = N^2 / S_h^{\,2}, \tag{3.98}$$

where $N^2 = g\overline{\Delta\rho/\Delta z}/\rho$ and $S_h^{\,2} = \overline{(\Delta u/\Delta z)}^2 + \overline{(\Delta v/\Delta z)}^2$. The averaging is performed on the corresponding depth surfaces along the individual R/V *Wecoma* sections. Note that the terms in the numerator and denominator of the expression for the Richardson number are averaged separately.

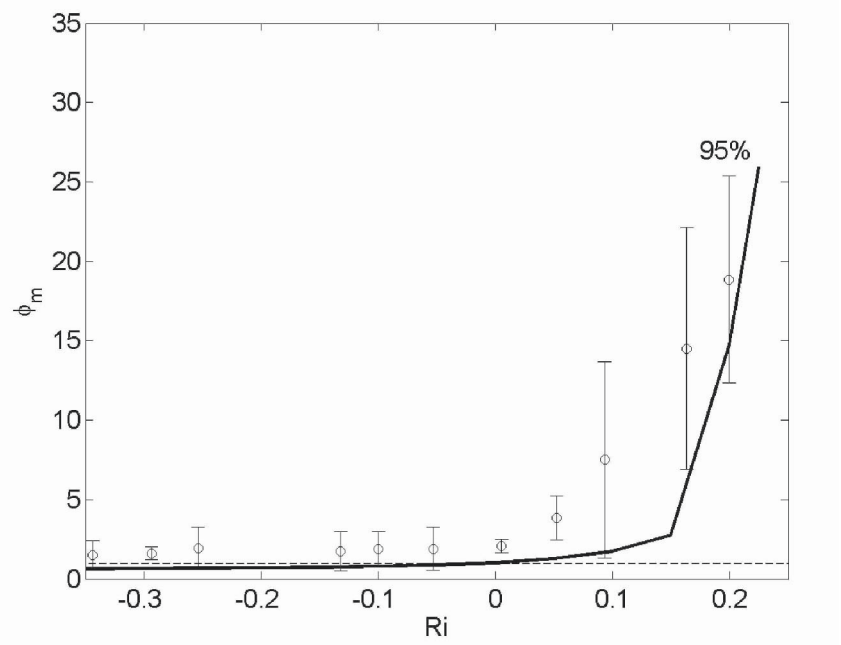


*Figure 3-23*. Dimensionless shear (from *Figure 3-22*) averaged within the mixed layer (i.e., $Ri <$ 0.25). Circles represent the mean for overlapping intervals of $\Delta Ri$ = 0.1. The 95% confidence limits are constructed on the basis of Student's distribution (Rabinovich, 1995). The bold line represents the theoretical turbulent boundary layer law averaged over the same *Ri* intervals. The horizontal dashed line is the logarithmic layer dependence. Adapted from Soloviev et al. (2001) by permission of American Geophysical Union.

The shear magnitude in *Figure 3-22* is normalized with the friction velocity calculated from the meteorological measurements with the COARE 2.5 bulk flux algorithm. There are 17 points within the Richardson number range $-0.1 < Ri < 0.05$ that correspond to the logarithmic layer regime. Most

of the shipboard ADCP measurements during the R/V *Wecoma* surveys are, however, taken at higher magnitudes of the Richardson number, when the influence of stratification cannot be neglected. Within the turbulent boundary layer ( $Ri < 0.25$) the boundary layer dependence is consistent with the experimental data, however the scatter of the individual points is relatively large. For $Ri > 0.25$ the data are more scattered. Note that the universal boundary layer dependences are not defined for $Ri > Ri_{cr}$ . (This implies criteria $Ri = Ri_{cr}$ as a definition of the surface mixed layer depth.)

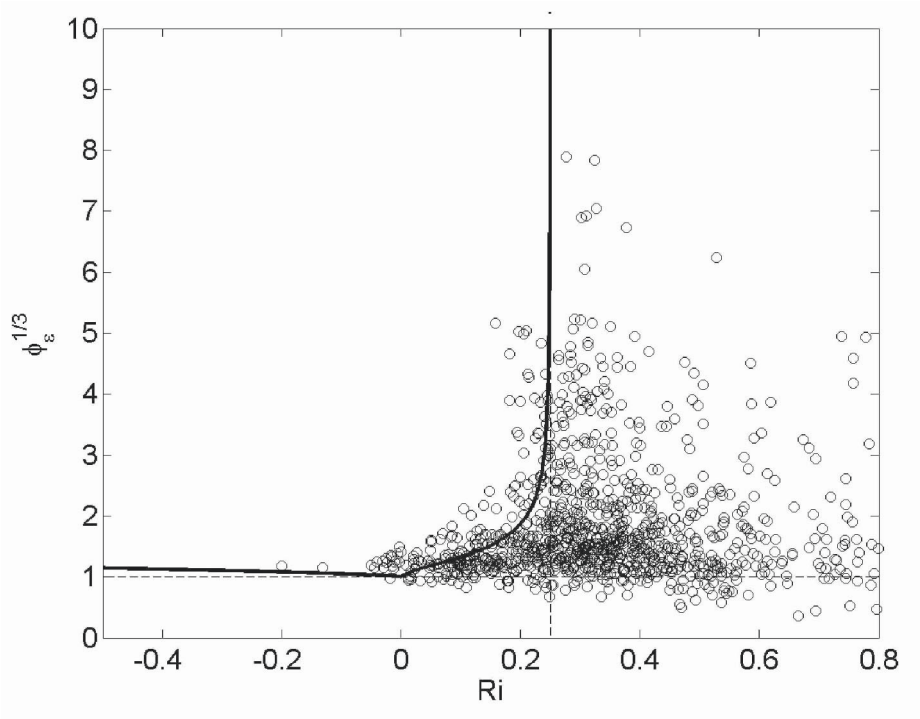


*Figure 3-24*. Dimensionless dissipation rate $\phi_\varepsilon = \varepsilon\kappa|z|/u_*^3$ as a function of *Ri* during *TOGA COARE*. The bold line corresponds to the turbulent boundary layer law. Points are the dissipation rate of turbulent kinetic energy $\varepsilon$ from Moum and Caldwell's (1994) and Smyth et al.'s (1996) turbulence measurements. Friction velocity $u_*$ is calculated from the WHOI mooring meteorology data using the COARE 2.5 bulk flux algorithm (Fairall et al., 1996). The horizontal dashed line corresponds to logarithmic layer dependence. Reproduced from Soloviev et al. (2001) by permission of American Geophysical Union.

In *Figure 3-23*, the shear data for $Ri < Ri_{cr}$ are averaged for overlapping Richardson number intervals, $\Delta Ri = 0.1$. The averaged shear is shown as a function of the averaged Richardson number. For consistency the theoretical boundary layer dependence is also averaged over the same *Ri* number

intervals on this plot. Within the turbulent boundary layer the averaged dissipation rates are consistent with the theoretical boundary layer dependence, demonstrating the striking effect of increased shear at $Ri \sim Ri_{cr} = 0.25$. Some points, however, deviate from the theoretical dependence by more than the 95% confidence interval.

Dimensionless dissipation rates are plotted as a function of the Richardson number in *Figure 3-24*. Measurements made under light winds ($u_* <$ 0.3 cm $s^{-1}$) are excluded. The boundary layer dependence for dissipation rate (bold line) is consistent with data from within the mixed layer (*i.e.*, $Ri < Ri_{cr}$). Outside the mixed layer ($Ri > Ri_{cr}$), the dimensionless dissipation rate data are almost randomly scattered; this can be explained by the fact that the boundary layer scaling is no longer valid outside the turbulent boundary layer. The rate of turbulence dissipation below the surface mixed layer relates to the statistics of internal wave shear rather than to the surface forcing (Peters et al., 1988). To some extent, internal wave breaking events may depend on surface wind stress as well (Thorpe, 1975), which is, however, beyond the scope of this book.

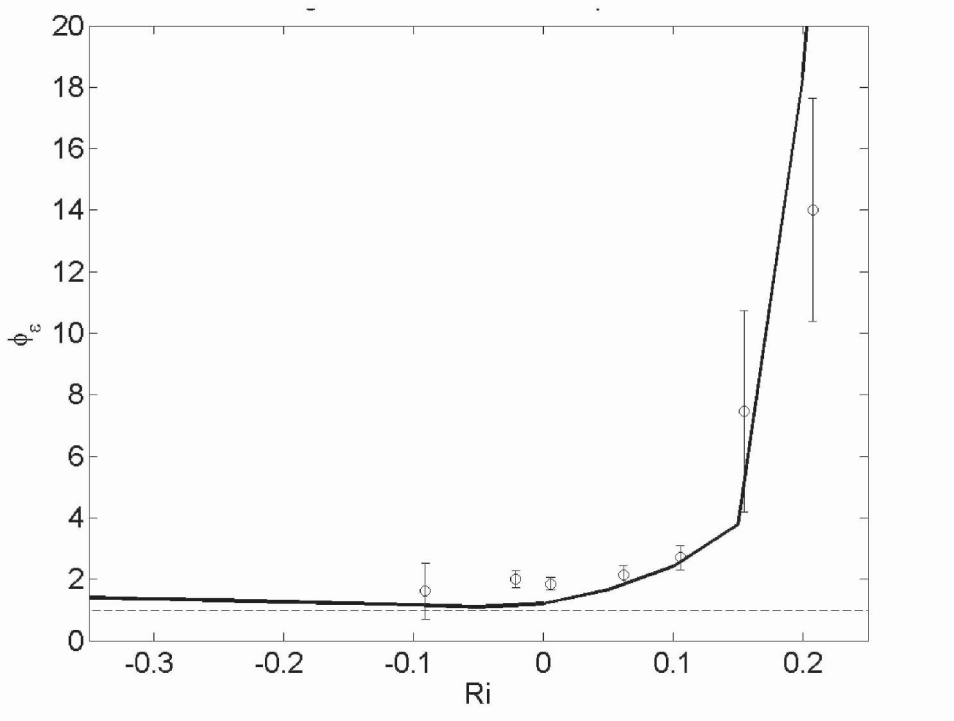


*Figure 3-25*. Dimensionless dissipation rate from *Figure 3-24* averaged within the mixed layer $Ri < 0.25$. Reproduced from Soloviev et al. (2001) by permission of American Geophysical Union.

In *Figure 3-25* the averaged dissipation rate data for $Ri < Ri_{cr}$ are presented as in *Figure 3-23*. The averaged data are consistent with the boundary layer dependence (three points, however, deviate from the theoretical dependence by more than the 95% confidence interval). The maximum dimensionless dissipation rate of TKE near the bottom of the mixed layer $\varepsilon \sim 5 \times 10^2 u_*^3 / (\kappa |z|)$, which substantially exceeds the log layer prediction, $\varepsilon = u_*^3 / (\kappa |z|)$. The strong increase of the dissipation rate as $Ri \to Ri_{cr}$, which corresponds to $\zeta \to \infty$, is in accordance with the Wyngaard et al. (1971) formula (1.154). Note that the increase of $\varepsilon$ at $Ri \sim Ri_{cr}$ is not in contradiction to the decrease of dimensionless mixing coefficient $K_M / (\kappa u_* z)$ predicted by (3.97); this is because $K_M$ also depends on the turbulent mixing scale that rapidly decreases at $Ri \to Ri_{cr}$.

## 3.5 Parameterization of Turbulent Mixing

### 3.5.1 Parameterization of wave-enhanced mixing coefficient

In the framework of the CB94 model, the vertical mixing coefficient due to wave breaking can be calculated from the following relationship:

$$K_M = S_M B^{1/3} \varepsilon^{1/3} l^{4/3} \approx \varepsilon^{1/3} l^{4/3}. \tag{3.99}$$

With the expression for the dissipation of turbulent kinetic energy in the form (3.44), and for the length scale defined by equation (3.33), formula (3.99) is as follows:

$$K_M = \kappa u_* \left( |z| + z_0 \right) \left[ 1 + \sqrt{3} \alpha_w \left( B S_q \right)^{-0.5} z_0{}^n / \left( |z| + z_0 \right)^n \right]^{1/3} . \tag{3.100}$$

Formula (3.100) is shown in *Figure 3-26* for surface roughness $z_0$ parameterized via significant wave height $H_s$ according to (3.47) with $c_0$ = 0.6.

As expected, the main enhancement of the vertical mixing is observed within the layer of approximately one significant wave height depth. Bubbles from breaking waves produce density stratification that may affect the turbulence close to the ocean surface. At this point, however, it is not yet clear how to include this effect into a mixing parameterization.

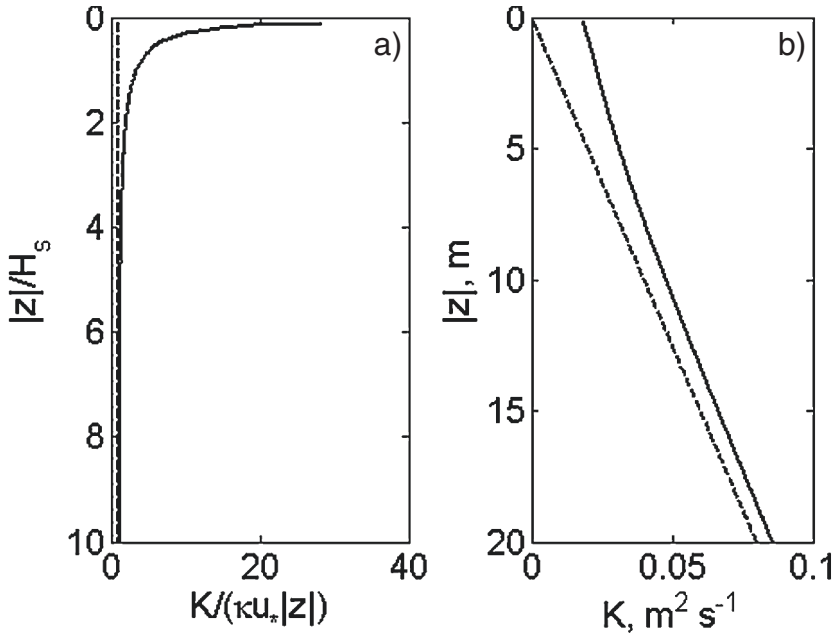


*Figure 3-26*. Vertical mixing coefficient in the wave-enhanced turbulent boundary layer (continuous line) in comparison with the logarithmic layer prediction (dashed line) in (a) nondimensional and (b) dimensional coordinates. In (b), the mixing coefficients are given for $u_* = 0.01$ m s$^{-1}$ and $H_s = 1.6$ m.

Asymptotically, as $z \to -\infty$, (3.100) tends to the log layer mixing parameterization (3.93). Parameterization (3.100), however, does not account for the Langmuir circulations. One possible approach to the parameterization of the Langmuir circulations contribution into vertical mixing is proposed Chapter 5, Section 5.7.2.

### 3.5.2 Richardson-number type mixing parameterization

The vertical variation of the wind-induced momentum flux is a common problem for the non-stationary oceanic (Large et al., 1994) and atmospheric (Tennekes, 1973) boundary layers. To test the constant stress layer hypothesis for the mixed layer in the western Pacific warm pool, Soloviev et al. (2001) examined profiles of the local friction velocity, $u_{*l} = sqrt(\tau_l)$, where $\tau_l$ is the vertical momentum flux magnitude calculated from measurements. The corresponding surface value $u_*$ was calculated from the meteorological observations using the COARE 2.5 bulk flux algorithm (Fairall et al., 1996).

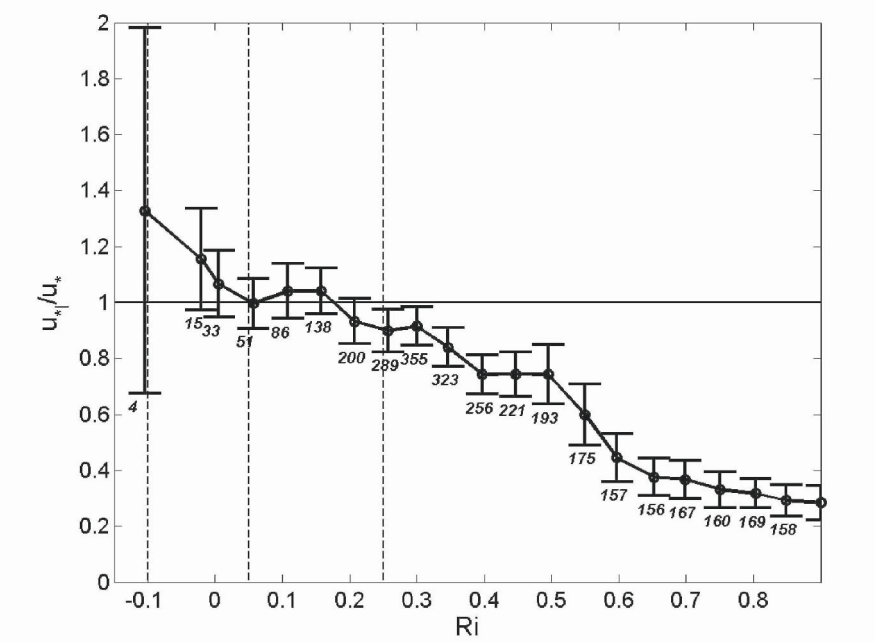


*Figure 3-27*. Test of the constant stress assumption. Friction velocities calculated from the turbulence data (Moum and Caldwell, 1994; Smyth et al., 1996), normalized by surface values $u_*$, are shown as a function of gradient Richardson number *Ri*. Each circle represents the mean for overlapping intervals of $\Delta Ri = 0.1$; the vertical bars cover the 95% confidence intervals, and the numbers below each bar are the number of points averaged. Averaging is done over all profiles (taken every 1 hour) during the R/V *Moana Wave* COARE cruise. *Ri* and $\tau_l$ are calculated using the data from the depth range of 16 to 100 m. Averages over intervals with $Ri < -0.1$ are not shown because there are less than five points falling into these intervals. Reproduced from Soloviev et al. (2001) by permission of American Geophysical Union.

The upper ocean is neither stationary nor horizontally homogeneous. Moreover, the heat and momentum fluxes within the surface turbulent boundary layer may change with depth. The *Ri*-type scheme, however, adjusts to the environmental conditions on the relatively short turbulence timescale, which substantially reduces effects of nonstationarity.

*Figure 3-27* shows the mean profile of $u_{*l}/u_*$ as a function of *Ri*. The number of points within the mixed layer ($Ri < 0.25$) and especially within the logarithmic layer ($-0.1 < Ri < 0.05$) is relatively small. Nevertheless, it is sufficient to provide acceptable confidence intervals because of the substantial volume of the data collected during TOGA COARE. According to *Figure 3-27*, within the stably stratified mixed layer ($0 < Ri < Ri_{cr}$) the maximum deviation of $u_{*l}$ from its surface value $u_*$ is about 30% and can be approximated as follows:

$$u_{*l} \approx u_* \left(1 - 0.7 Ri / Ri_{cr}\right). \tag{3.101}$$

A possible approach to account for the vertical momentum flux change with depth is to parameterize $K_M$ using the profile of local friction velocity rather than its surface value $u_*$. This does not follow directly from the boundary layer theory but was previously employed by several investigators (*e.g.*, Large et al., 1994) including non-equatorial (in fact, polar) conditions (McPhee, 1987).

The mixing parameterization should match to a small but finite turbulence level below the boundary layer because the background mixing levels are non-zero due to internal wave breaking. Comprehensive discussions of the eddy momentum exchange coefficient parameterization below the surface turbulent boundary layer are given in McComas and Muller (1981), Peters et al. (1988), Gregg et al. (1993), Polzin (1996), and Gregg et al. (2003). Peters et al. (1988) approximated the momentum eddy coefficient in the upper shear zone, 23–81 m depth, as follows:

$$K_{Mb} = 5.6 \times 10^{-8} Ri^{-8.2} \ \text{m}^2\,\text{s}^{-1}. \tag{3.102}$$

For the higher $Ri$ range, Peters et al. (1988) obtained the semi-empirical formula

$$K_{Mt} = 5 \times 10^{-4} \left(1 + 5Ri\right)^{-1.5} + 2 \times 10^{-5} \ \text{m}^2\text{s}^{-1}. \tag{3.103}$$

The final parameterization of the eddy viscosity coefficient $K_M$ by Peters et al. (1988) is obtained by adding (3.102) and (3.103):

$$K_M = K_{Mb} + K_{Mt} \tag{3.104}$$

The strong power dependence and unboundedness of (3.102) as $Ri \to 0$ eliminates its practical use within the mixed layer.

In this situation we replace (3.102) with the parameterization of the boundary layer type defined by (3.88). From (1.149), (1.152), (1.155), (1.156), and (3.85) the mixing coefficients for the momentum and a scalar property in the boundary layer can be expressed as follows:

$$K_{Mb} = \begin{cases} \kappa u_* z \left(a_m - c_m Ri\right)^{1/3}, & \text{for } Ri < Ri_m \\ \kappa u_* z \left(1 - \alpha Ri\right)^{1/4}, & \text{for } Ri_m < Ri < 0 \\ \kappa u_* z \left(1 - Ri / Ri_{cr}\right) + K_{m2}, & \text{for } 0 \le Ri < Ri_{cr} \end{cases} \tag{3.105}$$

$$K_{sb} = \begin{cases} \kappa u_* z \left(a_s - c_s Ri\right)^{1/3}, & \text{for } Ri < Ri_s \\ \kappa u_* z \left(1 - \alpha Ri\right)^{1/4}, & \text{for } 0 > Ri \geq Ri_s \\ \kappa u_* z \left(1 - Ri / Ri_{cr}\right), & \text{for } 0 \leq Ri < Ri_{cr} \end{cases} \tag{3.106}$$

where dimensionless constants $Ri_m$ = -0.20, $R_{is}$ = -1.0, $Ri_{cr}$ = 0.25, $\alpha$ = 16, $a_m$ = 1.26, $a_s$ = -28.86, $c_m$ = 8.38, and $c_s$ = 98.96 are derived from atmospheric measurements (see Chapter 1, section 1.7.2).

The first two lines in (3.105) and (3.106) are the boundary layer parameterization for the unstably stratified mixed layer; the third line is the boundary layer parameterization for the stably stratified mixed layer (which is similar to (3.97)).

In order to ensure a smooth transition from the mixed layer to the thermocline, the eddy mixing coefficient for momentum is finally defined as

$$K_M = \max(K_{Mb,} K_{Mt}) \tag{3.107}$$

where $K_{Mb}$ and $K_{Mt}$ are the mixing coefficients for momentum in the mixed layer and thermocline respectively. The mixing coefficient for scalar property $s$ is defined in the similar way:

$$K_s = \max\left(K_{sb}, K_{st}\right), \tag{3.108}$$

where $K_{sb}$ and $K_{st}$ are the mixing coefficients for scalar properties in the mixed layer and thermocline respectively. Furthermore, under the assumption that the turbulent Prandtl number is equal to unity in thermocline,

$$K_{st} = K_{Mt}\,. \tag{3.109}$$

To take into account the free convection above a stratified layer, $u_*$ in (3.105) and (3.106) can be replaced by $\left(u_*^2 + w_*^2\right)^{1/2}$, where $w_*$ is the Priestly (1959) convective velocity scale (3.95).

*Figure 3-28* compares parameterization (3.107) with the mixing coefficient for momentum that is derived from the R/V *Moana Wave* COARE IOP leg 2 turbulence data of Moum and Caldwell (1994) and Smyth et al. (1996). The mixing coefficient in the thermocline $K_{Mt}$ entering (3.107) is parameterized with equation (3.103). The vertical mixing coefficient for momentum is calculated using the "dissipation method" as in Peters et al. (1988):

$$K_M = \overline{\varepsilon} / \left[ \left( \Delta \overline{u} / \Delta z \right)^2 + \left( \Delta \overline{v} / \Delta z \right)^2 \right], \tag{3.110}$$

where $\Delta z$ = 4 m. The Richardson number is calculated from the formula,

$$Ri = g \left( \Delta \overline{\rho} / \Delta z \right) / \left[ \left( \Delta \overline{u} / \Delta z \right)^2 + \left( \Delta \overline{v} / \Delta z \right)^2 \right] \tag{3.111}$$

The hourly 4 m gridded vertical profiles of dissipation rate and velocity were averaged at each depth for 12 hours (with a 6 hour overlap). The original data set contained 550 hourly sampled vertical profiles of dissipation rate and velocity. After the averaging it turned out that a very few points with the magnitude of the velocity difference, $\left[ \left( \Delta \overline{u} \right)^2 + \left( \Delta \overline{v} \right)^2 \right]^{1/2} \le 1.2 \times 10^{-3}$ m s$^{-1}$, produced an enormous scatter in the calculated vertical eddy coefficient and Richardson number compared with the rest of points. These low-shear points (0.99% of the whole data set) were removed. Finally, the experimental points were averaged over overlapping Richardson number intervals, $\Delta Ri$ = 0.1; confidence intervals are calculated using Student's probability distribution. The average at $Ri = -0.2$ is calculated from four points only; it is not shown here because the confidence interval is quite large.

In the mixed layer ($Ri < Ri_{cr}$) parameterization (3.107) is in a good agreement with observational data shown in *Figure 3-28*. (Remember that the mixed-layer portion of the parameterization is mainly represented by equation (3.105).)

In the thermocline ($Ri \ge Ri_{cr}$), the parameterization (3.107) underestimates mixing. For $Ri \ge Ri_{cr}$, coefficient $K_{Mt}$ is of primary importance (although $K_{Mt}$ can also be relevant for $Ri$ slightly below $Ri_{cr}$). Nonlocal transport in the form of internal waves is one possible explanation for the discrepancy. Soloviev and Lukas (1996) reported observations of large amplitude internal waves in the diurnal thermocline and rain-formed halocline (see Chapter 5). Zilitinkevich and Calanca (2000) parameterized the effect of internal waves on the mixing coefficient in the atmospheric boundary layer; a comparable theory for the ocean is now under development (Vladimir Kamenkovich, private communication).

Two other mixing parameterizations, from Peters et al. (1988) and Monin and Yaglom (1971), are also shown in *Figure 3-28*. The parameterization of Peters et al. (1988) is based on the data taken from below the mixed layer, and its comparison with the mixed layer dependence, in particular with the logarithmic layer law, is not suitable. The parameterization taken from Monin and Yaglom (1971) has the correct neutral (logarithmic) layer

asymptote, but it is not valid for unstable stratification and apparently overestimates the mixing coefficient for $Ri > 0.05$.

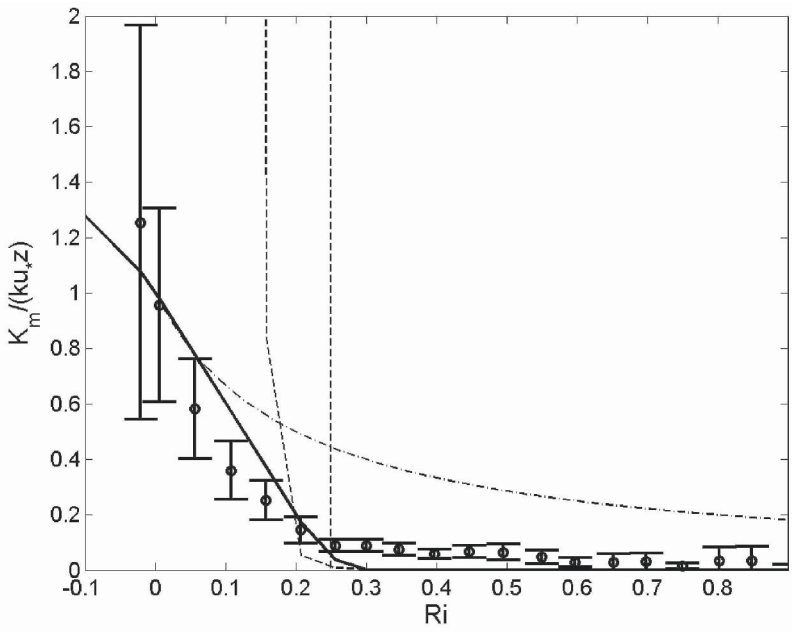


*Figure 3-28*. The vertical eddy coefficient for momentum $K_M$ (normalized by logarithmic layer eddy coefficient $\kappa u_*|z|$) as a function of *Ri*. Open circles are COARE data from the R/*V Moana Wave* (Moum and Caldwell, 1994; Smyth et al., 1996). Each circle represents the mean over *Ri* intervals as in *Figure 3-27*. The solid bold line is parameterization (3.107). The vertical dashed line corresponds to $Ri = Ri_{cr} = 0.25$. The bold dashed line is the parameterization of Peters et al. (1988) calculated for the heat and momentum flux conditions during the R/V *Moana Wave* COARE cruise. The dash-dotted line is the parameterization of Monin and Yaglom (1971). Reproduced from Soloviev et al. (2001) by permission of American Geophysical Union.

The important feature of the parameterizations (3.105) and (3.106) is that they have the correct boundary layer asymptotes for stable, unstable, and neutral stratification. As a result, these new parameterizations are capable of resolving such details of the actively mixed layer as the shear and stratification. Within the mixing layer, these are relatively small but dynamically important factors; they are associated with the vertical transfer of buoyancy and momentum.

Note that that if the mixing coefficient $K_M$ is scaled using the local friction velocity $u_{*l}$ determined from equation (3.101) rather than its surface value $u_*$, parameterization (3.105) is in better agreement with the data. The difference is, however, relatively small (Soloviev et al., 2001).

The scaling used in parameterizations (3.105) and (3.106) is consistent with the idea by Stommel (1960) that the shear within the mixed layer is proportional to the friction velocity. For the vertical eddy viscosity, Ekman (1905, cf. Santiago-Mandujano and Firing, 1990) proposed a parameterization $K_M \sim u_*^2$, which is not consistent with the logarithmic layer asymptote observed for neutral stratification conditions in the mixed layer. The analysis of Santiago-Mandujano and Firing (1990) shows that Ekman's parameterization $K_M \sim u_*^2$ appears as a result of assuming that the mixed layer depth is proportional to the Ekman scale, $L_E = u_* / f$. Ekman's parameterization ignores any dependence of $K_M$ on depth *z*.

The boundary layer parameterizations (3.105) and (3.106) results in $K_M \sim u_*$, which is consistent with the logarithmic layer asymptote $K_M = \kappa u_* |z|$. The parameterization of Large et al. (1994) based on boundary layer scaling also implies that $K_M \sim u_*$.

An important feature of turbulence that has to be taken into account in mixing parameterization schemes is that it is a fundamentally *nonlocal* process (Stull and Kraus, 1987; Large et al., 1994). This is because the turbulent transport is performed via a cascade of eddies. The nonlocal behavior of turbulence is associated with the presence of spatially coherent organized motions. There are numerous observations of coherent structures in the surface layer of the ocean, including Kelvin-Helmholtz billows (Thorpe, 1969), Langmuir cells (Weller and Price, 1988; Thorpe et al., 2003b), convective plumes and ramp-like structures (Thorpe, 1988; Soloviev, 1990), and sharp frontal interfaces (Soloviev and Lukas, 1997b). These structures are considered in detail in Chapter 5.

The *transilient* (Stull and Kraus, 1987) and *large eddy simulation* (LES, Skyllingstad et al., 1999) models involve some nonlocal features. Diffusive models, which are based on the parameterization of turbulent transports by eddy coefficients, are essential local. Systematic incorporation of the coherent structures into subgrid parameterizations is one of the important tasks to be performed for improving mixed-layer models.

### 3.5.3 Rotation effects

On a rotating sphere with no stratification effects, the boundary layer depends on the two components of rotation: $f = 2\Omega \sin\varphi$ and $f_y = 2\Omega \cos\varphi$, where Ω is the magnitude of the Earth's rotation vector and $\varphi$ is the latitude. The Coriolis parameter *f* contributes to the Ekman length scale, $L_E = u_* / f$. An interesting situation is observed at the equator because *f* vanishes; the classic Ekman layer is too deep there to influence strongly the

structure of the upper turbulent boundary layer of the equatorial ocean (*Table 3-2*). However, the Reynolds stress may interact with the horizontal component of Earth's rotation $f_y$ to exchange turbulent kinetic energy between horizontal and vertical components (Garwood and Gallacher, 1985; Garwood et al., 1985), resulting in the length scale $L_G = u_* / \left( f_y \sin\theta \right)$, where $\theta$ is the wind direction.

The effect of horizontal Coriolis acceleration on the turbulent eddies in the equatorial turbulent boundary layer, however, appears to be relatively small (Wang et al., 1996; Soloviev et al., 2001).

### 3.5.4 Boundary-layer horizontal pressure gradients

In the tropical ocean, the surface turbulent boundary layer has some unique features because of its proximity to the equator. As mentioned above, in Ekman's solution for the drift of water in a rotating homogeneous ocean when acted upon by a steady stress applied to the surface, the depth of the spiral and the amplitude of the current increase without limit as the latitude and vertical component of rotation approach zero. Stommel (1960) was first to show that there is actually no singularity at the equator. However, to remove the singularity, a zonal pressure gradient is required. At the equator, such a pressure gradient cannot be balanced by the horizontal Coriolis component but must be balanced by friction or inertial forces (Charney, 1960). The wind stress penetrates into the ocean through the surface mixed layer, and the vertical turbulent viscosity provides the principle balance for the zonal pressure gradient driving the Equatorial Undercurrent (McCreary, 1981).

Later, Lukas and Firing (1984) found evidence of geostrophic balance of the Equatorial Undercurrent, which provides an alternative perspective compared to the result of Charney (1960). The zonal pressure gradient and the vertical turbulent viscosity were nevertheless still principle components of the momentum balance at the equator.

It is known from hydraulics engineering that the longitudinal pressure gradient can influence the structure of the turbulent boundary layer (White, 1986). Following Yaglom (1979), one can construct the so-called pressure gradient length scale, $L_p = \rho u_*^2 / \partial p / \partial x$. $L_p$ may be derived from the momentum equations under the assumption that the horizontal pressure gradient is approximately balanced by vertical mixing. Veronis (1960) related a similar scale to the depth of the Equatorial Undercurrent.

Typical estimates of $L_p$ are given in *Table 3-2*. This horizontal pressure gradient length scale exceeds all of the other mixed layer length scales. This estimate suggests that the horizontal pressure gradient is not a major factor in determining the vertical structure of the ocean mixed layer. It may

nevertheless play an important role in the dynamics of sharp frontal interfaces to be considered in Chapter 5.

*Table 3-2*. Order of magnitude estimate of buoyancy ($D_B$), rotation ($D_E$ and $L_G$), pressure-gradient ($L_P$) length scales for different surface stress values[a].

| $u_*$ , cm s$^{-1}$ | $D_B$,, m | $L_P$, m | $D_E$, m | $L_G$, m |
|---|---|---|---|---|
| 0.1 | $0.1_b$ | 20 | 50 | 14 |
| 0.5 | $12.5_b$ | 100 | 250 | 69 |
| 1.0 | $100_b$ | 200 | 500 | 137 |
| 2.0 | 800 | 800 | 1000 | 274[b] |

[a] According to Kraus and Businger (1994), the depth of the mixed layer is $D_E \approx 0.25 L_E$ in the case of no stratification. Buoyancy forces apparently dominate over Coriolis forces, when $D_B << D_E$.

[b] Minimum values of the length scale

Chapter 4

# FINE STRUCTURE AND MICROSTRUCTURE

*Under light winds or heavy rainfall, upper ocean turbulence interacts strongly with stratification and large vertical gradients can develop in the upper few meters of the ocean.*

In the oceanographic literature, the term *fine structure* is traditionally reserved for inhomogeneities relating to stratification, while the term, *microstructure* has often been applied to inhomogeneities associated with small-scale turbulence (Gregg, 1975).

Air-sea momentum, heat, and freshwater fluxes are crucial factors determining the thermohaline structure of the near-surface layer of the ocean. Under moderate-to-high wind speed conditions, the upper ocean is usually well mixed due to strong turbulence. When the wind drops below about 5 m $s^{-1}$, and with solar warming, the turbulent regime dramatically changes. The stabilizing buoyancy flux suppresses turbulent mixing and the air-sea exchange is effectively trapped within a thin near-surface layer. Under these conditions, the diurnal thermocline can be found close to the ocean surface contributing to the fine structure and microstructure of the near-surface layer.

In addition to solar heating, the freshwater cycle may substantially modify the structure, dynamics, and thermodynamics of the near-surface layer of the ocean. The main components of the hydrologic cycle in the ocean are precipitation, evaporation, river discharge, and sea ice melting/formation.

Precipitation effects are pronounced in low latitudes, especially within intertropical convergence zones, warm pools, and monsoon regions. Lateral advection of freshwater may contribute to the fine structure of the near-

surface layer of the ocean in the coastal areas with river run-off, in the marginal ice zones, and in regions of strong mesoscale convection.

## 4.1 Near-Surface Thermohaline Structures

### 4.1.1 Diurnal mixed layer and diurnal thermocline

A fundamental mode of upper ocean variability is the diurnal cycle, which is forced by the diurnal cycle of solar irradiance. As a result of this forcing, a diurnal mixed layer and diurnal thermocline can develop near the ocean surface. Following Fedorov and Ginzburg (1988), three main types of vertical temperature structures are associated with this process as schematically illustrated in *Figure 4-1*.

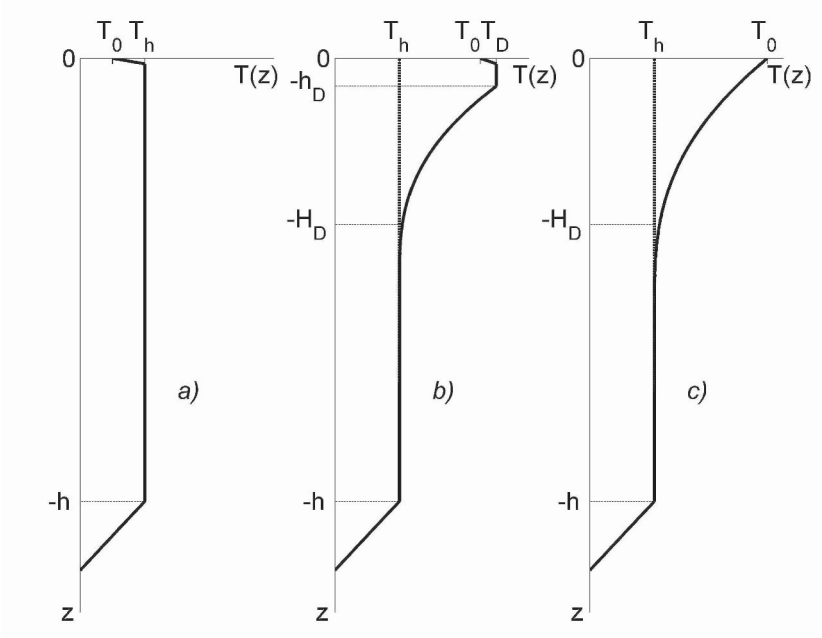


*Figure 4-1*. Typical vertical thermal structures of the upper ocean associated with the diurnal cycle: (a) Nighttime well-mixed layer; (b) Diurnal mixed layer and diurnal thermocline develop in the top of the mixed layer; (c) Diurnal mixed layer is stratified or does not exist. Here: $h$ is the depth of the upper ocean mixed layer, $H_D$ is the depth of the bottom boundary of diurnal thermocline (which can often, but not always, be considered as the lower boundary of the near-surface layer of the ocean, $h_D$ is the diurnal mixed layer depth; $T_h$ is the bulk temperature of the upper ocean mixed layer, $T_D$ is the bulk temperature of the diurnal mixed layer, and $T_0$ is the sea surface temperature.

Wind-wave mixing and/or nighttime convection produce a well-mixed layer (*Figure 4-1*a). This is the surface mixed layer of the ocean, which is

also referred to as the seasonal mixed layer wherever the climate has seasons.

During daytime, a warmer diurnal mixed layer and a diurnal thermocline form on the background of the mixed layer (*Figure 4-1b*), due to the absorption of solar radiation in the upper ocean. From Chapter 1 the reader knows that solar forcing $I_R(z)$ is a volume source of heat and strictly speaking should not be considered as a surface flux. The surface flux consists of latent ($Q_E$) and sensible ($Q_T$) heat fluxes and the net longwave radiation ($I_L$). Wind-wave mixing and convection produce a diurnal mixed layer. The diurnal mixed layer is clearly pronounced (as in the sketch shown in *Figure 4-1b*) when $Q_0$, the sum of $Q_E$, $Q_T$, and $I_L$, is positive (*i.e.*, net surface cooling takes place) and its magnitude is not too small compared to the solar heating.

For $Q_0 < 0$ (for example, in cases when air is warmer than water and relative humidity is close to 100%), the diurnal mixed layer can hardly be seen in temperature profiles (*Figure 4-1*c) but may still be resolved from turbulence or gradient Richardson number profiles. Similar temperature profiles can be observed under calm weather conditions during peak insolation. In this case, the sea surface can lose heat to the atmosphere ($Q_0 > 0$) but the volume source of heat (absorption of solar radiation) is so strong that convective mixing ceases, and there is no surface mixed layer (Soloviev and Lukas, 1997a).

Freshwater cycling may affect the ocean diurnal cycle in two ways: 1) Evaporation from the sea surface or ice formation results in increased surface salinity that adds to the convection due to surface cooling; 2) Precipitation, river discharge, or sea ice melting inhibits convection. These effects are considered elsewhere in this chapter (as well as in Chapter 2 in relation to the sea surface microlayer).

The structure of the diurnal mixed layer and diurnal thermocline depends on atmospheric forcing (wind speed, solar radiation, rain, heat fluxes), which is generally spatially inhomogeneous. The internal processes associated with pressure gradient equilibration and mass redistribution in the upper ocean are often quasi-two-dimensional and may exhibit features of organization. As a result, the diurnal thermocline can reveal spatial patterns in the form of nonlinear internal waves, billows, fronts, etc. Examples of the vertical and horizontal structure of the diurnal thermocline are given in the next section. Spatially coherent organized structures in the near-surface layer of the ocean are considered in Chapter 5.

### 4.1.2 Examples of near-surface structures associated with diurnal cycle

*Figure 4-2* illustrates the vertical structure of the turbulent boundary layer in the near-surface North Atlantic Ocean under strong, moderate and low wind speed conditions during afternoon hours when it was not raining. Pertinent information about these measurements is given in *Table 4-1*.

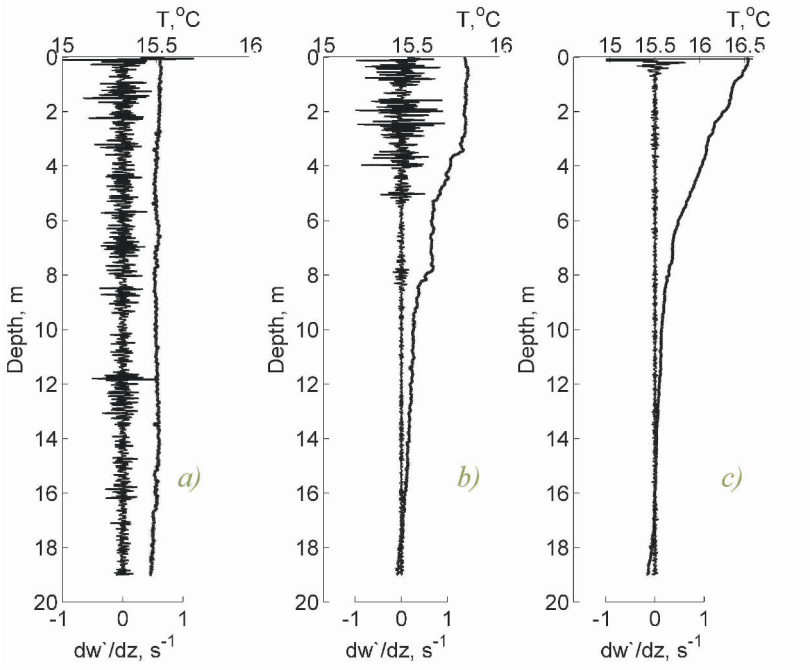


*Figure 4-2.* Examples of temperature *T* and strain fluctuation *dw'/dz* profiles under different wind conditions: (a) strong wind ($U_{18} = 8.3$ m s$^{-1}$), (b) moderate wind ($U_{18} = 6.2$ m s$^{-1}$), and (c) Low wind ($U_{18} = 3.3$ m s$^{-1}$) as observed in the North Atlantic during *GasEx-1998* with a free-rising profiler by Soloviev *et al.* (2001b). $U_{18}$ is the wind speed at 18 m height (shipboard observations). The vertical profile of *dw'/dz* is an indicator of the turbulent mixing processes.

The example shown in *Figure 4-2*a corresponds to 8.3 m s$^{-1}$ wind speed. As observed from the turbulent fluctuation velocity and temperature profiles, the upper 20 m layer of the ocean is well mixed, and there is no significant vertical stratification due to diurnal warming in this layer.

In the second example (*Figure 4-2*b), obtained at a moderate wind speed (6.2 m s$^{-1}$), there is a diurnal mixed layer and diurnal thermocline in the upper 8 meters of the ocean. The turbulent velocity fluctuations are intense within the upper 5 m. The turbulent area near 8 m presumably represents a

sporadic mixing event possibly driven by shear. Below 8 m, turbulence levels are close to the noise level of the sensor.

The third example (*Figure 4-2*c) represents low wind speed conditions. There is a diurnal thermocline near the surface. While the diurnal mixed layer is not clearly seen in the temperature profile, intense velocity fluctuations in the upper 0.5 m indicate the presence of mixing.

*Table 4-1.* Pertinent information for the example profiles shown in *Figure 4-2*. Here: $U_{18}$ is the wind speed at 18 m above the sea surface, $u_*$ is the friction velocity in the upper ocean, $I_\Sigma$ is the insolation (surface solar irradiance), $Q_0$ is the sum of latent $Q_E$ and sensible $Q_T$ heat fluxes and net longwave irradiance $I_L$.

| *Fig. 4-2* | Coordinates lat, lon | Date, 1998 | Time LT | $U_{18}$ $ms^{-1}$ | $u_*$ $ms^{-1}$ | $I_\Sigma$ $Wm^{-2}$ | $Q_0$ $Wm^{-2}$ |
|---|---|---|---|---|---|---|---|
| a) | 46°07'N, 20°25'W | 13 Jun | 14:41 | 8.3 | 0.0093 | 472 | 42 |
| b) | 46°03'N, 20°44'W | 5 Jun | 14:26 | 6.2 | 0.0068 | 645 | 103 |
| c) | 46°02'N, 20°54'W | 6 Jun | 15:51 | 3.3 | 0.0036 | 582 | 100 |

*Figure 4-3* shows three series of vertical temperature profiles obtained under different wind speeds in the equatorial Pacific on different days but during approximately the same afternoon time period. The series of 9 profiles shown in *Figure 4-3a* was obtained under relatively strong winds (~7 m $s^{-1}$) and clouds of medium altitude (cloud fraction 6/8). The depth of the diurnal mixed layer varied from 12 to 17 m and the maximum temperature increase in the upper 18 m was about 0.2°C.

The series of 10 temperature profiles shown in *Figure 4-3*b was obtained under light winds (~2 m $s^{-1}$) with midlevel clouds (cloud fraction 2/8), revealing a more substantial diurnal warming of the near-surface layer. The temperature difference across the diurnal thermocline was between 0.6°C and 0.8°C. The diurnal mixed layer depth varied from 1 to 7 m. The strong variations of the mixed layer depth as well as the depth and thickness of the diurnal thermocline were presumably caused by internal waves in the diurnal thermocline. The diurnal thermocline appears to be of almost constant thickness but of variable depth, changing from one cast to another.

The series of 5 temperature profiles (*Figure 4-3c*) obtained under calm weather conditions and high clouds (cloud fraction 2/8) shows that the diurnal heating is mainly localized in the upper meter. The temperature difference across the diurnal thermocline is larger than 3°C, with the sea surface temperature reaching 33.25°C. Based on cloud information, we can conclude that for the example shown in *Figure 4-3*c the shortwave solar

forcing was larger than for examples *a* and *b* which contributed to the large diurnal warming of the near-surface layer.

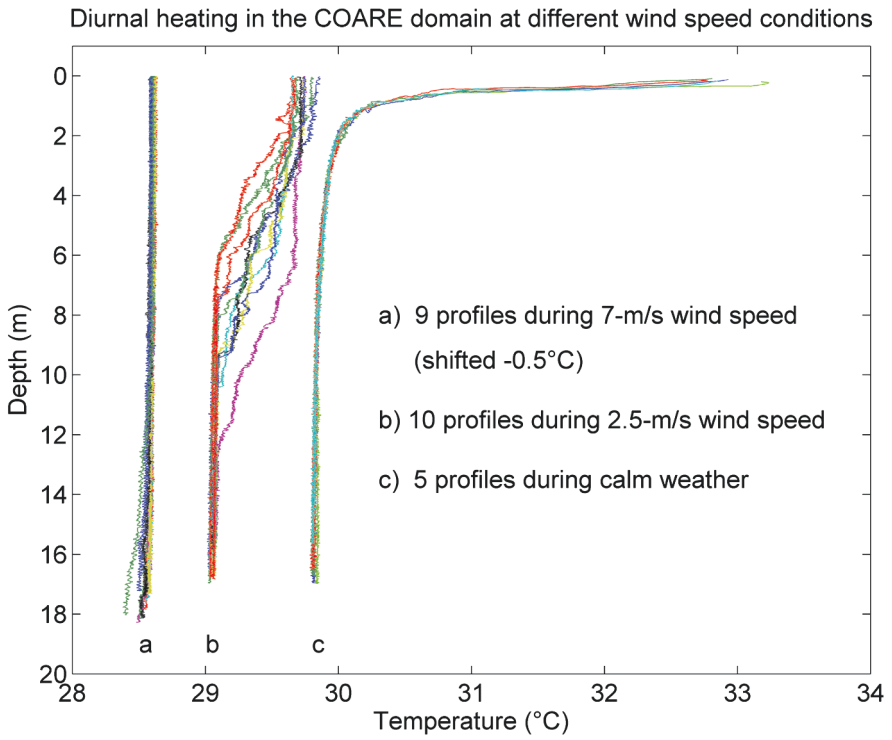


*Figure 4-3.* Vertical temperature profiles in the western equatorial Pacific obtained by a free-rising profiler during different wind speed conditions taken at approximately the same afternoon time on different days. Reproduced from Soloviev and Lukas (1997) with permission of Elsevier.

Examples from diverse climatic zones presented in this section and elsewhere in this chapter, from the equatorial Pacific (0°N) to the North Atlantic (59°N), demonstrate that a common feature of the upper ocean diurnal cycle is its strong dependence on the local wind speed. As we also know from Chapter 3, under light winds and strong insolation the turbulent regime in the upper ocean dramatically changes. Consequently, the diurnal thermocline is found very close to the ocean surface; the amplitude of the diurnal warming sometimes reaches a few °C.

### 4.1.3 Wave-like disturbances in the diurnal thermocline

Under certain conditions the diurnal thermocline can exhibit structures resembling large-amplitude internal waves. The contour plot of temperature

(*Figure 4-4*a) from measurements by bow sensors made on 26 April 1994, just before profiling shown in *Figure 4-3*b, reveals wave-like disturbances of the diurnal thermocline of ~200 m wavelength with amplitude > 1 m. Because of surface waves and pitching of the vessel, the bow probes profiled portions of the upper 4 m. This method, described in more detail in Chapter 3, provides an opportunity to study both vertical and horizontal structure of the near-surface layer of the ocean.

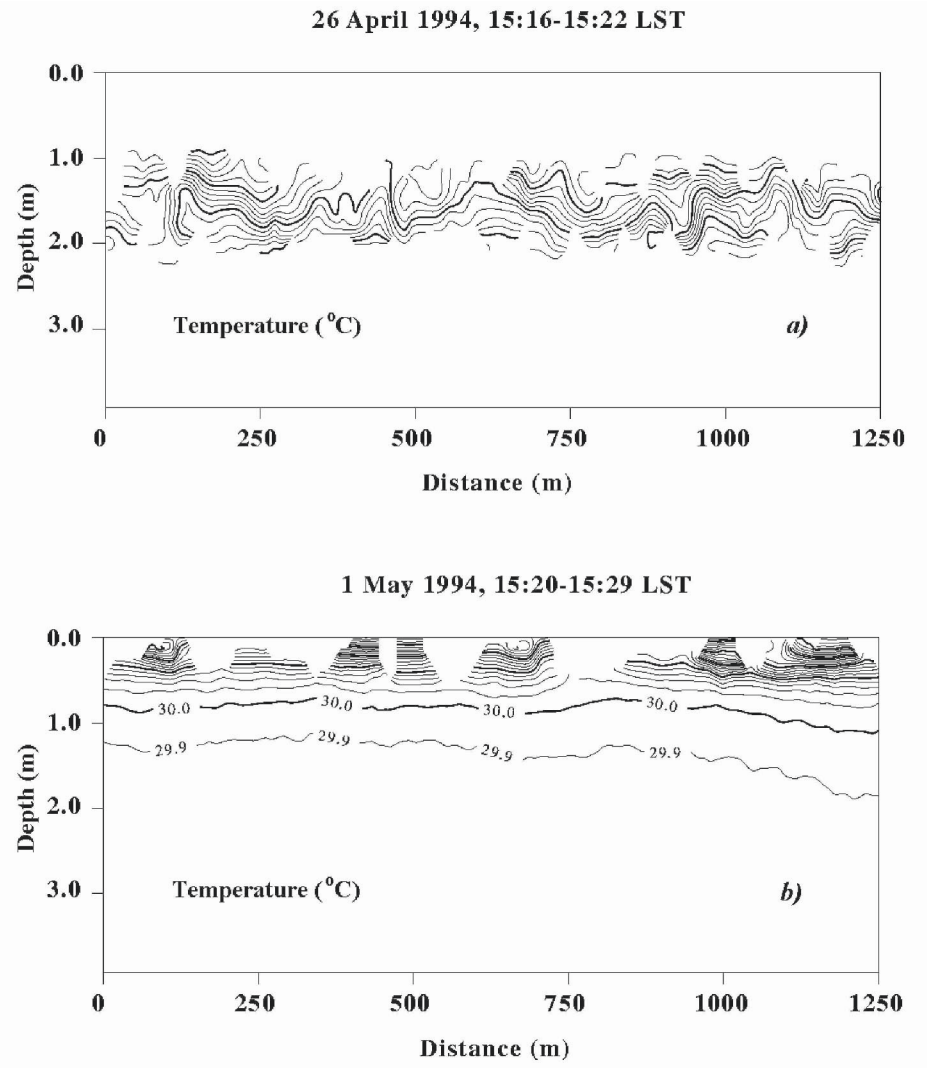


*Figure 4-4.* Contour plots of temperature in the coordinate system connected to the instantaneous position of the ocean surface. Measurements by bow sensors on (a) 26 April and on (b) 1 May 1994. Adapted from Soloviev and Lukas (1997) with permission of American Meteorological Society.

The contour plot of temperature from the bow record on 1 May 1994, just after the measurements of *Figure 4-3c,* is shown in *Figure 4-4b*. It is much more "quiet" than that in *Figure 4-4a*.

Other sources of the horizontal variability in the diurnal thermocline include spatially coherent organized motions, which are considered in Chapter 5.

### 4.1.4 Rain-formed mixed layer and halocline

In addition to the diurnal cycle, near-surface freshening due to rain is another fundamental mode of upper ocean variability. A rain-formed mixed layer and halocline can be formed in the upper ocean mixed layer. Three main types of vertical salinity structures associated with this process are schematically illustrated in *Figure 4-5*. This sketch implies conditions of no thermal stratification in the upper ocean.

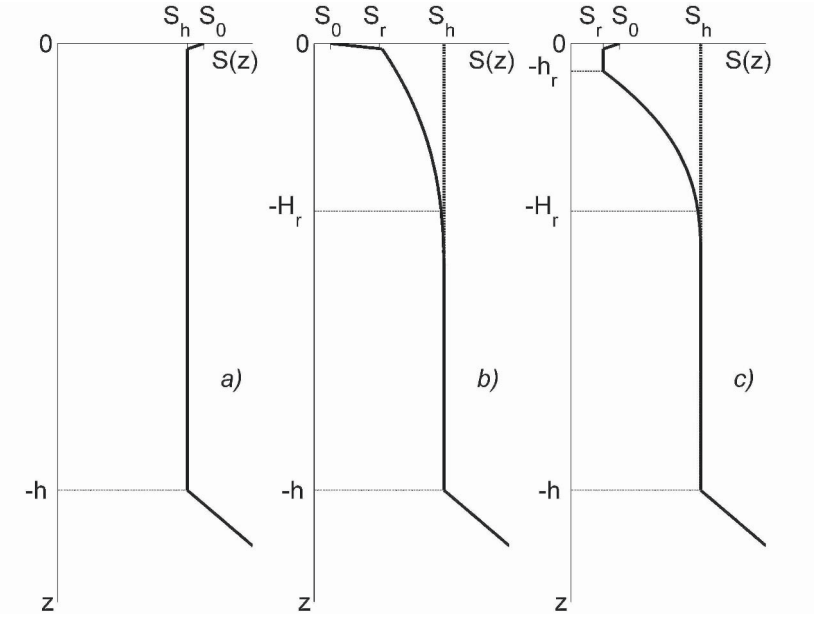


*Figure 4-5*. Typical vertical haline structures of the upper ocean layer associated with rainfall events compared with a well mixed layer (a) under no rain conditions. Under rainy conditions (b) a halocline develops at the top of the mixed layer; the rain-formed mixed layer may not be clearly seen in the vertical salinity profile. A rain-formed mixed layer and halocline after the end of rain is schematically shown in (c). Here, $h$ is the depth of the mixed layer, $H_r$ is the depth of the bottom boundary of rain-formed halocline (which can often, but not always, be considered as the lower boundary of the near-surface layer of the ocean, $h_r$ is the rain-formed mixed layer depth; $S_h$ is the bulk salinity of the mixed layer, $S_r$ is the bulk salinity of the rain-formed mixed layer, and $S_0$ is the sea surface salinity.

Wind-wave mixing and/or nighttime convection produce a well-mixed layer (*Figure 4-5*a). With no rain, salinity in the molecular diffusion sublayer just below the sea surface is slightly increased due to evaporation.

The rain forcing consists of a volume flux and a surface flux of freshwater (Section 1.5). When rain starts, the kinetic energy of raindrops, as well as the associated buoyancy flux, contributes to the turbulent kinetic energy balance in the near-surface layer. The rain-formed mixed layer may not be clearly seen in the vertical salinity profile (as in the sketch shown in *Figure 4-5*b) during strong rain. However, when the rain ceases, the rain-formed mixed layer is usually well defined from the vertical salinity profile (as schematically shown in *Figure 4-5*c).

Rains are often intermittent in time and space. As a result, the rain-formed halocline usually varies spatially. Examples of the vertical and horizontal structure of the rain-formed halocline are given in the next section.

### 4.1.5 Low salinity patches due to convective rains

Convective rains produce low salinity patches in the upper ocean. Measurements with bow sensors across such a patch (associated with strong rain event) are shown in *Figure 4-6*. Averaged vertical profiles of temperature ($T$), salinity ($S$) and density ($\sigma_t$) are shown in *Figure 4-7*. They are calculated by sorting the data in pressure (P) and averaging over the 10 minutes intervals, indicated on the time axis of *Figure 4-6* by heavy line segments. Segments marked by rectangles in *Figure 4-6* are shown in *Figure 4-8* in more detail.

This low salinity patch is also traced in the temperature record because the temperature of the raindrops is lower than the SST (Gosnell et al., 1996). High frequency fluctuations of $T$, $S$, and $\sigma_t$ primarily result from depth variations of the probes.

*Figure 4-8* gives a more detailed picture of the core of the rain patch (the $T$, $S$, and $\sigma_t$ records for the corresponding segment in *Figure 4-6* are marked by rectangles). The contour plot of $\sigma_t$ versus depth (*Figure 4-8*d) reveals disturbances that look like internal waves with apparent wavelengths of ~200 m or more. The true wavelengths cannot be estimated from these measurements because the ship‘s motion relative to the internal wave propagation is unknown.

Averaged vertical profiles of $T$, $S$, and $\sigma_t$ at 6:49LT (*Figure 4-7*) just before entering the rain zone show a well-mixed layer within the depth range of the bow probes. The wind speed was 7.8 m $s^{-1}$ and there were no signatures of diurnal heating or previous rain events in the upper 4 m of the ocean.

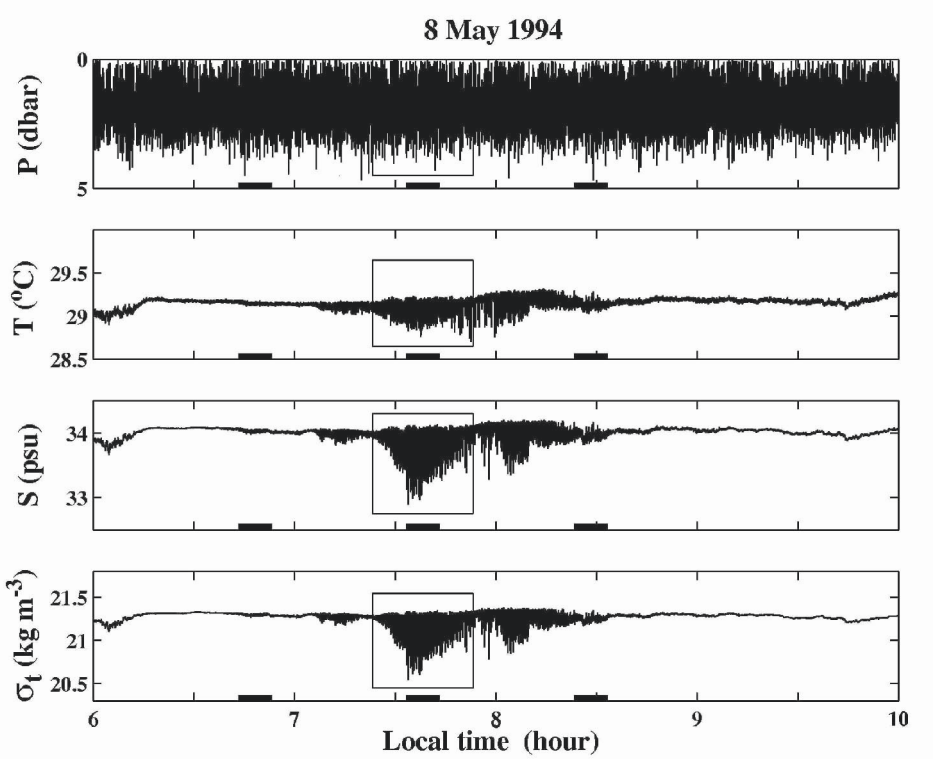


*Figure 4-6*. Example of records made by bow sensors in the western Pacific warm pool during a strong rain event while steaming at 10-11 knots. (Note that 1 dbar = 0.98 m.) Segments marked by rectangles are shown in more detail in *Figure 4-8*. Solid segments on the time axis correspond to 10 min averaging intervals for calculation of vertical profiles of $T$, $S$ and $\sigma_t$ shown in *Figure 4-7*. Reproduced from Soloviev and Lukas (1996) by permission of American Meteorological Society.

The vertical profiles at 7:39LT corresponding to the core of the freshwater patch showed a near-surface halocline with salinity difference $\Delta S$ ~ 1 psu localized in the upper ~2 m and accompanied by a temperature inversion of $\Delta T$~0.3°C. The $\sigma_t$ vertical profile at 7:39LT revealed a stably stratified layer of ~2 m depth; the turbulent mixing in the near-surface layer of the ocean was not sufficient to mix this near-surface stratified layer. (The wind speed fluctuated strongly both in magnitude (3.2 m $s^{-1}$ - 6.9 m $s^{-1}$) and in direction (230°-360°) because of squalls accompanying the rain event.)

The vertical profiles at 8:29LT (*Figure 4-7*) correspond to the end of the rain zone (*Figure 4-6*). Stratification in the upper 4 m of the ocean is much reduced in comparison with the core of the patch. Wind speed increased up to 10-12 m $s^{-1}$ and its direction became more stable (250°-280°).

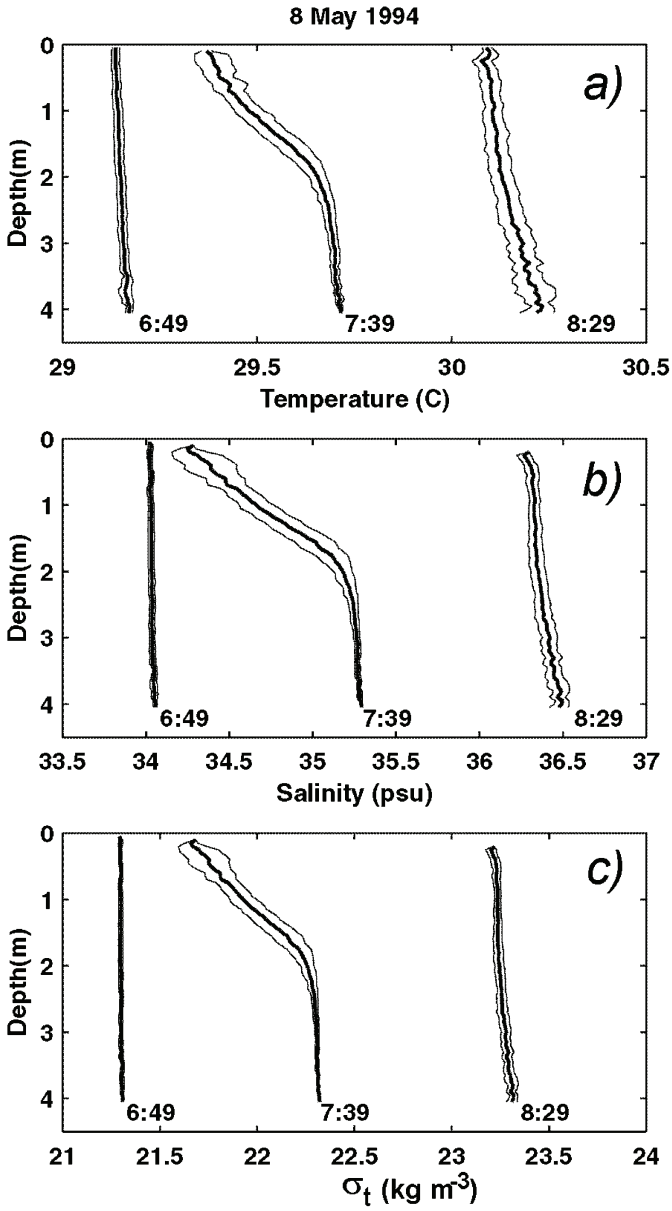


*Figure 4-7.* Vertical profiles of (a) temperature, (b) salinity, and (c) density obtained by averaging 10 minute intervals of bow sensor data within 0.1 dbar pressure bins. Each successive profile is shifted by $0.5P^{oP}C$ in temperature, by 1.2 psu in salinity and 1.0 kg $mP^{-3P}$ in $\sigma B_{tB}$ density in subplots (a), (b), and (c), respectively. The local time below each profile corresponds to the middle of the 10 minute segment. Thin lines represent one standard deviation. Adapted from Soloviev and Lukas (1996) by permission of American Meteorological Society.

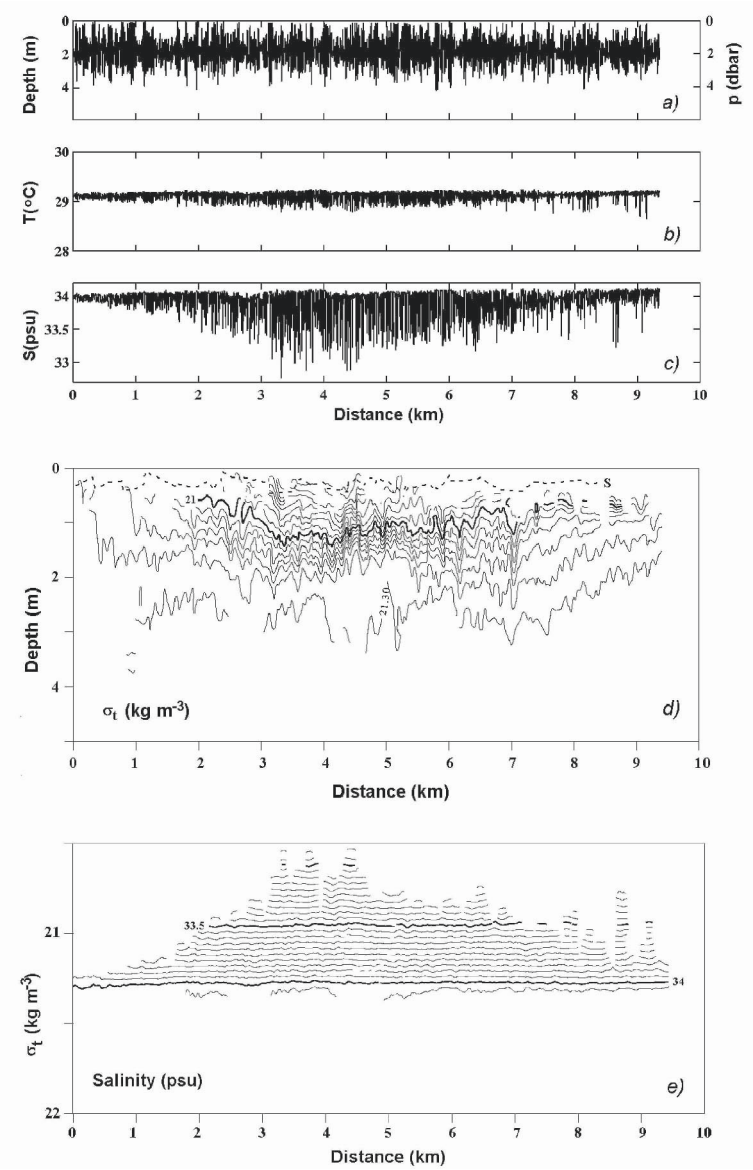


*Figure 4-8*. Intersection of a shallow fresh water patch near 4.43°N, 137.01°E during COARE cruise EQ-3. The upper part of the figure shows records of (a) depth (pressure), (b) temperature, and (c) salinity. The lower part shows (d) the corresponding contour plots of $\sigma_t$ versus depth and (e) *S* versus $\sigma_t$. The dashed line (*S*) in the contour plot $\sigma_t$ -*T* corresponds to the air-sea interface as indicated by the conductivity sensor using criteria *C* = 4.6 S/m, where *C* is the water conductivity. Wind speed is 3.3 m $s^{-1}$ - 6.9 m $s^{-1}$ (rain squalls), direction 338-353°; ship speed is 5.2 m $s^{-1}$, direction 1°; height of swell waves observed from the bridge ~2.5 m, direction ~30°. Adapted from Soloviev and Lukas (1996) by permission of American Meteorological Society.

The dashed line $S$ in the $\sigma_t$ – depth contour plot (*Figure 4-8*d) corresponds to the R.M.S. uncertainty of pressure-to-depth conversion (the hydrostatic pressure bias has already been removed) at occasional intersections of the water-air interface as detected by the conductivity cell. It illustrates the uncertainty of pressure-to-depth conversion due to the dynamic pressure component and the ~0.6 m horizontal spacing between the $C$, $T$ and $P$ sensors. The R.M.S. uncertainty in the pressure-to-depth conversion is estimated as being between 0.02 dbar and 0.1 dbar (Soloviev and Lukas, 1996).

The contour plot of salinity in density coordinates (*Figure 4-8*e) shows practically no anomalies. This supports the wavelike nature of the disturbances observed on the $\sigma_t$ – depth contour plot on the horizontal scales resolved by this contour plot ($l$ >100 m).

### 4.1.6 Combined effect of diurnal and freshwater cycles on the upper ocean structure

The schematics of the diurnal thermocline in *Figure 4-1* do not include cases with precipitation effects. Rainfalls produce near-surface salinity stratification, which helps to trap the net solar heating during daytime and cooling during nighttime in the near surface layer of the ocean, thus enhancing the diurnal SST amplitude.

The freshwater cycle may thus modify diurnal heating of the near-surface layer of the ocean. Buoyancy fluxes due to precipitation increase the static stability of the upper ocean, suppressing turbulent exchange with deeper waters. The rainfall influences the diurnal cycle by trapping heat near the surface (Anderson et al., 1996). An example is given in *Figure 4-9*. The salinity profile shows a salinity depression within the upper 5 m due to a previous rain. Turbulent mixing is mainly localized within this stably stratified near-surface layer (note larger velocity strain fluctuations $dw'/dz$ in the upper 5 m). Subsequent diurnal warming develops within this freshwater lens.

*Figure 4-10* gives additional experimental evidence of a strong modification of the near-surface layer due to rain. It helps to understand how the combined effect of daytime solar heating and previous freshwater influx due to rain results in the strong density stratification of the upper ocean. In the case shown in *Figure 4-10*, the diurnal mixed layer and diurnal thermocline evolve on the background of the temperature structure within the rain-formed mixed layer. According to *Figure 4-10* the temperature of the rain-formed mixed layer is lower than that of the underlying water mass. This is typical for a rain-formed mixed layer after previous nighttime surface cooling (Fedorov and Ginzburg, 1988; Lukas, 1990b). The profiles shown in

*Figure 4-10* are taken during the early evening and show a gradual deepening of the diurnal mixed layer.

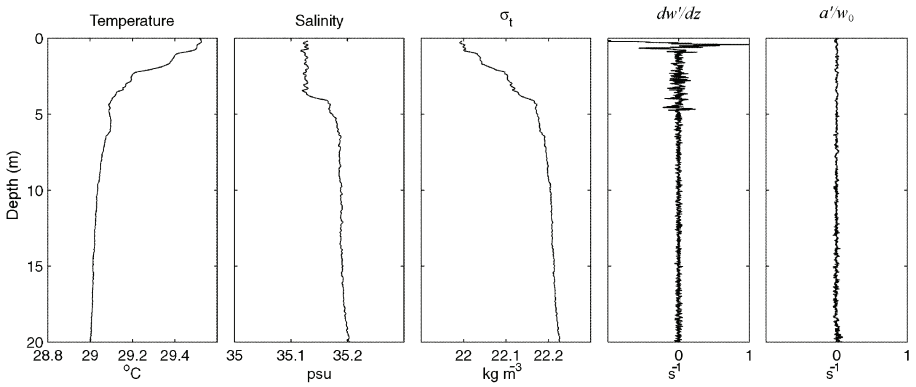


*Figure 4-9.* Temperature, salinity, sigma-t density, and turbulent velocity (strain) fluctuation profiles in the upper 20 m of the ocean as measured with a free-rising profiler within a shallow freshwater lens in the western equatorial Pacific (15 April 1994, 04:29 GMT, 1°58'N, 165° E) under light winds (2.1-3.7 m $s^{-1}$). Note the larger velocity strain fluctuations ( $dw'/dz$ ) within the upper 4.5 m. Acceleration fluctuations of the profiler ( $a'$ ) are scaled in such a way ( $a'/w_0$ ) that they are comparable with and are in fact much less than $dw'/dz$ , where $w_0$ is the nominal vertical velocity of the profiler. Vertical velocity $w'$ and acceleration $a'$ signals are high-passed with a 4 Hz cut-off frequency and low-passed with a 40 Hz cut-off frequency. Adapted from Soloviev et al. (1999) by permission of American Meteorological Society.

Double-diffusion effects may also contribute to mixing in the stably stratified near-surface layer. (See the description of the phenomena of salt fingers and layering convection, for instance, in Turner, 1973.)

Conditions leading to salt fingers can occur in the diurnal thermocline because excess salinity due to evaporation accumulates within the diurnal mixed layer. There is a slight but systematic increase of salinity within the diurnal mixed layer and diurnal thermocline in the profiles of *Figure 4-10*. The increase of salinity of about 0.01-0.02 psu within the layer of diurnal heating is also clearly seen in *Figure 4-23* (except at 19:00 LST because of rain). The corresponding density profiles are stable excluding the diurnal mixed layer where some inversions are associated with convective cooling and excess salinity. Remember that due to volume absorption of solar radiation in the upper ocean convective cooling may exist even during the daytime. Evaporation usually increases the destabilizing buoyancy flux on the order of 10%. The step-like structure after strong rain, presumably connected to layering convection, is shown in *Figure 4-11*.

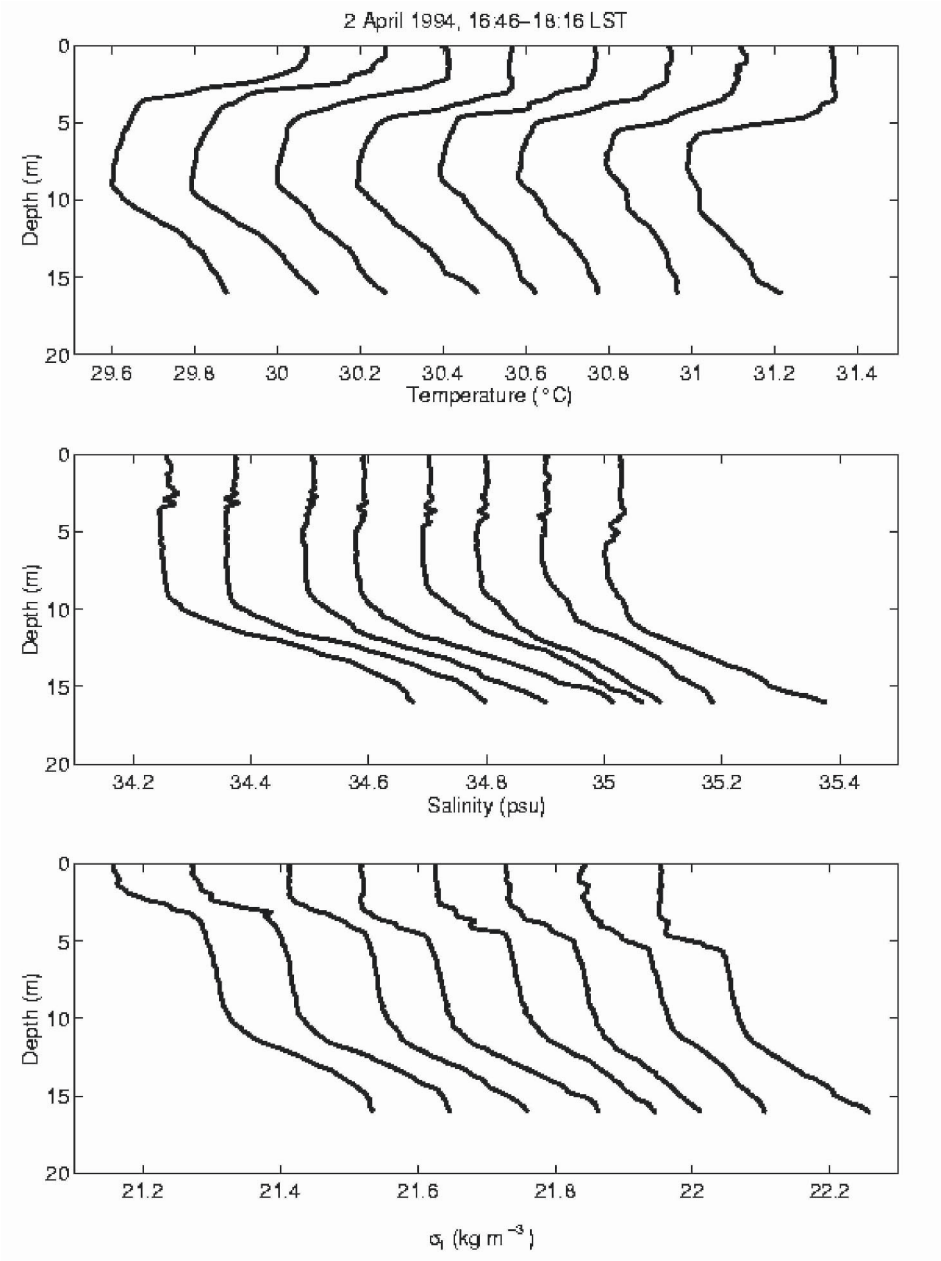


*Figure 4-10.* Vertical temperature, salinity and density profiles obtained by a free-rising profiler. Each successive profile is shifted by 0.2°C for temperature, by 0.1 psu for salinity and by 0.1 kg m$^{-3}$ for density. Reproduced from Kudrayvtsev and Soloviev (1990) with permission of American Meteorological Society.

*Figure 4-11* shows the temperature and salinity microstructure of the upper ocean after rainfall. These observations were made in the Inter-

Tropical Convergence Zone (ITCZ) where the hydrologic cycle is a crucial factor in upper ocean dynamics. Near-surface layers with distinctly lower salinity are formed, which suppress the turbulent exchange with the deeper water. Intense solar heating often alternates with heavy rains. A fraction of the solar energy is effectively trapped in the near-surface layer of the ocean, which in combination with the rain forcing results in complicated vertical stratification.

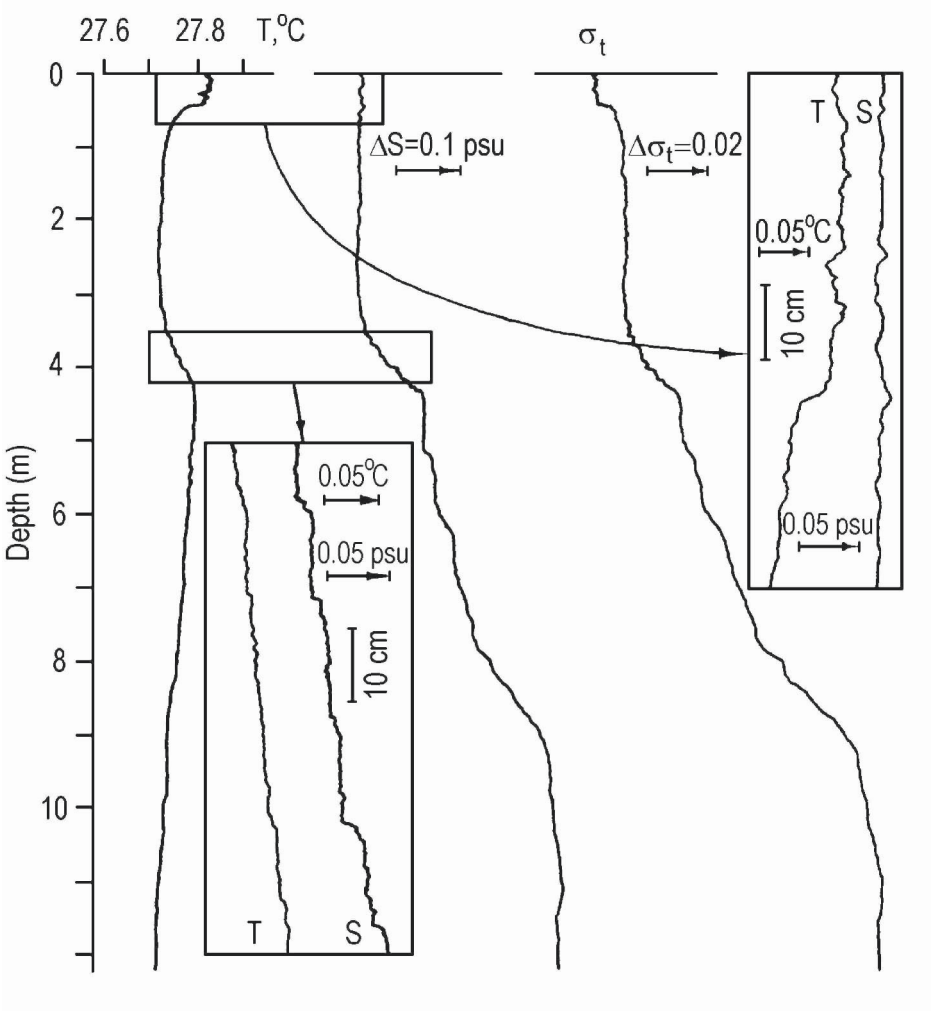


*Figure 4-11*. Vertical temperature *T*, salinity S, and $\sigma_t$ density profiles several hours after a rainfall. $\sigma_t$ Scale is in kg $m^{-3}$. The measurements are taken with a free-rising profiler by Soloviev and Vershinsky (1982).

These measurements shown in *Figure 4-11* were made during morning hours after a heavy nighttime rainfall. A salinity depression of about 0.3 psu

is observed in the upper 9 m of the ocean. Judging from the salinity profile the amount of precipitation was approximately 60 mm.

There is a 3.3-m deep quasi-homogeneous layer in the salinity profile. It presumably results from the nighttime convective mixing that worked against stable salinity stratification (*Figure 4-11*). The temperature inversion observed between 3.3 and 4.2 m is consistent with this interpretation.

In the upper right corner of *Figure 4-11*, the near-surface temperature and salinity profiles are shown with higher resolution. There is a 0.4 m thick diurnal mixed layer and the diurnal thermocline is found in the depth range from 0.4 m to 0.8 m. The diurnal mixed layer and diurnal thermocline are found close to the ocean surface due to low wind speed conditions.

The layer between 3.3-m and 4.2-m depth, with unstable temperature stratification, is expanded in the upper right corner of *Figure 4-11*. This temperarture inversion is overcompensated by the stable salinity stratification; thus the density profile is stable. The combination of unstable temperature stratification and stable salinity stratification provides favorable conditions for the development of layering convection due to double diffusion of heat and salt. It is remarkable that a step-like structure, typical for layering convection, is evident within the depth range from 3.3 to 4.2 m.

Freshwater input often results in forming a barrier layer in the upper ocean mixed layer (see Sections 1.7.4 and 7.6.3). The barrier layer has been recognized as a crucial element of tropical warm pool dynamics (Lukas and Lindstrom, 1991). The barrier layer isolates the warm water of the upper ocean layer by reducing the entrainment cooling from below the mixed layer and by providing slippery conditions within the mixed layer. The existence of the barrier layer plays a key role in the onset of El Niño, through a complex process that involves ocean vertical mixing, sea surface temperature, wind stress, freshwater flux, and large-scale ocean-atmosphere dynamics.

## 4.2 Surface-Intensified Jets

### 4.2.1 Slippery Near-Surface Layer of the Ocean Arising Due to Diurnal Warming

Woods (1968) hypothesized that the water above a strong thermocline can slide over the underlying water with a minimum of friction. Houghton (1969) called this phenomenon the *slippery seas*. He observed the slippery seas in the coastal region of Acapulco; the stratification was associated with lateral advection of warm water.

Montgomery and Stroup (1962) reported near-surface currents in the equatorial ocean intensify during daytime but obtained only fragmentary

data. Woods and Strass (1986) and Price et al. (1986) described the diurnal jet developing as a result of diurnal warming. Their studies, however, did not include conditions of low wind speed when the diurnal thermocline is localized very near the surface.

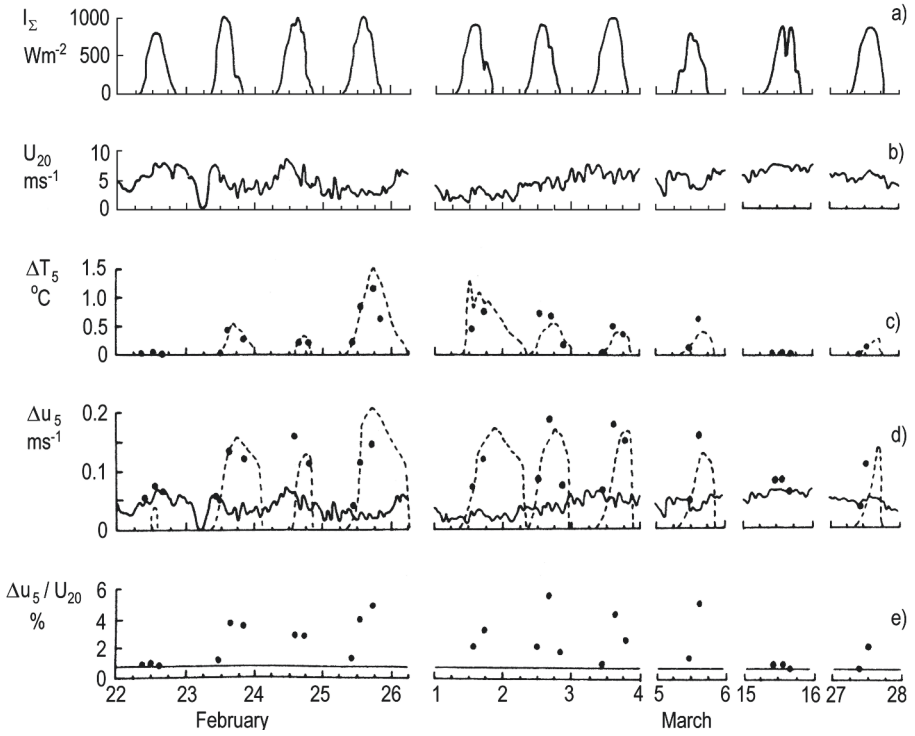


*Figure 4-12.* Observations of the slippery near-surface layer of the ocean arising due to daytime solar heating. Measurements in the Equatorial Atlantic and model-computed data encompass the period from 22 February to 28 March 1987. Time is UTC. (a) Insolation $I_\Sigma$;(b) wind speed 20 m above the ocean $U_{20}$; (c) temperature difference $\Delta T_5$ between the drogue depths (0.35 and 5 m) observed from a small boat (points) and model-computed time series of the temperature difference between the surface and 10 m depth (dashed line). (d) Current velocity difference $\Delta u_5$ between the drogue depths (0.35 and 5 m) registered by the drifters (points) and the model-computed time series of the current velocity difference between the surface and 10 m depth (dashed line). Solid line corresponds to the current velocity difference calculated between 0.35 and 5 m depth for an unstratified (constant stress) layer using formula (4.1); (e) coefficient of wind drift $\Delta u_5/U_{20}$: measured (points) and calculated from (4.1) (solid line). Adapted from Kudrayvtsev and Soloviev (1990) by permission of American Meteorological Society.

Kudryavtsev and Soloviev (1990) undertook simultaneous measurements of the vertical stratification and the current velocity difference in the upper layer of the ocean in the equatorial Atlantic using a combination a free-rising profiler deployed from research vessel and pairs of drifters simultaneously

deployed from a small boat. They found that during low wind speeds the jet is often localized in the upper few meters of the ocean.

Kudryavtsev and Soloviev (1990) concluded that the stabilizing buoyancy flux due to absorption of solar radiation reduces the turbulent friction. As a result, the near-surface warm layer slips over the underlying water mass practically with no turbulent friction. A similar slippery layer may result from positive buoyancy flux due to precipitation or due to the lateral advection (as in the fore mentioned observation by Houghton, 1969).

Kudryavtsev and Soloviev (1990) also noted the somewhat surprising fact that the speed of the diurnal jet did not drop with decreasing wind speed. This is nevertheless easy to understand, at least qualitatively. It is due to the diurnal mixed layer thinning at nearly the same rate as the wind stress decreases, thus concentrating the smaller momentum flux in a thinner layer.

*Figure 4-12* shows the solar radiation and wind speed during the experiment of Kudryavtsev and Soloviev (1990) in the equatorial Atlantic alongside with the temperature and velocity differences across the upper 5 m layer of the ocean. When the wind speed $U_{20}$ measured at 20 m height drops below approximately 6 m s$^{-1}$ the temperature difference, $\Delta T_5$, measured between depths of 0.35 m and 5 m dramatically increases (*Figure 4-12*c), as does the corresponding velocity difference $\Delta u_5$ (*Figure 4-12*d). These observations suggest that the temperature and velocity differences in the diurnal jet are interrelated.

*Figure 4-12e* shows the variability of the wind drift coefficient, $\Delta u_5 / U_{20}$. This coefficient is calculated from the velocity difference $\Delta u_5$ measured by a pair of drifters with drogue depths of 0.35 m and 5 m and from the wind speed 20 m above the sea surface, $U_{20}$ (*Figure 4-12*e). Solid lines in diagrams (d) and (e) indicate the current velocity difference, $\Delta u_5$, calculated between 0.35 m and 5 m depth from the logarithmic layer model as follows:

$$\Delta u_5 = C_{20}^{1/2} \left( \rho_a / \rho \right)^{1/2} \kappa^{-1} \ln\left( z_2 / z_1 \right) \approx 0.85 \times 10^{-3} U_{20}, \qquad (4.1)$$

where $C_{20} \approx 1.3 \times 10^{-3}$ is the bulk flux coefficient (for 20 m height), $\kappa = 0.4$ (the von Karman constant), $z_2$ = 5 m, and $z_1$ = 0.35 m.

The data from 22 February and March 15 (*Figure 4-12*) obtained during wind speeds $U_{20} \geq 7$ m s$^{-1}$ show that the measured velocity difference, $\Delta u_5$, and the wind drift coefficient, $\Delta u_5 / U_{20}$, were close to the logarithmic layer prediction. When the wind speed drops below approximately 6 m s$^{-1}$, the temperature and velocity differences in the upper 5 m layer of the ocean caused by the diurnal warming rapidly increase, and the wind drift coefficient exceeds the logarithmic layer prediction by up to a factor of 5.

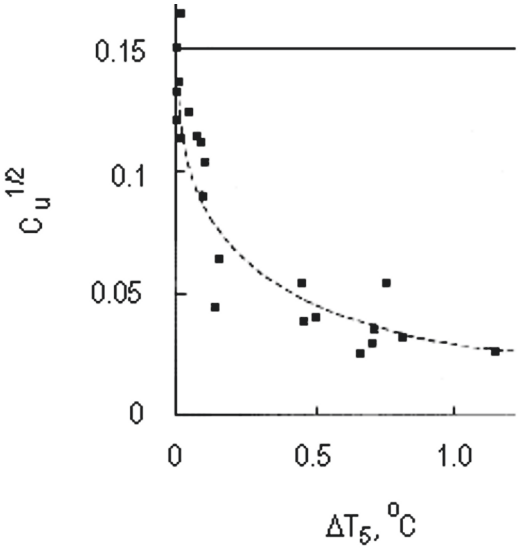


*Figure 4-13.* Dependence of the drag coefficient in the near-surface layer of the ocean on the temperature difference across the diurnal thermocline during a period of intense warming (morning and noon hours). Horizontal line corresponds to the drag law in the logarithmic boundary layer. Adapted from Kudrayvtsev and Soloviev (1990) by permission of American Meteorology Society.

In order to illustrate the near-surface slippery layer phenomenon, *Figure 4-13* shows the dependence of the drag coefficient defined as

$$C_u = \left(u_* / \Delta u_5\right)^2 \tag{4.2}$$

on the temperature difference $\Delta T_5$ in the upper 5 m layer of the ocean. This data indicates a systematic decrease of the drag coefficient as the temperature difference across the diurnal thermocline increases. For $\Delta T_5 = 1^{\circ}\mathrm{C}$, the drag coefficient $C_u$ is reduced by a factor of 25 to 30 compared to the case of neutral stratification. This result suggests that during periods of intense diurnal warming, the near-surface layer of the ocean can slip over the underlying water mass practically without friction.

### 4.2.2 Self-regulating state of the diurnal thermocline

From the theory of stratified turbulent boundary layers (cf., Turner, 1973), the mixed layer depth depends on the balance between positive buoyancy flux and the turbulent kinetic energy available for mixing. In the stationary case with no rotation effects, the depth of the mixed layer is proportional to the Oboukhov length scale $L_O$ (Niiler and Kraus, 1977)

$$h \sim L_O = u_*^3 / \left[ \kappa \alpha_T g Q_n / \left( c_p \rho \right) \right] = L_* / \kappa \,, \tag{4.3}$$

where $u_*$ is the friction velocity in water, and

$$Q_n = Q_0 - (1 - A) I_\Sigma \tag{4.4}$$

is the net heat flux into the ocean. (Note that for typical oceanic salinity S ~ 35 psu the sign of thermal expansion coefficient of water $\alpha_T$ is negative). In this analysis, we ignore the effect of volume absorption of solar radiation in the near-surface layer of the ocean (though it is incorporated at a later stage).

Under high wind speed conditions, the depth of the diurnal mixed layer is relatively large; the rate of diurnal warming, which is inversely proportional to the mixed layer depth, is small. When wind speed $U_{10}$ drops, the friction velocity $u_*$ also drops approximately as $U_{10}$, and according to (4.3) the mixed layer depth rapidly reduces.

From a simple model with isolating boundary conditions at the bottom of the diurnal mixed layer, the temperature of the of diurnal mixed layer with respect to the underlying water mass increases with time as

$$\Delta T = \frac{-Q_n t}{c_p \rho h_D} \sim \frac{-Q_n t}{c_p \rho L_O} = \frac{-\alpha_T g \kappa}{u_*^3} \left( \frac{Q_n}{c_p \rho} \right)^2 t = \frac{-\alpha_T g \kappa}{C_{10}^{3/2}} \left( \frac{Q_n}{c_p \rho} \right)^2 U_{10}^{-3} t \,. \tag{4.5}$$

The water within the mixed layer also accelerates horizontally under the action of the tangential wind stress $\tau_0 = \rho u_*^2$ according to the equation:

$$\Delta u = \frac{\tau_0 t}{\rho h_D} \sim \frac{\tau_0 t}{\rho L_O} = \frac{\kappa \alpha_T g Q_n}{c_p \rho u_*} t = \frac{\kappa \alpha_T g Q_n}{c_p \rho C_D^{1/2}} U_{10}^{-1} t \,. \tag{4.6}$$

Under very low wind speed conditions, the effect of volume absorption of solar radiation (which is ignored here but discussed in Section 4.5.1), limits the minimum depth of the diurnal mixed layer and thus the maximum values of $\Delta T$ and $\Delta u$.

According to (4.6), under the assumption of isolating boundary conditions a discontinuity of the temperature and velocity should occur at the bottom of the diurnal mixed layer. A discontinuity of the tangential velocity profile in incompressible fluid is always unstable (see, for instance, Landau and Lifshits, 1986). As a result, a transitional layer of finite thickness $\Delta H$ (which can be interpreted as the diurnal thermocline thickness $\Delta H_D$) is

formed below the mixed layer. The dynamic state of the diurnal thermocline depends on the bulk Richardson number,

$$Ri = -\alpha_T g \Delta T \Delta H / \Delta u^2 \tag{4.7}$$

where $\Delta T$, and $\Delta u$ are bulk temperature and velocity differences in the diurnal thermocline, respectively.

Substituting $\Delta T$ and $\Delta u$ in (4.7) from (4.5) and (4.6) gives:

$$Ri \sim \frac{\Delta H}{\kappa u_* t}. \tag{4.8}$$

According to (4.8) the Richardson number decreases inversely proportionally to the elapsed time, $t$. At a fixed $\Delta H$, $Ri$ unavoidably drops below its critical value $Ri_{cr} \approx 0.25$, at some point. The diurnal thermocline becomes dynamically unstable and an overturning event occurs increasing $\Delta H$ and, thus, returning $Ri$ to a stable (overcritical) value. Since the diurnal warming continues and the temperature and velocity differences across the diurnal thermocline continue increasing, after a certain time period the Richardson number should again drop below its critical value. This cyclic process will repeat itself while the diurnal warming continues. This is the regime of marginal stability, which maintains the diurnal thermocline in a quasi-equilibrium state:

$$Ri \approx Ri_{cr}. \tag{4.9}$$

This self-regulating regime of the diurnal thermocline is similar to the regime of marginal stability on the external boundary of turbidity currents described by Turner (1973). For the diurnal jet, the concept of the critical Richardson number was proposed by Price et al. (1986).

According to Turner's (1973) similarity theory for stratified turbulent boundary layers, in the self-regulating regime the local gradients of temperature ($\partial_z T$) and velocity ($\partial_z u$) can be expressed through the buoyancy ($-\alpha_T g \Delta T$) and velocity ($\Delta u$) differences across the diurnal thermocline as follows:

$$-\alpha_T g \partial_z T = K_2 \left(-\alpha_T g \Delta T / \Delta u\right)^2 \tag{4.10}$$

$$\partial_z u = K_1 \left(-\alpha_T g \Delta T / \Delta u\right) \tag{4.11}$$

where $K_1$ and $K_2$ are nondimensional constants.

Relations (4.10) and (4.11) describe linear temperature and velocity profiles. This is because the set of determining parameters no longer includes vertical coordinate z, and no length scale can be produced combining parameters $-\alpha_T g\Delta T$ and $\Delta u$. The interpretation is that in a stable boundary layer the vertical size of turbulence eddies is restricted; the turbulence is not directly affected by the presence of a boundary (the ocean surface). As a result, the boundary layer structure no longer explicitly depends on $z$ (Neuwstadt, 1984).

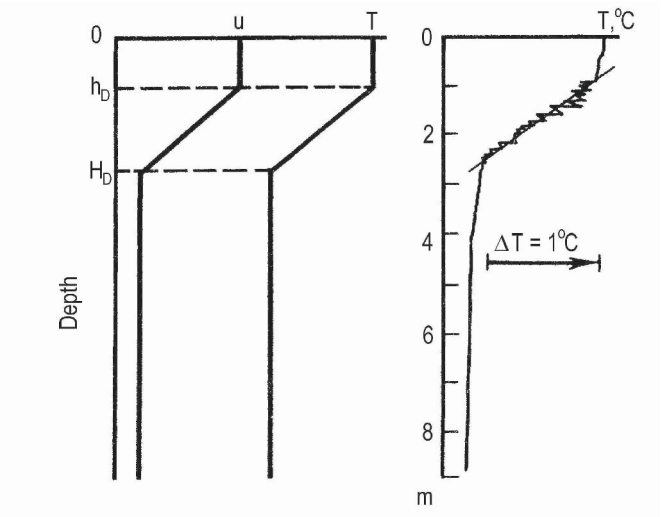


*Figure 4-14.* Vertical profiles of temperature and horizontal velocity in the diurnal jet: (a) schematic representation; (b) temperature profile obtained with a free-rising profiler. (After Kudrayvtsev and Soloviev, 1988.)

The vertical temperature and current profiles in the diurnal mixed layer and diurnal thermocline for the regime of marginal stability are schematically shown in *Figure 4-14a*. They include the diurnal mixed layer ($0 < z < h_D$) with constant $T$ and $u$ and the diurnal thermocline ($h_D < z < H_D$) with linear profiles of $T$ and $u$. In this notation the thickness of the thermocline is $\Delta H_D = H_D - h_D$.

The diurnal thermocline under conditions of low wind speed in fact often exhibits a linear temperature profile, which is prominent even in individual temperature profiles (*Figure 4-14b*). The temperature profiles in the diurnal thermocline may contain fluctuations (microstructure). Averaging over several casts produces smoother vertical profiles. *Figure 4-15* shows mean temperature profiles averaged over two or three successive individual profiles from Kudrayvtsev and Soloviev (1990). Only those profiles obtained

under conditions of daytime solar heating and when the lower boundary of the diurnal thermocline did not exceed 5 meters (*i.e.*, the maximum drogue depth of the drifter pair) are shown.

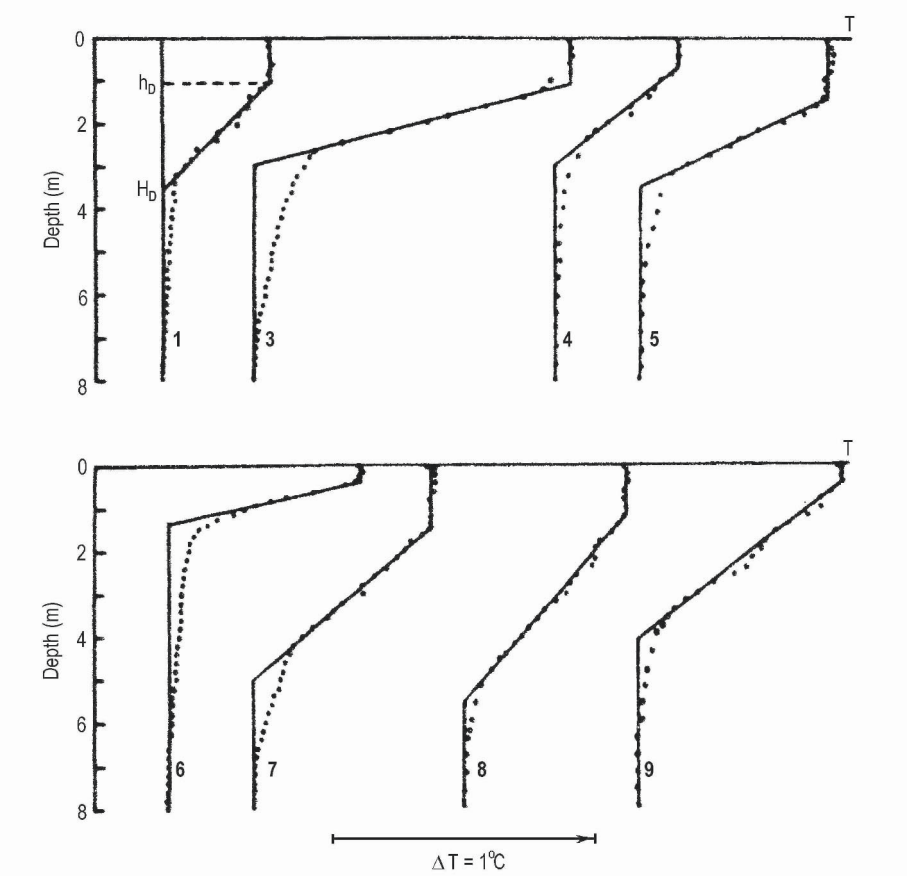


*Figure 4-15.* Average temperature profiles from measurements with a free-rising profiler during daytime solar heating. Pertinent information can be found in *Table 4-2*. Adapted from Kudrayvtsev and Soloviev (1990) by permission of American Meteorological Society.

According to *Figure 4-15*, during daytime the averaged vertical temperature profiles have linear segments in the diurnal thermocline. An appreciable deviation from linearity is observed only at the lower boundary of the diurnal thermocline. This deviation is likely due to the volume absorption of solar radiation below the diurnal thermocline or just the remains of a relic diurnal thermocline formed at a previous stage of the diurnal cycle.

*Table 4-2*. Pertinent information for the Kudryavtsev and Soloviev (1990) observations. LST is the local soalr time. The first column is the profile number in *Figure 4-15*. Profile #2 is a single one and is not shown in *Figure 4-15*. This profile can, however, be found in Figure 2 of the original publication by Kudryavtsev and Soloviev (1990).

| # | Date 1987 | Time LST | Coordinates | | $U_{20}$ m s$^{-1}$ | $\Delta H_D$ m | $\Delta T_5$ $^{o}$C | $\Delta u_5$ m s$^{-1}$ | *Ri* |
|---|---|---|---|---|---|---|---|---|---|
| | | | Lat N | Lon W | | | | | |
| 1 | 23 Feb | 13:51-13:55 | 01$^{o}$30’ | 22$^{o}$01’ | 3.9 | 2.5 | 0.45 | 0.131 | 0.19 |
| 2 | 25 Feb | 11:59 | 02$^{o}$29’ | 23$^{o}$29’ | 2.7 | 1.8 | 0.8 | 0.113 | 0.33 |
| 3 | 25 Feb | 14:51-15:08 | 03$^{o}$00’ | 23$^{0}$30’ | 2.9 | 1.8 | 1.15 | 0.143 | 0.30 |
| 4 | 1 Mar | 11:29-11:42 | 06$^{o}$30’ | 24$^{o}$59’ | 3.2 | 2.4 | 0.45 | 0.073 | 0.60 |
| 5 | 1 Mar | 14:56-15:10 | 06$^{o}$01’ | 25$^{o}$00’ | 3.3 | 2.0 | 0.7 | 0.118 | 0.30 |
| 6 | 2 Mar | 11:28-11:41 | 03$^{o}$03’ | 24$^{o}$59’ | 4.0 | 1.2 | 0.75 | 0.091 | 0.32 |
| 7 | 2 Mar | 15:10-15:33 | 02$^{o}$28’ | 24$^{o}$59’ | 4.4 | 3.8 | 0.7 | 19.0 | 0.22 |
| 8 | 3 Mar | 12:58-13:13 | 00$^{o}$28’ | 25$^{o}$00’ | 5.6 | 4.2 | 0.5 | 17.7 | 0.20 |
| 9 | 5 Mar | 13:16-13:36 | 06$^{o}$00’ | 26$^{o}$30’ | 3.0 | 3.7 | 0.65 | 15.6 | 0.29 |

In order to estimate the thickness of the diurnal thermocline, $\Delta H_D$, the temperature profiles in the diurnal thermocline were linearly extrapolated (*Figure 4-15*). The bulk Richardson number, *Ri*, is then estimated from (4.7) under an assumption that $\Delta H = \Delta H_D$, $\Delta T = \Delta T_5$, and $\Delta u = \Delta u_5$, where $\Delta T_5$ and $\Delta u_5$ are the temperature and current velocity difference between the drogue depths of the drifters, 0.35 and 5 m, respectively, and $\Delta H_D$ is the thickness of the diurnal thermocline obtained from the linear extrapolation as shown in *Figure 4-15*. The estimates of the Richardson number are given in *Table 4-2*. The average Richardson number, $\overline{Ri} = 0.3 \pm 0.1$, is close to the theoretical critical gradient Richardson number, $Ri_{cr} = 1/4$. This fact and the existence of linear temperature profiles in the diurnal thermocline are evidence in favor of a self-regulating state of the diurnal thermocline during the observations summarized in *Figure 4-15* and *Table 4-2*.

Thus, for the self-regulating state of the diurnal thermocline, the vertical temperature and current velocity profiles can be approximated in the simple way shown in *Figure 4-14*a. For the model temperature and velocity profiles of this type, the integrated heat and momentum balance equations (1.10) and (1.6) under the assumption of horizontal homogeneity and no rotation effects take the following shape:

$$\Delta T\left(h_D + 0.5\Delta H_D\right) = -\int_0^t \frac{Q_D}{c_p \rho} dt' , \tag{4.12}$$

$$\Delta u\left(h_D + 0.5\Delta H_D\right) = \int_0^t \frac{\tau_0}{\rho}\, dt', \tag{4.13}$$

where $h_D$ is the depth of the diurnal mixed layer, $\Delta H_D$ is the thickness of the diurnal thermocline, $\Delta T$ and $\Delta u$ are the temperature and current velocity differences across the diurnal thermocline; $\tau_0$ is the momentum flux at the air-sea interface,

$$Q_D = Q_0 - \left(1 - A\right) I_\Sigma \left[1 - f_R\left(H_D\right)\right], \tag{4.14}$$

is the net heat flux into the upper ocean layer of depth $H_D$ (taking into account the volume absorption of solar radiation), and $t$ is the elapsed time from the beginning of the diurnal warming.

An important feature of the model (4.12)-(4.13) is that it operates with integral rather than instanteneous fluxes, so the diurnal amplitudes depend on the "history" of fluxes $Q_D$ and $\tau_0$ (at least from sunrise). It is convenient to introduce time averaged parameters:

$$\overline{Q_D} = \frac{1}{t}\int_0^t Q_D dt', \tag{4.15}$$

$$\overline{\tau_0} = \frac{1}{t}\int_0^t \tau_0 dt'. \tag{4.16}$$

From equations (4.7), (4.9), (4.12), and (4.13) it follows that

$$\Delta T / \Delta H_D = Ri_{cr}^{-1}\overline{T_*} / \overline{L_*}, \tag{4.17}$$

$$\Delta u / \Delta H_D = Ri_{cr}^{-1}\overline{u_*} / \overline{L_*}, \tag{4.18}$$

$$\Delta H_D / h_D = \left(1 + 2Ri_{cr}\overline{L}_*\overline{u_*}t / h_D^2\right)^{1/2} - 1 \tag{4.19}$$

where $\overline{u_*} = \left(\overline{\tau_0} / \rho\right)^{1/2}$, $\overline{T_*} = -\overline{Q_D} / \left(c_p \rho \overline{u_*}\right)$, and $\overline{L_*} = c_p \rho \overline{u_*}^3 / \left(\alpha_T g \overline{Q_D}\right)$.

Equations (4.17) and (4.18) connect the mean temperature and velocity gradients in the diurnal thermocline with the accumulated heat and

momentum fluxes at the air-sea interface. These equations yield a simple relationship

$$\Delta u / \overline{u_*} = \Delta T / \overline{T_*} \ , \tag{4.20}$$

which can be used to estimate the velocity difference $\Delta u$ (here interpreted as the speed of the diurnal jet) from the temperature difference $\Delta T$ across the diurnal thermocline and the history of heat and momentum fluxes are known.

Equation (4.19) describes the evolution of the diurnal thermocline thickness $\Delta H_D$ as a function of time. At the initial stage of the diurnal warming when $t << \frac{1}{2} h_D^{\,2} / (Ri_{cr} \overline{u_*} \overline{L_*})$, (4.19) is approximated with

$$\Delta H_D \approx Ri_{cr} \overline{u}_* \overline{L}_* t / h_D \, . \tag{4.21}$$

At the stage when $t >> \frac{1}{2} h_D^{\,2} / (Ri_{cr} \overline{u}_* \overline{L}_*)$, equation (4.19) can be approximated as follows:

$$\Delta H_D \approx \left( 2 Ri_{cr} \overline{u}_* \overline{L}_* t \right)^{1/2} \tag{4.22}$$

Thus, initially the thermocline thickness $\Delta H_D$ grows proportional to time $t$, while at late stages $\Delta H_D$ grows as $t^{1/2}$.

### 4.2.3 Upper velocity limit for the diurnal jet

The model of the self-regulating diurnal thermocline allows a simple estimate of the upper velocity limit for the diurnal jet. In this model, the heat content of the warm layer is:

$$\Upsilon_D = c_p \rho \Delta T \left( h_D + 0.5 H_D \right) . \tag{4.23}$$

Since only a fraction of the solar radiation is absorbed in the diurnal mixed layer and diurnal thermocline,

$$\Upsilon_D < \int_0^t \left[ (1 - A) I_\Sigma - Q_0 \right] dt' \, . \tag{4.24}$$

where $t$ is the elapsed time from the beginning of the diurnal warming. From (4.7), (4.9), (4.24) and an obvious inequality $\left(h_D + 0.5H_D\right) > 0.5H_D$, it follows that $\left(\Delta u\right)^2 < 2Ri_{cr}^{-1}\alpha_T g \Upsilon_D / \left(c_p \rho\right)$. Hence, the upper limit of the diurnal jet velocity is

$$\Delta u_{\max} = \left[-2Ri_{cr}^{-1}\alpha_T g \Upsilon_D / \left(c_p \rho\right)\right]^{1/2}. \tag{4.25}$$

The heat accumulated in the upper ocean due to diurnal warming is mainly determined by solar radiation. The maximum quantity of the solar radiation absorbed by the ocean during daytime is roughly equal to 2 x $10^7$ J $m^{-2}$. Substituting this value into (4.25) gives an estimate $\Delta u_{\max} \approx 0.3$ m $s^{-1}$, which represents the upper velocity limit for the diurnal jet.

### 4.2.4 Upper velocity limit for the rain-formed jet

Slippery layers can also develop due to freshwater input from rain. An equation similar to (4.25) can be derived for estimating the upper velocity limit in the case of rain-formed jet:

$$\Delta u_{\max} = \left[2Ri_{cr}^{-1}\beta_S g S_0 M_r\right]^{1/2}, \tag{4.26}$$

where $M_r$ is the cumulative precipitation, defined from equation

$$M_r = \int_0^t P dt', \tag{4.27}$$

where $P$ is the precipitation rate and $t$ is the elapsed time from the beginning of the rain event. For a strong tropical rainfall with $M_r = 100$ mm, the upper estimate of the velocity following from (4.26) is $\Delta u_{\max} \approx 0.5$ m $s^{-1}$.

## 4.3 Evolution of the Diurnal Mixed Layer and Diurnal Thermocline Under Low Wind Speed Conditions

*Figure 4-16* offers the following classification of the diurnal mixed layer and diurnal thermocline evolution under low wind speed conditions. During Phase I, nighttime convection typically penetrates to the bottom of the mixed layer. After sunrise, increasing solar radiation gradually suppresses convective mixing forming a diurnal mixed layer, which rapidly thins (Phase

II). The diurnal mixed layer depth stabilizes at a depth of the order of 1 m or less (depending on the wind speed and surface heat fluxes); a diurnal thermocline develops with gradually increasing temperature difference and thickness (Phase III). The maximum temperature difference across the diurnal thermocline occurs around 2-3 pm local time. During Phase III the warm near-surface layer typically slips over the underlying water mass, with little turbulent friction; as a result, the diurnal jet develops.

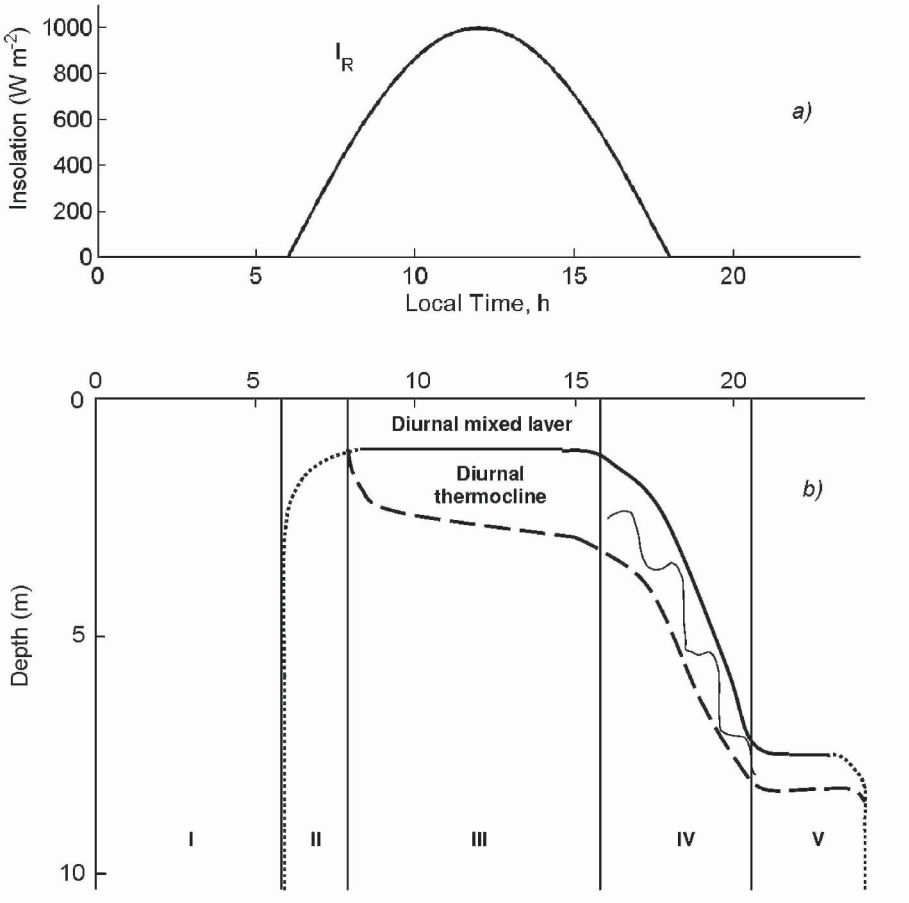


*Figure 4-16.* Schematic representation of the diurnal mixed layer and diurnal thermocline depth under low wind speed conditions. Here: a) surface solar irradiance cycle; b) diurnal mixed layer and diurnal thermocline evolution: Phase I is the nighttime convection; Phase II is the detrainment phase when the diurnal mixed layer is formed; Phase III is the daytime warming phase; Phase IV is the evening deepening of the diurnal mixed layer and diurnal thermocline; and Phase V is the erosion of the diurnal thermocline by convection. Light, wavy line in Phase IV signifies the Kelvin-Helmholtz instability.

When the surface solar irradiance drops below a certain level that depends on wind speed and surface heat fluxes, the diurnal mixed layer starts its evening deepening (Phase IV). The positive buoyancy flux can no longer stabilize the diurnal mixed layer and cannot maintain slippery conditions on its lower boundary. The diurnal jet releases its kinetic energy, which results in the Kelvin-Helmholtz type instability followed by overturning events (billows). The diurnal mixed layer and diurnal thermocline rapidly deepen. The intensive deepening of the diurnal thermocline is often associated with jumps of temperature between the diurnal mixed layer and diurnal thermocline. These jumps result from the Kelvin-Helmholtz instability accompanied by overturning events.

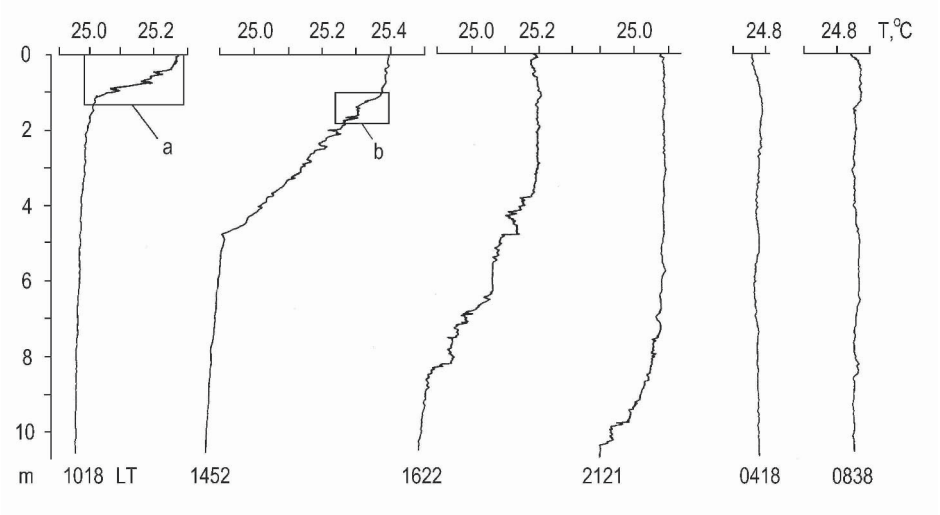


*Figure 4-17.* Vertical profiles of temperature in the upper 10 m of the Atlantic Ocean at 28°N, 21°W. Adapted from Soloviev and Vershinsky (1982) with permission of Elsevier. Local times are indicated at the bottom of each profile.

After reaching a depth of several meters the excess kinetic energy of the diurnal jet is pretty much spent on entrainment of colder water from below the thermocline; the deepening of the diurnal mixed layer and thermocline slows down. At this stage the diurnal thermocline mainly erodes from its top due to convective cooling from the ocean surface (Phase V). Turbulent entrainment is relatively small in this phase.

In order to illustrate the above classification, *Figure 4-17* shows a series of temperature profiles characterizing the diurnal warming of the subtropical ocean under conditions of low wind speed and strong insolation. This series of measurements was made with a free-rising profiler equipped with high-resolution temperature and conductivity sensors. The cold film temperature sensor (DISA) had a response time in water of ~3 milliseconds. For the

profiler speed of 1 m $s^{-1}$ this corresponds to a resolution of ~3 mm in the vertical. Vertical resolution of the conductivity sensor was better than 1 mm with practically zero response time.

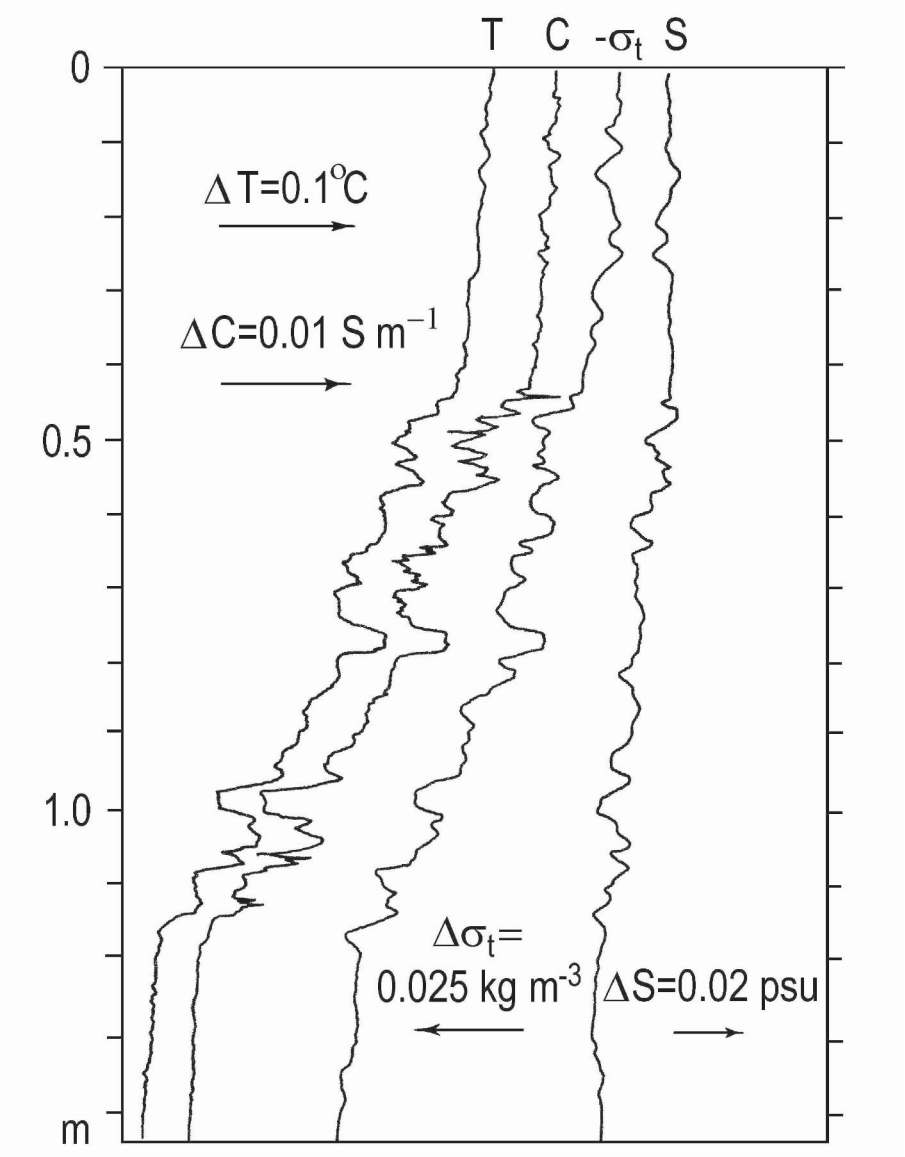


*Figure 4-18.* Microstructure of the diurnal thermocline at 10:18 LT (from *Figure 4-17*, box *a*. Adapted from Soloviev and Vershinsky (1982) with permission of Elsevier. *C* stands for conductivity; other symbols are standard.

The first profile shown in *Figure 4-17* reveals a 0.4-m thick diurnal mixed layer and a diurnal thermocline in the depth range from 0.4 to 1.2 m. Below 1.2 m the vertical temperature change is relatively small. According to the classification given in *Figure 4-16*, this profile corresponds to Phase III.

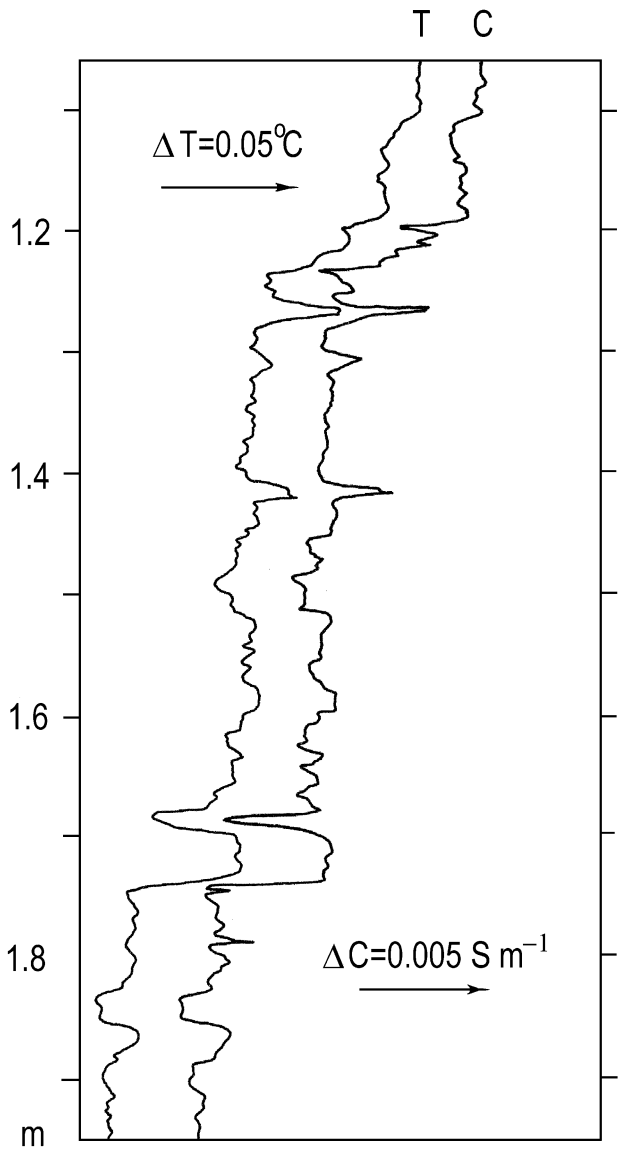


*Figure 4-19.* Microstructure of the diurnal thermocline at 14:52 LT (from *4-17*, box b. Adapted from Soloviev and Vershinsky (1982) with permission of Elsevier.

The subsequent temperature profiles demonstrate development (1452 LST) and evening deepening (1622 and 2121 LST) of the diurnal mixed layer and diurnal thermocline. These are Phase IV (16 22 LST) and Phase V (2121 LST). At 0418 LST next morning, the diurnal thermocline could not be seen within the upper 10 m. A slight temperature inversion near the surface was related to the convective cooling of the ocean surface. This is Phase I. The temperature profile taken after sunrise (0838 LST) indicated that a new warm layer had begun to form (Phase II).

The section of temperature profile marked by rectangle *a* in *Figure 4-17* is shown in *Figure 4-18* in more detail (including conductivity, salinity, and density). There are numerous small-scale temperature inhomogeneities within the diurnal thermocline, associated with intermittent turbulent mixing, which can be classified as microstructure. Local vertical gradients of temperature reach $6^{o}C\ m^{-1}$. Above and below the diurnal thermocline, the temperature gradients are considerably smaller.

The conductivity profile in *Figure 4-18* almost repeats the corresponding temperature profile. The conductivity profile reveals finer structure than the temperature profile, mainly because of a better spatial resolution of the conductivity sensor. These small-scale features partially disappear in the salinity profiles because, in order to avoid spikes, salinity was calculated from smoothed (over 1 cm) temperature and conductivity signals.

The salinity profile in *Figure 4-18* shows a small (~0.02-psu) increase of salinity toward the surface, associated with evaporation from the ocean surface. The salinity stratification is unstable and contributes to convective mixing within the diurnal mixed layer. Within the diurnal thermocline, the unstable salinity stratification is compensated by the stable stratification of temperature; the density profile is dominated by the temperature contribution and is therefore stable. Strong stratification in the diurnal thermocline makes it more difficult for the excess near-surface salinity to penetrate into deeper layers. This results in a slightly elevated level of salinity within the diurnal mixed layer and, in part, within the diurnal thermocline. In this situation (stable temperature and unstable salinity stratification), double diffusion convection may develop in the form of salt fingers.

The section of the temperature profile marked by rectangle *b* (*Figure 4-17*) is shown in *Figure 4-19* in more detail. In this example, the diurnal thermocline reveals a remarkable step-like structure. This profile was taken at the beginning of the evening deepening of the diurnal thermocline (Phase IV). Step-like structures often appear in the diurnal thermocline in this phase of the diurnal cycle. The next temperature profile taken at 16:22 also reveals step-like structures but with larger vertical scale (*Figure 4-17*). In Section 5.5, we consider two possible mechanisms leading to overturning and step-like structure in the diurnal thermocline, which are the Kelvin-Helmholtz (K-

H) instability and the resonant interaction between surface and internal waves.

Billowing due to the K-H instability is probably the most frequent cause of the observed step-like structures. As already mentioned at the beginning of this section, the diurnal jet can slip over the underlying water mass with little turbulent friction due to the stabilizing positive buoyancy flux from the absorbed solar radiation. When the solar radiation decreases in the evening (or due to clouds) the balance between turbulence and positive buoyancy flux is disturbed. As a result, the shear stress at the bottom of the mixed layer intensifies, which creates favorable conditions for the K-H instability followed by the overturning events.

The K-H instability is also a plausible explanation of step-like structures observed in the near-surface ocean in the example shown in *Figure 4-20*. This series of measurements was made in the North Atlantic during a period of relatively calm weather (see *Table 4-3*). The appearance of step-like structures in the profiles correlates well with the deepening phase of the diurnal thermocline (which occurred either due to changing atmospheric conditions like for the profile at 12:58 LT or reduction of insolation in the evening time as in the profile taken at 15:18 LT) can also be associated with the K-H instability.

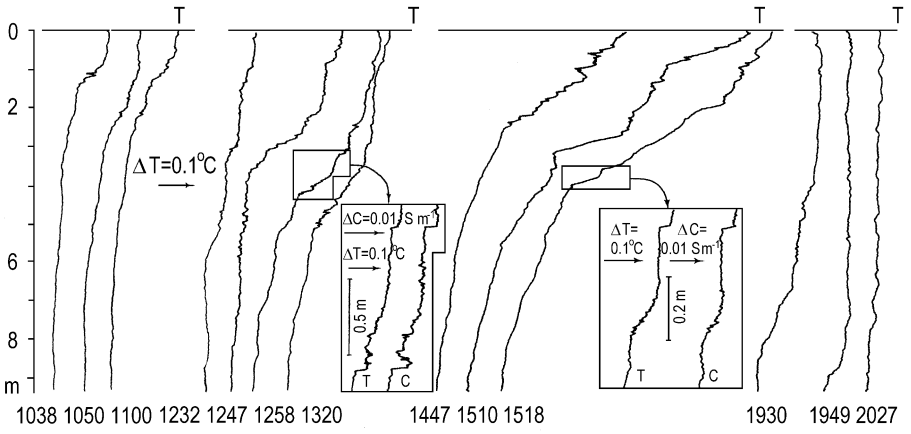


*Figure 4-20.* Vertical profiles of temperature in the upper 9 m obtained with a free-rising profiler at 59°N, 13°W during the Joint Air-Sea Interaction (*JASIN*.) experiment. *Figure 4-21.* Microstructure of the diurnal thermocline at 14:52 LT (from *4-17*, box b. Adapted from Soloviev and Vershinsky (1982) with permission of Elsevier.

*Figure 4-21* shows a series of near-surface measurements in the Atlantic Ocean during evening deepening of the diurnal thermocline and diurnal mixed layer. During these measurements the 10 m wind speed was about 2-2.5 m $s^{-1}$ and the surface waves were small. The temperature profiles shown in *Figure 4-21* are calculated from conductivity profiles under the

assumption of constant salinity. No rain was observed on the day of these measurements. No signs of previous rains were found in the upper 10 m of the ocean from a salinity profile measured 3 hours in advance of the data set shown in *Figure 4-21*.

In addition to the temperature profiles calculated from conductivity profiles, there are profiles of the vertical temperature gradient and velocity fluctuation. Fluctuation velocity profiles are high-pass filtered with a 12 Hz cut off frequency. Because free-rising profiler motions and surface wave orbital velocities are insignificant for frequencies above 12 Hz, velocity fluctuations shown in *Figure 4-21* are ascribed to small-scale turbulence.

The diurnal mixed layer and diurnal thermocline can be clearly seen in the temperature profiles (*Figure 4-21*). The mean velocity of the diurnal mixed layer deepening calculated from the least squares method is $\overline{w}_e \approx 0.1$ cm $s^{-1}$. Due to large amplitude internal waves developing in the deepening diurnal thermocline (presumably because of the Kelvin-Helmholtz instability), the depth of the diurnal mixed layer and diurnal thermocline oscillate. This depth may also vary due to horizontal variability of the studied phenomenon, since the ship drifted between the individual casts.

*Table 4-3.* Pertinent information for the field observations of near-surface microstructure.

| *Fig.* # | Date | Time LST | Position | $U_{10}$ m $s^{-1}$ | (1-A) $I_\Sigma$ W $m^{-2}$ | $Q_0$ W $m^{-2}$ |
|---|---|---|---|---|---|---|
| *4-11* | 27 Aug 79 | 09:00 | 09°N, 23°W | 0.5 to 2 | 630 | 70 to 120 |
| *4-17, 4-18* | 6 Oct 78 | 10:18 | 28°N, 21°W | 2 | 840 | 150 |
| *4-17, 4-19* | 6 Oct 78 | 14:52 | 28°N, 21°W | 3 | 620 | 190 |
| *4-17* | 6 Oct 78 | 16:22 | 28°N, 21°W | 3 | 210 | 170 |
| *4-17* | 6 Oct 78 | 21:21 | 28°N, 21°W | 4 | 0 | 190 |
| *4-17* | 7 Oct 78 | 04:18 | 28°N, 21°W | 5 | 0 | 240 |
| *4-20* | 3 Sep 78 | 08:38 | 59°N, 13°W | 4.5 | 510 | 220 |
| *4-20* | 3 Sep 78 | 10:38 to 11:00 | 59°N, 13°W | 2 | 270 to 380 | 30 |
| *4-20* | 3 Sep 78 | 12:32 | 59°N, 13°W | 2.5 | 260 | 40 |
| *4-20* | 3 Sep 78 | 12:47 | 59°N, 13°W | 2.5 | 270 | 40 |
| *4-20* | 3 Sep 78 | 12:58 | 59°N, 13°W | 2.5 | 260 | 40 |
| *4-20* | 3 Sep 78 | 13:20 | 59°N, 13°W | 2.5 | 250 | 40 |
| *4-20* | 3 Sep 78 | 14:47 | 59°N, 13°W | 1.0 | 400 | 20 |
| *4-20* | 3 Sep 78 | 15:10 | 59°N, 13°W | 1.0 | 280 | 20 |
| *4-20* | 3 Sep 78 | 15:18 | 59°N, 13°W | 1.0 | 240 | 20 |
| *4-20* | 3 Sep 78 | 19:30 to 20:27 | 59°N, 13°W | 4 | 0 | 50 |

A characteristic feature of the temperature profiles in *Figure 4-21* is the sharp temperature jump separating the bottom of the mixed layer and the top of the diurnal thermocline. In some cases, the local magnitude of the vertical temperature gradient exceeded $1^{o}C\ m^{-1}$. The conductivity sensor installed on the free-rising profiler had the spatial resolution of about 1 cm, thus smoothing temperature jumps and underestimating vertical gradients. In reality, jumps with local temperature gradients up to $30^{o}C\ m^{-1}$ have been observed in the deepening diurnal thermocline when measured with higher resolution sensors (Soloviev and Vershinsky, 1981).

According to Barenblatt (1982), for $w_e \sim \left(K_T / \tau\right)^{1/2}$ (here $K_T$ and $\tau$ are the turbulent diffusion coefficient and the relaxation time for temperature inhomogeneities in the diurnal thermocline respectively) the turbulent exchange is principally nonstationary (and nonlocal), and ordinary, diffusion type models of turbulent transport are no longer relevant. One of the consequences of the non-stationary nature of turbulence in a rapidly deepening thermocline is the appearance of a temperature jump or a discontinuity separating the mixed layer and the thermocline.

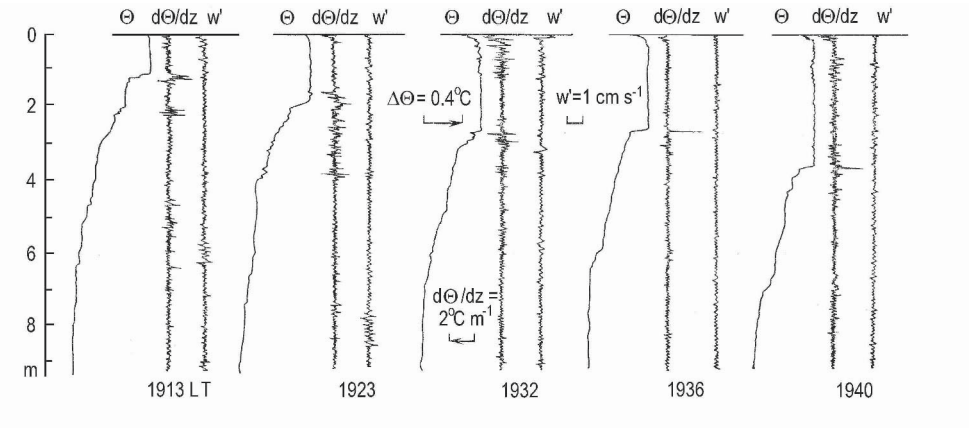


*Figure 4-21.* Series of vertical profiles of temperature (θ), temperature gradient ($\theta_z$'), and longitudinal (vertical) velocity fluctuation (*W*') during the evening deepening of the diurnal mixed layer and diurnal thermocline. The local time for each measurement is given below the profiles. (After Bezverkhny and Soloviev, 1986.) Adapted by permission from American Geophysical Union from Izvestiya, *Atmospheric and Oceanic Physics* 22, 72-77, © 1986 AGU.

A schematic temperature profile from Barenblatt's (1982) model is shown in *Figure 4-22*a. The temperature profile below the point of discontinuity has the exponential form:

$$\Theta = \Theta_1 \exp\left(-\alpha_B \xi\right) \tag{4.28}$$

where $\alpha_B = \left[ \left( K_T^2 + 4 w_e^2 \eta \right)^{1/2} - K_T \right] / 2 w_e \eta$ , $\eta = \tau K_T$ ,

$$\xi = z - w_e t - h_0 , \tag{4.29}$$

$z$ is the depth referenced to the ocean surface, $t$ is time, and $h_0$ is the depth of the upper boundary of the thermocline at the initial moment $t$ = 0. The temperature profile at the point of discontinuity is determined from relation

$$\Theta_1 = 2\Theta_0 / \left[ 1 + \left( 1 + \beta_B \right)^{1/2} \right], \tag{4.30}$$

where $\beta_B = 4 w_e^2 \tau / K_T$ . Order of magnitude estimates suggest that the non-stationary effect becomes important in the dynamics of the deepening thermocline for $w_e > 0.001 - 0.1$ cm s$^{-1}$ (Barenblatt, 1982).

Average temperature profiles calculated from five individual temperature profiles are shown in *Figure 4-21* in the depth coordinate $\xi$ according to (4.29). Note that $\xi$ is referenced to the top of the diurnal mixed layer rather than to the ocean surface, and that before averaging, the individual profiles were normalized by the corresponding total temperature difference across the diurnal thermocline.

Comparison of the model (*Figure 4-22a*) and experimental (*Figure 4-22*b) profiles shows good qualitative agreement between them. There is a sharp temperature jump at the top of the diurnal thermocline, and the temperature profile below the "discontinuity" point in general follows an exponential law (*Figure 4-22c*). The temperature jump constitutes about 16% of the overall temperature difference across the diurnal thermocline. The estimate of $\alpha_\tau$ derived from *Figure 4-22*c and equation (4.44) is $\alpha_B \approx 4.16 \times 10^{-1}$ m$^{-1}$. From (4.28) and (4.30), parameters $K_T$ and τ can be expressed via $\Theta_1 / \Theta_0$ and $\alpha_B$ as follows:

$$K_T = \frac{w_e \Theta_1}{\alpha_B \Theta_0} , \tag{4.31}$$

$$\tau = \frac{\Theta_0 - \Theta_1}{\alpha_B w_e \Theta_1} . \tag{4.32}$$

For $w_e = 0.1$ cm s$^{-1}$ and $\Theta_1 / \Theta_0 = 0.84$ , equations (4.31) and (4.32) result in the estimates, $K_T \approx 20$ m$^2$ s$^{-1}$ and $\tau \approx 460$ s.

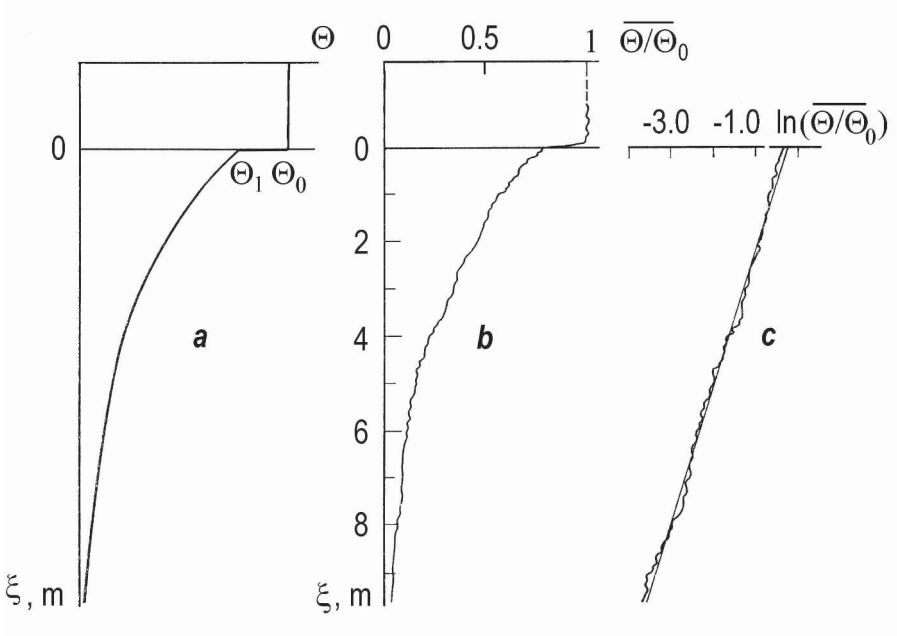


*Figure 4-22.* (a) Schematic representation of vertical temperature profiles for rapid evening deepening of the diurnal thermocline. (b) Average temperature profiles calculated from five individual temperature profiles shown in *Figure 4-22* in the depth coordinate system referenced to the bottom boundary of the diurnal mixed layer. (c) The average temperature profile in the diurnal thermocline plotted in semi-logarithmic coordinates approximated with a straight line. (After Bezverkhny and Soloviev, 1986.) Adapted by permission from American Geophysical Union from Izvestiya, *Atmospheric and Oceanic Physics* 22, 72-77, © 1986 AGU.

Bezverkhny and Soloviev (1986) provide independent estimates of the turbulent mixing coefficient $K_T$ obtained from fluctuation characteristics of the velocity and temperature profiles shown in *Figure 4-21*. From the fluctuation velocity signal they obtained estimates of $b^{1/2}$ ranging from 0.2 cm $s^{-1}$ to 0.3 cm $s^{-1}$ in the diurnal thermocline (where $b$ is the turbulent kinetic energy). The turbulence length scale, $l$, estimated from the temperature profiles (*Figure 4-21*) within the diurnal thermocline was in the range of 20 cm to 100 cm. Estimates of the mixing coefficient obtained with the Kolmogorov's (1942) formula

$$K_T = lb^{1/2}, \tag{4.33}$$

are within the range from 4 to 30 $cm^2$ $s^{-1}$, consistent with the estimate $K_T \approx 20\,cm^2\ s^{-1}$ following from comparison of the average temperature profiles with Barenblatt's (1982) model.

An alternate estimate of the turbulent mixing coefficient can be obtained from the Osborn and Cox (1972) equation:

$$K_T \approx (2 \pm 1) C_\kappa \kappa_T \tag{4.34}$$

where $C_\kappa = \overline{(\partial_z \Theta')^2} / (\partial_z \overline{\Theta})^2$ is the Cox number, and $\kappa_T$ is the coefficient of thermal molecular diffusion . The '+' sign pertains to the case for isotropic turbulence, while the '-' sign is intended for the case of anisotropic (layered) structure. The estimate of the Cox number within the diurnal thermocline following from the data shown in *Figure 4-21* is $C_\kappa \approx 40$. The mixing coefficient estimate from (4.34) is $K_T \approx 0.06 - 0.17$ cm$^2$ s$^{-1}$, which is much less than the estimate from (4.33). One possible explanation is that, strictly speaking, the Osborn and Cox (1972) formula is derived under the assumptions that may not be valid for non-stationary turbulence. Another possible explanation is that the temperature (conductivity) sensor did not fully resolve the convective-viscous subrange of turbulence, possibly leading to underestimation of the Cox number.

## 4.4 Large Diurnal Warming Events

### 4.4.1 *In situ* data

Another example of a large diurnal warming event from the western equatorial Pacific warm pool is given in *Figure 4-23*. These are measurements by bow sensors "scanning" the near-surface layer of the ocean as described in Section 4.1.3. In this experiment, the vessel was steaming at 4-5 knots perpendicular to the dominant surface waves to increase the ship pitching for ~15 min every 2 hours.

These observations illustrate the evolution of the vertical temperature profile in the near-surface layer of the ocean due to diurnal warming under conditions of very low wind speed. In this example the temperature difference across the diurnal thermocline is localized in the upper ~1 m and at 13:02 reaches as much as 3$^o$C.

A slight salinity increase within the diurnal mixed layer and diurnal thermocline at 11:03, 13:02, and 15:01, and 17:00 is related to evaporation and trapping excessive salinity within the diurnal mixed layer due to the underlying diurnal thermocline (see Section 4.1.6). Substantial salinity and density variability noticeable in the profile at 19:00 is because of convective rainfall.

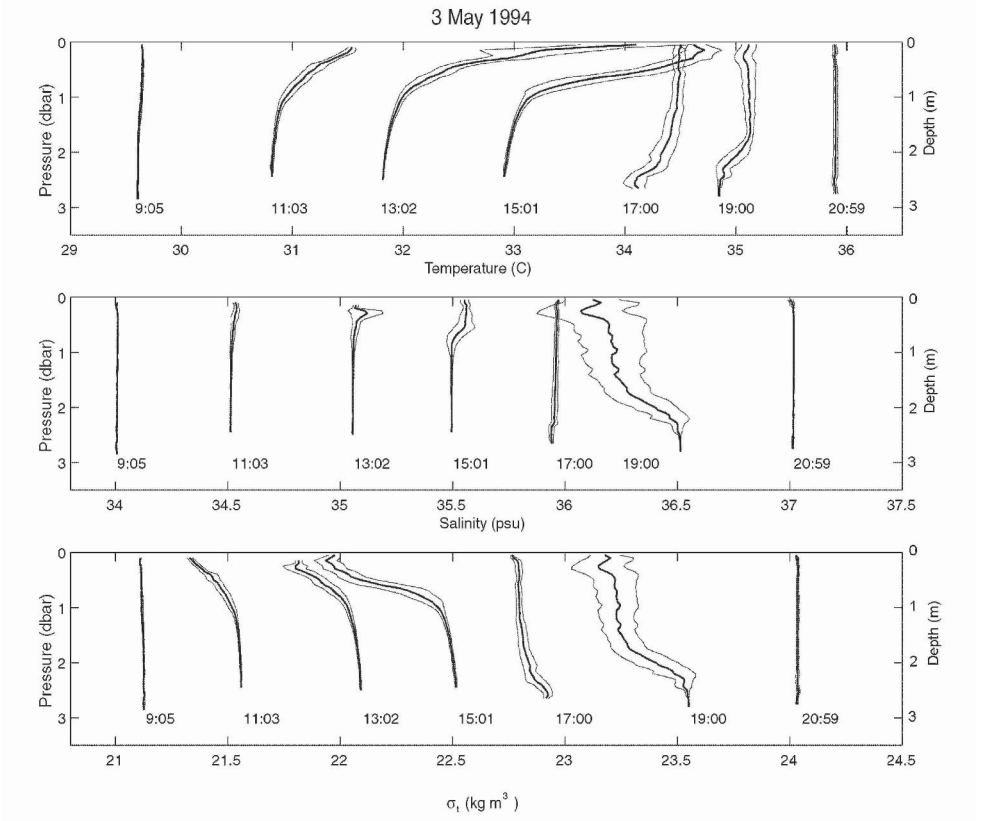


*Figure 4-23.* Vertical profiles of temperature, salinity and density obtained by averaging the bow sensor data within 0.1dbar pressure intervals in 10 minute segments. Successive temperature, salinity and density profiles are shifted by 1°C, 0.5 psu and 0.5 kg $m^3$ correspondingly. Under each profile the corresponding local solar time (LST) is given. The thin lines represent one standard deviation from the mean profiles. Reproduced from Soloviev and Lukas (1997a) with permission of Elsevier.

A series of individual vertical temperature profiles shown in *Figure 4-24* evidences that the depth of the diurnal mixed layer can decrease to ~10 cm or even disappear completely for some time under weak winds and strong insolation. The part of the vertical temperature profiles most near the surface sometimes has a slightly unstable stratification. Negative temperature gradients arise during daytime on account of a combination of the volume absorption of solar radiation in the upper cm of the ocean and the surface cooling (Kraus and Rooth, 1961; Turner, 1973; Soloviev, 1979; and Chapter 2).

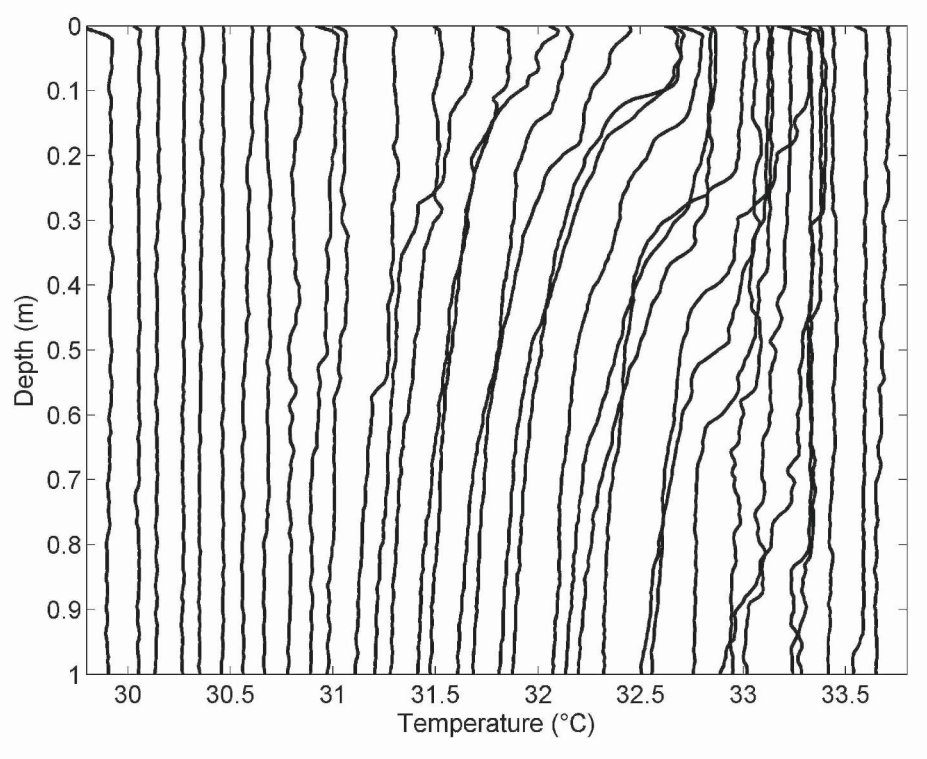


*Figure 4-24.* Temperature profiles in the upper meter of the ocean obtained by a free-rising profiler equipped with a 3 ms response time temperature sensor. These 35 profiles were obtained between 10:55 and 16:10 LST. Each successive temperature profile is shifted by $0.1P^{oP}C$. Note the cool skin effect in many of the profiles. Reproduced from Soloviev and Lukas (1997a) with permission of Elsevier.

The examples shown in *Figure 4-3c*, *Figure 4-23*, and *Figure 4-24* demonstrate that the diurnal cycle under low wind speed conditions is dramatically different from the high and moderate wind speed regime. Intensive insolation in low wind areas leads to large diurnal variations of sea surface temperature. There, the diurnal thermocline is found close to the ocean surface, where standard shipboard oceanographic measurements may be disturbed by the ship's hull. As a result, large diurnal warming events are often undetected during shipboard surveys and unaccounted for when quantifying sea surface temperature (SST).

### 4.4.2 Global distribution of large diurnal warming events

Satellites using infrared or microwave imagery provide a broad overview of SST and its spatial and temporal variability. Recent studies (Kawaii and Kawamura, 2002; Gentemann et al., 2003; Stuart-Menteth and

Robinson, 2003) indicate that extended regions of the World Ocean including the tropics, subtropics, mid- and, perhaps, a part of high-latitudes are subject to large diurnal warming events (*Figure 4-25*). These regions are correlated with low wind speed zones. The largest diurnal signal is observed in the tropics and the northern Indian Ocean. Freshening of the near-surface layer of the ocean by rainfalls and river discharges can also increase diurnal SST amplitudes. It is therefore not surprising that the regions highly susceptible to diurnal warming include the Inter-Tropical Convergence Zone, the northern Indian Ocean during the monsoon transitions, the western Pacific warm pool, and the waters off the west coast of Mexico. The regions experiencing larger diurnal warming are also the Mediterranean Sea and mid-North Atlantic in boreal summer and the southern mid-latitudes in austral winter.

Diurnal SST amplitude variability depends on the time of year (*Figure 4-26*), following the seasonal cycle of solar radiation. Satellite data also reveal remarkable interannual variability of diurnal SST amplitudes (*Figure 4-27*).

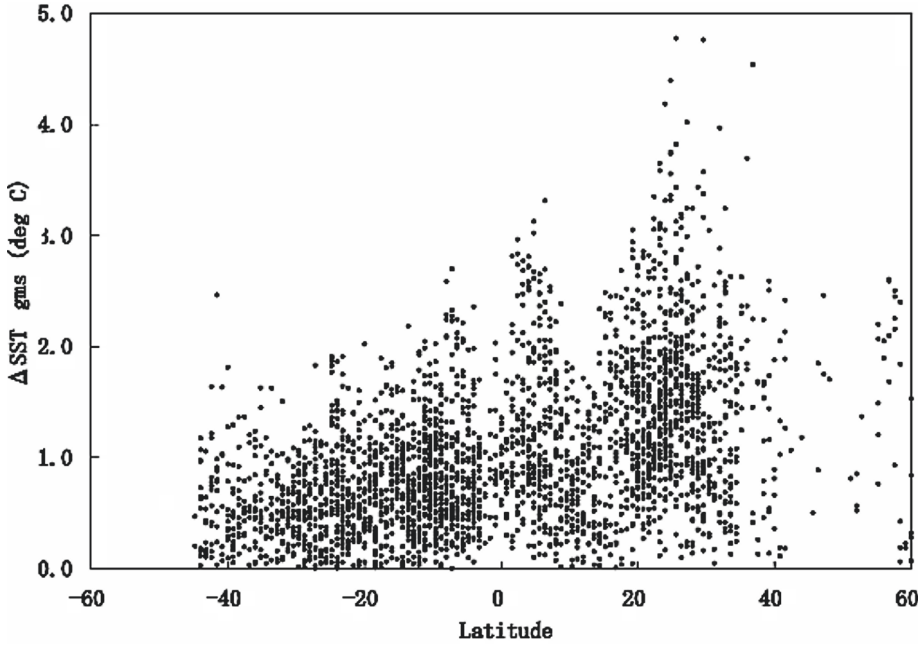


*Figure 4-25.* The latitudinal distribution of diurnal amplitudes (day minus night SST) on 15 June 1997 obtained from a geostationary satellite. Reproduced from Tanahashi et al. (2003) by permission of American Geophysical Union.

Accounting for diurnal SST variability is important for formulation of accurate boundary conditions for modeling the atmospheric general

circulation and weather prediction (Shinoda et al., 1998) and biophysical processes (McCreary et al., 2001). Diurnal cycling also has important implications for air-sea gas exchange (McNeil and Merlivat, 1996; Soloviev et al., 2001b). Relatively strong dependence of the $CO_2$ solubility on temperature suggests that diurnal warming shifts the partial pressure difference between atmosphere and the ocean surface towards lower $CO_2$ uptake by the ocean.

These studies also emphasize the necessity for improving theoretical methods of quantifying the SST variations due to diurnal cycling. The main reason is that clouds affect the space-based infrared imagery of the sea surface. The microwave measurement does not depend on clouds, but its R.M.S. accuracy is not better than 0.5 K (Gentemann et al., 2004), which may not always be sufficient to resolve the diurnal cycle of SST. Rains also affect the microwave signal.

An effective approach to resolve this situation is to enhance the remote sensing results with the diurnal mixed layer model forced with remotely sensed heat and momentum fluxes (the latter may not depend so critically on cloudiness as infrared SST methods). Under low wind speed conditions the diurnal warming, however, is a nonlinear function of heat and momentum fluxes. Simple regression type parameterizations of the diurnal SST amplitudes may not be effective in conjunction with remote sensing methods because, strictly speaking, they require tuning empirical coefficients for each region and event. An accurate model of the diurnal cycle combined with remotely sensed data may improve the accuracy of estimating the temperature difference across the diurnal thermocline globally (including regions with cloud cover) compared to the use of regression type parameterizations.

Adequate sampling is another critical factor for realistic simulation of large diurnal warming episodes because they depend not only on instantaneous fluxes but also on their history (at least from sunrise). The fundamental problem is that for polar orbiting satellites, track-repeat times are too long to resolve the diurnal cycle of SST. A multi-satellite approach including geostationary satellites can help in solving this problem. In particular, the International Satellite Cloud Climatology Project (see Section 1.4.4) has demonstrated the possibility of providing short wave radiation data globally every 3 hours.

A variety of retrieval schemes to derive boundary layer parameters from polar orbiting satellites of the NOAA and DMSP series have been developed (Katsaros et al., 1981; Schlüssel and Luthardt, 1991; Wick et al., 1992; Bauer and Schlüssel, 1993; Emery et al., 1994; Chou et al., 1995). These retrieval methods can be used to estimate surface heat and momentum fluxes (Schlüssel et al., 1995; Schlüssel , 1996; Quilfen et al., 2001).

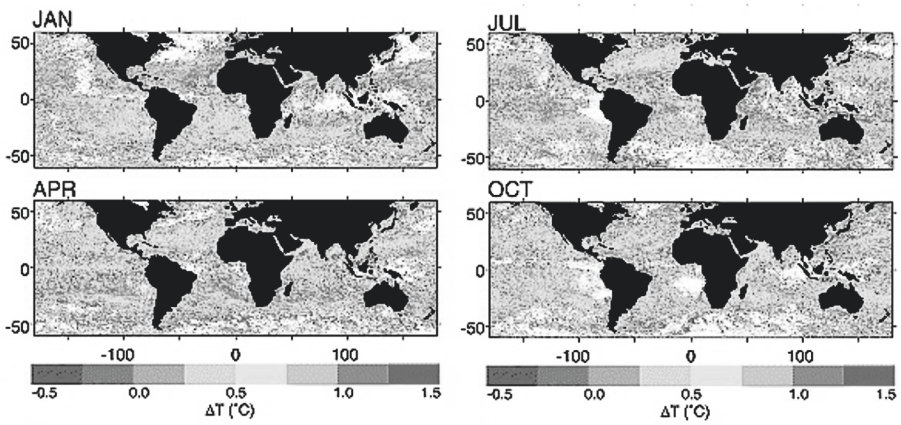


*Figure 4-26.* Seasonal distribution of diurnal warming for 1989: Monthly mean $\Delta T$ computed from daily day-night SST differences for January, April, July, and October. Reproduced from Stuart-Menteth et al. (2003.) by permission of American Geophysical Union.

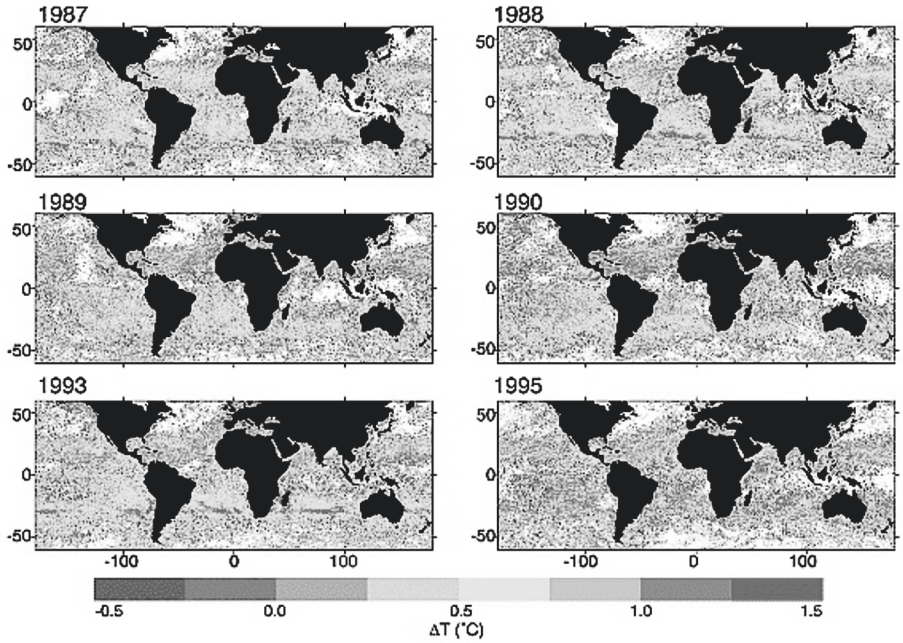


*Figure 4-27.* Interannual distribution of monthly mean $\Delta T$ computed from daily day-night SST differences. Monthly mean $\Delta T$ for January for 6 years (1987, 1988, 1990, 1993, and 1995). Reproduced from Stuart-Menteth et al. (2003.) by permission of American Geophysical Union.

Applying these data to mixed layer modeling faces some problems. In particular, the relative error of wind speed measurement with microwave methods approaches 100% in low wind speed zones. Fortunately, the sensitivities of the diurnal mixed layer depth and warming rate to wind diminish with decreasing wind speed, because of increased contributions from convection (Soloviev, 1981).

The convective mixing is driven by the net surface heat flux $Q_0$, which is the sum of sensible, latent, and net longwave radiation fluxes. The accuracy of the retrieval of these fluxes depends on averaging period. Achieving a time resolution of a few hours necessary for accurately modeling the diurnal cycle is still a challenge but one, which can be addressed with a multi-satellite approach.

### 4.4.3 Physics of large diurnal warming events

The Oboukhov buoyancy length scale,

$$L_O = u_*^3 / \left[ \kappa \alpha_T g Q_n / \left( c_p \rho \right) \right], \tag{4.35}$$

has a cubic dependence on friction velocity while the Ekman length scale,

$$L_E = u_* / f \,, \tag{4.36}$$

has a linear dependence. (Here $Q_n$ is defined according to (4.4).) When wind speed $U_{10}$ drops, the friction velocity $u_*$ also drops approximately as $U_{10}$, and according to (4.35) the Oboukhov length scale strongly reduces. The smaller of the two length scales, $L_O$ and $L_E$, determines the mixed layer depth (provided that $L_O$ is not negative), and the transition between "rotational" and "buoyant" regimes depends on the ratio between the Oboukhov and Ekman length scales. The buoyancy forces thus dominate Coriolis forces when

$$\frac{L_O}{L_E} = \frac{c_p \rho u_*^2 f}{\kappa \alpha_T g Q_n} << 1 \tag{4.37}$$

Qualitative analysis of (4.37) suggests that the buoyancy forces should dominate over rotational forces under low wind speed conditions. The range of wind speeds where buoyancy dominates over rotation increases towards the equator where $f \to 0$.

For the rotational regime, the equilibrium diurnal mixed layer depth is proportional to the Ekman length scale, ($h_D \sim L_E$). In the model with isolating boundary conditions at the bottom of the diurnal mixed layer the rate of diurnal warming is accordingly as follows:

$$\Delta T / \Delta t = \frac{-Q_n}{c_p \rho h_D} \sim \frac{-Q_n}{c_p \rho L_E} = \frac{-Q_n}{c_p \rho} \frac{f}{u_*} = \frac{-Q_n}{c_p \rho} \frac{f}{C_{10}^{1/2}} U_{10}^{-1} \sim U_{10}^{-1}. \qquad (4.38)$$

For the buoyant regime, which is associated with low wind speed conditions, the rate of the diurnal warming from equation (4.5) is $\Delta T / \Delta t \sim U_{10}^{-3}$. The cubic dependence of the diurnal warming rate on wind speed leads to substantial distinction between the high and low wind speed regimes, which are separated by a critical wind speed of about 4-5 m s$^{-1}$.

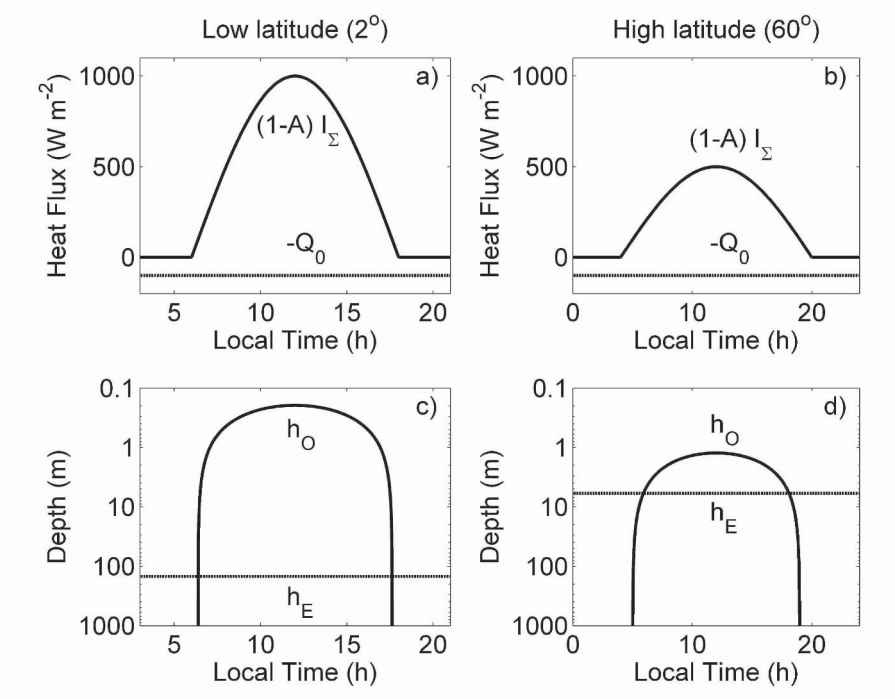


*Figure 4-28.* Idealized heat fluxes for low (a) and high (b) latitudes. Corresponding diurnal mixed layer depth estimates from relationships $h_O = c_O L_O$ and $h_E = c_E L_E$, where $c_O = 2$, $c_E = 0.25$, and $L_O$ and $L_E$ are determined from equations (4.35) and (4.36) respectively (b, c). In both examples, wind speed is $U_{10} = 2.5$ m s$^{-1}$, surface salinity $S_0 =$ 35 psu, and net heat flux $Q_0 = 100$ W m$^{-2}$. Surface temperature $T_0$ is 28°C for the low latitude example and 5°C for the high latitude example.

The above estimates imply that the entrainment at the lower boundary of the diurnal mixed layer is negligible. The entrainment conditions are incorporated into the analysis in Section 4.2.2, in the framework of parameterizations and numerical models. In particular, this leads to a $u_*^{-2}$ rather than $u_*^{-3}$ dependence for the diurnal temperature amplitude (as well as a $u_*^{0}$ rather than $u_*^{-1}$ dependence for the diurnal jet amplitude).

From the above analysis it is also obvious that large diurnal warming events are exclusively associated with the buoyant regime in the near-surface layer of the ocean. Inequality (4.37) is thus a necessary condition for the development of large diurnal warming events. *Figure 4-28* shows results of calculations of the equilibrium mixed layer depths for low and high latitudes at a low wind speed. Interestingly, during intense diurnal warming, inequality (4.37) can be satisfied for both low and high latitudes. This suggests that large diurnal events can be observed not only in mid- and low latitudes but also at relatively high latitudes (during the boreal or austral summer, respectively), which is consistent with the satellite-derived diurnal amplitudes shown in *Figure 4-25*.

Rotation effects nevertheless can indirectly influence the diurnal cycle even under low wind speed conditions by affecting dynamics of the diurnal jet (see Section 4.2). The Coriolis force deflects the diurnal jet to the right (left) of the wind in the northern (southern) hemisphere. Under the same environmental conditions, the magnitude of the diurnal jet is maximal in equatorial regions, where the direction of diurnal jet coincides with the wind stress direction.

It should be noted that similar relationships hold for the rain-induced mixed layer. The buoyancy flux due to rain can play a similar, stabilizing role as the buoyancy flux due to solar heating. This can explain substantial drops of salinity observed in the rain patches in low wind speed zones.

In the polar seas where SST can drop to $0^oC$ (or even below it), the thermal expansion coefficient is small. The buoyancy contribution due to the absorption of solar radiation diminishes, and the buoyancy effects can no longer dominate over rotation effects. An exception is the marginal ice zone with melting ice where the freshwater supply leads to restratification of the upper ocean mixed layer. Fine structure of the near-surface layer of the polar seas is considered in Section 4.6.

## 4.5 Modeling Large Diurnal Warming Events

### 4.5.1 Radiative-convective mixed layer

Raschke (1975) calculated vertical profiles of temperature in the upper ocean during equinoxes under the assumption of no turbulent mixing and no

surface cooling. These vertical profiles showed that the heating depends strongly on latitude and could amount to as much as 10 to 30°C per day in the uppermost centimeters of tropical and subtropical oceans. It is interesting that during midsummer the subpolar ocean in the summer hemisphere can be exposed to even more radiative energy than near the equator because of the longer days. These high heating rates do not result in so big actual changes of the water temperature because internal turbulent processes immediately transport the absorbed thermal energy into deeper layers, and because some energy is lost to the atmosphere above.

In the presence of both volume and surface sources of heat, the vertical flux of heat near the surface is

$$Q(z) = Q_0 - (1-A)I_\Sigma\left(1 - f_R(z)\right), \tag{4.39}$$

where $I_\Sigma$ is the insolation, $A$ is the sea surface albedo , function $f_R(z)$ characterizes the absorption of solar radiation with depth (see Section 1.4.6), and $Q_0$ is the surface heat flux, which is a sum of latent, sensible, and effective longwave radiation flux ($Q_0 = Q_E + Q_T + I_L$). $Q$ changes sign at some depth $z_c$. This is the *compensation depth* determined from the equation,

$$0 = Q_0 - (1-A)I_\Sigma\left(1 - f_R(z)\right). \tag{4.40}$$

During daytime, $z_c$ often amounts to only a few millimeters (Soloviev, 1979).

The layer $0 < |z| < z_c$ can become convectively unstable since $Q > 0$. Discrete convective elements from this layer overshoot the compensation depth and penetrate into the stably stratified layer below (Kraus and Rooth, 1961). The kinetic energy generated in the convectively unstable layer $0 < |z| < z_c$ works against the buoyancy forces in the stable layer $z_c < |z| < h_c$, where $h_c$ is the penetration depth of convection. When $z_c$ is very small, the convection is close to a laminar regime, and, as a first guess, we will ignore the viscous dissipation of the kinetic energy balance.

Remarkably, $z_c$ does not depend on the ocean turbulence regime. Equations (4.39)-(4.40), however, imply an unlimited depth of the surface mixed layer. In fact, this depth is limited and equal to $h_c$.

The depth of penetration of convection into the stably stratified layer, $h_c$, can be determined from an integral model including the differential equations for temperature, salinity, and kinetic energy balance (Soloviev, 1979):

$$c_p \rho \frac{\partial T}{\partial t} = -\frac{\partial Q}{\partial z} + \frac{\partial I_R}{\partial z}, \tag{4.41}$$

$$\rho \frac{\partial S}{\partial t} = -\frac{\partial J}{\partial z}, \tag{4.42}$$

$$0 = -\frac{\alpha_T g Q}{c_p \rho} - \frac{\beta_S g J}{\rho} - \frac{1}{\rho}\frac{\partial E}{\partial z}, \tag{4.43}$$

where $S$ is salinity, $J$ is the salinity flux; $\alpha_T gQ/\left(c_p\rho\right) + \beta_S gJ/\rho$ is the net buoyancy flux, which can be related to the buoyant energy source/sink, $E$ is the vertical flux of the kinetic energy. These equations can be derived from equations (1.10), (1.11), and (1.24) under the following assumptions: potential temperature is equal to the thermodynamic temperature; there is no wind, rain, or upwelling; penetrating convection works mainly against stable stratification, therefore the dissipation term is negligible compared to other terms in the equation for the turbulent kinetic energy. Equation (4.43) for the turbulent kinetic energy is given in the stationary form because the equilibration time for turbulence is much smaller than for thermal and salinity inhomogeneities. The processes that shape the vertical temperature profile under calm conditions and strong insolation are schematically shown in *Figure 4-29*.

Soloviev (1979) suggested that under conditions of strong insolation (and calm weather) convection might become non-turbulent (laminar), which has recently been confirmed in numerical experiment by Verevochkin and Startsev (2000). Fortunately, the system of equations in (4.41)-(4.43) is valid for laminar convection as well.

In theory, under extremely strong solar radiation, the thermal convection may be completely suppressed (see Section 2.4). In that case, the problem is reduced to that of molecular heat diffusion with volume sources, and equation (4.43) becomes irrelevant.

Boundary conditions for the sea surface are formulated as follows:

$$Q\left(0,t\right) = Q_0,\ \mathrm{J}\left(0,t\right) = -\left(S_0/L\right)Q_E,\ E\left(0,t\right) = 0. \tag{4.44}$$

Boundary conditions at the bottom of the mixed layer formed by penetrative convection are (Kraus and Rooth, 1961):

$$Q(-h_c, t) = 0,\ \mathrm{J}(-h_c, t) = 0, E(-h_c, t) = 0. \tag{4.45}$$

These are isolating boundary conditions; entrainment fluxes at the bottom of the mixed layer are ignored. This assumption should not lead to significant errors when $h_c$ does not change substantially.

A small amount of heat and salt can penetrate through the bottom of convective mixed layer because of double-diffusion. A warmer and slightly saltier layer is formed near surface, which may result in convecting layers (Stern and Turner, 1969). This effect is not accounted for here, but is discussed in Section 4.1.6.

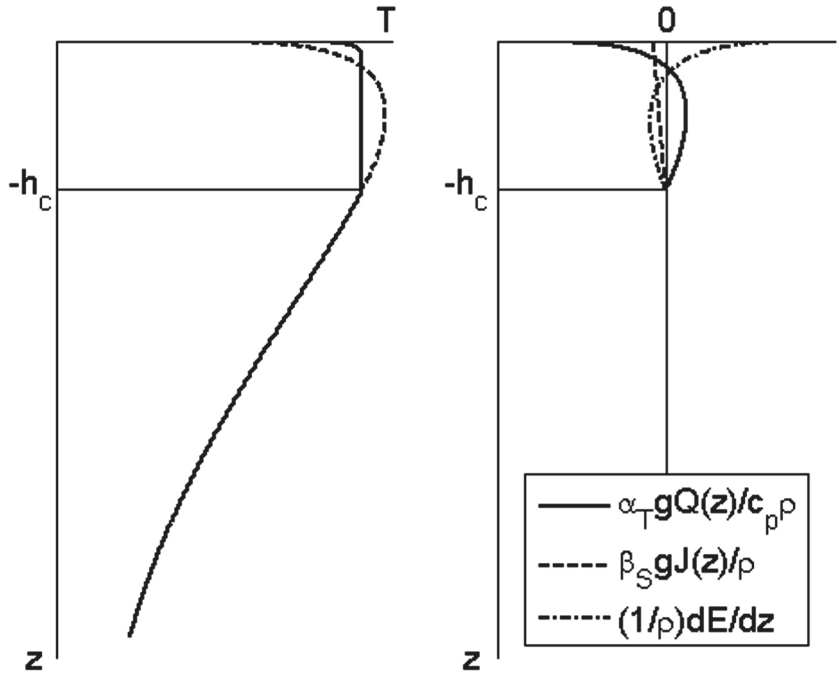


*Figure 4-29*, Formation of a convective mixed layer due to volume absorption of solar radiation and surface cooling under calm weather conditions. The penetration depth of convection for this example, $h_c$ = 0.073 m, is calculated from equation (4.48) for $Q_0$ = 140 W m$^{-2}$, $Q_E$ = 70 W m$^{-2}$, and (1-$A$) $I_\Sigma$ = 560 W m$^{-2}$. (a) Schematic representation of the temperature profile with penetrative convection (continuous line) and no convection (dashed line). (b) Terms of the turbulent kinetic energy (TKE) balance equation (4.43) within the convective mixed layer.

A customary constraint for integral models is that temperature and salinity profiles are constant with depth within the mixed layer (Kraus and Turner, 1967). The diurnal mixed layer, however, sometimes exhibits non-zero vertical temperature and salinity gradients (see examples in *Figure 4-2*c and

*Figure 4-2*0). Soloviev (1979) therefore relaxed the Kraus and Turner (1967) condition by requiring that $\partial T/\partial t$ and $\partial S/\partial t$ (rather than $T$ and $S$) do not depend on depth $z$. The latter condition does not prohibit dependence of $T$ and $S$ on $z$ within the radiative-convective layer.

By integrating equations (4.41) and (4.42) over $z$ with boundary conditions (4.44)-(4.45) and excluding terms $\partial T/\partial t$ and $\partial S/\partial t$, fluxes $Q$ and $J$ can be expressed as follows:

$$Q(z) = Q_0\left(1+\frac{z}{h_c}\right) - (1-A)I_\Sigma\left[1+\frac{z}{h_c} - f_R(z) - f_R(h_c)\frac{z}{h_c}\right], \tag{4.46}$$

$$J(z) = -\frac{S_0}{L}\left(1+\frac{z}{h_c}\right)Q_E, \tag{4.47}$$

and function $f_R(z)$ characterizes the absorption of solar radiation with depth..

Absorption of solar radiation in the upper meters of the ocean is then parameterized with 9 exponentials according to formula (1.62). The vertical profiles, $Q(z)$ and $J(z)$, expressed in terms of corresponding buoyancy fluxes are shown in *Figure 4-29*. Substituting $Q$ and $J$ in the energy balance equation (4.43) with their expressions (4.46) and (4.47), and integrating (4.43) over depth, a transcendental equation for the convective diurnal mixed layer depth $h_c$ is obtained:

$$1 - \frac{Q_0}{(1-A)I_\Sigma} + \frac{\beta_S Sc_p Q_E}{\alpha_T L(1-A)I_\Sigma} = \sum_{i=1}^{9}\left[\frac{2a_i}{\alpha_i h_c} - \left(1+\frac{2}{\alpha_i h_c}\right)a_i \exp(-\alpha_i h_c)\right], \tag{4.48}$$

Verevochkin and Startsev (2000) performed direct numeric simulation (DNS) of free convection taking into account the volume absorption of solar radiation. Results of their calculations are shown in *Figure 4-30*. Profile (a) corresponds to the ratio, $(1-A)I_\Sigma/Q_0 = 4$, showing a distinct convective-radiative mixed layer. Convective mixing confined within the quasi-homogeneous layer appears to be of laminar nature. The convection is completely suppressed for the ratio $(1-A)I_\Sigma/Q_0 = 4.75$ (profile b in *Figure 4-30*).

A convective diurnal mixed layer observed in the Sargasso Sea is shown in *Figure 4-31*. The vertical temperature profiles obtained with a free-rising profiler in the upper 5 m during afternoon hours under calm weather

conditions and 1.2 m swell revealed a shallow diurnal mixed layer and strong diurnal thermocline that developed at the top of the seasonal mixed layer of 20-25 m depth. Low relative humidity (~70%) and clear skies resulted in appreciable surface cooling ($Q_0 \approx 140$ W m$^{-2}$) even under calm weather conditions.

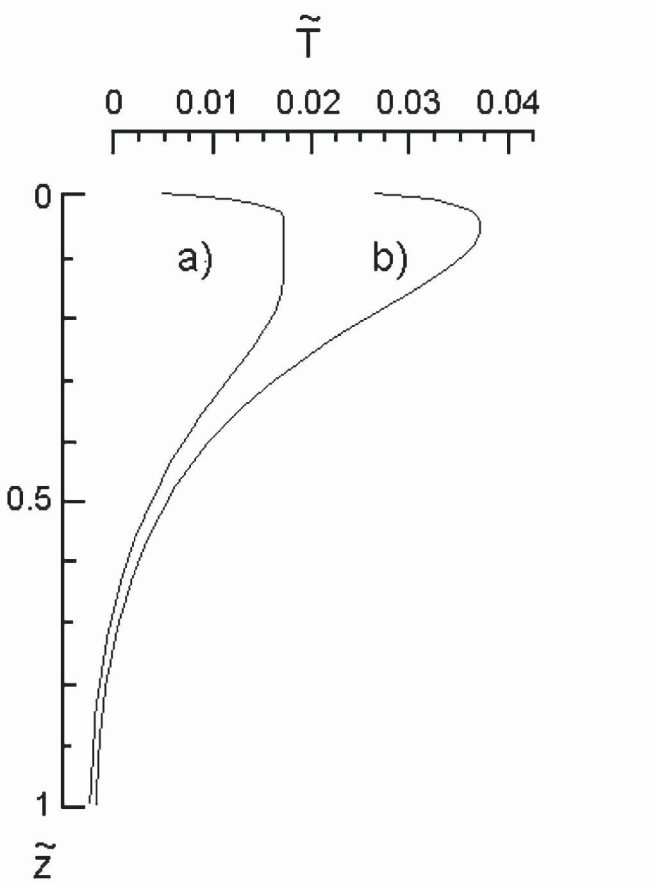


*Figure 4-30.* Numerical simulation of the radiative-convective equilibrium temperature profiles in the near-surface ocean by Verevochkin and Startsev (2000) for (a) $(1-A)I_\Sigma / Q_0 = 4$ and (b) $(1-A)I_\Sigma / Q_0 = 4.75$. Here $\tilde{T} = c_p \rho \kappa_T (T - T_h)/(Q_0 h)$ is the nondimensional temperature, $T_h$ is the bulk temperature of the upper ocean mixed layer, $\kappa_T$ is the molecular coefficient of kinematic thermal diffusivity; $\tilde{z} = z/h$ is the nondimensional depth, and $h$ is the layer depth determining the model domain. Note the similarity of the model profiles to the observations under calm weather conditions and strong solar insolation shown in *Figure 4-31*.

The solar irradiance during the first measurement (14:47 LT) was $(1-A)I_\Sigma$ = 594 W m$^{-2}$. There is a diurnal (convective) mixed layer in the

upper 7-12 cm of the ocean and a thermocline in the upper 1 m with a temperature difference of 1.3-1.4°C (*Figure 4-31a*). The vertical temperature profile obtained 17 minutes later (*Figure 4-31b*) has a similar diurnal mixed layer. The intermediate thermocline that is seen in *Figure 4-31b* near 3 m is presumably of advective nature.

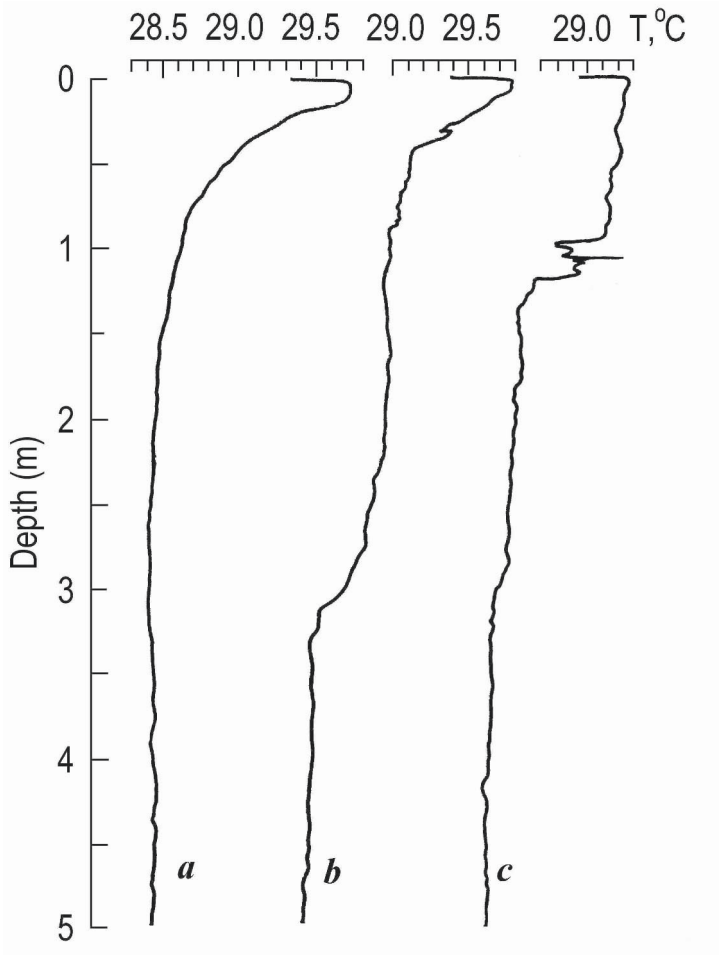


*Figure 4-31*. Vertical temperature profiles in the upper 5 m according to measurements with a free-rising profiler in the Sargasso Sea during POLYMODE on 1 October 1977 at (a) 14:47, (b) 15:04, and (c) 17:31. (After Soloviev, 1979.) Adapted by permission from American Geophysical Union from Izvestiya, *Atmospheric and Oceanic Physics* 15, 514–517, © 1980 AGU.

The temperature profile taken on the same day but in the evening time (17:31 LT) is shown in *Figure 4-31c*. The diurnal mixed layer depth increased to approximately 1 m. The diurnal thermocline became sharper; the temperature difference across the diurnal thermocline dropped to approximately 0.8°C. There are also inversions and other microstructure

features in the diurnal thermocline. They are presumably associated with overturning events, which are often observed in the diurnal thermocline during the deepening stage.

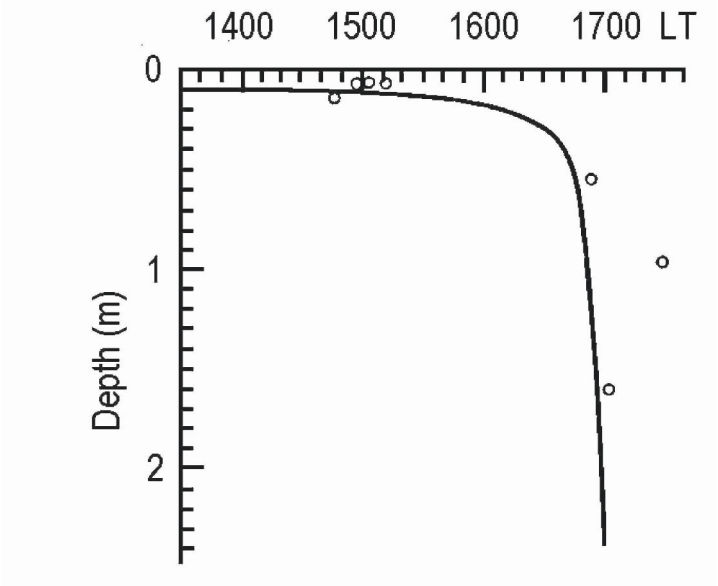


*Figure 4-32*. Diurnal mixed layer depth under calm weather conditions as a function of local time. Open circles are experimental data; continuous line is the depth of convective mixed layer calculated from (4.48). (After Soloviev, 1979). Adapted by permission from American Geophysical Union from Izvestiya, *Atmospheric and Oceanic Physics* 15, 514–517, © 1980 AGU.

Note that these measurements were made with a temperature sensor (DISA) having a response time of only 3 ms in water. At the 1 m $s^{-1}$ ascent speed of the profiler, this sensor partially resolved the cool skin of the ocean, which resulted in a remarkably sharp drop of temperature in the upper few millimeters of the ocean (*Figure 4-31*).

For estimated irradiance $(1-A)I_\Sigma$ = 560 W $m^{-2}$ and heat flux $Q_0$ = 140 W $m^{-2}$ for 14:47 LT, 1 October 1977 the compensation depth calculated from equations (4.40) is $z_c$ = 0.02 m. The discrete convective elements developing in this layer then penetrate to approximately 0.1 m depth according to the radiative-convective model (4.48), which is consistent with the vertical temperature profile taken at 14:47 LT

The DNS result for $(1-A)I_\Sigma / Q_0 = 4$ (*Figure 4-30*a) exhibits a temperature profile that is qualitatively consistent with the observations shown in *Figure 4-31*a, b. The temperature profiles taken around 1700-1800

LT showed that by 1700 LT the diurnal mixed layer had substantially deepened (*Figure 4-31*c). After 1700 LT, the evening deepening of the mixed layer slowed down significantly.

*Figure 4-32* shows the evolution of the diurnal mixed layer depth during afternoon and early evening hours estimated from the measurements with a free-rising profiler on 1 October 1977. Three of seven total profiles taken during this day are shown in *Figure 4-31*. In cases when a second quasi-homogeneous layer was observed, only the upper one is taken into account.

*Figure 4-32* also shows the radiative-convective mixed layer depth calculated from equation (4.48) for the case of no cloud conditions during POLYMODE (Soloviev, 1979). During daytime the model curve $h_c(t)$ is in good agreement with field data. It is remarkable that $h_c$ practically does not change during daytime hours although the solar radiation flux does change. At about 1600 LT, when the insolation drops below some level, $h_c$, starts a rapid increase. The model demonstrates an unbounded increase of the diurnal mixed layer depth around 1700 LT. The experimental mixed layer depth, however, does not follow the model prediction after 1700 LT. This is related to the fact that the model ignores entrainment fluxes at the bottom of the mixed layer, which become important when the diurnal mixed layer depth increases. The water densification due to evaporation only slightly increases $h_c$ (by about 5-10% during daytime).

### 4.5.2 Transition from radiative-convective to wind mixing regime

The wind induced mixing can be accounted for by adding the momentum balance equations (1.17) and (1.18) and by including the shear production term according to the equation for turbulent kinetic energy (TKE) balance (1.24). Under an assumption of horizontal homogeneity and with no rotation effects, the equations for momentum balance are:

$$\frac{\partial u}{\partial t} = \frac{1}{\rho}\frac{\partial \tau_{zx}}{\partial z}, \tag{4.49}$$

$$\frac{\partial v}{\partial t} = \frac{1}{\rho}\frac{\partial \tau_{zy}}{\partial z}, \tag{4.50}$$

Equation (1.24) for the TKE balance in stationary form then reads

$$0 = \tau_{xz}\frac{\partial u}{\partial z} + \tau_{yz}\frac{\partial v}{\partial z} - \frac{\alpha_T g Q}{c_p \rho} - \frac{\beta_S g J}{\rho} - \frac{1}{\rho}\frac{\partial E}{\partial z} - \varepsilon, \tag{4.51}$$

where $E = \overline{w'\left(b' + p'/\rho\right)}$ is the vertical flux of TKE. Dissipation term $\varepsilon$ is retained in (4.51). In contrast to the purely convective case described by equation (4.43), the dissipation term can no longer be ignored when turbulence production due to shear is included (Soloviev, 1982). Equation (4.51) is given in a stationary form because the turbulence regime equilibrates much faster than the diurnal mixed layer evolves.

Boundary conditions at the sea surface are formulated as follows:

$$Q(0,t) = Q_0,\ J(0,t) = -\left(S_0/L\right)Q_E,\ E(0,t) = E_0. \tag{4.52}$$

Boundary conditions at the bottom of the diurnal mixed layer, $z = -h_D$, are similar to (4.45):

$$Q(-h_D,t) = 0,\ J(-h_D,t) = 0,\ E(-h_D,t) = 0. \tag{4.53}$$

The boundary condition in the form (4.53) limits the model application only to conditions of no entrainment (decreasing or quasi-stationary mixed-layer depth).

The Kraus and Turner (1967) hypothesis is used to close the system of equations (4.41), (4.42), and (4.51):

$$-E_0 - \int_{-h_D}^{0}\left(-\tau_{xz}\partial u/\partial z - \tau_{yz}\partial v/\partial z\right)dz - \int_{-h_D}^{0}\varepsilon dz = m_1 u_*^3, \tag{4.54}$$

where $m_1$ is the nondimensional empirical constant.

Assuming again that $\partial_t T$ and $\partial_t S$ are not depth dependent within the mixed layer and integrating equations (4.41), (4.42), (4.49), (4.51) with boundary conditions (4.52), (4.53) and closure hypothesis (4.54), we obtain a transcendental equation with respect to the diurnal mixed layer depth, $h_D$, in the following form:

$$1 - \frac{Q_0}{(1-A)I_\Sigma} + \frac{\beta_S Sc_p}{\alpha_T L}\frac{Q_E}{(1-A)I_\Sigma} + \frac{2m_1 c_p \rho}{\alpha_T g}\frac{u_*^3}{h_D(1-A)I_\Sigma} = \sum_{i=1}^{9}\left[\frac{2a_i}{\alpha_i h_D} - \left(1 + \frac{2}{\alpha_i h_D}\right)a_i \exp(-\alpha_i h_D)\right], \tag{4.55}$$

Following Soloviev (1982), we select $m_1 = 0.9$.

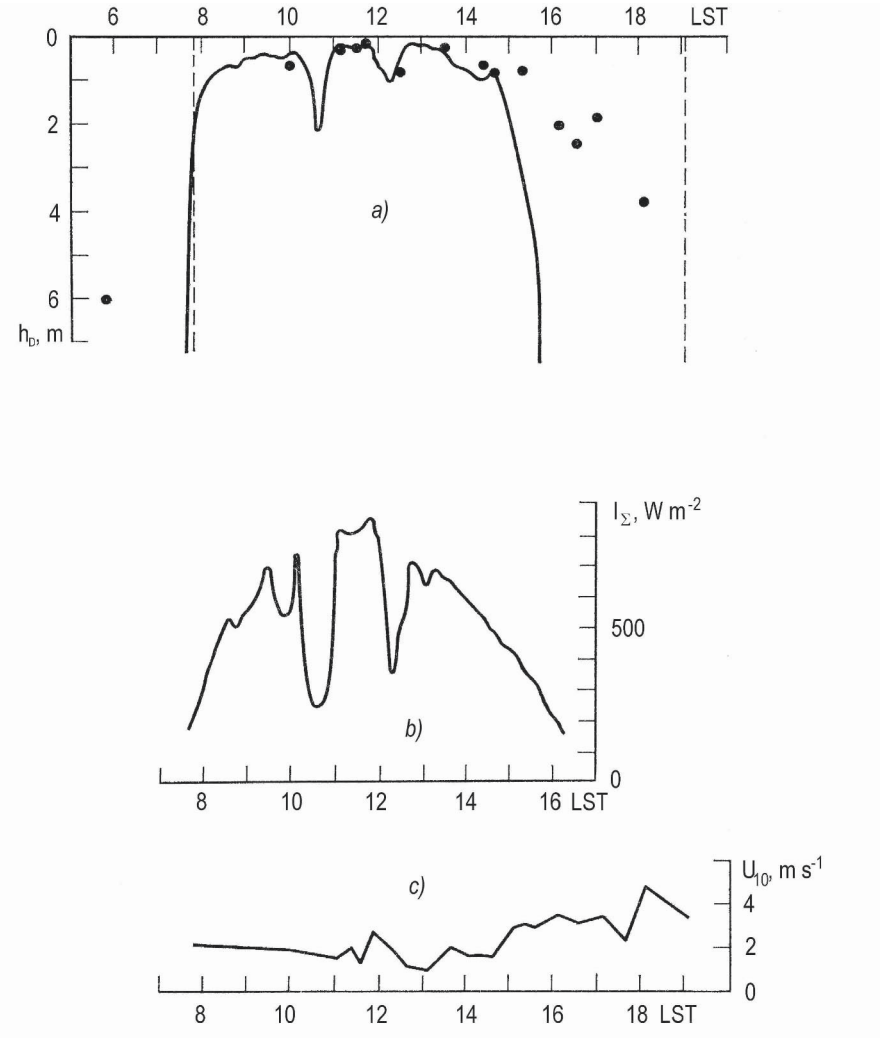


*Figure 4-33*. (a) Variation of the diurnal mixed layer depth at 35°03'N, 12°52'W derived from free-rising profiler measurements on 16 October 1978 (dots are experimental data, continuous line is the results of calculations from equation (4.55), vertical dashed lines indicate the measurements when no diurnal thermocline was found); (b) insolation (10 min averages); (c) wind speed measured in discrete time intervals (linearly interpolated in between the measurements). (After Soloviev, 1982.) Adapted by permission from American Geophysical Union from Izvestiya, *Atmospheric and Oceanic Physics* 18, 579–585, © 1983 AGU.

*Figure 4-33a* shows the variation of the diurnal mixed layer depth obtained from free-rising profiler measurements in the Atlantic Ocean. The insolation and wind speed also are shown (*Figure 4-33b, c*). The first profile

was made at 5:57 LST (before sunrise). There is a diurnal thermocline left from the previous diurnal cycle. The depth of this "relic" diurnal mixed layer is ~ 6 m (see *Figure 4-33a*). At the time of the temperature profile taken at 7:49 LST (immediately after sunrise), the relic thermocline had disappeared, though the new diurnal mixed layer and diurnal thermocline had not yet formed.

The temperature profile at 7:49 LST was practically homogeneous within the upper 10 m. This measurement is indicated in *Figure 4-33a* by a vertical dashed line. The temperature profiles taken later this day show the formation of a shallow diurnal mixed layer and diurnal thermocline and their subsequent evening deepening. By 19:06 LST, the diurnal thermocline disappeared from the depth range of the free-rising profiler. This measurement is indicated in *Figure 4-33a* by a second vertical dashed line.

The depth of the diurnal mixed layer calculated from equation (4.55) is in remarkable agreement with the experimental data even in the presence of substantial variability of the solar radiation due to clouds (*Figure 4-33b*). The situation, however, radically changes during the evening hours when the model depth tends to infinity and is no longer able to predict the actual depth of the diurnal mixed layer. This is because entrainment fluxes at the bottom of the diurnal mixed layer are not taken into account in (4.53).

Soloviev (1982) demonstrated that the effect of volume absorption of solar radiation leads to a reduced sensitivity of the model diurnal mixed layer depth to changes of external parameters. (This is true only at relatively small depths of the mixed layer, $h_D$ < 2 m.) For larger mixed layer depths, the effect works in the opposite direction, increasing the sensitivity of the mixed layer depth to changes in the air-sea heat fluxes and the wind speed. This, in particular, explains the characteristic $\Pi$ – shape of the diurnal mixed layer dependence on the time of the day clearly seen in *Figure 4-33*a.

In order to predict the diurnal mixed layer dynamics during the evening hours as well as the temperature difference across the diurnal thermocline, a numerical model is required that accounts for entrainment fluxes (see Section 4.5.4). Rotation effects can also then be included.

### 4.5.3 Parameterizations for the diurnal SST range

Early empirical parameterizations for diurnal SST amplitudes (for instance, Hasse, 1971; Deschamps and Frouin, 1984) operated with instantaneous wind velocities and instantaneous or peak solar radiation fluxes. Since the diurnal warming is a cumulative process, which depends on the "history" of the heat and momentum fluxes during the hours after sunrise, Lukas (1991) proposed connecting the SST range ($\Delta T_{\max}$) with daily average cloud fraction ($\bar{C}$) and daily average wind speed ($\bar{U}$) by a regression formula:

$$\Delta T_{\max} = 0.75 + 14.67 \frac{\left(1 - \bar{C}\right)}{\bar{U}^2}. \quad (4.56)$$

This parameterization was intended for the equatorial ocean, where the daily average cloud fraction is a good proxy for the cumulative daily insolation.

The presence of $\bar{U}^2$ in the right side of the regression implies that below some critical value of the wind speed the diurnal warming of the ocean surface layer rapidly increases. Equation (4.56) is derived using data only for wind speed exceeding 2.7 m $s^{-1}$, because the scatter of points strongly increases under very low wind speed conditions. This equation should not therefore be applied for very low and calm winds. It was not intended for use outside the western Pacific warm pool but it should be applicable to other regions with possible change of coefficients.

Clayson and Curry (1996) extended the Lukas (1991) approach to low wind speeds by modifying the set of determining parameters and separating wind speed conditions below and above a 2 m $s^{-1}$ threshold. Their regression parameterization of the diurnal SST range has the following form:

$$\Delta T_{\max} = a_0 + b_0\left(I_S\right) + c_0\left(\bar{P}\right) + d_0 \ln\left(\bar{U}\right) + c_0\left(I_S\right)\ln\left(\bar{U}\right) + f_0\left(\bar{U}\right), \quad (4.57)$$

where $I_S$ is the peak insolation, $\bar{P}$ is the daily average precipitation, and $\bar{U}$ is the daily average wind speed. The empirical coefficients for (4.57) as determined by Webster et al. (1996) from observations in the western Pacific warm pool are given in *Table 4-4*. Comparison of ship-measured $\Delta T_{max}$ variability with parameterization (4.57) shows a bias of 0.13°C (derived SST range lower than observed) with a standard deviation of 0.31°C and a correlation coefficient of 0.85 (Clayson and Curry, 1996). Inclusion of the nighttime rainfall into the parameterization is, however, problematic. In some cases it may improve the fit while in other case it can make prediction of the diurnal SST range even worse.

*Table 4-4*. Empirical coefficients for the Clayson and Curry (1996) parameterization (4.57) .

| $\bar{U}$ < 2 m $s^{-1}$ | | $\bar{U}$ > 2 m $s^{-1}$ | |
|---|---|---|---|
| Coefficient | Magnitude | Coefficient | Magnitude |
| $a_0$ | 0.328 | $a_0$ | 0.262 |
| $b_0$ | 0.002 | $b_0$ | 0.00265 |
| $c_0$ | 0.041 | $c_0$ | 0.028 |
| $d_0$ | 0.212 | $d_0$ | -0.838 |
| $e_0$ | -0.000185 | $e_0$ | -0.00105 |
| $f_0$ | -0.329 | $f_0$ | 0.158 |

The advantage of the regression type parameterizations is that they are simple and are easy for practical applications, especially when only limited information on the environmental conditions is available. A fundamental problem of such parameterizations is that, strictly speaking, they require adjustment of empirical coefficients to each geographical region, season, and, perhaps, even to synoptic conditions. Their application for the global coverage of large diurnal warming events is therefore very limited.

### 4.5.4 Numerical models

Early numerical models of the diurnal cycle employed the turbulent heat diffusion equation with constant mixing coefficient. Foster (1971a) undertook direct numerical simulation of an idealized diurnal cycle in the upper ocean by solving the equations of motion, heat, and continuity. Wind mixing was introduced by setting a constant turbulent mixing coefficient; the solar radiation was treated as a time dependent volume source. The surface cooling was represented by a constant heat flux from the ocean surface. The model in general reproduced some qualitative features of the diurnal cycle. Convection developed during nighttime but was suppressed by solar radiation during daytime. The initial wind induced turbulence was unimportant in the vertical transport after development of the nighttime gravitational convection. Yet for strong initial (wind-induced) mixing, the convection could not start during nighttime.

The main problem of Foster's (1971a) model was that the mixing coefficient did not depend on depth or on time. Thus, it could not be correct under light winds. Remember that an important feature of turbulent mixing in the upper ocean under light winds is that it both influences, and is influenced by, stratification arising due to diurnal heating. This results in a nonlinear response of the diurnal cycle to external forcing, which could not be captured by Foster's (1971a) model.

More realistic models of the diurnal mixed layer include the Kraus and Turner (1967) integral type model, a second moment turbulence closure mixed layer model (Wick, 1995), the KPP model (Large et al., 1994; Soloviev et al. 2001), the Price-Weller-Pinkel (PWP) model (Price et al., 1986), and the transilient model (Stull and Kraus, 1987; Soloviev and Lukas, 1997a). No perfect model of the diurnal cycle, however, has been developed: They all have advantages and disadvantages. Application of the integral model for the diurnal mixed layer and thermocline modeling is complicated by some limitations in parameterizing entrainment fluxes at the bottom of the diurnal mixed layer. The KPP model requires specifying the nonlocal transport term that has not been well defined. The PWP model does not have the correct asymptotic convective regime under conditions of very low wind

speed when the effect of volume absorption of solar radiation is of importance.

Below we consider modeling of the diurnal cycle for the example of the transilient model (though it also has a disadvantage in that it does not allow unstable stratification to develop). The transilient model deals with the parameterization of turbulent transports by a spectrum of eddies that transport fluid properties over a range of distances (Stull and Kraus, 1987). The transilient model specifies a velocity scale $u_l = u_*$ and a vertical length scale $l = \kappa |z|$, where $u_*$ is the frictional velocity in water, $\kappa$ is the von Karman constant, and $z$ is the vertical coordinate. For the unstably stratified near-surface layer (nighttime) Soloviev and Lukas (1997a) proposed to use a different scaling: $u_l = w_*$ and $l = L_c$, where according to Priestly (1959) $w_* = \left(L_c B_0\right)^{1/3}$, $L_c$ is the depth of the unstably stratified near-surface layer, and $B_0$ is the surface buoyancy flux. The absorption of solar radiation with depth was parameterized with a 9 exponential dependence (1.62).

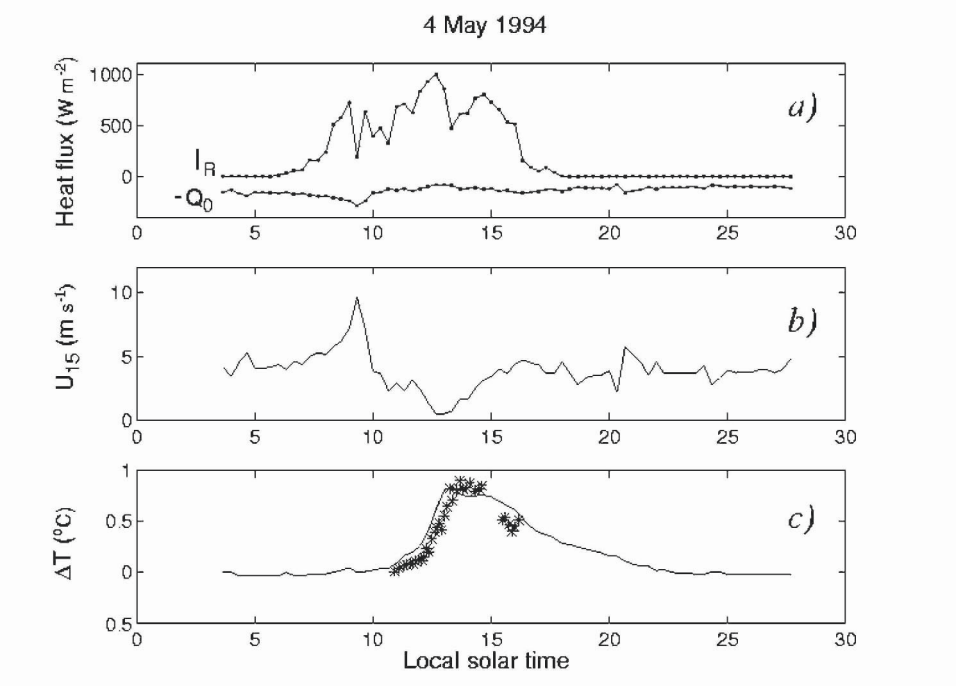


*Figure 4-34*. Evolution of the diurnal temperature increase averaged over 0-0.25 m. (a) Insolation ($I_\Sigma$) and surface cooling heat fluxes ($Q_0 = I_L+Q_T+Q_E$); (b) wind speed at 15 m height $U_{15}$; (c) temperature difference $\Delta T = T_0 - T_8$ in the near-surface layer of the ocean as measured by a free-rising profiler (asterisk) and simulated by the transilient model (contiguous line), here $T_0$ and $T_8$ are the temperature averaged over depth range 0-0.25 m and 8-8.25 m correspondingly. The free-rising profiler measurements are the same as shown in *Figure 4-24* Reproduced from Soloviev and Lukas (1997a) with permission of Elsevier.

*Figure 4-34* shows the results of a simulation of the diurnal cycle in the western Pacific warm pool area with the transilient model. The vertical resolution and the time step were 0.25 m and 15 s respectively. The vertical profiles of temperature and salinity were initialized to be a constant in the upper 20 m of the ocean, while the velocity profile was initialized with a 0.0004 $s^{-1}$ shear to ensure finite values of the Richardson number for the first step of the simulation. The model was forced with the wind stress and sensible and latent heat fluxes calculated with the TOGA COARE Version 2.5a bulk-flux algorithm. The net long-wave radiation flux was calculated using the parameterization of Simpson and Paulson (1979).

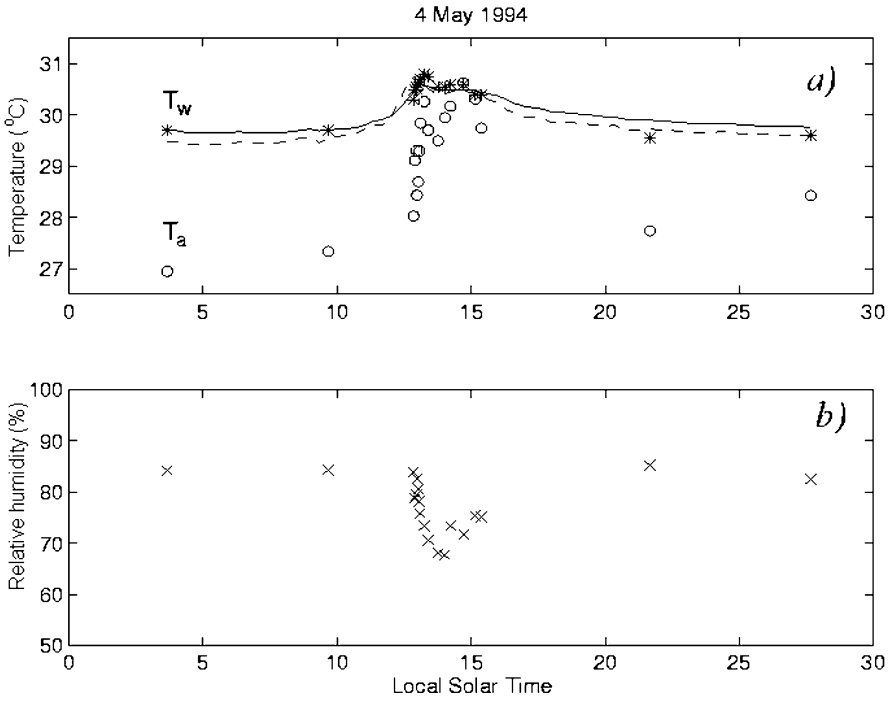


*Figure 4-35*. (a) Air and water temperatures on 4 May 1996. Here, asterisks are the bucket thermometer bulk temperatures, open circles are the dry air temperature (corrected to 10 m height), the contiguous line is the surface temperature (0-0.25 m average) calculated using the transilient model, and the dashed line is the SST calculated using the transilient model and the cool skin model. (b) relative humidity on 4 May 1996. Reproduced from Soloviev and Lukas (1997a) with permission of Elsevier.

*Figure 4-34* shows the heat fluxes and wind speeds for the vertical temperature profiles shown in *Figure 4-24*. Corresponding evolution of the temperature difference in the upper 8 m of the ocean according to the measurements with a free-rising profiler is compared to calculations of the same temperature difference with the transilient model. The model and field

data are in good agreement. The dependence of the diurnal heating on the wind speed is clearly seen in this figure. During the morning wind forcing, there is practically no rise in SST. Although diurnal warming is suppressed during morning hours, it increases strongly at 10 a.m. when the wind speed drops below 5 m $s^{-1}$.

According to *Figure 4-35a*, the daily variation in atmospheric temperature is even larger than it is in the ocean. Hoeber (1969) previously observed a similar effect in the equatorial region. This effect is supposedly because the moist equatorial atmosphere absorbs solar radiation directly during the daytime and is cooled again during the nighttime (see discussion in Kraus and Businger, 1994, p. 170).

Note the diurnal cycle of relative humidity (*Figure 4-35b*). The relative humidity decreases with the daytime SST increase, thus enhancing the latent heat flux. This is a manifestation of the negative feedback mechanism stabilizing the SST (Greenhut, 1978; Gautier, 1978; Lukas, 1990a; Katsaros and DeCosmo, 1990; Kraus and Businger, 1994).

Direct numerical simulation represents another possible approach to modeling the diurnal cycle of SST under low wind speed conditions. The model of Verevochkin and Startsev (2000) mentioned in Section 4.5.1 is one of the first attempts in this direction. The present version of this model, unfortunately, does not include wind mixing.

## 4.6 Fine Structure of the Near-Surface Layer in the Polar Seas

Few details are known about the near-surface layer of the polar seas. Barrier layers similar to those observed in the Indo-Pacific warm pool are possibly an important factor in the dynamics of the polar seas in marginal ice zones.

In the cold surface water of the polar seas, the coefficient of thermal expansion $\alpha_T$ is substantially smaller than in mid- and low latitude surface waters. The thermal component of the buoyancy flux, $-\alpha_T g Q_n / \left(c_p \rho\right)$, is therefore small. As a result, the suppression of turbulence due to absorption of solar radiation is less probable than in warmer environments. Substantial contribution to the buoyancy flux can, however, come from fresh water released by melting ice. (The salinity contraction coefficient $\beta_S$ does not depend as much on water temperature as $\alpha_T$ does.)

When the Arctic or Antarctic pack ice melts in spring, it releases fresher water, which leads to the formation of near-surface plumes. These plumes tend to spread horizontally in the near-surface layer, forming low salinity, stably stratified layers. The stable salinity stratification inhibits turbulent mixing, which effectively traps the air-sea heat and mass exchange near the

surface. This effect influences the process of spring melting of the pack ice as well as stimulating the spring algae bloom. The source of fresh water (melting ice) is often localized within the relatively thin near-surface layer of the ocean. In the Antarctic, for example, the typical thickness of the pack ice is 1 m.

Pack ice adds dramatic variation to all atmosphere-ocean interactions (McPhee, 1983; Muench, 1990; Gow and Tucker III, 1990). The classic problem of air-sea interaction obtains a new dimension when air-sea-ice interaction is considered. While the previous studies in polar seas (see Muench, 1990 and McPhee, 1990 for reviews) have revealed fundamental principles regarding the coupling of the ice cover, ocean, and atmosphere, applying these principles to conditions at the pack ice edge is not simple. The processes in the marginal ice zone are complicated by large spatial gradients and by strong temporal variability. For example, field data from the Greenland Sea (Buckley et al., 1979; Johannessen et al., 1983) show that the marginal ice zone is an area of extreme upper ocean variability with numerous fronts, upwelling or downwelling features, and eddies. In the marginal ice zone, the ice concentration varies from 100% in the interior to 0% at the edge, with large fluctuations occurring over distances of a few kilometers in both the across edge and along edge directions. Also, because of the effect of incoming surface waves, average floe size in the marginal ice zone changes from a few meters at the edge to thousands of meters at a distance of 100 km to 200 km into the interior (Wadhams, 1973).

Though the marginal ice zone represents a small percentage of the total ice cover in the polar region, its dynamical description is crucially important in many processes associated with the pack ice variation. These include (Brown, 1990): "…the growth, extent, and break up of the pack ice; the regional ocean circulations and associated problems of the ocean mixed-layer dynamics, biology, and thermal structure; the dynamics of bottom-water formation in the marginal ice zone; the enhanced biological activity with high phytoplankton concentration and large standing stock near the marginal ice zone; and the mechanics of the long-time influence of the pack ice and marginal ice zone on climatic and oceanic circulation."

The upper ocean processes and ice mass changes that control the vertical transfer of momentum, heat and salt between the ice and water are of fundamental importance in controlling ice extent and motion in the marginal ice zone. When the ice is blown over warm water, the underside melts; how fast it melts depends on the rate of heat exchange in the ocean-ice boundary layer (McPhee, 1990). At the same time, the transfer of heat, salt, and momentum modifies the upper ocean and changes the physics of subsequent ice and ocean interaction. When the upper surface ice is melted by radiative and sensible heat input, the resultant mass flux also has an impact on upper

ocean processes. The ice and upper ocean thus represent a strongly coupled system whose description should rely on a detailed understanding of these heat, salt, and momentum transfer processes.

Antarctic pack ice is relatively thin. The ice drift patterns prevent most Antarctic sea ice from reaching ages greater than 1-2 years. Wadhams et al. (1987) found the mean thickness of ice floes formed during one year to be about 50-60 cm only.

In the Antarctic, melt occurs mainly from the bottom and the sides of the ice, which are in contact with the ocean. Divergence of the pack creates more open water, allowing more solar radiation to be absorbed by the ocean with a subsequent warming of the surface water. As austral summer approaches the surface layer of the ocean warms up and the rate of melting of the ice increases. Ice edge retreat begins in November, accelerates in December and continues throughout February along the entire East Antarctic coastline. By November, areas of open water within the pack are no longer exclusively sites of enhanced ice production; rather they become a focus for the uptake of solar radiation and contribute to the rapid decay of the ice. By this process, the pack ice decays "from within" as well as by the retreat of the ice edge from north to south. Particularly rapid retreat occurs in regions where the ice edge extended furthest north at maximum extent.

*Figure 4-36* shows an example when a weak salinity-controlled upper-layer frontal structure was generated by melt water input in the summer marginal ice zone in the Antarctic. This front migrated as the ice edge retreated in spring, releasing melt-water to the upper ocean.

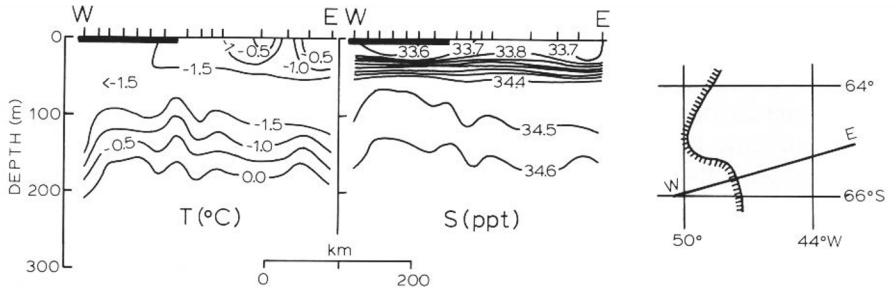


*Figure 4-36*. Vertical distributions of temperature (°C; left) and salinity (psu; middle) along a transect normal to the late summer ice edge in the northwestern Weddell Sea. Approximate location of the transect is shown to the right, with ice edge indicated by the heavy hachured line (ice cover to the left of the line). (After Muench, 1990.) Reprinted from *Polar Oceanography,* Academic Press © 1990.

McPhee (1983), Mellor et al. (1986) demonstrated that the stabilizing effect of the surface flux of freshwater reduces the interfacial drag coefficient and this appears to account for observed divergence of ice packs in the marginal ice zone. Strong stable salinity stratification in the marginal

ice zone can, however, lead to the coupling of the drifting ice with the internal wave field thus increasing the drag coefficient. This effect has been observed during MIZEX (Morrison et al., 1987; McPhee and Kantha, 1989).

At times when winds are blowing off the ice, the ice edges of the ocean are generally the site of regularly spaced (~20 km) surface bands of ice floes. McPhee et al. (1987) suggested that this is a result of the coupling between the internal wave field and ice floes; this coupling is possible due to stable salinity stratification in the near-surface layer of the ocean maintained by melting along the ice edges.

Smith and Nelson (1985) observed a dense phytoplankton bloom near a receding ice edge off the coast of Victoria Land in the Antarctic. The bloom area extended 250 km from the ice edge and was confined to waters where melting ice had reduced salinity. Presumably, stable salinity stratification in this area favored phytoplankton growth and accumulation.

An extensive phytoplankton bloom in the northern Gerlache Strait was studied during the Research on Antarctic Coastal Ecosystem Rates (RACER; see Karl, 1991). The bloom abruptly declined when the mixing layer depth changed. It was concluded that the phytoplankton bloom was controlled largely by the physical processes in the water column.

Chapter 5

# SPATIALLY-VARYING AND COHERENT STRUCTURES

*The upper ocean boundary layer is turbulent but not completely random…*

## 5.1 Introduction

The upper ocean is turbulent, in other words chaotic, because the Reynolds number is large. This chaos may include organized, so-called *coherent structures*.

In the presence of stochastic fluctuations and nonlinear interactions, quasi-stationary and stable states having an ordered structure can be formed naturally (Nicolas and Prigogine, 1977). Self–organization occurs in a variety of nonlinear dissipative systems; the formation of life may be regarded as one example of such a process.

Kraichnan (1967), Rhines (1975), Hasegawa (1985) and others developed the self-organization conjecture for hydrodynamic systems. Important common features of these systems are as follows: The system should contain more than one quadratic or higher-order conserved quantity in the absence of dissipation; when the dissipation is introduced, there exists a selective dissipation process among the conserved quantities, that is one conserved quantity decays faster than the other(s); and finally, the nature of the mode coupling through the nonlinear term(s) in the equation is such that

the modal cascade in one of the quadratic quantities is towards small wavenumbers.

An example of such a hydrodynamic system is the two-dimensional incompressible fluid. It conserves the total energy, $b(t) = \frac{1}{2}\rho \int_D |\vec{u}|^2 \, dV$, as well as a second quadratic quantity, the total squared vorticity (enstrophy), $W(t) = \frac{1}{2} \int_D \left|(\nabla \times \vec{u})\right|^2 dV$, where $\vec{u}(\vec{x},t)$ is the Eulerian velocity field defined in a three-dimensional domain $D$ (bounded or unbounded). The enstrophy is a measure for the total vorticity of the flow.

When finite viscous dissipation is introduced, the energy spectrum for two-dimensional hydrodynamic turbulence cascades to smaller wavenumbers. On the other hand, the enstrophy spectrum cascades to higher wavenumbers (normal cascade) and dissipates due to viscosity. Consequently, energy accumulates at the longest wavenumber permitted in the system. From an energy point of view, such a state is considered organized.

The process of self-organization in two-dimensional turbulence is discussed in detail in Section 5.2. On a horizontal scale $l$ exceeding the boundary layer thickness $h$, the vertical component of motion in the upper ocean boundary layer is effectively suppressed due to stratification, and the boundary layer processes are effectively two-dimensional. Mesoscale eddies and spirals, which are often seen in satellite images of the ocean surface, have been linked to two-dimensional turbulence. The baroclinic Rossby radius, $L_R$, determines the maximum horizontal scale of these coherent structures.

Another example of a nonlinear dissipative system with tendency to self-organization is the helical structure (Moffatt and Tsinober, 1992; Branover et al., 1999). The *helicity* of a fluid flow is defined as the integrated scalar product of the velocity field and the vorticity field in the following way: $\mathrm{H}(t) = \int_D \vec{u} \cdot (\nabla \times \vec{u}) \, dV$. On intuitive level the vortex that has a nonzero axial component of velocity is characterized by nonzero helicity. Langmuir circulations in the ocean and tornados and tropical cyclones in the atmosphere are examples of the helical structure.

Organized structures are a characteristic feature of the atmospheric boundary layer as well. For instance, atmospheric convection produces clouds. The clouds modulate radiative fluxes and are a source of freshwater flux at the air-sea interface and thus induce spatial patterns in the sea surface temperature and salinity. This effect is especially strong in the tropical warm pools, because of deep atmospheric convection accompanied by heavy rainfalls. The “images” of the atmospheric processes in the upper ocean turbulent boundary layer evolve according to the laws of two-dimensional

turbulence, producing organized structures in the upper layer of the ocean (possibly on scales different from the initial atmospheric scales). In Section 5.3, this process is described in the framework of a nonlinear diffusion model. This process is also interesting because the energy accumulation on large scales is accompanied by the development of narrow frontal zones between large-scale structures. If a front becomes sharp enough, it may interact with the wind stress via the mechanism of *Stommel's overturning gate* (Section 5.4).

Since the diurnal thermocline and rain-formed halocline are stably stratified, they can develop internal wave motions. Under low wind speed conditions the mixed layer depth reduces dramatically; as a result, the diurnal thermocline or rain-formed halocline is found in the upper few meters of the ocean. In this case, internal waves can be observed close to the ocean surface (Section 5.5). In some situations, perhaps due to interaction with shear or to resonant wave interactions, internal waves developing on the shallow diurnal thermocline become strongly nonlinear and exhibit billowing.

On horizontal scales $l \sim h$, the transition from two- to three-dimensional boundary layer regimes occurs. Various types of organized structures like penetrative convection, ramps, billows, and Langmuir cells are interpreted as modes of the turbulent boundary layer instability. These spatially coherent organized motions are discussed in Sections 5.6-5.8.

Ramp like-structures appear in near-surface horizontal temperature records. The ramp-like structures have been found under both stable and unstable stratification conditions. Their phenomenology and the theory of this type of organized motion are discussed in Sections 5.6.

In Section 5.7, we try to distinguish between the myths and realities regarding Langmuir circulations, one of the most controversial phenomena in the history of oceanography. Convection is discussed in the last section of this Chapter, Section 5.8. The importance of penetrative convection in the dynamics of the surface mixed layer has been addressed with a nonlocal parameterization scheme. How other types of organized structures contribute to nonlocal transport, however, is not yet completely clear.

## 5.2 Self-Organization in Two-Dimensional Turbulence

On horizontal scales exceeding the thickness of the upper ocean boundary layer, motions are quasi-two-dimensional due to stratification and/or rotation effects. Three-dimensional flow at large Reynolds numbers is chaotic and obeys statistical laws of isotropic turbulence, while a two-dimensional flow is governed by the anisotropic turbulence law and has the tendency to self-organization.

The upper ocean boundary layer is turbulent, yet it reveals features of organization. From this point of view, coherent structures in the ocean can be interpreted as a form of self-organization. Self-organization is a fundamentally nonlinear process; the mathematical description of the organized structures is hence complicated.

A distinction between three-dimensional and two-dimensional hydrodynamic processes is related to the effect of *vortex stretching*. Vortex stretching pulls matter towards the rotation axis of the vortex; owing to conservation of angular momentum it will rotate faster. Van Heijst (1993). compares this effect with the pirouette of a figure skater, who can increase her rotation rate by bringing both arms against her body. The absence of vortex stretching in two-dimensional flow leads to a spectral flux of the kinetic energy from small to large spatial scales. This property directly follows from the equation for the vorticity $\vec{\omega} = (\nabla \times \vec{u})$ of the flow, where $\vec{u}$ is the velocity vector in the Eulerian co-ordinate system.

In a two-dimensional flow field $\vec{u}$ = ($u$, $v$, 0), as a result, the vorticity vector $\vec{\omega} = (0,0,\omega)$ is always directed perpendicular to the flow direction. For inviscid flows the vorticity vector $\vec{\omega}$ is a conserved quantity. Two other conservation laws that follow from the inviscid vorticity equation are:

$$b = const \quad \text{and} \quad W = const \tag{5.1}$$

where $b$ is the kinetic energy and $W$ is the *enstrophy* (defined in Section 5.1).

The *inverse energy cascade* in the wavenumber domain, a fundamental property of two-dimensional flows, is illustrated below by considering the conserved quantities $b$ and $V$ in spectral form (Van Heijst, 1993). The kinetic energy and enstrophy are represented as follows:

$$b \sim \int_0^\infty e(k;t)dk = const \tag{5.2}$$

$$W \sim \int_0^\infty k^2 e(k;t)dk = const \tag{5.3}$$

where $e(k;t)$ is the wavenumber spectrum of kinetic energy at time $t$.

Suppose that the energy spectrum at some initial moment $t$ = 0 has a peak around a wavenumber $k_0$ (see schematic diagram in *Figure 5-1*). Due to nonlinear interactions in the flow, the kinetic energy peak will broaden with time. According to (5.2), the total kinetic energy (*i.e.*, the area underneath the curve of $e$) should remain constant. In order to satisfy (5.2) the spectrum broadening has to be associated with a decrease of the spectral peak value. At the same time, according to (5.3), the spectral distribution of enstrophy,

$k^2 e(k;t)$, must be conserved as well. In order to satisfy both (5.2) and (5.3) in the process of the peak broadening the energy has to be redistributed from larger $k$ to smaller $k$. As a result, the energy peak shifts to smaller $k$, and the energy spectrum becomes asymmetric (as schematically shown in *Figure 5-1*). This effect is called the inverse energy cascade, because the kinetic energy of the two-dimensional flow exhibits a spectral flux from smaller to larger length scales, which is opposite to the normal energy cascade that is observed in three-dimensional flows.

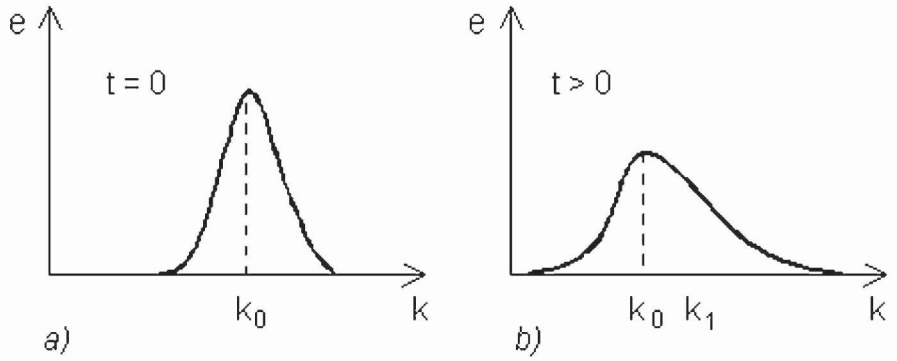


*Figure 5-1*. The kinetic energy peak that initially is at the wavenumber $k_0$ (a) shifts to smaller values of $k$ (b) in a two-dimensional flow due to nonlinear evolution of the system governed by conservation laws (5.2) and (5.3). (After Van Heijst, 1996.)

In two-dimensional flows, an initial chaotic state where the various characteristics are distributed over the whole wavenumber spectrum ("white noise" is an example), evolves into a spatially coherent vortex structure. The kinetic energy of the flow thus concentrates or, adopting the terminology from similar nonlinear processes in Quantum Mechanics, *condensates* in the large scale vortices. These vortices are often very stable and weakly dissipative.

The energy $b$ and the enstrophy $W$ are no longer conserved in two-dimensional turbulence in the presence of viscosity. If, however, the viscosity is not too large, the energy still shows a cascade to larger scales leading to organization. Two-dimensional flows are weakly dissipative, because molecular dissipation effects depend on velocity gradients and are relatively small on larger scales. In contrast to two-dimensional flows energy in three-dimensional flows cascades to smaller length scales and efficiently dissipates due to molecular viscosity.

An important insight into the process of self-organization in two-dimensional flows comes from numerical simulations. *Figure 5-2* shows the direct numerical simulation by McWilliams (1984). The striking result of

this simulation is that initially randomly distributed vortices evolve into isolated vortex structures concentrating much of the kinetic energy.

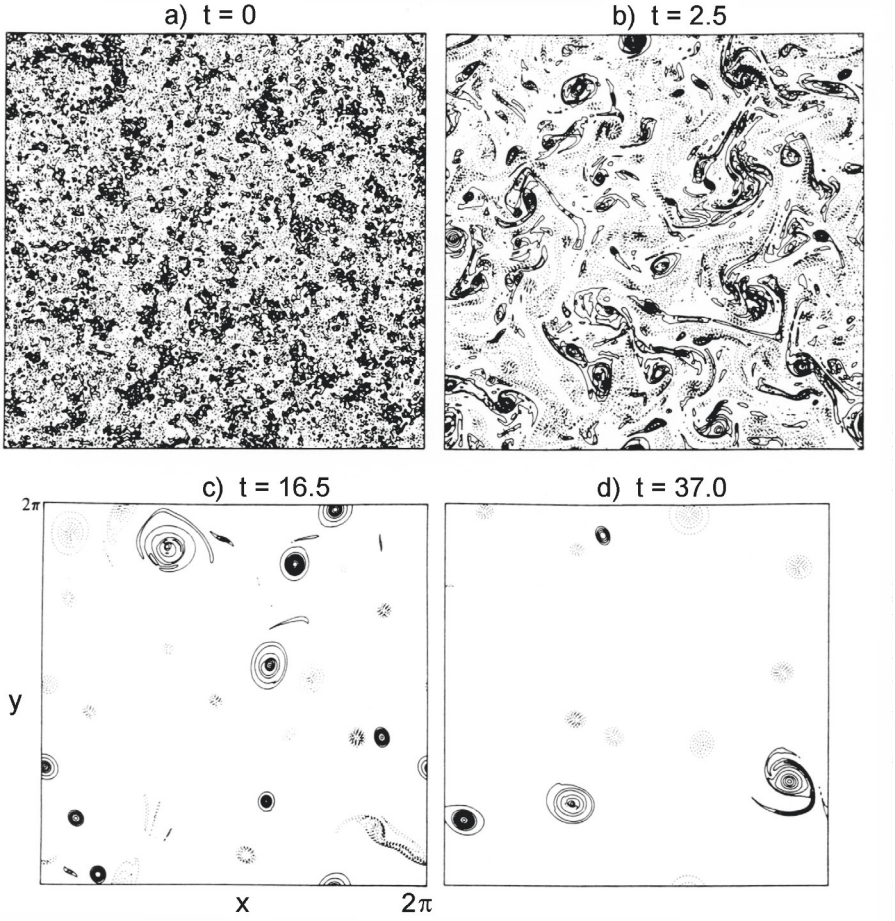


*Figure 5-2*. In a two-dimensional flow, initially randomly distributed vorticity (a) evolves into isolated vortex structures (b, c, and d). (Results of direct numerical simulation by McWilliams, 1984.) Reproduced with the permission of Cambridge University Press.

Many times, almost circular vortices develop, although the formation of other types of vortices is observed under certain conditions. Van Heijst and Kloosterziel (1989) proposed the following classification for stable vortices: 1) A *monopolar vortex*, approximately axis-symmetric (or slightly elliptic), possessing a net angular momentum; 2) A *dipolar vortex*, which consists of two counter-rotating vortices and has net linear momentum; 3) A *tripole vortex*, which consists of an elliptic central vortex, flanked by two weaker

satellite vortices of opposite circulation. Even higher order vortex structures form but seem to be unstable.

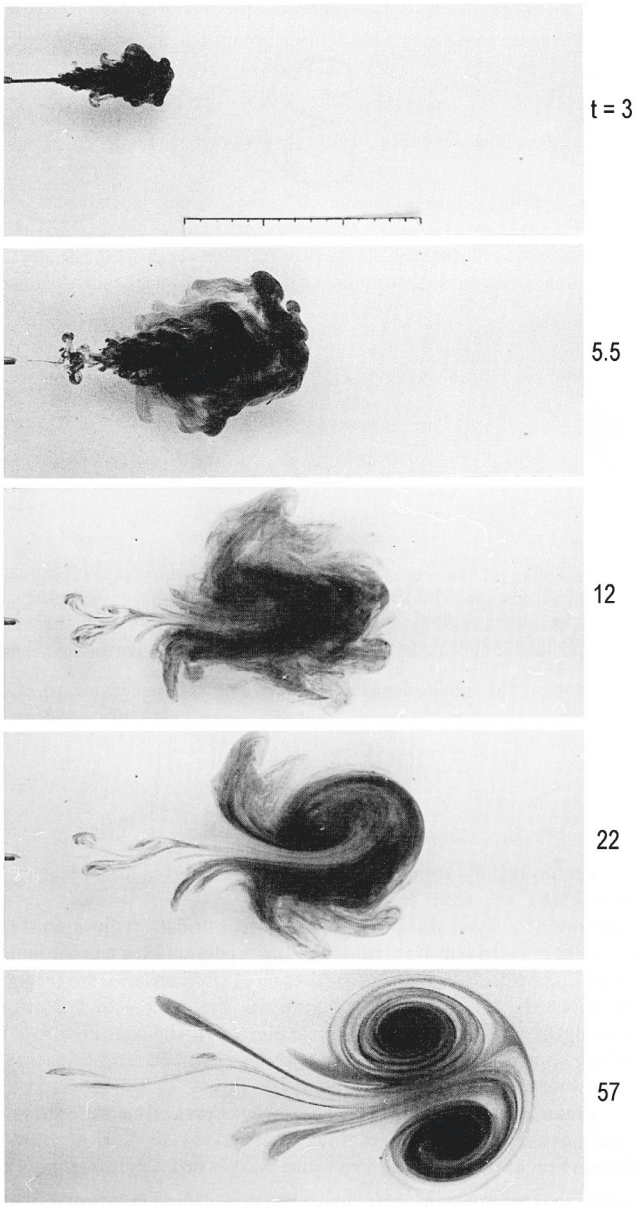


*Figure 5-3*. Top view photographs made during the laboratory experiment of Voropaev et al. (1991) in a stratified fluid: An organized dipolar vortex appears from a turbulent cloud. Scale is in cm, time (t) in s. Reproduced with the permission of Cambridge University Press.

In addition to numerical simulations, the dynamics of coherent vortices has been studied in laboratory experiments. The flow in the laboratory setting can effectively be made two-dimensional by the presence of rotation and/or stratification, magnetic fields, or geometry (Van Heist, 1993). Likely as a result of the variety of mechanisms used to make a flow two-dimensional, there is increasing interest not only within the field of geophysical fluid dynamics, but also in disciplines such as plasma physics and even astrophysics. In particular, the "Great Red Spot" on Jupiter is believed to be an organized structure – the eddy. Coherent structures are also likely present on the Sun and in the accretion disks of neutron stars.

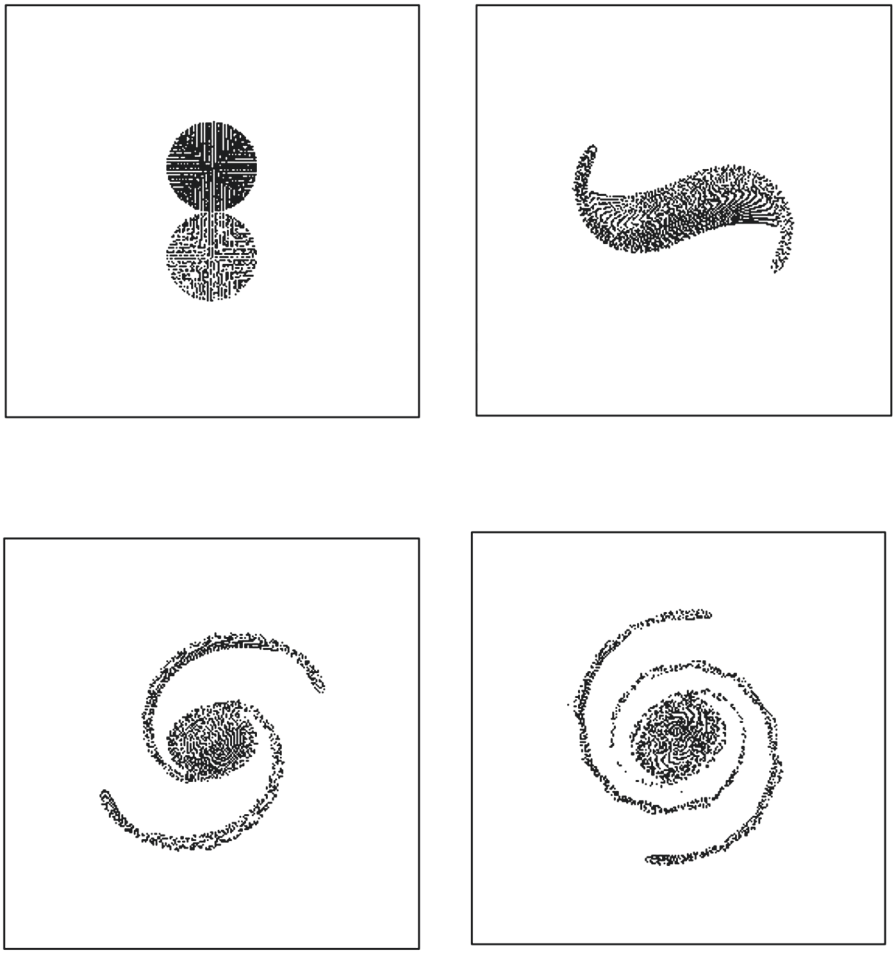

*Figure 5-4*. Merging of two identical monopolar vortices from the numerical simulation by Van Heijst (1993).

In the laboratory experiments of Van Heijst and Flor (1989) and Voropaev et al. (1991), a dipole was generated by horizontal, turbulent injection of a small amount of fluid in a tank filled with a continuously stratified fluid (*Figure 5-3*). Although the generated motion was initially three-dimensional, vertical motions of the injected turbulent cloud are rapidly suppressed by the surrounding stratification. As a result, the turbulence rather quickly assumes a two-dimensional character. Next, the effect of the inverse energy cascade increases the vortex scales, for instance, by merging vortices (as demonstrated in *Figure 5-4*), ultimately resulting in the appearance of an organized dipolar structure.

The interaction between separate vortices is an important part of the process of self-organization in two-dimensional flows. A basic interaction occurs between two monopolar vortices, either of equal or different size, strength and polarity. *Figure 5-4* illustrates merging of two identical monopolar vortices. At a specific distance from each other, the vortices merge to form a new vortex. At first the vortex is elliptic, but later it becomes axisymmetric. The 'strain' caused by the neighboring vortex causes the development of two characteristic spiral arms in both initial vortices, consisting of thin vorticity filaments. Formation of spiral arms is also observed in a single vortex placed in a non-uniform background flow, which may be caused by the presence of remote vortices.

The spiral eddies observed in the laboratory experiments can be seen in images of the ocean surface from manned space flights. Dr. Robert Stevenson was the first to discover such spiral eddies on the ocean surface. The spirals appear to be globally distributed, 10-25 km in size and overwhelmingly cyclonic in the northern hemisphere and anticyclonic in the southern hemisphere. *Figure 5-5* shows a visual image of spiral structures taken during a Space Shuttle mission. During this mission, the crew had excellent viewing conditions in the Southern Hemisphere:

"…During the first two days of the mission, the crew commander reported that the southern oceans were 'essentially featureless'. By the third day, the ocean had changed. The commander reported to Mission Control that the entire southern Indian Ocean, Tasman Sea, and southwestern Pacific Ocean were covered with spiral eddies and remained so for the rest of the mission. The crew took overlapping pairs of photographs showing the spiral eddy field in great detail. Streamlines of the flow into and between eddies formed slicks on the sea surface. At first the features were supposed to be the result of local wind action over the sea, but other data indicated that eddies extended to depths of several tens of meters and thus were an integral part of the dynamics of the upper ocean. Other data showed that the streamline slicks did indeed flow into eddies at speeds greater than the surrounding water." (Stevenson, 1998; 1999.)

*Figure 5-5.* Spirals on the ocean surface from the collection of NASA images (http://disc.gsfc.nasa.gov/oceancolor/shuttle_oceanography_web/oss_160.shtml).

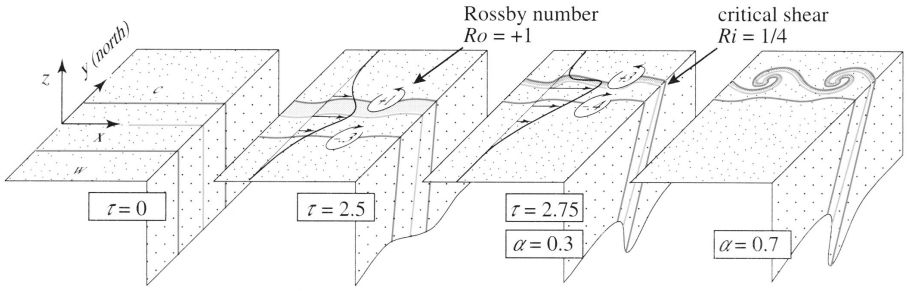


*Figure 5-6*. Cartoon of ocean spiral generation. An initial horizontal density gradient (cold to the north) in a mixed upper layer is portrayed by the central isopycnal (blue) and the two frontal isopycnals (red). With increasing time t, the isopycnals move together, tilt towards the north, translate northward and eventually converge at the surface on the positive frontal isopycnal. A developing eastward jet turns increasingly asymmetric, with strong cyclonic shear (large positive Rossby numbers) to the north and weak anticyclonic shear to the south. A downward tongue under the "north wall" and upwelling to the south modify the depth of the mixed layer. The Rossby number along the north wall increases rapidly from +1 to +3 between the times t = 2.5 and 2.75, when critical vertical shear develops near the surface. Horizontal shear instability develops along the north wall for $Ro > 1$, with an intensifying cat's-eye flow pattern characterized by nondimensional parameter $a$ (see Stuart, 1967 for details). Ambient surfactants are compressed and aligned along the north wall, and wound into cyclonic spirals. (After Munk and Armi, 2001.)

Munk and Armi (2001) proposed the explanation for spiral structures illustrated in *Figure 5-6*. The local frontogenesis process enhances the geostrophically balanced ambient ocean vorticity (which is of order $\pm 10^{-1} f$ ) and concentrates surfactants along a converging line. When the frontal shear becomes comparable to *f*, instabilities lead to cross-frontal flow accompanied by a twisting, *cat's-eye* circulation pattern. The cat's-eye circulation twists the convergence line and neighboring linear features into a cyclonic spiral, while stretching and further thinning the lines of surfactant concentration.

Near the Equator, thin lines on the sea surface rather than spirals are observed (*Figure 5-16*), due to diminished planetary vorticity. The next two sections, Section 5.3 and Section 5.4, elucidate the role of nonlinear interactions in the formation of organized structures in the near-surface ocean for the example of equatorial warm pools.

## 5.3 Horizontal Mixing as a Nonlinear Diffusion Process

Atmospheric convective complexes dominate the planetary boundary layer in the warm pool area and are responsible for the 3-5 m $yr^{-1}$ of precipitation. Convective rains produce surface *puddles* of the order of 10 km diameter containing appreciable salinity, temperature, and density anomalies. These puddles store significant potential energy, which when released in the form of gravity currents substantially contributes to mixing. This process is associated with vertical shearing, which involves nonlinear dynamics. Since it is a two-dimensional system, the initial disturbances have a tendency to self-organization.

### 5.3.1 Horizontal wave number statistics

We start our discussion from the analysis of some observable features of the horizontal wavenumber statistics in the warm pool area. *Figure 5-7* shows a record from a shipboard thermosalinograph (TSG) in the western Pacific warm pool obtained during TOGA COARE from a depth of 3 m (Delcroix et al., 1993). Rainfall was observed between $3^{o}$N and $3.5^{o}$N. This rainfall produced a localized salinity anomaly. In the temperature record, the freshwater puddle did not produce any prominent feature.

*Figure 5-7* represents one of 16 sections of the R/V *Le Noroit* made from $5^{o}$S to $5^{o}$N along $156^{o}$E during TOGA COARE from December 1992 through March 1993. The average density spectrum calculated from all 16 sections of the TSG data is shown in *Figure 5-8*. In the wavenumber range $k < 4 \cdot 10^{-4}$ $m^{-1}$, the experimental spectrum is approximated by a $k^{-1}$ dependence, which is consistent with the $k^{-1}$ law that follows from the theory of quasi-geostrophic two-dimensional turbulence for a passive tracer

(Batchelor, 1969; Kraichnan, 1975). According to the same theory, at even lower wavenumbers the $k^{-1}$ law transforms into a $k^{-5/3}$ spectral law. The statistics presented in *Figure 5-8*, however, are not sufficient to resolve the spectral dependence at low wavenumbers with sufficient confidence.

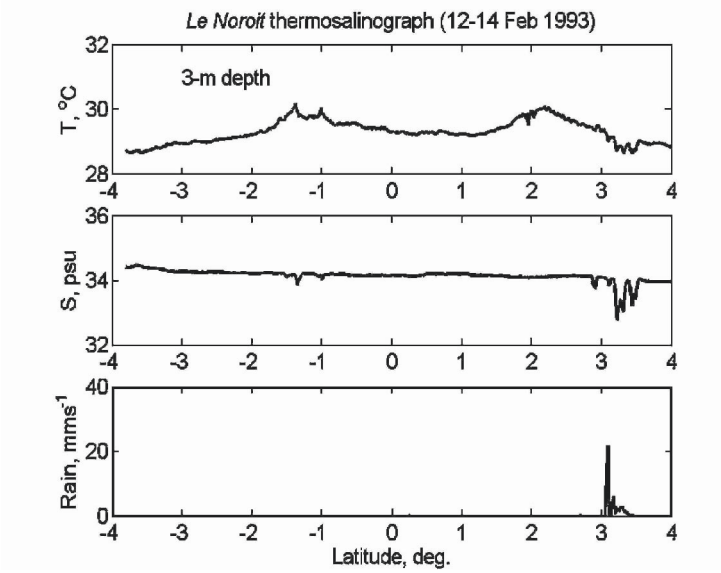


*Figure 5-7*. Patchy rainfall from convective clouds produces localized freshwater puddles in the near-surface layer of the ocean.

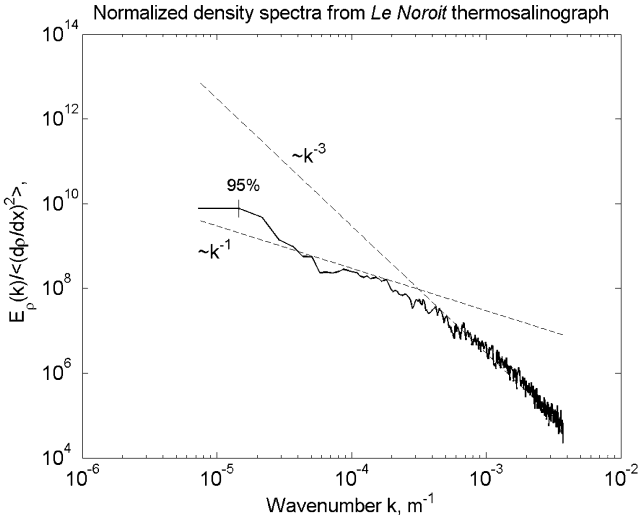


*Figure 5-8*. Scaled density wavenumber spectra from the *Le Noroit* thermosalinograph observations (averaged over 16 meridional sections).

For $k > 4 \cdot 10^{-4}$ m$^{-1}$, which corresponds to wavelengths $\lambda < 16$ km, the experimental spectrum switches to a $k^{-3}$ dependence. In this subrange, the experimental spectrum is not consistent with the theory of Batchelor (1969) and Kraichnan (1975). An explanation is that for submesoscales density can no longer be treated as a passive tracer.

The equatorial baroclinic Rossby radius for the density anomalies within the mixed layer of the warm pool area, $L_\beta$, is of the order of 10-20 km. Rotation effects therefore are not expected to be of primary importance on scales smaller than 10 km

### 5.3.2 Nonlinear advection-diffusion model

The process of puddle evolution is associated with vertical shearing, which involves Taylor's shear dispersion mechanism and nonlinear dynamics. Ferrari and Young (1997; hereafter FY97) and Ferrari et al. (2001) considered a non-rotating stratified fluid and developed a model for nonlinear horizontal diffusion. They used the Boussinesq approximation and a linear equation of state for seawater to derive the following system of equations:

$$D\vec{u} / Dt = -\nabla p + g(\rho - \rho_0) / \rho_0 \vec{z} + mix \tag{5.4}$$

$$\nabla \cdot \vec{u} = 0, \tag{5.5}$$

$$DS / Dt = mix \tag{5.6}$$

$$DT / Dt = mix \tag{5.7}$$

where $\vec{u} = (u, v, w)$, $g$ is the acceleration of gravity, $\rho$ is density, $\rho_0$ is a constant reference density; $D$ is the full (material) derivative operator, $\nabla$ is the gradient operator; and, "*mix*" indicates that an instantaneous homogenization is applied to momentum and the stratifying components.

Based on Taylor's shear dispersion mechanism, Young (1994) introduced a nonlinear dependence of the mixing coefficient on the buoyancy gradient, which, in the formulation of FY97, is as follows:

$$K_h = \gamma f(|\nabla_h B|)(\nabla_h B \cdot \nabla_h B), \tag{5.8}$$

where $\gamma = h^2\tau^3/96$, $h$ is the depth of the mixed layer, $\tau$ is the vertical homogenization time scale, $B = -g(\overline{\rho} - \rho_0)/\rho_0$ is the buoyancy, $\overline{\rho}$ is the fluid's density (averaged over the mixed layer depth and some time interval), $\rho_0$ is a constant reference density, $g$ is the acceleration of gravity, $\nabla_h$ is the horizontal gradient operator, and $f(|\nabla_h B|)$ is a non-dimensional function whose form depends on details of the hydrodynamic instabilities that dominate the flow.

Applying (5.8) to the equations for buoyancy (averaged over the depth of the upper ocean mixed layer), FY97 obtained the following nonlinear advection-diffusion equation:

$$\partial_t B + \vec{u} \cdot \nabla B = \gamma \nabla \cdot [f(|\nabla B|)(\nabla B \cdot \nabla B)\nabla B] + \Phi_B, \tag{5.9}$$

where $\vec{u}$ is the horizontal velocity field, and term $\Phi_B$ relates to the thermohaline fluxes from the top and bottom of the mixed layer.

### 5.3.3 Buoyancy flux through the bottom of the mixed layer

Turbulent entrainment, upwelling events, and internal wave effects can cause the horizontal modulation of the buoyancy flux through the bottom of the mixed layer. Horizontal wavenumber statistics below the mixed layer can help to understand this process.

*Figure 5-9* gives an example of the horizontal wavenumber spectrum averaged over 60 to 110 m depth range. These data are also from the western equatorial Pacific for approximately the same time period as the spectrum in the mixed layer shown in *Figure 5-8*. Comparison of the experimental spectra with the theoretical model of internal waves that accounts for the isotropic internal wave field and the lower modes of the $M_2$ baroclinic tide suggests that the internal wave processes could substantially determine the wavenumber statistics in this depth range and in the wavenumber range under consideration.

Internal waves modulate the vertical shear and the density gradient and, ultimately, the gradient Richardson number, $Ri$. The spectrum of the Richardson number associated with the Garrett and Munk model of internal waves is "white" (*i.e.*, it does not depend on frequency), except for the lowest few modes that are close to the inertial frequency. Near-inertial waves are associated with a drop in $Ri$. Overturning and turbulent entrainment occurs when $Ri$ drops below it critical magnitude (about 0.25). The buoyancy influx from the thermocline to the mixed layer caused by the isotropic internal wave field is therefore more probable on horizontal scales of inertia-gravity waves.

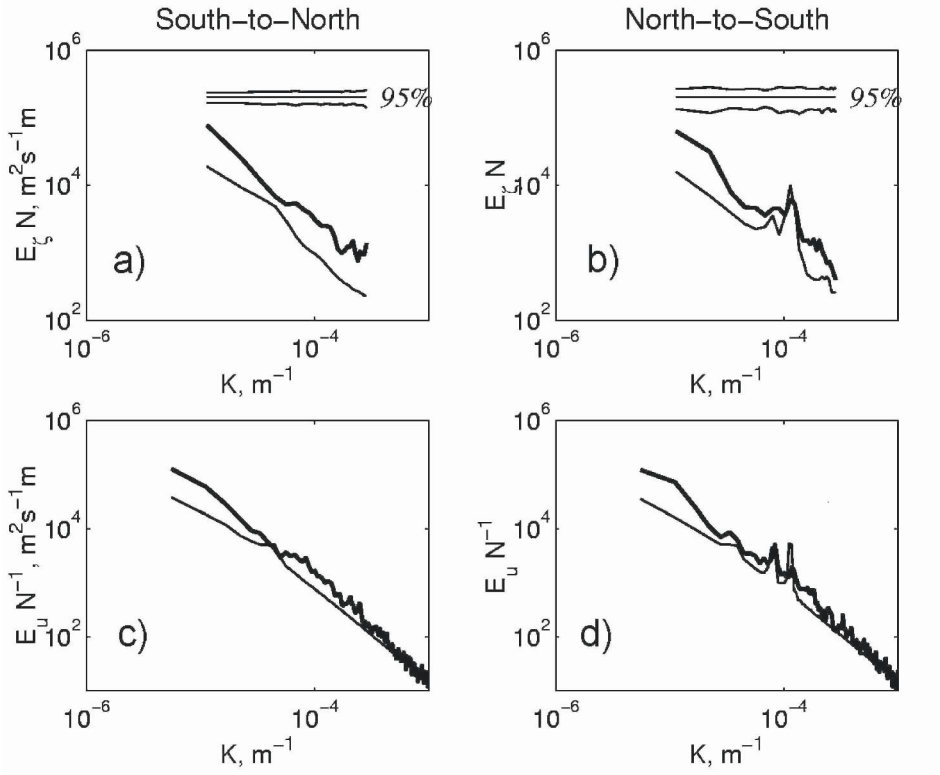


*Figure 5-9*. Comparison of the WKB-scaled (a, b) density displacement and (c, d) horizontal velocity spectra from the R/V *Le Noroit* South-to-North and North-to-South meridional sections (5°S to 5°N) with the internal wave towed spectral model. The experimental spectra (bold lines) are averaged within the depth range from 60 to 110 m. The model spectra (thin lines) represent the sum of the Feng et al. (1998b) tidal model and the Garrett-Munk wavenumber spectrum. Confidence intervals are also shown. The ADCP and SEASOAR data were collected by Eric Firing and Kelvin Richards.

Cabanes (1999) analyzed the modulation of the mixed layer thermodynamics by a long ($\lambda_{IG}$ ~1000 km), equatorial inertia-gravity wave using a quasi-two-dimensional model of PWP type (Price et al., 1994). He concluded that these waves could produce mixed layer temperature and salinity anomalies with the same horizontal length scale and a cascade of smaller scale anomalies due to the differential entrainment depending on the internal wave shear and atmospheric forcing.

Tidal motions constitute a significant fraction of the background velocity field in the COARE domain (note tidal peaks on the spectra from north-to-south sections in *Figure 5-9*). Having low vertical mode structure away from their generation region, the internal tidal waves have relatively small shear (Pinkel, 2000). The $M_2$ baroclinic tidal wave in the western equatorial

Pacific warm pool is, however, often accompanied by solitary internal wave packets (*solitons*), which, during spring tides, take the form of undular bores (*solibores*) (*Figure 5-10*).

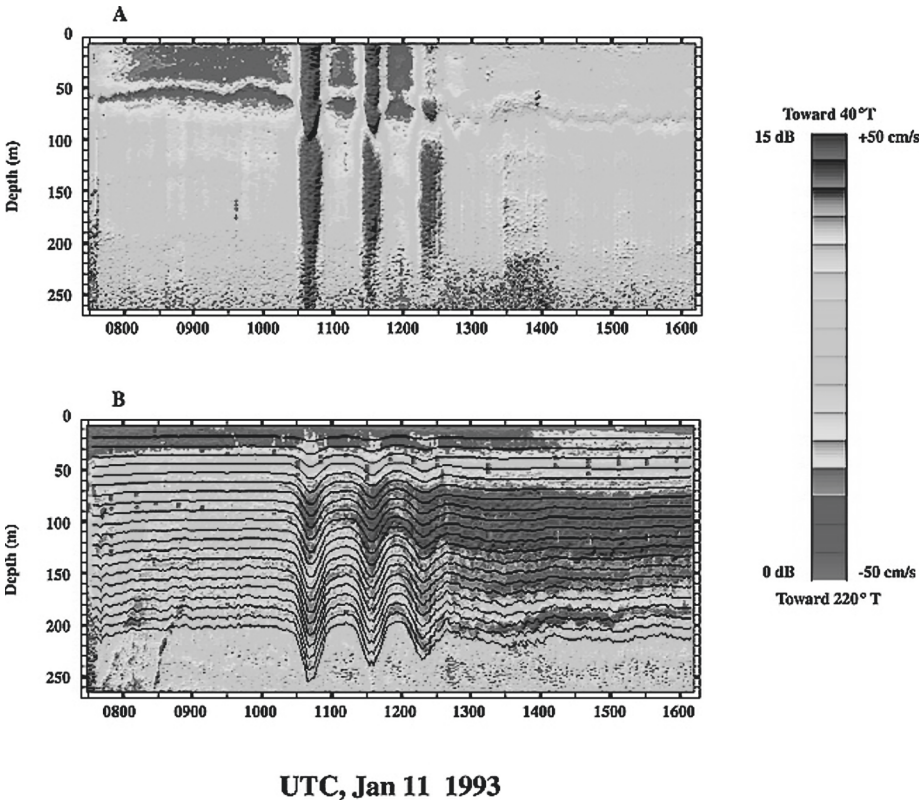


*Figure 5-10*. A solibore observed on 11 January 1993 in the COARE domain at 2°S, 156°E. (a) The along-path (40°–220°) component of absolute ocean velocity. Note that sonar precision degrades below 200 m, a consequence of low signal level at great range. (b) The acoustic scattering strength field at 161 KHz, following adjustment for inverse square spreading and attenuation. Colors represent variation on a logarithmic scale over a factor of thirty. Calculated flow streamlines are superscribed in black. Regions of the thermocline with unstable density gradient, as determined by the CTD, are indicated by purple rectangles. Reproduced from Pinkel (2000) by permission of American Geophysical Union.

The COARE solitons are phase-locked with the internal tides. The wavelength of the first $M_2$ baroclinic mode in the COARE domain is $L_{BT} \sim$ 100 km (Feng et al., 1998b). However, the wavelength of the soliton is only about 6 km.

In the example shown in *Figure 5-10*, three wave crests appear ordered in amplitude. The first crest is the largest one and has a horizontal velocity that exceeds 0.8 m $s^{-1}$ relative to the earth and 1.0 m $s^{-1}$ relative to the

background mixed layer. The crests are spaced by ~40 min apart (when interpolated to a fixed position of the ship).

The packet passage occurred several hours after the internal tide elevation of the thermocline reached maximum around 0800 UTC. The currents in the upper ocean (0–80 m) continued to be directed toward the southwest for several hours following the first soliton, reversing to a northwest flow only after passage of the third soliton.

According to Pinkel (2000), the intrinsic shear associated with solibores is not sufficient to trigger Kelvin-Helmholtz instability in a quiescent background. The minimum Richardson number remained relatively large (above 15). Solibores, however, may trigger instability of the background shear in an environment with gradient Richardson number not much larger than ¼ and can result in the thermohaline fluxes through the bottom of the mixed layer.

The rapid development of high-frequency internal waves on the equatorial shear has also been observed in association with the nocturnal convection in the eastern equatorial Pacific (Mack and Hebert, 1997). Nocturnal convection can also trigger packets of strongly nonlinear internal waves on the shear associated with the diurnal jet (see Section 5.5).

Mathematical modeling of the response of the mixed layer to the soliton forcing is complicated by the difficulty in solving the resulting nonlinear equations in the presence of vertical shear, which is ubiquitous in the upper ocean environment. As a result, the induced dynamic instability in a nearly critical background flow is still largely unexplored (Sandstrom and Oakey 1995).

### 5.3.4 Atmospheric buoyancy forcing

In general, the buoyancy flux into the mixed layer through the air-sea interface is as follows:

$$\Phi_{Ba} = -\frac{\alpha_T g}{c_p \rho}\left\{Q_E + Q_T + I_L - (1-A) I_\Sigma \left[1 - f_R(h)\right]\right\} + \beta_S g S_0 \left(\frac{Q_E}{\rho L} - P\right) + \alpha_T g P \frac{c_p \rho}{c_{pr} \rho_r}(T_r - T_0), \tag{5.10}$$

where $P$ is the rainrate; $c_p$ is the specific heat, and $\rho$ is the density of sea water; $c_{pr}$ is the specific heat, and $\rho_r$ is the density of rain water; $L$ is the latent heat of evaporation, $S_0$ is the surface salinity, $\beta_S$ is the coefficient of

salinity expansion, $T_r$ is the raindrop temperature, and $T_0$ is the sea surface temperature. The term in brackets on the right side of equation (5.10) is the buoyancy flux due to air-sea heat fluxes ($I_R$ is the insolation, $I_L$ is the effective longwave radiation, $Q_E$ and $Q_T$ are is the latent and sensible heat fluxes, respectively). The second term is the buoyancy flux due to the surface salinity change because of evaporation and rain. The third term is the buoyancy flux due to the heat flux because of the difference between the raindrops and seawater temperature. Here we ignore the volume nature of the rain induced buoyancy flux.

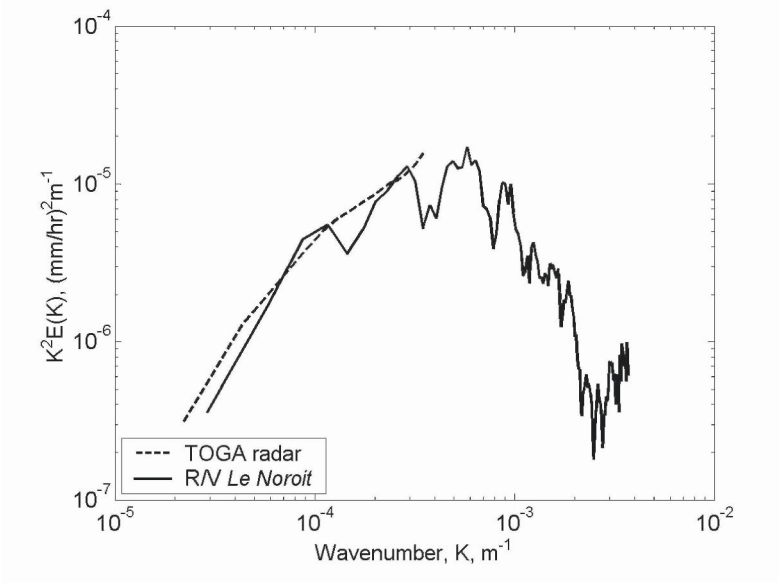


*Figure 5-11*. Comparison of the TOGA rain radar and the R/V Le Noroit rain gauge spectra averaged over the time period from 14 December 1992 through 2 January 1993 and over approximately the same latitude range in *Figure 5-8* (the longitudinal coverage is different, but overlapping). Here $E(k)$ is the rain rate wavenumber spectrum. (Rain radar data after Short et al., 1997; shipboard data are after Delcroix et al., 1993.)

Substantial spatial and temporal variability of the buoyancy flux into the mixed layer is observed in the tropics due to convective rainfalls. Rain rate spectra from the TOGA radar and the R/V *Le Noroit* rain gauge shown in *Figure 5-11* reveal a maximum in the spectrum of horizontal precipitation rate gradients, $k^2E(k)$, at approximately 20 km wavelength.

### 5.3.5 Equilibrium subrange

The analysis in the rest of Section 5 considers the effects of buoyancy flux into the top of the mixed layer. However, it is applicable to the

anomalies produced by internal forcing as well. In the latter case, parcels of heavier water would spread along the bottom of the mixed layer (in contrast to the parcels of lighter water spreading along the ocean surface).

During heavy rainfalls, low-salinity lenses of the order of $L_c \sim 10$ km diameter form at the surface (see Section 4.1.5). The initial buoyancy anomalies produced by convective rains tend to spread due to pressure gradient forces and produce frontal structures due to nonlinear interactions. On horizontal scales comparable to the thickness of the upper ocean boundary layer, the density inhomogeneities are three-dimensional and dissipate due to turbulent mixing. On these spatial scales, the boundary-layer mechanisms that eliminate horizontal density anomalies can be enhanced or suppressed due to the effects of wind stress crossing sharp frontal interfaces (see Section 5.4). Rotation effects are important on the horizontal scales comparable to the baroclinic Rossby radius $L_f$ (or to its equatorial version $L_\beta$).

Since there is frequent influx of buoyancy from convective rainfalls, there is a continuous creation, evolution, and dissipation of the density anomalies in the warm pool area. Here we hypothesize that there is a wavelength range, $h << \lambda << \min\{L_c, \lambda_{IG}, L_\beta, L_f\}$, in which the spectrum of horizontal buoyancy inhomogeneities in the warm pool area, $E_B(k)$, can be saturated. Analysis of equation (5.9) suggests that the equilibrium buoyancy spectrum in this subrange will depend on horizontal wavenumber vector $\vec{k}$, mixed layer depth $h$, vertical homogenization time $\tau$, and a parameter characterizing the horizontal variability of the density field, $\langle \nabla B \cdot \nabla B \rangle$.

A standard dimensional analysis then leads to the following formulation for the horizontal wavenumber spectrum of buoyancy:

$$\Psi_B(\vec{k}) / \langle \nabla B \cdot \nabla B \rangle = k^{-4} f_B(\alpha, kh, \mu), \tag{5.11}$$

where $\alpha$ denotes the direction of the wavenumber vector $\vec{k}$ (the polar angle relative to wind direction, for instance), $f_B$ is a function, and parameter $kh$ is associated with the turbulent boundary layer processes. For horizontal scales exceeding 1 km parameter $kh$ is very small and formally can be dropped from the number of determining parameters in (5.11). Parameter $\mu$ is given by

$$\mu = \tau^4 \cdot \langle \nabla B \cdot \nabla B \rangle. \tag{5.12}$$

Under the assumption of directional isotropy, the one-dimensional wavenumber buoyancy spectrum is obtained by integration over angle $\alpha$:

$$E_B(k_x)/\langle \nabla B \cdot \nabla B \rangle = \int_0^{2\pi} \Psi_B(\vec{k})\, k\, d\alpha \approx k_x^{-3} F(k_x h, \mu) \approx c(\mu) k_x^{-3}, \qquad (5.13)$$

where $F$ is a universal function of its nondimensional arguments $kh$ and $\mu$. For $kh \ll 1$, we assume that $F(kh, \mu) \approx c_B(\mu)$, since $kh$ can formally be dropped out of the number of determining parameters. The explicit form of $F$ as function of $kh$ can in principle be obtained by merging turbulent boundary layer spectra (Kamal et al., 1972; Wijesekera et al., 2001) with the spectrum of two-dimensional turbulence.

After replacing buoyancy $B$ in (5.13) with its expression via density $\rho$ the one-dimensional horizontal wavenumber spectrum of density is as follows:

$$E_\rho(k_x)/\operatorname{var}(\partial_x \rho) \approx c_B(\mu) k_x^{-3} \qquad (5.14)$$

where $c_B$ is another universal function of its nondimensional argument $\mu$.

As we can see from *Figure 5-8*, in the wavenumber range, $k_x > 4 \cdot 10^{-4}$ m$^{-1}$, which corresponds to the wavelength range $\lambda < 16$ km, the experimental spectrum follows the $k_x^{-3}$ law predicted by equation (5.14). Function $c_B(\mu)$ used to show the $k^{-3}$ spectral law in *Figure 5-8* depends on parameter $\mu$, which is related to the vertical mixing process and horizontal buoyancy gradients via equation (5.12).

### 5.3.6 Numerical diagnostics of nonlinear diffusion equation

Numerical diagnostics of the nonlinear diffusion equation (5.9) can help to understand the essential physics beyond the universal spectrum (5.14). We consider the following simplified form of equation (5.9):

$$\partial_t B = \gamma \partial_x \left[ \left( \partial_x B \right)^3 \right] + \Phi_B, \qquad (5.15)$$

where $B = -g\Delta\rho(x,t)/\rho_0$ and $\gamma = h^2 \tau^3/96$, $h$ is the mixed layer depth, and $\tau$ is the vertical mixing time scale. Boundary conditions are set as follows: $\partial_x B = 0$ at $x = -\Delta L/2$ and $x = \Delta L/2$, where $\Delta L$ is the domain size.

For an axisymmetric case, equation (5.9) can be written in polar coordinates ($r$, $\alpha$), where $r$ is the radial distance, and $\alpha$ is the polar angle. Being extended evenly for $r < 0$, the axisymmetric version of equation has the same form and the same boundary conditions as equation (5.15) but with $x$ replaced by $r$.

The preliminary numerical diagnosis of equation (5.15) was performed in *Matlab* with a partial differential equation (PDE) solver. This solver had been tested with an analytical solution of equation (5.15) given in Landau and Lifshitz (1993); the test showed a perfect agreement between the analytical and numerical solution.

The numerical solution for an axisymmetric smooth initial shape (Gaussian type profile) and at $\Phi_B = 0$ (*decay problem*) is shown in *Figure 5-12*. The initial shape of the density anomaly has a tendency to evolve into a *conic* structure (*Figure 5-12*b). Zones with increased curvature are localized at the top and the base of the conic structure, which appears to have important implications for the wavenumber statistics to be considered later. Between the top and the base of this cone, the solution asymptotically tends to a linear dependence on the radial distance *r*, which means that $\partial_r \rho(r) \to const$ and no length scale dependence is involved.

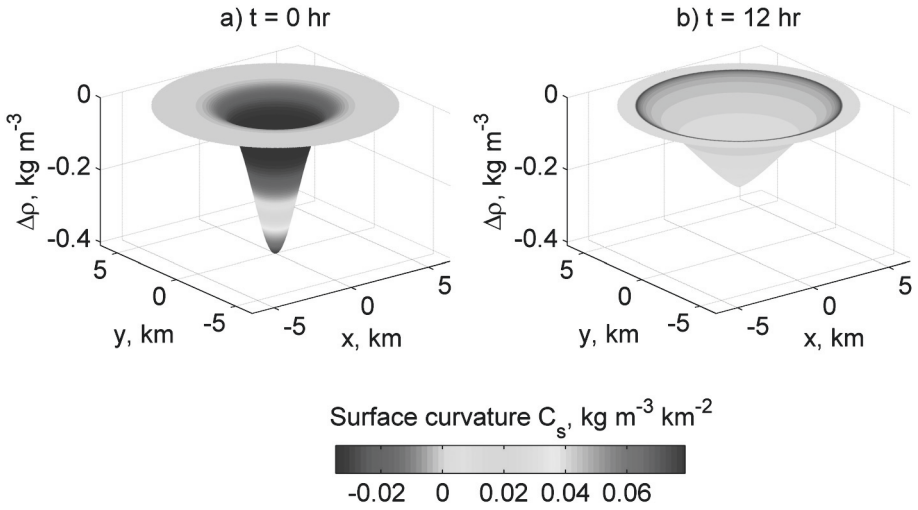


*Figure 5-12*. Evolution of a freshwater lens: (a) initial condition ($t = 0$), and (b) solution of the advective-diffusion equation for $t = 12$ hrs. Here $\Delta\rho = \rho - \rho_0$. The surface curvature, which is defined here as a Laplacian $C_s = \left(\partial^2_{xx}\rho + \partial^2_{yy}\rho\right)/4$, is indicated by color (scale given by color bar). In subplot (b) the surface curvature at the cone apex is so localized that it cannot be effectively displayed in color.

A projection of this axisymmetric solution onto the *x*-axis is shown in *Figure 5-13*. In this projection, the initial Gaussian profile evolves into a *triangular structure*. The triangular structure has curvature spikes at the top and base points. The wavenumber spectrum of such spikes is white noise. Double integrating the density anomaly curvature back to the buoyancy in the wavenumber domain spectrum is equivalent to multiplication by $k^{-4}$.

Integrating the density anomaly spectrum over all directions, as in (5.13), results in a $k_x^{-3}$ spectral law, which is consistent with experimental data shown in *Figure 5-8*.

The second numerical experiment used a random initial condition in the form of white noise. Results of this experiment are shown in *Figure 5-14*. In this case the initial white spectrum also evolves into a $k^{-4}$ dependence (which corresponds to a $k_x^{-3}$ spectrum after integrating over all directions).

The above tests indicate that the nonlinear system described by equation (5.15) tends to produce spikes in buoyancy curvature. According to Simpson and Linden (1989), increased curvature of buoyancy drives frontogenesis.

The model considered above is a vertically integrated, slab model of the mixed layer. It is not able to describe the vertical structure of fronts, which are characterized by the presence of an inclined pycnocline. In this type of model, the signature of a front is the increased curvature of the horizontal buoyancy (temperature, salinity) distribution.

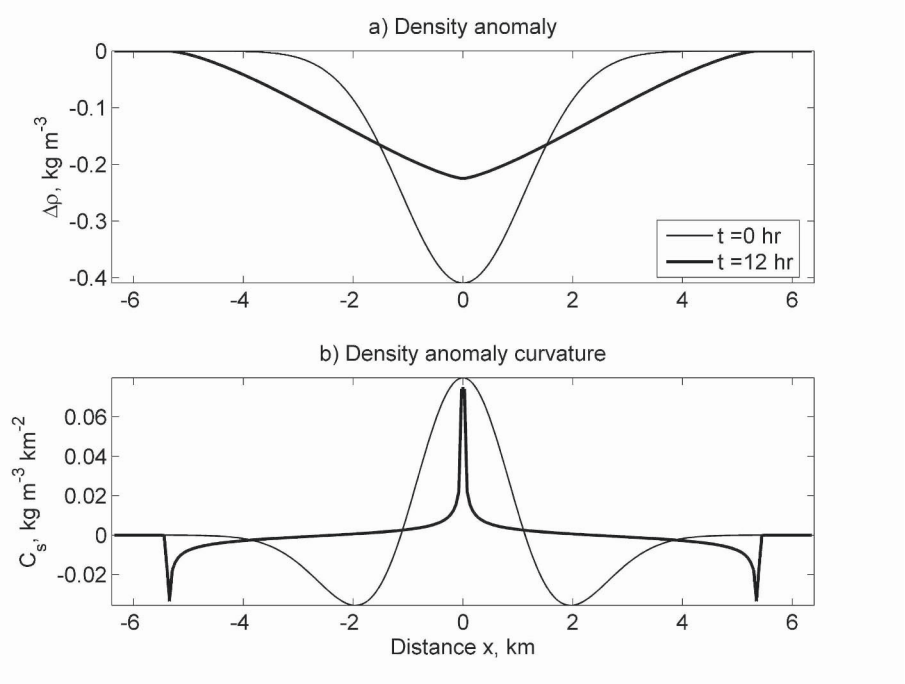


*Figure 5-13*. (a) A projection of the axisymmetric solution shown in *Figure 5-12* onto the x-axis. Note the tendency to form "spikes" of the horizontal buoyancy curvature (b), which leads to certain spectral laws.

The approach undertaken here to derive the theoretical spectrum (5.14) has some analogy with that used by Phillips (1977) to derive the wavenumber spectrum of surface waves in the saturation subrange.

According to Belcher and Vassilicos (1997), the surface wave field is a superposition of sinusoids plus sharp-crested breaking waves. The sharp-crested waves have a spike-like curvature, which leads to Phillip's spatial $F\left(\vec{k}\right) \sim k^{-4}$ and, thus, one-dimensional $f\left(k_x\right) \sim k_x^{-3}$ wavenumber spectra. In particular this analogy may be useful in specifying function $c_B\left(\mu\right)$ entering spectrum (5.14).

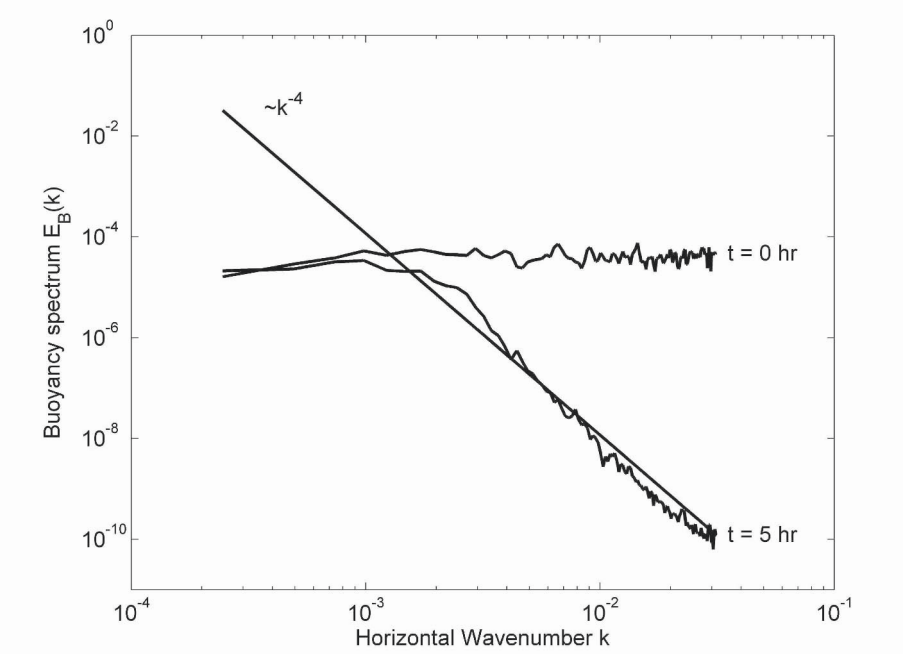


*Figure 5-14*. Spectral saturation due to nonlinear diffusion.

In this preliminary analysis, we have ignored the advection term $\vec{u} \cdot \nabla B$. Feng et al. (2000) showed the importance of advection on the salinity budget within the western Pacific warm pool. Comparative analysis of advection and atmospheric forcing may elucidate the difference between the warm pool and mid-latitude processes. In fact, when the advection forcing with no atmospheric forcing is considered, the wavenumber spectrum appears to be steeper than $k_x^{-3}$ (Ferrari and Paparella, 2003).

### 5.3.7 Relationship between vertical and horizontal mixing and atmospheric forcing conditions

Within the range of horizontal length scales exceeding the thickness of the mixed layer but not yet affected by the Coriolis force, the horizontal mixing coefficient is as follows:

$$K_h = \gamma \overline{\nabla B \cdot \nabla B} = \frac{h^2 \tau^3}{96} \frac{g^2 \overline{\nabla \rho \cdot \nabla \rho}}{\rho_0^2}, \tag{5.16}$$

which has been inspired by theoretical formula (5.8) and an assumption that $f \equiv 1$ (as in FY97). In the framework of this model, the vertical mixing coefficient is defined as

$$K_V = \frac{h^2}{4\tau}. \tag{5.17}$$

From (5.16), (5.17), and (5.12), the ratio between horizontal and vertical mixing coefficients is a follows:

$$\frac{K_h}{K_V} = \frac{\tau^4}{24} \frac{g^2 \overline{\nabla \rho \cdot \nabla \rho}}{\rho_0^2} = \frac{\mu}{24}. \tag{5.18}$$

The parameter $\mu = \tau^4 \langle \nabla B \cdot \nabla B \rangle$ that emerged from dimensional analysis in Section 5.3.5 thus characterizes the relative importance of the vertical and horizontal mixing processes in the equatorial region. A strong dependence of parameter $\mu$ on the somewhat uncertain relaxation time $\tau$ makes it difficult to make quantitative estimates of the horizontal to vertical mixing coefficient ratio. The estimates for typical conditions in the warm pool area given in *Table 5-1* should at this point be treated only as qualitative.

The first row in *Table 5-1* is an estimate for westerly wind burst conditions; the horizontal mixing coefficient $K_h$ is relatively small, on the order of the vertical mixing coefficient. Under low wind speed conditions and strong rainfalls (the second row in *Table 5-1*), $K_h$ equals to 420 $m^2\ s^{-1}$. (For comparison, Large et al. (2001) used a constant horizontal mixing coefficient of order 1000 $m^2\ s^{-1}$ in order to reproduce the equatorial zonal currents.) The ratio between the horizontal and vertical mixing is highly dependent on the regime of air-sea interaction; it dramatically increases under low wind speed conditions when the vertical mixing is suppressed by stratification.

*Table 5-1.* Estimates of horizontal mixing coefficient in the warm pool area from Eq. (5.16) ($h$ is the mixed layer depth, $\tau$ is the vertical homogenization time).

| Environmental conditions | $h$ m | $\tau$ s | $g^2\overline{\nabla\rho\cdot\nabla\rho}/\rho_0^2$ $s^{-4}$ | $K_h$ $m^2\,s^{-1}$ | $K_h/K_V$ |
|---|---|---|---|---|---|
| Westerly Wind Burst | 75 | 3600 | $1.6\times10^{-13}$ | 0.44 | 1.1 |
| Low wind and heavy rain | 10* | 12x3600 | $5\times10^{-12}$ | 420 | 726,000 |

* A barrier layer is assumed to be located below 10 m depth

Due to rotation effects the relationship between vertical and horizontal mixing may depend on latitude even relatively close to the equator, but it is essentially different from mid-latitude regions. In mid-latitudes the sheared flow within the mixed layer that arises due to horizontal density inhomogeneities can be partitioned between a geostrophic response and an ageostrophic response (Young, 1994; Tandon and Garrett, 1995; Roemmich et al., 1994). A relevant limitation on the horizontal length scale is the baroclinic Rossby radius ($L_f$), and the respective limitation on the timescale is the inertial timescale ($f^{-1}$). The analysis developed here section relates to the ageostrophic response. For the geostrophic response, the theory of quasi-geostrophic two-dimensional turbulence of Batchelor (1969) and Kraichnan (1975) must be used.

### 5.3.8 Implications for horizontal mixing parameterization

The numerical diagnostics performed in Section 5.3.6 with axisymmetric initial conditions indicate that the asymptotic (equilibrium) solution of equation (5.9) is a conic structure. Between the top and the base of the "cone" $\partial_r\rho(r)$ tends to a limiting (equilibrium) value and, hence, does not depend on the radial distance $r$. An important consequence of this fact is that the mixing coefficient is no longer an explicit function of the horizontal length scale. If the initial disturbance is represented by an ensemble of random disturbances, as in the example illustrated in *Figure 5-14*, in the process of nonlinear evolution only the disturbances that have maximal length scale possible in the system survive. A relevant limitation on the horizontal length scale in the ocean is the baroclinic Rossby radius ($L_f$) or the equatorial baroclinic Rossby radius ($L_\beta$). For the equilibrium subrange, we can therefore use a tentative approximation, $\overline{\nabla\rho\cdot\nabla\rho}\approx\left(\rho'/L_R\right)^2=\overline{\rho'^2}/L_R^2$, where $L_R$ is the appropriate baroclinic Rossby radius (either $L_f$ or $L_\beta$), and $\overline{\rho'^2}$ is the variance of the submesoscale density fluctuations. Equation (5.16) then reads:

$$K_h \approx \frac{h^2\tau^3}{96}\frac{g^2\overline{\rho'^2}}{L_R^2\rho_0^2}, \tag{5.19}$$

On the time and space scales where the determining parameters $h$, $\tau$, and $\rho'^2$ can be treated as stationary, formula (5.19) results in a constant (!) horizontal mixing coefficient. Parameterization of the horizontal mixing thus reduces to the classical problem described by a linear diffusion equation. An example is Brownian motion. According to Einstein's (1905) formula for Brownian motion:

$$D = 2\left(K_h t\right)^{1/2}, \tag{5.20}$$

where $D$ is the RMS distance.

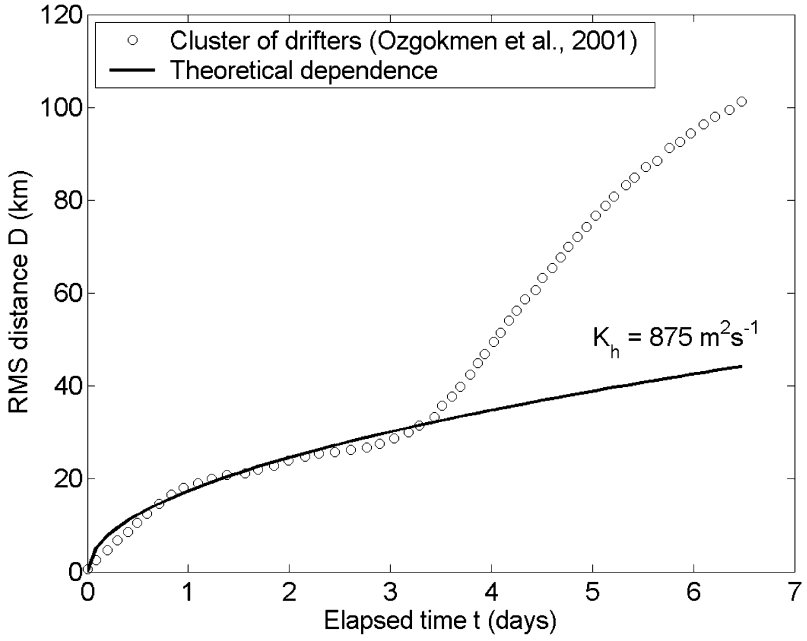


*Figure 5-15.* RMS distance $D$ in the cluster of 5 drifters released on 25 Oct 1993 (-5°S, 90°W) as a function of time $t$ elapsed from the drifter release.

Evidence in favor of (5.20) can be found from drifter cluster release experiments (Ozgokmen et al., 2001). *Figure 5-15* shows the RMS distance $D$ in the cluster of 5 drifters released on 25 October 1993 (5°S, 90°W) as a

function of elapsed time $t$ since the drifter release. Mean flow advection has been subtracted. Theoretical dependence (5.20) that follows from the nonlinear diffusion model is shown for a constant $K_h = 875$ m$^2$s$^{-1}$. According to *Figure 5-15*, the constant coefficient diffusion law (5.20) appears to be valid for about 3.5 days. During this time, the RMS distance between drifters increased to $D_0 = 35$ km, which is close to the values of the baroclinic Rossby radius estimated for typical stratification disturbances within the mixed layer of the tropical sea. On larger horizontal scales, (5.20) is apparently no longer valid.

The inhomogeneity of the buoyancy (or density) field in the upper ocean induced by atmospheric forcing can be estimated from a simple budget relationship as follows:

$$\nabla B = -g\frac{\nabla\rho}{\rho_0} = \int_0^\tau \nabla\left(\frac{\Phi_{Ba}}{h}\right)dt, \tag{5.21}$$

where $\Phi_{Ba}$ is net the buoyancy flux at the air-sea interface defined by equation (5.10) and $h$ is the depth of the mixed layer. Respectively, the variation of the mixed layer density $\rho'$ due to precipitation only can be estimated as follows:

$$\rho' = \rho_0 \int_0^\tau P/h \cdot dt \tag{5.22}$$

Formulas (5.19) and (5.22) then link the horizontal mixing coefficient with the atmospheric forcing (precipitation):

$$K_h \approx \frac{g^2\tau^3}{96L_R^2}\overline{M_r^2}\ . \tag{5.23}$$

where $M_r = \int_0^\tau P dt$ is the cumulative precipitation during rain event.

Rainfalls are in fact the major contributor to the temporal and spatial intermittency of the buoyancy flux between the atmosphere and ocean in the warm pool area. During TOGA COARE, the spatial and temporal structure of the rain rate was known from radar measurements (*Figure 5-11*) and from NCAR's cloud resolving models (Moncrieff et al., 1997; Redelsperger et al., 2000). For the implementation of the horizontal mixing parameterization in an ocean general circulation model (GCM), subgrid precipitation statistics with 1 km resolution can, in principle, be provided by the new generation of atmospheric cloud resolving models (Grabowski and Smolarkiewicz, 1999; Randall et al., 2003).

Brief conclusions for Section 5.3 are as follows:

1) The TSG data from the western Pacific warm pool reveal the $k_x^{-3}$ spectral subrange.
2) The hypothesis of an equilibrium spectrum leads to wavenumber dependence $E(k_x) \sim k_x^{-3}$, which is consistent with the field data.
3) Numerical experiments illustrate how nonlinear diffusion transforms initial horizontal density anomalies into conic structures with spike type buoyancy curvature at their corners, which leads to a $k_x^{-3}$ wavenumber spectrum.
4) For the equilibrium state, the nonlinear diffusion problem then reduces to a linear problem with the constant horizontal diffusion coefficient.
5) The increased horizontal curvature of buoyancy drives frontogenesis.

The last conclusion thus links the process of nonlinear diffusion to the problem of oceanic fronts. As we have seen from previous sections of this chapter, the process of self-organization involves a cascade of energy from smaller to larger scales. At the same time, horizontal gradients must simultaneously increase to satisfy the conservation law (5.3). One interpretation is that in the process of self-organization, boundaries of the spatially coherent organized structures become sharper. The data presented in the next section indeed show that sharp frontal interfaces are an observable feature of the near-surface layer of the ocean. The FY97 model is, however, hydrostatic and is not capable of simulating fronts.

## 5.4 Sharp Frontal Interfaces

Recent global surveys using the Pathfinder SST dataset reveal persistent fronts in many parts of the World Ocean (Belkin et al., 2001). Oceanic fronts have been linked to the process of subduction, where one water-mass sinks below another without substantial mixing (see for instance Rudnick and Luyten, 1996). Subduction appears to be an important process in maintaining the salt-stratified barrier layer often found below the warm, fresh mixed layer of the western Pacific warm pool (Lukas and Lindstrom, 1991; Shinoda and Lukas, 1995; Tomczak, 1995; You, 1995; Ando and McPhaden, 1997; Vialard and Delecluse, 1998).

Woods (1980) and Fedorov (1986) linked ocean fronts to dissipation of large-scale and mesoscale horizontal inhomogeneities of the physical fields in the upper ocean. Fronts sometimes are so narrow that in images from space they may look like “cracks” on the sea surface (*Figure 5-16*).

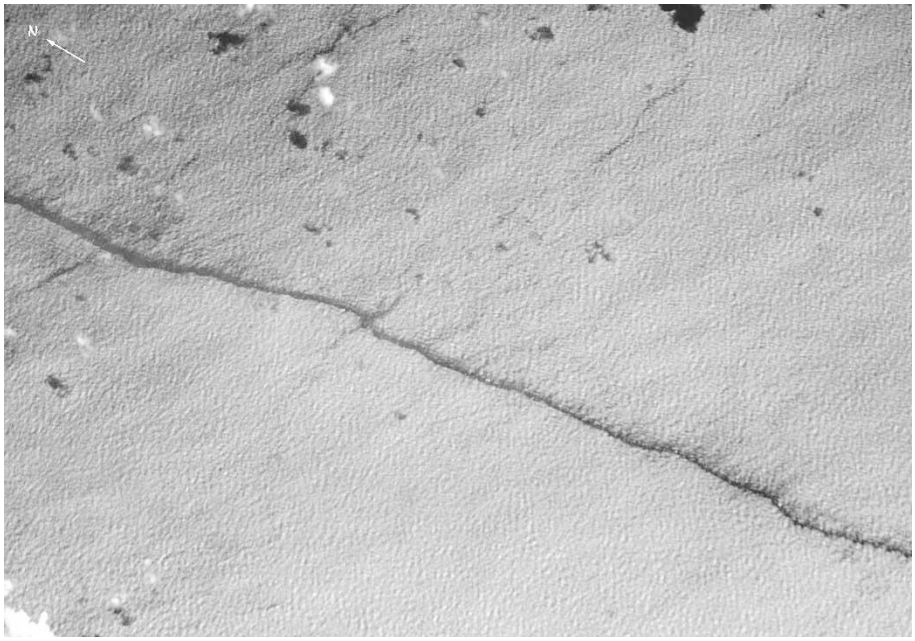


*Figure 5-16*. An image taken from International Space Station on May 24, 2001 in the Equatorial Pacific (2.3$^{o}$N 159.1$^{o}$E) by Increment 2 crew, Jim Voss and Susan Helms (© 2001 NASA, courtesy of Susan Runko.)

*Figure 5-17.* A sharp frontal line observed in the equatorial western Pacific warm pool from the *R/V Kaiyo* on 13 August 1996. Reproduced from Soloviev et al. (2002) by permission from Elsevier.

The front sometimes splits into a group of frontal interfaces. In mid- and high-latitudes, the Coriolis effect winds these lines up into spirals (*Figure 5-5*), but they may still be very narrow.

Although oceanic fronts are observed over a wide range of horizontal scales, turbulent mixing events in the ocean tend to occur on relatively small scales. The small-scale structure of oceanic fronts therefore potentially contains information about horizontal and vertical exchange processes in the upper ocean.

*In situ* measurements sometimes reveal sharp frontal interfaces in the upper ocean (Zenk and Katz, 1975; Soloviev and Zatsepin, 1992; Yoder et al., 1994; Soloviev and Lukas, 1997b). Many sharp frontal interfaces are found in the temperature, salinity, and density records made during TOGA COARE, using bow-mounted sensors (Soloviev and Lukas, 1997b; Wijesekera et al., 1999a; Soloviev et al., 2002).

### 5.4.1 Observations of sharp frontal interfaces in the western Pacific warm pool

The western equatorial Pacific warm pool region – the TOGA COARE domain – is characterized by heavy precipitation and generally light winds. As a result, both heat and freshwater fluxes contribute substantially to the buoyancy influx to the top of the surface mixed layer, and both temperature and salinity stratification is found in the upper ocean (Lukas and Lindstrom, 1991). The thermohaline fields in the warm pool area are heterogeneous and non-stationary to a surprising degree (Huyer et al., 1997); there are numerous instances of sharp fronts in the surface layer of the ocean (Soloviev and Lukas, 1997b).

*Figure 5-17* shows a sharp front in a photograph taken from the bridge of the R/V *Kaiyo* in the western equatorial Pacific warm pool during a TOCS cruise (This is believed to be the same type of front as in the image from space shown in *Figure 5-16*.) A description of the upper ocean currents, thermohaline structure, and atmospheric forcing during TOCS can be found in Matsuura et al. (2002).

The sharp frontal line in *Figure 5-17* is roughly aligned in the east-west direction and extended from one horizon to the other. The front is clearly seen in the photograph because the wind waves to the north of the front break much more intensively than those to the south of the front. There is also some difference in ocean color across the front.

CTD stations made along 156$^{o}$E from 8$^{o}$N to 3$^{o}$S (prior to crossing the front) reveal a surface salinity minimum at about 5$^{o}$N and the related meridional salinity gradient at the equator (*Figure 5-18*). A CTD station taken just north of the front (see map in *Figure 5-19*) reveals a nearly

isothermal layer 71 m deep (as determined from the criteria $T(1) - T(h) = 0.5^{o}C$) and a shallow halocline, starting from ~12 m (*Figure 5-18*).

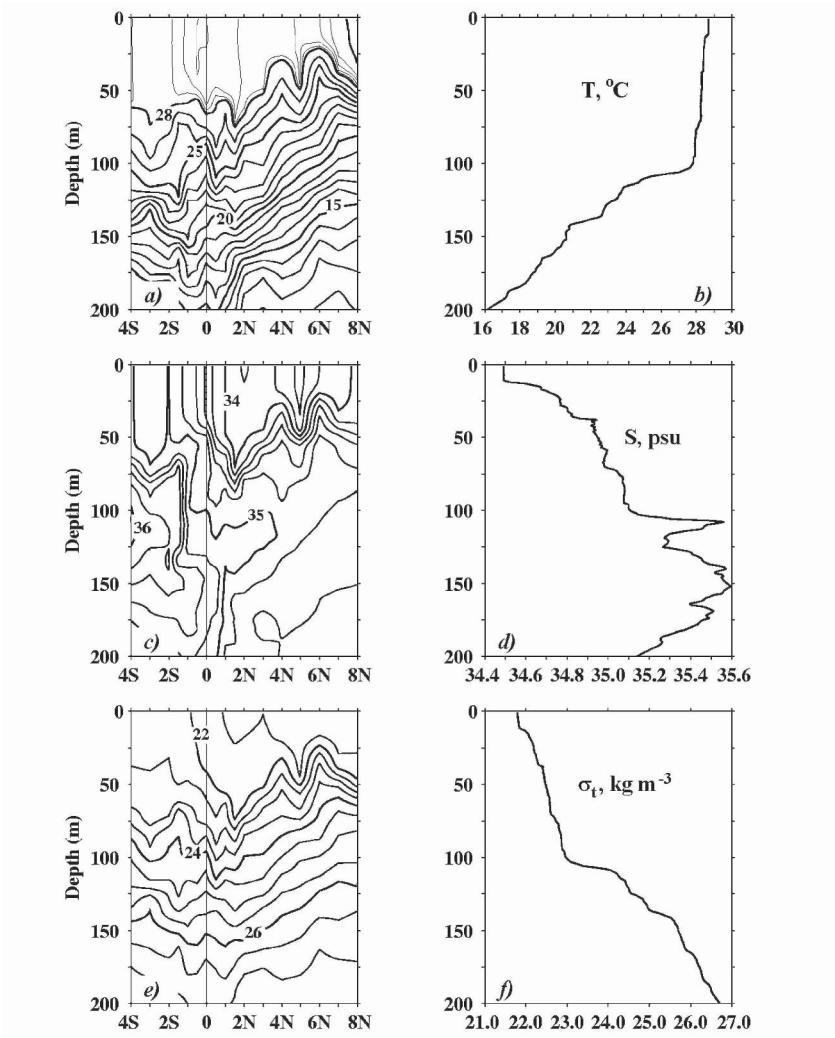


*Figure 5-18*. Contour plots of (a) temperature, (c) salinity, and (d) density during the R/V *Kaiyo* section along 156°E. Vertical profiles of (b) temperature, (d) salinity, and (f) density calculated from the CTD station taken north of the surface front (see *Figure 5-19* for the position of the station relative to front). There is a 4° difference in longitude between the meridional section and the CTD station. The contour interval in plot (a) is 0.2°C for $T > 28^{o}C$ and 1.0°C for $T < 28^{o}C$. Reproduced from Soloviev et al. (2002) by permission from Elsevier.

The shallow halocline was presumably related to the front. In *Figure 5-20*, the thermohaline structure of the upper 71 m at this CTD station is shown in more detail. The layer between the top of the shallow halocline

(the well-mixed layer) and the bottom of the nearly isothermal layer (the top of the thermocline) resembles a barrier layer, the feature often found in the western Pacific warm pool (Lukas and Lindstrom, 1991). This particular case has a temperature gradient reinforcing salinity stratification, though it is only approximately 1/2 of the salinity contribution to the stratification of the barrier layer.

There is a well-mixed near-surface layer in the upper 12 m of the ocean (*Figure 5-20*). Laboratory experiments described in Simpson (1987) suggest that the speed of a gravity current $U_b$ developing due to the density anomaly $\Delta\rho$ is controlled by the Froude number, $Fr = U_b / \sqrt{g' h_0}$, where $g'$ is the reduced gravity ($g\Delta\rho / \rho_0$) and $h_0$ is the effective depth of the near-surface density anomaly. Following Whitham (1974), we will use Favor's (cited from Whitham, 1974) critical value $Fr$ = 1.2. Simpson (1987) found that the critical Froude number could depend on $h_0 / H$, where $H$ is the depth of the nearly isothermal layer. For crude estimates we will ignore this dependence.

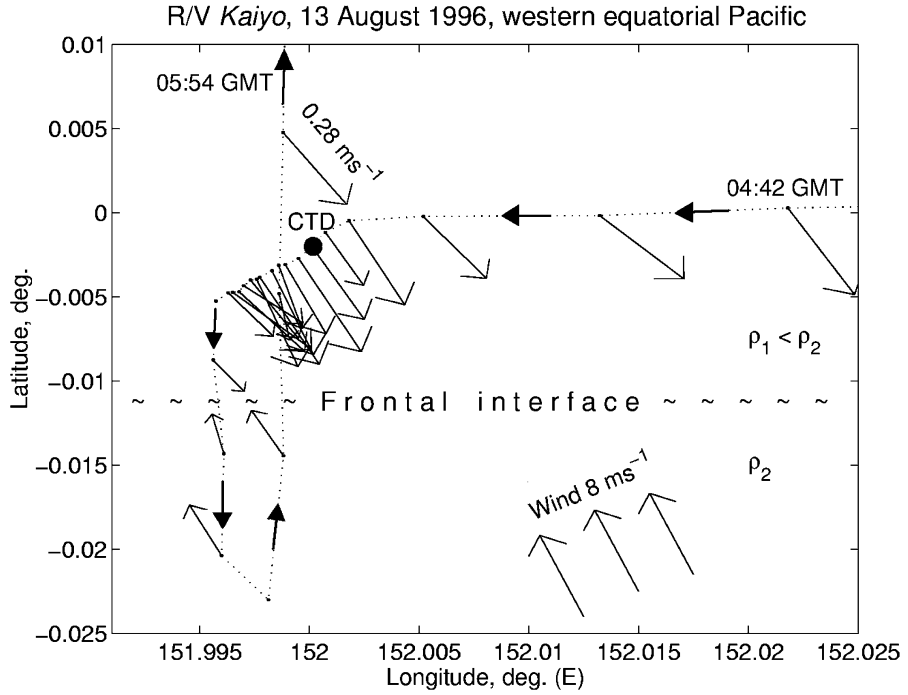


*Figure 5-19*. Track of the R/V *Kaiyo* on 13 August 1996 (during intersection of the sharp surface front shown in *Figure 5-17*) is given with dotted line; bold arrows indicate direction of ship. The time marks are on the upper right and left corners. The ADCP velocity shear vector $\Delta U = U_{16} - U_{24}$ is shown along the ship track, where $U_{16}$ and $U_{24}$ are the horizontal velocity vectors for the 16 m and 24 m bins respectively. The scale for the velocity shear vector can be found in the upper left corner. Position of the CTD station (*Figure 5-18* b, d, and *Figure 5-20*) is marked with a bold circle. Reproduced from Soloviev et al. (2002) by permission from Elsevier.

Assuming that in the example shown in *Figure 5-20*, $h_0$ = 12 m, $H$ = 71 m, $\Delta\rho$ = 0.54 kg m$^{-3}$, $\rho_0 = 1024$ kg m$^{-3}$, and $Fr = 1.2$ the speed of the gravity current due to the observed density anomaly within the mixed layer is estimated as $U_b \approx 0.30$ m s$^{-1}$. This is in fact a lower estimate, since the effective thickness of the near-surface density anomaly layer driving the gravity current is larger than 12 m. The effective thickness calculated as $h_0 = (\rho(0) - \rho(h))^{-1} \int_0^h (\rho(z) - \rho(h))\,dz \approx 27$ m results in $U_b$=0.44 m s$^{-1}$, which is an upper estimate. (However, both estimates do not account for the opposing wind stress.)

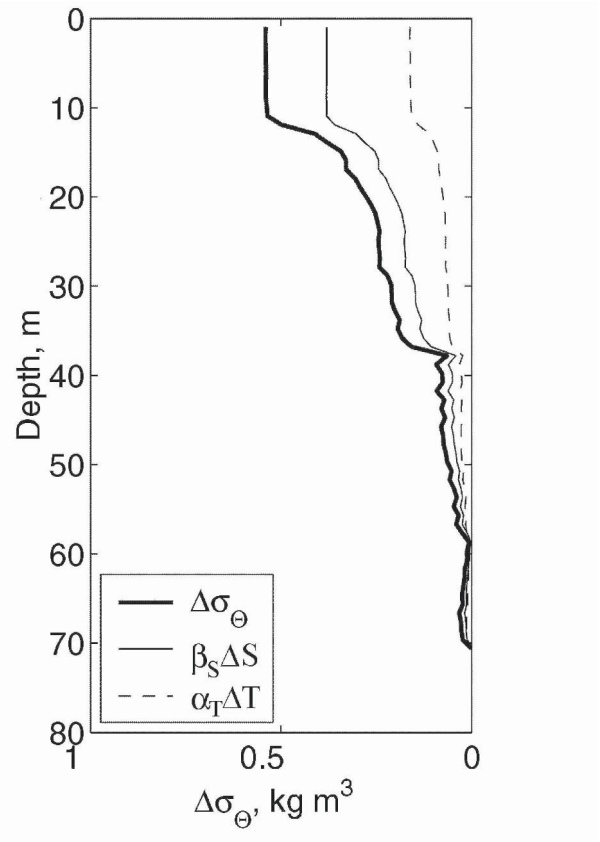


*Figure 5-20*. Vertical distribution of potential density ($\sigma_\Theta$) relative to the top of the thermocline (bottom of nearly isothermal layer) and the impact of salinity ($S$) and potential temperature ($\Theta$) on stratification within the upper ocean from the CTD station indicated in *Figure 5-19*. Here, $\alpha_T$ and $\beta_S$ are the respective thermal expansion and salinity contraction coefficients; $\Delta$ is the difference operator (with respect to the bottom of the nearly isothermal layer). The depth of the nearly isothermal layer, $H$ = 71 m, is determined from criteria $T(1) - T(H) = 0.5^{\circ}$C. Reproduced from Soloviev et al. (2002) by permission from Elsevier.

The ADCP record from the 16 m bin shows a jump of the relative velocity, $\Delta \boldsymbol{U} = \boldsymbol{U}_{16} - \boldsymbol{U}_{24}$, of approximately 0.4 m $s^{-1}$ at the intersection of the front (*Figure 5-19*). This is within the range of the preceding estimates for the gravity current speed. (Note that the shipboard ADCP data start only from 16 m.) The contour plot of the northward velocity component during the subsequent meridional section of the R/V *Kaiyo* along 152°E (*Figure 5-21*) reveals signatures of a strong SSE near-surface current. The sharp front visually observed in *Figure 5-17* can be associated with the leading edge of this near-surface current. According to the shipboard ADCP and meteorological observations, an 8 m $s^{-1}$ SSE wind opposed the buoyant spreading of the front (*Figure 5-19*).

There is a jump in the horizontal velocity component normal to the front (*Figure 5-19*). The breaking of surface waves observed north of the front (*Figure 5-17*) can be ascribed to the effect of surface wave–current interactions.

Another observation of the sharp frontal interface is presented in *Figure 5-22*. This is an east-west section from the R/V *Wecoma* during TOGA COARE. Visual observations of the ocean surface were not conducted for this section, but evidence of convergence lines was seen in sections during the preceding and following days. The data from the CTD sensor mounted on the bow of the vessel at 2 m mean depth (Wijesekera et al., 1999a) provided high-resolution data in the horizontal direction, and the data from a towed undulating CTD (SEASOAR) provided information on the upper ocean stratification during this case study. The 3 km horizontal grid of the interpolated SEASOAR and ADCP data is, however, too coarse to resolve small-scale horizontal features. In particular, the internal-wave train that presumably can accompany the propagation of the gravity current cannot be resolved with 3 km data since the theoretical wavelength of the wave train (see Section 5.2.3) is only $\lambda \approx 6h_0 \sim 10^2$ m.

A sharp front is clearly seen in the bow record of density at 45.6 km (*Figure 5-22*a), associated with a rain-formed freshwater surface lens. Note that only one boundary of this lens is sharp. The density and velocity contour plots for the upper 100 m of the ocean from SEASOAR and ADCP measurements (*Figure 5-22*b-d) reveal a density anomaly and signatures of the near-surface current associated with this frontal structure. Between 25 and 50 km, this density anomaly has cyclonic vorticity, which appears to have been caused by the inertial spin-down of an eastward equatorial jet (Feng et al., 2001).

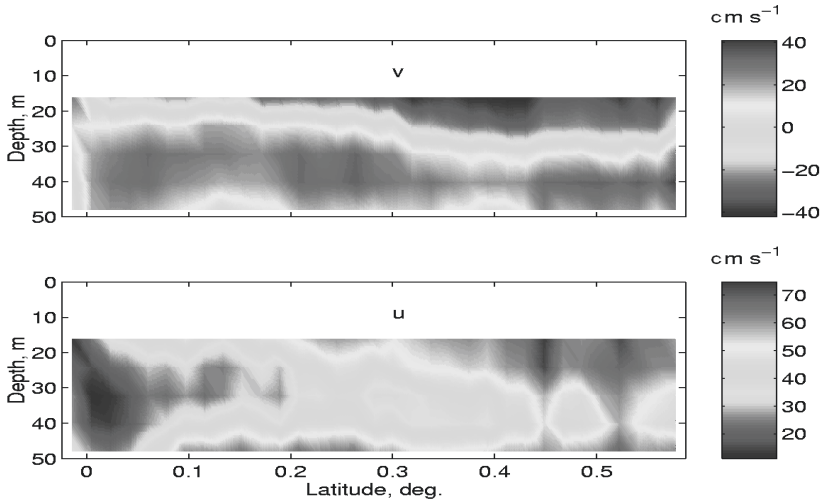


*Figure 5-21*. ADCP velocity contour plots for north *v* and east *u* components during the meridional section of the R/V *Kaiyo* on 13 August 1996 (corresponds to the northbound part of the ship trajectory in *Figure 5-19*)

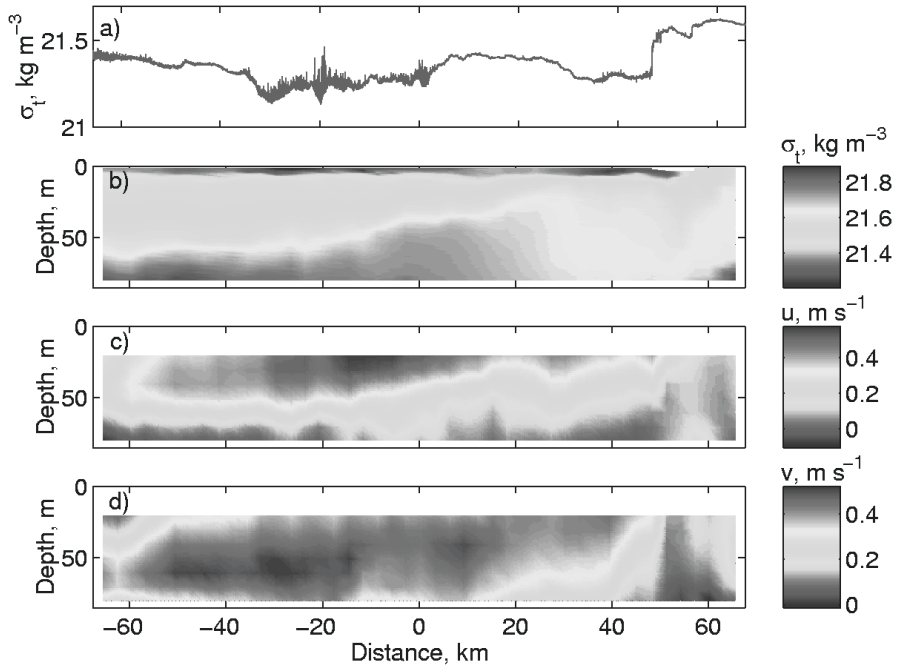


*Figure 5-22*. (a) Sharp frontal interface in the near-surface density field measured at 2 m mean depth by a bow-mounted CTD; (b) Density contour plot calculated from a towed undulating vehicle; (c, d) Eastward and northward velocity contour plots. Reproduced from Soloviev et al. (2002) by permission from Elsevier.

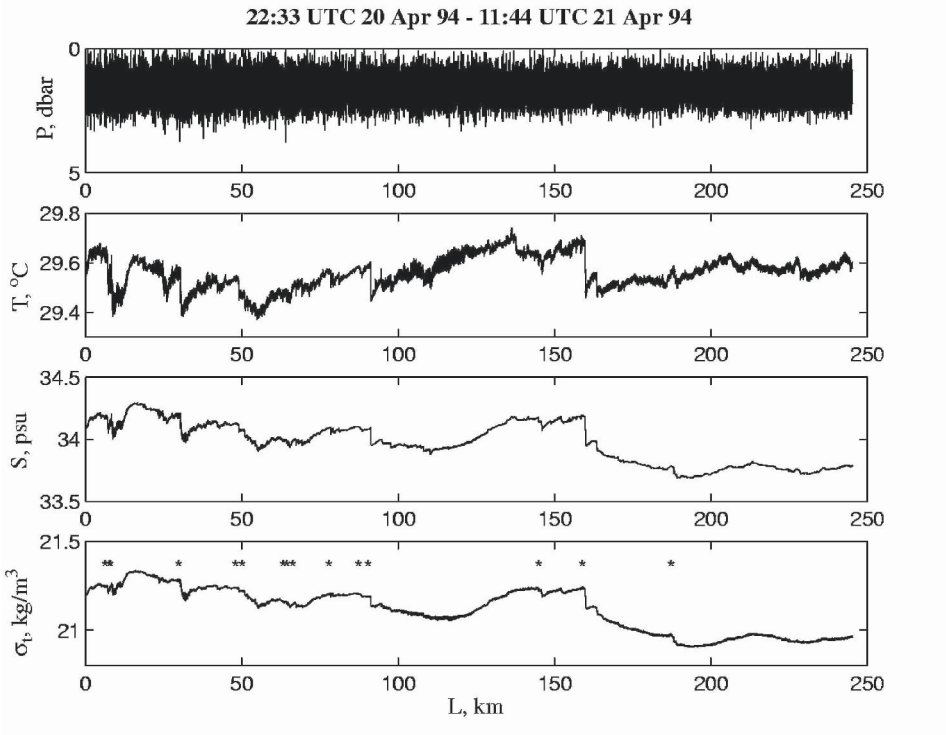


*Figure 5-23*. Example of repeating asymmetrical structure in the near-surface layer of the ocean in the western equatorial Pacific warm pool (1 dbar = 0.98 m). This is a 13-hour record obtained by bow sensors from 7°05' S, 164°21' E to 5°00' S, 163°12' E (ship heading ~330°). Sharp frontal interfaces detected in $\sigma_t$ with the algorithm described in Section 5.4.2 are marked by asterisk signs. Reproduced from Soloviev and Lukas (1997b) by permission of American Meteorological Society.

Several factors complicate shipboard observations of the sharp frontal interfaces. Such fronts are very localized in space; the moments of their intersection are usually unknown in advance. For their study, high-resolution measurements over a relatively long time period are therefore necessary. There are no conventional techniques for such measurements. (Remember that standard shipboard thermosalinographs usually don't resolve features with scales less than several hundred meters.) Moreover, the magnitude of the cross-frontal difference in temperature ($T$) and salinity ($S$) is typically only of the order of 0.01 °C or psu. Such frontal interfaces may be strongly masked at the surface by diurnal warming or precipitation effects in the near-surface layer of the ocean. In measurements by moored sensors, the fronts can be detected only for extreme situations, because the frequency range of the signal from frontal passages substantially overlaps the frequency range of the diurnal warming/precipitation variability. High-resolution towed

measurements, however, do reveal the sharp frontal interfaces due to the horizontal scale separation.

During TOGA COARE, fast-response temperature, conductivity, pressure (depth), and turbulence probes were mounted on the bow of the R/V *Moana Wave* at a nominal depth of 1.7 m (Soloviev et al., 1998; Soloviev et al., 1999). The data were collected almost continuously during several cruises, which provided representative statistics of frontal interfaces..

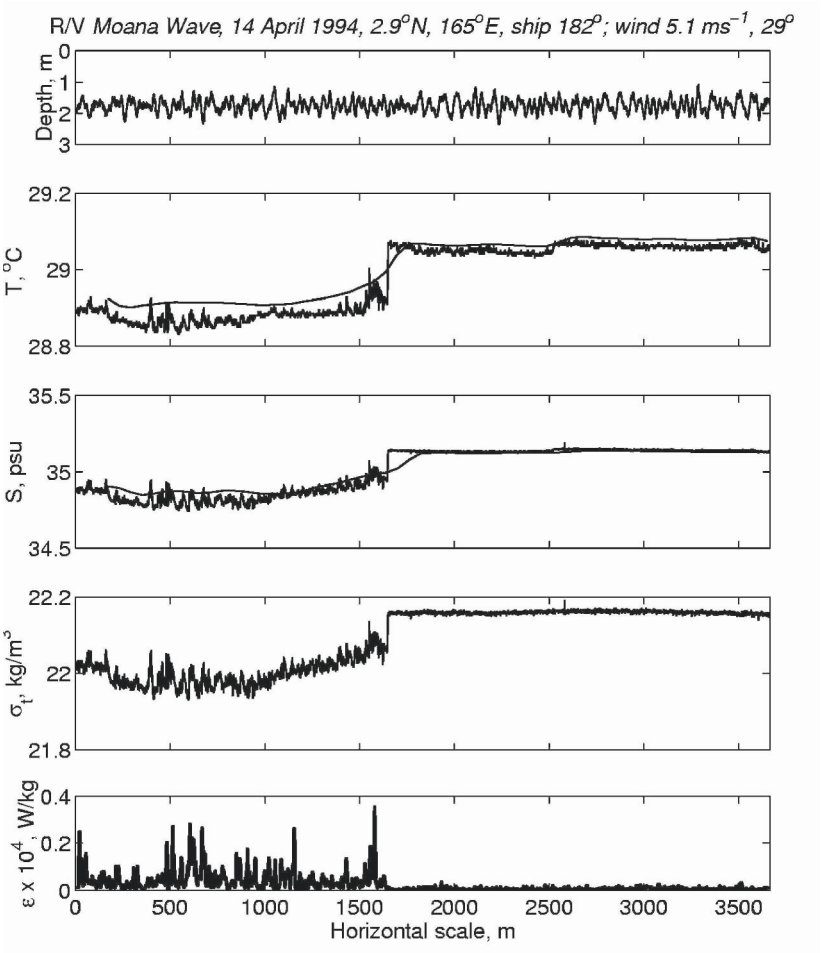


*Figure 5-24*. The depth (pressure), temperature (*T*), salinity (*S*), density ($\sigma_t$), and the dissipation rate of turbulent kinetic energy ($\varepsilon$) from bow sensors for the case of wind stress opposing the buoyant spreading of front. Corresponding records of temperature (bow thermistor at 3 m intake) and salinity (ship's thermosalinograph system) are shown with smooth lines. Reproduced from Soloviev et al. (2002) by permission from Elsevier.

It is intriguing that the frontal interfaces often appear in groups. *Figure 5-23* shows an example of such variation. The temperature, salinity, and density series reveal a quasi-periodic structure of about 10-60 km wavelength observed on the background of the mean horizontal density gradient of about 0.001 kg $m^{-3}$ $km^{-1}$. A feature of this structure is its strong asymmetry. A gradual rise of density is followed by its abrupt reduction.

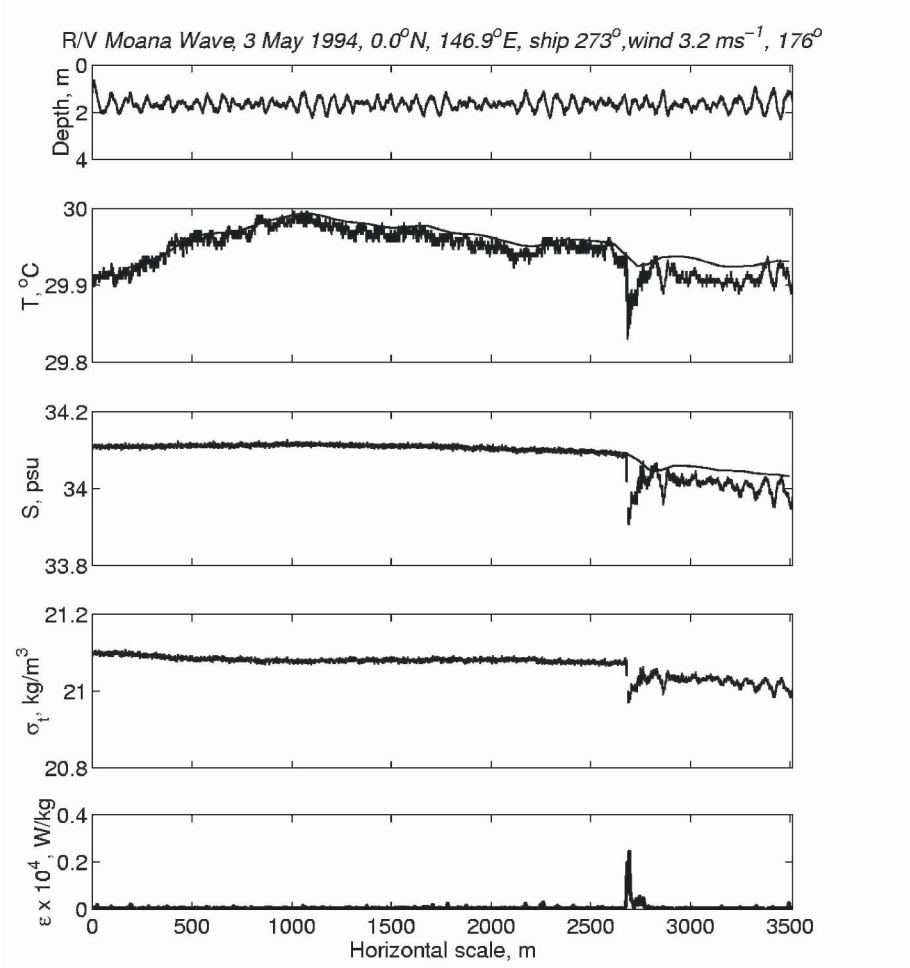


*Figure 5-25*. Same as in *Figure 5-24* but for a case where the wind stress was directed along frontal line. Reproduced from Soloviev et al. (2002) by permission from Elsevier.

Frontal interfaces can presumably interact with the wind drift current (Soloviev and Lukas, 1997b). *Figure 5-24*-*Figure 5-26* depict three examples of sharp frontal interfaces observed in the warm pool area during the R/V *Moana Wave* COARE EQ-3 cruise. In addition to high-frequency

signals from the bow sensors, the corresponding records of temperature and salinity from the ship's thermosalinograph system are also shown.

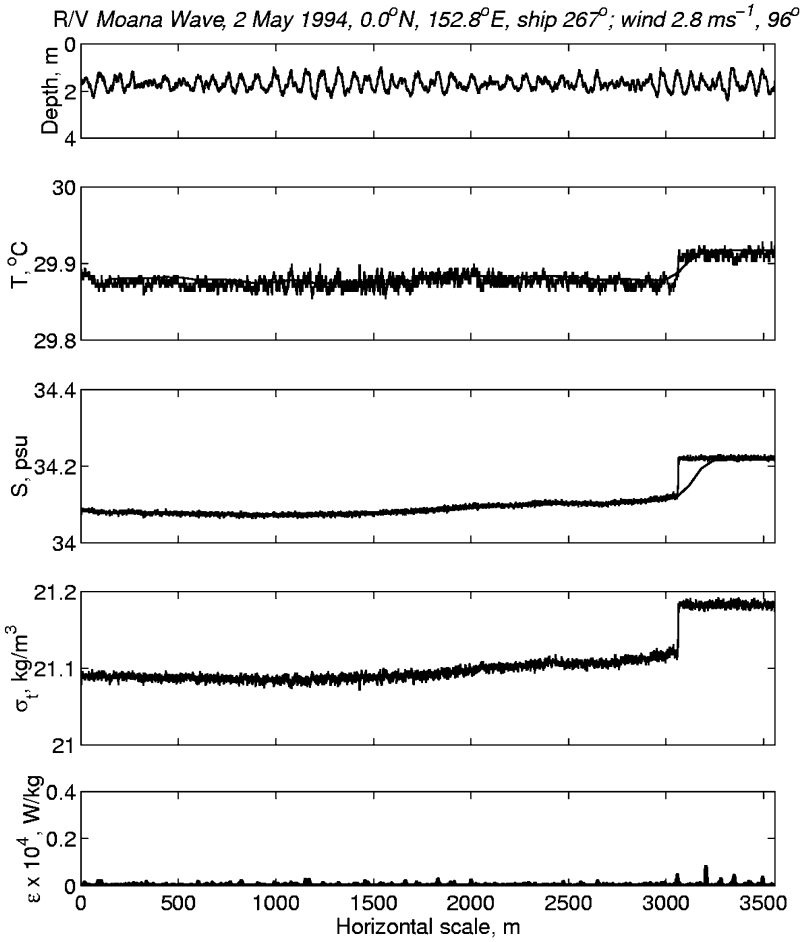


*Figure 5-26*. Same as in *Figure 5-24* but for a case with the wind stress directed from lighter to denser water. Reproduced from Soloviev et al. (2002) by permission from Elsevier.

There are dramatic changes in the turbulence dissipation rate associated with the frontal interface in the cases shown in *Figure 5-24* and *Figure 5-25*, while there are no signatures of turbulence variation related to the interface in the example shown in *Figure 5-26*. In *Figure 5-24*, the wind stress opposes the buoyant spreading of the front; the turbulence signal is substantially increased on the downwind side of the interface. In *Figure 5-25*, the wind stress is almost tangential to the front. There is a very localized increase in the turbulence signal associated with this frontal interface. Note that this front is relatively weak. *Figure 5-26* represents a

case where the wind stress was in the same direction as the direction of the buoyant spreading of the front. The turbulence dissipation level doesn't change at the interface intersection

These three cases represent noncompensated fronts. The differences in the turbulence signals in the vicinity of the fronts are possibly associated with the interaction of frontal interfaces with wind stress. *Figure 5-24* suggests that when the wind stress opposes the buoyant spreading of a sharp front, intensive mixing occurs at the front. It should be stressed that in most cases, however, the turbulence signals could not be confidently associated with the presence of sharp frontal interfaces. We also do not know the exact orientation of the front with respect to the ship track or wind.

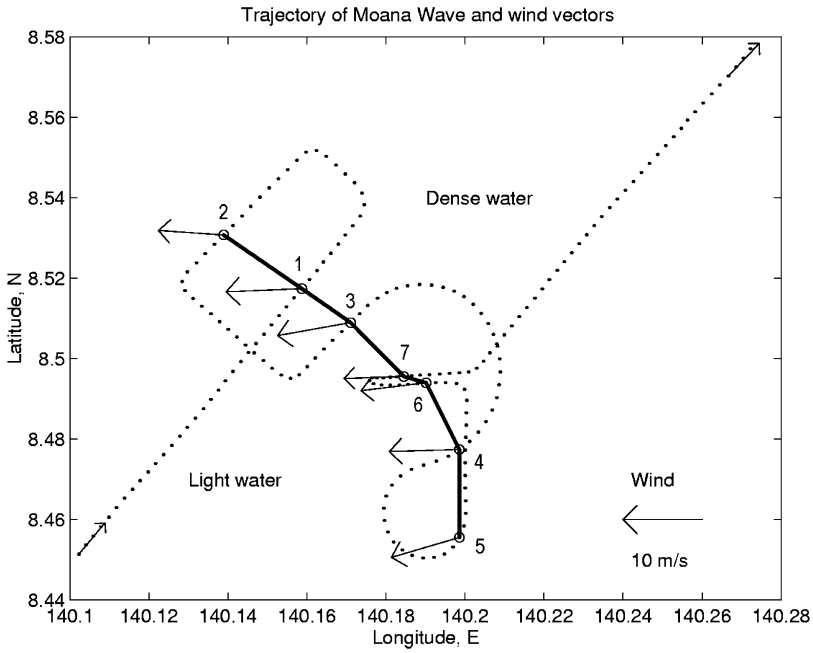


*Figure 5-27*. Snake-like trajectory of the ship and locations of intersection of the front. Position of the ship is shown by points; the time interval between points is 1 min. The front as determined by the points of its intersection (circles numbered from 1 through 6), is shown by a solid line. Corresponding values of the wind vectors from the ship's measurements are also shown. Reproduced from Soloviev and Lukas (1997b) by permission of American Meteorological Society.

A special survey in which the ship followed a snake-like trajectory was performed to determine the orientation of a particular frontal structure to the wind direction (*Figure 5-27*). The front was curved, and oriented approximately 45-80$^{o}$ to the wind direction. A reciprocal course was run at slower ship speed in order to obtain data at higher resolution while crossing the front.

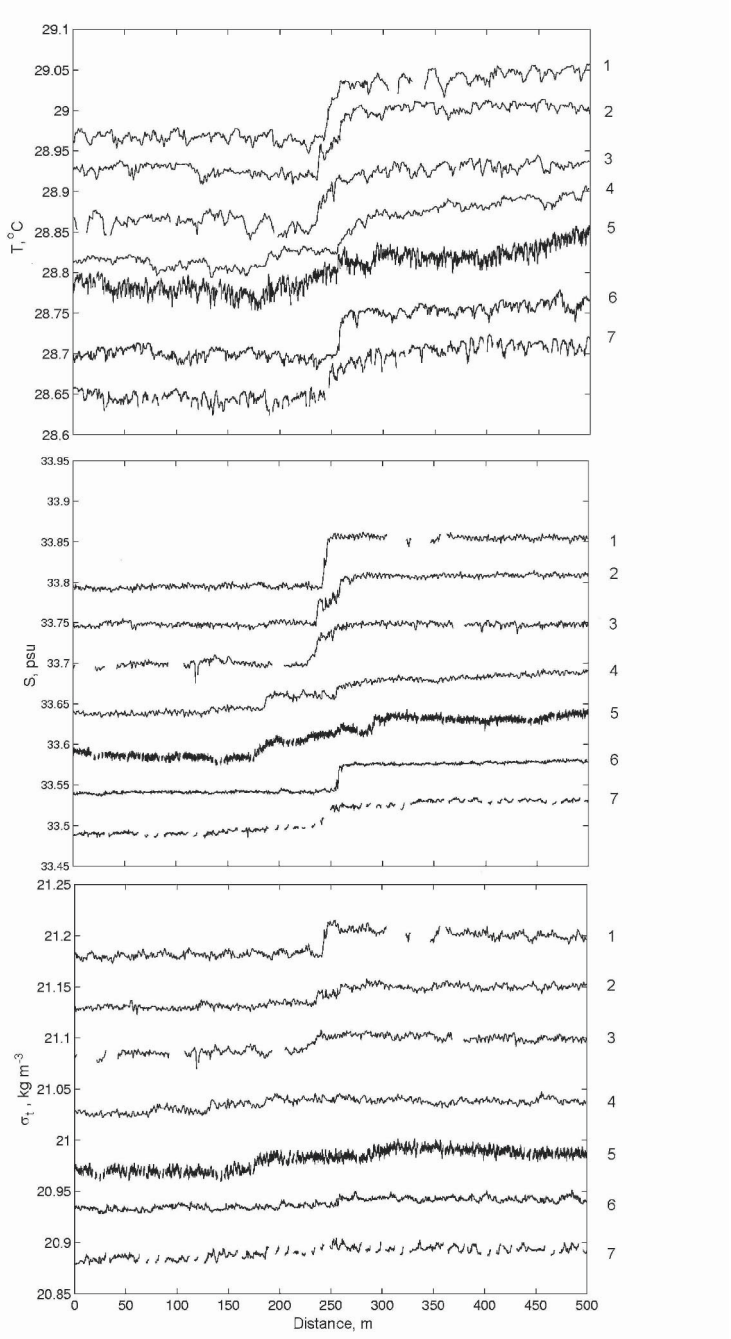


*Figure 5-28*. Small-scale structure of the sharp frontal interface shown in *Figure 5-27*. Blank spaces on S and $\sigma_t$ profiles correspond to surfacing of the probes due to ship pitching. Numbers along right axes indicate the successive cross-frontal sections. Reproduced from Soloviev and Lukas (1997b) by permission of American Meteorological Society.

*Figure 5-28* shows the individual intersections of the front on a high resolution distance scale. Intersections 2, 4 and, 6 are plotted in the inverse direction because of the reciprocal course of the ship at these intersections. For intersections 5, 6, and 7, the horizontal scale is multiplied by 0.15, 0.5, and 0.5 respectively to correct for the oblique angle of intersection with the front. A feature of this front is that it is seen in the $\sigma_t$ record only at intersections 1, 2, and 3. For the intersections 4, 5, 6, and 7 the frontal interface is almost compensated in the density field but is still seen in the *T* and *S* records. The front shown in *Figure 5-28* is of about one order of magnitude wider than that shown in Figure 5-26. We ascribe this difference to the wind stress direction opposing the buoyant spreading of the front in the former case.

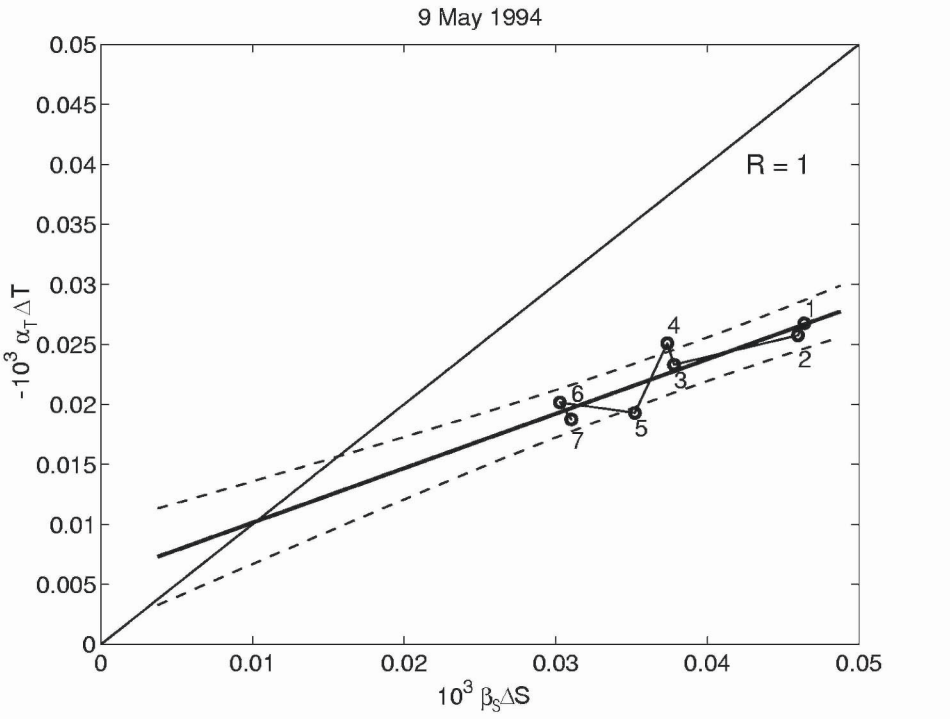


*Figure 5-29*. Evolution of the temperature-salinity relationship during multiple intersections of a sharp front in the warm pool area during the R/V *Moana Wave* COARE EQ-3 cruise. The successive frontal intersections are numbered from 1 to 7 (for more details see *Figure 5-27*). These points are linearly extrapolated (bold straight line) up to the intersection point with line *R* = 1, while the space between dashed lines contain at least 50% of the predictions. Reproduced from Soloviev et al. (2002) by permission from Elsevier. © 2002 Elsevier.

*Figure 5-29* demonstrates how the temperature-salinity relationship across this front evolved over time with the wind stress opposing the

buoyant spreading of front. During several hours the ship crossed back and forth across this front (*Figure 5-27*). The front appears to degrade considerably during the time period; the temperature-salinity relationship tends toward the equilibrium state, which is characterized by density ratio,

$$R = \alpha_T \Delta T / \beta_S \Delta S = 1 , \tag{5.24}$$

where $\alpha_T = \left(\partial_t \rho / \partial T\right)\Big|_{p,S}$ and $\beta_S = \left(\partial \rho_t / \partial S\right)\Big|_{p,T}$ are the expansion coefficients of temperature and salinity in units kg m$^{-3}$ $^{o}$C$^{-1}$ and kg m$^{-3}$ psu$^{-1}$, and the temperature and salinity differences $\Delta T$ and $\Delta S$ are taken across the frontal interface.

Equation (5.24) is shown by the straight diagonal line in *Figure 5-29*. (Note that some contribution from spatial variation of the front is possible in *Figure 5-29*.) According to the linear interpolation of the *T-S* tendency (*Figure 5-29*), the compensated state for this frontal interface could be achieved at $\alpha_T \Delta T \approx 1 \cdot 10^{-5}$ and $\beta_S \Delta S \approx 1 \cdot 10^{-5}$, which corresponds to $\Delta T \approx -0.030\,^{o}$C and $\Delta S \approx 0.013$ psu.

After the interface achieves the compensated state ($R$=1), it is no longer affected by wind stress (see Section 5.4.4). The density ratio $R$ is therefore an important parameter characterizing the dynamics of sharp frontal interfaces.

### 5.4.2 Statistics of sharp frontal interfaces in the western Pacific warm pool

The presence of sharp frontal interfaces is associated with the subduction process in the surface mixed layer, which is important in forming the barrier layer in the warm pool area. The cases of sharp fronts described in the previous section represent extreme situations. In many other cases, the temperature, salinity, and density differences across fronts are relatively small. Thus, these fronts cannot be seen visually on the ocean surface as in the case shown in *Figure 5-17*, they may not be detected from the available ADCP measurements because they are often shallower than 16 m (*Figure 5-21* and *Figure 5-22*), and they cannot be seen in the bow turbulence records as in the case shown *Figure 5-24-Figure 5-26*. These frontal interfaces, however, can be detected in the bow density, salinity, and temperature records due to huge local gradients within the interfaces.

Soloviev and Lukas (1997b) developed an algorithm for the automatic detection of sharp frontal interfaces. The sharp frontal interface is detected in a scalar property $C$ when $\left|dC/dx\right| > n \cdot std(dC/dx)$. In order to detect the sharpest frontal interfaces, Soloviev and Lukas (1997b) recommend to set $n$ = 4.

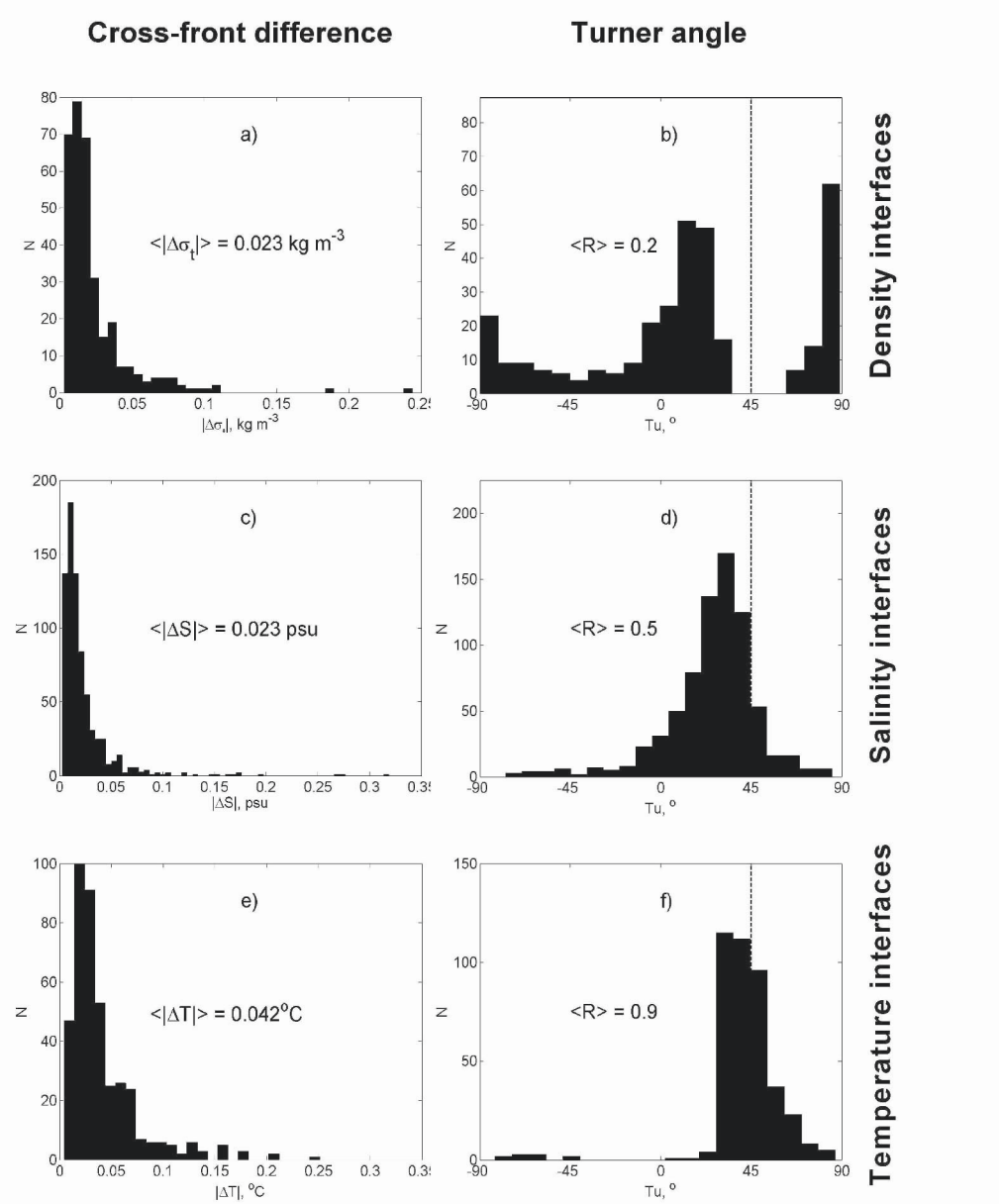


*Figure 5-30*. Statistics of sharp frontal interfaces acquired with bow sensors during four TOGA COARE cruises of the R/V *Moana Wave*. Histograms of cross-front differences for the sharp frontal interfaces detected in (a) density, (c) salinity, and (e) temperature data and respective histograms (b, d, and f) for the Turner angle.

The ability to detect an interface depends on the ratio of the maximum gradient within the interface to the level of background fluctuations. Background fluctuations depend strongly on environmental conditions such

as the wind speed, heat fluxes, presence of rain, diurnal warming and so on. An interface may be clearly seen, for example, in the salinity record but fall below the detection level in the temperature and/or density record(s). Some interfaces are therefore found simultaneously in two or three of these variables while others appear clearly in only one variable. We will hereafter refer to the sharp frontal interfaces found in density, salinity, and temperature records as the *density*, *salinity*, and *temperature interfaces* respectively.

In *Figure 5-30*, statistical properties of the density, salinity, and temperature interfaces obtained from bow records during four TOGA COARE cruises of the R/V *Moana Wave* are summarized in the form of histograms. The first, second, and third rows in *Figure 5-30* correspond to the density, salinity, and temperature interfaces. The total number of sharp fronts found in density, $N_\rho = 326$, in salinity, $N_S = 751$, and in temperature, $N_T = 412$. The statistics presented in *Figure 5-30* include the cross-front difference of density, salinity, and temperature (left column) and the density ratio $R$ for the density, salinity, and temperature interfaces expressed in terms of the Turner angle (the right column).

In the oceanographic literature, $Tu = \arctan(R)$ is known as the Turner angle (Ruddick and Turner, 1979), where $R$ is defined as in (5.24). The Turner angle is positive when temperature and salinity tend to compensate each other in density. For compensated fronts $R = 1$ and $Tu = \pi/4$. For fronts with no temperature difference ($\Delta T = 0$), $R = 0$ and $Tu = 0$, while for fronts with no salinity difference ($\Delta S = 0$), $R = \infty$ and $Tu = \pi/2$

As emphasized by Ferrari and Rudnick (2000), the advantage of using the Turner angle instead of the density ratio number is that the infinite scale of $R$ is replaced by a finite one running from $-\pi/2$ to $\pi/2$. Also, the temperature dominated regions ($1 < |R| < \infty$) and salinity-dominated regions ($0 < |R| < 1$) occupy the same space on the $Tu$ scale, which in particular means that the ensemble averaging over $Tu$ may be more accurate than that over $R$.

According to *Figure 5-30*, the average density ratio number defined as $\langle R \rangle = \tan(\langle Tu \rangle)$ is relatively small for density interfaces ($\langle R \rangle = 0.2$), is larger for salinity interfaces ($\langle R \rangle = 0.5$), and approaches unity for temperature interfaces ($\langle R \rangle = 0.9$). (The operator $\langle\rangle$ here denotes ensemble averaging). The interpretation is that all density interfaces and a part of the salinity interfaces are not compensated interfaces, while the majority of the temperature interfaces appear to be compensated interfaces.

*Figure 5-31* shows the dependence of sharp frontal interfaces on the wind-to-ship angle, $\theta$, (the left column) and on the wind speed, $U_a$ (the right column) separately for the density, salinity, and temperature interfaces (the first, second, and third rows respectively). Salinity and temperature

differences in *Figure 5-31*c-f are multiplied by the corresponding expansion coefficients, $\alpha_T$ or $\beta_S$, to have comparable (density) units on all graphs. *Figure 5-31* represents the bow data sets collected during the four COARE cruises of the R/V *Moana Wave* (same as in *Figure 5-29*). The data in *Figure 5-31* are averaged over $\theta$ within $\pm 24^o$ and $U_a$ within $\pm 2$ m s$^{-1}$. The vertical bars represent one standard error confidence limits calculated on the basis of Student's distribution (Rabinovich, 1995).

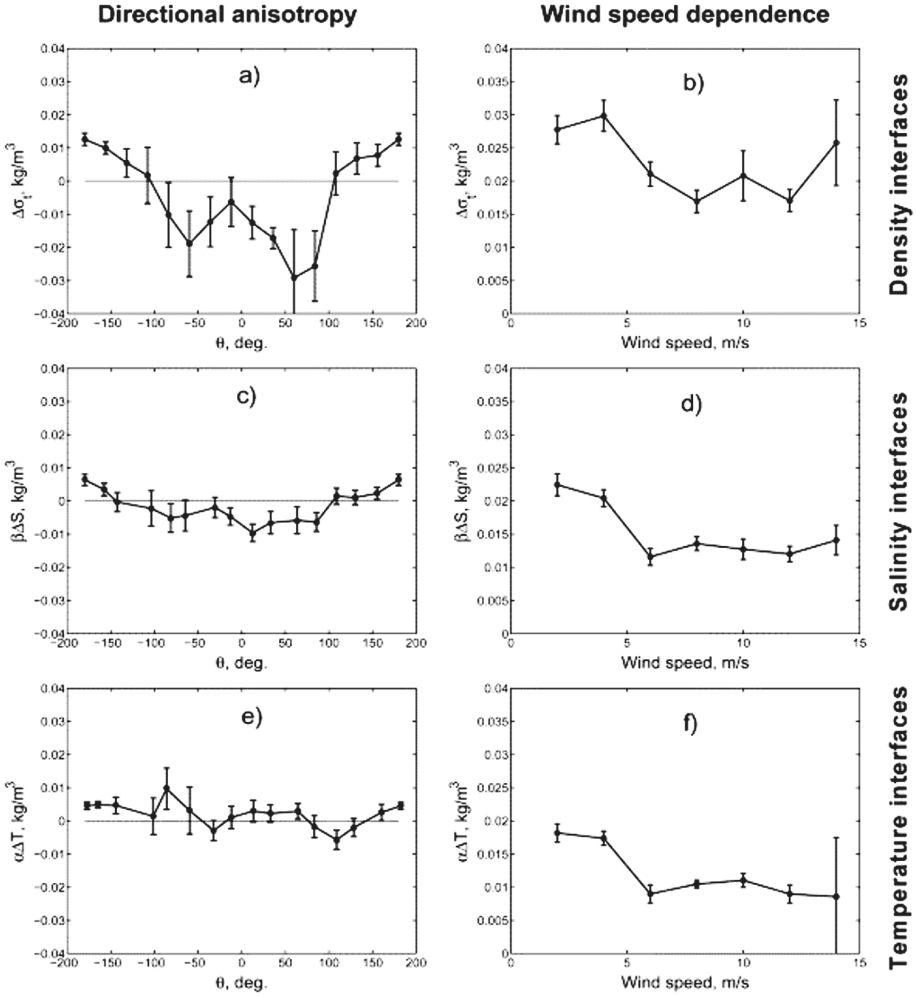


*Figure 5-31*. Directional and wind speed dependence of the sharp frontal interfaces detected in the (a, b) density, (c, d) salinity, (e, f) temperature bow data respectively. The data are from four TOGA COARE cruises. The temperature and salinity differences are shown as the equivalent density differences to simplify their visual comparison with the density differences in a) and b). The vertical bars represent one standard error confidence limits calculated from Student's distribution. Reproduced from Soloviev et al. (2002) by permission from Elsevier.

At the intersection of a particular frontal interface we do not know the intersection angle. Soloviev and Lukas (1997b) nevertheless showed that in a statistical sense for the frontal interfaces detected with their algorithm, the average wind-to-front angle, $<\phi>$, can be replaced with the average wind-to-ship angle, $<\theta>$, where $\theta = \beta - \gamma$, $\beta$ is the wind direction (we use the meteorological convention), and $\gamma$ is the ship's course. The front vector is defined here as a vector that is normal to the frontal line. The vector direction is positive from less to more dense water (*i.e.,* coinciding with the direction of the gravitational spreading of the front).

According to *Figure 5-31*, the density and salinity interfaces (which are mostly not compensated fronts) appear to depend on the wind-to-front angle. The spatial anisotropy is pronounced for the density interfaces (*Figure 5-31*a), is less pronounced (but still statistically significant) for the salinity interfaces (*Figure 5-31*c), and is practically non-resolvable for the temperature interfaces (*Figure 5-31*e).

It is remarkable that the density fronts do not seem to depend much on the wind speed magnitude (*Figure 5-31*b), while the salinity and temperature interfaces degrade with increasing wind speed. Larger error bars in *Figure 5-31*b and *Figure 5-31*f at 14 m $s^{-1}$ average wind speed are primarily due to a relatively small number of observations of the density and temperature fronts under high wind speed conditions (10 and 3 respectively). For the salinity interfaces, this number is larger (37), and the confidence limits for the 14 m $s^{-1}$ bin are smaller (*Figure 5-31*d).

Based on the theory developed in Section 5.4.4, the fronts that do not satisfy inequality (5.42) (*i.e.*, cannot interact with wind stress) are removed from the ensemble averaging in *Figure 5-31*. Removal of this relatively small number of interfaces (see histogram in *Figure 5-37*b) results in some reduction of error bars but does not modify the main conclusions about directional anisotropy and wind speed dependence of the sharp frontal interfaces.

### 5.4.3 Internal wave–shear flow interaction as a cause of repeating frontal interfaces

Soloviev and Lukas (1997b) hypothesized that the sharp frontal interfaces may occur as a result of nonlinear buoyant adjustment of the stably stratified near-surface layer of the ocean to external forcing. The external forcing includes the variable buoyancy flux and wind stress at the ocean-air interface, tidal motions, and so forth. Relatively small thickness of the near-surface anomalies is favorable for the development of nonlinear interactions. The frontal interfaces are often found in groups (as in the example shown in *Figure 5-23*). This feature of the frontal interfaces was

explained using a "buoyant" asymptotic of the problem (*i.e.*, neglecting rotational effects).

Laboratory studies indicate that any density anomaly in the upper layer tends to spread horizontally. The leading edge of the gravity current along a boundary through a uniformly stratified medium can generate several different modes of internal waves. According to a laboratory observation described by Simpson (1987), "…These waves affected the form of the gravity current behind the head in a rhythmical manner. The fluid in the original head was cut off from the flow, which formed a second head. The process was repeated and later a third new front appeared…" However, this striking effect was observed only when the Froude number,

$$Fr_0 = \frac{U_b}{NH} < \frac{1}{\pi} \tag{5.25}$$

and the fractional depth of the gravity current was less than 0.2 of the total depth $H$ (here: $U_b$ is the speed of the gravity current and $N$ is the Brunt-Vaisala frequency of stratified surroundings). This is a resonant type of mechanism; it provides a plausible explanation for the appearance of upper ocean sharp frontal interfaces in groups.

In the equatorial region, the maximum spatial scale of buoyancy driven anomalies is restricted by the baroclinic Rossby radius (Moore and Philander, 1977). The equatorial baroclinic Rossby radius is

$$L_\beta = \left( \frac{c}{2\beta} \right)^{1/2}, \tag{5.26}$$

where $\beta = \left( \partial f / \partial y \right)_{\varphi=0} = 2.3 \times 10^{-11}$ m$^{-1}$ s$^{-1}$, $f$ is the Coriolis parameter, and $c$ is the phase speed of internal perturbations. At $c = 0.1 - 0.4$ m s$^{-1}$ (typical for weakly stratified mixed layer), $L_\beta = 50 - 100$ km, which correlates with the maximum horizontal distance between the sharp frontal interfaces observed in the western equatorial Pacific warm pool.

The nature of interaction between the near-surface current and the internal wave field has been described in several theoretical studies (Romanova, 1984; Voronovich et al., 1998a). The vorticity and internal gravity waves interact and influence each other in the presence of density stratification. This influence is relatively weak when far from the resonance, but is greatly enhanced when the phase speed of the vorticity wave matches the celerity of one of the internal wave modes. The internal wave-shear flow resonance can lead to the splitting of the near-surface gravity current into a coherent series of frontal interfaces.

The sketch in *Figure 5-32* shows the flow geometry in the Romanova (1984) and Voronovich et al. (1998a) theory. The problem is formulated under a rigid-lid approximation. The shear is localized in the thin subsurface layer of thickness *h* and has no inflection points in the velocity profile *U*(z). The latter condition is to ensure that the flow is dynamically stable with respect to perturbations in the inviscid limit.

For resonance to occur in the flow configuration shown in *Figure 5-32*, the typical frequency of the vorticity waves should be of the same order as that of the internal wave $N_0$

$$u_0 / H = c_N N_0 = \max\left(N\right), \tag{5.27}$$

where equation (5.27) is formulated in dimensional variables and $c_N$ is a dimensionless coefficient.

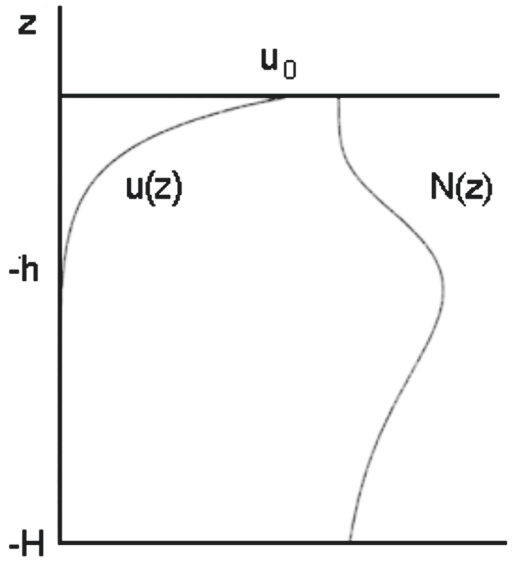


*Figure 5-32*. Flow geometry and notation in the theory of shear waves. (After Romanova, 1984.)

In an attempt to describe the nonlinear resonant interaction by means of an asymptotic analysis, Voronovich et al. (1998a) derived the set of two coupled equations for normalized wave amplitudes *a* and *b* of the internal and vorticity modes, respectively.

$$\begin{cases} a_t + \Delta a_x + a_{xxx} - b_x = 0, \\ b_t + 2bb_x - a_x = 0. \end{cases} \tag{5.28}$$

where $\Delta$ is a free parameter corresponding to a disparity in the coupled wave phase speeds.

Two types of solutions for plane solitary waves follow from (5.28). The first type of solutions ("supercritical") propagates with velocities greater than that of the current, which is expressed by inequality:

$$u_0 / H < c_N N_0 . \tag{5.29}$$

The supercritical solution has amplitudes limited by the critical value (*i.e.*, the value at which the solitary wave exhibits a sharp corner at the crest – see also *Figure 5-33*). This type of nonlinear instability leads to the formation of vertical slopes and, thus, to wave breaking in finite time. Solitary waves of the second type ("subcritical") have velocities smaller than the flow speed at the surface and are characterized by a series of smooth pulses.

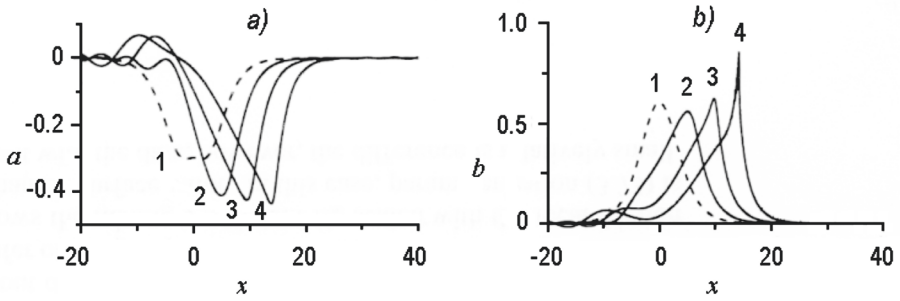


*Figure 5-33*. Nonlinear evolution of an initial pulse of supercritical amplitude. Graphs (a) and (b) represent solutions of (5.28) (for variables *a* and *b* respectively) at different dimensionless time *t*. (After Voronovich et al., 1998a.) Reprinted with the permission of Cambridge University Press.

It is easy to see that (5.29) is similar to (5.25). The supercritical solution following from the internal wave–shear flow interaction theory can therefore be identified as that describing the formation of repeating ageostrophic fronts.

This specific application of the internal wave–shear flow interaction theory described above has not yet been developed in detail. In particular, the effects of wind stress and turbulent mixing have to be incorporated into this theoretical analysis. We consider the interaction of sharp frontal interfaces with wind stress in the next section (which, however, is based on strong assumptions).

It should be noted that in contrast to the Kelvin-Helmholtz instability (Section 5.5.3) the critical layer contribution to the internal wave–vortex resonance is negligible. These are fundamentally different mechanisms.

### 5.4.4 Interaction of sharp fronts with wind stress

High-resolution horizontal measurements in the open ocean thus reveal frontal interfaces of width less than 100 m. These sharp frontal interfaces have been observed in a wide range of wind speed conditions (0–15 m $s^{-1}$). The frontal interfaces of less than ~100 m width reveal anisotropy with respect to the wind stress direction (*Figure 5-31*).

Some of the frontal interfaces are narrow–sometimes only a few meters. Detailed analysis of the record shown in *Figure 5-26* reveals that the width of the frontal interface is only about 1.5 m; the absolute values of the horizontal temperature, salinity, and density gradients within this interface reach 137.8°C $km^{-1}$, 125.8 psu $km^{-1}$, and 47.96 kg $km^{-1}$ respectively. In particular, the density gradient within the interface is about $5x10^4$ times larger (!) than the mean horizontal density gradient (which is ~0.001 kg $m^{-3}$ $km^{-1}$). This interface looks pretty much like a discontinuity or a "wall" in the upper ocean.

How can such discontinuities survive in the turbulent ocean? Soloviev and Lukas (1997b) suggested that this happens because noncompensated fronts narrower than 100 m could interact with the wind stress. When the wind stress is directed toward lower density, gravitational instability may trigger intensive vertical and cross-frontal mixing. In the process of mixing, the interface may either reach the compensated state or entirely disappear; in both cases, the interface is no longer prominent in the density field. When the wind stress is directed toward higher density, vertical stratification develops due to tilting, which inhibits mixing. As a result, the sharp interface "freezes" and can drift down wind until the wind substantially changes either its direction or speed with respect to the front. The lifetime of the sharp frontal interfaces can therefore be linked to the synoptic time scale for atmospheric processes (~5 days).

Soloviev et al. (2002) later identified this mechanism of the interaction between a sharp front and wind stress as Stommel's overturning gate (*Figure 5-34*). According to Stommel (1993):

"Future observational study of the three-dimensional structures within the 'mixed' layer may show that direct driving of shear within the layer by wind overwhelms the hypothetical density-driven exchanges of thermohaline regulations (…) In the presence initially of a horizontal density gradient in the direction of the displacement, one of two events will ensue. If the displacement is toward larger mixed-layer density, then vertical stratification develops. Vertical mixing eventually occurs. There is a horizontal exchange of properties. On the other hand, if the wind-forced displacement of the surface half of the mixed layer is toward smaller density below, rapid gravitational instability will mix the two halves immediately, effectively

short cutting the horizontal exchange (...) Therefore, there is a form of gate that opens or closes to allow horizontal flux of properties in the mixed layer, and it depends on the joint signs of displacement and local horizontal density gradient. For convenience this phenomenon may be called the *overturning gate.*"

Stommel's overturning gate is open when the surface wind drift current is directed toward higher density and closed when directed toward lower density, as it is schematically illustrated in *Figure 5-34*a, b. In case b, the wind drift current stabilizes the sharp frontal interface, which then resembles an arrested wedge.

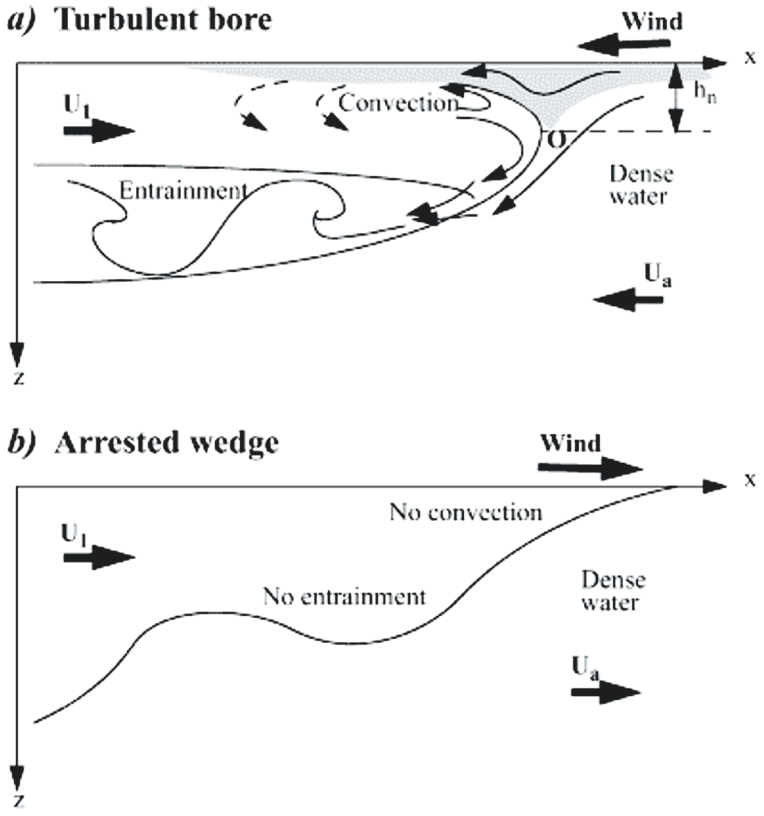


*Figure 5-34*. Interaction of sharp frontal interface with wind stress: (a) Stommel's overturning gate is closed; (b) Stommel's overturning gate is opened. Reproduced from Soloviev et al. (2002) by permission from Elsevier.

The spatial anisotropy of noncompensated interfaces (*Figure 5-31*a, c) can therefore be explained by the fact that most sharp frontal interfaces are observed when the wind stress is directed towards higher density (the overturning gate is opened). When the wind stress is towards lower density

(the overturning gate is closed) the intensive mixing effectively eliminates noncompensated sharp frontal interfaces (this process is illustrated in *Figure 5-28*). The lifetime of an noncompensated sharp frontal interface opposing the wind stress is relatively small; the probability of its observation is reduced.

Stommel's overturning gate is a complicated nonlinear problem. Its faithful solution in the framework of the hydrodynamics equations is not feasible now, though the internal wave–shear flow interaction theory described in the previous section has a good chance to succeed in this direction.

At the same time, the structural form of the sharp frontal interfaces has some similarity to that of the internal surge previously observed in long stably stratified lakes (Thorpe, 1971; Hunkins and Fliegel, 1973; Farmer, 1978). Evolution of an initially smooth perturbation with wavelength $\lambda >> h_0$ into an asymmetric shockwave structure can be described in the framework of shallow water theory similar to the analysis of Farmer (1978) for a long stably stratified lake, but in our case, $h_0$ is the depth of the intermediate thermocline associated with the front.

At the stage when the internal perturbation's slope becomes very steep, dispersion and dissipation effects are important in this nonlinear system. Whitham (1974) and Barenblatt and Shapiro (1984) applied an equation of Korteweg-deVries-Burgers type to explore a simple nonlinear system with dispersion and dissipation. Applied to a two-layer upper ocean with an infinitely deep lower layer this equation is as follows:

$$\eta_t + c_0(1+\frac{3}{2}\frac{\eta}{h_0})\eta_x + \frac{1}{6}c_0 h_0^{\,2}\eta_{xxx} = \nu_e \eta_{xx}\,, \tag{5.30}$$

where $\eta$ is the displacement of streamlines, $t$ is time, $x$ is the horizontal coordinate in the direction of propagation, $h_0$ is the undisturbed depth of the near-surface pycnocline, $c_0 = \left(g' h_0\right)^{1/2}$ is the phase speed of the disturbance, $g'$ is the reduced gravity, and $\nu_e$ is the effective (turbulent) viscosity.

The Korteweg-deVries-Burgers equation is a convenient tool in exploring the relative importance of dissipation and dispersion in a weakly stratified mixed layer of the ocean, since this equation represents the simplest form of nonlinear evolution including both dispersion and dissipation. (Some caution should however be exercised here because Whitham (1974) and Barenblatt and Shapiro (1984) did not derive (5.30) directly from the Navier-Stokes equation.)

Steady propagating solutions of (5.30) are of the form $\eta = h_0\zeta(X)$, $X = x - Ut$, where $U$ is the propagation speed of the disturbance. Integration of Eq (5.30) results in (Whitham, 1974):

$$\frac{1}{6}h_0{}^2\zeta_{xx} - \frac{\nu_e}{c_0}\zeta_x + \frac{3}{4}\zeta^2 - \left(\frac{U}{c_0} - 1\right)\zeta = 0\,, \tag{5.31}$$

which can be normalized in the following way:

$$z_{\xi\xi\xi} - mz_\xi + z^2 - z = 0\,, \tag{5.32}$$

where $\xi = \left[6\left(Fr-1\right)\right]^{1/2}\frac{X}{h_0}$, $z = \frac{3}{4\left(Fr-1\right)}\zeta$, $F = \frac{U}{c_0}$,

$$m = \left(\frac{6}{Fr-1}\right)^{1/2}\mathrm{Re}_*^{-1}, \tag{5.33}$$

$$\mathrm{Re}_* = h_0(g'h_0)^{1/2}\nu_e^{-1}. \tag{5.34}$$

Here $\mathrm{Re}_*$ is the dimensionless Reynolds number, which defines the relationship between the dissipative and dispersive properties of this nonlinear system (Barenblatt and Shapiro, 1984). According to Whitham (1974), for $m < 2$ the solution is a wavelike (soliton) type, while for $m > 2$, it is a shockwave (dissipative) type. The critical value of $m = 2$ at $Fr = 1.2$ (see Section 5.4.2) corresponds to $\mathrm{Re}_* = \mathrm{Re}_{cr} = 2.74$. This means that the solution of (5.30) is wavelike in nature (and finally evolves into a wavelike bore) for $\mathrm{Re}_* > \mathrm{Re}_{cr}$ and is turbulent in nature (and finally evolves into a turbulent bore) for $\mathrm{Re}_* < \mathrm{Re}_{cr}$.

The wavelength of the wave train that occurs at $\mathrm{Re}_* < \mathrm{Re}_{cr}$ can be estimated using Whitham's (1974) solution of (5.32) as follows: $\lambda \approx 6.5\left[6\left(F-1\right)\right]^{-1/2}h_0$. At $Fr = 1.2$ and $h_0 = 20$ m, this results in a 120 m wavelength.

One problem emphasized by Whitham (1974) is that the effective viscosity that can be obtained by parameterization via the mean shear flow is about 10 times smaller than necessary to achieve the critical value of $\mathrm{Re}_*$. This problem, however, can be resolved by incorporating Stommel's concept of the overturning gate. When the wind stress opposes buoyant spreading of the sharp front, the convective overturning enhances the effective viscosity at the sharp frontal interface. Soloviev and Lukas (1997b) parameterized the effective viscosity entering (5.34) as a sum of shear ($\nu_{shear}$) and convectively ($\nu_{conv}$) induced turbulent viscosity:

$$\nu_e \approx \nu_{shear} + \nu_{conv} = \nu_{shear} f_c , \tag{5.35}$$

where $\nu_{shear} = \kappa u_* h_0$, $f_c = \nu_{conv} / \nu_{shear} \approx 1 + \left[ 30 \frac{h_0}{L} \left( \cos\phi + |\cos\phi| \right) \right]^{1/3} \frac{Ri_*^{1/6}}{\kappa}$ is the factor describing convective enhancement of mixing in the frontal zone, $L$ is the width of the frontal interface, $Ri_* = g' h_0 / u_*^2 = \left( c_0 / u_* \right)^2$, $c_0$ is the phase speed of internal disturbances, $u_*$ is the friction velocity in water, $\kappa$ is von Karman's constant ($\kappa$ = 0.4), $\phi$ the wind direction relative to the direction of buoyant spreading of the front. For $\phi$ > 90° or $\phi$ < -90° and $f_c \equiv 1$, no convective instability is possible (Stommel's overturning gate is opened), while for –90° < $\phi$ < 90° and $f_c > 1$ convective instability at the leading edge of the gravity current can develop (Stommel's overturning gate is closed).

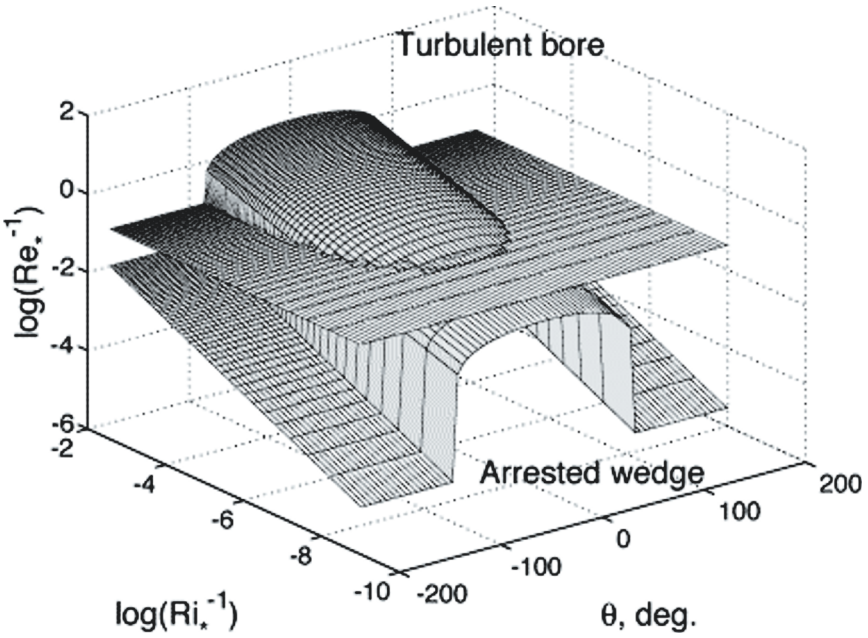


*Figure 5-35*. Diagram for the two regimes of wind-front interaction according to (5.36) –(5.37). Reproduced from Soloviev et al. (2002) by permission from Elsevier.

Incorporation of parameterization (5.35) into (5.34) leads to the following relationship:

$$\mathrm{Re}_*\left(Ri,\phi\right) \approx \frac{\kappa^{-1} Ri_*^{1/2}}{\left\{1+\left[30\left(\cos\phi+\left|\cos\phi\right|\right)h_0/L\right]^{1/3}\kappa^{-1}Ri_*^{1/6}\right\}}, \tag{5.36}$$

which is shown in *Figure 5-35*. The horizontal plane in *Figure 5-35* corresponds to the relationship

$$\mathrm{Re}_* = \mathrm{Re}_{cr} = 2.74, \tag{5.37}$$

which separates the arrested wedge and turbulent bore regimes.

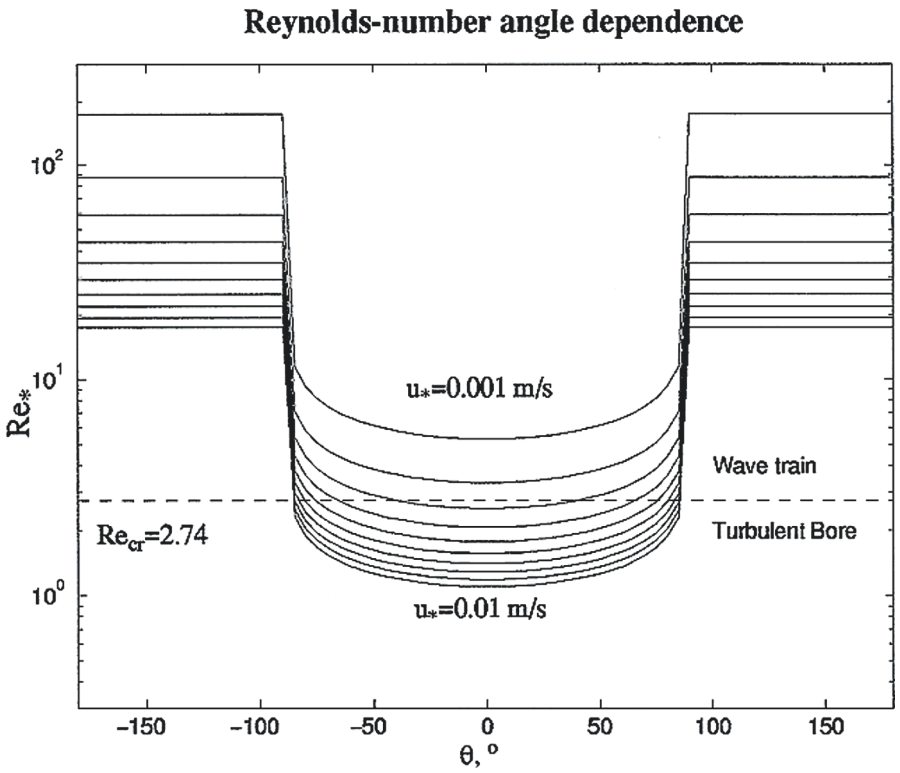


*Figure 5-36*. Dependence of Reynolds number $\mathrm{Re}_*$ on wind direction relative to the direction of the buoyant spreading of the front $\theta$, calculated for friction velocity $u_*$ from 0.001 to 0.01 m s$^{-1}$ in steps of 0.001 m s$^{-1}$. Dashed line represents critical value of the Reynolds number. Reproduced from Soloviev and Lukas (1997b) by permission of American Meteorological Society.

A two-dimensional version of *Figure 5-35* is given in *Figure 5-36*, which shows (5.36) for $h_0$ = 10 m, $L$ = 20 m, and $\Delta\sigma_t$ = 0.05 kg m$^{-3}$ for the friction

velocity range 0.001 m $s^{-1}$ < $u_*$ < 0.01 m $s^{-1}$. A turbulent bore solution is possible when the wind opposes the buoyant spreading of the front. Under light winds or in the case when the wind velocity is directed along the direction of buoyant spreading of the front, $\mathrm{Re}_* > \mathrm{Re}_{cr}$, and the solution is of the wave train type

For the case shown in *Figure 5-17-Figure 5-21*, $\mathrm{Re}_* \approx 2-4$; the sharp front is close to the regime of the internal turbulent bore. For the case shown in *Figure 5-22*, $\mathrm{Re}_* \approx 60$; the sharp frontal interface is in the arrested wedge regime. Since dispersion dominates over dissipation in the arrested wedge regime, an internal wave train may develop. The horizontal grid for the SEASOAR and ADCP data (3 km) is not sufficient to resolve short internal wave trains, however. Soloviev et al. (2002) speculated that from the bow data it is possible to see these short-wave oscillations at the front intersection only when the surface plume depth is relatively shallow (with respect to the sensor depth, which is ~2 m). In the cases presented in *Figure 5-17-Figure 5-21*, the plume depth was much larger than 2 m.

When the wind stress direction coincides with the buoyancy driven propagation of the front ($\theta = 180^o$), (5.36) reduces to

$$\mathrm{Re}_*\left(Ri, 180^o\right) = \kappa^{-1} Ri_*^{1/2}. \tag{5.38}$$

Since $Ri_* = \left(c_0 / u_*\right)^2$ and $c_0 >> u_*$, the development of a turbulent bore in this situation is practically impossible.

When the wind stress opposes the buoyant spreading of the front ($\phi = 0^o$), (5.36) correspondingly reduces to

$$\mathrm{Re}_*\left(Ri, 0\right) = \frac{\kappa^{-1} Ri_*^{1/2}}{\left\{1 + \left(60h/L\right)^{1/3} \kappa^{-1} Ri_*^{1/6}\right\}}. \tag{5.39}$$

Estimates show that the condition for the development of an internal turbulent bore,

$$\mathrm{Re}_*\left(Ri_*, 0\right) < \mathrm{Re}_{cr}, \tag{5.40}$$

can be easily satisfied for a weakly stratified mixed layer. For the seasonal thermocline, however, it is practically impossible to satisfy (5.40) due to considerable stratification and larger depth. The response to wind forcing in the form of an internal turbulent bore is therefore possible for weakly stratified mixed layers but not possible for the seasonal thermocline (perhaps except during hurricane conditions).

Since for most practical situations, $(60h/L)^{1/3}\kappa^{-1}Ri_*^{1/6} >> 1$, formula (5.39) can be simplified as follows

$$\mathrm{Re}_*(g',u_*,0) \approx {1}/{60^{1/3}}\left(g'L/u_*^2\right)^{1/3} = \mathrm{Re}_L, \tag{5.41}$$

which contains only parameters that are readily available from the ship's underway measurements ($g$'=$g\,\Delta\rho/\rho$ is the reduced gravity, $\Delta\rho$ the density difference across the frontal interface, $L$ the interface width, and $u_*$ the frictional velocity). $\mathrm{Re}_L$ exceeds $\mathrm{Re}_*$ by 7 % on average for $h_0$ = 10 m and by 16 % for $h_0$ = 2. The difference between $\mathrm{Re}_L$ and $\mathrm{Re}_*$ increases with decreasing $h_0$. Recall that algorithm for sharp frontal interfaces detection (see Section 5.4.2) does not detect the interfaces associated with plumes of less than approximately 2 m depth, as these plumes are above the mean depth of the bow sensors.

It is remarkable that no measurement of the intermediate pycnocline depth, $h_0$, is required to calculate the *frontal Reynolds number*, $\mathrm{Re}_L$, defined by formula (5.41). This number can therefore be estimated practically for all observations of sharp frontal interfaces made during TOGA COARE (*Figure 5-37*b). According to the theory considered here, Stommel's mechanism of the overturning gate (including the development of an internal bore) is possible in principle at

$$\mathrm{Re}_L < \mathrm{Re}_{cr}. \tag{5.42}$$

This is, however, only a necessary but not sufficient condition for the internal bore regime (remember that $\mathrm{Re}_L$ is an asymptote of (5.39). It does not account for the wind-to-front angle dependence described with (5.36)).

In terms of the interface width, (5.42) transforms into inequality

$$L < L_{cr}, \tag{5.43}$$

From (5.37) and (5.41), the critical width of the frontal interface is $L_{\mathrm{cr}}$ = 1234 $u_*^2/g'$. Inequality (5.43) means that only very sharp frontal interfaces (typically of less than 100 m width) can interact with wind stress.

As we already mentioned in Section 5.4.2, condition (5.42) had been applied to the data shown in *Figure 5-31*; as a result, the error bars for the directional dependence reduced. In fact, only 10% of the density interfaces detected from the COARE bow data with algorithm described in Section 5.4.2 do not satisfy condition (5.42); according to the theory developed here these interfaces cannot interact with wind stress at any wind-to-front angle.

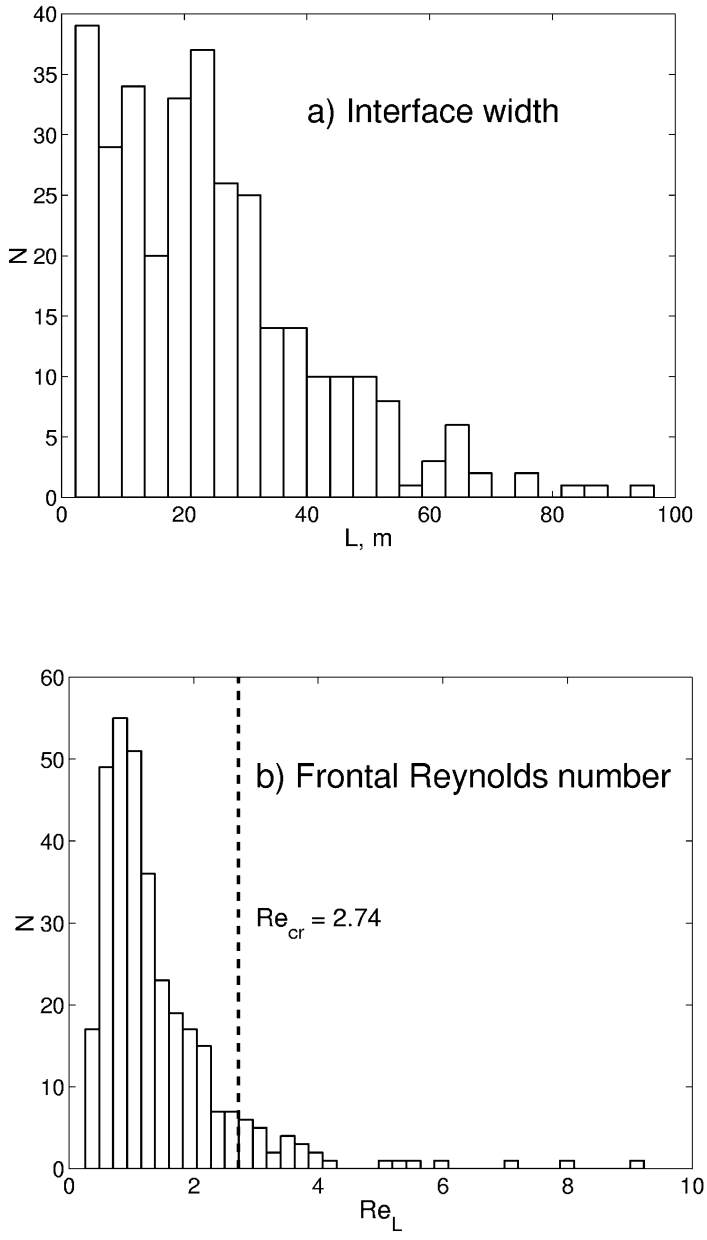


*Figure 5-37***.** Histograms of (a) width, $L$, and (b) frontal Reynolds number, $\mathrm{Re}_L$, for the sharp frontal interfaces detected in the bow density data for four TOGA COARE cruises of the R/V *Moana Wave*. Reproduced from Soloviev et al. (2002) by permission from Elsevier.

As follows from relationship (5.36) the transition from the wave-like to the turbulent regime occurs (if it occurs at all) almost sharply at $\phi = \pm 90^{\circ}$

(*Figure 5-35*). If a turbulent bore does develop, the frontal interface is intensively mixed and may disappear or reach a compensated state quickly. If no turbulent bore develops then the situation has some analogy to the arrested wedge, and the frontal interface may exist for a relatively long time, drifting with the wind. This means that observed fronts are mainly arrested frontal interfaces, which can explain their spatial anisotropy with respect to wind direction (*Figure 5-31*a, c).

Because the transition from turbulent to arrested front occurs when convective overturning starts, there should be dependence on the angle rather than on wind speed, which is consistent with observations (*Figure 5-31*b). This is because convection triggers development of billows, which are relatively large eddies providing an effective mixing mechanism.

In the case of compensated fronts, there is no interaction between the frontal interface and wind stress, and no spatial anisotropy is expected. This is consistent with observed temperature interfaces (*Figure 5-31*e), which are mostly compensated. Some dependence on wind speed observed in *Figure 5-31*f can be explained by the fact that the wind induced turbulent mixing increases with wind speed, thus affecting the erosion of compensated frontal interfaces.

The sharp frontal interfaces discussed here are different from the so-called *ramp-like* coherent structures. The ramp-like structures are described in Section 5.6.

### 5.4.5 Parameterization for cross-frontal exchange

From the concept of Stommel's overturning gate (*Figure 5-34*), a sharp frontal interface may evolve into:

(a) An arrested wedge, which "freezes" the frontal structure; or

(b) A bore-like structure, which dramatically intensifies the cross-frontal exchange and leads to a rapid elimination of the density difference across the interface.

According to the laboratory experiment of Simpson (1987), the gravitational instability induced at the leading edge of a surface gravity current by an opposing surface stress (wind stress in our case) may trigger Kelvin-Helmholtz instability and billowing in tale part of the gravity current head. The entrainment flux associated with this instability achieves a relatively large value, estimated by Simpson (1987) as 0.15 times the mass flux of the gravity current itself. These considerations lead to the following parameterization of the cross-frontal mass exchange (Soloviev et al., 2002):

$$\overline{u'\rho'} = \begin{cases} c_e V_g \Delta\rho, & \text{for } \mathrm{Re}_* \le \mathrm{Re}_{cr} \\ \sim 0, & \text{for } \mathrm{Re}_* > \mathrm{Re}_{cr} \end{cases}, \tag{5.44}$$

where $u'$ and $\rho'$ are deviations from the temporal or spatial mean cross-front velocity and density, $\Delta\rho$ is the density difference across the frontal interface, $c_e \approx 0.15$ is an empirical constant, and $V_g$ is the speed of the gravity current estimated here in the same way as in Section 5.4.1: $V_g = F\left(g'h_0\right)^{1/2} \approx 1.2\left(g'h_0\right)^{1/2}$. In accordance with (5.36) (see also *Figure 5-35*): $\mathrm{Re}_*\left(Ri,\phi\right) \approx \kappa^{-1} Ri_*^{1/2} \Big/ \left\{1 + \left[30\left(\cos\phi + \left|\cos\phi\right|\right)h_0 / L\right]^{1/3} \kappa^{-1} Ri_*^{1/6}\right\}$, $Ri_* = g'h_0 / u_*^2$, and $\mathrm{Re}_{cr} \approx 2.74$ Similar formulae can be derived for the heat, salinity, and chemical substance flux by replacing the density in (5.44) with the temperature, salinity, or concentration respectively.

Increased scatter of the experimental points near $\theta$ = -90° and $\theta$ = 90° in *Figure 5-31*a possibly indicates that there are some processes that are not controlled by Stommel's overturning gate mechanism. (The increased scatter may also be due to the uncertainty of the front alignment relative to the wind, which makes the sign of the cross-front component unknown when the wind is close to alignment with the front.) In particular, the tangential shear that is often observed at sharp fronts (see *Figure 5-21* and *Figure 5-22*) may result in the formation of quasi-geostrophic eddy pairs, advection within these eddies, and the ultimate destruction of eddies with subsequent dissipation of the thermohaline structure. For mid- and high-latitudes, this mechanism can be parameterized as follows (Spall and Chapman, 1998):

$$\overline{u'\rho'} = c_e V_m \Delta\rho \tag{5.45}$$

where $V_m$ is a scale for the along-front velocity, and $c_e \approx 0.045$ is an empirical constant. (Though constant $c_e$ does not appear to depend on rotation effects explicitly, the validity of parameterization (5.45) for low latitudes has not yet been proven.)

Parameterization (5.45) has a structure similar to (5.44). The ratio of the constants, $c_b/c_e \sim 3$, and of the velocity scales, $V_g / V_m \sim 1$, suggests that the cross-frontal exchange due to an internal bore is comparable to, or perhaps exceeds, the cross-frontal exchange due to eddies.

### 5.4.6 Implications for the T-S relationship in the mixed layer

As it follows from the discussion in Sections 5.4.4 and 5.4.5, on horizontal scales less than approximately 100 m the temperature-salinity relationship in the mixed layer of the ocean depends on the relative angle between the horizontal density gradient and the wind stress vector (!).

Ferrari and Rudnick (2000) found the horizontal density ratio $R$ in the subtropical Pacific mixed layer is close to 1 for horizontal scales > 100 m. Statistics for one month of low-latitude observations acquired during TOGA COARE (see *Figure 5-30*) indicate that there are numerous cases of non-compensated density fronts (*i.e.*, $R \neq 1$). These statistics, however, relate to the sharp interfaces only (*i.e.,* those less than ~100 m width) and are therefore not contradictory to the results of Ferrari and Rudnick (2000).

### 5.4.7 Observations of sharp frontal interfaces in mid- and high-latitudes

The substantial observational statistics of the sharp frontal interfaces reported here are from tropical latitudes only. Sharp fronts have been observed in mid-latitudes as well. To our knowledge there are only a few case shipboard observations (Zenk and Katz, 1975; Soloviev and Zatsepin, 1992); no representative statistics have been obtained in mid-latitudes.

In high latitudes, sharp frontal interfaces are expected to be present in the marginal ice zone during periods of ice meting. To our best knowledge there have been no horizontal microstructure measurements in the near-surface layer of the ocean in polar seas.

At this point, we do not know exactly how the sharp frontal interfaces are affected by Earth's rotation. From general considerations, the rotation should not directly affect the internal structure of sharp fronts because their width is so small. Fronts, nevertheless, are associated with larger scale anomalies; these anomalies may depend on Earth's rotation even near the equator. In particular, the sharp front shown in *Figure 5-22*a was found at the edge of a density anomaly with cyclonic vorticity, that appears to be caused by the inertial spin-down of an eastward equatorial jet (Feng et al., 2001). In mid-latitudes, mesoscale eddies wind the sharp fronts into spirals (Munk and Armi, 2001).

## 5.5 Internal Waves in the Near-Surface Pycnocline

As described in Section 4.1.3, the shallow diurnal thermocline and rain-formed halocline are subject to perturbations in the form of internal waves. In some instances, these internal waves become large, transform into billows or rolls, and can produce signatures in SST and on SAR images.

### 5.5.1 Large amplitude internal waves

The terminology "large amplitude" internal wave in this context means that the amplitude of the internal wave is of the order of the distance to the

surface (depth). Soloviev and Lukas (1996) reported an observation of a packet of large amplitude internal waves in the diurnal thermocline (*Figure 5-38*). The observation was made with bow-mounted sensors (see Section 4.1.3) while steaming at 10-11 knots.

CTD profiles made before and after this section revealed a barrier layer above the thermocline with a salinity difference of ~0.6 psu to ~1.0 psu from the top of the thermocline to the base of the mixed layer. The depth of the upper quasi-homogeneous layer identified in the CTD temperature profiles was 40 m before and 80 m after the section, respectively. Horizontal variability of the salinity in *Figure 5-38* was presumably because of the previous surface forcing (rainfall) or the spatial variability of the underlying barrier layer.

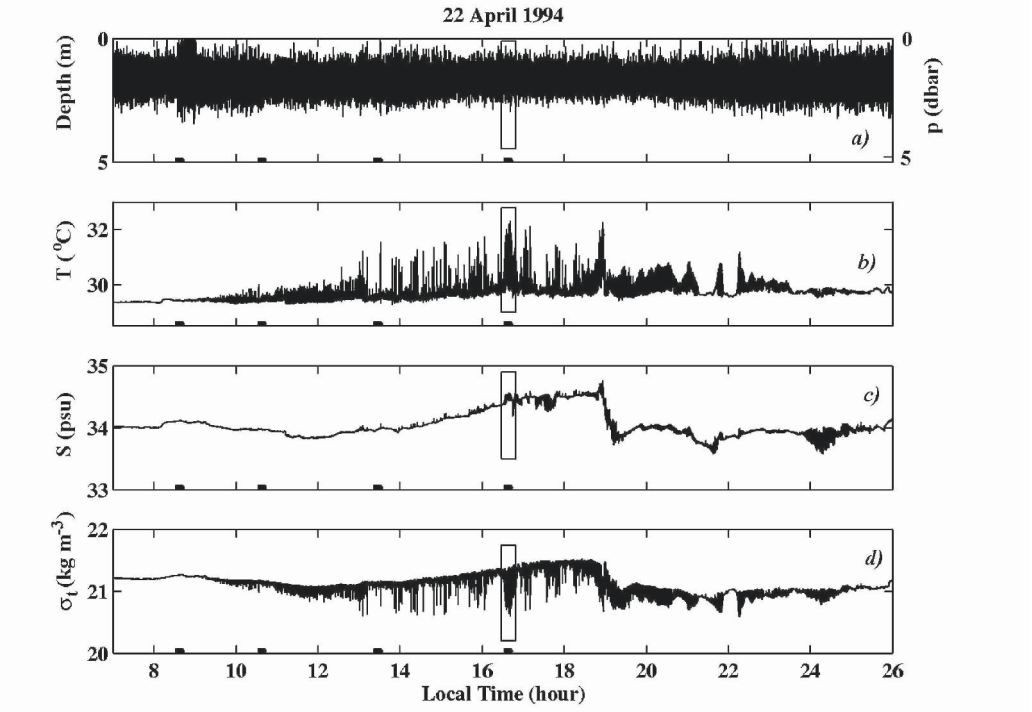


*Figure 5-38*. Example of records of (a) depth (pressure), (b) temperature, (c) salinity, and (d) sigma-t density made by bow sensors in the western Pacific warm pool during a strong diurnal warming event. Segments marked by rectangles are shown in more detail in *Figure 5-40*. Solid segments on the time axis correspond to 10 min averaging intervals for calculation of vertical profiles of $T$, $S$ and $s_t$ shown in *Figure 4-7*. (After Soloviev and Lukas, 1996.)

*Figure 5-39* documents the evolution of averaged vertical profiles of $T$, $S$ and $\sigma_t$ on the same day (22 April 1994) from early morning until late afternoon. At 8:37L, the profiles of $T$, $S$ and $\sigma_t$ showed a well-mixed near-

surface layer (within the 3 m depth variation range of the bow sensors). Wind speed was 2.2 m $s^{-1}$. The temperature profile at 10:37L indicated that the diurnal warming of the upper ocean layer had started; because of low wind speed conditions (1.5 m $s^{-1}$), the diurnal thermocline was within the upper meter of the ocean surface. At 13:27L, the diurnal thermocline was still in the upper 1 m because of calm conditions (0.9 m $s^{-1}$ wind speed); the temperature difference reached ~2°C. There was also ~ 0.1 psu salinity difference across the diurnal thermocline as a result of evaporation from the ocean surface and accumulation of the excess salinity within the diurnal mixed layer.

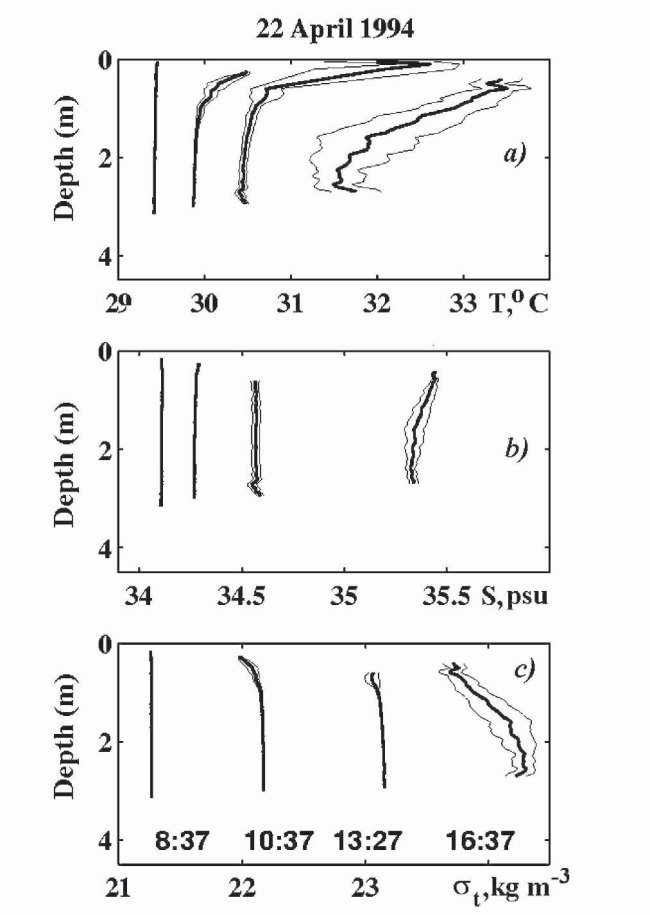


*Figure 5-39*. Vertical profiles of temperature, salinity, and density obtained by averaging 10 min intervals of the bow sensor data within 0.1 dbar pressure ranges. Each successive profile is shifted by 0.5°C in temperature, by 1.2 psu (in subplot a) and 0.3 psu (in subplot b) in salinity, and by 1.0 in $\sigma_t$. The local time below each profile corresponds to the middle of the 10 min segment. Thin lines represent one standard deviation. (After Soloviev and Lukas, 1996.)

At 16:37L (*Figure 5-39*), the beginning of the evening deepening of the diurnal thermocline, vertical profiles reveal increased scatter. This time interval is analyzed further in the contour plot shown in *Figure 5-40*. The corresponding section of the records is denoted in *Figure 5-38* by a rectangle. There are high-frequency oscillations of $T$, $S$ and $\sigma_t$ in this record (*Figure 5-40***,** b-d) because of the depth variation of the probes (*Figure 5-40*a). There are also variations in temperature of about 2°C in *b*, which are visible over several kilometers. The $\sigma_t - p$ contour plot (*Figure 5-40*d) reveals wavelike disturbances of the diurnal thermocline with a typical scale beginning from ~200 m.

The $T - \sigma_t$ contour plot in *Figure 5-40*e reveals an asymmetric anomaly between 5300 m and 6000 m associated with a salinity feature (*Figure 5-40*d). It is not clear, however, whether it has any connection with the large-amplitude shortwave train observed in the $\sigma_t - p$ contour plot (*Figure 5-40*d).

The $\sigma_t - p$ contour plot in *Figure 5-40*d shows an intermittent wavelike pattern. The intermittence in space and time, with energy predominantly in the first mode, is a typical feature of short-period internal waves trapped in the thermocline that is close to the surface (Brekhovskikh et al., 1975). There is also asymmetry in the perturbations in *Figure 5-40*d. When a thermocline is close to the surface, it is typical for the wave crest to flatten and the troughs to become sharper (Thorpe, 1968).

These observations revealed a near-surface spatial structure that looks like a packet of large amplitude internal waves. For the data shown in *Figure 5-40*d the amplitude of the wavelike perturbations is much larger than the uncertainty of the pressure-to-depth conversion (~0.1 m). The 30-day data set analyzed by Soloviev and Lukas (1996) contained several other cases of large amplitude internal waves within the diurnal thermocline to the amplitude comparable with the depth of the thermocline.

For comparison, Voropaev et al. (1981) observed a wave-like perturbation of the diurnal thermocline of ~200 m length and ~1 m height under 5 m $s^{-1}$ wind speed. Imberger (1985) presented detailed near-surface measurements from a freshwater lake during 21.5 hours, including observation of internal waves of ~1 m amplitude and billows associated with the diurnal thermocline.

Wijesekera and Dillon (1991) and Lien et al. (1996) observed packets of internal waves with approximately 200 m wavelength associated with diurnal cycling. Interestingly, Wijesekera and Dillon (1991) found for a large-amplitude wave packet that the wave-induced Reynolds stress below the mixed layer was of the same order of magnitude as the surface wind stress.

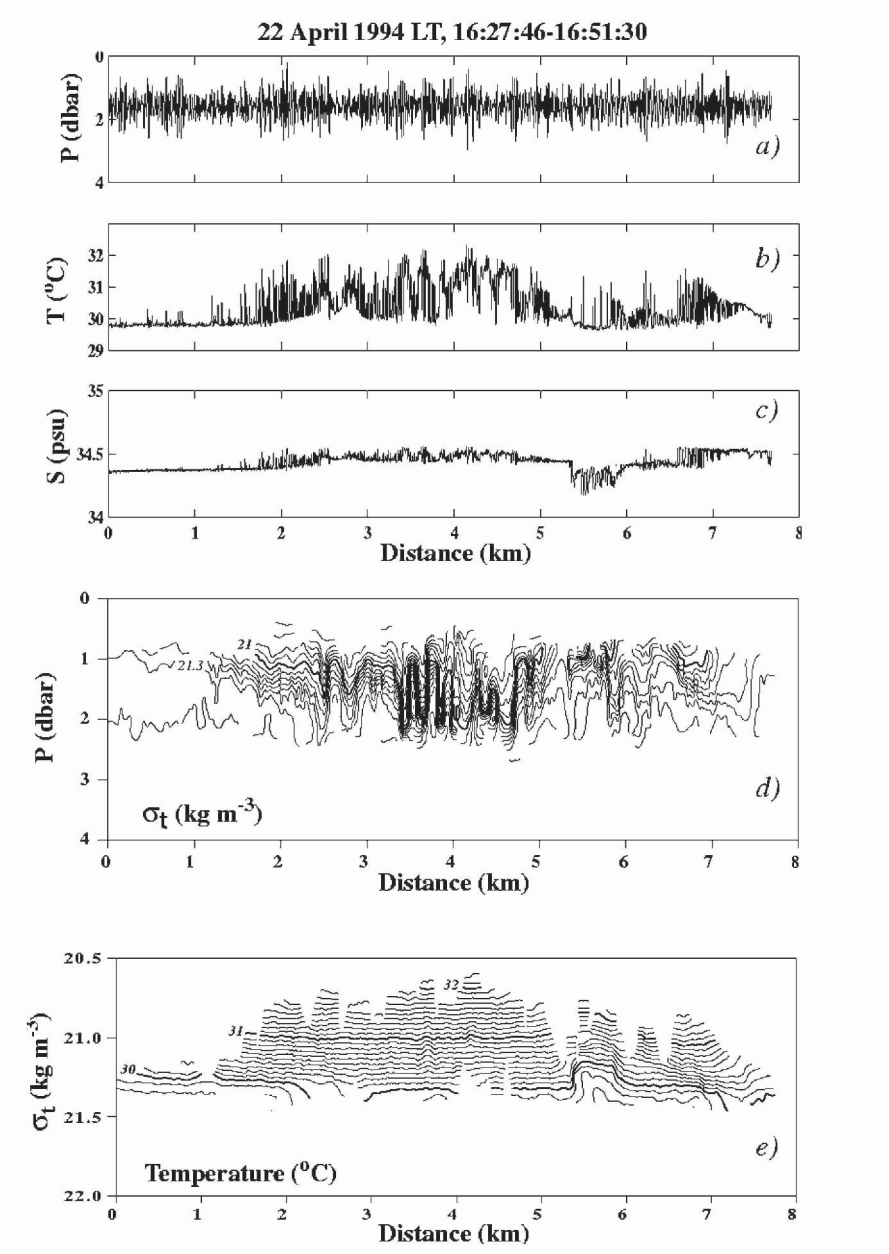


*Figure 5-40*. Observations during strong diurnal warming near 2.2°S, 161.7°E during COARE cruise EQ-3. The upper part of the figure shows records of (a) pressure, (b) temperature, and (c) salinity. The lower part shows corresponding contour plots (d) of $\sigma_\tau$ versus P and (e) of T versus $\sigma_\tau$. Wind speed is 0.5 m $s^{-1}$ - 1.0 m $s^{-1}$, direction 297-339°; ship speed is 5.5 m $s^{-1}$, direction 338°; height of swell waves observed from the bridge ~1 m, direction ~50°. Reproduced from Soloviev and Lukas (1996) by permission of American Meteorological Society.

Mack and Hebert (1997) found large amplitude internal waves in the upper layer of the eastern equatorial Pacific Ocean from towed thermistor-chain measurements. Occurrences of large-amplitude internal waves were consistent with solutions to the Taylor-Goldstein equation for shear flow instability (see Section 5.5.3). This instability is due to changes in the vertical structure of the mean horizontal velocity and density associated with diurnal cycling.

The two mechanisms presumably important for the generation of internal waves on the near-surface pycnocline are (a) resonant interactions between the internal mode and a pair of surface waves with almost equal frequency and direction and (b) the shear instability produced by the diurnal jet at the evening deepening due to convection. Below, we discuss both mechanisms in more detail.

### 5.5.2 Surface-internal waves resonant interactions

Nonlinear interaction of surface gravity waves can cause the excitation of internal waves in stratified near-surface layers. Observations of Apel et al. (1975), Briscoe (1983), and others suggest that a strong ocean swell can generate internal waves. A pair of surface waves with almost equal frequency and direction and an internal wave may satisfy the necessary conditions of the resonant triad (Phillips, 1977):

$$\vec{k} = \vec{k}_1 - \vec{k}_2 \text{ and } \omega\left(\vec{k}\right) = \omega\left(\vec{k}_1\right) - \omega\left(\vec{k}_2\right), \tag{5.46}$$

where $\vec{k}_1$ and $\vec{k}_2$ are the wavenumber vectors and $\omega_1 = \omega\left(\vec{k}_1\right)$ and $\omega_2 = \omega\left(\vec{k}_2\right)$ the frequencies of the pair of surface waves; $\vec{k}$ is the wavenumber vector and $\omega$ is the frequency of the internal wave.

Brekhovskikh et al. (1972) and Watson et al. (1976) used a *locked phase approximation* to theoretically describe two surface waves interacting with an internal wave. This mechanism is relatively strong, predicting the internal-wave growth timescale of the order of a few hours. It requires, however, a special situation: Each of the two surface waves must have a deterministic phase relationship for as long as it takes to generate the internal wave. This is possible for a narrow-band long ocean swell.

Models of *spontaneous creation mechanism* (Olbers and Herterich, 1979) and *modulation mechanism* (Dysthe and Das, 1981) are based on incoherent or statistical three-wave interactions. According to Olbers and Herterich (1979), the spontaneous creation mechanism may play an important role if there is strong stratification. Watson (1990) concluded that,

except for winds > 20 m $s^{-1}$, only the modulation mechanism is of practical significance (but with energy flow from the internal to the surface waves). In contrast to this result for the wind waves, Watson (1990) also found that a strong, narrow-band ocean swell can lead to rapid growth of high frequency internal waves. The application of the theoretical models cited above, however, demands advanced measurement for both internal and surface wave components, which has not yet been done.

### 5.5.3 Kelvin-Helmholtz instability of a sheared stratified flow

The kinetic energy accumulated by the diurnal jet during a period of intensive warming is a possible source of mechanical energy for the generation of internal waves and billows in the diurnal thermocline. During a period of intensive solar heating, the turbulent friction in the diurnal thermocline is substantially reduced due to buoyancy forces (Kudryavtsev and Soloviev 1990). The shallow diurnal jet accumulates the momentum transferred from the wind. In the evening the net surface buoyancy flux at the ocean-air interface decreases and when becomes negative convection develops (see Section 5.8.3); the slippery conditions within the diurnal thermocline disappear and the momentum flux at the lower boundary of the diurnal jet increases. This provides favorable conditions for the Kelvin-Helmholtz instability. The atmospheric forcing may significantly vary during the day (*e.g.,* because of clouds) producing short-term conditions for Kelvin-Helmholtz instability in the diurnal thermocline (see an example in *Figure 4-20*).

The instability of a continuously stratified shear flow can be described with the Taylor-Goldstein equation (Taylor, 1931; Goldsten, 1931). The Taylor-Goldstein equation is derived under the assumption of an inviscid, Boussinesq fluid; the vertical structure equation is linearized around the vertical profiles of horizontal velocity and density representing the basic state. The upper equatorial ocean typically has strong mean shear, which in general may not coincide with the direction of the diurnal jet (the latter largely depends on wind stress direction). Mack and Hebert (1997) generalized this equation for a three-dimensional case in the following way:

$$\partial_{zz}^2 w + \left[ \frac{\left|\vec{k}\right|^2 N^2}{\left(\vec{k}\cdot\vec{u}-\omega\right)^2} - \frac{\vec{k}\cdot\vec{u}_{zz}}{\vec{k}\cdot\vec{u}-\omega} - \left|\vec{k}\right|^2 \right] w = 0 \qquad (5.47)$$

where $w(z)$ is the vertical structure of vertical velocity, $\vec{u} = \{u(z), v(z)\}$ is the mean horizontal velocity vector consisting of zonal $u(z)$ and meridional

$v(z)$ components, $\vec{k} = \{k,l\}$ is the horizontal wavenumber vector consisting of the zonal $k$ and meridional $l$ components, $\omega$ is the complex frequency, $N^2(z) = g\partial_z \overline{\rho} / \rho_0$ is the mean squared buoyancy frequency, $\overline{\rho}$ and $\rho_0$ are the horizontal mean and the overall mean densities, respectively. The solution for (5.47) is sought in the form of a plane wave:

$$W(x,y,z,t) = w(z)\exp\left[i(kx + ly - \omega t)\right] \tag{5.48}$$

For complex frequency $\omega = \omega_r + i\omega_i$ the exponential in (5.48) has a real and growing part (for $\omega_i > 0$), so that all wave variables have a growth rate $\omega_i$.

The Howard (1961) theorem states that the complex phase speed of any unstable modal solution in parallel flows of an inviscid fluid must lie inside the semicircle in the upper half of the complex phase speed plane, which has the range of the mean flow as the diameter. Mack and Hebert (1997) altered slightly this theorem in application to the three-dimensional version of the Taylor-Goldstein equation (5.47) to obtain the following criteria for instability:

$$\begin{aligned} &\left\{\omega_r - \frac{1}{2}\left[\max\left(\vec{k}\cdot\vec{u}\right) + \min\left(\vec{k}\cdot\vec{u}\right)\right]\right\}^2 + \omega_i^2 \\ &\le \left\{\frac{1}{2}\left[\max\left(\vec{k}\cdot\vec{u}\right) - \min\left(\vec{k}\cdot\vec{u}\right)\right]\right\}^2 \end{aligned} \tag{5.49}$$

$$\omega_i > 0 \tag{5.50}$$

Mack and Hebert (1997) found that solutions were almost completely determined by the mean density and velocity profiles, which was in agreement with most of their field data (unfortunately, there was no information on velocity in the upper 20 m layer of the ocean). A necessary criterion for instability of a stratified parallel flow was a gradient Richardson number, $Ri = N^2 / \left(u_z^{\,2} + v_z^{\,2}\right) < 1/4$. The fastest growing, unstable first mode solutions had e-folding growth times of less than 10 min.

For a two-dimensional, two-layer model the criteria of instability is as follows (Turner, 1973):

$$\lambda < \pi(\Delta u)^2 / g' \tag{5.51}$$

where $\lambda$ is the wavelength, $\Delta u$ is the vertical velocity jump, $g' = g\Delta\rho/\rho_0$ is the reduced gravity. For the large-amplitude internal wave observations of Soloviev and Lukas (1996) (*Figure 5-40*), $\Delta\rho/\rho_0 \approx 5\times10^{-4}$. Typical velocity of the diurnal jet is 0.2-0.3 m s$^{-1}$. In the equatorial ocean, however, there is substantial background shear. For a total velocity difference $\Delta u \sim 0.5 - 0.7$ m s$^{-1}$, formula (5.51) results in an estimate $\lambda < 160 - 310$ m. The $\sigma_t$ -P contour plot in Figure 5-40d reveals wavelike disturbances of the diurnal thermocline with a typical scale beginning from ~200 m, which is consistent with the above estimate.

Observations from satellite images of strong diurnal warming events near the California coast (Flament et al., 1994) indicated the formation of coherent streaks, associated with the erosion and decay of the warming layers during the night following strong diurnal warming. The horizontal spacing of the streaks, observed at 1 km resolution, was ~4-8 km. This is consistent with *Figure 5-40* in which it is possible to trace a several kilometer scale variation of the near-surface temperature of ~2$^o$C amplitude. Internal waves of ~200 m wavelength cannot be resolved in the available satellite images. The patterns between the two successive images separated by 5 h 26 min (Flament et al. 1994, *Figure 12*b and c) look stationary, but appear consistent with internal waves propagating at ~0.1 m s$^{-1}$ in the diurnal thermocline.

The horizontal spacing of the streaks of 4-8 km observed by Flament et al. (1994) is probably too large for the Kelvin-Helmholtz instability because of the limitation on the maximum wavelength imposed by (5.51). The internal wave–vortex resonance mechanism considered in Section 5.4.3 allows for perturbations with a wavelength of a few km to develop (but those perturbations are not of Kelvin-Helmholtz type).

Internal waves in the near-surface stably stratified layers could modulate the roughness of the ocean surface in the same way as the internal waves in the main thermocline, making them visible in SAR images. Nonlinear internal waves and billows in the near-surface layer of the ocean associated with diurnal thermocline or rain-formed halocline may also modulate SST producing specific spatial patterns seen in the infrared images of Walsh et al. (1998).

## 5.6 Ramp-Like Structures

As emphasized in many studies (*e.g.,* Thorpe, 1985; 1988; Csanady, 1984; Soloviev et al., 1988), the turbulent boundary layer at the ocean surface has some similarity to the atmospheric turbulent boundary layer. The atmospheric boundary layer exhibits spatially coherent organized motions in the form of “ramps” (Antonia et al., 1979; Phong-Anant et al., 1980). Ramp-

like structures have also been found in the upper layer of the ocean under both stable (Thorpe and Hall, 1987) and unstable (Soloviev, 1990; Wijesekera et al., 1999b) stratification. Since the organized structures are of relatively large size (comparable to the boundary layer thickness), they may appreciably contribute to the vertical transport of heat, mass, and momentum as well as air bubbles.

### 5.6.1 Phenomenology of ramp-like coherent structures

The laboratory measurements of Brown and Thomas (1977), made in a coordinate system moving with the average convection velocity of coherent structures, suggest that the typical organized motion in the unstratified turbulent boundary layer resembles a three-dimensional horseshoe vortex that is inclined to the wall. Interaction of the velocity field in the vortex with the mean shear current leads to the vortex asymmetry. As a result of this asymmetry, the so-called ramp like structure forms, which is schematically illustrated in *Figure 5-41*. The velocity jump at the upstream interface has a tendency to increase with distance from the wall and is of the same order of magnitude as the mean speed of the boundary-layer flow.

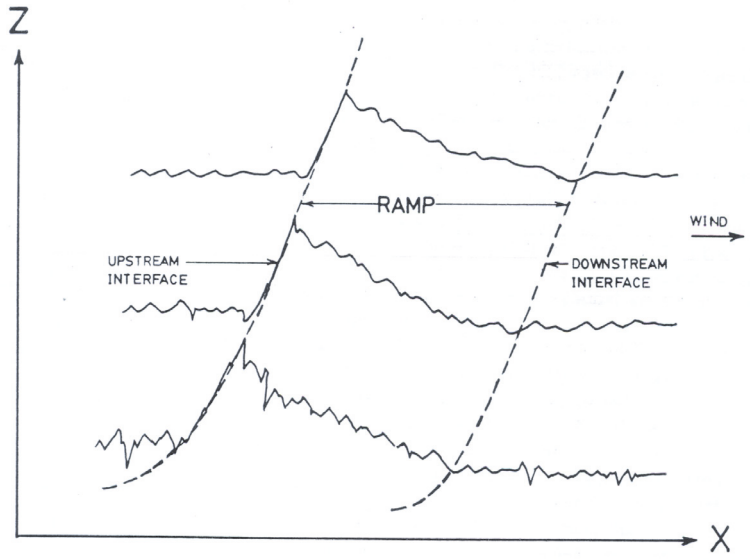


*Figure 5-41*. Phong-Anant et al. (1980) schematic representation of temperature ramps measured simultaneously at different heights. Upstream and downstream interfaces are indicated by dashed lines. Continuous lines are isotherms. Reproduced by permission of American Geophysical Union.

Temperature (density) features accompany vorticity features in stratified conditions. Observations of Phong-Anant et al. (1980) using a fixed probe in

the convectively unstable atmospheric boundary layer confirms that temperature has a characteristic ramp profile—a gradual rise followed by a relatively sharp decrease. Temperature ramps in the atmospheric boundary layer were suggested to be a signature of organized large-scale motion (Phong-Anant et al., 1980). In the unstably stratified atmospheric turbulent boundary layer, the coherent structures of this type have vertical scale proportional to the Oboukhov length scale ($L_O$), while their horizontal size is an order of magnitude bigger than the vertical.

An important question concerns the size of the contribution of the coherent structures to the vertical Reynolds shear stress and heat flux. From measurements in the atmospheric boundary layer, Phong-Anant et al. (1980) estimated the contribution of the organized motion to the vertical heat flux for unstable stratification conditions as being over 40% of the average vertical heat flux and about 20% of the average Reynolds stress. The relative contribution to the average vertical heat flux and Reynolds stress is less than 10% for nearly neutral and moderately stable conditions.

There are good reasons to assume that ramp-like coherent structures are important in the dynamics of the upper ocean turbulent boundary layer as well (Thorpe, 1985). At the same time, free-surface effects can modify the properties of the organized motion. Observation and theory of the coherent structures in the near-surface layer of the ocean are more complicated than in the atmosphere. One reason is that due to significant difference in density and specific heat capacity in air and water, the boundary layer temperature and velocity scales in the ocean are much smaller than in the atmosphere.

Thorpe (1985) observed ramp-like structures in the stably stratified near-surface ocean. Soloviev (1990) and Wijesekera et al. (1999b) reported the presence of ramp-like structures in the near-surface layer of the ocean under unstably stratified conditions as well. The next three subsections are devoted to the analysis of data on ramp-like structures taken in the upper ocean.

### 5.6.2 Observation of ramp-like coherent structures with bow-mounted sensors

A schematic diagram of Soloviev's (1990) experiment is shown in *Figure 5-42*. The underwater probe was mounted on the bow of the research vessel *Akademik Kurchtov* at 2 m depth and it measured temperature and conductivity fluctuations ahead of the moving vessel. Due to a "knife-edge" hull, the research vessel produced practically no bow wave ahead of itself, as confirmed by photographs and following from hydrodynamic estimates. In front of a moving sphere, streamlines are not appreciably disturbed at a distance greater than ~3 radii (see discussion of these techniques in Section 3.2.5b). At the probe mount location, the radius of curvature of the vessel's

hull was ~10 cm with a frontal angle of 16° (*Figure 5-42*). No turbulent or wave perturbations from the vessel's body were therefore expected in the measurement area. These measurements were made at 37°W between 1°N and 20°N in June 1985. Wijesekera et al. (1999b) performed a similar set of observations with a bow mounted CTD in the western equatorial Pacific during TOGA COARE.

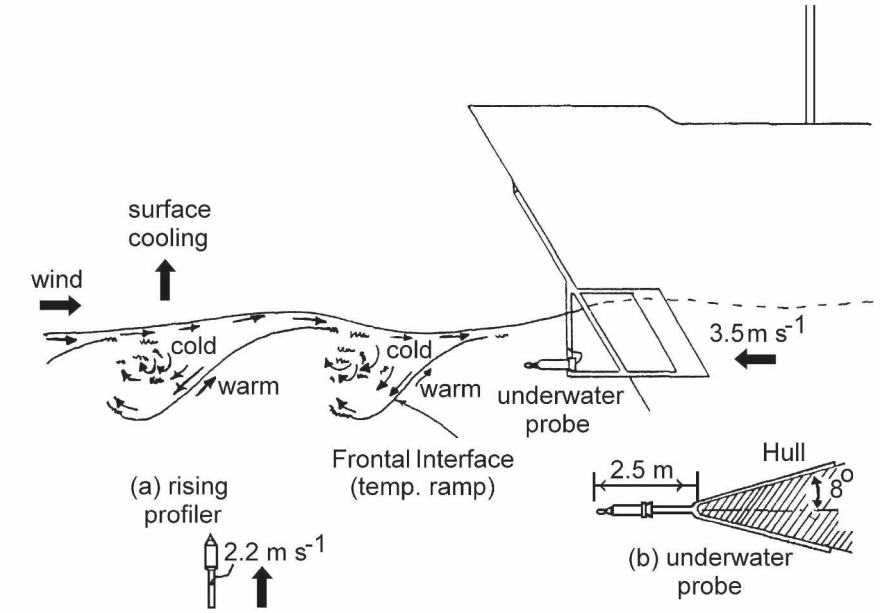


*Figure 5-42*. Schematic representation showing spatially coherent organized motion in the upper ocean boundary layer under unstably stratified conditions and experimental techniques and devices in Soloviev's (1990) experiment: (a) Free-rising profiler; (b) Top view at the probe mount (2 m below the waterline). Adapted by permission from Macmillan Publishers Ltd: *Nature* 346, 157-160, © 1990.

The observations reported here were made when it was not raining and outside frontal regions to simplify the identification of ramp-like structures. Information for the context of the observations is given in *Table 5-2*.

*Figure 5-43*, a and b, shows fragments of the bow temperature recordings at the nominal depth of 2 m, while the ship was steaming into the wind at 3.5 m $s^{-1}$. These measurements were taken during nighttime when the surface layer cools (unstable stratification). For comparison, a temperature record in the atmospheric boundary layer (at 12 m height) under unstable stratification is shown in *Figure 5-43*c. There is a striking similarity between the ramp-like structures observed in the ocean and in the atmosphere. Although absolute temperature scales in the ocean and the atmosphere are very different, the dimensionless characteristics, like $\langle|\Delta\theta|\rangle / T_*$ are consistent (see *Table 5-2*).

*Table 5-2*. Case studies of ramp-like structures in the oceanic and atmospheric turbulent boundary layers under unstably stratified conditions. Here, $U_{10}$ is the wind speed at 10 m height, $\tau_0$ is the wind stress, $h_s$ is the sensor depth (in the ocean) or sensor height (in the atmosphere), $L_O$ is the Oboukhov length scale, $\langle|\Delta\theta|\rangle$ is the average temperature ramp magnitude, $T_* = Q_0/(c_p \rho u_*)$ is the friction temperature, $Q_0$ is the net surface cooling, and $u_*$ is the friction velocity.

| Figure | Experiment | $U_{10}$, m s$^{-1}$ | $\tau_0$ Nm$^{-2}$ | $h_s/L_O$ | $<\|\Delta\theta\|>/T_*$ |
|---|---|---|---|---|---|
| Figure 5-43a, b | Ocean – bow sensors Soloviev and Bezverkhniy (1992) | 3.4 | 0.015 | -1.5 | 1.9 |
| *Figure 5-47* | Ocean - free-rising profiler Soloviev (1990) | 4.1 | 0.019 | | |
| *Figure 5-44* | Ocean – bow sensors Wijesekera et al. (1999b) | 8 | 0.1 | -0.1 | 2 |
| Figure 5-43c | Atmosphere – tower Antonia et al. (1979) | 5.6 | 0.048 | -0.8 | 2.9 |

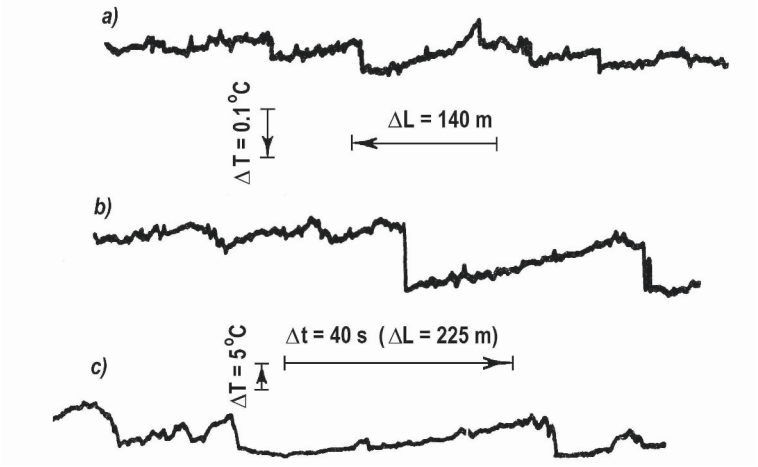


*Figure 5-43*. Fragments of (a, b) horizontal temperature profiles obtained with the bow-mounted sensors in unstably stratified conditions in comparison with (c) temperature records in the unstably stratified atmospheric boundary layer. The ship was steaming into the wind. The scales for subplots (a) and (b) are the same. For the atmospheric measurements done from a fixed tower (curve c) the equivalent distance scale is also shown (which is calculated from formula $\Delta L = U_{10}\Delta t$ ). (After Soloviev and Bezverkhny, 1990.)

For convenient comparison with the atmospheric boundary layer, the ocean temperature records (*Figure 5-43*, a and b) are plotted with time and temperature scales reversed. The reason for the temperature coordinate reversion is that unstable stratification in the upper ocean is caused by

surface cooling, which is opposite to its atmospheric counterpart where the unstable stratification is due to warming of the underlying surface. The reason for the reversion of the time coordinate in the oceanic data series is that the ship was traveling into the wind; the bow sensors crossed the structures in the ocean layer in the direction opposite to the relative direction of the air flow during the measurements with a fixed sensor in the Antonia et al. (1979) experiment (*Figure 5-43*c).

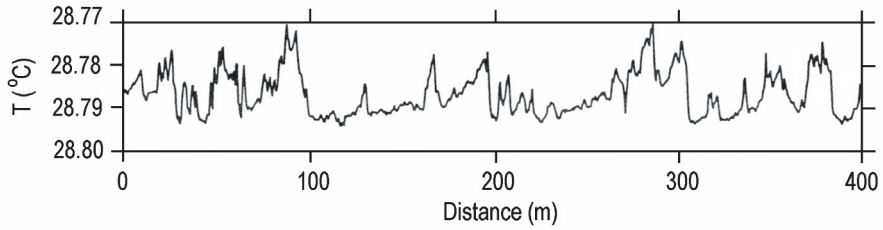


*Figure 5-44*. A horizontal series of temperature observed at 2 m during the night of December 31, 1992 from the R/V *Wecoma* moving downwind at 4 m $s^{-1}$. Wind stress (westerly) about 0.1 N $m^{-2}$, net surface cooling about 250 W $m^{-2}$, the stability parameter, $z_s/L_O$ = -0.1, where $L_O$ is the Monin-Oboukhov scaling length, and average bow sensor depth $z_s$ = 2 m. (After Wijesekera et al., 1999b.)

*Figure 5-44* shows the horizontal temperature series taken during nighttime measurements with bow sensors mounted at 2 m depth (nominal) by Wijesekera (1999b). In order to compare this record with the data shown in *Figure 5-44* the temperature scale is reversed. The distance scale, however, does not require reversion, because this measurement is made in the downwind direction. The temperature series in *Figure 5-44* reveals ramp-like structures similar to those in *Figure 5-43*.

Patterned on Figure 4 of Thorpe (1987), which shows processes of the vertical transport in a stably stratified shear boundary layer of the upper ocean, *Figure 5-42* reconstructs water circulation in unstably stratified conditions. As the ship moves upwind, the ramps are observed as the probe passes from the "warm water" to the "cold water" side of the inclined sharp interfaces (*Figure 5-42*). The ramps on the temperature record shown in *Figure 5-43*a, b and *Figure 5-44* are consistent with this sketch.

### 5.6.3 Skewness of temperature derivative

The presence of ramp-like structures in the temperature records leads to asymmetry of the probability distribution function (PDF) for the temperature derivative (Thorpe, 1985). A measure of PDF asymmetry is the skewness, $\mu_3$, which is defined as follows:

$$\mu_3 = M_3 / M_2^{3/2}, \tag{5.52}$$

where $M_3 = \left\langle \left( \partial T/\partial\alpha - \langle \partial T/\partial\alpha \rangle \right)^3 \right\rangle$, $M_2 = \left\langle \left( \partial T/\partial\alpha - \langle \partial T/\partial\alpha \rangle \right)^2 \right\rangle$, and $\partial T/\partial\alpha$ denotes the temperature derivative either over time, $\alpha = t$, for fixed-sensor measurements, or over the horizontal coordinate, $\alpha = x$ for towed measurements.

The skewness of the oceanic temperature derivative for the upwind direction of the ship in the observations of Soloviev (1990) under convectively unstable near-surface conditions ocean falls in the range –0.7 to –1.0. In the convectively unstable atmospheric boundary layer, the skewness in the presence of coherent structures falls in a similar range (Thorpe and Hall, 1987).

As mentioned before, based on the results of laboratory experiments the vortex motion associated with a ramp-like structure in the upper ocean has the rotation axis oriented perpendicular to the wind direction or, more exactly, to the wind drift current direction. As a result, the mean value of $\mu_3$ depends on the direction of the ship's motion relative to the wind. Directional dependence of $\mu_3$ on the wind heading relative to ship heading measured by Wijesekera et al. (1999b) is shown in *Figure 5-45*.

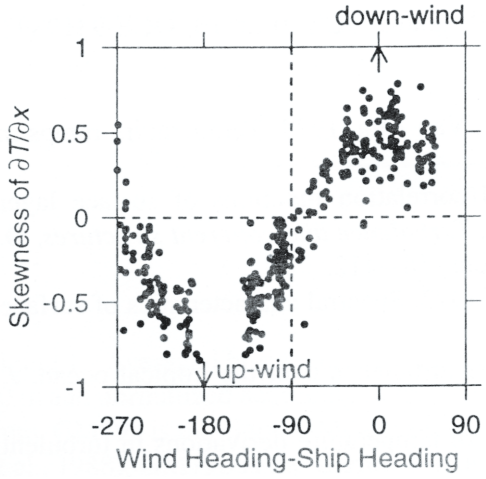


*Figure 5-45*. Skewness of $\partial T/\partial x$ versus the relative angle between the wind and ship heading under unstably stratified conditions in the western equatorial Pacific Ocean. (After Wijesekera et al., 1999b.)

Dependence of the temperature derivative skewness on the relative wind direction for mid-latitudes, including both stable and unstable upper ocean stratification, is shown in *Figure 5-46*. During the daytime when the stratification is stable, $\mu_3$ is positive. In order to account for the sign of

stratification, the skewness coefficient in *Figure 5-46* is multiplied by the sign of the Monin-Oboukhov stability parameter $z_s/L_O$.

The full series of measurements made in January 1990 in the Atlantic Ocean by Soloviev (1990) is compared in *Figure 5-46* with the data obtained by Thorpe (1985) under stable stratification conditions, and by Thorpe et al. (1988) under unstable stratification conditions in the North Atlantic. These data sets also include a range of relative wind directions. They reveal directional anisotropy of the coherent structures of this type with respect to the wind stress direction. The magnitudes of $\mu_3$ in Soloviev (1990) are near those reported by Thorpe (1985) and Thorpe and Hall (1987) at similar winds and towing angles.

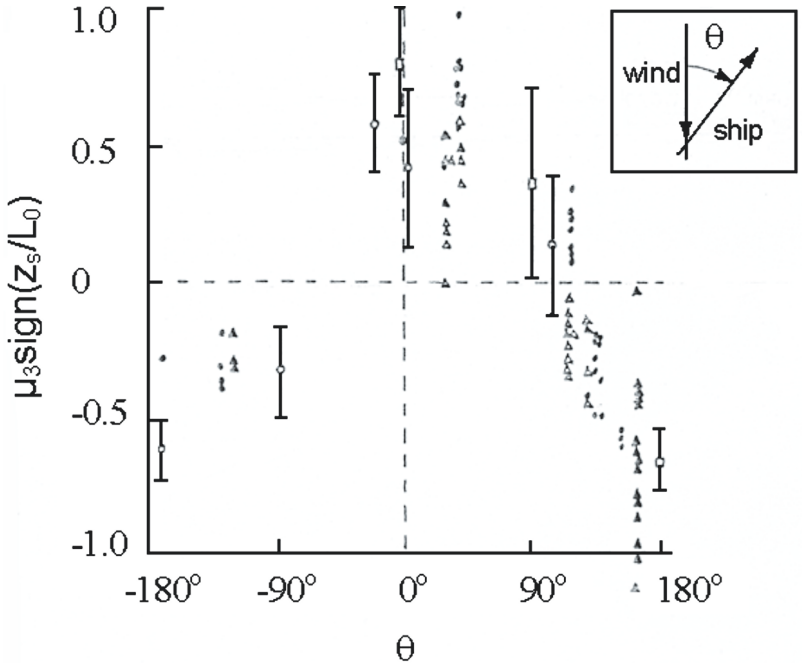


*Figure 5-46*. Skewness of $\partial T / \partial x$ multiplied by the sign of the Monin-Oboukhov stability parameter $z_s/L_O$ versus the relative wind direction according to Soloviev and Bezverkhny (1990). Dark and light circles represent measurements at 1.5 m average depth during nighttime ($L_O < 0$) and daytime ($L_O > 0$) conditions respectively. For comparison, data from Thorpe (1985) and Thorpe et al. (1988) obtained under stable stratification ($L_O > 0$) and unstable stratification ($L_O < 0$) are shown by light circles and squares and by light triangles respectively.

The observations of ramp-like structures in the upper ocean obtained from different sources under various wind speed and stratification conditions appear to be consistent. The difference between equatorial (*Figure 5-45*) and mid-latitude (*Figure 5-46*) directional diagrams is that in mid-latitudes, the

maximum of the skewness seems to be shifted to the right by 10-20°.This can be explained by the fact that away from the equator the wind drift current direction differs from the wind velocity vector direction because of the Ekman spiral (see Section 1.7.1). Data scatter in both figures is, however, marginal for making final conclusions.

### 5.6.4 Vertical profiles

Additional insight into spatially coherent organized motions in the near-surface layer of the ocean has been obtained from analysis of free-rising profiler data (*Figure 5-42*). The profiler measured vertical velocity profiles of conductivity and the vertical component of velocity fluctuations in the frequency range 2-250 Hz. The rise speed of the profiler was 2.2 m $s^{-1}$. Temperature profiles were calculated from the conductivity profiles neglecting salinity variation. For the convectively unstable near-surface layer of the ocean, these calculations resulted in only small error (see Section 2.2.1). The profiler tends to follow the wave-induced orbital motion in long surface waves (see Section 3.2.4). This reduces the influence of surface waves on turbulence measurements in the upper boundary layer of the ocean.

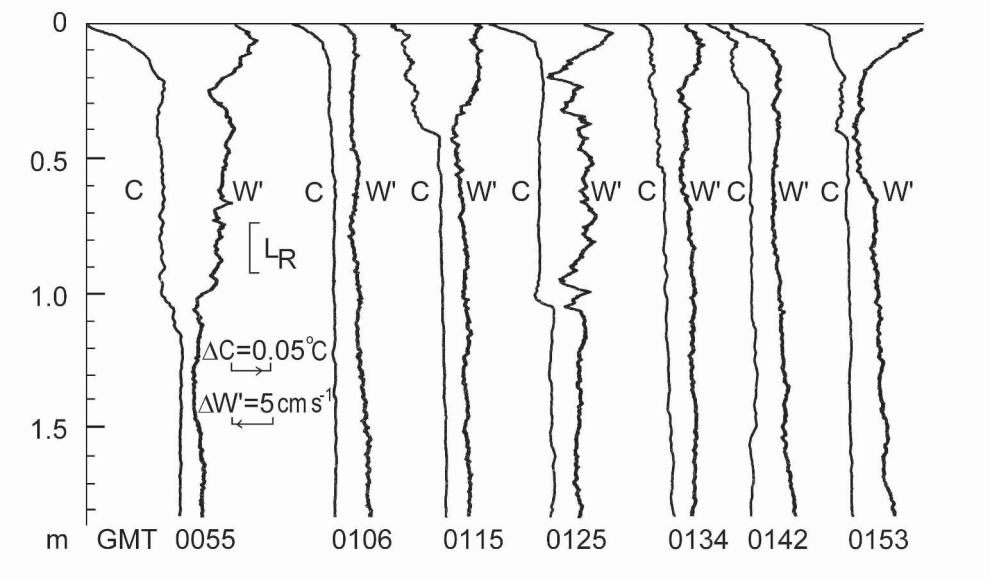


*Figure 5-47*. Vertical profiles of temperature (*C*, calculated from conductivity profiles assuming constant salinity) and vertical component of velocity fluctuation (*W'*) in the upper ocean in convectively unstable conditions (nighttime). A positive *ΔW'* indicates a positive velocity change of the flow along the profiler. The vertical length scale ($L_R$) represents the relaxation time of the fluctuation velocity sensor. Adapted from Soloviev (1990) by permission from Macmillan Publishers Ltd: *Nature* 346, 157-160, © 1990.

*Figure 5-47* shows a series of measurements of temperature and vertical velocity fluctuations made by free-rising profiler at 20°N, 37°W in the early morning hours. The weather conditions were similar to those during the measurements shown in *Figure 5-43*. The time interval between successive measurements was ~10 min, and the vessel drift during this time period was several tens of meters. The structures investigated supposedly had time and space scales of the same order. From these data, it would then be difficult to trace any space-time connections between the successive vertical profiles in relation to ramp-like structures.

*Figure 5-47* suggests that in a few cases the profiler crossed the temperature interfaces presumably related to ramp-like structures. In particular, in the profiles obtained at 00:55 and 01:25 UTC, the temperature interfaces were correlated with abrupt vertical velocity features. In the interpretation of the velocity profiles it is important to remember that the sensor measured only velocity fluctuations within the frequency range 2 to 250 Hz. Since the profiler moved quickly with respect to the water (at a 2.2 m $s^{-1}$ vertical speed), abrupt velocity changes were observed correctly.

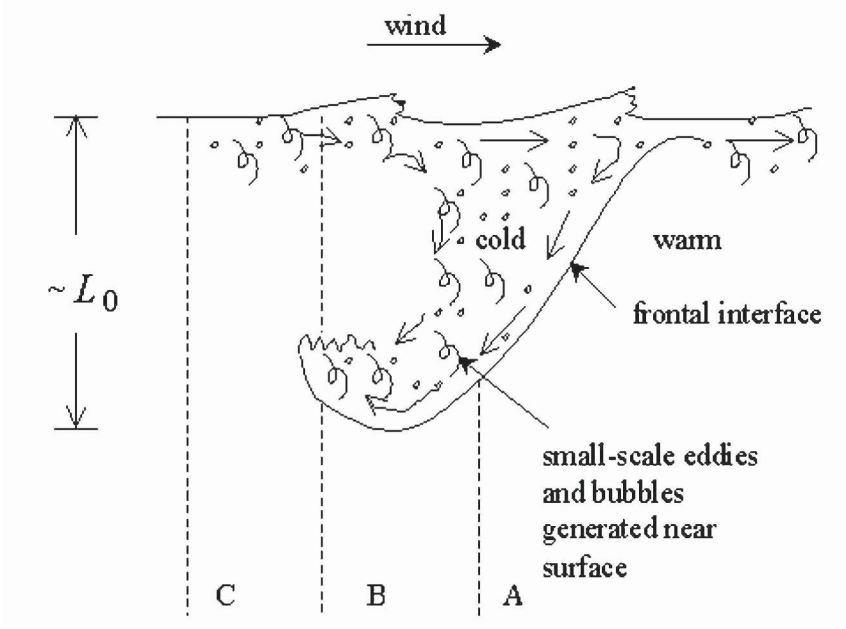


*Figure 5-48*. Schematic representation of the cooled water, small-scale eddies, and bubble transport from the near-surface zone to deeper layers due to ramp-like coherent structure under convectively unstable conditions. Vertical dashed lines (A, B, and C) indicate some of the possible free-rising profiler trajectories with respect to the organized structure.

Similar profiles obtained at 00:55 (*Figure 5-47*), but having the opposite sign of vertical velocity change at 0.95 m depth and the same sign of

temperature change as the profiles discussed above, may be interpreted as the result of intersection of a region where cold water was moving along the frontal interface toward the ocean surface. This corresponds to profiler trajectory B in *Figure 5-48*

The profiles obtained at 01:06 GMT have no substantial changes either in temperature or in vertical component of velocity. These profiles might be located in the space between the large-scale eddies (trajectory C in *Figure 5-48*. The other four pairs of profiles shown in *Figure 5-47* are supposedly related to the cases when the profiler passes through less pronounced regions of the vortex structure.

The vertical profiles shown in *Figure 5-47* are thus consistent with the presence of ramp-like coherent structures in the near-surface layer of the ocean. This is, however, fragmentary information; alternate interpretations are not excluded.

Before moving on to theoretical aspects of the problem of ramp-like coherent structures we would like to point the reader to one unresolved question relating to the problem of organized motions in the upper ocean. The field study performed by Thorpe et al. (2003) using an autonomous underwater vehicle suggests that both types of coherent structures do coexist. How can ramp-like structures coexist with Langmuir circulations? Vortices associated with ramp-like structures have transverse axes, while Langmuir circulations have a longitudinal axis, relative to the wind. Moreover both phenomena have similar space and time scales. Each of these motions in isolation is two-dimensional. However, two uncorrelated two-dimensional motions with mutually perpendicular axes represent a three-dimensional motion, which, according to principles of self-organization should have a tendency to randomization rather than organization. At first glance, the ramp-like structure and Langmuir circulations should not coexist at all. This appears possible only if they are synchronized in some way in space and time.

Microstructure measurements in the near-surface layer of the ocean are still very rare. Further studies will have to address the question posed above, as well as some other important questions relating to the problem of coherent structures in the upper ocean. Though previous studies in the atmospheric boundary layer can provide guidance to ocean boundary layer studies, the analogy between the atmospheric and oceanic boundary layers, however, is not exact. The oceanic turbulent boundary layer differs from its atmospheric analog due to the presence of a free surface. The importance of free-surface effects (including breaking waves) increases towards the surface. Processes in the near-surface layer are therefore crucial to understanding the coherent structures in the upper ocean turbulent boundary layer and must be sampled adequately.

### 5.6.5 Townsend's hypothesis and ramp-like structures

Townsend (1961) conditionally divided the turbulence near a wall into two parts–an active part, which transports momentum, and an inactive part, which does not. In addition, he hypothesized that these two types of turbulent motion do not interact. In Townsend's (1961) model, active turbulence is generated by wind shear; its properties can be scaled by local parameters of the flow. Inactive turbulence is the product of energetic processes remote from the surface; its properties are scaled with the outer-layer parameters. The Monin-Oboukhov similarity theory, which is formulated in terms of local parameters, can apply to active motions only.

McNaughton and Brunet (2002) proposed a mechanism for how inactive motions could initiate active, coherent ejection/sweep structures that carry much of the momentum and heat (*Figure 5-49*). They found evidence that the inactive motions take the form of streak patterns of faster and slower air, which are aligned with the surface wind. The streaks are induced by the pressure effect of the large eddies passing overhead. Sharp convergence lines of uplifted, slower air are created in the flow by the high-speed streams of subsiding air spreading laterally. The slow streaks are therefore narrower than the subsiding zones between (*Figure 5-49*).

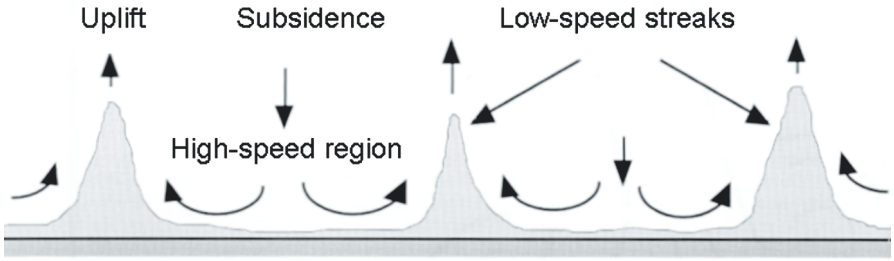


*Figure 5-49*. Schematic cross-flow section of the low-speed streaks near the ground. Reproduced from Smith and Walker (1997): Advances in Fluid Mechanics ISBN: 1-85312-453-2, www.witpress.com

The difference in speeds of the various parts of the flow thus creates convergence zones where the high-speed streams overtake the slower-moving streaks. In each of these zones the faster air stream at first simply passes about the slower streak, creating a zone of strong shear between the faster and slower air streams. The velocity profile along normals to this interface is strongly inflected, forms a classic source of instability in the flow. It initiates a series of transverse roll vortices, just as similar inflections do in plane mixing layers, but here the roll vortices are draped across the spine of the engulfed streak. These vortices describe gentle arcs where the streak is low and board, but become croissant- or horseshoe vortices over

taller, more upright parts of streaks. Well-formed horseshoe vortices can then assume a life of their own, continuing to grow by taking vorticity and turbulent kinetic energy from the mean flow itself. The mean shear also rotates these coherent vortices forward until, by a combination of growth and rotation, they contact the ground to form a dam with strong inflows along the ground produced by the rotation of the vortex arms and the main flow presenting pressing in from behind. With nowhere else to go, the trapped air squirts backwards and outwards into the flow. This squirt is usually described as an ejection/sweep event. *Figure 5-50* illustrates a schematic of the first ejection formation on a streak.

McNaughton and Brunet (2002) assume that their model is consistent with information from many sources and provide a historical excursion into studies of the bursting process. Theodorsen (1952) was probably the first who gave theoretical arguments for initiation of horseshoe vortices about slow-moving masses of fluid attached to the ground, with subsequent vortex roll-up and ejection. In the 1950's, he could not know of wall streaks nor appreciate the power of the ejection. In a series of laboratory experiments, Kline et al. (1967) discovered wall streaks and described their oscillation and break-up with sudden ejection of fluid from very near the wall. Kline et al. (1967) did not detect the overtaking fluid or the horseshoe vortices. Corino and Brodkey (1969) observed the colliding masses of fluid and realized the power of the ejections in the boundary-layer dynamics; their visualization methods unfortunately could not detect the formation of horseshoe vortices. Hinze (1975) and Offen and Kline (1975) proposed a relationship between wall streaks and horseshoe vortices. Hagen and Kurosaka (1993) were the first who demonstrated the connection between horseshoe vortices and powerful ejections. From a large-eddy simulation (LES) of a convective atmospheric boundary layer, Lin (2000) deduced a sequence of horseshoe eddies followed by a vigorous ejection. Finally, McNaughton and Brunet (2002) used his results to develop the schematic diagram shown in *Figure 5-50*.

McNaughton and Brunet's mechanism thus appears to be consistent with a wide range of results from laboratory and atmospheric boundary layer experiments. The new element introduced by these researchers is the pressure mechanism for streak formation. This mechanism has an important consequence, since it allows the wall streaks to form within fully turbulent layers. Previously, wall streak formation has been associated only with viscous sublayers, though the importance of pressure rather than vorticity in creating motions near the ground was shown from LES results by Moeng (see Peltier et al., 1996).

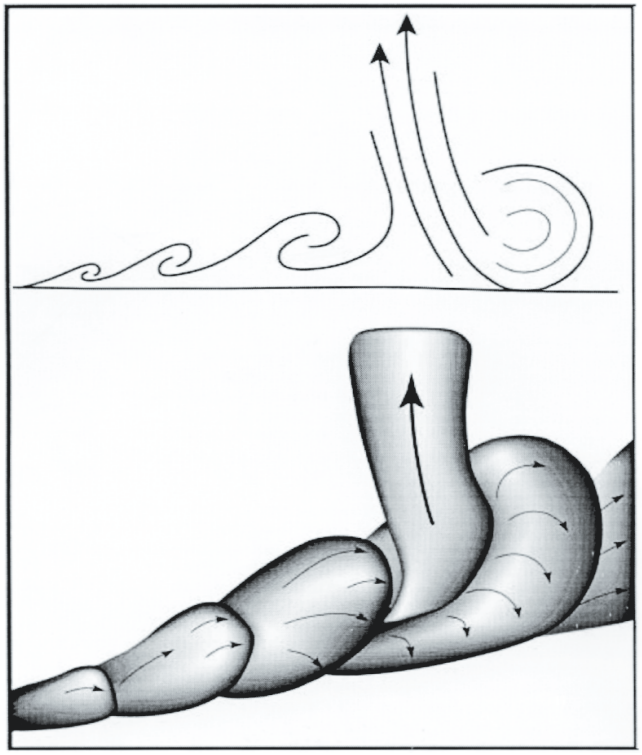

*Figure 5-50*. Schematic diagram of a series of vortices forming across the spine of a low-speed streak. The upper panel shows a longitudinal section down the streak while the lower panel represents an outline of the air of the streak as the vortices form. The vortices lying across the spine of the streak take on a 'horseshoe' or 'hairpin' shape where the streak is sufficiently upright, and these can grow to the point where they contact the ground and cause a vigorous ejection of fluid. Reproduced from McNaughton and Brunet (2002) with permission from Springer Science and Business Media.

The phenomenological model of McNaughton and Brunet (2002) justifies some important underlying assumptions made in the theory of coherent structures as vorticity waves described in the next section (Section 5.6.6):

1) Wall streaks can form within fully-turbulent layers
2) A zone of strong shear is created between the faster and slower air streams, and
3) On certain time scales the viscosity effects are negligible.

Since temperature transport is significantly affected, the dimensional assumptions of Monin-Oboukhov theory are undermined. This circumstance has important application for mixing parameterizations, which can no longer rely on local diffusion only but must include nonlocal transport due to coherent structures.

### 5.6.6 Vorticity waves in shear flows

The vorticity waves introduced in Section 5.4.3 for a stratified ocean (in relation to sharp frontal interfaces) can also exist in a uniform density fluid (Lin, 1966). In stratified flows the vorticity waves are not directly affected by stratification, though the presence of stratification may affect the vorticity waves indirectly, via modifying the mean velocity profile or due to resonance with the internal waves that can develop in the underlying stratified layer (Section 5.4.3).

The theoretical analysis below is based on the hypothesis that ramp-like structures are associated with vorticity waves. Ramp-like structures have been observed within the actively mixed turbulent boundary layer (*i.e.*, at $Ri < Ri_{cr} = 1/4$) that, according to condition (5.25) (or (5.27)), can be far from internal wave–shear resonance. The system of equations describing the internal wave–shear flow resonance in Section 5.4.3 is replaced with a single nonlinear evolution equation (Shrira, 1989; Voronovich et al., 1998b):

$$\partial_\tau A - \alpha A \partial_x A - \beta \hat{G}\left[\partial_x A\right] = 0, \tag{5.53}$$

where $\alpha = u'|_{z=-0}$, $\beta = \left(u^2/u'\right)|_{z=0}$, and $\hat{G}$ is an integral operator of the form

$$\hat{G}\left[\varphi(\vec{r})\right] = \frac{1}{4\pi^2}\int_{-\infty}^{\infty} Q\left(\vec{k}\right)\varphi(\vec{r}_1)\exp\left(i\vec{k}\left(\vec{r}-\vec{r}_1\right)\right)d\vec{k}\,d\vec{r}_1 \tag{5.54}$$

This class of evolution equation is specified by the kernel $Q\left(\vec{k}\right)$ that depends on the structure of eigenfunctions of the boundary layer problem. In the two-dimensional case, equation (5.53) reduces to the well-known equation of Benjamin-Ono type (previously derived in a similar context by Romanova (1984)). The coefficients of the related Benjamin-Ono equation appear to be finite only when the condition $u(z) \sim \alpha z$ is satisfied at $z \sim 0$. For this special case of the linear velocity profile (see dashed line in *Figure 5-51*) and $N = 0$, the Romanova (1984) solution represents a vorticity wave, which is defined as a long wave having the maximum of its modal function at the vorticity jump at $z = h$.

For a smooth shear profile localized near the surface (see continuous line in *Figure 5-51*), the solution is much more complicated but still preserves some basic properties of the simplest model. Voronovich et al. (1998b) demonstrated that on horizontal length scales $L >> h\,\mathrm{Re}^{1/4}$ arbitrary wave perturbations still behave like discrete modes in Romanova's solution while

the viscous terms are negligible on length scales $L << h\,\mathrm{Re}^{1/2}$. Here $\mathrm{Re} = u_0 h/\nu$; velocity $u_0$ and depth $h$ scales are defined as shown in *Figure 5-51*, and $\nu$ is the molecular coefficient of kinematic water viscosity.

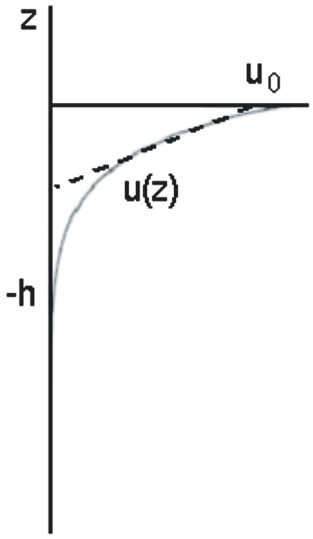


*Figure 5-51*. Schematic representation of the wind-drift current in the surface layer of the ocean. (After Voronovich et al., 1998b.)

The waves of the continuous spectrum thus form an intermediate asymptotic solution; its leading terms coincide with the solution for the simplest model of Romanova (1984). A continuous spectrum replaces the discrete modes on intermediate times

$$h\,\mathrm{Re}^{1/4} << L << h\,\mathrm{Re}^{1/2}, \tag{5.55}$$

For $h = 1$ m, $u_0 = 0.1$ m, and $\nu = 10^{-6}$ $\mathrm{m^2 s^{-1}}$, inequality (5.55) corresponds to the range of horizontal scales, 18 m $<< L <<$ 316 m, which is consistent with the typical horizontal scales of ramp-like structures in the upper ocean (see *Figure 5-43*b and *Figure 5-44*).

The dispersion relationship for the linear analog of equation (5.53) is as follows:

$$\omega = \left(c - \beta\left|\vec{k}\right|\right)k_x, \tag{5.56}$$

where $c = U|_{z=0}$ For a two-dimensional case $k = k_x$; the spectrum of $\omega(k)$ in (5.56) is "nondecaying" because the conditions for three-wave

synchronization, $\omega(k_3) = \omega(k_1) + \omega(k_2)$ at $k_3 = k_1 + k_2$ are never fulfilled. At the same time for three-dimensional waves, the synchronism conditions can be satisfied for certain oblique perturbations (Voronovich et al., 1998b). Plane (three-dimensional) solitary waves in infinitely deep water appear to be unstable with respect to transverse perturbations (Pelinovsky and Shrira, 1995).

The properties of the intermediate asymptotic solution of equation (5.54) are consistent with the qualitative scheme of Townsend (1961) discussed in the previous section (Section 5.6.5). Perturbations that develop across the spine of a low-speed streak (*Figure 5-50*) are apparently long enough to satisfy the left side of inequality (5.55). The fact that the three-dimensional solution of (5.53) is unstable with respect to transverse perturbations is also qualitatively consistent with the McNaughton and Brunet (2002) phenomenology stating (see *Figure 5-50*) that the flow instability is initiated by transverse roll vortices

The active motions are dissipative; the viscosity effects can therefore no longer be ignored. This imposes an upper bound on the horizontal length scale, which is determined by the right side of inequality (5.55).

The interpretation of the ramp-like coherent structures as non-linear wave-like perturbations in shear flow due to the inhomogeneous mean vorticity field is consistent with observational data. The theory of vorticity waves can therefore serve as the basis for the interpretation of the ramp-like coherent structures. This theory, however, describes evolution of weakly nonlinear waves only and cannot handle the dynamics of the horseshoe vortex.

## 5.7 Langmuir Circulations

### 5.7.1 Phenomenology

Long before oceanography developed as a distinct branch of science, sailors and seafarers noted long narrow “bands,” “streaks,” or “lanes” on the sea surface, which were often nearly aligned with wind. This phenomenon appears in the notes of Charles Darwin from his voyages on the *Beagle* (Leibovich, 1983). In 1938, Langmuir came to the conclusion that the streaks or “windrows” are the visible manifestations of a parallel series of counter-rotating vortices in the surface layers of the water with axes nearly parallel to the wind. At present, while the existence and many features of Langmuir circulations are generally accepted, their role in the mixed layer dynamics is still ambiguous.

Different floating substances ranging from seaweed and marine organisms to organic films and foam from breaking waves tend to

concentrate in the convergence zones. Flotsam makes the bands visible directly. These bands are sometimes observed even in the absence of floating objects — compressed films make them visible due to suppressing capillary waves, thereby giving the bands a smoother appearance in surface reflectance. In some cases, the amplitude of the surface gravity waves increases in convergence zones leading to wave breaking. Though convergences at the ocean surface can be caused by different factors including internal waves, oceanic fronts, convection etc., Langmuir circulations are an important and frequent cause of the near-surface convergence lines.

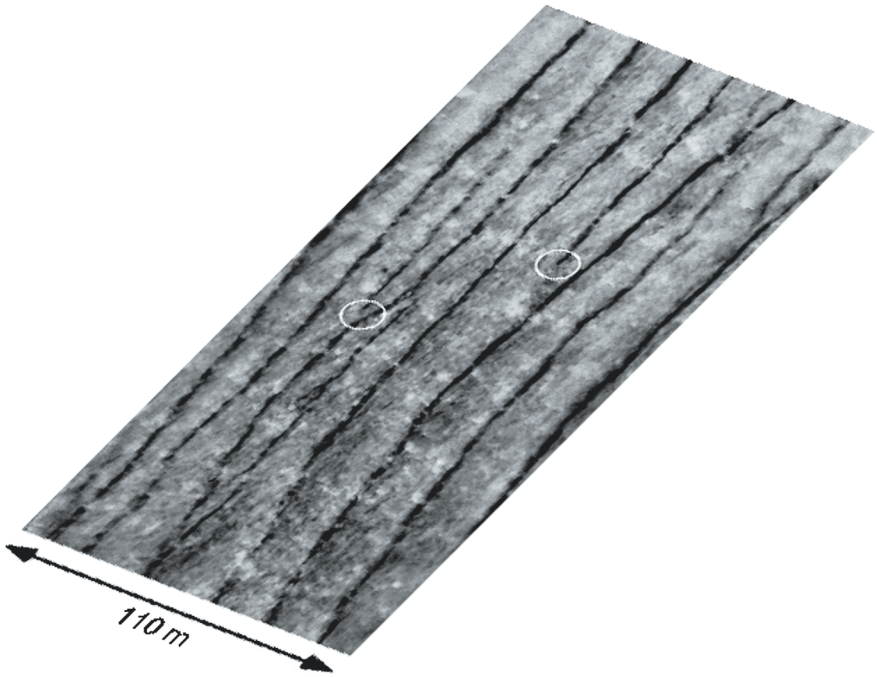


*Figure 5-52*. Langmuir cells (dark streaks) in nighttime infrared imagery. The streaks are about 0.2°C cooler than the ambient surface water. The circle on the right highlights the termination of one streak. The left circle indicates where two streaks merge. Such features persisted over several minutes and drifted with the downwind surface current. Bright (warm) spots occurring throughout the image represent microscale wave breaking events. (This image is from the public domain of the Naval Research Laboratory Web Site http://www.nrl.navy.mil.)

The convergence zones are sometimes seen in infrared imagery through their interaction with the ocean's cool skin. The infrared imagery shown in *Figure 5-52*a depicts long, dark (cool) streaks associated with Langmuir

circulations (Marmorino et al., 2005). Surface convergences between successive pairs of Langmuir cells interact with the cool skin producing the cool streaks in the imagery. This observation was made from an aircraft flying over the inner West Florida continental shelf where the water depth was only 3 m. The wind of about 5 m $s^{-1}$ was blowing nearly parallel to the streaks. The spacing of the streaks in *Figure 5-52* is 10 to 20 m, which gives each cell an unusually large width-to-height aspect ratio of about 2.5. In the open ocean, the aspect ratio of the largest Langmuir cells is believed to be close to unity.

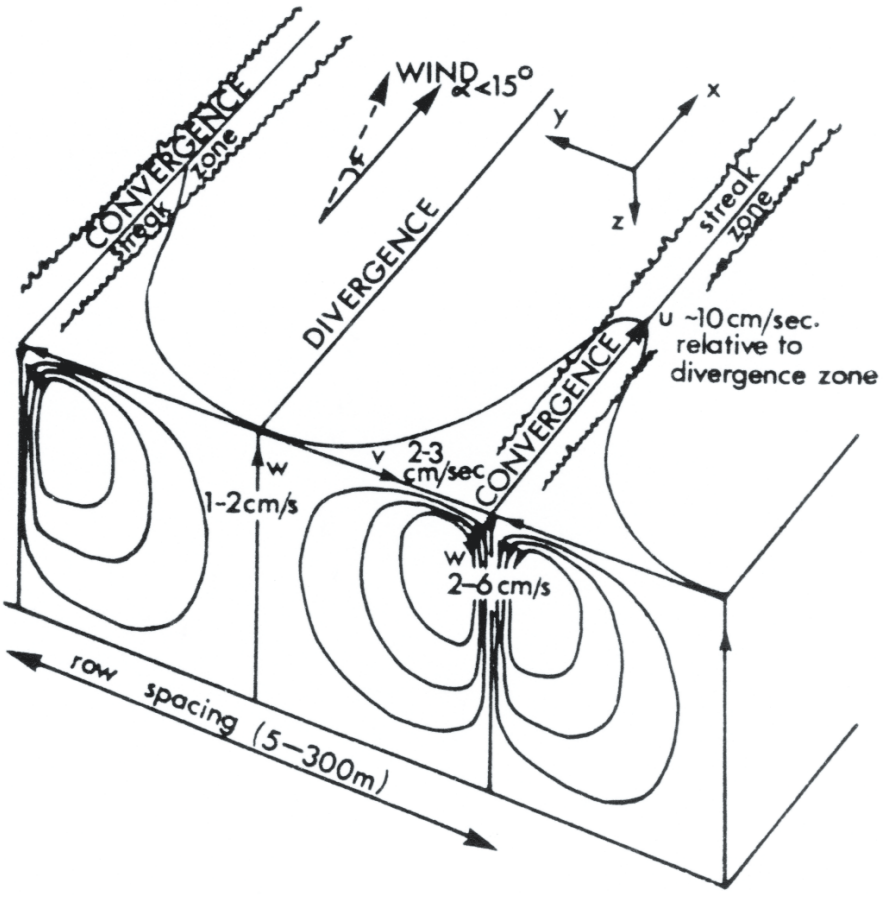


*Figure 5-53*. Pollard's (1979) sketch of Langmuir circulations.

The Langmuir cells are parallel and oriented nearly downwind with alternating longitudinal vorticity (*Figure 5-53*), producing convergence and divergence zones. The downwelling zones are substantially narrower than

the upwelling zones. The typical distance between the Langmuir vortices is from a few meters to a few hundred meters.

Langmuir circulations appear to be a transient and variable process. A hierarchy of Langmuir circulations is often observed with smaller, more irregular, and less well-defined streaks occurring between stronger and more widely spaced streaks. In the hierarchy of spacings between the lanes, the small cells continually form and gradually merge into the more permanent larger cells (Thorpe, 1992). Evidence for the adjacent streaks merging and individual streaks terminating can also be found in the infrared imagery shown in *Figure 5-52* (two circled areas).

According to observations, the speed of near-surface current in the wind direction is maximal in convergence zones, reaching 0.2 m $s^{-1}$ with respect to the current speed in divergence zones. The typical speed of downwelling in the convergence zones is of the order of several cm $s^{-1}$ near the surface according to some investigators. At the same time, downward vertical velocities estimated by Weller and Price (1988) appear to be even larger, perhaps because the vertical velocity increases with depth to some point ~$h$/2. Interestingly, the D'Asaro et al. (1996) attempt to identify motions below the surface as Langmuir circulations using Lagrangian tracking did not provide clear evidence for the presence of circulatory flows.

The Langmuir circulations form within a few minutes of onset of a wind of 3 m $s^{-1}$ or faster (Pollard, 1979). Langmuir circulations are observed regardless of surface heating or cooling. Nevertheless, under conditions of surface cooling (unstable stratification), the Langmuir circulations may form at a lower wind speed. For wind speeds exceeding 3 m $s^{-1}$, surface fluxes (cooling or heating) do not appear to appreciably modify their strength and form.

Under high wind speed conditions the Langmuir cells are not clearly seen on the ocean surface because of wave breaking though they may still exist (Leibovich, 1983). Most observations of Langmuir circulations are reported in the wind speed range from 3 to 10 m $s^{-1}$, although there are observations of the Langmuir type streaks at wind speeds less than 3 m $s^{-1}$.

Weller and Price (1988) found that Langmuir cells rapidly destroy the surface thermal stratification in shallow diurnal mixed layers. They, however, could not find evidence that Langmuir vortices directly participate in mixing in the deeper parts of the oceanic mixed layer.

Craik and Leibovich (1976) developed a list that abstracts a minimum of qualitative features than any viable theory of Langmuir circulations must be able to reproduce:

1) A parallel system of vortices nearly aligned with the wind.
2) A means must be given by which these vortices are driven by the wind.

3) The resulting cells must have the possibility of an asymmetric structure with downwelling speeds larger than upwelling speeds.
4) Downwelling zones must be under lines where the wind-directed surface current is greatest.
5) The Langmuir circulations must have maximum downwelling speeds comparable to the mean wind-directed surface drift.

Apparently, this checklist helped Craik and Leibovich to develop their famous theory of Langmuir circulations.

### 5.7.2 Concepts and theories

Many mechanisms for Langmuir circulations have been proposed since the publication of the pioneer work of Langmuir in 1938. An overview of the early ideas concerning the mechanism of the Langmuir circulations can be found in Leibovich (1983). Potentially important mechanisms can be grouped as follows: 1) convection; 2) wind forcing; 3) action of surface gravity waves; 4) joint influence of wind and waves. Most of these mechanisms have been shown to be nonessential to or incompatible with the phenomenon, and therefore have been dismissed. A combination of theories, field, and laboratory observations pointed out an interaction between wave motions and surface sheared currents as a mechanical cause for the phenomenon.

In the 1970s, Garrett, Craik and Leibovich developed a theory capable of predicting observable features of Langmuir circulations. The theory involved the distortion of vortex lines in the current by the action of surface waves. This theory was based upon a set of nonlinear equations derived from the Navier-Stokes equations by perturbation procedure. Craik-Leibovich, or "CL" theories described circulatory motions by two distinct theoretical mechanisms, which are considered below. Both mechanisms depended on wave-current interactions.

The orbital motion of irrotational surface gravity waves usually dominates the instantaneous velocity field in the near-surface surface layer of the ocean. An important component of CL models is the Stokes drift associated with the surface waves,

$$\vec{U}_s = \int_t \overline{\vec{u}_w \partial t \cdot \nabla \vec{u}_w} \,. \tag{5.57}$$

The Stokes drift results from the nonlinear rotational component of the surface wave field and is defined in (5.57) following Phillips (1977). The overbar in (5.57) correspond to a proper averaging operator; $\vec{u}_w$ is the velocity vector of the orbital motion induced by the waves.

The surface wind stress is an important source of vorticity in the surface layer of the ocean. Vorticity in the surface layer of the ocean may also arise from shear currents driven by horizontal pressure gradients, which are not necessary directly related to the surface stress. The surface waves (that develop due to a prolonged action of the wind stress on the sea surface) perturb the vorticity field in the near-surface layer of the ocean. In particular, surface waves stretch and rotate vortex lines. The rectified (*i.e.*, irreversible) effects of the waves arise from additional advection and stretching of mean vorticity by the wave-induced Stokes drift (Leibovich and Ulrich, 1972).

The governing equations in the model for the rectified water motion under the Boussinesq approximation are based on the assumption of constant eddy diffusivity of momentum ($\nu_T$) and heat ($\chi_T$) and are as follows (Leibovich, 1977b):

$$\frac{\partial \vec{u}}{\partial t} + \vec{u} \cdot \nabla \vec{u} = -\nabla \pi + \vec{U}_s \times curl \vec{u} + \alpha_T g \theta \vec{k} + \nu_T \nabla^2 \vec{u}, \tag{5.58}$$

$$\frac{\partial \theta}{\partial t} + \vec{u} \cdot \nabla \theta = -w \frac{\partial \overline{T}(z)}{\partial z} + \chi_T \nabla^2 \theta,$$

$$\nabla \cdot \vec{u} = 0,$$

where $\overline{T}(z)$ is the temperature distribution in the absence of circulations, $\theta$ is the perturbation of temperature, $\alpha_T$ is the coefficient of thermal expansion, $g$ is the acceleration of gravity, $\vec{u}$ is the mean velocity vector in the current, and $\pi$ is a modified pressure term that includes the mean pressure as well as terms involving wave kinetic energy.

The boundary conditions for the equation system (5.58) are as follows:

$$\frac{\partial u}{\partial z} = u_*^2 / \nu_T; \ \frac{\partial v}{\partial z} = 0; \ w = 0; \ \theta = 0 \text{ at } z = 0; \tag{5.59}$$

$$\vec{u} \to 0, \ \theta \to 0 \quad \text{as } z \to -\infty, \tag{5.60}$$

where $u_*$ is the friction velocity in water. The ocean at the initial moment is motionless, except that surface waves are present. The wind drift current does not change in the longitudinal direction $x$. If the wave-mean current interactions are ignored (which means that the currents may be specified in advance), then the Stokes drift is given a priori; the system of equations (5.58) is closed.

This model is able to address the problem of the generation of Langmuir circulations from the motionless state. It meets the criteria of Craik and

Leibovich (Section 5.7.1) and thereby explains many observable features of the Langmuir circulations.

Leibovich (1977a, b) further extended the CL model to allow time development of the currents and density stratification under the Boussinesq approximation. These works, however, greatly simplified the problem by parameterizing the effects of turbulent fluctuations by constant eddy diffusivities. More sophisticated turbulence models like those described in Chapter 3 were not yet available in the 1970s.

A remarkable feature of (5.58) is the presence of a vortex force:

$$\vec{f}_v = \vec{U}_s \times \vec{\omega} \tag{5.61}$$

where $\vec{\omega}$ is the mean vorticity. Note that as $\vec{U}_s \to 0$ (which is achieved, for instance, when $z \to \infty$), the vortex force term (5.61) vanishes and equations (5.58) reduce to the classical Navier-Stokes equations of a Boussinesq fluid.

In order to explore the role of the vortex force term (5.61), let us follow Leibovich (1983) and assume that the wind blows in a fixed direction over initially undisturbed water of unlimited horizontal extent and depth. Only one fixed direction is involved in the problem formulation, thereby symmetry dictates the development of a surface wave field with unidirectional Stokes drift aligned with the wind or $\vec{U}_s = U_s \vec{i}$ . Since this is a two-dimensional hydrodynamic system, it has tendency to self-organization.

For simplicity, Coriolis acceleration is neglected; the total momentum transferred to the surface layer of the ocean is in the same direction as the Stokes drift velocity vector. The horizontally averaged velocity is $\vec{u} = u(z,t)\vec{i}$ , while the positive *y*-vorticity is $\vec{\omega} = \left(\partial u / \partial z\right)\vec{j}$ . It is remarkable that the vortex force

$$\vec{f}_v = \vec{k} U_s \partial u / \partial z \,, \tag{5.62}$$

is oriented vertically upward and is formally analogous to the buoyancy force in (5.58).

If the Stokes drift $u_s$ would depend only on depth *z*, then the vortex force could be balanced by the analog of a hydrostatic pressure gradient (developing unidirectional current). If for any reason the Stokes drift varies across the wind (in the *y*-, or transverse direction), the vortex force cannot be balanced just by pressure gradients, and an overturning is possible.

Longuet-Higgins (1962) exploited the fact that the directional spectrum of wind-generated surface waves in a "short-crested" sea is bimodal and symmetric with respect to the wind. If the spectrum is bimodal (with peaks of wave energy at angles +/-θ with respect to the wind), and if the wave spatial structure remains coherent for long enough for the rectification

responsible for the Stokes drift to take place (many times a typical wave period), then the Stokes drift would be spatially periodic with a cross wind wave number of $2k \sin\theta$, where $k$ is the characteristic wave number of the surface waves. This horizontally periodic wave drift produces a torque due to horizontal variations of vortex force that drives the roll motions (Craik and Leibovich, 1976). This mechanism is known in literature as the CL1 mechanism.

Leibovich and Ulrich (1972) proposed an alternate, kinematic interpretation of the CL1 mechanism. In this interpretation, the Stokes drift deforms the vortex lines associated with the current and produces the streamwise vorticity periodically (in $y$) altering in sign.

*Figure 5-54* summarizes both the dynamic and kinematic interpretations of the CL1 mechanism. This figure also includes a schematic diagram of idealized "cross-wave trains" assumed in the CL1 mechanism.

Leibovich (1977a) extended the CL1 theory to include time evolution of the coupled (wind-directed) currents and circulations. He formulated the problem as an initial-value problem, with currents and circulations initially zero and initiated by a step function in surface stress, which resulted in a well-posed mathematical problem. Since by assumption the wave field is steady and invariant in the $x$-(wind) direction and symmetric with respect to the $x$-axis, the problem is independent of $x$ and any emerging circulations appear in the form of rolls. This initial-value problem depends upon an angle representing the directional properties of the waves and a single dimensionless parameter called the *Langmuir number,*

$$La = \left( \nu_T^3 k^2 / \sigma a^2 u_*^2 \right)^{1/2} \tag{5.63}$$

where $u_*$ is the friction velocity (corresponding to a constant wind stress for $t \geq 0$), and $\nu_T$ is the eddy viscosity; $\sigma$, $k$, and $a$ are the characteristic surface waves frequency, wave number, and amplitude respectively. The Langmuir number describes the balance between the rate of diffusion of streamwise vorticity and the rate of production of streamwise vorticity by the vortex stretching accomplished by the Stokes drift. This number can also be interpreted as an inverse Reynolds number. The appropriate scalings of the Langmuir circulations characteristics are given in *Table 5-3*. Since these scalings emphasize a balance between vortex force and the applied shear stress when $x$-variations are negligible, they are also appropriate to problems involving the CL2 instability mechanism under the same set of assumptions. In that case, however, the angle representing the directional properties of the waves is not invoked.

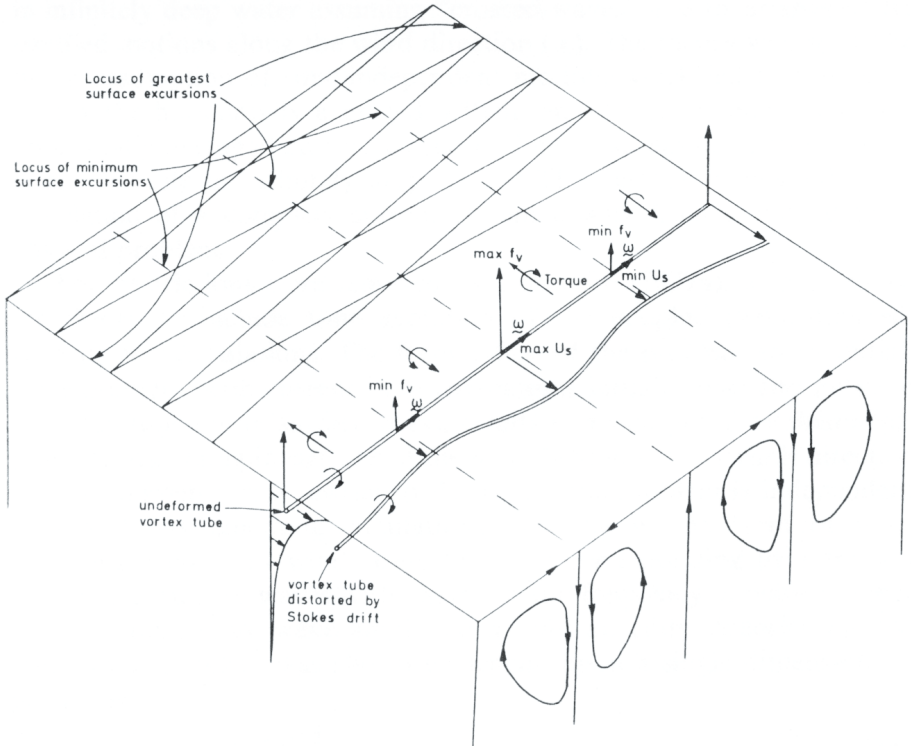


*Figure 5-54*. Sketch illustrating the direct-drive generation mechanism for Langmuir circulations. Wave crests of the assumed crossed-wave pattern are shown; the Stokes drift variations distort vortex lines of the primary current. The resulting variations of vortex force create a torque leading to overturning. Reprinted from Leibovich (1983) with permission by Annual Reviews www.annualreviews.org

The formation of a periodic Stokes drift pattern, which is basic to the CL 1 theory, requires a given wave pattern to be phase-locked for several wave periods. Moreover, the formation of a well-developed circulation by the CL1 mechanism seems to require that the Stokes drift pattern remain fixed for times of the order of hundreds of wave periods. Phase locking for times as long as this is not expected in a wind-generated sea; it has, however, been achieved in the laboratory (Faller and Caponi, 1978).

Craik (1977) and Leibovich (1977b) proposed another mechanism for Langmuir circulations, which does not require the presence of a coherent surface-wave pattern. It is known in the literature as the CL2 mechanism. The linear stability of a unidirectional sheared current in the presence of a parallel, spanwise uniform Stokes drift is the basis of the CL2 mechanism.

*Table 5-3*. Scalings for the Craik and Leibovich model of Langmuir circulations.

| Length | Time ($T_d$) | Wind-directed component of rectified current | Crosswind velocity component of rectified currents |
|---|---|---|---|
| $k^{-1}$ | $(\nu_T/\sigma)^{1/2}/a\kappa u_*$ | $u_*^2/\nu_T\kappa$ | $(au_*/\nu_T)(\sigma\nu_T)^{1/2}$ |

The Langmuir cells are produced via the vortex force as an inviscid instability of the unidirectional current. The vortex force represented by (5.61) in this case is balanced by a vertical pressure gradient. Assuming that $u_s$ and $u$ and the vortex force typically decrease monotonically with depth below the surface, the joint effect of typical distributions of $U_s$ and $u$ appears to be analogous to a statically unstable density distribution (Leibovich, 1983). If dissipation is sufficiently weak, the rectilinear current could become unstable. It is interesting that if the waves and current are opposed, then the vortex force is stabilizing and Langmuir circulations cannot be generated by the CL2 mechanism.

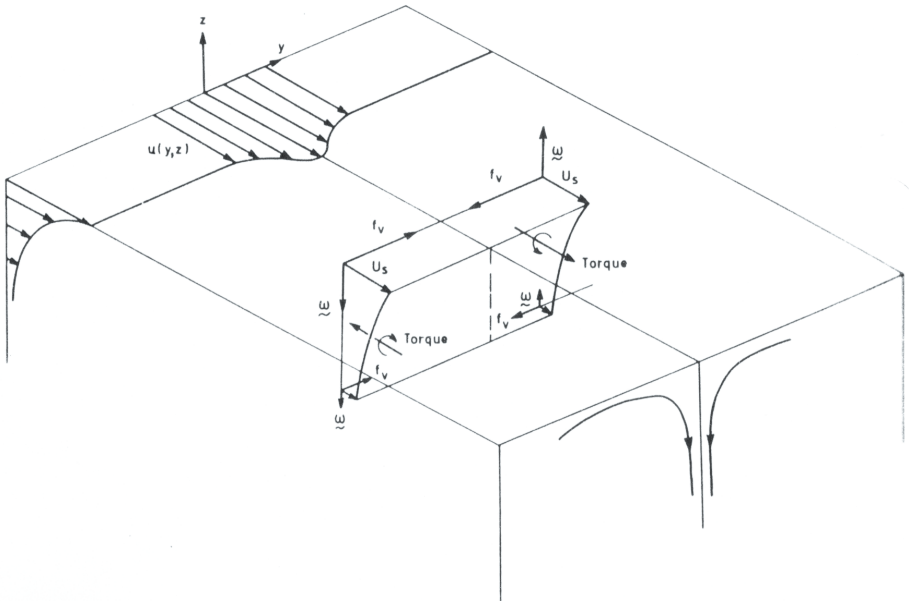


*Figure 5-55*. Sketch illustrating the Craik and Lebovich instability mechanism of Langmuir-circulations generation. The Stokes drift is horizontal but decays in depth. Streamwise vorticity is induced by the current. Variations of vortex force caused by the current perturbation create torques leading to overturning. Reprinted from Leibovich (1983) with permission by Annual Reviews www.annualreviews.org

*Figure 5-55* illustrates both the dynamics and kinematics of the CL2 mechanism. If a horizontally uniform current $u(z)$ has an infinitesimal spanwise irregularity $u(y,z,t)$, this produces vertical vorticity $\omega_z = -(\partial u/\partial y)$ and a horizontal vortex-force component $-U_S\omega_z\vec{j}$. The horizontal vortex-force component is then directed toward the planes of maximum *u*. The converging horizontal forces cause acceleration toward these planes, where, by continuity, the fluid must sink. Under the assumption that $\partial u/\partial z > 0$ and shear stresses are vanishing, conservation of *x*-momentum for a thin slab of fluid centered on the convergence plane shows that as the fluid sinks, *u* must increase. Thus a current anomaly will lead to convergence and therefore be amplified, which in turn further amplifies the convergence. This positive feedback results in development of Langmuir type circulations. Frictional effects are included in this conceptual mechanism. A kinematic interpretation of the CL2 mechanism is that the vertical vorticity is rotated and stretched by the Stokes drift, leading to convergence and amplification of the anomaly (Leibovich, 1983).

Craik (1977) and Leibovich (1977b) suggested an interesting analogy between the Langmuir instability induced in stably stratified flow and turbulent flows in the regime of marginal stability. These authors concluded that an inviscid, non-heat-conducting fluid of infinite depth is stable if

$$M(z) = \frac{\partial U_S(z)}{\partial z}\frac{\partial u(z)}{\partial z} - N^2(z) \tag{5.64}$$

is everywhere negative, and it is unstable otherwise. Here $N^2 = -\alpha_T g \partial \overline{T}(z)/\partial z$ is the Brunt-Vaisala frequency of the basic state; $\partial U_S/\partial z$ and $\partial u/\partial z$ are vertical gradients of the Stokes drift and of the shear currents. In an unstable system with a stable density stratification, $N^2 \geq 0$, no disturbances penetrate below some characteristic depth. As it follows from (5.64), stability for the inviscid case occurs for

$$Ri_* = \min\left[ N^2(z) \Big/ \left( \frac{\partial U_S}{\partial z}\frac{\partial u}{\partial z} \right) \right] > 1 \tag{5.65}$$

when the minimum is taken over depth. $Ri_*$ resembles a gradient Richardson number, with the geometric mean of $\partial u/\partial z$ and $\partial U_S/\partial z$ replacing the usual shear.

It is interesting that the appearance of the gradient Richardson number in the theory of Langmuir circulations for a stably stratified ocean layer opens

an opportunity to parameterize the mixing produced by this type of organized motion within a simple, first order scheme based on the gradient Richardson number, which is similar to that developed by Soloviev et al. (2001a).

### 5.7.3 Numerical models of Langmuir circulations

*a) Direct numerical simulation (DNS)*

Leibovich and Lele (1982) computed cases with constant $N$, together with other examples with variable $N$ simulating preexisting mixed layers bounded by a thermocline. *Figure 5-56* demonstrates how the horizontally averaged temperature evolves into a sharp thermocline from an initially linear profile due to developing cellular circulation motion. For gradient Richardson numbers $Ri_* > 0.125$ growth rates were smaller and the unstable motions were oscillatory. Surprisingly, the motions appear qualitatively to be a mixture of monotonically growing circulations in homogeneous water and internal waves. Apparently, the internal waves support a nonlocal transport of the kinetic energy away from the near-surface layer. In this connection, it is interesting to mention the work of Zilitinkevich and Calanca (2000) who included internal waves in a mixed-layer parameterization for the atmospheric boundary layer. The Zilitinkevich and Calanca (2000) theory is pending implementation for upper ocean mixed layer dynamics (V.M. Kamenkovich, private communication).

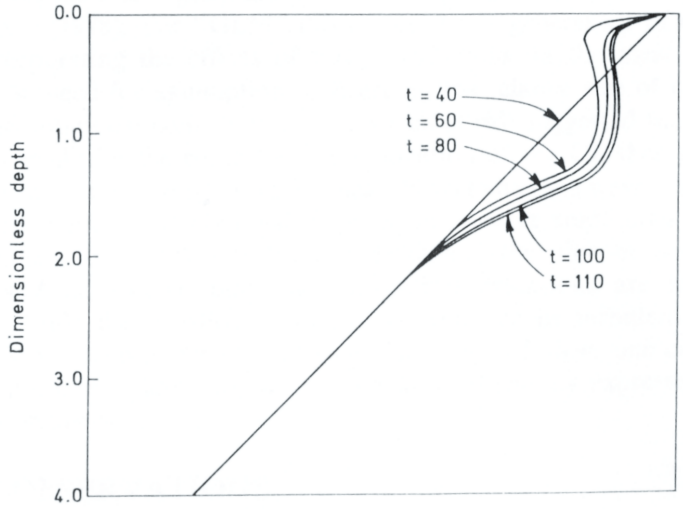


*Figure 5-56*. Horizontally averaged temperature at various times after onset of Langmuir circulations by the instability mechanism. (After Leibovich and Lele, 1982.)

For $Ri_* \geq 1/4$, but well below the inviscid criterion (5.65), the system appears to be stable at the Langmuir number of 0.01 used in the calculations. Leibovich and Lele (1982) found that sufficiently thick preexisting thermoclines with sufficiently strong temperature gradients act as an impenetrable "bottom" for the induced circulations. This is in accord with Langmuir's (1938) ideas.

*b) Large Eddy Simulation (LES)*

One problem of DNS is that the maximum Reynolds number is limited in principle. This complicates the application of DNS to geophysical situations. LES is able to handle typical geophysical situations with larger Reynolds number than is possible with DNS. Skyllingstad and Denbo (1995) performed LES studies of Langmuir circulations under a variety of conditions. These conditions included wind- and convection-driven mixing with and without Stokes drift to highlight their importance in the structure of the upper layers. They indicated the limited effect of surface heating and cooling on the near-surface structure of Langmuir circulations during their simulation. Cases with the wind- and wave-forced simulations (with or without cooling or heating) reveal the organized structure; conversely, runs without surface wave forcing do not reveal this type of organization. Remarkably, the characteristic elongated structures associated with Langmuir cells were evident in the near-surface layer only but not at greater depths in the upper ocean mixed layer. The enhancement of vertical velocity variance and the increased entrainment heat flux in the case with Stokes drift relative to the case with no Stokes drift led Skyllingstad and Denbo (1995) to the conclusion that Langmuir circulations might be important to the dynamics of the upper ocean mixed layer.

McWilliams et al. (1997) added Coriolis and pressure terms to the mean momentum equation for Stokes drift that was ignored by Skyllingstad and Denbo (1995). McWilliams et al. (1997) performed LES studies with the improved model formulation and demonstrated an elevated TKE and dissipation rate of TKE in the mixed layer, especially in the upper part, as well as a significant increase in eddy viscosity. The velocity profiles in the Ekman layer were also more homogeneous in the case with Langmuir circulations.

LES results show significant increase of the dissipation rate in the upper ocean mixed layer, which is in contradiction to the concept of self-organization. Organization should not increase, but rather reduce, chaos and thus reduce dissipation in the system. LES might then not be completely appropriate to the modeling of Langmuir circulations. LES models are based on the idea of separation between large and small-scale motions (Deardorff,

1980; Moeng, 1984). Strictly speaking, in order for the LES scheme to be effective, a trough in the wavenumber spectrum is required. In the case of Langmuir circulations, the scale separation might not be sufficient. This aspect concerned Skyllingstad and Denbo (1995) since they could not verify that there was a proper separation between Langmuir circulations and subgrid turbulence in the LES.

*c ) Models with second order closure schemes*

Kantha and Clayson (2004) tried to reproduce the McWilliams et al. (1997) LES results on Langmuir circulations with a one-dimensional mixed layer model, based on second moment closure of turbulence. They incorporated the effect of Langmuir circulations in the model by modifying the TKE and dissipation rate of TKE equations to account for the additional turbulence and dissipation production terms:

$$\begin{aligned}&\frac{\partial}{\partial t}\left(\frac{q^2}{2}\right)-\frac{\partial}{\partial z}\left[qlS_q\frac{\partial}{\partial z}\left(\frac{q^2}{2}\right)\right]=\\&-\langle uw\rangle\left(\frac{\partial u}{\partial z}+\frac{\partial U_S}{\partial z}\right)-\langle vw\rangle\left(\frac{\partial v}{\partial z}+\frac{\partial V_S}{\partial z}\right)+\beta g\langle w\theta\rangle-\frac{q^3}{B_1 l}\end{aligned} \tag{5.66}$$

$$\begin{aligned}&\frac{\partial}{\partial t}\left(q^2 l\right)-\frac{\partial}{\partial z}\left[qlS_1\frac{\partial}{\partial z}\left(q^2 l\right)\right]=E_1 l\left(-\langle uw\rangle\frac{\partial u}{\partial z}-\langle vw\rangle\frac{\partial v}{\partial z}\right)\\&+E_6 l\left(-\langle uw\rangle\frac{\partial U_S}{\partial z}-\langle vw\rangle\frac{\partial V_S}{\partial z}\right)+E_3\left(\beta g\langle w\theta\rangle\right)\\&-E_2\frac{q^3}{B_1}\left[1+E_4\left(\frac{l}{\kappa l_w}\right)^2\right]+E_5\left(2\Omega\right)q^2 l\end{aligned} \tag{5.67}$$

where $U_S$ and $V_S$ are the components of the Stokes drift velocity vector $\vec{U}_S$. Mellor and Yamada (1982) recommended that $E_1$ = 1.8. $E_2$ = 1, $E_3$ = 1.8, $E_4$ = 1.33, and $E_5$ = 0.

In the Kantha and Clayson (2004) model, the enhancement of the mixing coefficient $K_m$ due to Langmuir circulations critically depends on the value of $E_6$. At this point, the value of constant $E_6$ can only be determined empirically. By analogy between the vortex force (5.61) and the buoyancy force suggested in the works of Craik and Leibovich, the value of $E_6$ is expected to be close to unity. For $E_6$ = 1, the $K_m$ values in the Kantha and

Clayson (2004) model are, however, only slightly higher than those for the case without the Langmuir term. This new model constant introduced into the mixing model has to be greater than unity to simulate the vigorous mixing produced by Langmuir cells. Only in the case when $E_6$ is set as large as 4 is the increase in the mixing coefficient of similar magnitude to that in McWilliams et al. (1997) simulations. Such a high value of $E_6$ enables the turbulence length scale (and hence the mixing) in the mixed layer to be increased significantly in the presence of Langmuir cells. Though this seems to be consistent with the fact that these cells are indeed large-scale structures, there is no known physical basis to increase empirical constant $E_6$ so much. In fact, $E_6$ is expected to be of the order of magnitude of constants $E_1$ or $E_3$. If $E_6$ is of the order of unity, then the additional (Stokes) term in equation (5.67) is unimportant.

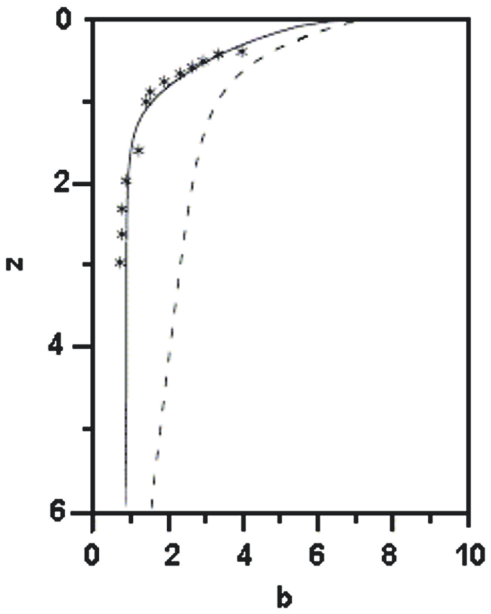


*Figure 5-57*. Vertical profiles of turbulent kinetic energy for parallel flow (---) and in the presence of secondary motions (——). Experimental points obtained in laboratory wind-wave flume are indicated by stars. Reprinted from (After Araujo et al., 2001.) with permission from Elsevier.

Araujo et al. (2001) ignored the Stokes terms both in (5.66) and (5.67). They nevertheless were able to reproduce the Langmuir circulations. The close fit between laboratory measurements and numerical results in Araujo et al. (2001) suggests that the Craik-Leibovich equations associated with the $k$-$\varepsilon$ turbulence model provides a good description of flow characteristics (*Figure 5-57*). Model results confirm that secondary motions have

remarkable influences over the vertical distribution and transport of momentum and TKE. Wind-wave boundary conditions, resulting from a balance between diffusion and dissipation of TKE are capable of reproducing the realistic scales of phenomena in this model. It is remarkable that vertical profiles of the turbulent kinetic energy in the presence of Langmuir circulations demonstrate a reduction of TKE rather than its increase as in LES. This appears to be consistent with the data from laboratory experiment (*Figure 5-57*). The explanation is that the organized motion increases the vertical transport of properties, while reducing dissipation in the system. This is consistent with the concept of self-organization introduced in the beginning of this chapter.

## 5.8 Convection

*Free convection* is fluid motion due to unbalanced buoyancy forces. Free convection, also referred to as simply *convection*, is driven by the static instability that results when relatively dense fluid lies above relatively light fluid. In the ocean, greater density is associated with colder and/or saltier water, and it is possible to have *thermal convection* due to the vertical temperature gradient, *haline convection* due to the vertical salinity gradient, or *thermohaline convection* due to the combination.

Since convection has a preferred direction (determined by the gravity force), it is a two-dimensional hydrodynamic process, which, therefore, has tendency to self-organization. Soloviev and Klinger (2001) provided a comprehensive review of convection in the upper layer of the ocean. Here we focus on the coherent properties of convection.

Since seawater is about 1000 times denser than air, the air-sea interface from the waterside can be considered a free surface. So-called *thermo-capillary convection* can develop near this surface due to the dependence of the surface tension coefficient on temperature. There are experimental indications that in the upper ocean layer more than 2 cm deep, buoyant convection dominates. Surfactants, however, may substantially affect the surface renewal process (see Section 2.2). Here, we consider convection without these capillary effects.

Convection is one of the key processes driving mixed layer turbulence, though mechanical stirring driven by wind-stress and other processes is also important. Therefore understanding convection is crucial to understanding the mixed layer as well as property fluxes between the ocean and the atmosphere.

Thermal convection is associated with the cooling of the ocean surface due to sensible ($Q_T$), latent ($Q_E$), and net long-wave radiation ($Q_L$) heat fluxes. $Q_T$ may have either sign; its magnitude is, however, much less than

that of $Q_E$ or $Q_L$ (except perhaps in some extreme situations such as cold air outbreaks over warm western boundary currents). The top of the water column becomes colder and denser than the water below, and convection begins. In this way, cooling is associated with the homogenization of the water column and the deepening of the mixed layer. Warming due to solar radiation occurs in the surface layer of the ocean and is associated with re-stratification and reduction in mixed layer depth (see Chapter 4). The most prominent examples of this mixing/re-stratification process are the diurnal cycle (night-time cooling and day-time warming) and the seasonal cycle (winter cooling and summer warming).

There are also important geographical variations in convection, with net cooling of relatively warm water occurring more at higher latitudes and a net warming of water occurring closer to the equator. For this reason, mixed layer depth generally increases towards the poles, though at very high latitudes ice-melt can lower the surface salinity enough to inhibit convection. Over most of the ocean, annual average mixed layer depths are in the range of 30 to 100 m, though very dramatic convection in such places as the Labrador Sea, Greenland Sea, and western Mediterranean Sea can deepen the mixed layer to thousands of meters. The deep convection can be significantly affected by the rotation of the Earth.

Convection directly affects several aspects of the near-surface ocean. Most obviously, the velocity patterns of the turbulent flow are influenced by the presence of convection, as is the velocity scale. The convective velocity field then controls the vertical transport of heat (or more correctly, internal energy), salinity, momentum, dissolved gases, and other properties, and the vertical gradients of these properties within the mixed layer. Convection helps to determine property exchanges between the atmosphere and ocean and the upper ocean and the deep ocean. The importance of convection for heat and gas exchange has implications for climate studies, while convective influence on the biologically productive euphotic zone has biological implications as well.

### 5.8.1 Phenomenology

The classical problem of free convection in the ocean is to determine the motion in a layer of fluid in which the top surface is kept colder than the bottom surface (Soloviev and Kilnger, 2001). This is an idealization of such geophysical examples as an ocean being cooled from above or the atmosphere being heated from below. The classical problem ignores such complications as wind stress on the surface, waves, topographic irregularities, and the presence of a stably stratified region below the convection region. The study of convection started in the early twentieth

century with the experiments of Benard and the theoretical analysis of Rayleigh. One might expect that heavier fluid would necessarily exchange places with lighter fluid below due to buoyancy forces. This happens by means of convective cells or localized plumes of sinking dense fluid and rising light fluid. However, such cells or plumes are retarded by viscous forces and are also dissipated by thermal diffusion and entrainment as they fall or sink into an environment with a different density. When the buoyancy force is not strong enough to overcome the inhibitory effects, the heavy-over-light configuration is stable and no convection forms. The relative strengths of these conflicting forces is measured by the Rayleigh number, a nondimensional number given by

$$Ra = g\alpha_T \Delta T h^3 / (k_T \nu), \tag{5.68}$$

where $g$ is the acceleration of gravity, $\alpha$ is the thermal expansion coefficient of seawater ($\alpha_T = -2.6 \cdot 10^{-4}\ ^{o}\mathrm{C}^{-1}$ at $T$ = 20°C and $S$ = 35 psu), $\Delta T$ is the temperature difference between the top and bottom surfaces, $h$ is the convective layer thickness, and ν and $k_T$ are the molecular coefficients of viscosity and thermal diffusivity, respectively ($\nu = 1.1 \cdot 10^{-6}\ \mathrm{m^2 s^{-1}}$ and $k_T = 1.3 \cdot 10^{-7}\ \mathrm{m^2 s^{-1}}$ at $T$ = 20°C and $S$ = 35 psu). The term, $\alpha_T \Delta T = \Delta\rho/\rho$, represents the relative density difference between top and bottom.

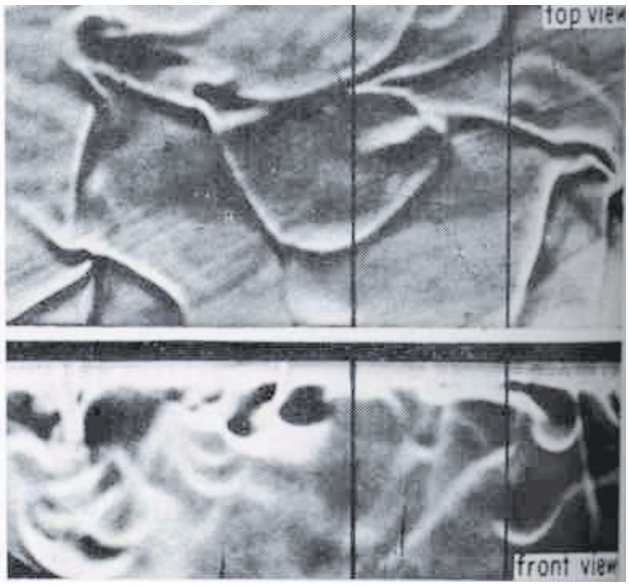


*Figure 5-58*. Orthogonal views of convective streamers in the warm water that is cooling from the surface. The constantly changing patterns appear as intertwining streamers in the side view. Reprinted from Spangenberg and Rowland (1961) with permission of American Institute of Physics.

Turbulent convection is usually characterized by the formation of descending parcels of cold water. In laboratory experiments, it has been found that water from the cooled surface layer collects along lines producing thickened regions that become unstable and plunge in vertical sheets (*Figure 5-58*). In analogy to the atmospheric convection, we will call these parcels *thermals*, although in contrast to the atmosphere, in the ocean they are colder than the surrounding fluid. Howard (1966) formulated a phenomenological theory that represented turbulent convection as the following cyclic process. The thermal boundary layer forms by diffusion, grows until it is thick enough to start convecting, and is destroyed by convection, which in turn dies down once the boundary layer is destroyed. Then the cycle begins again. This phenomenological theory has implications for the development of parameterizations for the air-sea heat and gas exchange under low wind speed conditions with a renewal model (see Chapter 2).

*Figure 5-59*. Shadowgraph picture of the development of secondary haline convection. (After Foster, 1974. © Centre National de la Recherche Scientifique.)

The descending parcels of water have a mushroom-like appearance. In the process of descending to deeper layers, the descending parcels join and

form larger mushroom-like structures. The latter descend faster and eventually form bigger structures. This cascade process produces a hierarchy of convective scales, which is illustrated in *Figure 5-59* for the example of haline convection. As a result, the energy cascades to larger scales. This is consistent with the fact that the free convection represents a type of two-dimensional hydrodynamic system and thus has a tendency to self-organization.

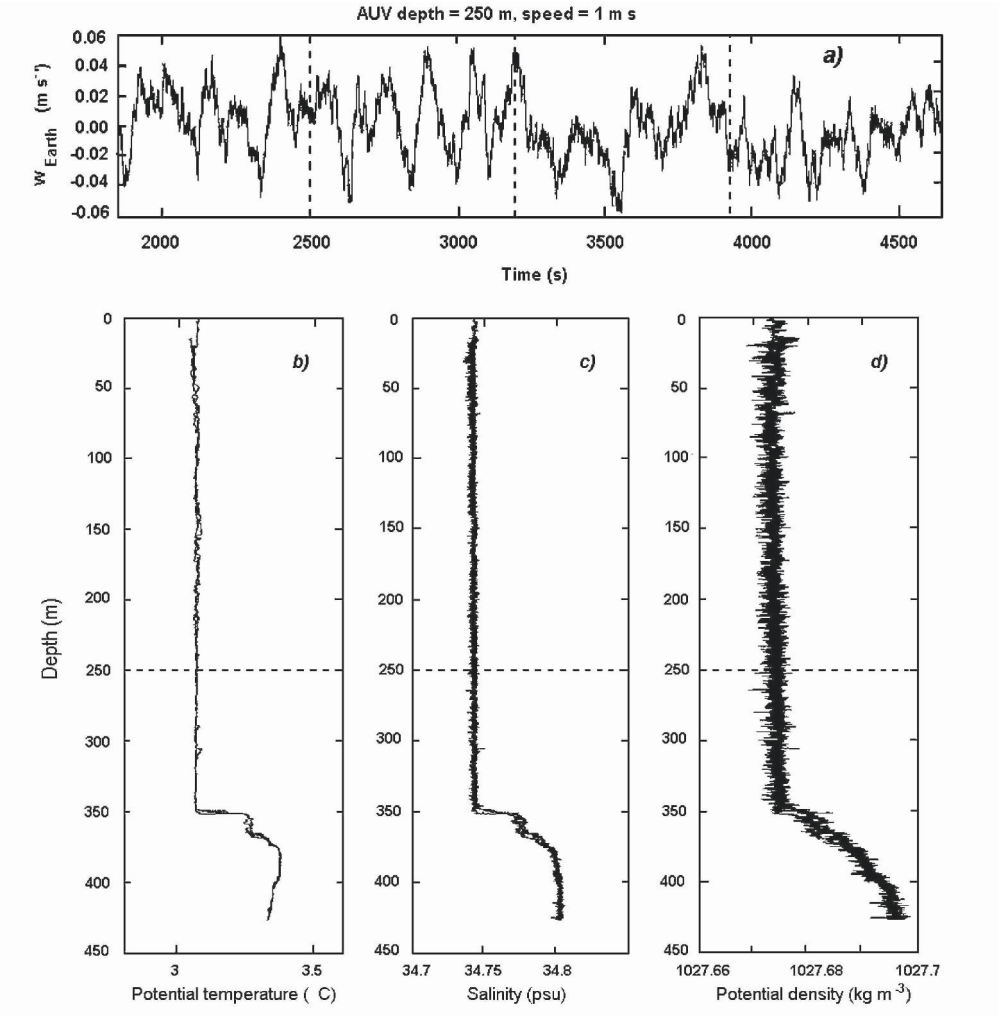


*Figure 5-60*. (a) The Earth-referenced vertical flow velocity $w_{Earth}$ at 250 m depth measured during an autonomous underwater vehicle (AUV) mission in the Labrador Sea. The vertical dashed lines show the AUV 90$^{o}$ turning points. The profiles of potential temperature, salinity, and potential density during this AUV mission are shown on panel b, c, and d, respectively. The depth of the AUV mission is shown by horizontal dashed line. (After Zhang et al., 2001.) © 2001 IEEE.

The size of convective parcels of cooler water increases with depth. If the mixed layer is deep, as in the example form the Labrador Sea shown in *Figure 5-60*, the horizontal size of the convective cells can exceed one hundred meters. In this experiment the depth of the convective mixed layer is equal to 350 m (*Figure 5-60*b). The horizontal profile of the vertical velocity taken at 250 m (*Figure 5-60*c) reveals quasi-periodic structure. Zhang et al. (2001) identified this structure as convection. The peak in the spectrum calculated from the velocity record is at 0.007 Hz, which corresponds to a 143 m wavelength for AUV speed 1 m $s^{-1}$.

### 5.8.2 Penetrative convection

The unstable stratification of the mixed layer is usually bounded below by a stratified pycnocline. One can imagine the mixed layer growing in depth with thermals confined to the statically unstable depth range. In reality, the largest thermals acquire enough kinetic energy as they fall through the mixed layer that they can overshoot the base of the mixed layer, working against the stratification. This is penetrative convection, which is a type of organized motion. The penetrative convection produces a counter-gradient flux that is not properly accounted for if convective mixing is modeled as merely a very strong vertical diffusion.

The cooling of the ocean from its surface is countered by the absorption of solar radiation. The latter is a volume source for the upper meters of the ocean. The thermals from the ocean surface, as they descend deeper into the mixed layer, produce heat flux that is compensated by the volume absorption of solar radiation.. This is another type of penetrative convection in the upper ocean, which is considered in more detail in Section 4.5.1.

### 5.8.3 Diurnal and seasonal cycle of convection

Below the wave-turbulent layer shear and convection are the main sources of turbulent mixing (Section 3.1.4). Experimental studies conducted in the atmospheric boundary layer show that for $|z|/L_O < -0.1$ the flow is primarily driven by buoyant convection, where $L_O = u_*^3 / \left[ \alpha_T g Q_0 \kappa / \left( c_p \rho \right) \right]$ is the Oboukhov buoyancy length scale.

For 5 m $s^{-1}$ wind speed and net surface cooling $Q_0$ = 100 $Wm^{-2}$, the Oboukhov length scale in the upper ocean is $L_O \sim$ -15 m. This means that the shear driven turbulent flow is confined within the upper approximately 1.5 m. In a 50 m deep mixed layer 97% of its depth will be driven by buoyant convection during nighttime.

For much of the year, most of the ocean experiences a cycle of daytime heating and night-time cooling which leads to a strong diurnal cycle in

convection and mixed layer depth. Such behavior is illustrated in *Figure 5-61*. At night, when there is cooling, the convective plumes generally reach the base of the mixed layer. During the day, convection is inhibited within the bulk of the mixed layer but may still occur near the surface, even if the mixed layer experiences a net heat gain. This is because the solar radiation is a volume source of heat (see Chapter 4).

Usually, the rate of turbulent kinetic energy production in the mixed layer is dominated by the convective term at night, but by the wind stress term during most of the day. Because the compensation depth (see Section 4.5.1 for definition) is generally quite small, turbulent kinetic energy generated by convection during daytime makes no contribution to turbulent entrainment at the bottom of the mixed layer, which lies much deeper.

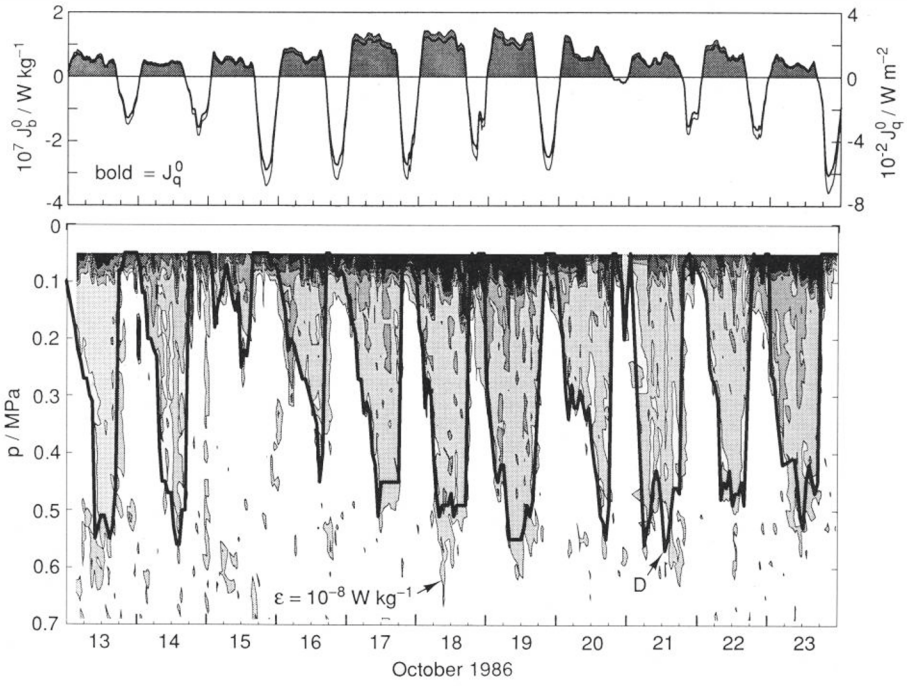


*Figure 5-61*. Diurnal cycles in the outer reaches of the California Current (34°N, 127°W). Each day the ocean lost heat and buoyancy starting several hours before sunset and continuing until a few hours after sunrise. These loses are shown by the shaded portions of the surface heat and buoyancy fluxes in the top panel. In response, the surface turbulent boundary layer slowly deepened (lower panel). The solid line marks the depth of the surface turbulent boundary layer, and the lightest shading shows $10^{-8}$ W kg$^{-1}$ < ε < $10^{-7}$ W kg$^{-1}$. The shading increases by decades, so that the darkest shade is ε > $10^{-5}$ W kg$^{-1}$. Note that 1 MPa in pressure $p$ corresponds to approximately 100 m in depth, $J_b^0 = -B_0$, and $J_q^0 = -(Q_0 + I_R)$, where $I_R$ is the solar radiation flux penetrating ocean surface. Reproduced from Lombardo and Gregg (1989) by permission of American Geophysical Union.

Stable stratification inhibits turbulent mixing below the relatively thin near-surface convection layer. Vertical mixing of momentum is confined to the shallow diurnal mixed layer, so that during the day, flow driven directly by the wind stress is confined to a similarly thin current known as the diurnal jet. In the evening, when convection is no longer confined by the solar radiation effect, convective thermals penetrate deeper into the mixed layer, increasing the turbulent mixing of momentum at the bottom of the diurnal jet. The diurnal jet then releases its kinetic energy during a relatively short time period. This process is so intense that the kinetic energy released cannot be dissipated locally. As a result, a Kelvin-Helmholtz type of instability is formed, which generates billows – another type of organized structure. The billows intensify the deepening of the diurnal mixed layer. The theoretical basis for this mechanism is described in Section 5.5.3.

Although the energy of convective elements is relatively small, it serves as a catalyst for the release of the kinetic energy by the mean flow. In most of the equatorial ocean, the Equatorial Undercurrent intensifies the shear in the upper ocean; the evening deepening of the diurnal jet is therefore sometimes so intense that it resembles a shock wave, which radiates very intense high frequency internal waves in the underlying thermocline.

The diurnal cycle is often omitted from numerical ocean models for reasons of computational cost. However, the mixed layer response to daily-averaged surface fluxes is not necessarily the same as the average response to the diurnal cycle (Shinoda et al., 1998; McCreary et al., 2001).Neglecting the diurnal cycle replaces periodic nightly convective pulses with chronic mixing that does not reach as deep.

Upper ocean convection is a mechanism effectively controlling the seasonal cycle in the ocean as well (Woods and Barkman, 1986b). Resolution of diurnal changes is usually uneconomical when the seasonal cycle is considered. Because of the nonlinear response of the upper ocean to atmospheric forcing, simply averaged heat fluxes cannot be used to estimate the contribution of convection on the seasonal scale. The sharp transition between the nocturnal period, when convection dominates mixing in the surface layer, and the daytime period, when the Sun severely limits the depth of convection leaving the wind stress to control mixing, may in fact simplify the design of models for the seasonal cycle of the upper ocean. Parameterization of the convection on the seasonal and global scale is therefore an important task for the prediction of climate and its changes.

Though free convection is probably one of the most studied types of organized motion, many intriguing questions regarding convection in the open ocean still remain. Some of them, like the role of penetrative convection in mixed layer dynamics, are of crucial importance for improvement of global ocean circulation modeling. Others, like the role of

surfactants in the surface renewal process, are of substantial interest for studying the air-sea exchange and global balance of *greenhouse gases* like $CO_2$.

## 5.9 Conclusions

Spatially coherent organized motions are an inherent part of the upper ocean turbulent boundary layer dynamics. These motions perform nonlocal transport of properties.

Observation of coherent structures in the open ocean is not a simple experimental task. Though several types of these structures have been observed in oceanic turbulence studies, most of our knowledge of this phenomenon in the ocean is either fragmentary or mainly based on the analogy between atmospheric and oceanic boundary layers, and on laboratory studies. A major problem of applying the knowledge acquired in the atmospheric boundary layer to its oceanic counterpart is in the huge difference between the air and water densities. In particular, the air-sea interface from the waterside behaves like a free surface (which, in particular, requires different surface boundary conditions.)

The elements of the theory for the coherent structures in the upper ocean do exist, but they often come from different areas of science and still require substantial efforts to apply them to the upper ocean situation. The theoretical models of organized structures are often detached from real observations, while the existing observations could validate theories only in a few successful cases. This is an indication that this area of physical oceanography requires special attention.

Chapter 6

# HIGH WIND SPEED REGIME

*Under high wind speed conditions breaking waves disrupt the air-sea interface producing a two-phase zone—air-bubbles in water and sea spray in air. This mixed-phase environment changes the dynamics and thermodynamics of air-sea interaction especially within tropical cyclones.*

Breaking waves intermittently disrupt the air-sea interface. With increasing wind speed, the sharp interface between the air and water disappears for longer intervals (*Figure 6-1*). Under extreme conditions of very high wind speeds, the concept of the air-sea interface becomes problematic: A two-phase environment with gradual transition from bubble-filled water to spray-filled air is formed.

The effects of bubbles and sea spray appear to be of crucial importance for air-sea exchanges in tropical cyclones. These effects can also be important for extratropical winter storms.

In Section 6.1 of this chapter, we consider air-bubbles in the near-surface layer of the ocean. Effects of the bubbles produced by breaking surface waves include the modification of upper ocean turbulence by a buoyant surface layer, their contribution to air-sea gas exchange, and to the acoustic and optical environments. Sea spray and marine aerosol generation is the subject of Section 6.2. Section 6.3 discusses the issues of modeling air-sea exchanges in high wind conditions. Section 6.4 intends to explain the recently discovered phenomenon of the limiting state of the aerodynamic roughness under hurricanes conditions.

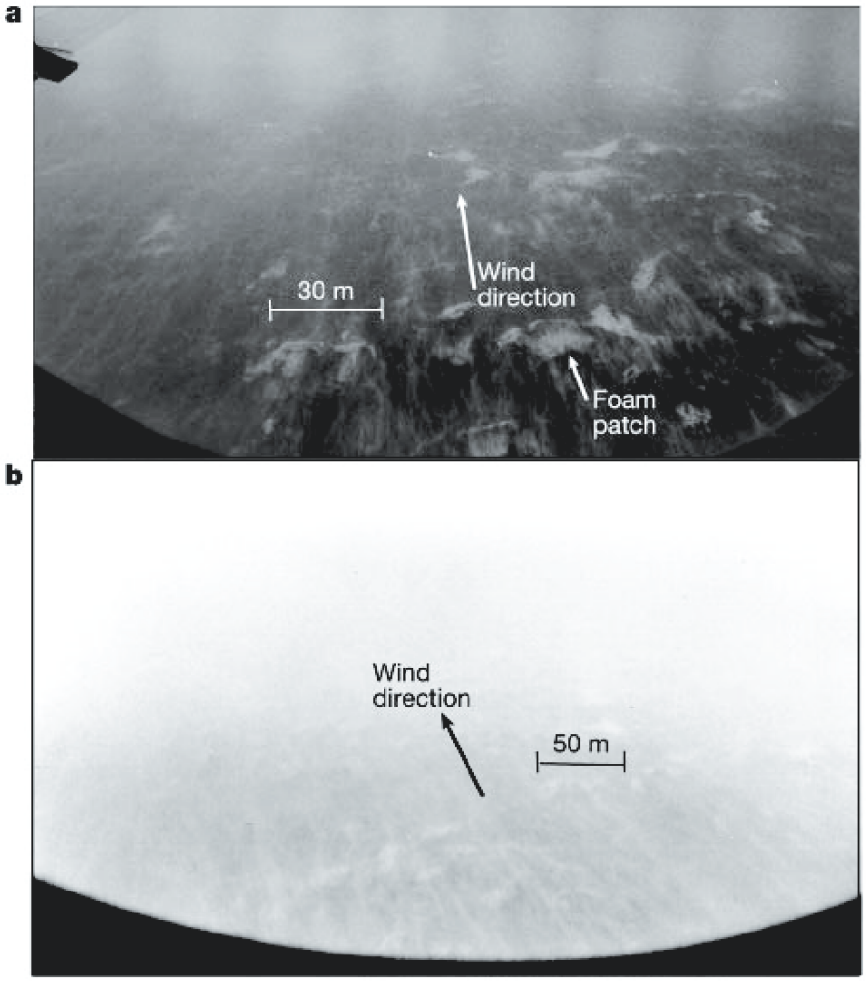


*Figure 6-1.* Sea state photographs taken from a research aircraft during a hurricane eye-wall penetration: (a) from 253 m altitude with flight level wind speed of 46 m $s^{-1}$; (b) from 450 m altitude with flight level wind speed of 55 m $s^{-1}$. Arrows show the wind direction, and scales suggest approximate sizes of the wave features. Reprinted from Powell et al. (2003) by permission from Macmillan Publishers Ltd: *Nature* 422, 279-283, © 2003.

## 6.1 Air Bubbles in the Near-Surface Turbulent Boundary Layer

### 6.1.1 Active and passive phases in bubble life

The high wind speed regime is associated with energetic wave breaking events. The fraction of the ocean surface covered with wave breakers increases approximately proportionally to the cube of the wind speed.

Breaking waves entrain air and create bubble plumes, which are highly transient and localized phenomena. Based on laboratory experiments of Leifer and De Leeuw (2001), the lifetime of wave-generated bubbles can be divided into four phases: 1) Formation; 2) Injection, 3) Rise, and 4) Senescence. The first phase is observed to occur during the first 0.1 s or less. During the second phase, the plume rapidly descends, initially at roughly a $30^o$ angle, then tilting towards the vertical. The second (injection) phase ends at the maximum penetration depth; it is followed by the third phase, when the mass of bubbles rises towards the surface. The Injection and rise phases last roughly the same time. Once the bubble creation process ceases, a newly formed bubble plume becomes acoustically quiescent and evolves under the influence of turbulent diffusion, advection, buoyant degassing and dissolution. This is the fourth, senescence, phase, which corresponds to typical bubble observations (that is the background distribution). During the senescence phase the plume consists of the smaller, mostly $r < 0.2$ mm bubbles.

Size-dependent bubble rise velocity mainly determines the residence time of larger bubbles, but the residence time of smaller bubbles may also be affected by the turbulent flow in the near-surface layer. Bubble plumes consisting of small bubbles can extend well into the mixed layer. As a result, the smaller bubbles act as tracers and map out the surface signatures of Langmuir cells (Farmer and Li, 1995), or the edges of current fronts and rips (Marmorino and Trump, 1996).

### 6.1.2 Bubble rise velocity

Bubble hydrodynamics depend on bubble size, temperature, and the presence of surfactants (Leifer et al., 2000a). Depending on size, the bubble form varies from spherical to spheroid for small bubbles ($r < 0.5$ mm) to ellipsoid for larger bubbles ($r > 0.5$ mm). The radius of transition between the spheroidal and ellipsoidal form depends on the temperature and on the presence of surfactants. Small bubbles are nearly perfect spheres because surface tension dominates over the drag stress that acts upon the rising bubble. The surface tension force, however, decreases inversely proportional to the bubble radius. At the same time, the drag force increases since larger bubbles rise faster and have larger effective cross sectional area. Bubbles with radius larger than approximately 0.7 mm (at $T = 20^oC$) can oscillate, in both path and shape, affecting the rise velocity. The trajectory oscillations (zig-zag or helical) are important for bubbles that just start oscillating and reduce their speed. For large bubbles ($r > 3.5$ mm) the shape or deformation oscillations are more important. The latter results in the reduction of the drag coefficient and thus an increase of rise speed.

The important factor in bubble hydrodynamics is the presence of surfactants, which can partially immobilize the surface, increasing drag and decreasing rise velocity. In the bubble radii range from approximately 0.25 mm to 10 mm, clean bubbles have different hydrodynamics from *dirty (i.e.*, surfactant covered) bubbles.

Thorpe (1982) proposed a formula for the buoyant rise speed of bubbles:

$$w_b(r) = \left(\frac{2r^2 g}{9\nu}\right)\left[\left(y^2 + 2y\right)^{1/2} - y\right], \tag{6.1}$$

where $y = 10.82\nu^2 / \left(gr^3\right)$. This equation is derived for dirty bubbles (small bubbles become covered with surfactants within a short time period).

Patro et al. (2001) proposed an analytical parameterization formula for clean non-oscillating bubbles:

$$w_b = \frac{c}{3} g r^d \nu^n, \tag{6.2}$$

where the coefficients *c*, *d*, and *n* for this equation are given in *Table 6-1*.

*Table 6-1*. Coefficients for equation (6.2) parameterizing the rise velocity for clean non-oscillating bubbles. (After Patro et al., 2001.)

| Re | $r$ (μm) | c | d | n |
|---|---|---|---|---|
| <1 | <60 | 0.666 | 2.0 | -1.00 |
| 1-150 | 60-500 | 0.139 | 1.372 | -0.64 |
| 150-420 | 550-660 | 11.713 | 2.851 | -0.64 |
| 420-470 | 660-700 | 0.156 | 1.263 | -0.64 |
| 470-540 | 700-850 | 0.021 | 0.511 | -0.64 |

For clean oscillating bubbles Patro et al. (2001) developed the following analytic parameterization:

$$w_b = \left[w_{bm} + H_1\left(r - r_c\right)^{m_1}\right]\exp\left[K_1\left(r - r_c\right)^{m_2 T}\right], \tag{6.3}$$

where the coefficients *H*, *K*, $m_1$, and $m_2$ and the critical radius $r_C$ (below which the parameterization suggests bubbles do not oscillate for any temperature *T*), the minimum velocity $w_{bm}$ for oscillating bubbles is given in *Table 6-2*. Parameterization (6.3) is applicable for oscillating bubbles for $0^0\text{C} < T < 30^0\text{C}$ and $r_p < r < 4$ mm. The radius $r$ for the onset of oscillation varies with temperature *T* according to the parameterization relationship,

$$r_p = 1086 - 16.05\,T_p \qquad (6.4),$$

where $r_p$ and $T_p$ are the peak radius and temperature.

*Table 6-2*. Coefficients for equation (6.3) parameterizing clean oscillating bubbles. (After Patro et al., 2001.)

| $H_1$ | $K_1$ | $r_C$ | $w_{bm}$ | $m_1$ | $m_2$ |
|---|---|---|---|---|---|
| $-4.792 \times 10^{-4}$ | 0.733 | 0.0584 | 22.16 | -0.849 | -0.815 |

A comparison of observed bubble rise velocities in clean and natural waters is shown in *Figure 6-2*, together with the parameterizations for clean and dirty bubbles (Clift et al., 1978). The parameterization for clean bubbles demonstrates a monotonic increase of $w_b$ with radius $r$ until the onset of oscillation, after which $w_b$ decreases to some level and then starts increasing again. In contrast, the parameterization for dirty bubbles shows a monotonic increase with $r$.

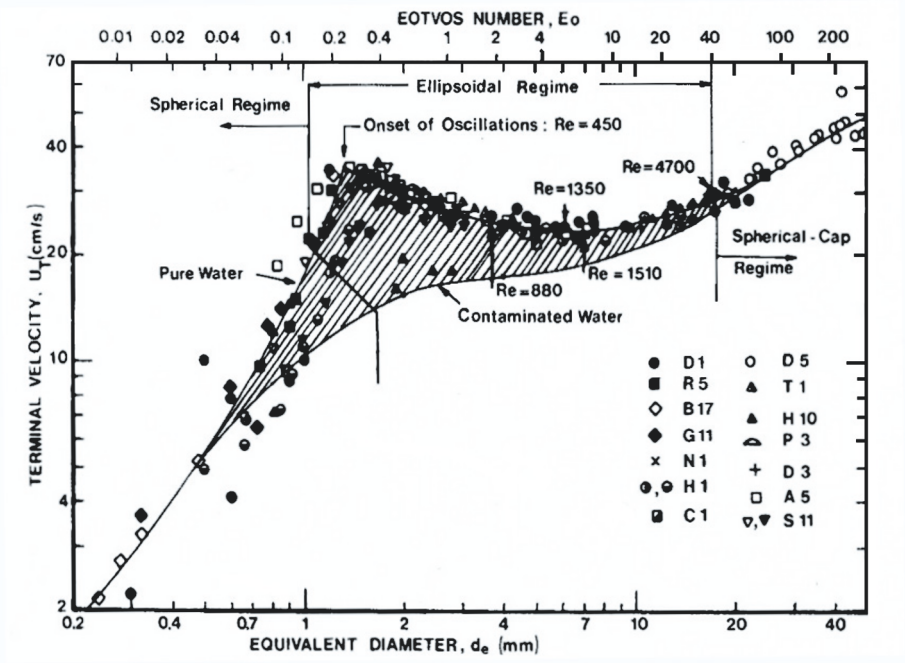


*Figure 6-2*. The bubble rise velocity for hydrodynamically clean and dirty bubbles as a function of the bubble size. (After Clift et al., 1978.) Reprinted from *Bubbles Drops and Particles*, Academic Press. © 1977.

The observational data given by Clift et al. (1978) suggest that the rise velocity for seawater bubbles with radii larger than approximately 0.6 mm is close to that of hydrodynamically clean bubbles. An explanation is that larger bubbles rise quickly to the surface and thus do not have sufficient time to collect surfactants (Keeling, 1993; Woolf, 1993). Small bubbles (less than approximately 0.3 mm radius) are assumed to perform as hydrodynamically dirty bubbles (Woolf and Thorpe, 1991). Their surface becomes covered with surfactants almost instantaneously.

Patro et al. (2001) proposed to treat small bubbles in seawater as dirty and large bubbles as clean with a transition at circa 0.6 mm. The transition radius somewhat increases with the increase of the time period the bubbles are in the water column. The assumption about clean and dirty bubbles is however, somewhat uncertain. Adding to the uncertainty is the collective behavior of bubbles in bubble clouds.

### 6.1.3 Bubble size distribution function

The bubble-mediated component of the air-sea gas exchange, production of spray droplets and aerosols, optical properties of the sea surface, generation of ambient noise and sound transmission within the oceans, and scavenging of biological surfactants also essentially depend on the size distribution of bubbles. The size distribution of entrained bubbles is also an important factor in controlling turbulence and dynamics in wave breakers. In addition, bubbles of different sizes behave differently in the turbulent surface layer. Bubble size distribution data potentially lead to a dynamical description of air-sea interaction based on near surface turbulence, advection, and other properties.

Different approaches for measuring bubble size spectra, from acoustical to optical, have been developed. Each technique has advantages and disadvantages and is effective over different size ranges and bubble density regimes (Leifer et al., 2003). Acoustic methods have played a definite role in observing bubble size distributions because bubbles have a high resonance quality factor leading to an acoustical cross-section some three orders of magnitude greater than their geometrical cross-section (Farmer et al, 1998). This effect reaches a maximum, usually at a frequency of 30 kHz, which corresponds to a bubble radius of 100 μm. Different frequencies excite bubbles of different radii, which allow an estimate of the bubble size distribution from acoustic measurements. However, acoustic methods have difficulties with large bubbles ($r$ > 0.5-0.7 mm), which are non-spherical in turbulent flow, and at high bubble concentrations. Laser techniques are noninvasive but, in common with acoustic methods, have problems when multiple bubbles enter the beam (high bubble density) and with large

bubbles ($r$ > 1 mm), whose mean shape is elliptical and is subject to oscillations. The optical methods based on the analysis of video or photo images are able to measure at high bubble concentrations and over a wide range of bubble sizes. The optical methods are, however, invasive in general and may disturb the measurement area.

The initial bubble formation, breakup, coalescence, dissolution, vertical motion caused by buoyancy forces, and turbulent mixing are the processes that determine the bubble size distribution in the ocean. Air is initially entrained into relatively large bubbles as a wave breaks. These bubbles rapidly break into smaller bubbles. During this active phase the bubble fragmentation process determines the bubble size distribution. Breaking waves directly inject air into the wave-stirred layer (see Benilov's classification of the upper ocean turbulence given in *Figure 3.1*). As soon as the wave breaker spends its energy, the air entrainment ceases and the bubble creation process stops. The bubble size distribution then evolves rapidly because larger bubbles leave the area and surface more quickly than smaller ones.

The bubbles with radius $r$ >0.7 mm have rise velocities of the order of 0.2 m $s^{-1}$ - 0.4 m $s^{-1}$ (*Figure 6-2*); after the end of the wave breaking process the remaining turbulence has little effect on their dynamics. The large bubbles immediately return to the surface, rarely penetrating below the wave-stirred layer. Note that the wave-stirred layer depth is typically less than one significant wave height (see Chapter 3, *Figure 3.20*). Smaller bubbles ($r$ ~ 0.1 mm) have rise velocities of the order of 0.01 m $s^{-1}$. The background turbulence as well as organized structures can transport these small bubbles to greater depths (see Chapter 5).

The bubble size spectra can be separated into the regions within the wave-stirred layer and below the wave-stirred layer. The spectra within the wave-stirred layer can additionally be separated into those taken during wave-breaking events and those in between wave-breaking events.

*Figure 6-3* shows averaged bubble spectra measured at 0.6 m depth including and excluding wave-breaking events. These observations are presumably in the wave-stirred layer. The density of bubbles, especially of large bubbles, is significantly higher during wave-breaking events. In this example, the slope of the spectrum for large bubbles changes in logarithmic coordinates from approximately -2.9 during wave-breaking events to approximately -4.3 between the wave breaking events.

Two mechanisms for large bubble fragmentation are possible in the wave breaker: 1) Turbulent fragmentation represented by the turbulent kinetic energy dissipation rate $\varepsilon$; 2) Rising-bubble fragmentation, characterized by the rising velocity $w_b$ and the collective behavior of rising bubbles.

From dimensional considerations Garrett et al. (2000) derived a bubble size spectrum for the turbulent fragmentation mechanism

$$N(r) \propto Q\varepsilon^{-1/3} r^{-10/3}, \tag{6.5}$$

where $N(r)$ is the number of bubbles per $m^3$ per mm radius increment (bubble density), $Q$ is the volume of air entrained per volume of water per second (with dimension $s^{-1}$), and $r$ is the bubble radius. The turbulent fragmentation mechanism is important during wave-breaking events. Theoretical spectrum (6.5) is compared in *Figure 6-3* with the field data of Bowyer (2001). For bubbles larger than approximately 1 mm, the slope of the theoretical spectrum is in fact consistent with the experimental spectrum averaged over wave-breaking events.

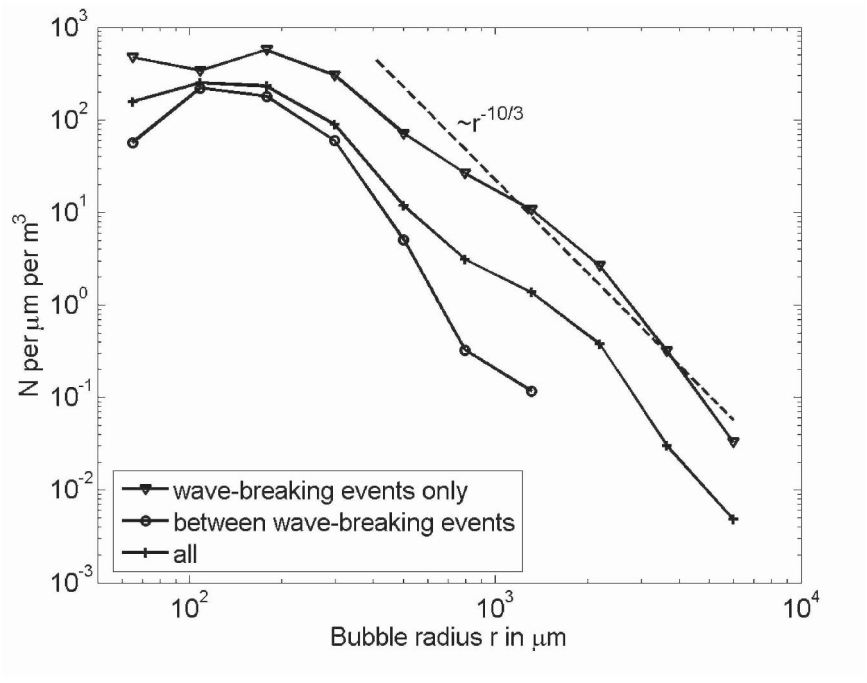


*Figure 6-3*. Bubble size distributions at 0.6 m depth excluding and including wave breaking events (Bowyer, 2001). These measurements are taken at 11-13 m $s^{-1}$ wind speed, 2.5 m wave height, and 15-120 km fetch.

Spectrum (6.5) is based on the concept of turbulent fragmentation formulated by Kolmogorov (1949) and Hinze (1955). They pointed out that at high Reynolds number a droplet of any different fluid or a gas bubble is likely to break up under the influence of differential pressure forces on its surface if these forces exceed the restoring forces of surface tension.

Turbulent fragmentation thus depends on the ratio of these forces, which is characterized by the Weber number,

$$We = \left(\rho / \sigma_s\right) u^2 d \,, \tag{6.6}$$

where $\rho$ is the water density, $\sigma_s$ is the surface tension, $u$ is the turbulent velocity fluctuation on the length scale of the bubble, and $d$ is the bubble diameter. Within the Kolmogorov inertial sub-range, the fluctuation velocity relates to the dissipation rate of the turbulent kinetic energy as,

$$u \sim \left(\varepsilon d\right)^{2/3} . \tag{6.7}$$

Turbulent bubble fragmentation is expected when the Weber number exceeds its critical value, $We_{cr}$. This condition corresponds to inequality $d > a_H$, where

$$a_H = We_{cr}^{\,3/5} \left(\sigma_s / \rho\right)^{3/5} \varepsilon^{-3/5} \tag{6.8}$$

is the *Hinze scale*, which is typically of the order of 1 mm. Hinze (1955) estimated the critical value of the Weber number as 0.2. More recent experiments by Lewis and Davidson (1982), Martinez-Bazan et al. (1999), and Deane and Stokes (2002) suggest that $We_{cr}$ lies in the range from 3 to 4.7.

Bubbles smaller than the Hinze scale are stabilized by surface tension, and the process of turbulent fragmentation is believed to be less important for these small bubbles.

Garrett et al. (2000) pointed out a major caveat for the turbulent fragmentation theory. Though the considerations leading to (6.5) are similar to those leading to Kolmogorov's inertial subrange in the energy spectrum of isotropic turbulence, there is one significant difference. In the Kolmogorov cascade the energy ultimately cascades into eddies at the Kolmogorov scale $\eta_T = \left(\nu^3 / \varepsilon\right)^{1/4}$ or less, and then dissipates into heat due to viscosity. In the case of bubbles, the input air fragments into smaller and smaller bubbles until surface tension halts the cascade at the Hinze scale. Air would thus tend to accumulate in a large spectral peak at the Hinze scale that would only slowly disappear since bubble dissolution is a relatively slow process. At the time of the Garrett (2000) publication such a peak was not observed in either field or laboratory experiments. However, the most novel laboratory results of Leifer et al. (2003) suggest that bubble plumes can be bimodal (*Figure*

*6-4*). This additional peak can perhaps be interpreted as a spectral accumulation near the Hinze scale.

Previously published distributions (Farmer et al., 1998; Bowyer, 2001 and others) were unimodal. These averaged together many plumes of diverse types along with the background, thereby eliminating the multiple peaks. Leifer et al. (2003) developed a plume-type classification scheme. When analyzed separately, populations of different plume types (measured in a wind-wave tank) appeared to be multimodal (*Figure 6-4*).

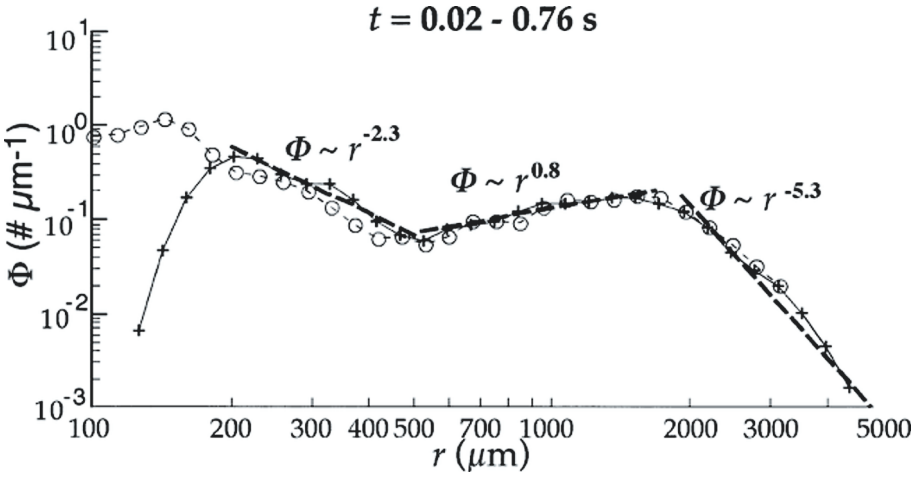


*Figure 6-4.* Bubble population distribution in the major bubble plume averaged over tine period from 0.02 to 0.76 s. These are optical measurements with wide (+) and narrow (o) field-of-view cameras. Reproduced from Leifer et al. (2003) by permission from American Meteorological Society.

Spectrum (6.5) is based on the assumption that the total air fraction is not large enough to have a feedback effect on the fragmentation process. At first glance, this assumption seems to be supported by the Deane and Stokes (2002) laboratory observation that "...the measured [bubble] separation velocity was always a factor of 5 or greater than the expected rise velocity of the bubble products, and the buoyancy effects were therefore assumed to be an unimportant source of bias." However, the Deane and Stokes experiment studied plunging breakers, which are not typical for open ocean conditions. In addition, the collective behavior of bubbles can result in significant fluctuations of the rising velocity of individual bubbles (Göz et al., 2001). (Remember that the velocity fluctuations are mainly responsible for bubble fragmentation.) The second mechanism, the rising-bubble fragmentation due to buoyancy forces, cannot therefore be completely discounted on the basis of the Deane and Stokes (2002) observation.

The spilling wave breaker resembles a turbulent bore (Section 1.6.4), which is an organized structure characterized by the regime of marginal stability in which the buoyancy and inertial forces are balanced in such a way that the Richardson number is close to its critical value (Turner, 1973). The rising-bubble fragmentation mechanism is not a Kolmogorov cascade. The Kolmogorov cascade is replaced here with the concept of marginal stability in the bore-like wave breaker.

If we assume that the mechanism of bubble fragmentation due to buoyancy forces dominates in spilling breakers and identify $w_b$ as the determining parameter (replacing dissipation rate $\varepsilon$), then standard dimensional analysis leads to the following size spectrum:

$$N(r) \propto Q w_b^{-1} r^{-3}. \tag{6.9}$$

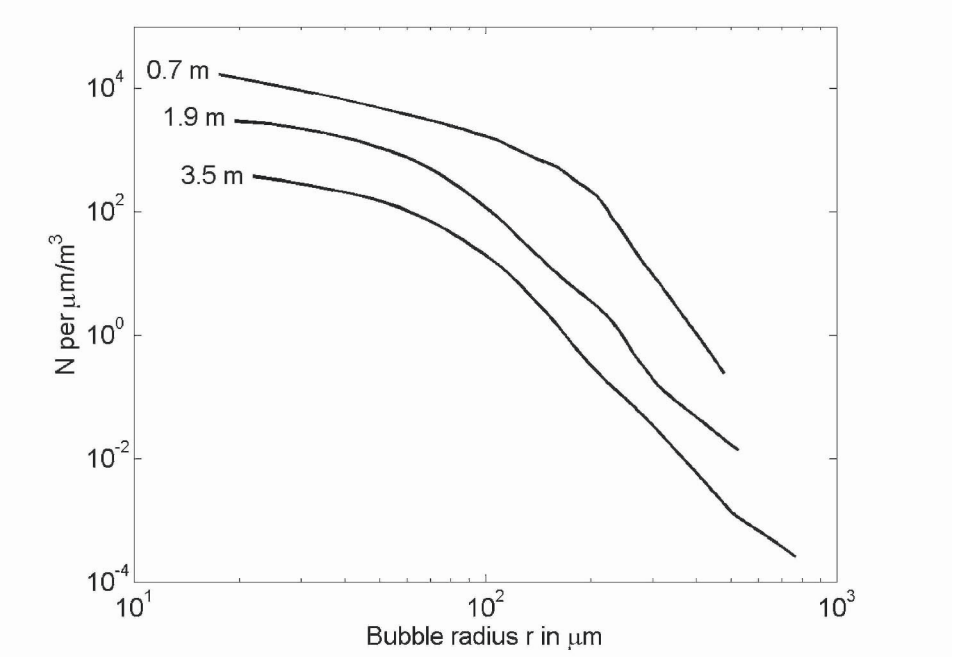


*Figure 6-5*. The average bubble size spectrum at three depths below the surface, obtained at a wind speed of 11.9 m s$^{-1}$ (Garrett et al., 2000).

An assumption that for large bubbles the rise velocity is approximately constant results in the –3 power law, which is close to the –10/3 power law in (6.5). Since bubble rise velocity $w_b$ depends on the bubble radius $r$ (*Figure 6-2*) the power-law scaling in (6.9) can be different for different parts of the

spectrum. Spectrum (6.9) should be used with parameterization formulas (6.2) and (6.3).

Remarkably, equation (6.9) does not contain $\varepsilon$ as a determining parameter. (From Chapter 3 the reader knows how difficult would be to measure the dissipation rate in a breaking wave.)

*Figure 6-5* shows bubble size distributions acquired in the Gulf of Mexico by Farmer et al. (1998) at depths 0.7 m, 1.9 m, and 3.5 m. The bubble density decreases with depth. The most significant drop of the bubble population is observed between 0.7 m and 1.9 m depths for large bubbles ($r$ > 200 μm). A plausible explanation is that the 0.7 m depth is within the wave-stirred layer, while the observations at 1.9 m depth are outside this layer.

The spectra shown in *Figure 6-5* are averages over a sufficiently large time period (30 minutes). Since this time period included different types of wave-breaking events, bimodal spectral structures (like those shown in *Figure 6-4*) could not be revealed.

### 6.1.4 Bubble dispersion and diffusion

A bubble plume injected in the near-surface layer of the ocean during a wave-breaking event is subject to dispersion and turbulent diffusion. Larger bubbles rise to the surface within a few seconds, forming the whitecaps. Wave breaking also leaves numerous smaller bubbles that can persist for minutes.

Garrettson (1973) derived an equation governing the size distribution $N$ of a cloud of bubbles at depth $z$. Thorpe (1982) simplified this equation by considering the cloud composed of small bubbles of a single gas (for instance, nitrogen) and of almost equal size. Ignoring acceleration and volume source terms (but retaining the dissolution term), and assuming horizontal isotropy transport equation (1.12) in application to bubbles respectively takes the following form:

$$\frac{\partial C}{\partial t} = \frac{d}{dz}\left( K_B \frac{dC}{dz} \right) - w_b \frac{dC}{dz} - \sigma_* C \,, \tag{6.10}$$

where $C$ is the volume concentration of bubbles, $w_b$ is the bubble rise speed, and $K_B$ is the turbulent diffusion coefficient for bubbles.

The terms on the right side of equation (6.10) represent the downward turbulent diffusion of bubbles from the surface wave-breaking zone, the vertical rise of bubbles towards the surface, and the dissolution and decay of bubbles. In the Thorpe (1982) model an additional assumption was that the total number of bubbles decreases at the same rate as the radius decreases.

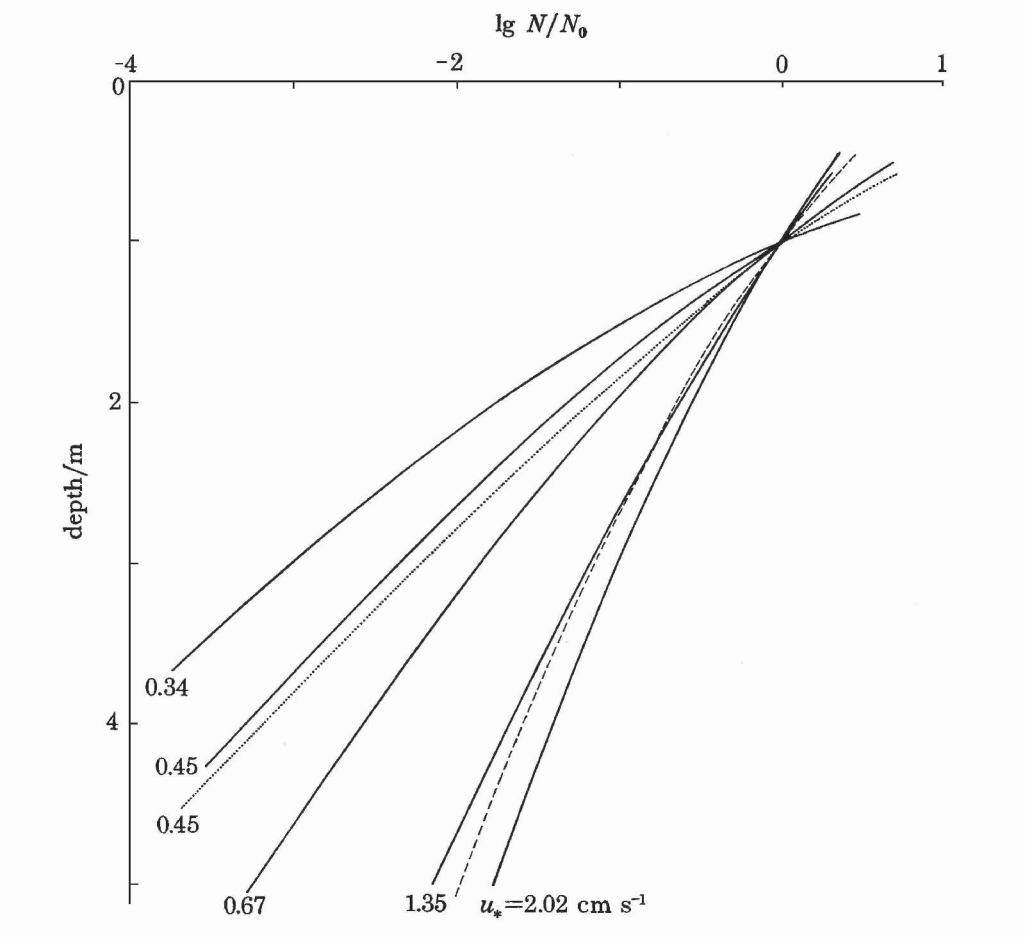


*Figure 6-6.* Logarithm of the normalized number of bubbles against depth from (6.13) at various values of $u_*$ with parameters chosen to correspond to $a_0$ = 50 mm. Reproduced from Thorpe (1982) with the permission of the Royal Society of London.

With a simplified parameterization for the turbulent mixing coefficient

$$K_B = \kappa u_* |z| \tag{6.11}$$

and the bubble decay rate

$$\sigma_* = \alpha z / \left(1 + |z| / H_0\right) \tag{6.12}$$

(here $H_0 = p_0 / g\rho \approx 10$ m, and $p_0$ is the atmospheric pressure), Thorpe (1982) obtained the following solution of (6.10):

$$N / N_0 = \left(\mu |z|\right)^{-\lambda/2} H_{\lambda/2}\left(\mu |z|^{1/2}\right) \tag{6.13}$$

where $H_{\lambda/2}$ is the modified Bessel function chosen so that $N \to 0$ as $z \to -\infty$, $\lambda = w_b / (\kappa u_*)$, $\mu = \left(\alpha / (\kappa u_*)\right)^{1/2}$, and $N_0$ is a constant.

The solutions for bubbles with radius $a_0 = 50$ μm, $w_b = 0.54 \times 10^{-2}$ m s$^{-1}$, and $\alpha \approx 4 \times 10^{-3}$ s$^{-1}$ m$^{-1}$ are plotted in *Figure 6-6* for different values of the friction velocity. They are qualitatively consistent with the observations of Johnson and Cooke (1979). The assumptions about the mixing coefficient and choice of other parameter values are, however, tenuous.

Since wave-breaking turbulence is not included in the mixing parameterization, there is a singularity of the air-bubble flux at $z = 0$. In order to preserve the flux $K_{tb} \partial N / \partial z$, the value $\partial N / \partial z \to \infty$ was avoided by selecting $z_0 = 0.5$ m, $z_{max} = 10$ m. This selection of initial depth away from the ocean surface also avoids discussion of the near-surface breaking wave zone where the assumed form of $K_B$ is not valid.

In addition to dispersion and turbulent diffusion, small bubbles are drawn into the convergence zones produced by spatially coherent organized motions in the near-surface layer of the ocean (Chapter 5).

### 6.1.5 Buoyancy effects in bubble plumes

The process of surface wave breaking and air entrainment have considerable dynamical coupling. A substantial part of the fluctuation energy during wave breaking may go to the work against buoyancy forces (Woolf, 1997). Buoyancy effects due to bubbles are believed to dominate the dynamics of the spilling breaker.

Buoyancy effects in a two-phase environment have yet to be included in theoretical models of turbulence in the near-surface layer of the ocean. These effects can sometimes be understood from the classic budget equation for TKE, similar to that in the theory for the flow with suspended particles developed by Barenblatt and Golitsyn (1974) for modeling dust storms. This theory predicts reduction of the turbulent drag coefficient in the suspension flow (see Section 6.3.2). Application of the Barenblatt and Golitsyn theory to the air-bubble plumes produced by breaking waves, however, is not straightforward. In particular, the Kolmogorov number criteria (which is an analog of the Richardson number for suspension flows) cannot be applied directly to the bubble infested upper ocean because the near-surface turbulence is mainly produced by breaking waves rather than by shear (as in dust storms). The discussion in this section is therefore mainly qualitative rather than quantitative.

*Table 6-3*. Average fraction of air at different depths for the conditions of developed seas. The measurements are taken from wave-following buoys.

| Source | Depth (m) | Fraction of air due to bubbles (%) | Wind speed (m $s^{-1}$) | Wave height (m) | Fetch |
|---|---|---|---|---|---|
| Bowyer (2001) | 0.1 | 0.016 | 10-12 | 2 | Unlimited |
| Bowyer (2001) | 0.6 | 0.0054 | 11-13 | 2.5 | 15-120 km |
| Garrett et al. (2000) | 0.7 | 0.0060 | 12 | | >100 km |
| Garrett et al. (2000) | 1.9 | 0.00030 | 12 | | >100 km |
| Garrett et al. (2000) | 3.5 | 0.000044 | 12 | | >100 km |

The average volume fraction of air due to bubbles from the measurements of Farmer et al. (1998) (cited in Garrett et al., 2000) and of Bowyer (2001) is given in *Table 6-3* as a function of depth. In its contribution to the buoyancy, the maximum air fraction of 0.016% observed at 0.1 m depth is equivalent approximately to a 0.5°C change in water temperature. The average air fraction rapidly drops with depth (*Table 6-3*).

At this point it is impossible to say definitely how important the bubble buoyancy contribution is for the balance of the turbulent kinetic energy in the near-surface layer of the ocean. The relatively high concentration of bubbles that is required for buoyancy effects to be important is primarily observed in breakers. During an active phase the bubble plume may contain a volume fraction of air that is much greater than the average (over many wave periods) value. For comparison, the observations of Bowyer (2001) (the first row in *Table 6-3*) when averaged over wave breaking events only gives the volume air fraction of as much as 0.12%, which is equivalent to a 3.75°C change in water temperature.

Under moderate wind speeds wave breaking events last only about 1 s; the white cap area associated with the wave breaker occupies a relatively small fraction of the sea surface. The whitecap coverage increases rapidly with wind speed. According to Monahan and O'Muircheartaigh (1980), the fractional coverage of the stage B whitecaps, which are the surface expression of decaying bubble plumes, is a strong function of wind speed:

$$W_c \approx 3.84 \times 10^{-4} U_{10}^{3.41}, \tag{6.14}$$

where $U_{10}$ is the wind speed at 10 m height. Bortkovskii (1983) found that the whitecap coverage varies with temperature (though he offered no parameterization for its temperature dependence).

Equation (6.14) predicts that $W_c = 1$ at $U_{10} = 38.7$ m s$^{-1}$. Extrapolation of (6.14) to such high wind speed of course does not make sense. Nevertheless, sea state photographs taken during a hurricane (*Figure 6-1*) show that at very high wind speeds, the sea surface in fact becomes completely covered with whitecaps. This suggests that a significant part of the energy transferred from the atmosphere to the ocean in hurricanes may go to air entrainment in breaking waves.

Sufficiently large rising bubbles by themselves induce turbulence in the near-surface layer of the ocean. Bubbles with radius exceeding approximately 1 mm shed unsteady vortices; the bubble trajectory also becomes unstable, changing from rectilinear to zig-zagging (Lima-Ochoterena and Zenit, 2003). Which leads to collective behavior. Generally, the bubble-induced water turbulence and the rise velocity of bubble swarms are different from those of single bubbles, due to bubble interactions (Göz et al., 2001). Also, the rising bubbles interact with the sea surface microlayer, influencing its structure and dynamics. So far neither the bubble buoyancy contribution to near-surface turbulence nor the bubble-induced turbulence has been investigated thoroughly.

## 6.2 Sea Spray and Marine Aerosol Production

### 6.2.1 Introduction

The ocean surface layer is a source of *sea spray* and *marine aerosols*. According to estimates given in Monin and Krasitskii (1985), about 0.3% of the World Ocean surface is covered with breaking waves, and the total salt flux into the atmosphere is about $10^{12}$ kg per year.

The sea spray is an important factor in the air-sea transfer of heat, moisture, and momentum under high wind speed conditions. The primary marine aerosol is composed of seawater enriched with chemical compounds as well as with bacteria and viruses. Both natural (biogenic) and anthropogenic sources, dissolved in the near-surface layer of the ocean or as a thin film on the ocean surface, contribute to the content of marine aerosols. Large spray drops return to the ocean before evaporating. Smaller drops are entrained into the turbulent flow in the marine boundary layer and, under favorable conditions, completely evaporate producing sea salt aerosol particles, which are effective cloud condensation nuclei. Influencing the lifetime and albedo of clouds, sea salt aerosols can influence climate.

Sea salt particles are an important part of the atmospheric sulfur cycle (Chamides and Stelson, 1992). According to O'Dowd et al. (1999), natural and anthropogenic sulfate aerosols influence the climate. The Intergovernmental Panel on Climate Change (2001) estimated the direct and indirect radiative forcing of sulfate aerosols to be in the range -0.2 to -0.8 W $m^{-2}$ and 0 to -1.5 W $m^{-2}$, respectively. This is comparable in magnitude to the radiative forcing of anthropogenic greenhouse gases. It is important that sulfate aerosols produce a radiative effect that is opposite in sign to that of anthropogenic greenhouse gases.

In addition to affecting climate, marine spray and aerosols transfer pollutants from the ocean to the atmosphere, serve as a tracer in the climate record of Arctic and Antarctic snow and ice cores, play a role for corrosion, and cause vegetation stress in coastal regions. The optical properties of the marine boundary layer depend substantially on the type and concentration of aerosols.

Note here that some studies cited below, like that of Andreas (1998), use the diameter of wet particles (*i.e.*, of droplets), while others like that of Mårtensson et al. (2003) use the diameters of dry particles. This can be attributed to different applications of marine aerosol results. Air-sea interaction scientists are interested in the influence of marine aerosols on the air-sea fluxes, while climatologists are mostly concerned with the presence of dry aerosol particles in the atmosphere. Respectively, different definitions for the sea spray and aerosol generation functions can be found in the literature. In particular, Mårtensson et al. (2003) uses the marine aerosol generation function defined via the dry diameter of aerosol particle; while, Monahans's sea spray generation function operates with the radius of a droplet at its formation $r_0$.

### 6.2.2 Mechanisms of sea spray production

There are basically three varieties of spray droplets: film droplets, jet droplets, and spume droplets. First consider film and jet droplets.

Bursting air-bubbles create film and jet droplets. Bubbles are primarily generated through entrainment by breaking waves (Thorpe, 1986). After being carried to some depth by a plunging wave jet, a bubble then rises to the surface where it bursts. The process of bursting is schematically illustrated in *Figure 6-7*. As the bubble emerges from the water, a thin film forms at the upper surface of the bubble; the film thins by drainage and eventually ruptures. When the bubble film opens, the rim of the receding film cap ejects tens to hundreds of film droplets with radii ranging roughly from 0.5 to 5 μm (Spiel, 1998). The collapsing bubble cavity shoots up a jet of water from its bottom. Due to velocity differences along this jet, it soon

breaks up into a few jet droplets with radii typically ranging from 3 to 50 μm, depending on the size of the bubble that created them.

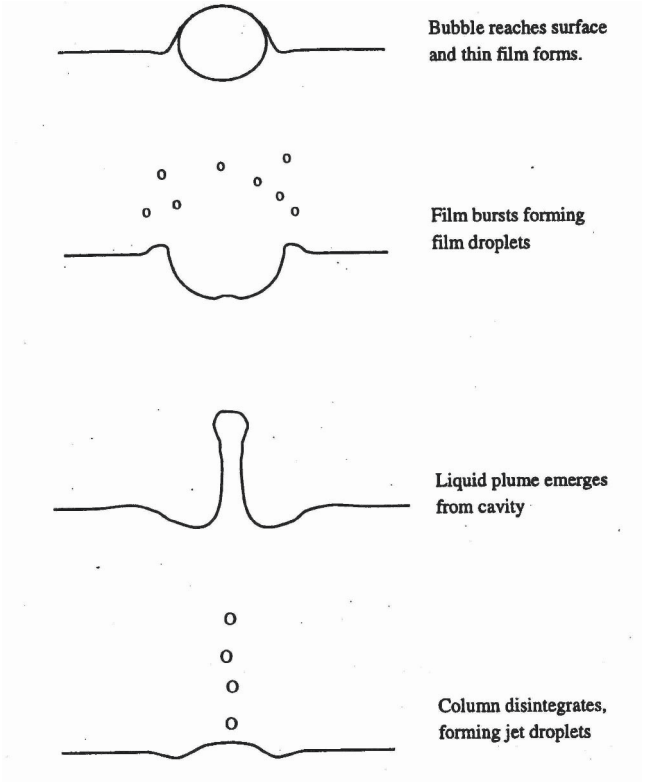


*Figure 6-7.* Creation of droplets by bursting bubble at water surface. Reproduced from Pattison and Belcher (1999) by permission from American Geophysical Union.

The number and size distribution of film and jet drops is connected to the bubble size distribution. Small bubbles produce only jet drops. The size of the jet drops is about 1/10 of the parent bubble diameter size; the bursting bubble produces a maximum of six jet droplets; bubbles larger than 3.4 mm produce no jet drops (Spiel, 1997). Jet drops hence dominate in the super-micrometer aerosol range.

Laboratory experiments suggest that most of the particles generated in whitecap areas are sub-micrometer size (Cipriano et al., 1987; Resch and Afeti, 1992). Spiel (1998) proposed that the film of bubbles with diameter < 3 mm has a tendency to roll up instead of disintegrating; the rim of the bubble attains an irregular structure with mass density fluctuations. The areas with larger mass obtain a higher momentum and can be ejected. The ejected parcels attain a large horizontal velocity component. The film disintegration, however, is not the main component of this process; the particles are

presumably formed by splashing or via formation of secondary bubbles of smaller size that collapse and eject jet drops. According to Leifer et al. (2000b), in addition to bubble formation through air entrainment by breaking waves, bursting of initial bubbles can form secondary bubbles. Bubble-burst bubble production is dispersed and primarily produces bubbles of less than 250 μm radius. Video or microwave images of whitecaps may not easily detect these secondary bubbles.

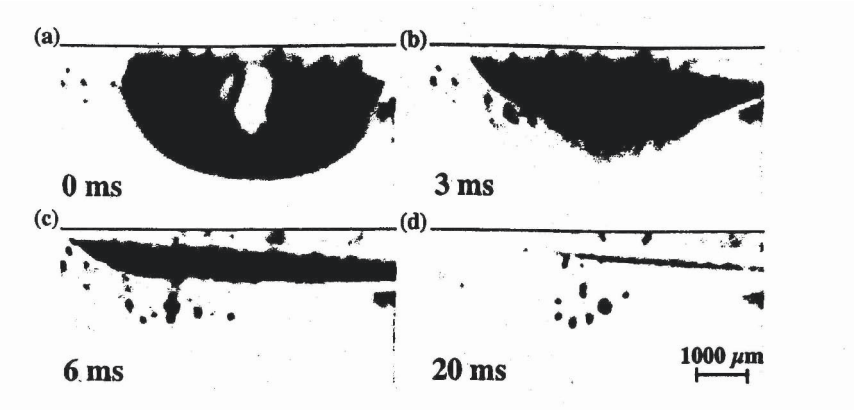


*Figure 6-8*. Time sequence of images illustrating the bubble-burst bubble production mechanism. Reproduced from Leifer et al. (2000) by permission from American Geophysical Union.

Leifer et al. (2000b) conducted a series of laboratory experiments to examine bubble-burst bubble production and to measure the resulting bubble size distribution. *Figure 6-8* shows a series of images taken with a high-speed video camera during these experiments. A bubble with an approximately 2.5 mm equivalent spherical radius bursts at the surface and produces a cloud of smaller bubbles. Several small bubbles in the upper left corner of *Figure 6-8*a-c (floating on the surface) are from a previous burst bubble event.

The bubble burst indicated by a slight deformation in the bubble subsurface interface supposedly began about 1 ms before the image shown in *Figure 6-8*a was taken. After 3 ms (*Figure 6-8*b) small bubbles are injected from the bubble's left edge. At 6 ms (*Figure 6-8*c), several bubbles initially obscured behind the bubble become visible. Leifer et al. (2000b) reported that the larger of these burst-produced bubbles did not penetrate deeper than perhaps half a centimeter, while smaller bubbles did.

The secondary bubbles produced by the burst mechanism may result in dramatically increased concentrations of small bubbles in the near-surface layer of the ocean, which are difficult to detect from conventional measurements that are typically made at a depth exceeding the wave height

and then extrapolated to the surface. Due to the burst mechanism in the vicinity of whitecaps a shallow layer may exist where the small bubble concentration is significantly greater than elsewhere (Leifer et al., 2000b).

In addition to the effects on marine aerosol generation, the near-surface layer populated by small bubbles may affect gas transfer. Very small bubbles dissolve rapidly due to Laplace pressure; the water adjacent to the whitecap can be supersaturated with atmospheric gases, thus contributing to the supersaturation term, $\Delta_e$, in the Woolf and Thorpe (1991) bulk-flux formula for air-sea gas exchange (7.22).

Bubbles produced by the bubble-burst mechanism may also influence the surface microlayers and their chemistry and microbiology (Blanchard, 1988). Rising bubbles accumulate surfactants and bacteria and transport them to the surface. The bubble-burst bubbles thus represent a source of materials to the surface microlayer, which modifies the balance between diffusion to the interface due to turbulence and loss due to processes such as aerosol generation, photochemistry, and surface disruption. The enhanced oxygenation near the interface from dissolving micro-bubbles can modify the microbiological environment of the sea surface microlayer

Detection of the secondary bubbles from measurements of whitecap coverage is difficult since bubble bursting is dispersed horizontally, and the production is localized very close to the ocean surface (*e.g.*, shallower than a significant wave height) where bubble measurements are extremely complicated. The secondary bubbles have a short lifetime if they are not transported away from the surface by turbulence or other fluid motions. The turbulence generated by a surfacing bubble plume may also diffuse these burst-bubbles deeper into the water column.

In addition to film and jet droplets, spume drops are produced by direct tearing of water from wave crests at wind speeds higher than about 9 m $s^{-1}$. (Monahan et al., 1983). The spume drops are the largest spray droplets; minimum radii are generally about 20 μm and there is no definite maximum radius. Spume generation is associated with eliminating the clearly defined air-sea interface under high wind speed conditions. Koga (1981) has shown from observations in a wind-wave tank that near the crest of the wave, where the wind stress is generally highest, small projections develop, which then break up to form droplets. The maximum diameter of these droplets was about 3 mm in diameter. The projections were supposedly developing due to Kelvin-Helmholtz instability.

Droplets with radii in the range 10–500 μm contribute most to the heat fluxes at high wind speeds (Andreas, 1992). This size range is dominated by spume droplets, implying that spume generation is the most important mechanism of droplet generation for mediating fluxes under very high wind speed conditions.

The terminal velocity of the largest drop that is stable in the gravitational field (assuming an oblate-spheroid shape of the droplet) scales according to Pruppacher and Klett (1978) as follows:

$$w_t \approx \left( \frac{4\pi b_a}{3aC_D} \right)^{1/2} \left( \frac{\rho g \sigma_s}{\rho_a^2} \right)^{1/4}, \tag{6.15}$$

where $b_a$ is the axial ratio of the oblate spheroid ($b_a \approx 0.55$), and $C_D$ is the drag coefficient ($C_D \approx 0.85$), $\sigma_s$ is the surface tension at the air-sea interface. For air-temperature of 20°C and normal atmospheric pressure of 101.3 kPa, the terminal velocity, $w_t \approx 7.8$ m s$^{-1}$. Equation (6.15) is relevant for drops $r > 2$ mm.

The transport equation for a large droplet in an equilibrium thermodynamics state and in a statistically steady and horizontally homogeneous marine boundary layer is as follows (Iida et al., 1992):

$$w_t \frac{dC}{dz} + \frac{d}{dz}\left( K_D \frac{dC}{dz} \right) = 0 . \tag{6.16}$$

A plausible parameterization for the turbulent diffusion coefficient in a coordinate system connected to the sea surface is

$$K_D = Sc_T^{-1} \kappa \left( z + z_{0a} \right) u_{*a}, \tag{6.17}$$

where $Sc_T$ is the turbulent Schmidt number for water droplets (of the order of unity), and $z_{0a}$ is the surface roughness parameter from the air-side of the air-sea interface, for instance expressed via Charnock's (1955) type parameterization,

$$z_{0a} = 0.0185 u_{*a}^2 / g . \tag{6.18}$$

The solution for equations (6.16) and (6.17) for $C$ is as follows:

$$C = C_0 \left( 1 + z / z_{0a} \right)^{-w_t / \kappa u_{*a}}, \tag{6.19}$$

where $C_0$ is some reference concentration.

For hurricane force winds, $u_{*a} \approx 2$ m s$^{-1}$ and the terminal velocity for the largest spray droplets $w_t \approx 8$ m s$^{-1}$, which means that $w_t / \left( \kappa u_{*a} \right) \approx 10$. As a

result, in a one-dimensional model the concentration of the largest droplets should drop dramatically with distance from the sea surface. The surface roughness length scale following from the Charnock (1955) parameterization is of the order of 1 cm. From (6.19) it follows that the initial concentration at $z$ = 1 cm should decrease by a factor $2^{10} \approx 10^3$. Though the turbulent diffusion mechanism apparently is not effective for the largest droplets, after tearing from the wave crest these droplets are taken up by the wind and may fly some distance in the horizontal direction before reentering the ocean surface.

### 6.2.3 Sea spray generation function

Essential for many applications is the sea spray generation function defined as the rate at which spray droplets of any given size are produced at the sea surface. The sea spray generation function, commonly denoted as $dF/dr_0$ (e.g., Monahan et al., 1986), where $F_0$ is total particle flux from the ocean and $r_0$ is the radius of a droplet at its formation, has units of number of droplets produced per square meter of surface per second per micrometer increment in droplet radius. For the consideration of spray momentum, heat, and moisture transfer, the generation function as a volume flux, $\left(4\pi r_0^3/3\right) dF/dr_0$, is more relevant.

Andreas (1998) compared the results of different authors only to find that the existing parameterizations of the primary marine aerosol source differ 6-10 orders of magnitude (*Figure 6-9*). He nevertheless found some consistency in the predicted shape of the spray generation function. The volume flux is relatively small for droplets with radii less than 2 μm or exceeding 500 μm; there is a 2 to 3 order-of-magnitude peak in the spray generation function between approximately 10 μm and 200 μm. This peak appears in the spume droplet region, which contributes most to the heat and momentum fluxes at high wind speeds. Parameterization of spume droplet production is therefore essential for evaluating the effects of spray on air-sea heat and moisture transfer.

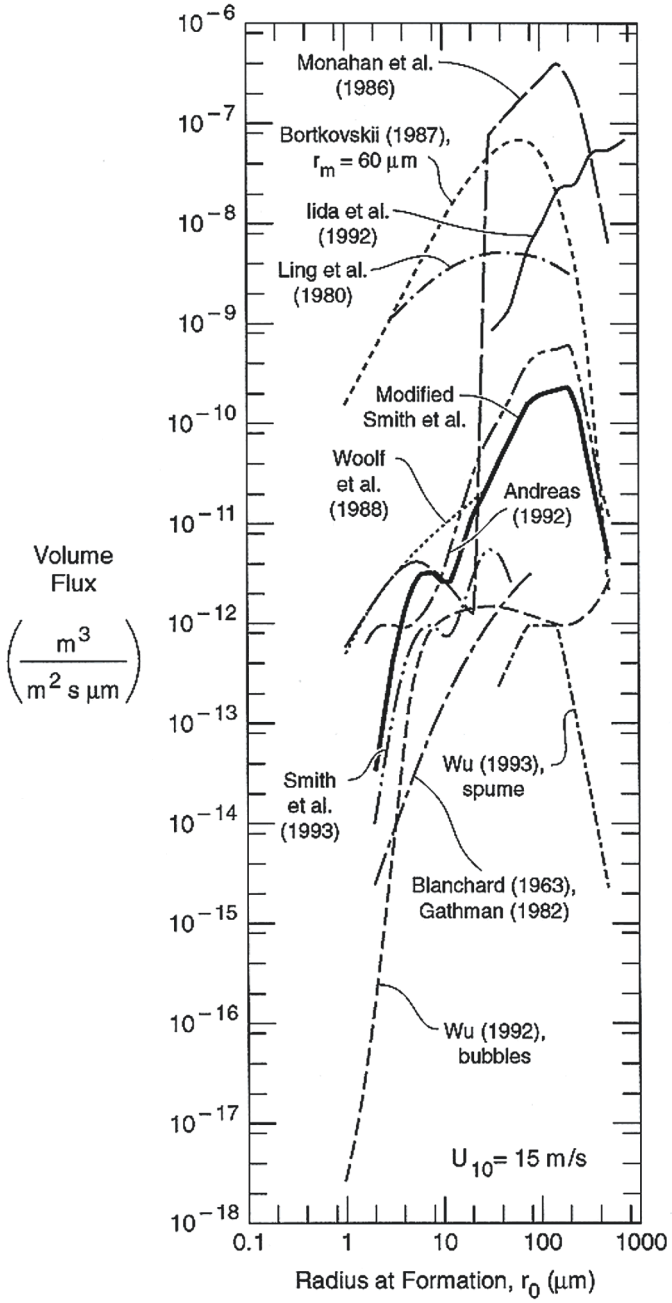


*Figure 6-9*. Various estimates of the sea spray generation function expressed as the volume flux, $\left(4\pi r_0^3/3\right)\, dF/dr_0$, for $U_{10}$ of 15 m s$^{-1}$. Reproduced from Andreas (1998) by permission from American Meteorological Society.

The predicted generation rates differ so greatly mainly due to the use of different sets of droplet concentration data and differences in the assumptions made regarding droplet trajectories. The process of droplet evaporation also adds to the uncertainty. Ultimately, Andreas (1998) discounts some of the parameterizations shown in *Figure 6-9* based on different grounds and ultimately focuses his analysis on the results of Smith et al. (1993) and Monahan et al. (1986) to produce the following parameterization:

$$\frac{dF_s}{dr_{80}} = \begin{cases} C_1(U_{10})\, r_{80}^{-1}, & 10 \le r_{80} \le 37.5\ \mu\text{m} \\ C_2(U_{10})\, r_{80}^{-2.8}, & 37.5 \le r_{80} \le 100\ \mu\text{m} \\ C_3(U_{10})\, r_{80}^{-8}, & 100 \le r_{80} \le 250\ \mu\text{m} \end{cases} \tag{6.20}$$

in which the spume extrapolation (third line) is based on droplet concentration data obtained within 0.2 m of the surface by Wu (1984). Here $C_1$, $C_2$, and $C_3$ are the wind-speed dependent coefficients ($\sim U_{10}^3$) that are evaluated by matching wind-dependent coefficient $C_1$ to the Smith et al. (1993) parameterization at $r_{80} = 10\ \mu\text{m}$, where $r_{80}$ is the radius of spray droplets in equilibrium at a relative humidity of 80%. Coefficient $C_2$ is determined from the continuity condition in (6.20) at $r_{80} = 37.5\ \mu\text{m}$. Coefficient $C_3$ is then found in the similar way from continuity condition at $r_{80} = 100\ \mu\text{m}$. The relationship between $r_{80}$ and $r_0$ (the radius of a droplet at its formation) is as follows:

$$r_{80} = 0.518\, r_0^{0.976}. \tag{6.21}$$

In fact, the parameterizations that are currently in use for various applications already show better agreement, though still with a few orders of magnitude differences. Andreas (2002) assumes that uncertainties can be further reduced to an order of magnitude range, even based only on the existing data sets. These datasets, however, do not cover hurricane wind conditions ($U_{10}$ > 30 - 40 m s$^{-1}$). The sea spray generation function for hurricane conditions remains practically unknown. Andreas (1998) has concluded that there is no trustworthy spray generation function even for a wind speed exceeding only 20 m s$^{-1}$. Extrapolation of parameterization (6.20) to hurricane conditions undertaken by some authors is not based on any data.

The dynamics of large droplets is a critical issue in developing the spray generation function for high wind speed conditions. After the initial ejection or splashing from the wave crest region these droplets fall quickly and do not

diffuse to any significant height above the ocean (though can be taken up by the wind gust and fly some distance in the horizontal direction before reentering the ocean surface). The largest droplets may therefore have eluded complete characterization during previous experiments.

### 6.2.4 Primary aerosol number distributions

The size distribution function of bubbles in the upper ocean, which are the primary source of marine aerosols, depends on the temperature, salinity, and surfactants. The primary marine aerosol generation is expected to depend on these parameters as well. *Figure 6-10* and *Figure 6-11* show results of a laboratory experiment for quantifying the salinity and temperature dependence of primary marine aerosol generation.

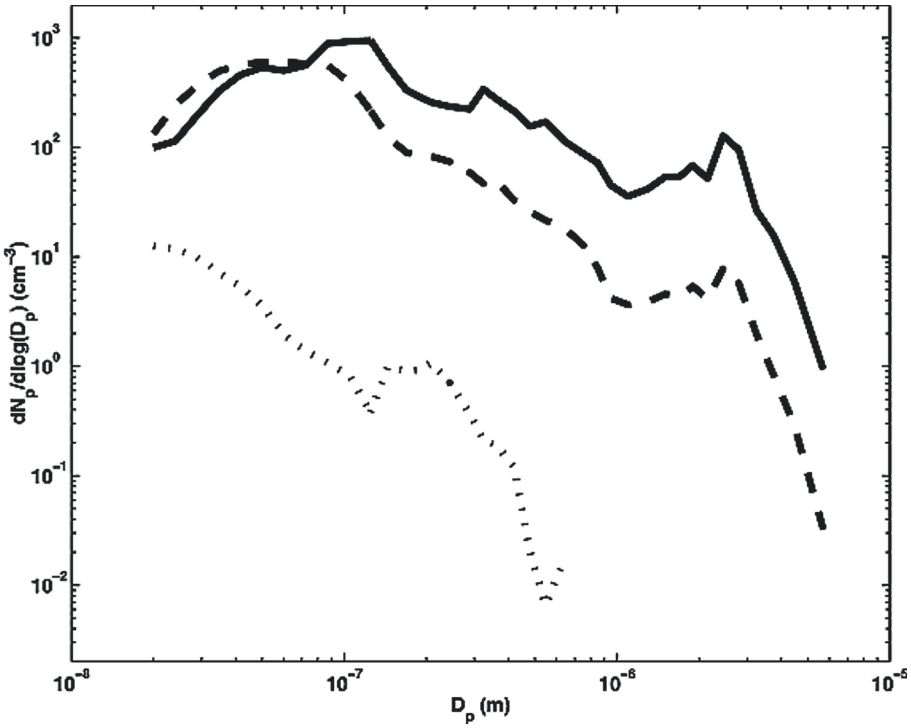


*Figure 6-10*. Number distributions of primary aerosols produced from bubbles in water with salinity of 0.0‰ (dotted line), 9.2‰ (dashed line), and 33.0‰ (solid line) in a laboratory experiment. Water temperature was 23°C. Reproduced from Mårtensson et al. (2003) by permission from American Geophysical Union.

*Figure 6-10* illustrates the effect of salinity on the dry aerosol number concentration ($N_p$ $cm^{-3}$). For the interpretation of this graph recall that for a similar drop size spectrum at formation, the less saline droplets produced at

the lower salinity will evaporate to particles with smaller diameter $D_p$. The ratio between the diameters of dry particles resulting from 33.0 and 9.2‰ salinity following from simple considerations is determined as $(33.0/9.2)^{1/3} \sim 1.5$.

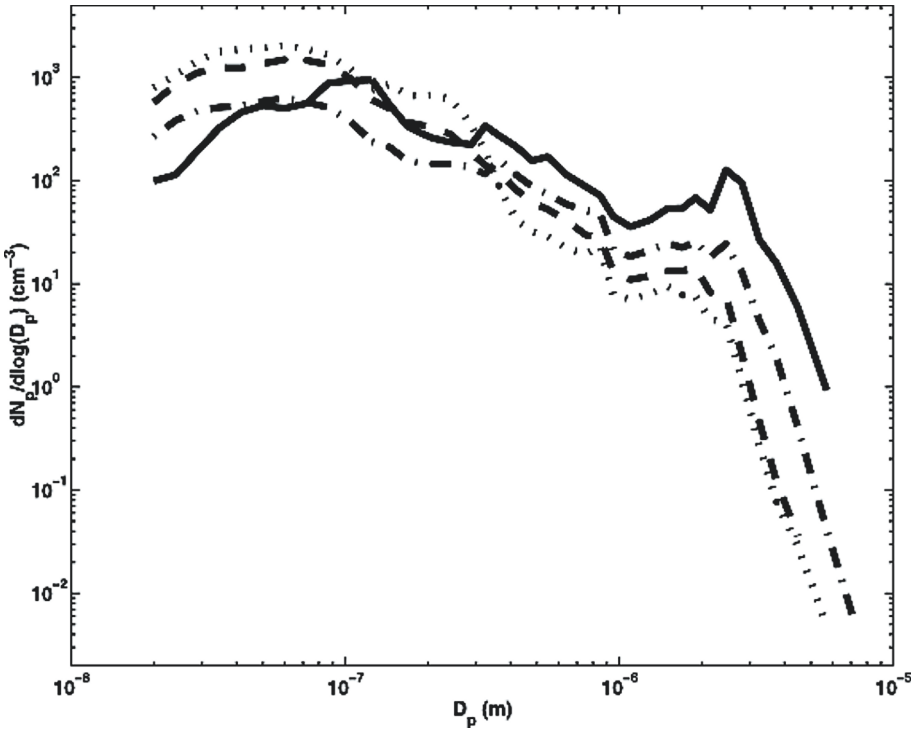


*Figure 6-11*. Number distributions of primary aerosol produced at water temperatures of -2°C (dotted line), 5°C (dashed line), 15°C (dot-dashed line), and 23°C (solid line) in laboratory conditions. The salinity was 33‰. Reproduced from Mårtensson et al. (2003) by permission from American Geophysical Union.

For aerosols generated by bubbles in the saltwater solutions ($S_w$ = 9.2‰ and 33.0‰), two modes are observed depending on the particle size (*Figure 6-10*). For the higher salinity, the small particle mode appears as a peak at ~0.1 μm $D_p$, whereas for the lower $S_w$ the small particle mode appears as a peak at a $D_p$ that is roughly a factor 1.5 smaller. This is consistent with the above ratio estimate for the dry particle diameters evaporated from the same size wet particle but with different sea-salt concentration. For particles from the $D_p < 0.2$ μm range, the total volume varies approximately proportionally to the water salinity.

On the other hand, for $D_p > 0.2$ μm (with a peak at ~2 μm) the aerosol spectra have a similar shape for both salinities; the concentrations, however, are an order of magnitude different. This leads to the conclusion that for $D_p <$

0.2 μm, salinity does not affect the original droplet production, just the size of the residual dry aerosol. Note that at formation, droplets are assumed to have the salinity of the seawater (Andreas, 1998). *Figure 6-10* thus indicates different droplet formation processes for particles with $D_p$ smaller than ~0.2 μm and for particles larger than this size.

Aerosol number size distributions for four water temperatures are presented in *Figure 6-11*. For $D_p > 0.35$ μm, the number concentration increases with increasing temperature, and the shapes of the size distributions are similar at all temperatures. For $D_p < 0.07$ μm, the number concentration decreased with increasing temperature. The curves cross in a transitional range $0.07 < D_p < 0.35$ μm, however no clear trend with water temperature has been revealed for this transition. Similar to the salinity dependence (*Figure 6-10*), the temperature dependence in *Figure 6-11* indicates different droplet formation processes, in this case below and above 0.07–0.35 μm $D_p$.

### 6.2.5 Marine aerosol generation function

The large concentration of aerosols in the sub-micrometer particle size range observed in laboratory air-sea interaction tanks is consistent with existing field data. The particle size distribution for dry aerosol particles includes two modes producing a peak near the 2 $\mu$m (median) diameter due to jet drops and a peak near 0.2 $\mu$m (median) diameter due to film drops (O'Dowd and Smith, 1993). The marine aerosol size distributions increase rapidly with wind speed for both modes.

Below we consider a recent parameterization for the primary marine aerosol generation function proposed by Mårtensson et al. (2003). This parameterization, intended for the dry diameter of aerosol particles in the $0.02$ μm $< D_p < 3$ μm range, is as follows:

$$\frac{dF_0}{d\log D_p} = \Phi W_c, \tag{6.22}$$

where $D_p$ is the dry diameter of aerosol particle,

$$\Phi = \frac{dF_p}{d\log D_p} = A_k T_w + B_k, \tag{6.23}$$

$F_p$ is the resulting particle flux per whitecap area; $W_c$ is the whitecap cover parameterized as a function of wind speed, $U_{10}$, at 10 m above the sea surface according to (6.14).

Coefficients $A_k$ and $B_k$ on the right side of equation (6.23) describe the size dependence. Mårtensson et al. (2003) utilized salinity and temperature dependences shown in *Figure 6-10* and *Figure 6-11* (plus a size distribution dependence from the same laboratory experiment) to derive the following polynomial fit:

$$\left.\begin{aligned} A_k &= c_4 D_p^4 + c_3 D_p^3 + c_2 D_p^2 + c_1 D_p + c_0 \\ B_k &= d_4 D_p^4 + d_3 D_p^3 + d_2 D_p^2 + d_1 D_p + d_0 \end{aligned}\right\} \qquad (6.24)$$

In *Figure 6-12*, the Mårtensson et al. (2003) parameterization at 9 m $s^{-1}$ wind speed and water temperatures of 25°C and 5°C is compared with the Monahan et al. (1986) and Smith et al. (1993) source parameterizations. For consistency, the expressions for the source fluxes have been converted to $dF_0/d\log D_p$ ($m^{-2}$ $s^{-1}$), where $D_p$ is the dry diameter of aerosol particles.

*Table 6-4.* Coefficients for the polynomial fits of $A_k$ ($c_4$–$c_0$) and $B_k$ ($d_4$–$d_0$) in equation (6.24) for the three size intervals ($D_p$) (after Mårtensson et al., 2003).

| Size Interval, $10^{-6}$ m | $c_4$ | $c_3$ | $c_2$ | $c_1$ | $c_0$ |
|---|---|---|---|---|---|
| 0.020–0.145 | -2.576 × 1035 | 5.932 × 1028 | -2.867 × 1021 | -3.003 × 1013 | -2.881 × 106 |
| 0.145–0.419 | -2.452 × 1033 | 2.404 × 1027 | -8.148 × 1020 | 1.183 × 1014 | -6.743 × 106 |
| 0.419–2.8 | 1.085 × 1029 | -9.841 × 1023 | 3.132 × 1018 | -4.165 × 1012 | 2.181 × 106 |
| Size Interval, $10^{-6}$ m | $d_4$ | $d_3$ | $d_2$ | $d_1$ | $d_0$ |
| 0.020–0.145 | 7.188 × 1037 | -1.616 × 1031 | 6.791 × 1023 | 1.829 × 1016 | 7.609 × 108 |
| 0.145–0.419 | 7.368 × 1035 | -7.310 × 1029 | 2.528 × 1023 | -3.787 × 1016 | 2.279 × 109 |
| 0.419–2.8 | -2.859 × 1031 | 2.601 × 1026 | -8.297 × 1020 | 1.105 × 1015 | -5.800 × 108 |

Mårtensson et al.'s (2003) source function describes the aerosol flux down to $D_p$ = 0.020 μm, with modes centered at ~0.07 μm and 2 μm $D_p$. In accordance with the experimental data shown in *Figure 6-11*, the source function depends on the water temperature: Below $D_p$ = 0.1 μm the number

flux is higher for colder water; above 0.2 μm $D_p$ the number flux is higher for warmer water.

Gong et al. (1997) and Lohmann et al. (2000) extrapolated the Monahan et al. (1986) parameterization below 0.9 μm (shown in *Figure 6-12* with a dotted line). This extrapolation demonstrates monotonically increasing flux with decreasing $D_p$ below 0.9 μm. The Mårtensson et al. (2003) parameterization, based on the size spectra observed in the laboratory as well in the available field data, offers a different dependence for $D_p < 0.9$ μm.

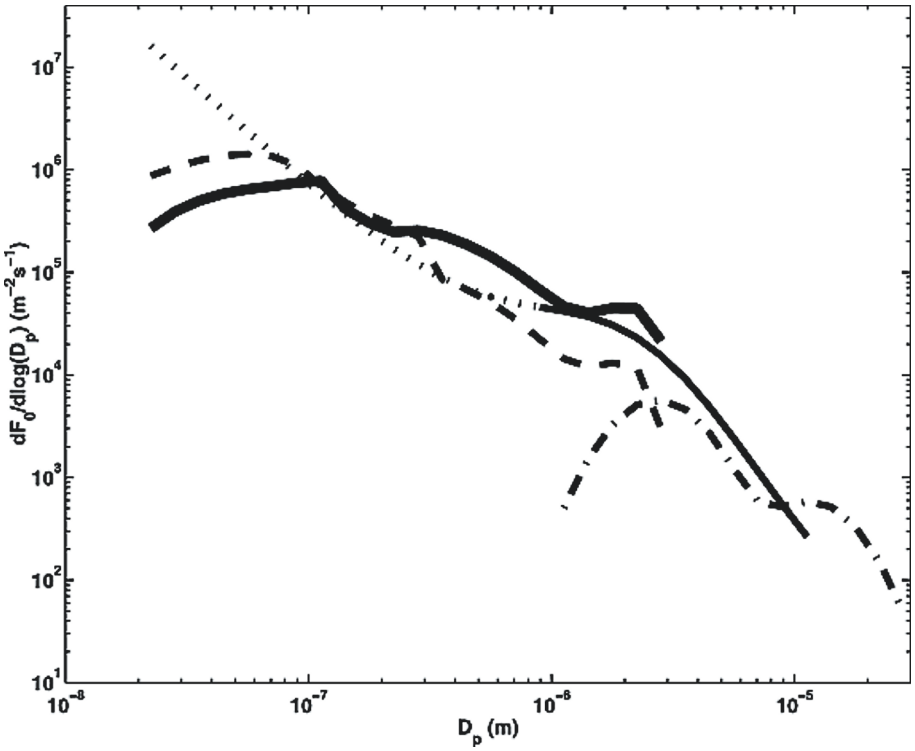


*Figure 6-12*. Parameterization (6.22)-(6.24) of the primary aerosol production shown as a function of the dry particle diameter $D_p$, for a wind speed of 9 m $s^{-1}$ and water temperatures 25°C (solid bold line) and 5°C (dashed line). This parameterization is also compared with the source flux from Monahan et al. (1986) in the size interval 0.9 –11.2 $D_p$ μm (solid line) and extrapolated down to 0.02 μm, *i.e.*, in the size interval 0.020–0.9 μm $D_p$ (dotted line). The flux derived by Smith et al. (1993) is shown by a dot-dashed line. Reproduced from Mårtensson et al. (2003) by permission from American Geophysical Union.

In the size range $D_p$ = 0.07–0.9 μm, Monahan et al. (1986) may underestimate the flux, while below 0.07 μm $D_p$, they overestimate the flux, compared to Mårtensson et al. (2003). The deviation of the Monahan et al. (1986) parameterization below 1 μm $D_p$ is presumably because it is based on

a simple power law fit to an aerosol mode located at ~1 μm $D_p$, which might be too simple to reproduce the observed properties.

The underestimation in the 0.07–0.9 μm $D_p$ range and the overestimation in the $D_p$ < 0.07 μm range partly cancel each other when the total number flux is determined. However, the differences below 0.9 μm $D_p$ may have serious implications concerning the contribution of the primary marine aerosol source to the cloud condensation nuclei (CCN) population. Consequently, these two parameterizations are likely to result in different cloud properties and radiative forcing. The parameterization of Mårtensson et al. (2003) in the $D_p$ < 0.9 μm range is probably more realistic, because this range is outside the range of the experimental data on which Monahan et al. (1986) based their parameterization.

For $D_p$ = 0.9–3.0 μm, both Mårtensson et al. (2003) and Monahan et al., (1986) predict almost the same aerosol generation rates.

Spray droplets that eventually become the main component of the marine aerosol are typically smaller than those that most influence air-sea heat and moisture transfer. The latter are in the range $r_0$ = 2–500 μm (remember that $r_0$ is the radius of droplets, while $D_p$ is the diameter of dry aerosol particles).

## 6.3 Air-Sea Exchange During High Wind Speeds

### 6.3.1 Effect of spray on air-sea exchanges

Spume droplets, which are relatively large, are particularly important for the fluxes carried by sea spray. Andreas (1998) and Andreas and Emanuel (2001) made an estimate of the effect of the sea spray on heat, moisture, and momentum transfer involving the sea spray generation function that was extended into the range of spume droplet sizes. These authors employed a sea spray generation function valid in the droplet radius range from 2 μm to 500 μm based on the Andreas (1992) and modified Smith et al. (1993) parameterizations.

*Figure 6-13* shows estimates of the magnitude of the sensible and latent heat fluxes based on the Andreas (1992) spray model and two formulations for the spray generation function—the one developed in Andreas (1992) and the modified parameterization of Smith et al. (1993). Differences between these generation functions are observed only for $U_{10}$ < 15–16 m $s^{-1}$, when the contributions of sea spray to air-sea fluxes of heat and moisture are small. *Figure 6-13* suggests the possibility of extremely large contributions of sea spray to heat and moisture transfer during storms.

Sea spray represents a volume source of heat and humidity in the marine boundary layer. The temperature and humidity profiles can be so strongly modified near the surface by the effects of evaporating spray that additional feedbacks may occur (Katsaros and de Leeuw, 1994). The contribution of

this feedback is still largely unknown due to the lack of reliable field data under very high wind speed conditions. Andreas' (1998) estimate does not include this feedback, though Fairall et al. (1994) have made an attempt to quantify the resulting sensible and latent heat flux above the droplet evaporation layer.

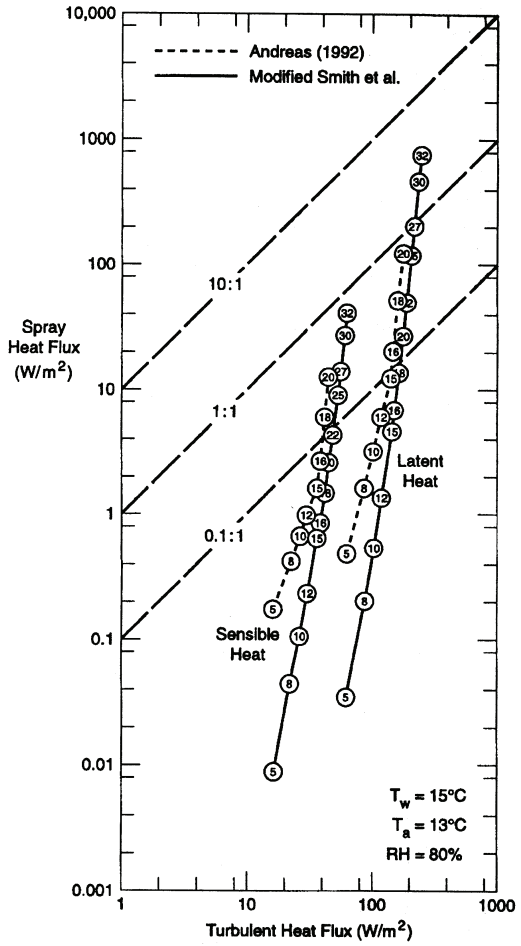


*Figure 6-13*. Estimates of the sensible and latent heat fluxes from the Andreas (1992) spray model and two formulations for the spray generation function. The turbulent heat fluxes are estimated from bulk aerodynamic formulas. The surface water temperature (which is the initial temperature of the spray droplets) is $T_w$, the air temperature is $T_a$, and the relative humidity is *RH*. The number in each circle is the 10 m wind speed in m s$^{-1}$. The diagonal lines indicates where the spray and turbulent fluxes are equal (1:1), where the spray flux is 10% of the turbulent flux (0.1:1), and where the spray flux is 10 times the turbulent flux (10:1). Reproduced from Andreas (1998) by permission from American Meteorological Society.

An important feature of the spray thermodynamics is that the heat and mass exchange of a spray droplet with the air are decoupled. *Figure 6-14* demonstrates this for a 100 μm radius spray droplet ejected into typical tropical cyclone conditions. The initial droplet temperature equal to the sea surface temperature drops from 28°C to its equilibrium temperature within 1 s, while only 1% of the droplet mass must evaporate for the droplet to reach this equilibrium temperature (Andreas and Emanuel, 2001). Remarkably little evaporation occurs until at least 100 s after droplet formation.

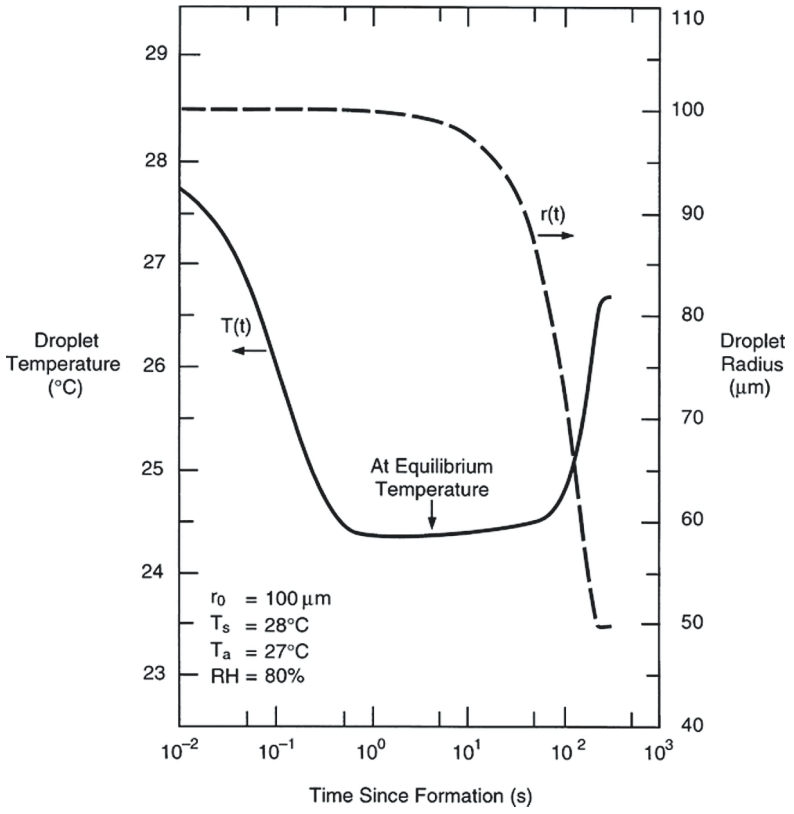


*Figure 6-14.* Evolution of temperature and radius of a spray droplet of initial radius $r_0$ = 100 $\mu$m, which is ejected from the sea surface at temperature $T_s$ = 28°C into the air at temperature $T_a$ = 27°C and relative humidity 80%. The droplet has initial salinity 34 psu, and the barometric pressure is 1000 mb. Reproduced from Andreas and Emanuel (2001) by permission from American Geophysical Union.

After spray is ejected into the atmosphere, wind can accelerate it. The time required for sea spray droplets starting with no horizontal speed to accelerate to within $e^{-1}$ of the nominal wind speed $U_{10}$ is shown in *Figure 6-15*. This exchange extracts momentum from the flow, which is transferred to the ocean when spray droplets land back in the water (Andreas and

Emanuel, 2001). In surface-level winds of 10 m $s^{-1}$ and higher, droplets with radii up to 500 μm reach a speed equal to $e^{-1}$ of the local speed within 1 s. An estimate of droplet residence time for all droplets up to 500 μm in radius suggests that this time is sufficient to accelerate to the local wind speed.

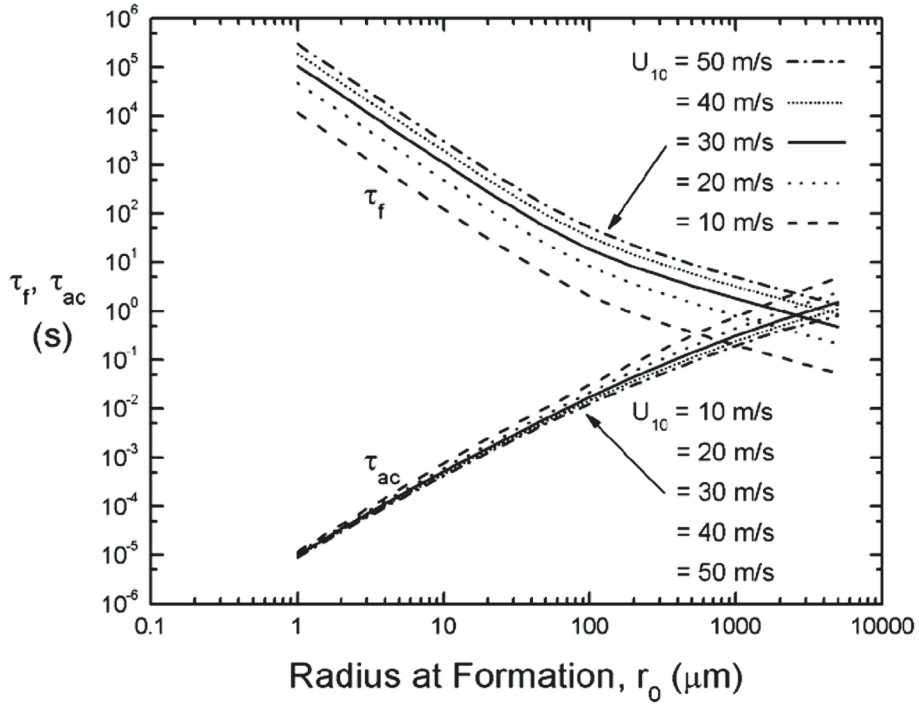


*Figure 6-15.* Time $\tau_{ac}$ required for sea spray droplets to accelerate to wind speed $U_{10}$. Here, $\tau_f$ is the typical atmospheric residence time for droplets of initial radius $r_0$ at the indicated wind speed calculated from relation $\tau_f = A_{1/3}/w_t$, where $A_{1/3}$ is the significant wave amplitude determined as $A_{1/3} = 0.015U_{10}^2$ ($A_{1/3}$ is in m and $U_{10}$ is in m $s^{-1}$). The air temperature is taken as 20°C, and the barometric pressure as 1000 hPa. Reproduced from Andreas (2004) by permission from American Meteorological Society.

Thus, spray droplets with relatively short atmospheric residence time (the re-entrant spray) effectively transfer momentum flux and sensible but not latent heat flux. Note that the latent heat flux is usually much larger than the sensible heat flux.

The spray momentum flux is defined from the following formula (Andreas and Emanuel, 2001):

$$\tau_{sp} = \frac{4\pi}{3}\rho U \int_{r_{lo}}^{r_{hi}} r_0^3 \frac{dF_0}{dr} dr_0 , \qquad (6.25)$$

where $dF_0/dr_0$ is the sea spray generation function, and $U$ is the wind speed at one significant wave height above the mean sea level. Equation (6.25) implies that all droplets reach this level. Some justification for this assumption comes from the fact that the droplets that contribute most to the spray momentum flux are the large ones torn right off the wave crests.)

Equation (6.25) is nevertheless only an upper bound on the surface stress that falling spray droplets produce on the ocean surface layer. In fact, some small spray droplets are entrained in the turbulent flow and never return back to the ocean. The droplets that return to the sea partially evaporate and therefore have a reduced radius $r_0$, and thus reduced momentum.

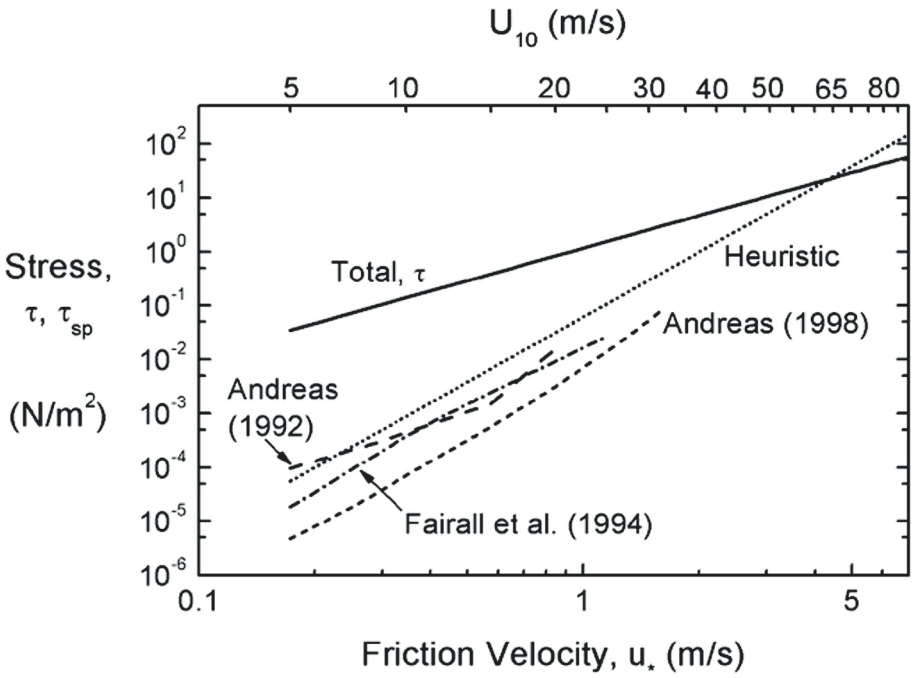


*Figure 6-16*. Estimates of the total and sea spray stresses. The sea spray stresses are calculated from equation (6.25) for three versions of the sea spray generation function. The extent of these curves reflects the wind speed range over which the functions are appropriate The total stress line is equation (6.26); the heuristic line is equation (6.27). Reproduced from Andreas (2004) by permission from American Meteorological Society.

*Figure 6-16* shows the results of the estimation of $\tau_{sp}$ from equation (6.25) for two versions of the sea spray generation function in comparison with the total surface stress,

$$\tau = \rho_a u_{*a}^2 , \tag{6.26}$$

where $\rho_a$ is the air density, and $u_{*a}$ is the friction velocity in the air. The sea spray generation function has not yet been determined for friction velocities $u_{*a} \geq 2$ m s$^{-1}$. In the range $u_{*a} < 2$ m s$^{-1}$, $\tau_{sp}$ estimated with (6.25) is much less than $\tau$. Nevertheless, the estimated spray stress increases approximately as the fourth power of $u_{*a}$, because $dF_0 / dr_0 \sim u_{*a}^3$ and $U$ is linear in $u_{*a}$. At the same time, $\tau$ is just quadratic in $u_{*a}$. Andreas (2004) therefore assumes that when the winds reach hurricane strength, spray stresses may become comparable to the total stress. Andreas and Emanuel (2001) proposed the following parameterization for the spray stress,

$$\tau_{sp} = 6.2 \times 10^{-2} \rho_a u_{*a}^4 \ , \tag{6.27}$$

which gives $\tau_{sp}$ in N m$^{-2}$, when $\rho_a$ is in kg m$^{-3}$, and $u_{*a}$ is in m s$^{-1}$. They call parameterization (6.27) "Heuristic" because it is based on their intuition rather than on any data. According to *Figure 6-16*, the sea spray stress becomes comparable to the interfacial wind stress at about 60 m s$^{-1}$ wind speed. Note that the sea spray contribution to the sensible and latent heat fluxes becomes comparable to the corresponding interface fluxes at about 30 m s$^{-1}$ wind speed.

### 6.3.2 Dynamics of suspension flow

The spray-saturated atmospheric boundary layer can be represented as a suspension flow. The Barenblatt and Golitsyn (1974) theory for the flow with suspended particles in a dust storm can provide a theoretical basis for the analysis of the sea spray effects in the marine boundary layer. In this conceptual theory, a stationary turbulent flow of a dust-gas suspension is considered in the semi-infinite region $z \geq 0$ bounded from below by the horizontal plane $z = 0$. The suspension is a two-phase medium consisting of a gas with small particles; the concentration, volume, and weight of particles are small. The horizontal velocity components for the particles and gas are the same while the vertical components differ by the constant value *a*, which is the fall velocity of a single particle in unbounded space. Contributions due to particle interactions with the pressure and viscous stress are neglected due to the smallness of the particle concentration. Only density variations connected to the action of gravity are taken into account, which is the Boussinesq approximation. Under the Boussinesq approximation the direct contribution of the solid phase to the momentum and momentum flux of the suspension are neglected. The analogy is of course not complete because in contrast to dust particles, sea spray experiences phase transformation (evaporation).

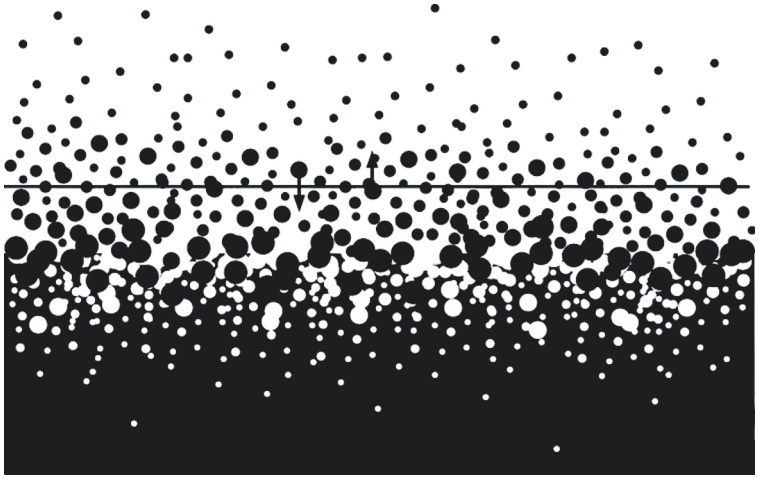

*Figure 6-17*. Momentum and enthalpy transfer through an emulsion. Spray droplets are ejected upward and accelerate toward the free stream velocity, absorbing momentum from the atmosphere. Reproduced from Emanuel (2003) by permission from American Meteorological Society.

The laws of momentum and mass conservation for the suspension are as follows:

$$-\rho\overline{u'w'} = \tau = \rho u_*^2 = const\,, \tag{6.28}$$

$$\overline{C'w'} = aC\,, \tag{6.29}$$

where $C$ is the volume concentration of particles ($C = 4\pi r^3 n/3$), $r$ is the particle radius, and $n$ is the number of particles in the unit volume. Equation (6.29) reflects the fact that the vertical turbulent flux of the admixture is equal to its gravitational fallout.

The density of suspension is defined through its components:

$$\rho = \rho_g\left(1-C\right) + \rho_p C \tag{6.30}$$

where $\rho_g$ is the gas density, and $\rho_p$ is the particle density. The velocity vector $\vec{u}$ that consists of the longitudinal $u$ and the vertical $w$ components is defined in the following way:

$$\vec{u} = \left[\rho_g\left(1-C\right)\vec{u}_g + \rho_p C\vec{u}_p\right]/\rho \tag{6.31}$$

where $\vec{u}_g$ and $\vec{u}_p$ are the gas and particle velocity vectors respectively. For small volume ($C \ll 1$) and weight ($\sigma C \ll 1$) concentrations the density fluctuations are:

$$\rho' = \sigma \rho C', \tag{6.32}$$

where

$$\sigma = \left(\rho_p - \rho_g\right)/\rho_g . \tag{6.33}$$

For water drops in the air $\sigma = \left(\rho - \rho_a\right)/\rho_a \approx \rho/\rho_a$.

The equation for the turbulent energy balance of the admixture is as follows:

$$\rho\overline{u'w'}du/dz + \overline{\rho'w'}g + \varepsilon = 0 \tag{6.34}$$

where is the dissipation of the turbulent kinetic energy. With (6.32), this equation can be presented in the form:

$$\rho\overline{u'w'}du/dz + \sigma\rho\overline{C'w'}g + \rho\varepsilon = 0 \tag{6.35}$$

The physical meaning of this equation is that the energy of turbulence from the mean shear flow is then spent partially for suspension and partially for dissipation. Introducing the nondimensional parameter,

$$K_t = \frac{g\overline{C'w'}\rho/\rho_a}{\overline{u'w'}du/dz} \tag{6.36}$$

which is known as the *Kolmogorov number*, equation (6.35) can then be presented in the following form:

$$\overline{u'w'}\left(du/dz\right)\left(1 - K_t\right) + \varepsilon = 0 \tag{6.37}$$

The solution of the problem appears to depend on a nondimensional parameter already familiar to us (see Section 6.2.2)

$$\omega = w_t/\left(\kappa u_{*a}\right), \tag{6.38}$$

where $w_t$ is the terminal velocity of the particle. For $\omega \geq 1$, the vertical distributions of the horizontal velocity $u$ and concentration $C$ are determined by the classical laws for the logarithmic boundary layer (Prandtl, 1949):

$$U(z) = \frac{u_{*a}}{\kappa} \ln z + const_1, \; C(z) = \frac{const_2}{z^{\omega}}, \tag{6.39}$$

which means that the particles do not affect flow dynamics.

For $\omega < 1$, the saturation-limited flow regime is possible, which is described by the following relation for the velocity and concentration profiles (Barenblatt and Golitsyn, 1974):

$$u(z) = \frac{u_{*a}}{\kappa\omega} \ln z + const, \quad C(z) = \frac{a^2 K_t}{\sigma g z}. \tag{6.40}$$

For $\omega > 1$ the vertical mixing coefficient is defined as $K_m = \kappa u_{*a} z$, while for $\omega < 1$ it is given by equation

$$K_m = \omega \kappa u_{*a} z = w_t z, \tag{6.41}$$

which means that the stratification effect reduces turbulent friction by a factor of $\omega^{-1}$.

Equation (6.38) at $\omega = 1$ combined with the formula for the terminal velocity of raindrops (2.112) gives an equation for the droplet radius separating the two regimes according to the Barenblatt and Golitsyn theory. This critical droplet radius $r_c$ is as follows:

$$r_c = r_\upsilon \left[1 - \ln\left(\kappa u_{*a} / w_t\right)\right]^{1/\lambda} \tag{6.42}$$

Dependence (6.42) is shown in *Figure 6-18* as a function of the friction velocity in air. Spray droplets with radii $r > r_c$ are the re-entrant spray, while smaller droplets are effectively transported by turbulence. Note that for 15 m s$^{-1}$ wind speed, which corresponds to the friction velocity in air $u_{*a} \approx 0.6$ m s$^{-1}$, the critical droplet radius is $r_c \approx 70$ μm. It is interesting that most of the spray generation functions shown in *Figure 6-9* reveal peaks around $r = 100$ μm, which may be an indication that the turbulent diffusion is not an effective mechanism for transporting these relatively large droplets. This, however, might also be an indication that the known spray generation functions underestimate the contribution of large droplets, because the

largest droplets might elude detection during the measurements conducted at some distance from the sea surface.

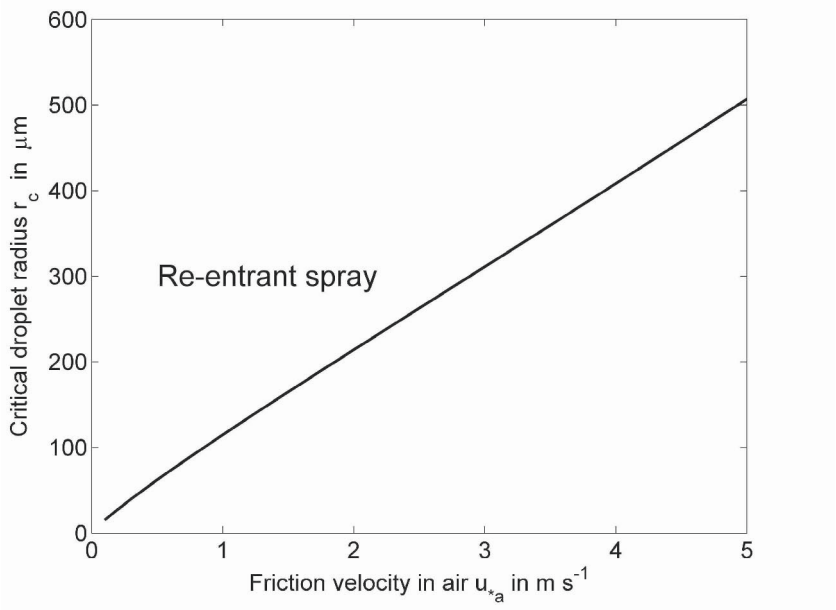


*Figure 6-18*. Critical radius separating re-entrant and entrained droplets according to the Barenblatt and Golitsyn (1974) theory.

The saturation-limited flow implies an infinite supply of particles from the boundary to the flow. If the particle supply is not infinite (*e.g.*, due to the surface tension effect in the case of air-sea interface), then at small distances from the surface the velocity and concentration profiles follow the laws of the classic logarithmic boundary layer (6.39), while switching to the saturation-limited regime (6.40) at some distance $h$ from the boundary. In the latter case a new parameter, enters the problem--surface buoyancy flux of particles $B_0$--and a new length scale appears:

$$L_* = \frac{u_{*a}^3}{\kappa B_0}, \tag{6.43}$$

which is an analog to the Oboukhov buoyancy length scale in the thermally stratified turbulent boundary layer (see Chapter 1). A surface mixed layer is formed with thickness $h \sim L_*$. This regime is schematically illustrated in *Figure 6-19* for $\omega = 0.1$.

In application to the marine boundary layer, the buoyancy flux due to sea spray is defined in the following way:

$$B_0 = g \int_0^{r_c} \frac{4}{3} \pi r_0^3 \frac{dF}{dr_0} dr_0 , \qquad (6.44)$$

where is $dF / dr_0$ the sea spray generation function. Rough estimates for 15 m $s^{-1}$ wind speed using the spray generation function determined from (6.20)-(6.21) and integrated from 10 μm to 70 μm results in the vertical length scale estimate from (6.43) far exceeding the thickness of the atmospheric boundary layer. Since $dF / dr_0$ defined from (6.20)-(6.21) increases with friction velocity as $u_{*a}^3$, which is the same dependence on friction velocity as in the denominator of equation (6.43), the estimate for $L_*$ should not change with wind speed.

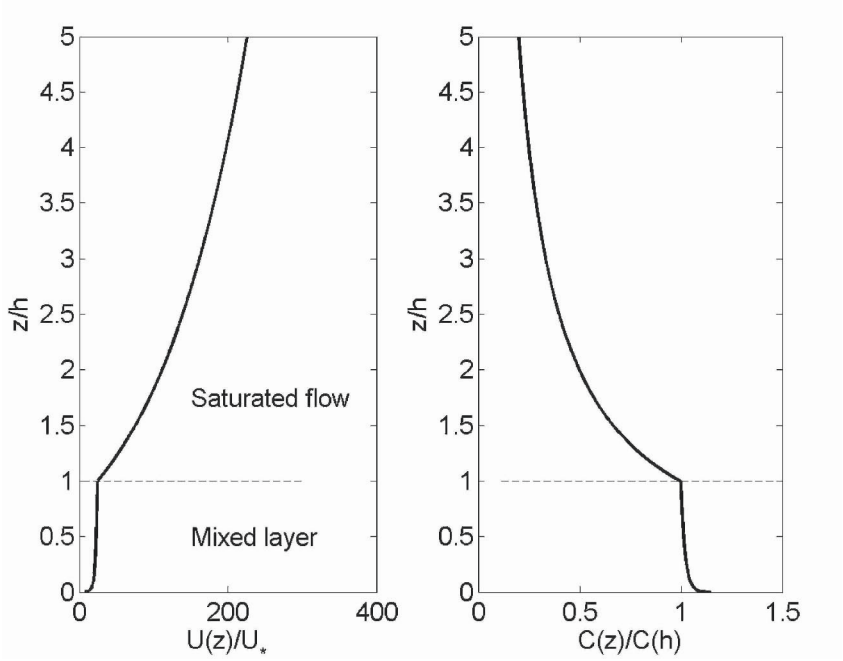


*Figure 6-19*. Vertical profiles of velocity and concentration in the suspension-limited flow according to the Barenblatt and Golitsyn (1974) model.

Theoretically, the sea spray concentration in the marine boundary layer can reach the level at which its associated stratification may suppress turbulent fluctuations, reducing wind stress at the ocean surface. However, if the spray generation function (6.20) holds for very high wind speed conditions, then the influence of the sea spray on the atmospheric boundary layer dynamics is relatively small even during hurricanes.

### 6.3.3 Drag coefficient in very strong winds

The dynamics of cyclonic storms cannot be fully predicted without proper knowledge of the physical processes at the air-sea interface under high wind speed conditions. The drag coefficient formula of Large and Pond (1981) derived from field measurements under low and moderate wind speed conditions gives a linear increase of the drag coefficient with wind. There are, however, indications that this formula may not work in the high wind speed regime.

*Figure 6-20* and *Figure 6-21* show the results of laboratory and in situ evaluations of the drag coefficient under high wind speed conditions. Both data sets suggest that the drag coefficient does not increase (or perhaps even decreases) with wind speed starting from approximately 30 m $s^{-1}$. Several hypotheses have been offered to explain this phenomenon (Powell, 2003; Emanuel, 2003; Donelan, 2004; Andreas, 2004).

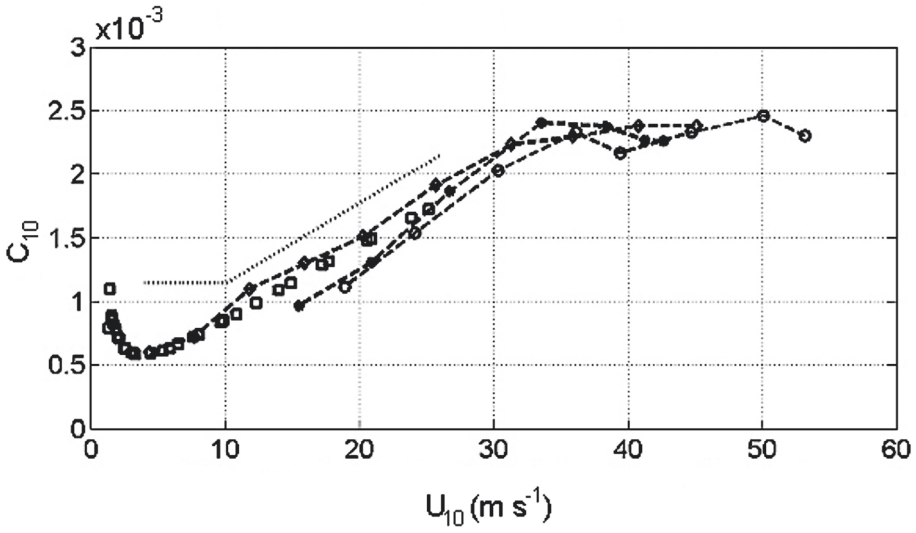


*Figure 6-20.* Laboratory measurements of the neutral stability drag coefficient by profile (asterisks), eddy correlation (diamonds) and momentum budget (circles) methods. The squares represent the data obtained in a different tank by Ocampo-Torres et al. (1994). Squares denote the measurements of the drag coefficient $C_{10}$ appropriate to the wind speed $U_{10}$ measured at the standard anemometer height of 10 m. The drag coefficient formula of Large and Pond (1981) derived from field measurements under relatively low winds is shown by dots. (After Donelan et al., 2004.)

According to the estimates described in the previous section, the buoyancy effect of spray by itself cannot explain the deviation of the drag coefficient dependence on wind speed under very high wind speed

conditions observed either in the laboratory experiments of Donelan et al. (2004) or the in situ experiment of Powell et al. (2003). Donelan et al. (2004) hypothesized that the probable cause of the effect of reduction of the drag coefficient under very strong winds is airflow separation above the leading slope of the waves.

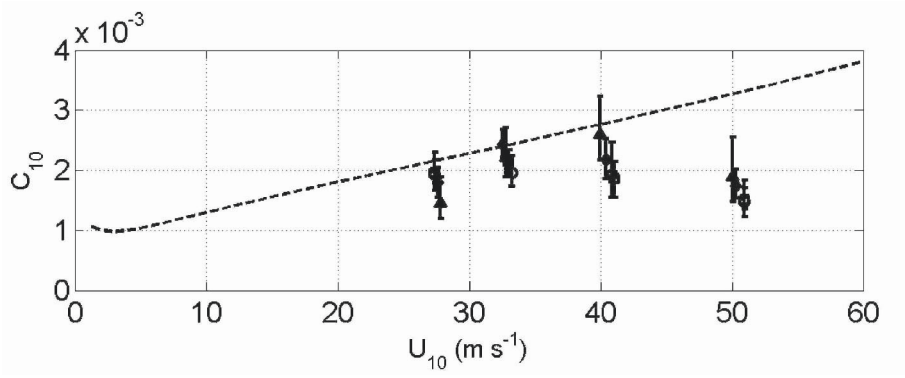


*Figure 6-21*. Drag coefficient under high wind speed conditions. Dashed line is the Large and Pond (1981) type parameterization derived by extrapolating relatively low wind speed measurements. Also shown are the experimental data of Powell et al. (2003) derived from GPS sonde profiles and the corresponding 95% confidence limits.

Andreas (2004) suggested that when the wind speed reaches about 30 m $s^{-1}$, the flux of spray droplets is equivalent to a heavy rainfall. As discussed in Chapter 2 (Section 2.5.5 and 2.5.6), rainfall damps the shortest surface waves, which contribute most to the surface roughness (Donelan, 1998; Schlüssel et al, 1998; Makin and Kudryavtsev, 1999). In analogy with rainfall, spray droplets penetrating the sea surface produce significant mixing in the near surface layer of the ocean, absorbing the energy of surface waves and smoothing the ocean surface. A smooth ocean surface makes it easier for the airflow to separate from waves. From classic hydrodynamics, it is known that the transition to turbulence delays boundary-layer separation, which is related to the difference in the shape of the velocity profile in the laminar and the turbulent boundary layer (Kundu et al., 2004). The adverse pressure gradient (that causes the boundary layer to separate from the body) more easily overcomes laminar rather than turbulent boundary layer. The airflow can thus separate sooner from a smooth wave surface than from a rough surface.

Another possible reason for the airflow separation from waves is the distraction of the aqueous viscous sublayer under very strong winds by the Kelvin-Helmholtz (K-H) instability. Due to the presence of aqueous viscous sublayer the sea surface moves slightly faster than the phase speed of the

wave. According to Kraus and Businger (1994), boundary-layer separation of the airflow from surface waves under this condition is rather rare event.

Banner and Phillips (1974) identified the presence of a stagnation point accompanied by a gravity-capillary wave train near the wave crest linked to the microscale wave breaking. When wind reaches the speed at which the surface wind drift speed exceeds the minimum phase speed of the gravity-capillary waves, a K-H instability of the gravity-capillary wave train disrupts the air-sea interface destroying the viscous sublayer. This leads to the separation of the airflow form waves and reduction of the drag coefficient.

The disruption of the air-sea interface also generates spume. As it has already been pointed in Section 6.2.2, the largest droplets are produced by the mechanism of direct splashing. The initial instability is of the K-H type. According to Koga (1981), small projections in fact develop near the crest of the wave, where the wind stress is generally highest, and then break up to form droplets.

The following nondimensional number characterizes the condition for development of the K-H instability at the air-water interface:

$$K = \frac{u_{*a}}{\sqrt{g\sigma_s \rho / \rho_a^2}}. \tag{6.45}$$

The instability first occurs at $K \geq K_{cr}$. An estimate of $K_{cr}$ from the laboratory experiment of Koga (1981) is $K_{cr} \approx 0.038$, which at a 20°C air temperature and normal atmospheric pressure corresponds to the friction velocity in air $u_{*a} = 1.24$ m s$^{-1}$ (or to friction velocity in the water $u_* = 0.043$ m s$^{-1}$), and the wind speed at 10 m height $U_{10} \approx 30$ m s$^{-1}$.

The spreading mechanism of the droplets varies according to the size of the droplets. Koga and Toba (1981) concluded that for droplets with radius of 75 μm or more, the diffusion by air turbulence is not of great importance (which is consistent with the graph shown in *Figure 6-18*). More important is the initial speed at the instant of the droplet production and the acceleration by wind.

*Figure 6-22* shows the spatial distribution of the velocity vector of the splashing droplets relative to the wave profile in the laboratory experiment of Koga (1981). The experimental set up was able to resolve droplets with radius larger than 0.4 mm. Most of these large droplets are produced on the leading slope near the crest of wave with initial speeds of the same order, or somewhat larger than, the speed of the projection. They spread upward and forward by the acceleration due to the drag of the pulsating wind flowing over wave profile. Due to gravity most of the droplets return to the water surface on the windward slope near the crest of the next wave; their

trajectories through the air are making an angle of nearly 15 degrees with the horizontal. According to *Figure 6-22* most of the droplets collide with the wave surface when they are accelerated to about half the local wind speed.

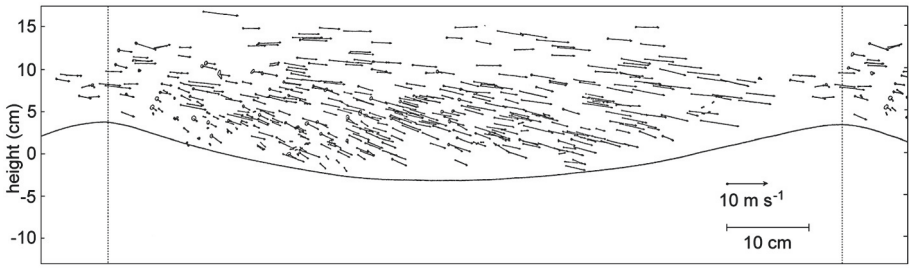


*Figure 6-22*. Movements of directly produced droplets along the representative wave for the case of 16 m fetch at $u_{*a}$ =1.97 m s$^{-1}$. Each droplet in the figure indicates actual size traced from photographs. Direction of the airflow and wave propagation is from left to right. Arrows indicate the droplet velocity vector in the coordinate system moving with the phase speed of the wave. Reproduced from Koga (1981) with permission from *Blackwell Publishing.*

In some cases Koga (1981) observed jumping of small droplets over the next crest. This usually took place when the steepness of the next crest was large. In this case, even large droplets sometimes jumped upward with some inclination over the next crest. This observation suggests that there is a strong jet flow in the air near the crest. On the leading slope of the wave near the crest, the droplet velocity is generally small, even for small droplets. This is an indication of the airflow separation, which is expected above the leading slope of the wave. Remember that the airflow separation was a striking effect observed under very high wind speed conditions in the laboratory experiment of Donelan et al. (2004) (results if which are presented in *Figure 6-20*).

A plausible scenario is that at wind speeds $U_{10}$ ~ 25-30 m s$^{-1}$ the K-H instability of the gravity-capillary wave train near wave crests develops effectively eliminates the aqueous viscous sublayer. This leads to the separation of the airflow from the wind waves and, as a consequence, to the reduction of the air-sea drag coefficient.

Another consequence of the K-H instability is the disruption of the water surface and dramatic increase of the spume production. Spume drops precipitate on the ocean surface, perhaps causing its additional smoothing.

Under very strong winds ($U_{10}$ ~ 60 m s$^{-1}$) a two-phase environment is formed at the air-sea interface. The spume becomes a significant component of the air-sea momentum flux, which, according to Section 6.3.1, may lead to the opposite effect—an increase of the drag coefficient.

Chapter 7

# APPLICATIONS

*In this final chapter, practical applications of the results obtained from the studies of the near-surface layer of the ocean are considered. These applications range from remote sensing and air-sea interaction to acoustics, optics, and biophysical coupling.*

The near-surface layer of the ocean is a principal component in several important applications. Traditional applications such as remote sensing and air-sea coupling in numerical models have been augmented by recent developments in ocean color, acoustic sensing and near-surface biology. Remote sensing from space can be efficiently complemented with remote sensing of the sea surface from inside the ocean. Optical and acoustical methods provide exciting opportunities in this direction.

Section 7.1 is devoted to the role of near-surface processes in remote sensing of the ocean from space. The study of ocean color appears to be one of the fastest developing areas of remote sensing. It is related to the inherent optical properties of the upper ocean, which we discuss in some detail in Section 7.2. Section 7.3 is devoted to the biochemistry of the near-surface layer of the ocean. Sections 7.4 and 7.5 analyze acoustic and gas-exchange applications, respectively. Section 7.6 is a discussion of parameterizing the near-surface layer processes for ocean and global climate modeling.

## 7.1 Remote Sensing of the Ocean

An increasing number of satellites, as well as a few Space Shuttle, Mir, and International Space Station missions, have been devoted to collecting oceanographic data. These observations have revealed new phenomena, and

have allowed studies of processes on unprecedented space and time scales compared to traditional in situ observations. Important data acquired with satellites include sea surface temperature, surface wind speed and direction, surface wave height and direction, ocean color, ocean current velocity, and sea ice thickness and extent in the high latitudes. Remote sensing methods have found numerous applications in studies of the coastal and shelf waters adjacent to continental margins where inflow and mixing of river waters substantially contribute to the observed patterns. Obvious advantages of satellite remote sensing methods are in the frequent global coverage and generally consistent accuracy of the data. However, the interpretation of the remote sensing data often requires detailed knowledge of the processes at the air-sea interface.

### 7.1.1 Remote sensing of surface winds

The surface wind stress (as well as heat and moisture fluxes) over the global ocean represents the boundary condition for global circulation models. Satellites provide exciting opportunities to measure wind stresses at the sea surface remotely, with global coverage.

Passive (radiometric) and active (radar) ocean sensors have orbited Earth, at various times since *SeaSat* in 1975. Presently flying is NASA's *QuikSCAT,* one of the most sophisticated satellites, equipped with the *SeaWinds* radar scatterometer. It is capable of measuring wind speeds from 3 to 20 m $s^{-1}$ with an accuracy of 2 m $s^{-1}$ and an accuracy of $20^{o}$ for direction with 25 km resolution. In order to utilize these measurements in the most effective way, understanding of both the detailed structure and dynamics of the ocean surface and the physics of electromagnetic wave scattering from the sea surface is required.

The remote sensing of the wind velocity vector is possible due to the amplitude and directional correlation between the wind and sea state parameters. The sea surface roughness almost entirely determines the scattering of radar signals. Capillary-gravity waves with wavelengths of ~0.01 m directly influence microwave scattering and radiance emission; a precise knowledge of the short-scale-wave roughness is therefore required. Due to nonlinear interactions, short waves are intimately coupled with intermediate and long waves. Full wavenumber models of the surface roughness such as that of Donelan and Pierson (1987), Apel (1994), Elfouhaily et al. (1997) have been widely used in microwave radar scattering studies. The problem, however, has not yet been completely solved because of the complex nature of the processes governing sea surface roughness and the physics of electromagnetic wave interaction with the sea surface (Lemaire et al., 1999; Voronovich and Zavorotny, 2001). Research in this

direction continues both with phenomenological description and in theoretical formulation.

The problem of inverting the backscattered radar signal into useful information is related to 1) better understanding of how the various parameters of wind speed and direction, atmospheric thermal stability, sea-surface temperature (SST), salinity, currents, and bathymetry determine the surface state, and 2) how the statistical properties of the sea surface can be extracted from backscattered radar signal. The first issue is inherently related to physics of the near-surface layer of the ocean. In particular, near-surface turbulence (Chapter 3) and surface-intensified jets (Chapter 4) can affect capillary-gravity waves and, thus, the sea surface roughness. These effects may explain some discrepancies between theoretical and field results on electromagnetic scattering from the sea surface and have yet to be incorporated into remote sensing algorithms.

### 7.1.2 Sea surface temperature

Thermal infrared imagery from satellites is an important source of information about the ocean. There are two atmospheric windows where absorption is a minimum (*Figure 7-1*). The instruments deployed on aircraft usually utilize the 3-5 μm and 8-14 μm wavelength ranges, while the satellite-based sensors normally use the 3-4 μm and 10.5-12.5 μm windows. In the 10.5-12.5 μm range the radiant energy is absorbed by ozone. Water vapor and carbon dioxide absorb some of the radiation energy across the entire spectrum. As a result, both windows require corrections to account for the atmospheric absorption. In addition to the water vapor absorption, the solar beams reflected form the ocean surface can contaminate the 3-4 μm window during daytime hours.

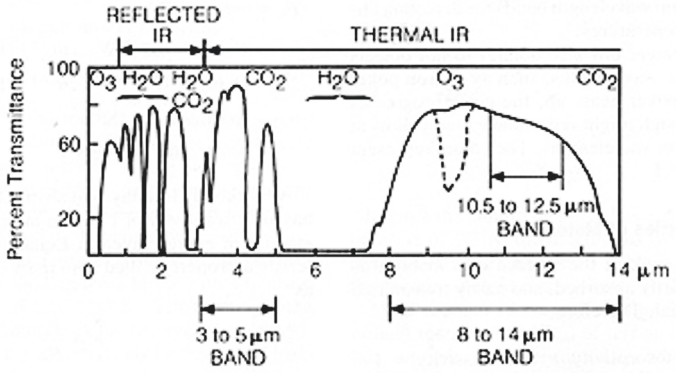


*Figure 7-1*. Spectral plot of the atmospheric transmission in the infrared band. (Reproduced from Sabins, F.F., *Remote Sensing Principles and Interpretation, 2nd ed. 449* PP © 1987 *WH Freeman & Co.*)

The primary infrared sensor on the U.S. meteorological satellites has been the Advanced Very High Resolution Radiometer (AVHRR). AVHRR has five measuring channels. Channel 3 ($\lambda$ = 3.55-3.93 μm), Channel 4 ($\lambda$ = 10.30-11.30 μm), and Channel 5 ($\lambda$ = 11.50-12.50 μm) are in the window of atmospheric transparency and are used for SST measurements.

The Terra and Aqua satellites carry the Moderate Resolution Imaging Spectroradiometer (MODIS), which is a 36-band spectroradiometer measuring, among other parameters, visible and infrared radiation. The accuracy of the SST measurement with MODIS is several times higher than with AVHRR, approaching 0.1$^{o}$K in favorable conditions.

The infrared satellite sensor receives signals from the upper several micrometers of the ocean. The SST depends on many factors. Among the most important factors causing SST to deviate from the bulk temperature of the upper ocean mixed layer are the effects of short and longwave radiation, latent and sensible heat fluxes, freshwater input, convection, and wind and wave mixing.

The wind-wave mixing and convection produce the surface mixed layer. The surface mixed layer participates in large-scale air-sea interaction, has substantial heat capacity, and is an important element of the weather and climate system. How the SST is connected to the temperature structure of the surface mixed layer is of interest for many practical applications, including the development of remote sensing techniques for monitoring the climate and global carbon cycles. In fact, the SST differs from the temperature of the bulk of mixed layer due to the aqueous thermal molecular sublayer, the cool skin of the ocean (Section 2.1.2), diurnal warming (Section 4.1.1), and freshwater addition by precipitation (Sections 2.5 and 4.1).

The temperature difference across the cool skin of the ocean is typically of the order of 0.2-0.3$^{o}$C but can increase to 0.4-0.6$^{o}$C under low wind speed conditions. Intense insolation at midday and/or air temperature exceeding water temperature can reverse the temperature gradient within the thermal molecular sublayer; the sea surface can become slightly warmer than the underlying water (Section 2.4). With the accuracy of the satellite techniques approaching 0.1$^{o}$C, the aqueous thermal molecular sublayer has already been included in some advanced remote sensing algorithms (*e.g.*, Schlüssel *et al.,* 1990).

Under light winds the near-surface layer of the ocean is often re-stratified due to diurnal warming and/or precipitation effects. A thin near-surface mixed layer is formed. Its heat capacity is comparable to the heat capacity of the atmospheric boundary layer. Under these conditions, the near-surface layer of the ocean can rapidly respond to changes in the atmospheric state; as a result, both oceanic and atmospheric processes determine the SST.

Katsaros and DeCosmo (1990) hypothesized that the air-sea heat flux could control the interface temperature and result in smoothing of spatial inhomogeneities of SST. This effect is illustrated in *Figure 7-2* with an example from the Florida Straits, which shows three-day composite AVHRR during (a) winter and (b) summer. The Gulf Stream is clearly traced in the SST winter image, while it is almost completely masked in the SST image acquired during summer. Katsaros and Soloviev (2004) explain this observation as an effect of atmospheric regulation of diurnal SST amplitudes (see also Katsaros et al. (2005). The cooling of the sea surface by sensible and latent heat fluxes and net longwave radiation would be larger from the warmer water than from the cooler side of fronts or eddies, leading to to greater diurnal heating on the cool side. This results in a decrease of the horizontal SST differences and possible erroneous conclusions about the ocean processes (Katsaros *et al.,* 1983; Katsaros and Soloviev, 2004; Katsaros et al., 2005). The atmospheric regulation can be additionally enhanced due to a positive correlation between SST and wind speed often observed on the mesoscale: Regions with lower SST typically have lower winds, which leads to stronger diurnal warming. Interpretation of remotely sensed SSTs requires that this phenomenon becomes better understood and its frequency and importance in nature is assessed.

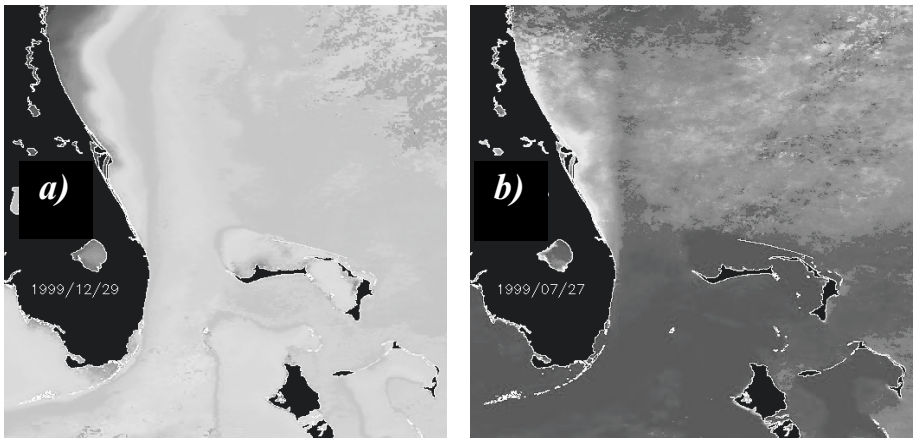


*Figure 7-2*. Three-day composite Advanced Very High Resolution Radiometer (AVHRR) images of the Florida Straits during (a) winter and (b) summer. Note that the Gulf Stream clearly seen in the winter image is substantially masked by solar warming that not only produces the near-surface vertical temperature gradients but also diminishes the horizontal temperature gradients due to the effect of atmospheric regulation. Adapted from Katsaros and Soloviev (2004) with permission from Springer Science and Business Media.

Clouds are the major obstacles in obtaining useful oceanographic information from satellite infrared imagery. They may cover extended areas of the ocean up to 90% of time. Microwave thermal measurement of the

ocean surface (for instant with SSM/I) is not affected by clouds, but its accuracy is far below that of infrared sensors. Also, rains affect the microwave measurement by modification of the sea surface reflectance.

The fundamental approach to address the problem of cloud interference of SST measurements is to enhance the remote sensing techniques with mixed-layer modeling capable of reproducing diurnal warming and precipitation effects (as well as the cool skin) and being forced with remotely sensed heat and momentum fluxes (Soloviev and Schlüssel, 2001). This approach, however, requires assimilation of multi-satellite and multi-sensor data. Several issues have yet to be resolved for this approach. Substantial progress has been made in the development of remote sensing techniques for latent and sensible heat fluxes with accuracies of satellite products approaching the accuracy of buoy and shipboard bulk-flux measurements (Benthamy et al., 2003; Jo et al., 2004).

### 7.1.3 Sea surface salinity

The measurement of the sea surface salinity from space can significantly improve understanding of ocean circulation, air–sea interaction, and the global climate as a result (Lagerloef et al., 1995; Topliss et al., 2002). The water emissivity in the microwave range depends on salinity. In the long wavelength end of the microwave spectrum (L or C band), the response due to changes in salinity is sufficiently strong to distinguish from the temperature dependence though it is still a second order effect. In order to obtain adequate resolution at the surface for longer wavelengths, large antennas must be placed in space.

The measurement of salinity from space becomes more practical with the emergence of aperture synthesis, the new microwave radiometer technology that does not require such large antennas. Le Vine et al. (1998) have shown the theoretical possibility of measuring sea surface salinity with airborne synthetic aperture radar. *Figure 7-3* compares remote (airborne) and shipboard measurements of sea surface salinity made by these authors in the vicinity of the Delaware coastal current. The remote sensing measurements were made from an aircraft with the Electronically Scanned Thinned Array Radiometer (ESTAR), which is an L-band synthetic aperture microwave radiometer. Both thermosalinograph- and microwave radiometer–derived salinity maps clearly show the freshwater signature of a coastal current and generally are in agreement to within about 1 psu

The sensors working in the L ($\lambda$ = 24 cm) and C ($\lambda$ = 6 cm) bands receive signals from approximately the upper 12 cm and 3 cm of the ocean respectively. Increasing the accuracy of salinity remote sensing will require incorporation of detailed knowledge of near-surface salinity structure into

the analysis. For instance, appreciable salinity difference in the near-surface layer of the ocean can develop due to rainfalls (Sections 2.5 and 4.1).

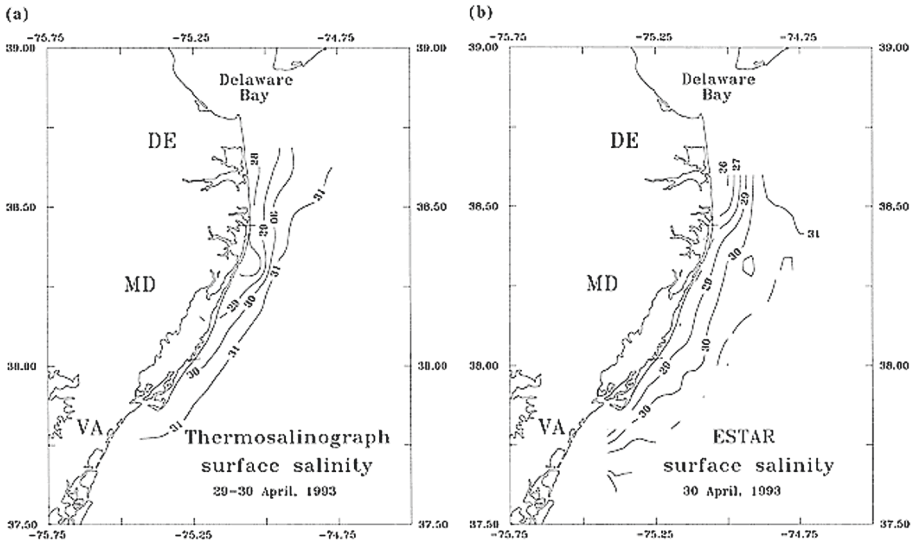


*Figure 7-3*. Comparison of salinity fields obtained from (a) the thermosalinograph data and (b) from an airborne remote sensing instrument (ESTAR). Reproduced from Le Vine et al. (1998) by permission from American Meteorological Society.

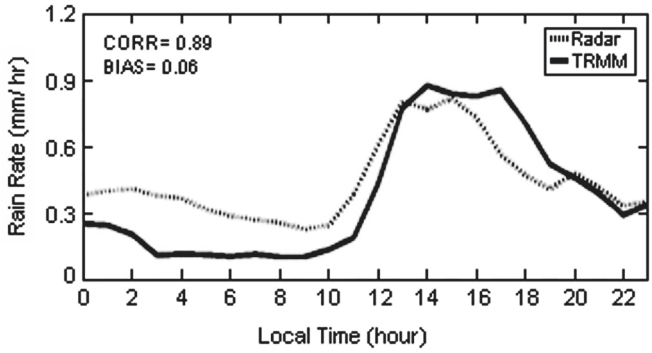


*Figure 7-4*. The composite diurnal cycle from rainfall measurements during the Tropical Rainfall Measuring Mission (TRMM) using the Microwave Imager and Precipitation Radar, compared with the composite diurnal cycle from the TOGA COARE rain radar. The correlation coefficient and bias between the radar and satellite data are shown in the upper left corner of the graph. (After Sorooshian et al., 2002.)

Knowledge of the precipitation distribution will be helpful for the interpretation of remotely sensed salinity (as well as for many other issues). The first specialized satellite for precipitation measurements was the Tropical Rainfall Mapping Mission (TRMM), a joint research project

between the U.S. (NASA) and Japan (National Space Development Agency: NASDA). The results of the intercomparison between this satellite and the TOGA COARE rain radar shown in *Figure 7-4* are very promising. Note that the satellite derived rain rates can be used to force the mixed layer model aimed at enhancing the remote sensing of SST (see the previous section).

### 7.1.4 Surface ocean currents

Ocean surface currents can be measured remotely with high-frequency (HF) radio waves due to the Bragg scattering effect. This effect results from coherent reflection of the transmitted energy by ocean surface waves whose wavelength is exactly one-half of the transmitted radar waves (Paduan and Graber, 1997). These coherent reflections produce a strong peak in the backscatter spectrum. Note that scatterometers exploit Bragg scattering from capillary waves (~1 cm) to obtain information about winds. HF radars exploit Bragg scattering from surface gravity waves ($\lambda \sim 10$ m) to obtain information about currents (as well as waves and winds). Combining simultaneous measurements from two separated sites, maps of surface current vectors can be created.

At this point, HF radars have found important applications in coastal ocean studies (Shay et al, 2002). There have also been attempts to employ the HF radar for offshore surface current measurements (Skop and Peters, 1997). Ship-based observations, however, suffer from motion of the ship, which complicates the measurement due to the degradation of spectral returns. Pierre Flament and Cedric Chavanne are working on the solution to this problem. (Ship motion used to be a problem for atmospheric radars on ship as well; but it is solved at this point.)

HF radar provides information about currents from the near-surface layer of the ocean with effective thickness equal to one half of the radio wavelength, $\lambda/2 \sim 5$ m. The slippery near-surface layer of the ocean that develops due to solar heating and/or freshwater influx (Chapter 4) can affect the interpretation of the HF radar data relative to surface currents. This problem, however, has not yet received proper attention.

Determination of surface currents is also possible from SAR imagery (Chapron et al., 2004), which opens a new exciting opportunity to study global ocean circulation from space. This method exploits electromagnetic waves of a several-cm wavelength and is based on the Doppler shift in the radio signal reflected from the surface waves of comparable wavelength. The short surface waves are advected by the near-surface shear and modulated by the orbital velocities of longer waves. In addition to the surface intensified jets (Section 4.2), the aqueous viscous sublayer (Section 2.1.1) appears to be

of critical importance for extracting useful information about ocean currents from SAR imagery, since for this case $\lambda/2$ is comparable to the thickness of the viscous sublayer.

### 7.1.5 Microwave imagery

A variety of the oceanic structures such as fronts, meanders, eddies, and river plumes can be studied using microwave imagery. *Figure 7-5* shows a convergent front on the continental shelf detected by airborne X-band radar operating in the 2.4-3.8 cm wavelength range. This is an image collected by Farid Askari (NRL) near Cape Hatteras, NC during the first High Resolution Remote Sensing Experiment. This converging front (rip) developed at the shoreward boundary of a Gulf Stream meander and the continental shelf waters. The red line indicates high backscatter, while the dark blue line supposedly corresponds to low backscatter due to an accumulation of surfactants on the north side of the rip.

The appearance of sharp frontal interfaces is usually an indication of an active subduction process (Chapter 5). Remotely sensed images of sharp frontal interfaces may therefore potentially contain information about the vertical structure of the upper ocean.

### 7.1.6 Monochromatic and color imagery

Monochromatic aerial photography was the first method to trace spatial structures manifested on the ocean surface. Introduction of color photography provided wider opportunities for studying and monitoring the ocean from space.

In addition to photographic methods, non-photographic sensor systems and space imaging systems have been intensively developing. A significant advance in sensor technology resulted from subdividing spectral ranges of radiation into bands (intervals of continuous wavelengths), and allowing sensors in several bands to form multi-spectral images.

A system for remote sensing of the ocean color consists of a sensor with a narrow field of view, aimed at a point on the ocean surface (IOCCG, 2000). Special devices allow for the sensor to scan the ocean surface (also due to the motion of the satellite with respect to the earth surface). The data acquired from different points on the ocean surface constitute its color image. The sensor receives radiometric signals in the visible and near infrared bands of the electromagnetic spectrum. The information content of the signal depends on the spectral resolution and the number of selected wavelengths. For example, on the SeaWiFS satellite, several bands cover the blue, green, and red parts of the visible spectrum and the near infrared range.

*Figure 7-5*. Convergent front on the continental shelf detected by airborne radar. This X-band radar image (~2.25x1.25 km) was one of several collected by Farid Askari (NRL) near Cape Hatteras, NC during the first High Resolution Remote Sensing Experiment. (This image is from the public domain of the Noval Research Laboratory Website http://rsd-www.nrl.navy.mil/7250/)

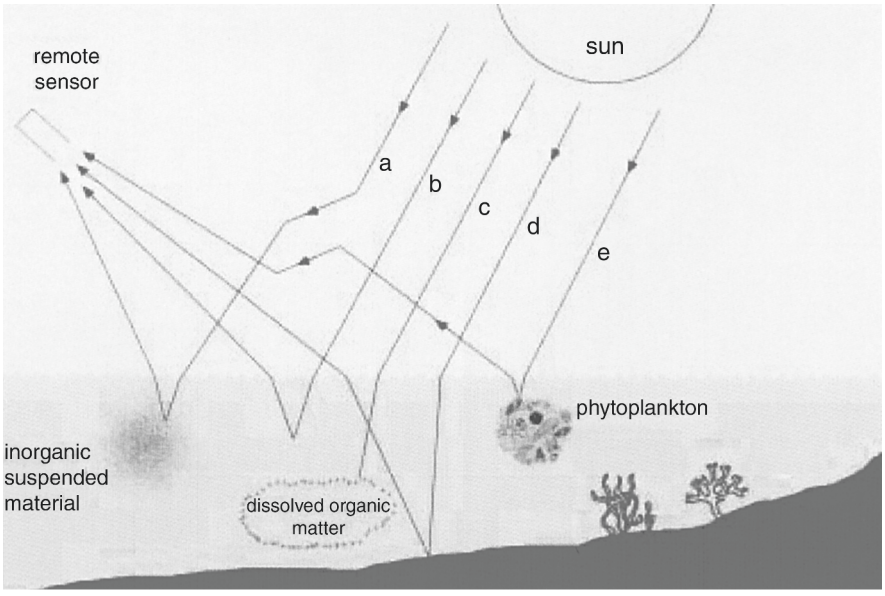


*Figure 7-6*. Schematic representation of the factors that influence upwelling light leaving the sea surface: (a) upward scattering by inorganic suspended material; (b) upward scattering from water molecules; (c) absorption by the yellow-substances component; (d) reflection from the bottom; and (e) upward scattering from phytoplankton. (After IOCCG, 2000.) Courtesy of Shubha Sathyendranath.

Higher spectral resolution potentially leads to more informative remote sensing systems. The so-called *hyperspectral* remote sensing involves systems with very fine spectral resolution and many wavelengths. Hyperspectral remote sensing is expected to improve the interpretation of the complex biophysical processes controlling optical properties of the coastal ocean.

Remote sensing of ocean color is a passive method, since the sun is the source of light. The photons from the sun follow different pathways before reaching the remote sensor. The light entering the sensor originates from scattering of photons by the atmosphere, reflection of direct sunlight from the sea surface (specular reflection), and the upwelling light that is back-scattered from below the sea surface (*Figure 7-6*).

The upwelling light scattered from below the sea surface carries useful information in relation to the water body properties. This light is, however, attenuated on its pathway from the sea surface to the remote sensor because of absorption and scattering by the atmosphere.

The specular reflection at the sea surface and atmospheric attenuation represent noise for remote sensing of ocean water properties using color. Specular reflection from the sun can be avoided by changing the orientation of the detector with respect to the position of the sun. This, nevertheless, does not help in eliminating the flux scattered from the atmosphere that reaches the sensor at many angles. More than 80% of the light reaching satellite sensors may be of atmospheric origin (Morel, 1980). Techniques for atmospheric correction are therefore an essential component of remote sensing of the ocean color (Gordon, 1997).

*Figure 7-6* illustrates the main factors that influence upwelling light back-scattered from below the sea surface. (This diagram is a bit simplified, because it does not show multiple reflections and scattering.) Direct and scattered (diffuse) solar radiation penetrating the sea surface is absorbed and scattered by the water molecules and suspended and dissolved materials contained in the near-surface water. In coastal areas, sunlight may reflect from the ocean bottom.

Ocean color imagery represents properties of a thicker layer than the microwave and infrared imagery. The color is therefore a more conservative characteristic of the water mass than the surface roughness or SST, and it better defines dynamical ocean features. These features are often well clearly seen in the chlorophyll-$\alpha$ band (Yentisch, 1984), though, strictly speaking, phytoplankton is not a conservative tracer. In coastal regions, other color imagery products such as the yellow substance and suspended sediment may be even better tracers than chlorophyll (Kopelevich et al., 1998).

The intrinsic color of the ocean is defined by spectral variations in reflectance $R_s$ which according to IOCCG (2000) is defined as follows:

$$R_s(\lambda,z)=\frac{E_u(\lambda,z)}{E_d(\lambda,z)}, \tag{7.1}$$

where $E_u(\lambda,z)$ is the spectral irradiance in all the upward directions, or upwelling spectral irradiance, at wavelength λ and depth z; and $E_d(\lambda,z)$ is the spectral irradiance in all the downward directions, or the downwelling spectral irradiance, at the same wavelength and depth.. Irradiance $E_u$ or $E_d$ is the flux received by a flat collector facing downward or upward, respectively (see definitions of $E_u$ or $E_d$ in Section 1.4.1).

The upwelling spectral irradiance $E_u$ is a measure of all the light that leaves the sea surface. The remote sensor with a narrow field of view receives only a small fraction of this flux. The description of the light field should hence include information on directional distribution of the light. Spectral radiance $L(\theta,\phi,\lambda,0)$, introduced in Section 1.4.1 and defined as the spectral radiant energy with wavelength λ per unit area and per unit solid angle, can provide this information.

A parameter closely related to the sea surface reflectance is the remote sensing reflectance, which is defined in the following way (IOCCG, 2000):

$$R_{rs}(\theta,\phi,\lambda,0)=\frac{L(\theta,\phi,\lambda,0)}{E_d(\lambda,0)}. \tag{7.2}$$

The remote-sensing reflectance makes use of upwelling radiance rather than irradiance. It decomposes the reflectance $R_s$ into its component radiances as a function of the viewing angles $\theta$ (zenith angle) and $\phi$ (azimuth angle).

Note that the definition of the remote sensing reflectance by IOCCG (2000) differs from the traditional definition of the reflectance coefficient of the sea surface given in Section 1.4.5. The latter does not include the upwelling light back-scattered from below the sea surface, which is the essential component of the ocean color signal. Since the color imagery of the ocean is a rapidly evolving area of science, we have decided to keep both definitions in this book.

According to Section 1.4.6, the ocean color, or remote-sensing reflectance, is an apparent optical property, because it can be modified by the zenith-angular structure of the incident light field as well as by the nature and quantity of substances present in the medium. Variations in the spectral form and magnitude of the ocean-color signal potentially contain quantitative information on the types of substances present in the water and on their concentrations. In order to obtain this information it is necessary is to express remote-sensing reflectance in terms of inherent optical properties,

which are independent of the incident light field, and are determined entirely by the type and concentration of substances present in the upper ocean water. The relationship between ocean color and inherent optical properties of seawater is consequently of great interest for the interpretation of remote sensing data. The inherent optical characteristics of the ocean in application to remote sensing are discussed in more detail in the next section.

## 7.2 Marine Optics

### 7.2.1 Inherent optical characteristics of the upper ocean water

Remote sensing of ocean color requires understanding the optical properties in the upper ocean water. Optical properties of the near-surface ocean water can be separated into the properties of pure water and the properties of the dissolved and suspended matter. The presence of dissolved salts in the water only slightly modifies its optical properties; which, nevertheless, can make a difference for certain applications. Suspended matter can influence the light propagation in a more significant way.

Three main components influencing the optical properties of seawater in addition to pure water itself and the light reflection off the bottom (in coastal areas) are as follows (IOCCG, 2000):

- Phytoplankton (which also includes other phytoplankton microscopic organisms);
- Inorganic suspended material;
- Yellow substances represented by colored, dissolved, organic substances and "detail" particulate material (the latter generally has absorption characteristics similar to yellow substances).

Jerlov (1976) proposed an optical classification of oceanic surface waters by distinguishing three major water types (I, II, and III), two intermediate types (IA and IB), and coastal turbidity types (1, 3, 5, 7, 9). Morel and Priuer (1977) partitioned the oceanic waters into Case 1 and Case 2 water. They defined Case 1 waters as those waters in which phytoplankton and accompanying biochemical and particulate environment are mainly responsible for variations in optical properties of the water. Case 2 waters, according to their classification, are the waters that are also influenced by inorganic particles in suspension and yellow substances.

The inherent optical properties of the water that are relevant to remote sensing of the ocean color are the absorption and scattering coefficients, which describe the exponential rate of decay of flux per unit path length of light in the water due to absorption and scattering of light, respectively. The observed color of the ocean results from the interaction of incident flux (downwelling, direct-solar and diffuse-sky, irradiances) with water and with its organic and inorganic substances. The processes of absorption and

scattering control the manner in which impinging photons propagate through a natural water body and substantially determine the color of the ocean). The process of absorption is simply the removal of photons from the light field, while scattering changes the direction of photon propagation. Scattering of photons can occur in both an elastic and inelastic manner. Elastic scattering does not change the photon wavelength, while inelastic scattering does. Fluorescence of dissolved organic matter or phytoplankton is an example of inelastic scattering (IOCCG, 2000).

The absorption and scattering coefficients are defined for the idealized conditions of collimated, monochromatic flux incident normally on the water, and traversing an infinitesimally thin layer of the water. (Scattering coefficients are defined separately for elastic and inelastic scattering processes.) Unlike the apparent optical properties (*e.g.*, diffusive attenuation coefficient for downwelling irradiance $K_d$ defined in Section 1.4.6) the inherent properties do not depend on natural light conditions. A complete description of the scattering process requires knowledge of the distribution of the scattered light as a function of scattering angle.

Inherent optical properties of Case 1 waters primarily depend on phytoplankton populations and accompanying materials. In Case 2 waters, suspended particulate material and dissolved organic matter of aqueous or terrestrial origins can influence inherent optical properties (in addition to and independently on phytoplankton). The optical properties of substances other than phytoplankton often dominate the bulk optical properties of Case 2 waters (Siegel and Michaels, 1996). In order to retrieve quantitative information on the constituents of the water body from ocean color, information on the inherent optical properties of each of major constituents is required.

The development of techniques for the interpretation of ocean color in the remote sensing context has been focused on the theoretical modeling of ocean color as a function of inherent optical properties and on the cataloguing of the inherent optical properties of substances encountered in the near-surface ocean waters, as well as their variations with the concentrations of the substances (IOCCG, 2000). Remarkably, the inherent optical properties allow a simple addition of the contributions of the individual components that can constitute a multi-component medium (which may not work for apparent optical properties, especially in highly scattering media). It is therefore feasible to resolve individual components and their concentrations from remote sensing of the ocean color. Detailed cataloguing of the inherent optical properties of the near-surface ocean waters is important for development of the most sophisticated inverse algorithms that also take into account the natural variability in the optical signatures of these substances especially due to the influence of air-bubbles populating the near-surface layer of the ocean.

### 7.2.2 Influence of bubbles on optical scattering in the upper ocean

The top few meters of the ocean are most important for remote sensing of ocean color. Morel's and Prieur (1977) classification into Case 1 and Case 2 waters, however, ignores the fact that the optical scattering in the near-surface waters can be largely modified by the presence of bubbles. Air bubbles efficiently scatter light in water because their refractive index is considerably less than that of the surrounding water, and their size is typically large compared to wavelengths of light. The intermittent nature of bubble entrainment depending on near-surface turbulence and, to some extent, on biochemical processes leads to strong fluctuations in light scattering near the ocean's surface (Terrill et al., 2001).

Air bubble concentration and size distribution (*i.e.*, major determinants of optical scattering) vary greatly in time and space as a function of wind and wave conditions. Large areas of the ocean surface may experience significant bubble entrainment at any given time.

Part of the error in the data products generated by existing ocean color algorithms can be related to variable concentrations of air bubbles in the near-surface layers; the existing parameterizations of backscattering coefficient in the semi-analytical algorithms for inverting reflectance measurements are most likely biased by the presence of the wind-wave dependent bubble backscatter. In addition, submerged bubbles can influence the validation of atmospheric correction, which is based on the comparison of in situ and satellite derived water-leaving radiances (Terrill et al., 2001).

Stramski (1994) assessed the significance of bubbles for the scattering of light in the ocean in quiescent seas (no breaking waves). He found that even the biologically formed and stabilized bubbles that dominate the bubble population during quiescent sea states can contribute to the total scattering and backscattering coefficients of seawater on the order of 1-10 %.

Zhang et al. (1998) studied the optical properties of bubbles coated with an organic film. The coatings exerted a small influence on total scattering by bubbles larger than 10 μm in size. The estimated effect on backscattering was found as being much more significant: the backscattering efficiency enhanced by as much as a factor of 4 for coated bubbles.

Terrill et al. (2001) performed light scattering calculations for acoustically measured bubble size distributions and size-dependent scattering efficiencies in rough weather conditions. Light scattering from a single air bubble in water was determined from the Mie theory (Chandraesekhar, 1950), which allowed for the solution of the angular distribution of light scattered from the bubble when illuminated by a monochromatic source. The Mie solution to the angular distribution of light scattering from a sphere operates with the radiant energy either completely scattered into all directions, $Q_b$, or the

energy backscattered, $Q_{bb}$ , as a fraction of radiant energy intercepted by the projected area of the sphere. The backscattering efficiency, $Q_{bb}$ , is relevant to the bubble mediated effects on remotely sensed ocean color.

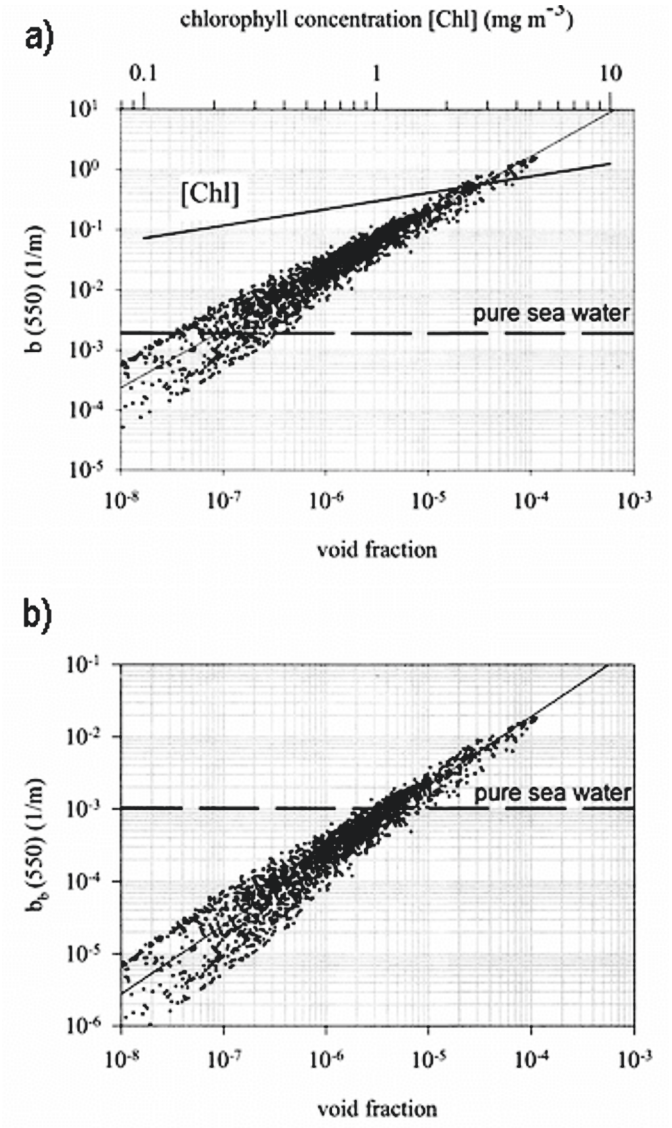


*Figure 7-7*. Scatterplots of (a) $b$ and (b) $b_b$ calculated from acoustic data and Mie theory versus the void fraction of the bubble density. The data suggest that the optical effects of the bubbles on $b_b$, and hence the remote sensing reflectance, will be significant at void fractions above $10^{-6}$. Reference values for pure seawater scatter at 550 nm are from Smith and Baker (1981). The empirical relationship between scatter at 550 nm and [Chl] for case 1 waters presented in plate (a) is taken from Loisel and More (1998). Reproduced from Terrill et al. (2001) by permission from American Geophysical Union.

The bulk scattering coefficient and backscattering coefficient respectively for a given bubble size distribution are calculated in the following way (Terrill et al., 2001):

$$b(bubbles) = \int Q_b \pi r^2 N(r)\, dr, \tag{7.3}$$

$$b_b(bubbles) = \int Q_{bb} \pi r^2 N(r)\, dr, \tag{7.4}$$

where $N(r)$ is the bubble size distribution function (see Section 6.1.3). Equations (7.3) and (7.4) treat the bubbly water as a mixture of random, single-scattering particles. The inherent bulk properties are the sum of the contributions by the individual bubbles (Mobley, 1994).

The range of bubble radii present in the near-surface layer of the ocean defines the limits of the integrals. Small bubbles with radii less than $r$ = 4 μm, however, have practically no contribution to the integrals and thereby to light scattering. Larger bubbles, which do contribute to the light scattering, practically do not depend on the wavelength of photons. Hence, bubble mediated effects on the scattering and backscattering coefficients are expected to have little spectral dependence.

*Figure 7-7* showing scatter-plots of $b$ and $b_b$ versus the void fraction indicates the correspondence between the bubble densities and the bubble contribution to the bulk light scattering properties. The void fraction of entrained air is defined as $\beta = 4/3\pi \int r^3 N(r)\, dr$.

According to *Figure 7-7*, scattering levels span a range of 4-5 decades. Backscatter coefficients $b$ and $b_b$ vary from $10^{-5}$ $m^{-1}$ to over 1 $m^{-1}$ and $10^{-6}$ $m^{-1}$ to over $10^{-2}$ $m^{-1}$, respectively. (Note that this is for only 20 min of observations.) The level of bubble contribution to the total backscatter becomes significant compared to the pure seawater scattering at bubble densities with void fractions above $10^{-6}$.

Terrill et al. (2001) evaluated the contribution of entrained bubbles to optical scattering in the open ocean by comparison with commonly accepted relationships between the light scattering coefficient $b$ and chlorophyll α concentration [Chl] (*Figure 7-7*a). For oligotrophic (Case 1) waters the bubble contribution to total scatter may be a significant fraction of the contribution by chlorophyll. At low chlorophyll concentrations, the errors in the bio-optical interpretation of measured optical properties may be very large due to surface waves breaking. For example, at a void fraction of $10^{-6}$, scatter from bubbles can be almost as large as the scatter by particles at a low chlorophyll [Chl] of 0.02 mg $m^{-3}$, while in more productive waters with [Chl] levels at 0.5 mg $m^{-3}$, scatter from the same bubble density is only 10%

of the scatter from particles (the chlorophyll). For the void fraction of order $10^{-5}$ (note that average void fractions of $10^{-5}$ are observed at wind speed of ~12 $ms^{-1}$), the bubble scatter is about equal with that of chlorophyll for 0.5 mg $m^{-3}$ concentration.

The remote sensing relevant parameter is the backscatter parameter $b_b$. The bubble backscatter exceeds the backscatter for pure water at average void fractions of $10^{-5}$ (*Figure 7-7*b). Terrill et al. (2001) unfortunately do not provide the corresponding backscatter parameter for chlorophyll α. It is therefore impossible to make quantitative estimates of the distortion of color imagery by bubbles from their results. The effect of bubbles is most likely strong under high wind speed conditions, especially if the assumption of Zhang et al. (1998) regarding the role of organic films in coating the bubbles and enhancing their ability to scatter the light is correct.

## 7.3 Marine Chemistry and Biology

Chemical and photochemical reactions in the near-surface layer of the ocean ensure the growth and accumulation of phytoplankton and neuston. Some of the chemical processes in the upper ocean do not require light (*dark* chemical processes). Other chemical processes are excited by chemical absorption of sunlight (photochemical processes). The biological cycling and supply of inorganic and organic elements necessary for phytoplankton growth can depend on both dark chemical and photochemical reactions (Bissett et al., 2001). The cycling of dissolved inorganic macronutrients (nitrogen, phosphorous, silica, etc.) is mostly related to biological activity in the water, with plant growth removal and microbial regeneration, rather than to photochemical reactions. In some situations, mixing processes can lead to substantial redistribution of chemical properties in the upper ocean, overshadowing in situ chemical reactions. The supply of materials such as cobalt, iron, manganese, vitamins and some other essential micronutrients depends on biological, dark-chemical, and photochemical reactions.

The majority of ultraviolet irradiance ($\lambda < 400$ nm) in the sea is absorbed by chromophoric (colored) dissolved organic matter (CDOM). This absorbed energy drives photochemical reactions in the near-surface layer of the ocean. The photochemical reactions include photo-destruction of chemical bonds and fragmentation of complex molecules into smaller compounds; both reactions are of fundamental importance for bio-productivity in the upper ocean (Plane et al., 1997; Bissett et al., 2001). These photochemical reactions can both promote (by breaking down complex molecules and increasing accessibility of organic carbon and some inorganic nutrients) and retard (by damaging cellular constituents) biological processes. In addition, secondary reaction between energized organic molecules and dissolved

oxygen in seawater form highly reactive chemical compounds including hydrogen peroxide and hydroxyl radicals. Another type of secondary reaction occurs between "excited" CDOM and other chemical compounds such as trace metals and sulfur compounds. Since CDOM strongly absorbs the solar radiation in the UV, it regulates the penetration depth of the biologically harmful UV radiation into the ocean (Zepp et al., 1995).

A complex mixture of photochemical reaction products (reactive oxygen species, inorganic nutrients, and trace gases) accumulates in the near-surface layer of the ocean affecting the biological availability of dissolved organic matter as well as the optical properties of surface water. Remotely sensed spectral radiance can therefore provide estimates of CDOM absorption and concentration (Bissett et al., 2001).

An interesting phenomenon, sometimes observed in the upper ocean, is the formation of thin biologically active layers. The layers of phytoplankton, zooplankton, and *marine snow* ranging from a few cm to a few m thick, extending up to many km horizontally, and lasting for days have been reported in estuaries, fjords, and coastal shelves (Donaghay et al., 1992; Rines et al., 2002). These thin layers may have elevated levels of nutrient uptake, increased intensity of competition and predation, higher accumulation of chemical waters and toxins, and higher levels of microbial degradation and remineralization than found in the seawater immediately above and below them (Sieburth and Donaghay 1993). The thin layers also affect optical and acoustical characteristics of the upper ocean (see Section 7.4).

Alldredge et al. (2002) observed thin layers of phytoplankton and marine snow and in the distributions of associated zooplankton in the near-surface layer of a shallow fjord (*Figure 7-8*). Four days before the measurements shown in *Figure 7-8*, strong winds advected a plume of fresher and warmer water (generated by a river) into the experimental area. The wind speed then dropped to 1 - 1.5 m $s^{-1}$.

Profiles of physical and optical structure suggest that the position of thin biota layers was related to the near-surface pycnocline. There are two distinct thin layers in *Figure 7-8*. The thin layer associated with phytoplankton fluorescence is at the bottom of the near-surface mixed layer (~ 3 m depth). There is also a layer of marine snow, an accumulation of microscopic aggregates of detritus particulate matter > 0.5 mm in diameter, which occurred about 1.5 to 2 m below the layer of high fluorescence.

The data shown in *Figure 7-8* was obtained under low wind speed conditions. When wind increased later, the snow layer and phytoplankton layers merged.

There was a pattern of maximum zooplankton abundance in the surface layer and minimum abundance within the marine snow layer. Zooplankton

(measured acoustically) concentrated in the layer from 0 to 5 m, which was above the marine snow layer (there was 4 times more zooplankton at 2 m than within the marine snow layer at 6 m). Total zooplankton abundance below the snow layer was increased compared to the marine snow layer but still at about 1/3 to ½ of the abundance in the near-surface layer.

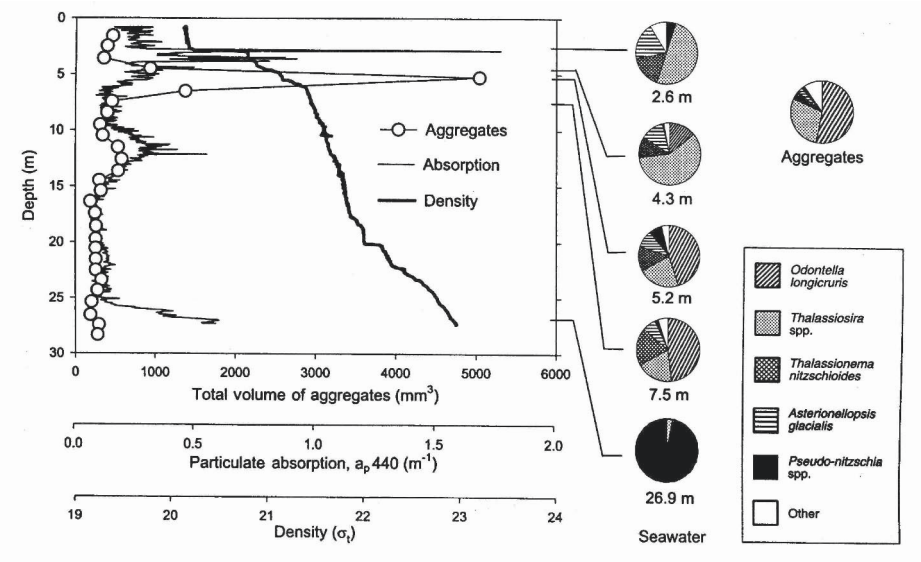


*Figure 7-8*. Thin biological layers as indicated in absorption and by the accumulation of microscopic aggregates in relationship to seawater density ($\sigma_t$), and particulate absorption at 440 nm in a shallow Pacific fjord. The phytoplankton thin layer is observed about 2 m above the marine snow thin layer. Diatom community composition is shown in the pie diagrams. Reproduced from Alldredge et al. (2002) with permission of Inter-Research Science Publisher.

Both the layer of high plankton concentration at ~3 m depth and the marine snow layer at ~5 m depth tended to occur at small discontinuities in the density profile (*Figure 7-8*). Marine snow contains a significant fraction of non-living organic matter. The mechanism by which the non-living matter accumulates into thin layers is supposedly different from that for living organisms (plankton). Plankton presumably concentrates in the turbulent entrainment zone, which is at the bottom of the near-surface mixed layer, while the marine snow aggregates sink until they reach neutral density.

The turbulence measurements made simultaneously with biological and optical observations by Alldredge et al. (2002) revealed relatively low dissipation rates within the marine snow layer, which indicated that the latter is below the actively mixed layer. According to Asper (1987), aggregates of 0.5 mm in diameter sink at rates of 40 to 50 m $d^{-1}$. It would require only a few hours for a 0.5 mm aggregate formed at the surface to reach a depth of 5 m (and much less time for larger, more rapidly sinking aggregates).

Aggregates collide and form larger aggregates. The large aggregates sink until they reach neutral density. If this does not occur, then the thin layer will never form because the aggregates will continue sinking and no accumulation will occur. Attainment of neutral density is a requirement for the persistence of any layer of passively sinking particles. Alldredge and Crocker (1995) proposed that neutral buoyancy of an aggregate sinking from a lower salinity surface layer into a halocline could be attained if some proportion of the aggregate's interstitial volume was occupied by lower-density mucus, which is resistant to the diffusion of salts and water. Interstitial mucus would form from the gelatin and aggregation of polysaccharides exuded by the diatoms in the lower-salinity layer (Alldredge et al., 1993). The sharp salinity gradient in the fjord created the sharp density interfaces that accumulated marine snow in the form of thin layers observed in *Figure 7-8*.

The thin biologically active layers have mostly been observed in the coastal zones of the ocean. Terrestrial runoff and river outflows provide organic rich waters to the coastal ocean. In the open ocean, observations of biological and chemical thin layers near the surface are nevertheless quite rare. The importance and the frequency of occurrence of this phenomenon in the open ocean are therefore largely unknown (which can in part be explained by the absence of proper techniques for the measurement of biochemical parameters near the air-sea interface).

Theoretical studies indicate that thin near-surface layers of biota can change remote sensing reflectance $R_{rs}$ defined by (7.2) up to several percent (Petrenko et al., 1998). The color imagery methods described in Section 7.1.6) are based on the assumption of a vertically homogeneous ocean. Further development of remote sensing techniques may enable identification of thin biological layers in the upper ocean.

## 7.4 Ocean Acoustics

The sea surface is an important element of the acoustic environment of the ocean (Brekhovskich and Lysanov, 1978). However, in contrast to other types of ocean boundaries such as the sea bottom or ice cover, the free sea surface by itself does not absorb acoustical energy—it just scatters it. The scattering of sound at the wave disturbed surface leads to space and time fluctuations of the propagating sound; as a result, spectral and statistical characteristics of the sound change. Sound scattered from the ocean surface may represent a serious disturbance to the effectiveness of hydro-acoustical systems.

In addition to scatter from the ocean surface, the acoustic signal may scatter due to near-surface turbulence, microstructure, and fine structure. Sound refraction due to internal waves in the near-surface thermocline or

rain-formed halocline may lead to a distortion of the acoustic signal and to its intensity fluctuations. In the process of sound scattering by the fine structure and microstructure, the contribution of temperature inhomogeneities usually dominates over the effect of salinity and velocity fluctuations. The sound speed dependence on salinity and velocity are second order effects in the ocean compared to that of temperature.

Thin, concentrated layers of phytoplankton and zooplankton sometimes occurring in the near-surface layer of the ocean (see Section 7.3) can effectively scatter and absorb acoustic signals. Air bubbles also substantially contribute to sound scatter, absorption, and noise generation. High concentration of bubbles is observed in the near-surface layer of the ocean below breaking waves and in ship wakes. The actions of wave breaking and bubble production generate easily detectable ambient noise that has been used as a signal to determine variables such as wind speed and rain rate. This noise can strongly degrade the performance of Navy systems that attempt to detect unnatural acoustic signatures or map objects using acoustics.

### 7.4.1 Effects of stratification

Under light winds, fine structure and microstructure can develop in the near-surface layer of the ocean due to solar warming and rainfalls. Local gradients of temperature and salinity may have significant magnitudes (see Chapter 4). In such a medium, sound speed may fluctuate along the acoustic path. Orbital motions due to surface wave action cause undulation of inhomogeneities in temperature and salinity, which cause phase changes in the sound propagation near the surface. The near-surface stratification is believed to affect the horizontal propagation more than vertical propagation of sound in the ocean.

The speed of sound at 10 dbar pressure, 36 psu salinity, and 19°C is $c$ = 1520 m $s^{-1}$. The fluctuation of the speed of sound due to temperature and salinity change is respectively as follows

$$\left(\Delta c/\Delta T\right)_{S=36\,psu,T=19^{o}C} = 2.83 \text{ m s}^{-1} \text{ }^{o}\text{C}^{-1}, \tag{7.5}$$

$$\left(\Delta c/\Delta S\right)_{S=36\,psu,T=19^{o}C} = 1.13 \text{ m s}^{-1} \text{ psu}^{-1} \tag{7.6}$$

The maximum temperature difference in the diurnal thermocline of 5°C corresponds to a 14 m $s^{-1}$ difference in the sound speed. Statistics of near-surface salinity anomalies in the ocean are, however, poorly known. During rainfalls, sea surface salinity depressions of a few psu have been reported

(Paulson and Lagerloef, 1993; Soloviev and Lukas, 1997a), which corresponds to a few m $s^{-1}$ difference in the speed of sound.

Significant surface salinity (as well as temperature) changes have been observed near icebergs. Lugt and Uglimchius (1964) estimated that the sound propagating horizontally through the cool and fresh water in the vicinity of an iceberg could refract up to about $18^{o}$.

### 7.4.2 Biological scattering layers

Objects containing internal gas volumes may resonate at certain frequencies and produce very intense scatter of sound. Thin, concentrated layers of phytoplankton and zooplankton in the near-surface layer have episodically been observed in the coastal ocean (Section 7.3). These thin layers range from only a few tens of centimeters to a few meters in vertical extent (Cowles *et al.* 1998, Hanson and Donaghay 1998). Biota in these layers is often highly concentrated. Layers can be continuous horizontally for at least kilometers and persistent for days to weeks, strongly affecting the optical and acoustical properties of the water column (Donaghay and Osborn, 1997, Rines et al*.,* 2002).

*Figure 7-9* reveals the persistence of a thin layer of zooplankton (green line, about 65 dB) over a 48-hour period. The thin layer was close to the thermocline. During the night hours it was masked by the vertical migration of zooplankton .(Presumption is that feeding is the driving force for these migrations.)morning hours when the convection is inhibited due to the absorption of solar radiation. Note that the near surface layer of intense scatter (red regions in *Figure 7-9*) is due to bubbles generated in the process of wave breaking.Under high wind speed conditions, wind-wave turbulence destroys biological scattering layers in the near-surface layer.

The frequency of the appearance of sound scattering biological layers in the near-surface layer of the open ocean is practically unknown. In the open ocean, these layers can supposedly appear during algae blooms. One of the authors of this book (AVS) observed a thin layer of biota in the North Atlantic Ocean ($39^{o}$N, $20^{o}$W) during a calm weather period in July 1982. This layer produced an appreciable disturbance to the electromagnetic velocity sensor (this type of sensor is described in Chapter 3) during measurements with a free-rising profiler. The layer was first detected at about 20 m depth and was gradually moving towards to the ocean surface.

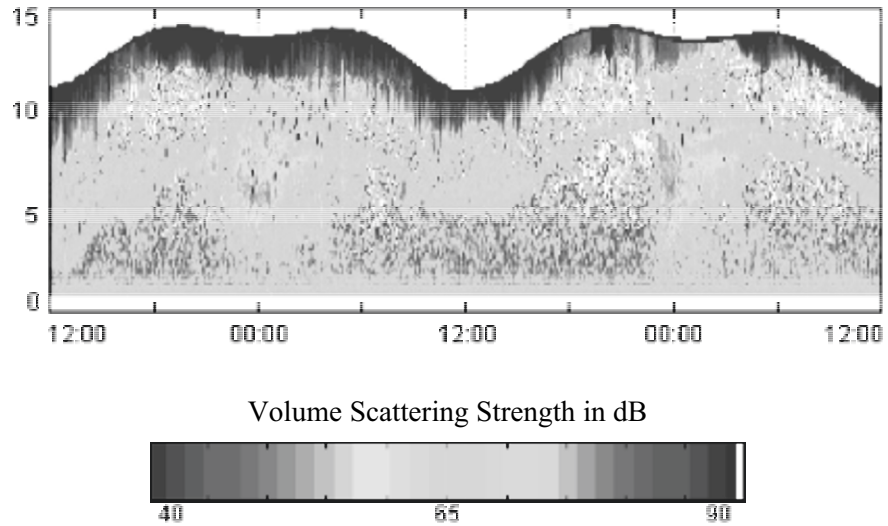


*Figure 7-9*. An example of a thin layer of zooplankton, as visualized with acoustical scattering at 265 KHz in East Sound, WA. Here: X axis = time, 24 - 26 June 1998, Y axis = depth, in meters, bottom referenced. Courtesy of D.V. Holliday (http.//www.gso.uri.edu/criticalscales/about/index.html). More details are in McManus et al. (2003).

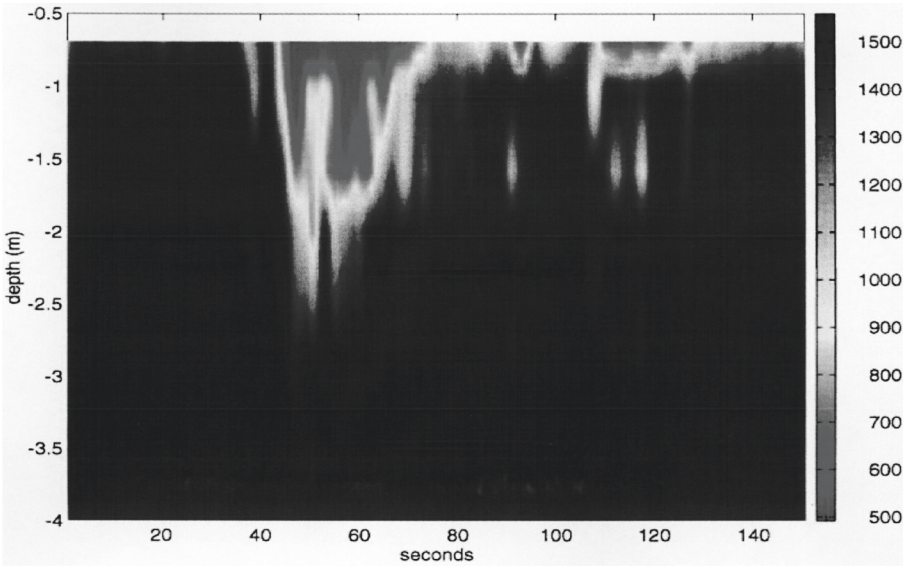


*Figure 7-10*. The response of the sound-speed field to a single large wave-breaking event. A region of very low sound speed exists near the surface for about half a minute, while the reductions are smaller but dissipate more quickly at depth. Orbital motions of the waves advecting the bubble cloud past the sensors produce high-frequency oscillations visible in this figure. Reproduced with permission from Eric Terrill and W. Kendall Melville, The Journal of the Acoustical Society of America, 102, 2607 (1997). © 1997 Acoustical Society of America.

The nature of the influence on the electromagnetic velocity sensor by the individual types of plankton is not completely clear. The interference signal from plankton was of significantly higher frequency than that from the turbulent velocity signal. The plankton layer did not affect the microstructure conductivity sensor signal. Professor Percy Donaghay (URI) (private communication) suggested that this disturbance might be caused by plankton species accumulating iron (magnetic material).

Most information about the thin layers of biota comes from a single fjord in the Pacific Northwest (the same fjord where the data illustrated in *Figure 7-9* are taken). Evidence of thin layers has also been reported in Monterey Bay, in the South Atlantic Bight, as well as on the shelf off west Florida, Oregon, and southern California

### 7.4.3 Effects of bubbles on sound propagation

Wave breaking at the surface of the ocean entrains air and produces bubbles. Raindrops can also generate bubbles. Bubbles represent a great disturbance to sound propagation in the ocean. Populated with bubbles, the near-surface layer under high wind speed conditions represents a two-phase medium, which significantly modifies the phase speed (*Figure 7-10*), scattering, and absorption of acoustic waves (Farmer and Lemon, 1984). Intense near-surface bubble layers formed during heavy rains may also effectively absorb sound energy (see Section 7.4.6). Bubbles also change the value of the buoyancy frequency in the near-surface layer of the ocean, which can result in the so-called *bubble mode* of the internal wave field (Grimshaw and Khusnutdinova, 2004).

The big difference in density and compressibility between an air bubble and the surrounding water provides a mechanism for bubbles to both generate and interact with acoustic (pressure) waves. Bubbles resonate at characteristic frequencies that are determined by their radius. The lowest eigenfrequency of a single bubble oscillation is known from the work of Minnaert (1933):

$$\omega_0 = \frac{1}{r_0}\left(\frac{3\gamma p_0}{\rho}\right)^{1/2}, \tag{7.7}$$

where $\rho$ is the water density, $\gamma = c_p / c_v \approx 1.4$ is the polytropic index for air ($c_p$ and $c_v$ are the specific heat capacity of water under constant pressure and volume respectively), and $p_0$ is the ambient pressure.

Resonant bubbles cause especially strong scatter and absorption effects. For acoustic frequencies at or near its lower resonant frequency, a bubble has

a scattering cross section up to three orders of magnitude larger than that of a solid particle of the same dimension. For acoustic frequencies much less than the resonant frequencies of the bubbles, the speed of sound depends solely on the volume of air present in the water. At higher frequencies, bubble resonances cause the sound speed to become dependent on the bubble size distribution.

A complex dispersion relationship for linear wave propagation and attenuation through a polydisperse (*i.e.*, of different sizes) population of bubbles is as follows (Commander and Prosperetti, 1989):

$$\frac{c^2}{c_m^2} = 1 + 4\pi c^2 \int_0^\infty \frac{r_0 N(r_0)\, dr_0}{\omega_0^2 - \omega^2 + 2ib\omega}, \tag{7.8}$$

where $c$ is the bubble-free sound speed, $c_m$ is the complex sound speed in the mixture, $\omega_0$ is the radian resonant frequency of a bubble of radius $r_0$ defined from equation (7.7), $\omega$ is the radian frequency of the sound, $b$ is the damping coefficient, and $N(r_0)d\,r_0$ is the number of bubbles per unit volume in the range ($r_0$, $r_0 + d\,r_0$).

The real and imaginary parts of the complex sound speed dispersion relationship (7.8) describe the phase speed and attenuation of sound propagating through the medium, respectively. This bubble acoustics model compares well with a number of historical measurements that contain a wide range of radii at void fractions up to 1% (Commander and Prosperetti, 1989). Relationship (7.8) may no longer be valid at higher void fractions because of the effect of multiple scattering ignored in the model. High void fractions of the order of 10% that exist directly beneath breaking waves in the ocean quickly degas over timescales of a wave period or less to bubble densities suitable for acoustic sizing techniques (the latter neglect multiple scattering). The typical mean void fractions in the upper ocean, depending on depth, range from $10^{-7}$ to $10^{-4}$ in winds of 10-13 m s$^{-1}$ (*Table 6.3*).

*Figure 7-11* demonstrates the attenuation and phase speed as a function of frequency calculated from (7.8) for two different idealized bubble size distributions. These two distributions (*Figure 7-11*a) are a power law with a slope of 3.5 (solid line) between $r_0$ = 30 and 600 μm and a narrow distribution centered at 60-μm radius (dashed line). The number densities of the bubble populations are normalized by setting void fractions for both distributions to $\beta = 1.91 \times 10^{-7}$.

*Figure 7-11*b shows the resulting frequency-dependent attenuation curves. (Note that the $x$ axis in subplots *b* and *c* is the frequency rather than the bubble radius as in subplot *a*.) The narrow size distribution (dashed line) results in large attenuation in a narrow frequency band centered at the resonant frequency of a 60 μm bubble. The power-law size distribution

demonstrates attenuation across a wider frequency band. This is consistent with the wider range of radii present in the power-law size distribution.

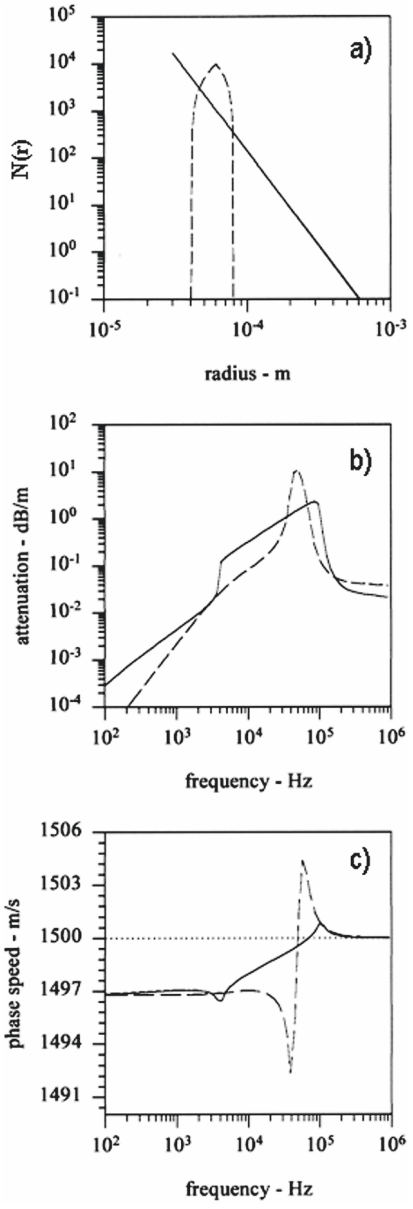


*Figure 7-11.* (a) Two sample bubble size distributions and the corresponding (b) frequency-dependent attenuation and (c) dispersion curves calculated from (7.8). Solid line represents a power law size distribution with a slope of 3.5 (between radiuses $r_0$ = 30 and 600 μm); dashed line corresponds to a narrow distribution centered at $r_0$ = 60 μm. Reproduced from Terrill and Melville (2001) by permission from American Meteorological Society.

It is remarkable that there are three different regimes for the phase speed that are common to both distributions (*Figure 7-11*c). The phase speed becomes non-dispersive at frequencies much lower than the resonant frequencies of the bubbles. The phase speed also asymptotes to the value for bubble-free water at frequencies much greater than the resonant frequencies of the bubbles. Strong frequency dependence is observed in the intermediate region where the dispersion varies according to the range of bubble sizes and the shape of the size distributions.

*Figure 7-10* shows the sound-speed field disturbed by a large bubble cloud from a wave-breaking event. For this particular event, the sound speed was dramatically reduced at the surface (to approximately 500 m $s^{-1}$) for 30-40 s. At a depth of a few meters, the sound speed was reduced by only about 100 m $s^{-1}$ and for a shorter time period. Short-lived events like this one are primarily responsible for injecting air into the water column and lowering the mean sound speed.

The average sound-speed reduction is at a maximum near the ocean surface and monotonically decreases with depth (because the average bubble concentration does so). The flux of bubbles into the surface waters apparently increases as the incidence of wave breaking increases, further reducing the sound speed in the near-surface layer.

In order to describe the depth dependence of the layer of reduced sound speed, Terrill and Melville (1997) calculated a contour representing the depth, $z_{0.99c}$, at which the mean sound speed is 99% of the bubble-free value. They derived a linear relationship between the depth of the reduced sound-speed layer and the significant wave height $H_s$:

$$z_{0.99c} = 0.26H_s + 0.31, \tag{7.9}$$

with the correlation coefficient, $r^2 = 0.97$. Since the significant wave height is approximately four times the RMS wave amplitude (Komen et al, 1994), the results suggest that the 99% contour depth has a characteristic length that scales with the RMS wave amplitude.

Significant wave height and the wind speed have often been used for obtaining correlations with bubble-driven acoustic phenomena such as backscatter and ambient noise, though with limited success. The correlation between $z_{0.99C_0}$ and significant wave height in the experiment of Terrill and Melville (1997) was high, though under certain conditions it could be disturbed. Presence of swell can significantly alter the measured significant wave height only contributing second-order effects to the wave breaking, or the acoustically active portion of the wave field (Felizardo and Melville, 1995). Some other factors can also affect the wave breaking process. For example, Terrill and Melville (1997) report the effect of strong surface

currents (due to the passage of an eddy that spun off the nearby Gulf Stream) on the small-scale wave breaking and the sound speed pattern in the near-surface layer of the ocean.

### 7.4.4 Acoustic technique for measuring bubble size distributions

Vagle and Farmer (1998) published a fine review of acoustical methods to measure bubble size distributions in the near-surface layer of the ocean including the acoustical resonator (Breitz and Medwin, 1989; Farmer et al., 1998; Su et al., 1994), acoustic pulse propagation sensor (Lamarre and Melville, 1994; Terrill and Melville, 2000), backscatter measurement with multiple- and single-frequency sonars (Thorpe, 1982; Vagle and Farmer, 1992). We discuss here in detail only the acoustic pulse propagation approach.

The sound speed, $c_m$, in the low frequency limit of dispersion relationship (7.8) is a function of the density $\rho_m$ and compressibility $K_m$ of the bubble mixture, and is determined from the formula,

$$c_m = \left(\rho_m K_m\right)^{-1/2} \tag{7.10}$$

where $\rho_m = \beta\rho_a + \left(1-\beta\right)\rho_w$, and $K_m = \beta K_a + \left(1-\beta\right)K_w$. $K_a$ and $K_w$ are the compressiblity of air and water, respectively. In the low frequency limit, the sound speed is simply a function of the void fraction $\beta$.

Asymptotic relationship (7.10) has provided the basis for the development of a single frequency sound velocimeter for measurement of entrained air beneath breaking waves. Lamarre and Melville (1995) measured propagation times of a narrowband acoustic pulse across a fixed path length, which provided a direct measurement of the sound speed and determination of the void fraction. This method, however, does not provide information about the size distribution of bubbles constituting the void fraction.

In order to calculate the size distribution of bubbles, the dispersion relationship (7.8) should be inverted, which requires sound velocity measurement in a range of frequencies. Terrill and Melville (2000) developed a broadband sound velocimeter that allowed the simultaneous measurement of sound speed and attenuation over a wide range of frequencies. Their velocimeter measured the attenuation and dispersion of a broadband acoustic pulse over frequencies ranging from 4 to 100 kHz across a fixed pathlength using a two-transducer system. The acoustic data were inverted to derive the bubble size distributions over bubble radii in the range from 30 μm to 800 μm.

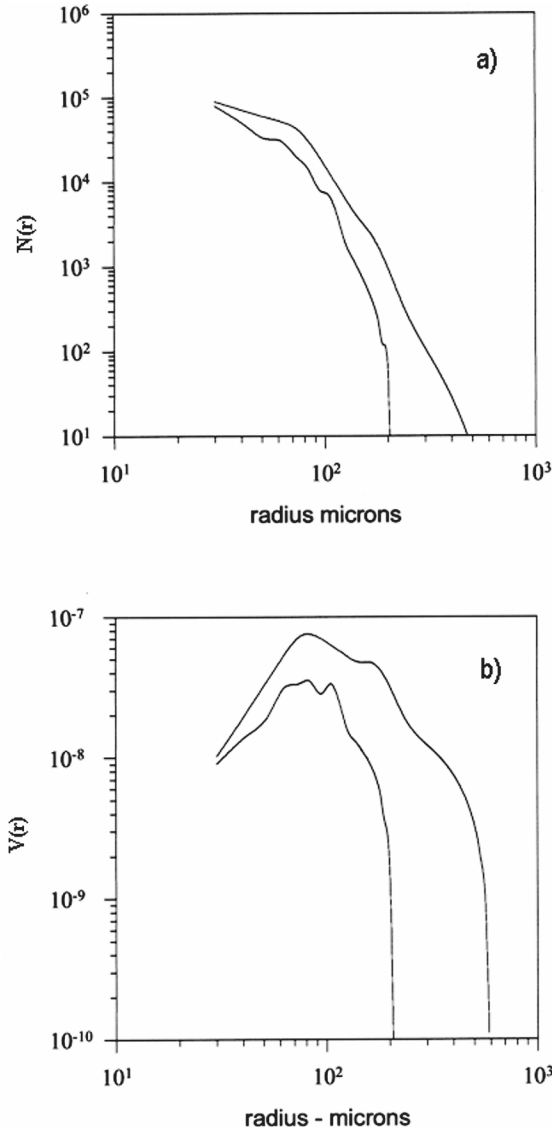


*Figure 7-12*. (a) The mean bubble size distributions and (b) the resulting mean volume scaled distributions the two measurement locations in the laboratory tank with different wave-breaking intensity. Each mean is calculated using $O(100)$ size distributions that were inverted on a per-ping basis for $t$ = 18–42 s and $t$ = 31–50 s at the two locations. The upper solid line is the 1 m downstream location and the lower solid line is the 2 m downstream location in the wave tank. The volume-scaled distribution reveals that bubbles with radii ranging from 60–90 μm (resonant frequencies of 36–54 kHz) contribute most to the void fraction at these locations. Note the similarities in numbers of small bubbles and the differences for the larger bubbles for the two measurement locations. This is attributed to the larger bubbles rising out of solution faster. Reproduced from Terrill and Melville (2000) by permission from American Meteorological Society.

The results of laboratory tests of the Terrill and Melville (2000) method are shown in *Figure 7-12*. Bubbles with radii in the range of 60–90 μm contribute most to the total void fraction. This bubble size range corresponds to a peak in the acoustic attenuation at frequencies of 36–54 kHz. Similar numbers of bubbles exist at the smaller radii; significant differences in the number of larger bubbles are, however, observed. The rise velocity of the bubbles is proportional to the square of the radius; as a result, the larger bubbles reach the surface at a significantly faster rate. The terminal rise velocity of an air bubble (see Section 6.1.2) with a 30 μm radius is 0.0008 $ms^{-1}$, while the rise velocity for an 800 μm air bubble is approximately 0.3 m $s^{-1}$, an increase of over 350 times. This provides a plausible explanation of the difference for large bubbles.

### 7.4.5 Ambient noise produced by bubbles

The fundamental problem of identifying an underwater sound source by its acoustical signature requires knowledge of the ambient noise spectra under different hydrometeorological conditions. The first studies of ambient noise were undertaken in relation to the development of underwater acoustics after World War II, revealing the dependence of ambient noise on the wave height and wind velocity (Knudsen et al., 1948). Since that time many efforts have been made to develop qualitative and quantitative descriptions of the phenomenon.

Wind is indirectly responsible for the ambient noise generation, namely via breaking wind waves (Medwin and Beaky, 1989). The fraction of dissipated wave energy radiated as sound waves is of the order $10^{-8}$ (Loewen and Melville, 1991a). Two approaches to understanding the nature of the sound radiated by oscillating air-bubbles in a bubble cloud under breaking waves have been formulated. Medwin and Daniel (1990) and Loewen and Melville (1991b) assume that individual bubbles radiate sound, while Carey and Bradley (1985) and Prosperetti (1985) focus on collective oscillations.

The bubbles with radii from 30 μm to 1000 μm, which are less than the Hinze scale (see Section 6.1.3 for definition), are believed to dominate the spectrum of bubbles produced by breaking waves. According to (7.7) a bubble with a radius within this size interval must have a natural frequency within 3-100 kHz. The available data, however, indicates that the ambient noise produced by breaking waves has somewhat lower frequencies. The collective oscillation mode can explain the observed shifting of the ambient noise to lower frequencies compared to the noise that could be produced by individual bubbles. Tkalich and Chan (2002) developed a theoretical model for the prediction of ambient noise level due to collective oscillations of air bubbles under breaking wind waves. The model predicts the sound intensity

spectra from wind speed or wave height of breaking waves as an environmental input. The model is also able to explain the main observed features of ambient noise produced by breaking waves, including the slope and frequency range of the spectra.

Crum (1995) and Kolaini et al. (1995) suggested that the bubbles could change their oscillation mode from individual to collective in a transition from a less violent to more violent type of wave breaking. The question of which mode, individual or collective, is most important in the process of noise generation has not yet been answered.

### 7.4.6 Ambient noise produced by rain

Rainfall generates sounds in the ocean. The underwater sound of rain is the ensemble of individual raindrop splashes on the water surface. These splashes represent a loud and distinctive sound, allowing detection, classification, and measurement of rainfall parameters in the ocean (Shaw et al., 1978; Nystuen et al, 2000).

The acoustic sensor (hydrophone) collects data from a relatively large area on the ocean surface, which is proportional to the depth of the hydrophone. Since the area of averaging for an acoustic sensor can be orders of magnitude larger than for other types of rain gauges, much higher temporal resolution of the rainfall measurement can be achieved. The acoustic measurement of rainfall with a 5 s temporal resolution has revealed instantaneous rainrates exceeding 1000 mm/hr under conditions of an extremely strong rain event (>100 mm/hr, according to conventional rain gages). These extreme rain rates could not be detected with conventional rain gages typically using the longer temporal resolutions (Nystuen and Amitai, 2003).

Acoustic analysis of underwater sound applied to identifying and quantifying geophysical processes consists of two steps (Nystuen et al., 2000): 1) The source of sound is identified from the spectral characteristics of the sound; 2) The geophysical quantity of interest is quantified.

Distinctive spectral shapes for different geophysical or anthropogenic noise sources aid the first step. *Figure 7-13* shows examples of the sound spectra generated by geophysical sources during an experiment in the South China Sea. The spectral shape of wind-generated sound is attributed to breaking wind waves (see Section 7.4.7). A relatively uniform negative spectral slope from a peak near 500 Hz to over 25 kHz characterizes the wind-generated sound. It is remarkable that five minutes after the start of an extreme rainfall event (rainfall rate 200 mm $h^{-1}$), the sound level at 40 kHz dropped 15 dB relative to the start of the downpour. This is presumably because of sound absorption by the intense bubble layer formed due to heavy

rain. Farmer and Lemon (1984) observed the deviations at frequencies over 10 kHz that were caused by acoustic absorption by bubbles (but for sea-state conditions with $U_{10} > 10$ m s$^{1}$ with high levels of wave breaking).

Two spectral features characterize the acoustic signal from rain (*Figure 7-13*):

1) Light rain or drizzle (typically containing only small drops) produces a broad peak in the sound spectrum between 13 and 25 kHz. Under high wind speed conditions this signal may not be detected above the background of wind-induced noise.
2) Rainfalls generate a loud sound in the near-surface layer of the ocean. The spectrum of sound produced by the raindrops exceeding 2 mm in diameter is a broadband one (2–50 kHz).

Sound levels in the surface layer of the ocean due to precipitation are much higher relative to the wind-generated sound level. Moreover, the variance of sound intensity within different acoustic frequency bands can be used as an aid to classify rainfall type and wind wave conditions (Nystuen and Selsor, 1997).

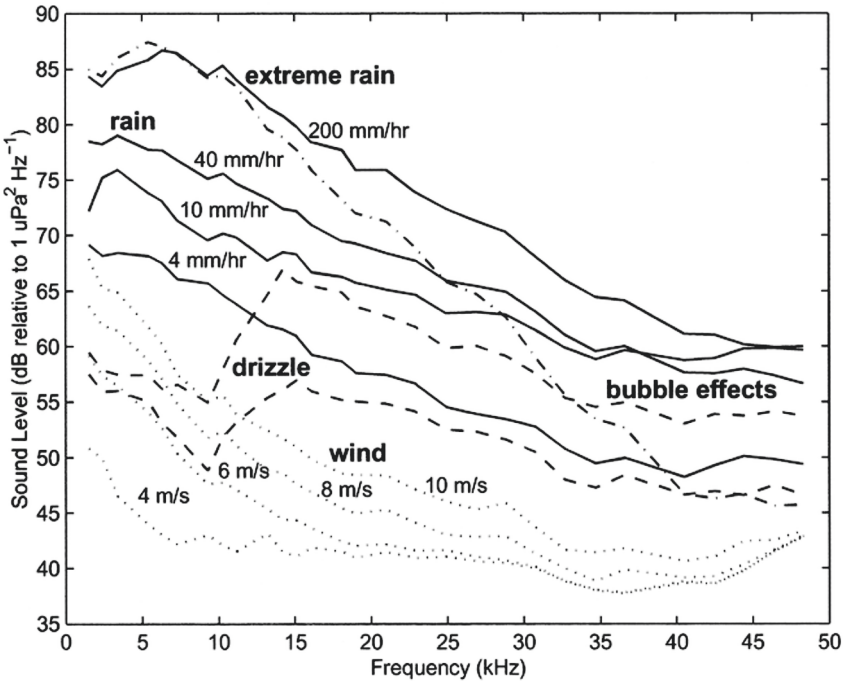


*Figure 7-13*. Examples of the sound spectra generated by geophysical sources during an experiment in the South China Sea: Periods of wind only (dotted line), drizzle (dashed line), rain (solid line), and extreme rain (top solid line). Five minutes after the start of an extreme rain, the sound levels above 20 kHz dropped to substantially lower values (dash–dot line), which is an indication of bubble layer formation by the rainfall. Reproduced from Nystuen et al. (2000) by permission from American Meteorological Society.

In addition to the known geophysical sounds created by air-sea interaction (wind, precipitation, subsurface bubbles), the ocean is also full of natural and anthropogenic noise sources. Shipping is one the most common anthropogenic noises in the ocean. Human activities other than shipping can also create loud sounds. Marine mammals produce significant acoustic signals. In addition, snapping shrimps can produce a very loud, broadband sound that can dominate the underwater sound field. Fortunately, these shrimp live on hard substrata in shallow tropical water and are not present in the open ocean. There are also unidentified sources of sound in the ocean. All together, 7.1% of the noise recorded by Nystuen et al. (2000) in the South China Sea was contaminated by unrelated sounds. Removal of contaminating sounds is an important part of identifying acoustical signals produced by wind, precipitation, and sub-surface bubbles. Fortunately, the spectral properties of these sounds are usually distinctively different from the other (contaminating) sounds.

For a sound source at the free ocean surface modeled as an acoustic dipole radiating sound energy downward in a $\cos^2\theta$ pattern, the intensity of sound at some depth $h$ below the surface is expressed as follows (Nystuen, 2001):

$$I(h) = \int I_0 \cos^2 \text{atten}(p)\, dA\,, \tag{7.11}$$

where $I_0$ is the sound intensity at the surface, $\theta$ is the zenith angle, and atten($p$) describes the attenuation due to geometric spreading and absorption along the acoustic path $p$.

Absorption of sound in the ocean depends on its frequency. The frequency dependence varies with the water properties (salinity, pressure, chemical composition) and the bubble density. Large diurnal warming events and freshwater flux due to rain can produce appreciable stratification in the near-surface layer of the ocean (Chapter 4). If the speed of sound varies along the path, acoustic refraction occurs. For short distances, acoustic refraction is a minor effect; as a result, a $p^{-2}$ (spherical) law can well approximate the spreading of sound. Vagle et al. (1990) found that even in strongly refracting environments only a minor correction is required, since most of the acoustic energy arrives at steep angles.

For straight acoustic paths equation (7.11) can be rewritten in the following way:

$$I(h) = \int I_0 \cos^2\theta \frac{\exp(-\alpha p)}{4\pi\rho^2} dA\,, \tag{7.12}$$

where α is the sound absorption coefficient. According to Medwin and Clay (1998), the absorption coefficient of sound in the ocean is a strong function of frequency, ranging from 0.5 dB $km^{-1}$ at 1 kHz to 10 dB $km^{-1}$ at 40 kHz. It is much higher in seawater than in freshwater. (The change of $\alpha$ for a small salinity change at a fixed frequency in the range from 0.1 to 100 kHz can be approximated as $\Delta\alpha/\alpha \approx \Delta S/S$.)

For acoustic rain estimation, it is important to know the effective listening area of the hydrophone. Rainfall measurements are needed on relatively large temporal or spatial scales, because rainfall is inhomogeneous. Larger inherent sampling area should produce better mean rainfall statistics. The sound spectrum of any single raindrop is variable in spectral character (except for small raindrops). The inversion techniques aimed at determination of rain parameters from its acoustic signature are based on the mean spectrum. It is therefore important to integrate over many discrete events (individual splashes) to obtain a smooth mean spectrum.

Equation (7.12) can provide an estimate for the effective listening area. Nystuen (2000) concluded from the analysis of (7.12) that for a uniform source of sound on the ocean surface (and absorption neglected), 50% of the sound energy arrives from an area equal to $\pi h^2$ over the hydrophone, while 90% of the sound energy arrives from an area equal to $\pi(3h)^2$, where $h$ is the depth of the hydrophone.

### 7.4.7 Passive acoustic monitoring of sea surface processes

Several air-sea interaction processes are responsible for the production and modification of underwater sound in the ocean as discussed in the previous section. Passive monitoring of the underwater sound field thus offers a means to make measurements of these processes. In particular, breaking wind waves and precipitation are the natural sources of underwater sound in the frequency range from 500 Hz to 50 kHz. Unique spectral characteristics of these sound sources allow them to be identified and then quantified (Nystuen, 2001). Distortion of these acoustic signals by sub-surface ambient bubbles in principle permits the detection and quantification of the near-surface bubbles, which are a potential indicator of the gas transfer velocity and sea state condition.

Since the resonant frequency depends on the bubble radius, it is important to know the bubble size distribution and its dependence on depth and environmental conditions, especially on surface wave parameters. The surface wave characteristics depend on several factors including wind speed and its history, fetch etc. For the interpretation of acoustical data, it is important to know the spectral and other statistical characteristics of surface waves. The dissipation of wave energy into turbulence appears to be a

convenient integral parameter for characterizing the bubble and related sound generation (Gemmrich and Farmer, 1999).

As stated in Section 7.4.6, inversion of the underwater ambient sound field consists of identifying the source of the sound, and then quantifying it. Nystuen and Selsor (1997) identify the following four ocean surface features producing distinctive features in the sound spectrum from 1-50 kHz: wind, drizzle, heavy rain and ambient bubbles present (*Figure 7-13*). Once the acoustic classification is done, several algorithms are available to quantify wind speed and precipitation.

*a) Acoustical wind speed measurements*

Vagle et al. (1990) developed an empirical algorithm for the acoustic quantification of wind speed using 8 kHz data from the North Atlantic Ocean. The sound level is empirically related to 10 m height wind speed by the following formula:

$$U_{10} = \left(10^{SL_8/20} + 104.3\right)/53.91, \tag{7.13}$$

where $SL_8$ is the sound level at 8 kHz, and $U_{10}$ is the 10 m wind speed. This method is valid for wind speeds $U_{10} > 2.2$ m s$^{-1}$ (no wind-wave breaking and practically no acoustic signature of the wind field is available in the ocean under very low wind speed conditions). The algorithm, however, is not capable of providing accurate wind speed data under rainy conditions

*b) Acoustic rain rate measurements*

Several types of acoustic rainfall rate algorithms are available in the literature. An acoustic estimate of rainfall rate can be made from an empirical relationship between the sound level within a particular frequency band and the rainfall rate. For instance, Nystuen (2001) derived the following relationships:

$$\log_{10} P = \left(SPL_{2-5} - 51.5\right)/17 \tag{7.14}$$

$$\log_{10} P = \left(SPL_{4-10} - 50\right)/17 \tag{7.15}$$

that were tuned to match the total rainfall accumulation from a disdrometer. Here $SPL_{2\text{-}5}$ and $SPL_{4\text{-}10}$ are the sound levels in the frequency bands 2–5 kHz and 4–10 kHz in decibels relative to 1 $\mu$Pa$^2$ Hz$^{-1}$, respectively. While these

relationships are easy to apply, they lead to outliers and also may overestimate rainfall when the rain contains relatively more large drops.

*Figure 7-14* shows a comparison of wind speed observations from the buoy anemometer and from the acoustic data. The acoustic wind speed is in reasonable agreement with the anemometer record, although the acoustic estimates appear to be biased high above 7 m $s^{-1}$.

Since raindrops of different sizes have distinctive acoustic signatures underwater (*Table 7-1*), the underwater sound can be decomposed into components associated with each drop size. The sound field can be "inverted" to estimate the drop size distribution in the rain (Nystuen, 2001).

*Table 7-1*. Raindrop size categories for acoustic estimation. The raindrop sizes are identified by different physical mechanisms associated with the drop splashes (Medwin et al. 1992; Nystuen, 1996). (After Nystuen, 2001.)

| Drop size | Diameter, mm | Sound source | Frequency range, kHz | Splash character |
|---|---|---|---|---|
| Tiny | <0.8 | Silent | | Gentle |
| Small | 0.8-1.2 | Loud bubble | 13-25 | Gentle, with bubble every splash |
| Medium | 1.2-2.0 | Weak impact | 1-30 | Gentle, no bubbles |
| Large | 2.0-3.5 | Impact<br>Loud bubble | 1-35<br>2-35 | Turbulent irregular<br>bubble entrainment |
| Very large | >3.5 | Loud impact<br>Loud bubbles | 1-50 kHz<br>1-50 kHz | Turbulent irregular<br>bubble entrainment<br>penetrating jet |

According to equation (7.12), the observed sound intensity at the hydrophone is associated with the sound intensity at the surface, modified by attenuation. The sound intensity, $I_0$, at the surface can be related to the drop size distribution in the rain as follows (Nystuen, 2001):

$$I_0(f) = \int A(D,f) V_T(D) N(D) dD \tag{7.16}$$

where $f$ is frequency, $A(D, f)$ is the transfer function describing the radiated sound as a function of frequency for a given drop size $D$, $V_T$ is the terminal velocity of the drop, and $N(D)$ is the drop size distribution in the rain. A discrete version of this equation is given by

$$\vec{I}_0(f) = \boldsymbol{A}(D,f) \cdot \boldsymbol{D}_{\boldsymbol{RD}}(D) \tag{7.17}$$

where $\boldsymbol{D_{RD}}$ is the drop rate density, $\boldsymbol{D_{RD}} = V_T \cdot N(D)$. Since the inversion matrix $\boldsymbol{A}$ is supposed to be known, using singular value decomposition Equation (7.17) can be inverted as follows

$$\boldsymbol{A} = \vec{U}\Lambda\vec{V}^T, \tag{7.18}$$

$$\boldsymbol{D_{RD}} = \boldsymbol{V}\left[\Lambda^{-1}\left(\boldsymbol{U}^T\boldsymbol{I_0}\right)\right], \tag{7.19}$$

which provides an estimate of the drop size distribution in the rain. Once a drop size distribution is derived, the rain rate is calculated by integrating over all drop sizes.

The sound spectrum produced by different sizes of droplets has some specific features (*Figure 7-15*), which makes a straightforward application of the inversion technique unrealistic. Nystuen (2001) proposed a constrained inversion technique to address this problem. It takes into account the following spectral features of the rain-generated sound:

1) The sound of drizzle, which has a peak at 13–25-kHz (*Figure 7-13*), is only detected when raindrops larger than 0.8-mm diameter are present in the rain, because drops smaller than 0.8 mm do not produce a detectable sound signal and cannot be measured acoustically. This sets the lower size limit for small raindrops. The upper size limit for small raindrops is set to 1.2 mm (see *Table 7-1*) based on laboratory studies.
2) Medium drop splashes, which do not generate bubbles (*Table 7-1*), are relatively quiet. Whenever the rain contains drops larger than 2.0 mm, the sound levels below 10 kHz are much increased. Thus, the lower size limit for large raindrops is set at 2.0 mm. *Table 7-1* therefore defines the medium drop size to be 1.2–2.0 mm diameter. The small drops are so much louder than the medium drops from 13 to 30 kHz that the sound signature for the medium drops had to be interpolated through this frequency range. The signal from the medium drops is small, though it appears to be louder than expected from laboratory studies. Presumably, this sound is from the impact of the drop onto the water surface and thereby is a broadband signal.
3) Large drops sound loud underwater. The sound generated by any individual large drop is, however, at the very narrow bands associated with any bubbles that are generated plus a broadband signal from the impact. According to laboratory results, larger drops produce, on average, larger bubbles. The largest bubbles tend to be loudest, producing a spectral peak in the mean spectrum at the

resonance frequency of these sound-dominating bubble sizes. The "large" drops produce the spectral peak between 2 and 5 kHz, while the peak for the very large drop category extends down to 1–2 kHz.

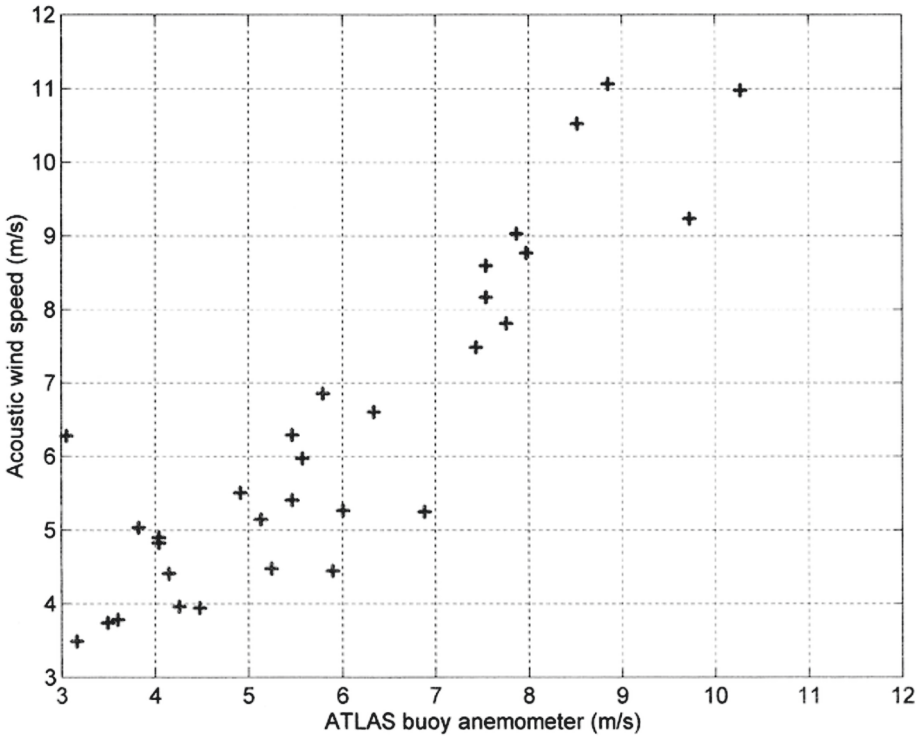


*Figure 7-14*. Wind speed measured by the anemometer at 4 m height versus the acoustic estimate of wind speed from equation (7.13). Reproduced from Nystuen et al. (2000) by permission from American Meteorological Society.

The sound energy radiated by very large raindrops is relatively large compared to their water volume. In order to address this problem, the Nystuen (2001) constrained algorithm performs an iterative inversion. If the number of very large drops per square meter of sea surface per second appears to be greater than a chosen value, 10 $m^{-2}$ $s^{-1}$, then very large drops are assumed to be present. If very large drops are not present, the second iteration of the inversion is repeated with the very large drop population set to zero.

Since the medium raindrops have a weak acoustic signal, another constraint is imposed. The medium raindrops are difficult to hear, especially on the background of very large raindrops. Unrealistic values of the medium drop category produced by inversion algorithms are unfortunately common. Medium-sized raindrops, however, often comprise a significant part of the

liquid content of rainfall; accurate estimates of their populations are very important. In order to address this problem, Nystuen's (2001) algorithm assumes that if very large raindrops are detected within the rain, then the medium drops that might be present cannot be heard. In the case of very large drops present, the algorithm therefore makes no attempt to acoustically invert for the medium drop population; instead, the medium drop population is set based on the small drop population count. If during the initial iteration very large raindrops are not detected, then the next iteration acoustic inversion estimate of the medium drop population is obtained from the singular value decomposition with the very large drop population set to zero. The resulting drop size distribution is also additionally constrained to be monotonically decreasing with drop size above the medium drop size category. In addition, the medium drop count is not allowed to be greater than twice the small drop population. Though the last two constraints are artificial, they are nevertheless consistent with most of the observed drop size distributions recorded by a conventional disdrometer.

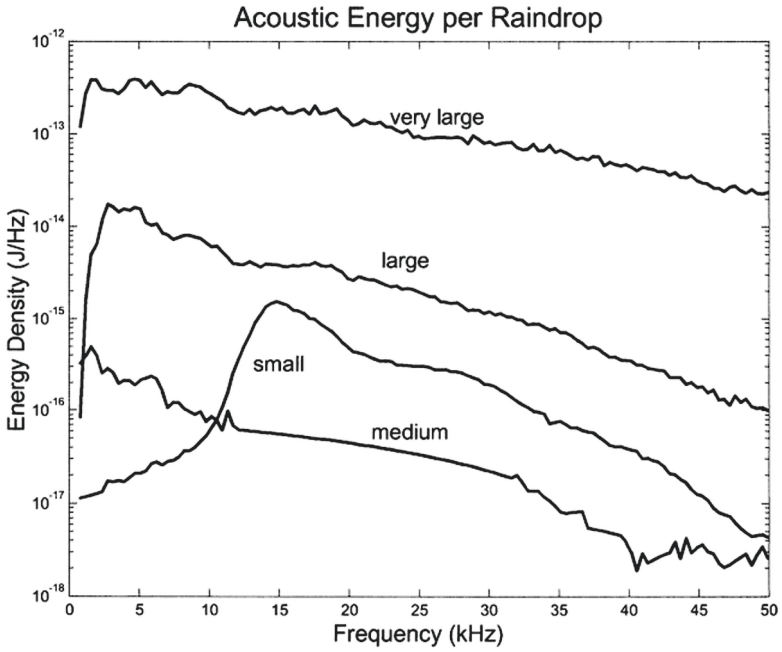


*Figure 7-15*. The acoustic signature of individual drop size categories. This forms the basis for the inversion of the sound field to obtain the drop size distribution. Reproduced from Nystuen (2001) by permission from American Meteorological Society.

*Figure 7-16* demonstrates the performance of the inversion to obtain rainfall rate with a limited data set obtained in a mangrove-lined pond near Miami. For this data set, the acoustic rain accumulation total is 900 mm,

which compares well to 969 mm from the disdrometer, 963 mm from the capacitance rain gauge, and 1031 mm from the optical rain gauge. Though there are some outliers, the overall correlation between the logarithms of the disdrometer rainfall rate and the acoustic inversion rainfall rate is 0.90.

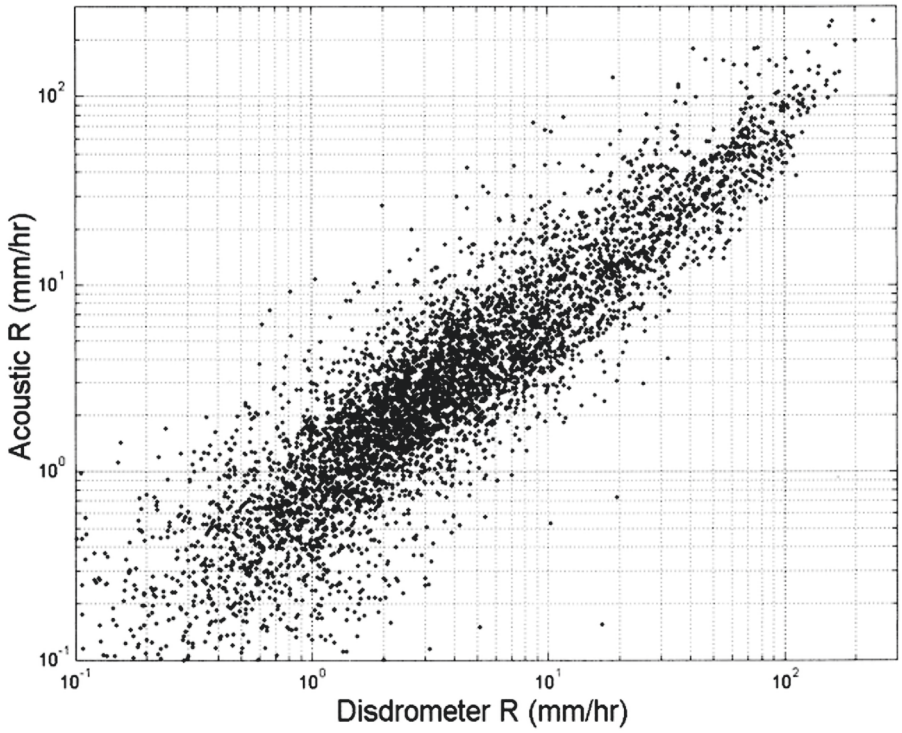


*Figure 7-16*. Acoustic rainfall rate versus disdrometer rainfall rate for over 6000 minutes of rainfall from Apr to Dec 1994. Reproduced from Nystuen (2001) by permission from American Meteorological Society.

The acoustic inversion based on equation (7.19) and the additional constraints mentioned above represents an improvement over the direct acoustic methods (7.14) and (7.15) because it makes an optimal use of the available information. The inversion method has the additional advantage of being used to calculate other rainfall parameters such as the size distribution of rain droplets. This technique, however, is still pending validation for oceanic conditions.

*c) Acoustic classification of rainfall type*

Black et al. (1997) proposed an acoustic classification of the two general rainfall types, convective and stratiform, based on the physics of sound generation. Small raindrops (0.8 μm – 1.1 μm diameter) effectively

produce sound in the high-frequency band; while, the rain containing large raindrops (diameter >2.0 mm) produces sound in both frequency bands. The ratio of the sound intensity in a high frequency band (10–30 kHz) to a lower frequency band (4–10 kHz) can therefore serve as a characteristic of the raindrop distribution and, hence, of the rainfall type.

Atlas et al. (1999) extended the Black et al. (1997) acoustic classification of rainfall types by using additional features of the sound field. They proposed to link systematic variations in the raindrop size distribution to four different rainfall categories: convective, transition convective, and two types of stratiform rain (type 1 and type 2).

## 7.5 Air-Sea Gas Exchange

The flux of gases like carbon dioxide across the air-sea interface is an important part of the global climate and its changes (Tans et al., 1990). Substantial efforts have been made toward parameterizing the air-sea gas exchange. Modeling and parameterization of the interfacial gas transport is a turbulent boundary layer problem, which is inherently linked to the physics of the near-surface layer of the ocean (Soloviev and Schlüssel, 2001).

### 7.5.1 Bulk-flux formulation

Woolf and Thorpe (1991) proposed to extend bulk-flux formulation (1.45) for the net air-sea gas flux, $G_0$ as follows:

$$G_0 = K\,[C_w - S_\mu p_a (1 + \Delta_e)], \tag{7.20}$$

where

$$K = K_{\text{int}} + K_b, \tag{7.21}$$

$K_{\text{int}}$ is the interfacial (direct) transfer velocity, $K_b$ is the bubble-mediated gas transfer velocity, $p_a$ is the gas partial pressure in the air, $S_\mu$ is the solubility of the gas, $C_w$ is its concentration in the bulk of the water (according to Henry law $C_w = p_w S_\mu$), and $\Delta_e$ is the equilibrium supersaturation defined as the fractional increase in partial pressure of the gas in the water caused by bubble overpressure and dissolution. If the supersaturation term is neglected, (7.20) reduces to a well-known parameterization formula for the air-sea gas exchange (1.45).

Woolf and Thorpe (1991) parameterized the equilibrium supersaturation term as follows:

$$\Delta_e^{\,i} \approx 0.01(U/U_i)^2, \tag{7.22}$$

where $U_i$ is the wind speed for a particular gas at which the equilibrium supersaturation is 1% (nitrogen, 7.2 $ms^{-1}$; oxygen, 9 $ms^{-1}$; argon, 9.6 $ms^{-1}$; carbon dioxide, 49 $ms^{-1}$). According to (7.22), the equilibrium supersaturation may reach several percent for poorly soluble gases such as oxygen, but is relatively small for more soluble gases, including carbon dioxide. Note that the presence of the supersaturation term in the bulk-flux parameterization implies an asymmetry between gas evasion and invasion.

The supersaturation term $\Delta_e$ in (7.20) might be even more important for air-sea gas exchange than Woolf and Thorpe (1991) initially assumed. In a laboratory experiment, Leifler et al. (2000) found that small secondary bubbles produced by the bubble-burst mechanism (see Section 6.2.2) may result in dramatically increased small-bubble concentrations in the near-surface layer of the ocean. Very small bubbles dissolve rapidly, contributing to the supersaturation of the water adjacent to whitecaps with atmospheric gases. Moreover, anomalous concentrations of small bubbles in the near-surface layer of the ocean are difficult to detect because the measurements are typically made at a depth exceeding the wave height and then extrapolated to the surface.

The gas transfer velocity, $K$, entering bulk-flux formula (7.20) mainly depends on local air-sea interactions. It can be partitioned into interfacial ($K_{\text{int}}$) and bubble mediated ($K_b$) gas transfer velocities. Though most of the known parameterizations for $K$ tend to converge to a single curve at moderate wind speed conditions, they differ greatly under low and high wind speed conditions. Under low wind speed conditions the air-sea gas transfer velocity depends to some extent on the air-sea heat (buoyancy) flux, while under high wind speed conditions, it depends on surface wave breaking and bubbles.

The gas partial pressure in the atmosphere $p_a$ is formed as a result of global atmospheric processes though inhomogeneity may exist in space and time. Two other parameters entering (7.20), the gas concentration in water ($C_w$) and the gas solubility $S_\mu$, are dependent on the temperature and salinity. Under conditions of low wind speed, $C_w$ and $S_\mu$ may vary because of restratification of the surface mixed layer due to diurnal warming and/or precipitation effects.

Soloviev and Schlüssel (2002) suggested that modeling of the air-sea gas exchange on global scales should include the following components:

1) Interfacial component
2) Bubble-mediated component
3) Mixed-layer component
4) Remote sensing component.

Discussion of these components based on the physics of the turbulent boundary layer and the properties of the sea surface is given below.

### 7.5.2 Interfacial component

Monahan and Torgersen (1990) proposed the following partitioning of the interfacial air-sea gas transfer velocity:

$$K_{\text{int}} = K_t(1 - W_c) + K_w W_c, \tag{7.23}$$

where $K_t$ is the interfacial transfer velocity everywhere except in the interior of whitecaps, $K_w$ is the interfacial transfer velocity associated with the turbulent diffusion of gas via the top of the bubble plume (*i.e.,* through the whitecap), and $W_c$ is the fraction of the sea surface covered by oceanic whitecaps.

Chanson (1996) summarizing studies of the air-bubble entrainment in free-surface turbulent shear flow concluded that the diffusion of air bubbles within the flow is primarily an advective-diffusive process. The bubble-mediated gas transport is therefore assumed to be a more effective mechanism than the turbulent diffusion of gas via the top of the bubble plume (*i.e.* $K_b >> K_w W_c$). Except in very high winds, $W_c << 1$ and thus $K_t(1 - W_c) \approx K_t$, formula (7.23) simply reduces to: $K_{\text{int}} \approx K_t$

The gas transfer velocity $K_t$ is associated with patches of turbulence in the near-surface layer of the ocean generated by shear, surface waves, or convective instability. Since turbulence is inhibited near interfaces, viscous, thermal, and diffusion molecular boundary layers develop near the air-sea interface. Conceptual models of the aqueous molecular sublayers can be conditionally divided onto two classes (see Chapter 2): surface renewal and boundary layer models. In renewal models, the properties of molecular sublayers are parameterized via the surface renewal time scale. The renewal time is then associated with the environmental parameters causing hydrodynamic instabilities and thus controlling the properties of molecular sublayers. Boundary layer models are based on the quasi-stationary representation of turbulent processes. The classical work of Kim et al. (1971) demonstrated that the turbulent momentum transport and production in the wall layer takes place intermittently in time and space through small-scale bursting motions. This work provided strong evidence in favor of the renewal concept for the analysis of near-wall molecular sublayers. The discussion in the literature about which approach, renewal or boundary layer, better represents the aqueous molecular sublayers adjacent to the air-sea interface still continues (Fairall, 2000). In fact, the analogy between the

molecular sublayers at the free ocean surface and at a rigid wall may not be complete. Here, we explore only the application of the surface renewal approach for modeling the interfacial component of gas exchange.

The renewal of the ocean surface water can occur because of convective, shear or surface wave instabilities. Portions of fluid are ejected from the molecular boundary layers into deeper layers, thus providing the renewal of the surface water. The renewal rate therefore determines the interfacial fluxes. Csanady (1990) linked the surface renewal with the presence of flow convergences. The surface convergence zones are usually relatively narrow and quasi-periodic in space and/or time. The so-called "rollers" (or micro-scale wave breakings) provide maximum flow convergence.

Modeling surface renewal is based on the relationships connecting the renewal rate to the environmental parameters such as friction velocity, heat fluxes etc. Surface films can influence the surface renewal process, especially under low wind speed conditions (Frew, 1997).

The thermal molecular sublayer of the ocean (cool skin) does not substantially influence the heat exchange between ocean and atmosphere except in some extreme conditions (Paulson and Simpson, 1981). At the same time, air-sea gas transport does substantially depend on parameters of the oceanic diffusion sublayer. Due to low gas diffusivity in water compared to the rather high gas diffusivity in air, the diffusion sublayer provides the main resistance to the interfacial atmosphere-ocean gas transport (Bolin, 1960).

Despite different roles in the heat and gas exchange at the air-sea interface, the thermal and diffusion sublayers are governed by similar laws. Soloviev and Schlüssel (1994) proposed relating the temperature difference across the thermal sublayer (cool skin of the ocean), $\Delta T$, to the interfacial (direct) gas transfer velocity ($K_t$) (Section 2.3). The more readily available cool skin data are then used for an adjustment of the gas transfer parameterization. A further extension of the renewal model includes the effects of solar radiation and rainfall on the molecular boundary layers (Sections 2.4 and 2.5).

Jaehne et al. (1987) proposed the controlled heat flux method for estimating the gas transfer velocity. However, according to the laboratory test of Richardson et al. (2000), this method exhibited significant differences between the heat and gas exchange data for large upward net-flux conditions. The version of this method recently developed by the same team of investigators but employing the properties of the "natural" cool skin on the ocean surface, which is basically the Soloviev and Schlüssel (1994) approach, performs very well (Garbe et al., 2002).

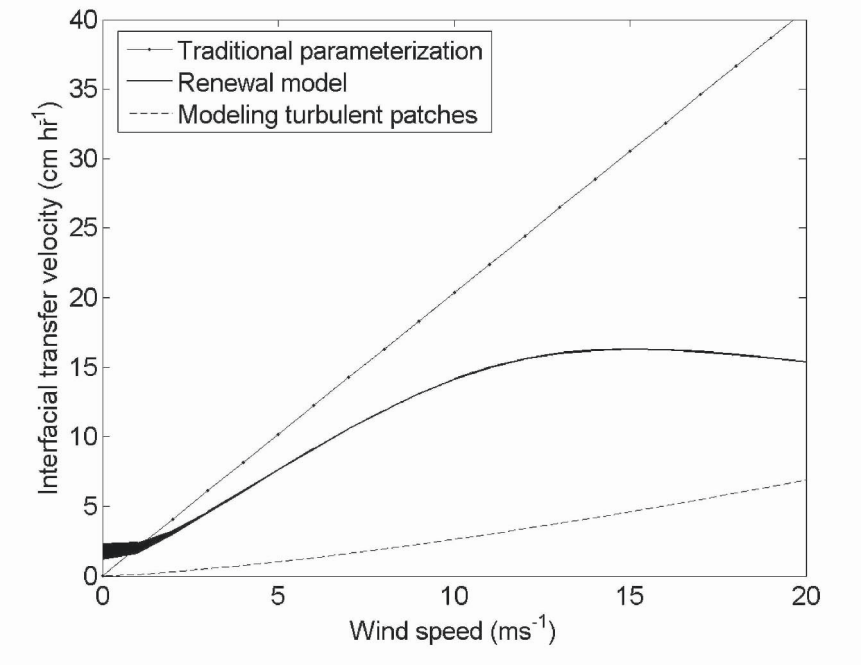


*Figure 7-17*. Comparison of the renewal model with the traditional parameterization of interfacial gas transfer $K = const$. The calculation is made for $Q_0$ = 80 Wm$^{-2}$, and $Q_L$ = 40 Wm$^{-2}$. The shadowed area is bounded by model curves calculated for $Q_R$ = 0 Wm$^{-2}$ (upper curve) and $Q_R$ = 1000 Wm$^{-2}$ (lower curve). The model of interfacial gas transfer by wave-breaking turbulence patches (Woolf, 1995) is shown by dashes.

The renewal model does not explicitly include the effect of turbulent patches in the upper ocean due to surface wave breaking. However, this can be estimated using the relationship (Kitaigorodskii and Donelan, 1984; Dickey et al., 1984):

$$K_{wp} \approx B_1 \left[ \varepsilon_0 \nu Sc^{-2} \right]^{1/4}, \tag{7.24}$$

where $B_1$ is a dimensionless coefficient, and $\varepsilon_0$ is the near-surface dissipation rate of the turbulent kinetic energy. Woolf (1995) developed a model of gas transfer by wave-breaking turbulent patches that resulted in relationship

$$K_{wp} = 2.5 \times 10^{-4} U_{10}^{39/28} (\nu Sc^{-2} h_{w-s})^{1/4}, \tag{7.25}$$

where $h_{w-s}$ is the depth of the wave-enhanced turbulent layer.

*Figure 7-17* shows the results of modeling surface renewal in comparison with the traditional parameterization of interfacial air-sea gas exchange. The contribution of wave-breaking patches to the interfacial gas flux represented by formula (7.25) for $h_{w-s}$ = 1 m is shown by dashes. Differences between the traditional parameterization and the renewal model are observed under low and high wind speed conditions. In contrast to the traditional parameterization, the renewal model predicts non-zero interfacial gas transfer velocities under calm weather conditions (depending on the heat flux) and smaller transfer velocities at high wind speeds.

For highly soluble gases (like $CO_2$) the interfacial gas exchange may exceed the bubble-mediated gas exchange even under relatively high wind speed conditions and is therefore believed to contribute substantially to the global air-sea gas exchange (Woolf and Thorpe, 1991; Soloviev and Schlüssel, 2001).

### 7.5.3 Bubble-mediated component

Bubbles generated by wave breaking can significantly enhance the air-sea gas exchange under high wind speed conditions, especially for low solubility gases. The asymmetry between evasion and invasion, solubility dependence on sea surface temperature and salinity, and equilibrium supersaturation caused by bubble gas transfer make the problem of parameterization of the bubble-mediated gas transfer quite complicated.

Several studies have been performed in this area (see reviews in Woolf and Thorpe (1991), Keeling (1993), and Asher and Wanninkhof, 1998). The study of Merlivat et al. (1993) resulted in the following parameterization for the bubble mediated gas transfer

$$K_b = W_c \left( a_1 / \alpha + b_1 \alpha^{-m} Sc^{-n'} \right) \tag{7.26}$$

where $\alpha$ is the Ostwald solubility coefficient (dimensionless), $a_1$ and $b_1$ are empirical coefficients (which, strictly speaking, may be different for evasion and invasion), and $W_c$ the fractional area coverage of actively breaking waves defined by (6.14). Note that (7.26) is specific to evasion when the air-water concentration is not near equilibrium (*i.e.*, $C_w / (S_\mu p_a) - 1 >> \Delta$).

Woolf (1997) proposed parameterizing the bubble-mediated gas transfer based on the asymptotes at large and small values of the solubility coefficient $\alpha$ as follows:

$$K_b = b W_c / \alpha \left[ 1 + \left( 14 \alpha Sc^{-0.5} \right)^{-1/1.2} \right]^{-1.2} \tag{7.27}$$

where $W_c$ is the whitecap coverage, and $b$ is an empirical constant. The empirical constants entering (7.27) have been determined only for clean bubbles.

The Merlivat et al. (1993) parameterization is defined with empirical coefficients determined for dirty bubbles by Asher and Wanninkhof (1998):

$$K_b = W_c \left( -37\alpha^{-1} + 6120\alpha^{-0.37} Sc^{-0.18} \right). \tag{7.28}$$

The asymmetry between evasion and invasion can be accounted for with the equilibrium supersaturation term (see equation (7.20)). According to (7.22) the effect of equilibrium supersaturation is more important for less soluble gases like $O_2$ and less important for highly soluble gases like $CO_2$.

### 7.5.4 Comparison with field data

Examples of modeling the $CO_2$ exchange for *GasEx-98* cruise legs 2 and 3 are shown in *Figure 7-18*. The model includes the interfacial component described in Section 2.4 and the bubble-mediated component represented by equation (7.28). The model is forced with the air-sea heat and momentum fluxes measured by Edson et al. (1999).

Moderate wind speed conditions prevailed during *GasEx-98* with several storms and a few periods of calm weather in leg 2 and with several calm weather periods and a few cases of high wind speeds in leg 3. The contribution of bubble-mediated transport achieves peak values of 20% during leg 2 and 10% during leg 3. The averaged contribution of bubbles into the $CO_2$ exchange appears to be relatively small for both legs: It does not exceed several percent for leg 2 and a few percent for leg 3.

The effect of solar radiation on the $CO_2$ transfer velocity is even smaller. Its relative contribution achieves peak values of about 25% in a few cases during leg 2 and leg 3. This is only for short time periods, a few midday hours. The average effect of solar radiation on the $CO_2$ exchange is far less than 1% for both cruises.

In *Figure 7-19*, the contributions of the interfacial and bubble-mediated components to the $CO_2$ air-sea exchange are shown as a function of the wind speed. The data are from modeling the $CO_2$ exchange in the *GasEx-98* leg 2 and leg 3 (see *Figure 7-18*). The scatter of the gas-exchange velocity under low wind speed conditions is because of its dependence on the buoyancy flux across the air-sea interface. Note that in the wind speed range 5 to 15 $ms^{-1}$, the total gas exchange exhibits near linear wind speed dependence. Under very high wind speeds (>17 $ms^{-1}$), the bubble-mediated component, which is proportional to the cube of wind speed, dominates.

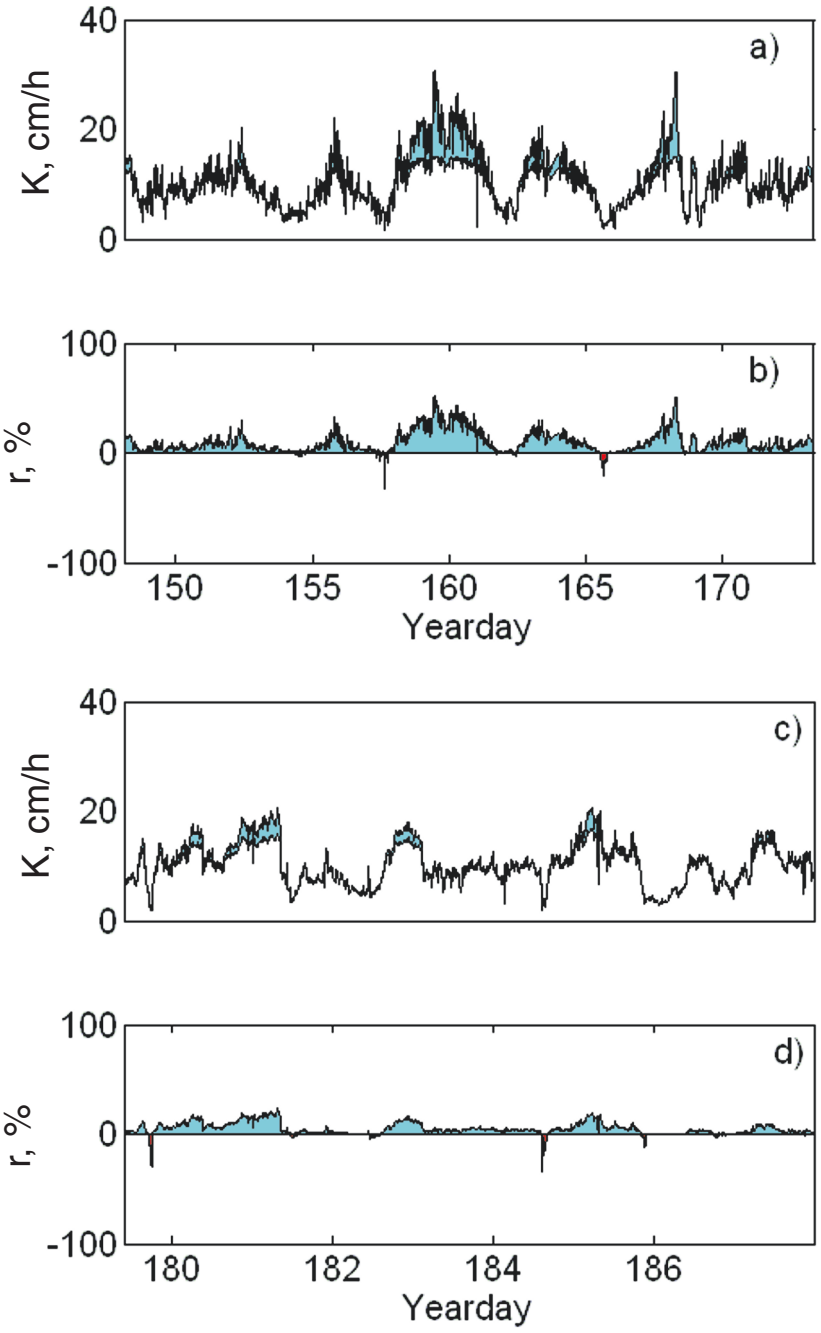


*Figure 7-18*. Modeling of the $CO_2$ transfer coefficient ($K$) and its relative change ($r$) due to bubbles (enhancement) and due to solar radiation (suppression) for *GasEx-98* leg 2 (a, b) and leg 3 (c, d). Bubble contribution is highlighted in blue; the solar radiation effect is given in red.

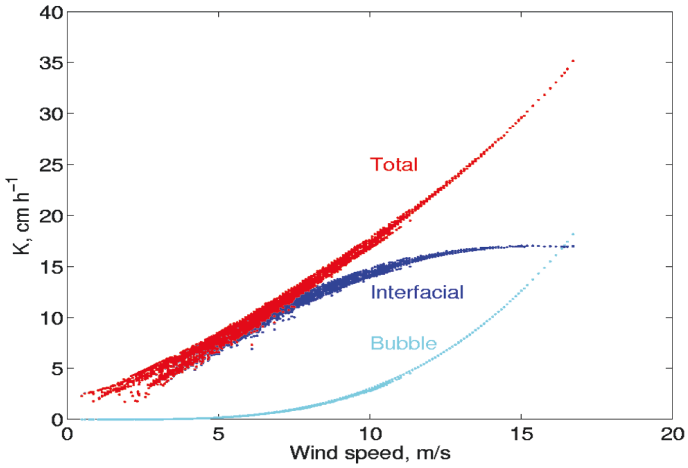


*Figure 7-19*. Contributions of interfacial and bubble mediated components to the total $CO_2$ air-sea transfer velocity at different wind speeds.

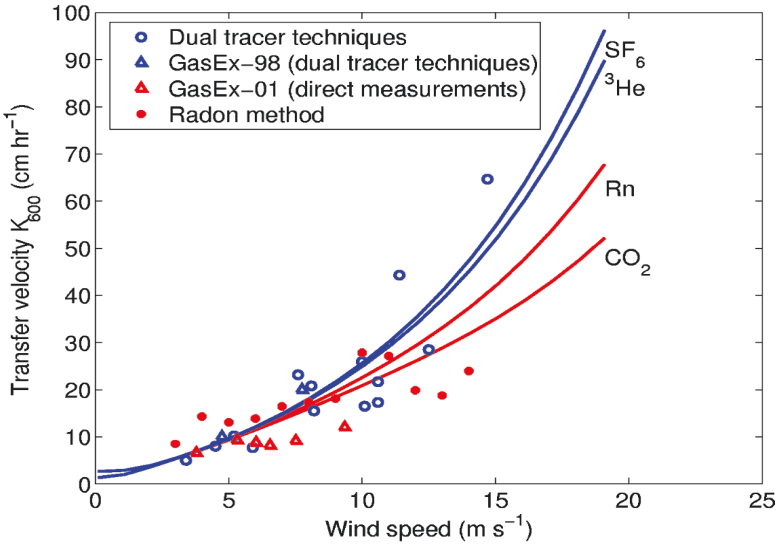


*Figure 7-20*. Summary of the gas transfer results over the ocean using the dual tracer and radon techniques as well as direct measurements. The continuous lines are the theoretical relationships for the gases involved in the corresponding measurement techniques ($SF_6$ and $^3$He, Rn). The theoretical dependence for $CO_2$ is also shown. The dual tracer data are from Wanninkhof et al. (1997), Asher and Wanninkhof (1998), and Nichtingale et al. (2000). The radon data are from Peng et al. (1974), Peng et al. (1979), and Cember (1985). The *GasEx-98* data are from Wanninkhof and McGillis (1999), and the *GasEx-01* data are from Hare et al. (2004). To illustrate the effect of surface heat flux and insolation on the air-sea gas exchange at low wind speed the model curves for all gases are calculated for $Q_0$ = 130 W m$^{-2}$, $Q_E$ = 60 W m$^{-2}$ and for two values of $I_\Sigma$: 0 Wm$^{-2}$ and 1000 Wm$^{-2}$ (see also *Figure 7-17*).

*Figure 7-20* shows a summary of gas transfer results over the ocean. The theoretical dependencies correspond to the sum of an interfacial component (renewal model described in Section 2.3.2), gas transfer by wave-breaking turbulent patches described by (7.25), and a bubble-mediated component described by equation (7.28).

Both theoretical relationships and field data are color-coded. Blue color indicates low solubility gases ($SF_6$ and $^3He$); red color indicates high solubility gases (Rn and $CO_2$). Under high wind speed conditions, the theoretical dependencies are quite different depending on gas solubility but are consistent with the available data.

The model shown in *Figure 7-20* is able to explain the difference between the Wanninkhof (1992) and Liss and Merlivat (1986) empirical parameterizations for gas transfer velocity. The former was derived from dual tracer data (using low solubility gases $SF_6$ and $^3He$), while the latter was derived from a laboratory experiment with a highly soluble gas ($CO_2$).

### 7.5.5 Fine thermohaline structure and gas exchange

The near-surface layer is not always well mixed. Appreciable temperature, and salinity differences can develop in the upper few meters of the ocean caused by the diurnal cycle and precipitation effects under low wind speed conditions. The temperature difference across the diurnal thermocline can reach as much as several $^oC$ and the salinity difference across the rain-formed halocline as much as several psu (see Chapter 4 for details). Dependence of the $CO_2$ solubility on temperature suggests that diurnal warming may shift the concentration difference between atmosphere and uppermost layer of the sea towards lower or negative $CO_2$ uptake by the ocean.

In addition, the presence of the diurnal thermocline (or a rain-formed halocline) may cause depletion or accumulation of gas in the near-surface layer. This effect, however, is not expected to change appreciably the $CO_2$ concentration in uppermost layer of the ocean due to the large buffer capacity of the carbonate system in seawater (but may be significant for other gases like $O_2$).

In the commonly used parameterization formulation for the net air-sea gas flux (1.45), the gas partial pressure $p_w$ in the bulk of water is usually taken from the ship's intake or from CTD measurements at roughly 3-5 m depth. Thermosalinograph or CTD data from the same depth are also usually used to calculate the gas solubility, $S_\mu$, which is a function of temperature and salinity. As a result, the large diurnal warming events, which are localized in the upper few meters of the ocean, are often undetected during shipboard surveys and unaccounted for when quantifying air-sea gas fluxes.

Measuring high-resolution $pCO_2$ profiles near the surface is still a challenge. At the same time, some of the dissolved oxygen sensor designs are able to resolve fine near-surface features associated with the diurnal cycle under low wind speed conditions. Atkinson et al. (1987) and Soloviev et al. (2002) reported significant $O_2$ concentration differences associated with the shallow mixed layer; an example is shown in *Figure 7-21*. This measurement was made during *GasEx-98* leg 1 with a sensor system mounted in front of the bow of the R/V *Ronald Brown*. The bow sensors were "scanning" the upper 3 m of the ocean because of the ship pitching. The vertical profile of temperature reveals an exceptionally strong diurnal thermocline in the upper 0.5 m. There is also a salinity increase and dissolved oxygen (DO) decrease. The turbulent mixing below the diurnal mixed layer is suppressed by the stable stratification. Excess salinity is accumulated within the diurnal mixed layer because of surface evaporation. A similar mechanism results in the depletion of $O_2$ within the diurnal mixed layer. (During this observation, the DO in the bulk of the mixed layer water was 117% of the saturation level.) The temperature and salinity dependence of $O_2$ solubility is also important.

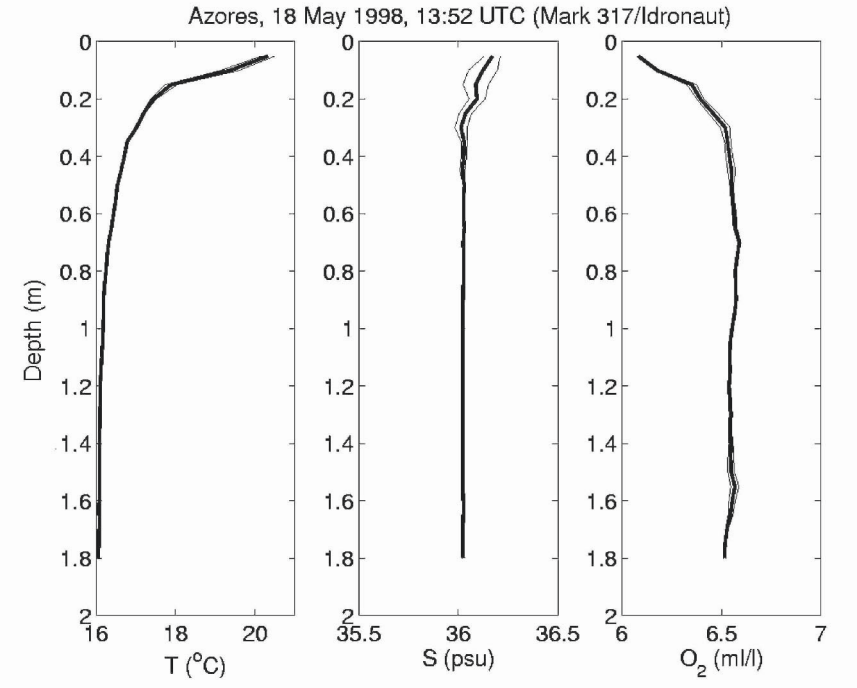


*Figure 7-21*. Vertical profiles of temperature (*T*), salinity (*S*), and dissolved oxygen concentration $O_2$ during a strong diurnal warming event observed in the North Atlantic during *GasEx-98 leg 1* (low wind conditions). The vertical profiles are calculated by averaging bow sensor records within 5 cm bins over 1 minute. Reproduced from Soloviev et al. (2002) by permission of American Geophysical Union.

Soloviev et al. (2002) evaluated the effect of mixed layer dynamics on the air-sea $O_2$ exchange during *GasEx-98* leg 2. This study employed a 1-D model with mixing parameterization (3.105)-(3.106). The equation for gas diffusion without biology effects was added to estimate the influence of the mixed layer dynamics on the bulk-flux for the air-sea gas exchange. The averaged error due to diurnal warming for leg 2 was relatively small (~4%).

Extrapolation of the results obtained with $O_2$ to $CO_2$ cannot be done directly. One reason is that the effect of the gas depletion/accumulation is less important for $CO_2$ than for $O_2$ since the former is a part of the carbonate system with large buffering capacity. Temperature dependence of solubility therefore primarily determines the effect of the fine thermal structure on the $CO_2$ exchange in the near-surface layer of the ocean.

The temperature dependence of $CO_2$ solubility in seawater can be described with the Takahashi et al (1993) coefficient:

$$\gamma_T = \partial(\ln pCO_2)/\partial T\,, \tag{7.29}$$

where $pCO_2 = S_\mu p_a$, and the partial derivative denotes isochemical conditions. At 15°C and 35 psu, $\gamma_T \approx 0.033\ ^{o}C^{-1}$.

McNeil and Merlivat (1996) combined (7.29) and (1.45) to obtain formula for the relative deviation of the $CO_2$ flux $\delta G_{CO_2}/G_{CO_2}$ as follows:

$$\delta G_{CO_2}/G_{CO_2} = \gamma_T\,\delta T\left(pCO_{2w}/(pCO_{2w} - pCO_{2a})\right), \tag{7.30}$$

where $\delta T$ is the perturbation of the sea surface temperature; $p\mathrm{CO}_2$ is the $CO_2$ partial pressure (indices *a* and *w* refer to the atmosphere and water respectively). During *GasEx-98* leg, the ratio $pCO_{2w}/(pCO_{2w} - pCO_{2a})$ varied between 2.7 and 4.1 (McGillis et al., 2004) and the diurnal warming in a few cases exceeded 1°C.

Calculation of the temperature difference within the upper 4 m due to diurnal warming is possible with a one-dimensional model of diurnal mixed layer and diurnal thermocline. Under the assumption of horizontal homogeneity, equations (1.6), (1.7), (1.10), and (1.11) are as follows:

$$\frac{\partial u}{\partial t} = \frac{\partial}{\partial z}\left(K_M \frac{\partial u}{\partial z}\right) + fv\,, \tag{7.31}$$

$$\frac{\partial v}{\partial t} = \frac{\partial}{\partial z}\left(K_M \frac{\partial v}{\partial z}\right) - fu\,, \tag{7.32}$$

$$c_p\rho\frac{\partial T}{\partial t}=c_p\rho\frac{\partial}{\partial z}\left(K_T\frac{\partial T}{\partial z}\right)+\frac{\partial I_R}{\partial z}, \tag{7.33}$$

$$\frac{\partial S}{\partial t}=\frac{\partial}{\partial z}\left(K_S\frac{\partial S}{\partial z}\right), \tag{7.34}$$

where $K_M$ and $K_T$ are the turbulent exchange coefficients for momentum and heat determined from the TOGA-COARE mixing parameterizations (3.105) and (3.106) as a function of the gradient Richardson number $Ri=g\rho^{-1}\partial_z\rho/[(\partial_z u)^2+(\partial_z v)^2]$. The turbulent exchange coefficients for salinity $K_S$ and gas concentration $K_C$ are determined as $K_C = K_S = K_T$. The absorption of solar radiation with depth ($I_R$) is given by formulas (1.61)-(1.62). The salinity balance equation (7.34) does not contain the volume source function, which implies that the rain is treated here as surface flux of freshwater.

The surface boundary conditions are as follows:

$$\rho\left(K_M\partial u/\partial z\right)\big|_{z\to-0}=\tau_{x0},\quad K_M\left(\partial v/\partial z\right)\big|_{z\to-0}=\tau_{y0}$$
$$-K_T\partial T/\partial z\big|_{z\to-0}=Q_T+Q_E+I_L,\quad K_S\partial S/\partial z=S_0\left(Q_E/L-\rho P\right),$$

where $\tau_{x0}$ and $\tau_{y0}$ are the surface eastward and northward components of the momentum flux; $Q_T$, $Q_E$, and are the sensible and latent heat fluxes, $I_L$ is the net longwave irradiance (note that the solar irradiance does not enter the surface boundary condition because it is treated as a volume source of heat), $S_0$ is the surface salinity, and $P$ is the rain rate.

A calculation illustrating the relationship between the gas exchange and the diurnal cycle has been made with a 1m vertical grid over the top 50 m of the ocean. The initial temperature and salinity profiles were taken from the CTD profiles obtained during leg 2 of *GasEx-98*. The model is forced with the air-sea heat and momentum fluxes measured by Edson et al. (1999). The results of the mixed layer calculation are shown in *Figure 7-22*. The mixed layer depth is defined using the gradient Richardson number criteria, $Ri = Ri_{cr} = 0.25$.

The simulated mixed layer depth (*Figure 7-22*a) is consistent with the depth of the actively mixed layer as determined from the turbulence profiles taken during *GasEx-98* leg 2 with a free-rising profiler. Both the modeling and experimental results demonstrate that under light winds, the surface-generated turbulence is confined relatively near the surface. As a result, appreciable temperature differences were formed in the upper few meters of the ocean. This is illustrated in *Figure 7-23*, which shows three examples of

the measurements taken with a free-rising profiler during *GasEx-98 leg 2* under different wind speed conditions.

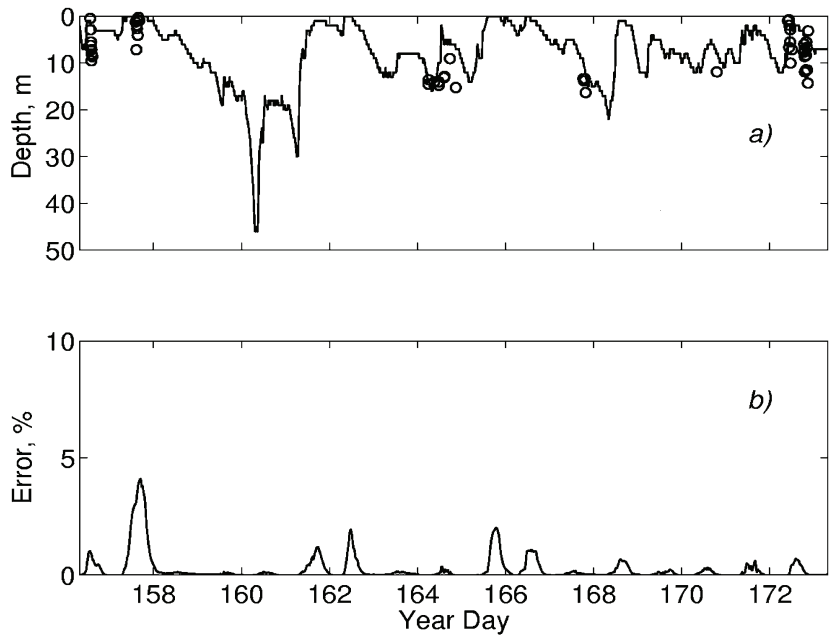


*Figure 7-22*. Effect of the diurnal warming on the bulk-flux formulation for the air-sea exchange of $CO_2$: (a) Depth of the actively mixed layer according to modeling (contiguous line) and turbulence measurements with a free-rising profiler (white circles) during *GasEx-98* leg 2; (b) Relative error in the bulk $CO_2$ flux calculation due to the effect of diurnal warming.

During *GasEx-98*, the measurements of *T*, *S*, and $p_w$ were routinely taken from the 4 m depth of the thermosalinograph intake at the bow of the ship, assuming that the near-surface layer of the ocean was well mixed. To evaluate the extent to which mixed layer processes may influence the bulk-flux formulation (1.45) of air-sea gas exchange, *Figure 7-22*b shows the relative error that occurs if mixed layer dynamics are ignored. This error is calculated from equation (7.30) implying that $\Delta T = T_0 - T_4$, where $T_4$ and $T_0$ are the temperature at the surface (upper bin) and at 4 m depth. During a few periods of low wind speed conditions observed during *GasEx-98* leg 2, the relative error for $CO_2$ approaches several % in a few cases (*Figure 7-22*b). The averaged error for leg 2 is, however, relatively small (~0.7%). *Figure 7-24* represents the modeling results from leg 2 as a function of wind speed. The effect of diurnal warming on the $CO_2$ flux calculation from the thermosalinograph data and a bulk-flux algorithm increases at light winds. The effect is presumably more pronounced in tropical seas.

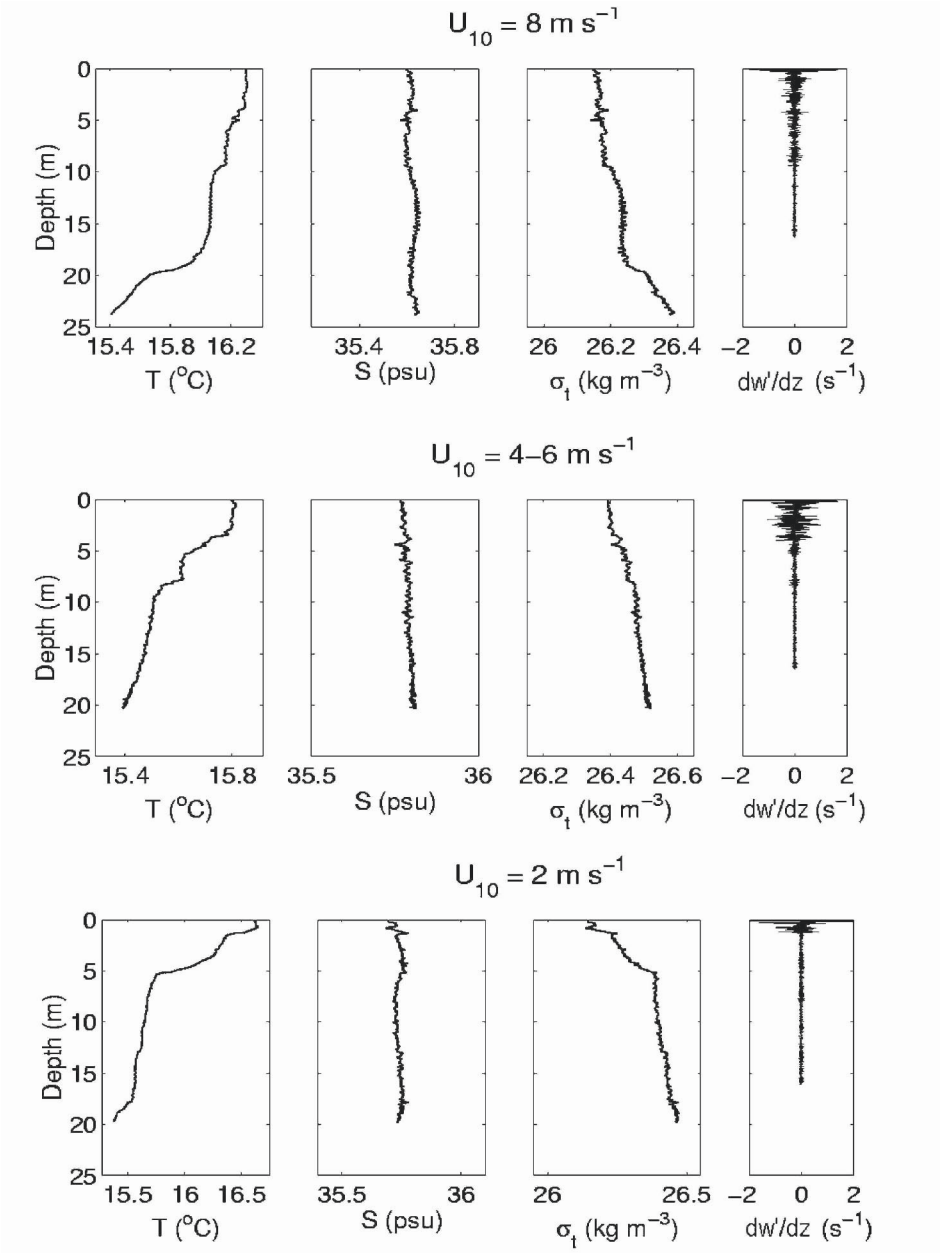


*Figure 7-23*. Examples of near-surface structure and turbulence under different wind speed conditions obtained with free-rising profiler during *GasEx-98 leg 2*. (After Soloviev et al., 2002.)

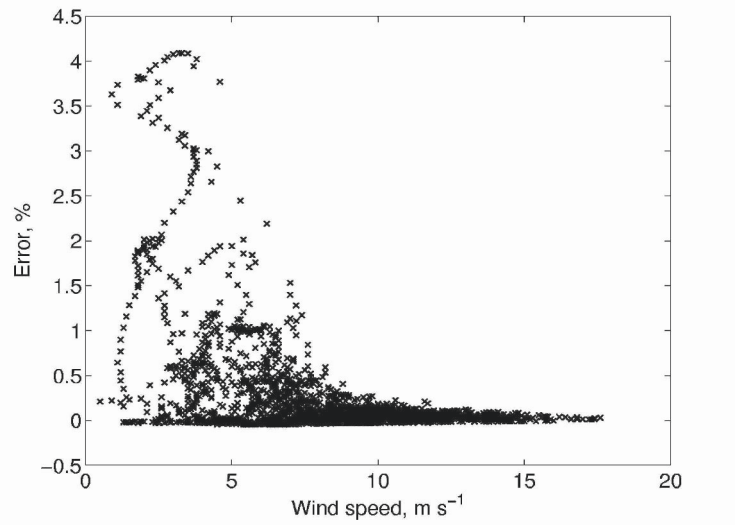


*Figure 7-24*. The relative error of calculating air-sea flux of $CO_2$ from the bulk flux algorithm using standard thermosalinograph data because of diurnal warming as a function of wind speed at 18 m height.

### 7.5.6 Remote sensing of gas exchange

A broader view of the air-sea exchange processes and their spatial and temporal variability in the vicinity of the experimental area and beyond can be obtained from satellite data. Infrared and microwave images from the Advanced Very High Resolution Radiometer and from the Special Sensor Microwave/Imager have been used to retrieve boundary layer variables for the time period corresponding to *GasEx-98*. These variables include the sea surface temperature, surface friction velocity, low-level atmospheric humidity, near-surface stability, and the atmospheric back radiation. They are used to calculate energy and momentum fluxes which in turn are used together with a surface renewal model to parameterize the temperature difference across the thermal molecular boundary layer of the upper ocean and the air-sea gas exchange coefficient.

Oceanic whitecaps (spilling wave crests) are the sea surface features detectable from satellites in the microwave emissivity signal. The bubble-mediated component of the air-sea gas exchange can be linked to the fraction of sea surface covered by whitecaps (Monahan, 2002).

Surface films can dramatically reduce the air-sea gas exchange through modification of capillary waves (Frew et al., 1995). According to Bock et al. (1999) and Jaehne et al. (1987), regardless of the surfactant concentrations, the gas transfer velocity shows a reasonable correlation with the mean square slope of the sea surface. Due to the fact that the remotely sensed wind

velocity (like that shown in *Figure 7-25*) is determined from the mean square slope, this substantially reduces (but does not completely eliminate) the dependence of the gas transfer coefficients on surface films.

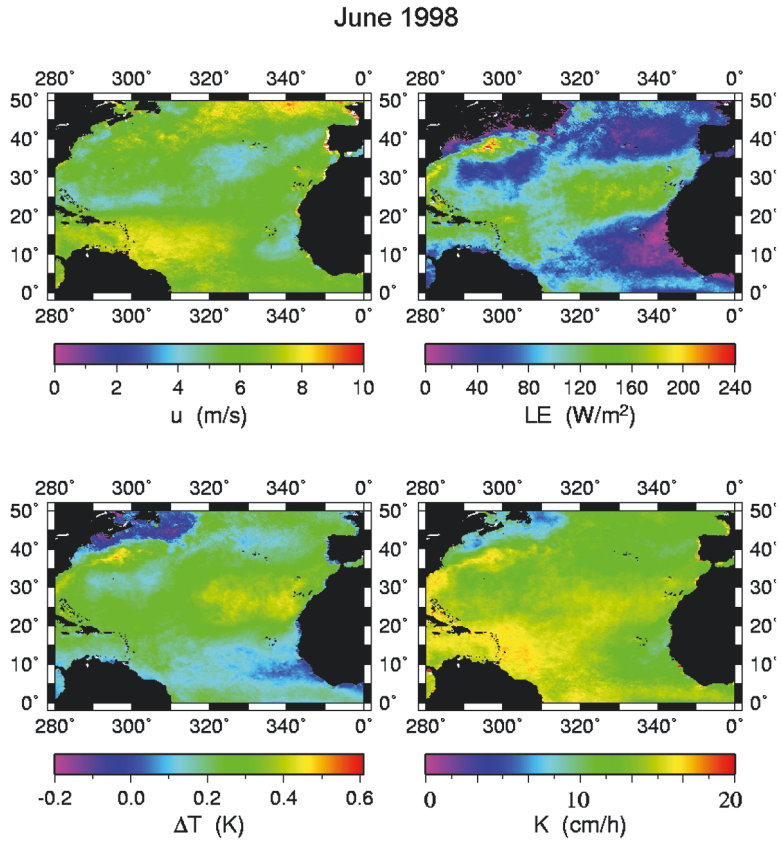


*Figure 7-25*. Wind speed ($u$), cool skin ($\Delta T$), latent heat flux ($LE$), and total ($K=K_{int}+K_b$) air-sea gas transfer velocity for the *GasEx-98* period of June 1998 as calculated from satellite data and the parameterization developed by Schlüssel and Soloviev (2002). Reproduced by permission from American Geophysical Union.

## 7.6 Ocean and Climate Modeling

Accurately modeling the near-surface layer of the ocean is important for a number of reasons. The near-surface layer is the portion of the ocean that humans are most affected by, and which humans affect most. The fluxes of energy into and through the near-surface ocean are responsible for driving the general circulation of the ocean. The heat and freshwater fluxes into and through this layer are responsible for the stratification of the ocean and for the formation of water masses that fill the ocean. The distribution of heat in

the near-surface ocean affects the overlying atmosphere on a variety of time and space scales. The exchanges of gases with the near-surface ocean, and fluxes of aerosols and salt into the atmosphere are crucial elements of the climate system as well.

The ocean plays a vital role in the Earth's climate and its variations. Thus, numerical models of the ocean are essential tools for understanding, assessing and predicting climate variability and change, along with the associated impacts. For example, understanding the relative roles of different ocean processes during El Niño-Southern Oscillation (ENSO) events has depended strongly on experiments with forced ocean models and coupled ocean-atmosphere models. Ocean models are now used routinely to assimilate observations to provide initial conditions for coupled ocean-atmosphere models that are used to predict seasonal-to-interannual climate variability. Global climate models that are used in greenhouse gas scenarios of future climates depend significantly not only on accurate representation of ocean physics, but also on representation of ocean biogeochemistry because the absorption and sequestration of $CO_2$ in the ocean is a very important element of global change projections.

Ocean models are important in their own right as tools for managing marine transportation, for search and rescue efforts, to support coastal engineering, for marine hazards mitigation, and for management of marine ecosystems, among other applications. The international Global Ocean Data Assimilation Experiment is underway as this is written, aimed at significantly advancing our ability to assess the state of the oceans, with these and other applications as objectives.

Successfully modeling the ocean requires adequate boundary conditions (usually expressed in the form of air-sea fluxes) and accurate parameterization of the grid-scale impacts of processes that are not resolved by the model grid. Forcing and parameterization errors may accumulate unevenly in the model domain, and in coupled models they may be amplified considerably by positive feedback mechanisms. For oceanic general circulation models (GCMs) on global and regional scales, the near-surface processes discussed throughout this book cannot be resolved. Global parameterizations of such processes are sought, but in many cases this is an elusive goal.

Another approach to parameterization is to incorporate submodels that can be used to provide a statistical representation of the grid-scale impacts of physics that cannot be resolved by the main model. An example of such an enhanced-resolution submodel is the non-hydrostatic cloud-resolving model embedded in an atmospheric GCM (Randall et al., 2003).

Submodels may be needed to represent variables that cannot easily be represented in the main model. For example, growing recognition of the

important role of waves in determining the momentum fluxes across the air-sea interface motivated the inclusion of spectral wave submodels in operational numerical weather prediction models at NOAA/NCEP and ECMWF. For some applications, the wave fields are of direct utility. Another example is the use of a biological submodel to predict turbidity for an ocean GCM. However, the biogeochemical processes and their interaction with physics near the air-sea interface represent a fundamental challenge for modeling climate variability and change because the appropriate equations are not yet fully developed.

Below, we discuss the representation of near-surface processes in the context of surface boundary conditions and near-surface subgrid scale parameterizations for numerical ocean models, and the possible roles of these processes in ocean and climate simulation and prediction.

### 7.6.1 Air-Sea Fluxes

Air-sea fluxes depend not only on the conditions in the atmosphere, but also on processes in the upper ocean boundary layer. Surface gravity waves are only the most obvious example. Thus, there is a coupled nature to ocean surface boundary conditions, and ocean models that are driven by specified fluxes cannot take these feedbacks into account. Coupled ocean-atmosphere models can, in principal, take them into account, but they generally do not have the vertical resolution to do so. Thus, these effects must be parameterized.

*a) Wave-mediated momentum fluxes*

At the present time, neither ocean general circulation models nor coupled climate models include the effects of surface waves, except as crudely parameterized by a wind-speed dependent drag coefficient. The flux of momentum from the atmosphere to the ocean (or vice-versa under calm winds) intimately involves the surface wave field, which depends on the history of the wind locally and at remote locations. The surface wind stress depends on the wave roughness, and the accurate partitioning of atmospheric momentum into the wave field and into the surface currents is a challenging problem. Properly accounting for these influences includes consideration of the Stokes drift due to wave radiation stress, spray effects (see below), and of the turbulence created when waves break.

*b) Rain-mediated fluxes*

Section 1.5 discussed the heat, freshwater and momentum fluxes associated with rainfall. These effects are generally ignored in ocean and coupled models, even though they can have substantial impacts in some regions and at some times. Even on climate time scales, the net effects can be significant. For example, for the four months of the TOGA COARE intensive observing period there was a net sensible heat flux of 6 W $m^{-2}$ due to rainfall (Weller and Anderson, 1996). This may seem insignificant, but the net heat flux for the same period was only about 20 W $m^{-2}$.

Parameterization of rainfall contributions to air-sea fluxes is moot at this time because obtaining accurate estimates of rainrates, which vary strongly in time and space, is so problematic. Even in atmospheric analyses and coupled models, where rainrates are known for grid-scale averages, the errors are large. Because of the small spatial scales and large temporal variability, and the nonlinearity of the rainfall-mediated processes, parameterization using grid-scale rainrates is not likely to be successful.

*c) Spray-mediated fluxes*

Under the very high winds in tropical and midlatitude cyclones, momentum, heat, and moisture fluxes are significantly altered from those estimated from Monin-Oboukhov similarity profiles, due to the presence of spray. Spray redistributes air-sea energy fluxes from sensible to latent heat, and it enhances the momentum flux from the atmosphere to the ocean (Section 6.2). Both positive and negative feedbacks are involved with spray modification of heat and momentum fluxes (Zhang and Perrie, 2001). Because the effects of spray are not completely understood and well modeled, it remains undecided whether tropical cyclones may become more intense due to spray (Andreas and Emmanuel, 2001; Wang et al., 2001).

Air-sea fluxes within extratropical cyclones are apparently altered by spray effects, leading to changes in surface winds and rainfall within the storms. Meirink (2002) compared latent and sensible heat fluxes in modeled North Sea storms with and without spray effects using a parameterization based on Makin (1998) and Andreas (1998). Maximum differences of latent fluxes were over 100 W $m^{-2}$, while sensible heat flux differences were reduced by comparable amounts. The net heat flux difference was as large as 50 W $m^{-2}$. Because of enhanced evaporation, the inclusion of spray effects resulted in an increase in rainfall by as much as 7 mm $d^{-1}$.

*d) Solar absorption and turbidity*

The volume absorption of penetrating solar radiation in the ocean plays an important role in determining the temperature and density structure of the upper ocean. Changes of turbidity alter the profile of shortwave radiation, and episodic or seasonal changes of productivity may significantly affect turbidity (Lewis et al., 1990; Siegel et al., 1995; Ohlmann et al., 1996). The impact of altered penetration of shortwave radiation can be significant for climate models (Schneider and Zhu, 1998; Murtugudde et al., 2002; Miller et al., 2003). Biological influences on turbidity are not amenable to parameterization at this time. Biogeochemical submodels are required (Christian et al., 2002). Though for the upper ten centimeters of the open ocean the effect of turbidity on the absorption of solar radiation is nevertheless relatively small (see Section 1.4.6.)

*e) $CO_2$ uptake by the ocean*

Greenhouse gas exchanges are important for global climate change. The $CO_2$ uptake by the oceans is largely controlled by the physical processes in the near-surface layer of the ocean. The estimates of the global ocean $CO_2$ uptake depends on the parameterization for the gas transfer velocity (Tans et al, 1990; Takahashi, 2000). The realistic parameterizations of the air-sea gas exchange should be based on the physics of the turbulent boundary layer and the properties of the sea surface rather than on empirics (Soloviev and Schlüssel, 2001). The parameterization of the former type described in Section 7.5 appears to be consistent with the reanalysis of the bomb $^{14}C$ global data by Sweeny et al. (2005) using the inverse method.

A strong dependence of $CO_2$ solubility on temperature suggests that the diurnal warming and the cool skin may cause deviations from bulk-flux formulation (7.20). For example, for the typical western equatorial Pacific $pCO_{2a}$ ~350 μatm and $pCO_{2w}$ ~360 μatm, the McNeil and Merlivat (1996) formula (7.30) gives an error of about 150% per $^oC$, while in the eastern equatorial Pacific the difference, $\Delta pCO_{2w}$, can achieve ~100 μatm, which results in an error of about -10% per degree C. (Remarkably, the McNeil and Merlivat (1996) formula is invariant with respect to the type of gas transfer parameterization.)

According to Robertson and Watson (1992), a 0.3$^o$C difference in SST due to the cool skin results in an increased oceanic global uptake of about 0.7 Pg of carbon per year, which constitutes a substantial correction, from 17% to 36%, of the global carbon uptake by the oceans. (A high-resolution approach by Van Scoy et al. (1995) showed a somewhat lower effect of the cool skin on the global estimate.) Global estimates of the $CO_2$ uptake by the ocean may also have to be corrected for the large diurnal warming events as

well, which has not yet been done. The effects of the diurnal cycle and the cool skin on the SST, however, have opposite signs and therefore tend to compensate each other.

Influence of air-bubbles on the fluxes of gases between the atmosphere and ocean has not yet been properly accounted in gas-exchange parameterizations. The contribution of the bubble-mediated component into the total $CO_2$ transfer between the ocean and atmosphere is, however, expected to be relatively small on average because $CO_2$ is a well soluble gas.

### 7.6.2 Subgrid Scale Mixing Parameterization

*a) Vertical mixing*

The projection of momentum from the surface wind into the interior of the ocean depends strongly on the vertical structure of turbulence, which is only crudely parameterized in coupled climate models, and in many ocean GCMs. Turbulence from wave-breaking is presently not considered in ocean models, yet this is a large source of turbulent kinetic energy in the near-surface layer.

One of the approaches to parameterizing the vertical mixing coefficient in the ocean is the so-called KPP scheme proposed by Large et al. (1994). A further development of this approach undertaken in Chapter 3 of this monograph provides a robust and computationally effective mixing parameterization scheme.

In some situations (like nighttime convective mixing) nonlocal processes dominate transport of properties within the upper ocean mixed layer. This transport is performed by coherent structures considered in Chapter 5 of this monograph. Incorporation of coherent structures into parameterization schemes has not yet been done in a systematic way.

*b) Horizontal mixing*

Horizontal mixing is a complex process including multi-scale nonlinear interactions. On the submesoscale, horizontal pressure gradients due to spatially varying buoyancy fields produce quite intensive mixing. Influx of buoyancy though the air-sea interface is an important component of this process. In the tropical ocean rainfalls substantially contribute into the spatial inhomogeneity of buoyancy flux at the air-sea interface. The horizontal mixing coefficient therefore appears to be intimately linked to freshwater cycling and salinity effects.

As the spatial resolution of numerical ocean models increases, processes that were completely unresolved may become partially resolved. Horizontal mixing is a case in point: When the model grid fully resolves mesoscale

eddies, then smaller scales on which rotational effects are less effective become more important to parameterize.

### 7.6.3 Interactions

While some subgrid processes have been parameterized, the interactions among these processes are generally not considered. For example, due to freshwater cycling and salinity effects, a salt-stratified barrier layer (Lindstrom and Lukas, 1991) may exist over a broad region covering many grid points in a numerical model. But the barrier layer is maintained by the interaction of resolved processes and unresolved processes acting on subgrid scales (Vialard and Delecluse, 1998b). The subduction process that plays a role in barrier layer maintenance involves large-scale advection, but also involves small-scale frontal processes including subgrid vertical and horizontal mixing.

The barrier layer favors the maintenance and displacement of the warm pool into the central Pacific by isolating the mixed layer from entrainment cooling and by confining the response of westerly wind events to a relatively shallow mixed layer (Vialard and Delecluse, 1998a). This process is an important part of the ENSO cycle (Maes et al., 2003; see Section 1.7.4). It can also be important in the dynamics of coastal regions with river run-off (like the Bay of Bengal) and in the marginal polar seas under conditions of ice melting.

Vinayachandran et al. (2002) captured the formation of a barrier layer at 17°30'N, 89°E in the northern Bay of Bengal. On 28 July 1999, the upper 30 m layer was homogeneous in both temperature and salinity (*Figure 1-18*). Subsequently, a freshwater plume from river discharge and rainfall was advected to the experimental area. The arrival of the freshwater plume caused the depth of the mixed layer to decrease to about 10 m and the salinity in the surface layer to drop by about 4 psu. As a result, a new halocline and thus a barrier layer formed within the upper 30 m of the ocean (*Figure 7-27*.). Air-sea interaction was then restricted to this thinner mixed layer; a 0.5°C inversion in temperature just below the mixed layer provided evidence that the surface cooling was restricted to this thin layer.

Such a thin surface layer is more strongly coupled to the atmosphere. The salt-stratified barrier layer may thus be involved in the processes of deep atmospheric convection and cyclogenesis by reducing the entrainment cooling from below the mixed layer (Murty et al., 2002; Subrahmanyam et al., 2005).

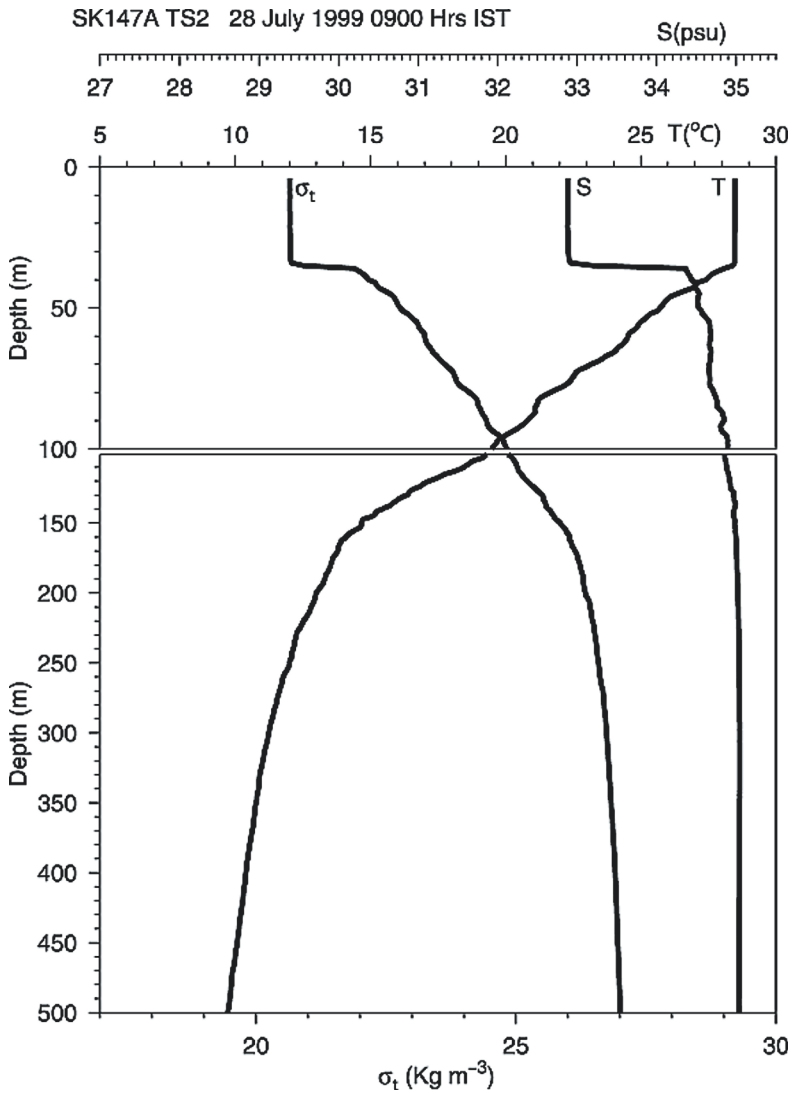


*Figure 7-26*. Vertical profiles of temperature, salinity and density measured at 17°30N, 89°E in the northern Bay of Bengal. Reproduced from Vinayachandran et al. (2002) by permission of American Geophysical Union.

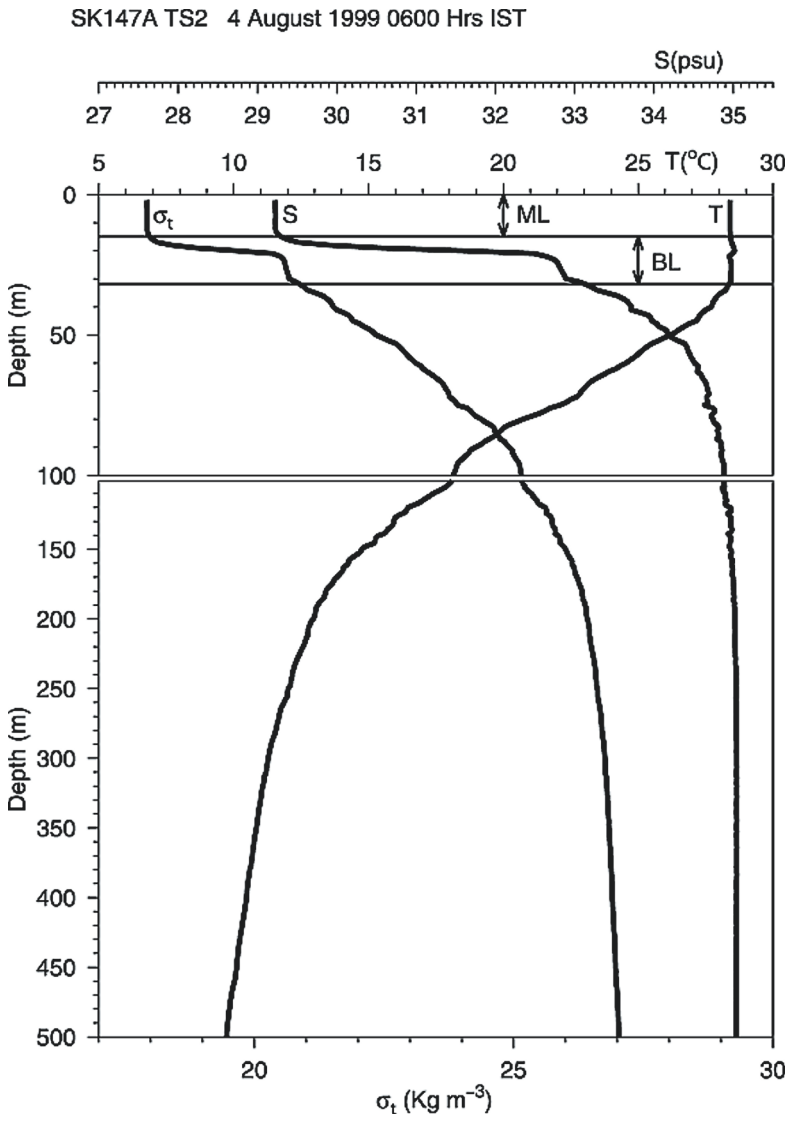


*Figure 7-27.* Vertical profiles of temperature, salinity and density after arrival of the freshwater plume. ML and BL indicate mixed layer and barrier layer respectively. Reproduced from Vinayachandran et al. (2002.) by permission of American Geophysical Union.

## Mathematical Notations

| Symbol | Description | | |
|---|---|---|---|
| $a$ | wave amplitude | | 1.6.2 |
| $a_i$ | weights corresponding to the spectrally distributed absorption coefficients $\alpha_i$ | (1.62) | 1.4.6 |
| $a_0$ | dimensionless constant in microlayer parameterization | (2.47) | 2.3.2 |
| $A$ | albedo | (1.54) | 1.4.5 |
| $A_d$ | parameter determining free-rising profiler dynamics | (3.10) | 3.2.4 |
| $A_w$ | wave age | | 1.6.6 |
| $A_0$ | dimensionless coefficient in parameterization for gas transfer | (2.41) | 2.3.2 |
| $b$ | turbulent kinetic energy (TKE) | (1.24) | 1.2.4 |
| $b_w$ | surface wave kinetic energy | (3.57) | 3.3.3 |
| $B$ | dimensionless constant in Craig and Banner (1994) model | (3.32) | 3.3.2 |
| $B_0$ | vertical flux of buoyancy just below the sea surface | (2.120) | 2.5.4 |
| $c$ | phase speed of wave | (1.105) | 1.6.2 |
| $c$ | bubble-free sound speed | (7.8) | 7.4.3 |
| $c_p$ | phase speed at the spectral peak of wind waves | | 1.6.6 |
| $c_p$ | specific heat capacity of water at constant pressure | (1.10) | 1.2.2 |
| $c_{pr}$ | specific heat of rain water | (1.80) | 1.5.4 |
| $c_{pa}$ | specific heat capacity of air at constant pressure | (1.35) | 1.3.2 |
| $C$ | conductivity of seawater | | 2.2.1 |
| $C$ | volume concentration of bubbles | (6.10) | 6.1.4 |
| $C_i$ | concentration of tracer | (1.12) | 1.2.2 |
| $C_w$ | concentration of tracer in the bulk of water | | 2.3.2 |
| $C_0$ | surface concentration of tracer | | 2.3.2 |
| $C_D$ | drag coefficient | (1.34) | 1.3.2 |
| $C_E$ | bulk transfer coefficient for latent heat | (1.36) | 1.3.2 |
| $C_T$ | bulk transfer coefficient for sensible heat | (1.35) | 1.3.2 |
| $C_u$ | drag coefficient in the near-surface layer of the ocean | (4.2) | 4.2.1 |
| $D_r$ | diameters of dry particles | | 6.2.4 |
| $e(k)$ | wavenumber spectrum of kinetic energy | (5.2) | 5.2 |
| $E$ | evaporation rate | (1.27) | 1.3.1 |

| | | | |
|---|---|---|---|
| $E$ | vertical flux of the kinetic energy | (4.43) | 4.5.1 |
| $E_B$ | one-dimensional (horizontal) wavenumber spectrum of buoyancy | (5.13) | 5.3.5 |
| $E_\rho$ | one-dimensional (horizontal) wavenumber spectrum of density | (5.14) | 5.3.5 |
| $E_u(k_x)$ | one-dimensional wavenumber spectrum of turbulence | (3.8) | 3.2.3 |
| $f$ | Coriolis parameter | (1.1) | 1.2.1 |
| $f$ | frequency in Hz | (3.8) | 3.2.3 |
| $f_y$ | horizontal component of the Coriolis parameter | (1.1) | 1.2.1 |
| $f_V$ | source function for penetrating rain | (1.78) | 1.5.3 |
| $f_R(z)$ | function characterizing the absorption of solar radiation with depth | (1.61) | 1.4.6 |
| $F_k$ | flux of kinetic energy carried by rain droplets | (2.126) | 2.5.6 |
| $F_0$ | flux of kinetic energy to waves from wind | (1.127) | 1.6.6 |
| $g$ | acceleration due to gravity | (1.3) | 1.2.1 |
| $G_i$ | flux of $i$-th component of tracer admixture | (1.12) | 1.2.2 |
| $G_{Vi}$ | volume source of $i$-th tracer | (1.12) | 1.2.2 |
| $G_0$ | net air-sea flux of gas | (1.44) | 1.3.2 |
| $h$ | layer depth, mixed layer depth, turbulent boundary layer depth | | |
| $h_c$ | penetration depth of convection | (4.45) | 4.5.1 |
| $h_r$ | rain-formed mixed layer depth | | 4.1.4 |
| $h_D$ | diurnal mixed layer depth | | 4.1.1 |
| $h_E$ | Ekman layer depth | (1.141) | 1.7.1 |
| $h_{TD}$ | turbulent diffusion layer depth | | 3.1.4 |
| $h_{w\text{-}s}$ | wave-stirred layer depth | | 3.1.4 |
| $h_0$ | depth of the near-surface density anomaly | | 5.4.1 |
| $H$ | depth of nearly isothermal thermal | | 5.4.1 |
| H | helicity | | 5.1 |
| $H_D$ | depth of the bottom boundary of diurnal thermocline | | 4.1.1 |
| $\Delta H_D$ | thickness of the diurnal thermocline | | 4.2.2 |
| $H_r$ | depth of the bottom boundary of rain-formed halocline | | 4.1.4 |
| $H_s$ | significant wave height | (1.117) | 1.6.5 |
| $I_L$ | net longwave irradiance | (1.46) | 1.3.3 |
| $I_R$ | volume source of heat due to absorption of solar radiation | (1.10) | 1.2.2 |
| $I_\Sigma$ | insolation (surface solar irradiance) | | 1.4.2 |
| $I_0$ | solar constant | | 1.4.2 |

| | | | |
|---|---|---|---|
| $J$ | salinity flux | (1.11) | 1.2.2 |
| $J_{rV}$ | volume source of freshwater due to the decay of raindrops | (1.11) | 1.2.2 |
| $k$ | wavenumber ( $k = 2\pi / \lambda$ ) | (1.102) | 1.6.2 |
| $\vec{k}$ | wavenumber vector with components $k_x, k_y$ | (1.100) | 1.6.2 |
| $K_b$ | bubble-mediated transfer velocity | (7.26) | 7.5.3 |
| $K_B$ | turbulent diffusion coefficient for bubbles | (6.10) | 6.1.4 |
| $K_D$ | turbulent diffusion coefficient for droplets | (6.17) | 6.2.2 |
| $K_h$ | horizontal mixing coefficient | (5.16) | 5.3.7 |
| $K_{int}$ | interfacial (direct) transfer velocity | (7.23) | 7.5.2 |
| $K_{Ci}$ | diffusion coefficient for *i*-th tracer | (1.15) | 1.2.2 |
| $Ke$ | Keulegan number | (2.1) | 2.2.3 |
| $K_M$ | kinematic viscosity | (1.5) | 1.2.1 |
| $K_S$ | diffusion coefficient for salinity | (1.14) | 1.2.2 |
| $K_T$ | thermal diffusion coefficient | (1.13) | 1.2.2 |
| $K_\mu$ | gas transfer (piston) velocity | (1.44) | 1.3.2 |
| $K_0$ | mixing coefficient in the logarithmic boundary layer | (3.93) | 3.4.2 |
| $l$ | characteristic length scale of turbulence | (3.30) | 3.3.2 |
| $L$ | width of frontal interface | | 5.4.4 |
| $L$ | specific heat of vaporization for water | (1.28) | 1.3.1 |
| $L(z,\theta,\phi)$ | radiance in the direction defined by the zenith angle $\theta$ and azimuth angle $\phi$, and z is the depth | (1.47) | 1.4.1 |
| $L_c$ | diameter of low-salinity lense | | 5.3.5 |
| $L_E$ | Ekman length scale | (3.5) | 3.1.2 |
| $L_f$ | baroclinic Rossby radius | | 5.3.5 |
| $L_G$ | Garwood et al. (1985) length scale | | 3.5.3 |
| $L_O$ | Oboukhov buoyancy length scale | (3.6) | 3.1.2 |
| $L_p$ | pressure-gradient length scales | | 3.5.4 |
| $L_\beta$ | equatorial baroclinic Rossby radius | | 5.3.1 |
| $m_d$ | mass of the free-ascending device | (3.9) | 3.2.4 |
| $M_r$ | cumulative precipitation | (4.27) | 4.2.4 |
| $n(r_0)$ | initial drop size distribution (at $z = 0$) | (1.65) | 1.5.2 |
| $N$ | Brunt-Vaisala frequency | (3.98) | 3.4.3 |
| $Nu$ | Nusselt number | (2.66) | 2.3.3 |
| $p$ | pressure | (1.1) | 1.2.1 |
| $p_a$ | gas partial pressure in air | (1.45) | 1.3.2 |
| $p_w$ | gas partial pressure in water | (1.45) | 1.3.2 |
| $p_0$ | atmospheric pressure | (1.93) | 1.6.1 |

| | | | |
|---|---|---|---|
| $P$ | precipitation rate | (1.27) | 1.3.1 |
| $Pr$ | Prandtl number | (2.2) | 2 |
| $q_a$ | specific humidity of air | (1.36) | 1.3.2 |
| $q$ | turbulent velocity scale | (3.30) | 3.3.2 |
| $q_R(z)$ | scaled solar irradiance as a function of z | (2.69) | 2.4.1 |
| $q_{R0}$ | scaled solar irradiance just below the air-sea interface | (2.79) | 2.4.1 |
| $q_0$ | scaled net heat flux at the sea surface | (2.10) | 2.3.1 |
| $Q$ | heat flux | (1.10) | 1.2.2 |
| $Q_E$ | latent heat flux | (1.28) | 1.3.1 |
| $Q_{rs}$ | surface component of rain-induced heat flux | (1.81) | 1.5.4 |
| $Q_{rV}$ | volume component of rain-induced heat flux | (1.80) | 1.5.4 |
| $Q_T$ | sensible heat flux | (1.26) | 1.3.1 |
| $Q_v$ | virtual cooling | (2.60) | 2.3.2 |
| $Q_0$ | net surface heat flux | (1.26) | 1.3.1 |
| $r$ | drop radius | (1.71) | 1.5.3 |
| $r$ | bubble radius | | 6.1.2 |
| $r_0$ | initial drop radius | | 1.5.1 |
| $R_{rs}$ | remote sensing reflectance | (7.2) | 7.1.6 |
| $R_s$ | surface reflectance (traditional definition) | (1.55) | 1.4.5 |
| $R_s$ | surface reflectance (IOCCG, 2000 definition ) | (7.1) | 7.1.6 |
| $Ra$ | Rayleigh number | (1.20) | 1.2.4 |
| $Ra_f$ | flux Rayleigh number | | 2.2.1 |
| $Re$ | Reynolds number | (1.20) | 1.2.6 |
| $Rf$ | flux Richardson number | (2.19) | 2.3.1 |
| $Rf_0$ | surface Richardson number | | 2.3.1 |
| $Ri$ | Richardson number | (3.84) | 3.4.1 |
| $Ri_{cr}$ | critical Richardson number | (3.86) | 3.4.1 |
| $Ro$ | Rossby number | (1.16) | 1.2.3 |
| $S$ | salinity | (1.11) | 1.2.2 |
| $S_h$ | shear | (3.98) | 3.4.3 |
| $S_h$ | bulk salinity of the mixed layer | | 4.1.4 |
| $S_M, S_q$ | dimensionless constants in Craig and Banner (1994) model | | 3.3.2 |
| $S_r$ | bulk salinity of the rain-formed mixed layer | | 4.1.4 |
| $S_u(f)$ | frequency spectrum of turbulence | (3.8) | 3.2.3 |
| $S_w$ | bulk salinity | (2.107) | 2.5.2 |
| $S_\mu$ | gas solubility | (1.45) | 1.3.2 |
| $S_0$ | sea surface salinity | (1.27) | 1.3.1 |
| $Sc$ | Schmidt number | (2.3) | 2 |

| | | | |
|---|---|---|---|
| $Sc_T$ | turbulent Schmidt number | (6.17) | 6.2.2 |
| $t$ | time, elapsed time | | |
| $t_*$ | renewal time | (2.30) | 2.3.2 |
| $T$ | thermodynamic temperature | | |
| $T_h$ | bulk temperature of the upper ocean mixed layer | | 4.1.1 |
| $T_r$ | raindrop temperature | (1.80) | 1.5.4 |
| $T_w$ | bulk water temperature | (1.80) | 1.5.4 |
| $T_D$ | bulk temperature of the diurnal mixed layer | | 4.1.1 |
| $T_0$ | sea surface temperature (SST) | (1.35) | 1.3.2 |
| $u, v, w$ | mean velocity components in $x, y, z$ directions, respectively | | 1.2.1 |
| $u_l$ | typical velocity scale | (1.19) | 1.2.4 |
| $u_S$ | stokes surface drift | | 2.3.2 |
| $u_w$ | current velocity of the bulk of water | | |
| $u_{wd}$ | wind-induced surface drift | (2.62) | 2.3.2 |
| $u_0$ | current velocity at the sea surface (relative to the background ocean current) | (2.62) | 2.3.2 |
| $u_*$ | friction velocity in the upper ocean boundary layer | | 1.6.6 |
| $u_{*a}$ | friction velocity in the atmospheric boundary layer | | 1.3.2 |
| $u_{*l}$ | local friction velocity | | 3.5.2 |
| $u_{*r}$ | equivalent friction velocity scale induced in the upper ocean corresponding to the flux of kinetic energy carried by the rain | (2.131) | 2.5.6 |
| $\overline{\Delta u}$ | ensemble averaged velocity difference across the aqueous viscous sublayer | | 2.3 |
| $U_a$ | mean wind speed relative to the ocean surface | (1.32) | 1.3.2 |
| $U_0$ | Relative flow speed (towed or mean flow advection speed) | (3.8) | 3.2.3 |
| $U_{10}$ | wind speed at 10 m height | | 1.3.2 |
| $V_x$ | longitudinal component of the bow velocity signal | | 3.2.5 |
| $w_b$ | buoyant rise speed of bubbles | (6.1) | 6.1.2 |
| $w_e$ | entrainment velocity | | 4.3 |
| $w_i$ | impact (terminal) velocity of raindrops | | 1.5.1 |
| $w_0$ | nominal ascending speed of the free-rising profiler in still water | (3.11) | 3.2.4 |
| $w_*$ | convective velocity scale | (3.95) | 3.4.2 |
| $W$ | total squared vorticity (enstrophy) | | 5.2 |

| | | | |
|---|---|---|---|
| $W_c$ | fraction of sea surface covered by oceanic whitecaps | (6.14) | 6.1.5 |
| $We$ | Weber number | (1.63) | 1.5.1 |
| $x, y, z$ | Cartesian coordinate system with origin at the sea surface ($x$ directed eastward, $y$ directed northward, $z$ directed upward or downward) | | 1.2.1 |
| $z$ | depth | | |
| $z_c$ | compensation depth | | 4.5.1 |
| $z_0$ | surface roughness length scale | (3.3) | 3.1.2 |
| $z_{0a}$ | surface roughness length scale from the air side of the air-sea interface | (1.42) | 1.3.2 |
| $\alpha$ | Ostwald solubility coefficient (dimensionless) | (7.26) | 7.5.3 |
| $\alpha$ | polar angle | | |
| $\alpha_T$ | thermal expansion coefficient of seawater | | 1.2.4 |
| $\alpha_i$ | spectrally distributed absorption coefficients | (1.62) | 1.4.6 |
| $\alpha_w$ | proportionality coefficient for kinetic energy flux from wind to waves | (1.128) | 1.6.6 |
| $\beta$ | void fraction of entrained air | | |
| $\beta_S$ | coefficient of saline contraction | | 1.2.4 |
| $\beta_w$ | $e$-folding scale for the temporal growth of wave energy in the absence of nonlinear interactions and dissipation | (1.126) | 1.6.6 |
| $\gamma$ | dimensional parameter in nonlinear diffusion equation | (5.15) | 5.3.6 |
| $\delta$ | solar declination angle | (1.53) | 1.4.3 |
| $\delta_\nu$ | thickness of the viscous sublayer | | 2.3.1 |
| $\delta_\mu$ | thickness of the diffusion sublayer | (2.4) | 2.1.3 |
| $\Delta_e$ | equilibrium supersaturation | (7.22) | 7.5.1 |
| $\varepsilon$ | viscous dissipation of the turbulent kinetic energy | | 1.2.4 |
| $\varepsilon_0$ | viscous dissipation of the turbulent kinetic energy in water near the sea surface | (3.61) | 3.3.3 |
| $\zeta$ | Stability parameter in the Monin-Oboukhov theory | (1.41) | 1.3.2 |
| $\eta$ | surface wave displacement | | 1.6.1 |
| $\eta_D$ | internal diffusivity length scale of turbulence | (2.3) | 2 |
| $\eta_T$ | internal thermal length scale of turbulence | (2.2) | 2 |
| $\eta_\nu$ | Kolmogorov's internal length scale of turbulence | (2.1) | 2 |
| $\theta$ | zenith angle | (1.51) | 1.4.3 |
| $\theta$ | wind direction | | 3.5.2 |

| | | | |
|---|---|---|---|
| $\Theta$ | potential temperature | (1.10) | 1.2.2 |
| $\kappa$ | von Karman constant | | 1.3.2 |
| $\kappa_T$ | molecular coefficient of thermal diffusivity | | 1.2.4 |
| $\lambda$ | wavelength | | |
| $\lambda_{IG}$ | wavelength of equatorial inertia-gravity wave | | 5.3.3 |
| $\lambda_S$ | nondimensional coefficient in cool-skin parameterization | | 2.1.2 |
| $\Lambda_0$ | dimensionless constant in microlayer parameterization | (2.39) | 2.3.2 |
| $\mu$ | molecular coefficient of kinematic tracer diffusivity (for gas, salinity etc.) | | |
| $\mu$ | parameter relating to the vertical mixing process and horizontal buoyancy gradients | (5.12) | 5.3.5 |
| $\nu_a$ | molecular kinematic viscosity of air | | |
| $\nu_T$ | eddy viscosity in Benilov and Ly (2003) model | (3.55) | 3.3.3 |
| $\xi$ | solar elevation angle | | 1.4.5 |
| $\rho$ | water density | | |
| $\rho_a$ | air density | | |
| $\rho_r$ | density of rain water | (1.80) | 1.5.4 |
| $\sigma_s$ | surface tension | | 1.5.1 |
| $\sigma_t$ | sigma-t density | | |
| $\sigma_*$ | Bubble decay rate | (6.12) | 6.1.4 |
| $\sigma_\eta^2$ | variance of surface wave elevation | | 3.3.2 |
| $\tau$ | relaxation time | (4.32) | 4.3 |
| $\tau_{ij}$ | components of the viscous stress tensor (where $i$ and $j$ can be $x$, $y$, or $z$) | (1.5) | 1.2.1 |
| $\tau_{rs}$ | surface component of rain-induced stress | (1.85) | 1.5.5 |
| $\tau_{rV}$ | volume component of rain-induced stress | (1.84) | 1.5.5 |
| $\tau_r$ | stress due to rain | (1.83) | 1.5.5 |
| $\tau_t$ | tangential component of air-sea momentum flux | (2.8) | 2.2.3 |
| $\tau_0$ | magnitude of wind stress | (1.34) | 1.3.2 |
| $\Upsilon$ | heat content | (4.23) | 4.2.3 |
| $\varphi$ | geographical latitude | | 1.2.1 |
| $\phi$ | potential function | (1.91) | 1.6.1 |
| $\Phi_\eta(\vec{k},\omega)$ | surface wave spectrum | | 3.1.1 |
| $\Phi(\omega)$ | frequency spectrum of surface waves | (1.113) | 1.6.5 |
| $\Psi(\vec{k})$ | wavenumber spectrum of surface wave | (1.122) | 1.6.5 |
| $\omega$ | frequency ($\omega = 2\pi/f$) | | |

| | | | |
|---|---|---|---|
| $\omega_p$ | frequency of the wave spectrum peak | | |
| $\omega_0$ | lowest eigenfrequency of a single bubble oscillation | (7.7) | 7.4.3 |
| $\Omega$ | magnitude of the Earth's rotation vector | | 1.2.1 |

# References


Agrawal, Y.C., E.A. Terray, M.A. Donelan, P.A. Hwang, A.J. Williams III, W.M. Drennan, K.K. Kahma, and S.A. Kitaigorodskii, 1992: Enhanced dissipation of kinetic energy beneath surface waves. *Nature* 359, 219-220.

Alldredge, A.L., T.J. Cowles, S. MacIntyre, J.E.B. Rines, P.L. Donaghay, C.F. Greenlaw, D.V. Holliday, M.M. Dekshenieks, J.M. Sullivan, and R. Zaneveld, 2002: Occurrence and mechanism of formation of a dramatic thin layer of marine snow in a shallow Pacific fjord. *Marine Ecology Progress Series* 233, 1-12.

Alldredge, A.L., and K.M. Crocker, 1995: Why do sinking mucilage aggregates accumulate in the water column? *Sci. Total Environ.* 165, 15-22.

Alldredge, A.L., U. Passow, and B.E. Logan, 1993: The abundance and significance of a class of large, transparent organic particles in the ocean. *Deep-Sea Res.* 40, 1131-1140.

Anderson, S.P., R.A. Weller, and R.B. Lukas, 1996: Surface buoyancy forcing and mixed layer of the western Pacific warm pool: Observations and 1D Model Results. *J. Climate* 9, 3056-3085.

Ando, K., and M.J. McPhaden, 1997: Variability of surface layer hydrography in the tropical Pacific Ocean. *J. Geophys. Res.* 102(C10), 23,063-23,078.

Andreas, E.L., 1990: Time constants for the evolution of sea spray droplets. *Tellus* 42B, 481-497.

Andreas, E.L., 1992: Sea spray and the turbulent air-sea heat fluxes. *J. Geophys. Res.* 97, 11,429-11,441.

Andreas, E.L., 1998: A new sea spray generation function for wind speeds up to 32 m $s^{-1}$. *J. Phys. Oceanogr.* 28, 2175-2184.

Andreas, E.L., 2002: A review of sea spray generation function for the open ocean. *Atmosphere-Ocean Interaction*, Volume 1, W. Perrie, Ed., WIT Press, Southampton, UK 1-46.

Andreas, E.L., and K.A. Emanuel, 2001: Effects of sea spray on tropical cyclone activity. *J. Geophys. Res.* 58, 3741-3751.

Andreas, E.L., 2004: Spray stress revisited. *J. Phys. Oceanogr.* 34, 1429-1440.

Antonia, R.A., A.J. Chambers, C.A. Friehe, and C.W. Van Atta, 1979: Temperature ramps in the atmospheric surface layer. *J. Atmos. Sci.* 36, 99-108.

Apel, J.R., 1994: An improved model of the ocean surface wave vector spectrum and its effects on radar backscatter. *J. Geophys. Res.* 99, 16,269-16,291.

Apel, J.R., H.M. Byrne, J.R. Proni, and R.L. Charnell, 1975: Observations of oceanic internal and surface waves from the Earth Resources Technology Satellite. *J. Geophys. Res.* 80, 865-881.

Araujo, M., D. Dartus, P. Maurel, and L. Masbernat, 2001. Langmuir circulation and enhanced turbulence beneath wind-waves. *Ocean Modeling* 3, 109-126.

Arjannikov, A.V., Y.E. Golubev, and V.A. Zvickevich, 1979: Apparatus for velocity measurement in the water flow. *USSR Patent N679878. Bulletin of inventions*, N30 (in Russian only).

Arsenyev, S.A., S.V. Dobroklonsky, R.M. Mamedov, and N.K. Shelkovnikov, 1975: Direct measurements of some characteristics of fine structure from a stationary platform in the open sea. Izvestiya, *Fizika Atmosphery i Okeana* 11, 845-850 (English translation).

Asher, W.E., and R. Wanninkhof, 1998: The effect of bubble-mediated gas transfer on purposeful dual-gaseous tracer experiment. *J. Geophys. Res*. 103, 10,555-10,560.

Asper, V.L., 1987: Measuring the flux and sinking speed of marine snow aggregations. *Deep-Sea Res.* 34, 1-7.

Atkinson, M.J., T. Berman, B.R. Allanson, and J. Imberger, 1987: Fine-scale oxygen variability in a stratified estuary: Patchiness in aquatic environments. *Mar. Ecol. Prog. Ser.* 36, 1-10.

Atlas, D., C.W. Ulbrich, F.D. Marks, E. Amitai, and C.R. Williams, 1999: Systematic variation of drop size and radar–rainfall relations. *J. Geophys. Res.* 104, 6155–6169.

Azizjan G.V., Y.A. Volkov, and A.V. Soloviev, 1984: Experimental investigation of vertical thermal structure of thin boundary layers of the sea and atmosphere. : *Atmospheric and Oceanic Physics* 20(6), 511-519.

Baier R.E., D.W. Goupil, S. Perlmutter, and R. King, 1974: Dominant chemical composition of sea surface films, natural slicks and foams. *J. de Rech. Atmos,* 8*,* 571-600.

Baker, M.A., and C.H. Gibson, 1987: Sampling turbulence in the stratified ocean: Statistical consequences of strong intermittency. *J. Phys. Oceanogr.* 17, 1817-1837.

Balk, A.M., and V.E. Zakharov, 1998: Stability of weak-turbulent Kolmogorov spectra, *Amer. Math. Soc. Transl. Ser. 2* 182, 31-81.

Banner, M.L., and W.L. Peirson, 1998: Tangential stress beneath wind-driven air-water interface. *J. Fluid Mech.* 364, 107-137.

Banner, M.L, and O.M. Phillips, 1974: On the incipient breaking of small scale waves. *J. Fluid Mech.* 65, 647-656.

Barenblatt, G.I., 1982: A model of unsteady heat- and mass exchange in a fluid with a strong stratification. Izvestiya, *(Bulletin), USSR Academy of Sciences, Atmospheric and Oceanic Physics* 18(3), pp. 201-205 (English Translation).

Barenblatt, G.I., and A.Y. Benilov, 1982: Influence of internal waves on inhomogeneities of the ocean surface hydrophysical characteristics. In: *The Effect of Large-Scale Internal Waves on Sea Surface. Gorkii*, 52-74 (in Russian).

Barenblatt, G.I., and G.S. Golitsyn, 1974: Local structure of mature dust storms. *J. Atmos. Sci.* 31, 1917-1933.

Barenblatt, G.I., and G.I. Shapiro, 1984: A contribution to the theory of the wave fronts in dispersive media. Izvestiya, *Akad. Nauk SSSR, Atmospheric and Oceanic Physics* 20(4), 277-284.

Batchelor, G.K., 1969: Computation of the energy spectrum in homogeneous two-dimensional turbulence. *The Physics of Fluids*, Suppl. II, 12, 233-239.

Bauer, P., and P. Schlüssel, 1993: Rainfall, total water, ice water and water vapour over sea from polarized microwave simulations and SSM/I data. *J. of Geophys. Res.* 98, 20,737-20,760.

Belcher, S.E., and J.C. Vassilicos, 1997: Breaking waves and the equilibrium range of wind wave spectra. *J. Fluid Mech.* 342, 377-401.

Beljaars, A.C.M., 1994: The parameterization of surface fluxes in large-scale models under free convection. *Q. J. Roy. Meteor. Soc.* 121, 255-270.

Beljaars, A.C.M., and A.A.M. Holstlag, 1991: Flux parameterization over land surfaces for atmospheric models. *J. Appl. Meteorol*. 30, 327-341.

Belkin, I., P. Cornillon, and Z. Shan, 2001: Global survey of ocean fronts from Pathfinder SST data. The Oceanography Society Biennial Scientific Meeting, 2-5 April, 2001, Miami Beach, Florida USA. *Oceanography* 14(1), p. 10.

Benilov, A.Y., 1973: Generation of turbulence in the ocean by surface waves. Izvestiya,*Fizika Atmosphery i Okeana* 9, 293-303.

Benilov, A.Y., and L.N. Ly., 2002: Modeling of Surface Waves Breaking Effects in The Ocean Upper Layer. *Math. .Comput. Model.* 35, 191-213.

Benilov, A.Y., and B.N. Filyushkin, 1970: Application of the linear filtration methods to the fluctuation analysis in the sea upper layer. Izvestiya,*Fizika Atmosphery i Okeana* 6, 477-482.

Bentamy, A., K.B. Katsaros, A.M. Mestas-Nuñez, W.M. Drennan, E.B. Forde, and H. Roquet, 2003: Satellite Estimates of Wind Speed and Latent Heat Flux over the Global Oceans *J. Climate* 16, 637-656.

Best, A., 1950: The size distribution of raindrops. *Q. J. Roy. Meteor. Soc.* 76, 16-36.

Bethoux, J.P., 1968: Adaptation d'une thermipile à la mesure de éclairement sousmarin. Thèse 3ème cycle, Faculté des Sciences de Paris.

Bezverkhny V.A., and A.V. Soloviev, 1986: Experimental data on the vertical structure of the non-stationary near-surface thermocline. Izvestiya, *(Bulletin), USSR Academy of Sciences, Atmospheric and Oceanic Physics* 22, No. 1, pp. 71-77 (In Russian).

Bishop, J.K.B., and W.B. Rossow, 1991: Spatial and temporal variability of global surface solar irradiance. *J. Geophys. Res.* 96, 16,839-16,858.

Bishop, J.K.B., T. Potylitsina, and W.B. Rossow, 2000: Documentation and description of surface solar irradiance data sets produced for SeaWiFS. NASA Grant NAG5-6450, Department of Applied Physics, Columbia, University (http://www.ocean.lbl.gov/seawifs/seawifs.000217.htm).

Bishop, J.K.B., W.B. Rossow, and E.G. Dutton, 1997: Surface solar irradiance from the International Satellite Cloud Climatology Project 1983 - 1991. *J. Geophys. Res.* 102, 6883-6910.

Bissett, W.P., O. Schofield, S. Glenn, J.J. Cullen, W.L. Miller, A.J. Plueddemann, and C.D. Mobley, 2001: Resolving the impacts and feedbacks of ocean optics on upper ocean ecology. *Oceanography* 14(3), 30-53.

Black, P.G., J.R. Proni, J.C. Wilkerson, and C.E. Samsury, 1997: Oceanic rainfall detection and classification in tropical and subtropical mesoscale convective systems using underwater acoustic methods. *Mon. Wea.ther Rev.* 125, 2014–2024.

Blanchard, D.C., 1963: The electrification of the atmosphere by particles from bubbles in the sea. *Prog. Oceanogr.* 1, 72-202.

Blanchard, D.C., and L.D. Sydzek, 1988: Film-drop production as a function of bubble size. *J. Geophys. Res.* 93, 3649–3654.

Blanchard, D.C., and A.H. Woodcock, 1957: Bubble formation and modification in the sea and its meteorological significance. *Tellus,* 9, 145-148.

Bock, E.J., and N.M. Frew. 1993: Static and dynamic response of natural multicomponent oceanic surface films to compression and dilation: Laboratory and field observations. *J. Geophys. Res.* 98*,* 14,599-14,617.

Bock, E.J, T. Hara, N.M. Frew, and W.R. McGillis, 1999. Relationship between air-sea gas transfer and short wind waves. *J. Geophys. Res*. 104, 25,821-25,831.

Bohren, C.F., and D.R. Huffman, 1983: *Absorption and Scattering of Light by Small Particles.* John Wiley and Sons Inc., New York, 530 pp.

Bolin, B., 1960: On the exchange of carbon dioxide between atmosphere and sea. *Tellus* 12(3), 274-281.

Bortkovskii, R.S., 1983: *Heat and Moisture Exchange Between Atmosphere and Ocean Under Storm Conditions*, 160 pp., Hydrometeorol. Publ., Leningrad, Russia.

Bortkovskii, R.S., 1973: On the mechanism of interaction between the ocean and the atmosphere during a storm. *Fluid Mech. Sov. Res.* 2, 87-94.

Borue, V., S.A. Orszag, and I. Staroselsky, 1995: Interaction of surface waves with turbulence: direct numerical simulations of turbulent open-channel flow. *J. Fluid Mech.* 286, 1-23.

Bowyer, P.A., 2001: Video measurements of near-surface bubble spectra. *J. Geophys. Res.*, 106: 14,179-14,190.

Bradley, E.F., C.W. Fairall, J.E. Hare, and A.A. Grachev, 2000: An old and improved bulk algorithm for air-sea fluxes: COARE 2.6A. *14th Symposium on Boundary Layer and Turbulence, AMS. 7 - 11 August 2000, Aspen CO,* 294-296.

Branover, H., A. Eidelman, E. Golbraikh, and S. Moiseev, 1999: *Turbulence and Structures. Chaos, Fluctuations, and Self-Organization in Nature and in the Laboratory*. Academic Press, San Diego, 270 pp.

Breitz, N.D., and H. Medwin, 1989: Instrumentation for in-situ acoustical measurements of bubble size distributions. *J. Atmos. Ocean. Tech.* 86, 739-743.

Brekhovskikh, L.M., V.V. Goncharov, V.M. Kurtepov, and K.A. Naugol'nykh, 1972: Resonant excitation of internal waves by nonlinear interaction of surface waves Izvestiya,. *Atmos. Ocean. Phys*. 8, 192-203.

Brekhovskich, L.M., and Y.P. Lysanov, 1978: Acoustic of the ocean. In: *Physics of the Ocean* 2, V.I. Voitov, Ed., Moscow, Nauka, 49-145.

Briscoe, M.G., 1983: Observations on the energy balance of internal waves during JASIN. *Philos. T. Roy. Soc. London*, *A*308, 427-444.

Brown, P.A., 1990: Meteorology. In: *Polar Oceanography*, W.O. Smith, Jr., Ed., Academic Press, San Diego,1-46.

Brown, G.L., and A.S.W. Thomas, 1977: Large structure in a turbulent boundary layer. *Phys. Fluids* 20**,** S243–S252.

Budyko, M.I., (1963): Atlas of the heat balance of the earth. *Gidrometeorozdat,* Moscow, 255 pp.

Buckley, J.R., T. Gammelsrod, J.A. Johannessen, O.M. Johannessen, and I.P. Roed, 1979: Upwelling: Oceanic structure at the edge of the Arctic ice pack in winter, *Science* 203, 165-167.

Businger, J.A., 1982: Equations and concepts. *Atmospheric Turbulence and Air Pollution Modeling*, F.T.M. Nieuwstadt and H. van Dop, Eds., D. Reidel Publishing Co., Dordrecht, 1-36.

Bye, J.A.T., 1988: The coupling of wave drift and wind velocity profiles. *J. Mar. Res.* 46, 457-472.

Cabanes, O., 1999: Modulation of mixed layer thermodynamics by equatorial waves in the tropical western Pacific. Report. *ENM Meteo France and SOEST University of Hawaii*, 74 p.

Caldwell, D.R., and W.H. Elliott, 1971: Surface stresses produced by rainfall. *J. Phys. Oceanogr.* 1, 145-148.

Callahan, P.S., C.S. Morris, and V. Hsiao, 1994: Comparison of TOPEX/POSEIDON $\sigma_0$ and significant wave height distributions to Geosat. *J. Geophys. Res.* 99, 25,015-25,024.

Carey, W.M., and M.P. Bradley, 1985: Low-frequency ocean surface noise sources. *J. Acoust. Soc. Amer.* 78, S1-S2.

Cember, R., 1989: Bomb radiocarbon in the Red Sea: A medium scale gas exchange experiment. *J. Geophys. Res.* 94, 2111-2123.

Chamides, W.L., and A.W. Stelson, 1992: Aqueous-phase chemical processes in deliquescent sea-salt aerosols: A mechanism that couples the atmospheric cycles of S and sea salt. *J. Geophys. Res.* 97, 20,565-20,580.

Chandraesekhar, S., 1950: *Radiative Transfer*. Oxford University Pressreprinted by Dover Publications, New York, 393 pp., 1960.

Chanson, H. (editor), 1996: *Air Bubble Entrainment In Free-Surface Turbulent Shear Flows*. Academic Press, San Diego, 348 pp.

Chapron, B., F. Collard, and V. Kerbaol, 2004: Satellite synthetic aperture radar sea surface Doppler measurements. Proceedings of the Second Workshop on Coastal and Marine Applications of SAR, 8-12 September 2003, Svalbard, Norway, (ESA SP-565), pp. 133-140, ESA Publications Division.

Charney, J.G., 1960: Non-linear theory of a wind-driven homogeneous layer near the equator. *Deep-Sea Res.* 6, 303-310.

Charnock, H., 1955: Wind stress on a water surface. *Q. J. Roy. Meteor. Soc.* 81, 639-640.

Chapman, D.S., and P.R. Critchlow, 1967: Formation of vortex rings from falling drops. *J. Fluid Mech.* 29, 177-185.

Cheung, T.K., and R.L. Street, 1988: The turbulent layer in the water at an air-water interface. *J. Fluid Mech.* 194, 133-151.

Chou, S.-H., R.M. Atlas, C.-L.Shie, and J. Ardizzone, 1995: Estimates of surface humidity and latent heat fluxes over oceans from SSM/I data. *Mon. Weather Rev.* 123, 2405-2425.

Christian, J., M. Verschell, R. Murtugudde, A. Busalacchi, and C. McClain, 2002: Biogeochemical modeling of the tropical Pacific Ocean I: Seasonal and interannual variability. *Deep-Sea Res*., 49, 509.

Churchill, J.H., and G.T. Csanady, 1983: Near-surface measurements of quasi-Lagrangian velocities in open water. *J. Phys. Oceanogr.* 13, 1669-1680.

Cipriano, R.J., E.C. Monahan, P.A. Bowyer, and D.K. Woolf**,** 1987: Marine condensation nucleus generation inferred from whitecap simulation tank results. *J. Geophys. Res.* 92*,* 6569–6576.

Clayson, C.A., and J.A. Curry, 1996: Determination of surface turbulent fluxes for TOGA COARE: Comparison of satellite retrievals and in situ measurements. *J. Geophys. Res.* 101, 28,503-28,513.

Clift, R., J.R. Grace, and M.E. Weber, 1978: *Bubbles Drops and Particles.* Academic Press, New York, 380 pp.

Commander, K.W., and A. Prosperetti, 1989: Linear pressure waves in bubbly liquids: Comparison between theory and experiments. *J. Acoust. Soc. Amer.* 85**,** 732–746.

Corino, E.R., and R.S. Brodkey, 1969: A visual investigation of the wall region in turbulent flow. *J. Fluid Mech.* 37, 1–30.

Cowles, T.J., R.A. Desiderio, and M-E. Carr, 1998: Small-scale planktonic structure: Persistence and trophic consequences. *Oceanography* 11(1), 4-9.

Cox, C., 2001: Sea surface micro-structure: Relation to air-sea fluxes, bubble transport and electromagnetic wave radiation**.** SIO Report A969093, La Jolla, CA.

Cox, C., and W. Munk, 1956: Slopes of the sea surface deduced from photographs of sun glitter. *Bull. Scripps Inst. Oceanogr. Univ. Calif.* 6, 401-487.

Craeye, C., and P. Schlüssel, 1998: Rainfall on the sea: Surface renewal and wave damping. *Bound.-Lay. Meteorol.* 89, 349-355.

Craig, P.D., and M.L. Banner, 1994: Modeling wave-enhanced turbulence in the ocean surface layer. *J. Phys. Oceanogr.* 24, 2546-2559.

Craik, A.D.D., 1977. The generation of Langmuir circulations by an instability mechanism. *J. Fluid Mech*. 81, 209-223.

Craik, A.D.D., and S. Leibovich, 1976: A rational model for Langmuir circulations. *J. Fluid Mech.* 73, 401–426.

Crum, I.A., 1995: Unresolved issues in bubble-related ambient noise. In: *Proceedings of III Int. Meeting on Natural Physical Processes Related to Sea Surface Sound "Sea Surface*

*Sound'94," University of California, Lake Arrowhead, 7-11 March 1994*, M.J. Buckingham and J. R. Potter, Eds., (World Scientific, Singapore), 243-269.

Csanady, G.T., 1978: Turbulent interface layers. *J. Geophys. Res.* 83, 2329-2342.

Csanady, G.T., 1984: The free surface turbulent shear layer. *J. Phys. Oceanogr.* 14, 402-411.

Csanady, G.T., 1990: The role of breaking wavelets in air-sea gas transfer. *J. Geophys.Res.* 95, 749-759.

D'Asaro, E.A., 2001: Turbulent vertical kinetic energy in the ocean mixed layer. *J. Phys. Oceanogr*. 31, 3530-3537.

D'Asaro E.A., D.M. Farmer, J.T. Osse, G.T. Dairiki, 1996: A Lagrangian float. *J. Atmos. Ocean. Tech.* 13, 1230-1246.

daSilva, A., A.C. Young, and S. Levitus, 1994: Atlas of surface marine data 1994, Volume 1.: Algorithms and procedures. *Tech. Rep. 6, U.S. Department of Commerce, NOAA, NESDIS*.

Deane, G.B., and M.D. Stokes, 2002: Scale dependence of bubble creation mechanisms in breaking waves. *Nature* 418, 839–844.

Deardoff, J.W., 1980: Stratocumulus-capped mixed layer derived from a three-dimensional model. *Bound.- Lay. Meteorol* 18, 495-527.

Debnath, L., 1994: Nonlinear waves. Academic Press, London, 544 pp.

Deschamps, P.Y., and R. Frouin, 1984: Large diurnal heating of the sea surface observed by the HCMR experiment. *J. Phys. Oceanogr.* 14, 177-184.

Delcroix, T., G. Eldin, C. Henin, F. Gallois, J. Grelet, M. Inall,S. Keene, M.-J. Langlade, , C. Menkes, F. Masia, and K. Richards, 1993: Campagne COARE-POI a bord du N.O. Le Noroit, 1 dec 92 - 2 mar 93. *Technical Report, ORSTOM, BP A5, Noumea, New Caledonia.* Rapports de Missions, Sci. mer, Oceanogra. phys., 10, 338 pp.

Dickey, T.D., B. Hartman, D. Hammond, and E. Hurst, 1984: A laboratory technique for investigating the relationship between gas transfer and fluid turbulence. In: *Gas Transfer at Water Surfaces*, W. Brutsaert and G.H. Girka, Eds., 93-100.

Dillon, T.M., J.G. Richman, C.G. Hansen, and M.D. Pearson, 1981: Near-surface turbulence measurements in a lake. *Nature* 290, 390-392.

Donaghay, P.L., and T.R. Osborn, 1997: Toward a theory of biological-physical control of harmful algal bloom dynamics and impacts. *Limnol. Oceanogr*. 42(5), 1238-1296.

Donaghay, P.L., H.M. Rines, and J.M. Sieburth, 1992: Simultaneous sampling of fine scale biological, chemical and physical structure in stratified waters. *Ergeb Limnol.* 36, 97-108.

Donelan, M.A., 1998: Air-water exchange processes. *Physical Processes in Lakes and Oceans,* J. Imberger, Ed., Coastal and Eustarine Studies 54, American Geophysical Union, 19-36.

Donelan, M.A., B.K. Haus, N. Reul, W.J. Plant, M. Stiassnie, H.C. Graber, O.B. Brown, and E.S. Saltzman, 2004: On the limiting aerodynamic roughness of the ocean in very strong winds, *Geophys. Res. Lett. 31*, L18306, doi:10.1029/2004GL019460.

Donelan, M.A., and W.J. Pierson, 1987: Radar scattering and equilibrium ranges in wind-generated waves with application to scatterometry. *J. Geophys. Res.* 92, 4971-5029.

Doney, S.C., 1995: Irreversible thermodynamics and air-sea exchange. *J.Geophys.Res.*. 100, 8541-8553.

Dozenko, S.V., 1974: Theoretical basis of measuring physical fields in the ocean. *Hydrometeoizdat*, Leningrad, 152 p. (in Russian only).

Drennan, W., M.A. Donelan, E.A. Terray, and K.B. Katsaros, 1996: Oceanic turbulence dissipation measurements in SWADE. *J. Phys. Oceanogr.* 26, 808-815.

Duncan, J.H., 2001: Spilling breakers. *Ann. Rev. Fluid Mech.* 33, 519-547.

Dysthe, T.H., and K.P. Das, 1981: Coupling between a surface wave spectrum and an internal wave: Modulation interaction. *J. Fluid Mech.* 104, 483-503.

Ebuchi, N., H. Kawamura, and Y. Toba, 1987: Fine structure of laboratory wind-wave surfaces using an optical method. *Bound. -Lay. Meterol*. 39, 133–151.

Edson, J.B., W.R. McGillis, J. Ware, J.E. Hare, and C.W. Fairall, 1999: Direct $CO_2$ flux measurement at the Air-Sea Interface. *Supplement to EOS*, *Transactions*, April 27, S45.

Einstein, A., 1905: On the motion of small particles suspended in liquids at rest required by the molecular-kinetic theory of heat. *Annalen der Physik* 17, 549-560.

Ekman, V.W., 1905: On the influence of the earth's rotation on ocean currents. *Arkiv Met. Astr. Fysik.* 2, 1-53.

Elfouhaily, T., B. Chapron, K. Katsaros, and D.A. Vandemark, 1997: United directional spectrum for long and short wind-driven waves. *J. Geophys. Res.* 102, 15,781-15,796.

Emanuel, K., 2003: Q similarity hypothesis for air-sea exchange at extreme wind speeds. *J. Atmos. Sci.* 60, 1420-1428.

Emery, W.J., Y.Yu, G.A. Wick, P. Schlüssel, and R. Reynolds, 1994: Improving satellite infrared sea surface temperature estimates by including independent water-vapor observations. *J. Geophys. Res.* 99, 5219-5236.

Emery, W.J., and R.E. Thompson, 1998: *Data Analysis Methods in Physical Oceanography*. Pergamon Press, 634 pp.

Engel, O. G., 1966: Carter depth in fluid mechanics. *J. Appl. Phys*. 37, 1798-1808.

Fairall, C.W., J.D. Kepert, and G.J. Holland, 1994: The effect of sea spray on the surface wind profile during conditions of strong wind. *Bound. -Lay. Meteorol.* 55, 305-308.

Fairall, C.W., R. Markson, G.E. Schacher, and K.L. Davidson, 1980: An aircraft study of turbulence dissipation rate and temperature structure function in the unstable marine atmospheric boundary layer. *Bound.- Lay. Meteorol.* 19, 453-469.

Fairall, C.W., E.F. Bradley, J.E. Hare, A.A. Grachev, and J.B. Edson, 2003: Bulk parameterization of Air-Sea Fluxes: Updates and verification for the COARE algorithm. *J. Climate* 16, 571-591.

Fairall, C.W., E.F. Bradley, D.P. Rogers, J.B. Edson, and G.S. Young, 1996: Bulk parameterization of air-sea fluxes in TOGA COARE. *J. Geophys. Res.* 101, 3747-3767.

Fairall, C.W., J.E. Hare, J.B. Edson, and W. McGillis, 2000: Parameterization and micrometeorological measurements of air-sea gas transfer. *Bound.-Lay. Meteorol.* 96, 63-105.

Faller, A.J., and E.A. Caponi, 1978: Laboratory studies of wind-driven Langmuir circulations, *J. Geophys. Res.* 83, 3617-3633.

Farmer, D.M., 1978: Observations of Long Nonlinear Internal Waves in a Lake. *J. Phys. Oceanogr.* 8(1), 63-73.

Farmer, D.M., and D. Lemon, 1984: The influence of bubbles on ambient noise in the ocean at high wind speeds. *J. Phys. Oceanogr.* 14, 1761–1777.

Farmer, D.M., and M. Li. 1995: Patterns of bubble clouds organized by Langmuir circulation. *J. Phys. Oceanogr*. 25, 1426-1440.

Farmer, D.M., S. Vagle, and A.D. Booth, 1998: A free-flooding acoustical resonator for measurement of bubble size distributions. *J. Atmos. Ocean. Tech.* 15(5), 1132-1146.

Fedorov, K.N., 1986: *The physical nature and structure of oceanic fronts*. Springer-Verlag, Berlin and New York.

Fedorov, K.N., and A.I. Ginzburg, 1988: The near-surface layer of the ocean, Hydrometeoizdat, Leningrad. Translated into English in 1992 by VSP, P.O. Box 346, 3700 AH Zeist, The Netherlands.

Fedorov, K.N., V.L. Vlasov, A.K. Ambrosimov, and A.I. Ginzburg, 1979: Investigating the surface layer of evaporating sea water by optical interferometry. Izvestya, *Academy of Sciences, USSR, Atmospheric and Oceanic Physics* 15, 742-747.

Felizardo F.C., and W.K. Melville, 1995: Correlations between ambient noise and the ocean surface wave field. *J. Phys. Oceanogr.* 25, 513-532.

Feng, M., P. Hacker, and R. Lukas, 1998a: Upper ocean heat and salt balances in response to a westerly wind burst in the western equatorial Pacific during TOGA COARE. *J. Geophys. Res.* 103, 10,289-10,311.

Feng, M., M.A. Merrifield, R. Pinkel, P. Hacker, A.J. Plueddemann, E. Firing, R. Lukas, and C. Eriksen, 1998b: Semidiurnal tides observed in the western equatorial Pacific during the Tropical Ocean-Global Atmosphere Coupled Ocean-Atmosphere Response Experiment. *J. Geophys. Res*. 103, 10,253-10,272.

Feng, M., R. Lukas, P. Hacker, R.A. Weller, and S.P. Anderson, 2000: Upper ocean heat and salt balances in the western equatorial Pacific in response to the intraseasonal oscillation during TOGA COARE. *J. Climate* 13, 2409-2427.

Feng, M., R. Lukas, and P. Hacker, 2001: Spin-up of a sub-mesoscale eddy in the TOGA COARE Intensive Flux Array during the spin-down of an intense eastward jet. *J. Phys. Oceanogr.* 31(3), 711-724.

Ferrari, R., and W.R. Young, 1997: On the development of thermohaline correlations as a result of nonlinear diffusive parameterizations, *J. Mar. Res.* 55, 1069-1101.

Ferrari, R., and D.L. Rudnick, 2000: Thermohaline variability in the upper ocean*, J. Geophys. Res.* 105(C7), 16,857-16,883.

Ferrari, R., and F. Paparella, 2003: Compensation and alignment of thermohaline gradients in the ocean mixed layer. *J. Phys. Oceanogr.* 34, 247–257.

Ferrari, R., F. Paparella, D.L. Rudnick, and W.R. Young, 2001: The temperature-salinity relationship of the mixed layer. In: *Proceedings, Hawaiian Winter Workshop, University of Hawaii at Manoa, January 16-19, 2001*. Editors: Peter Muller and Diane Henderson. SOEST Special Publication 2001, 95-104.

Fiedler, L., and S. Bakan, 1997: Interferometric measurements of sea surface temperature and emissivity. *German J. Hydrogr.* 49(2/3), 357-365.

Flament, P., J. Firing, M. Sawyer, and C. Trefois, 1994: Amplitude and horizontal structure of a large diurnal sea surface warming event during the Coastal Ocean Dynamics Experiment. *J. Phys. Oceanogr*. 24, 124-139.

Flack, K.A., J.R. Saylor, and G.B. Smith, 2001: Near-surface turbulence for evaporative convection at an air-water interface. *Phys. Fluids* 13, 3338-3345.

Fornwalt, B., G. Terray, G. Voulgaris, and J. Trowbridge, 2002: Flow modeling around an autonomous underwater vehicle with applications to turbulence measurements. Abstract to 2002 Ocean Sciences Meeting, 11-15 February 2002, Honolulu, Hawaii. Published in Supplement to *EOS, Transactions, American Geophysical Union* 83(4), p. 143.

Foster, T.D., 1971a: A convective model for a diurnal cycle in the upper ocean. *J. Geophys. Res.* 76(3), 666-675.

Foster T.D., 1971b: Intermittent convection. *Geophys. Fluid Dyn.* 2, 201-217.

Foster, T.D., 1974: The Hierarchy of Convection, *Colloques Internationaux du C.N.R.S. N215.* – Processus de Formation Des Eaux Oceaniques Profondes, 235-241.

Foukal, P., 2003: Can slow variations in solar luminosity provide missing link between the sun and climate? *EOS, Transactions, American Geophysical Union* 84(22), 205-208.

Frew, N.M., E.J. Bock, W.R. McGillis, A.V. Karachintsev, T. Hara, T. Muensterer, and B. Jaehne, 1995: Variation of air-water gas transfer with wind stress and surface viscoelasticity, in Air-Water Gas Transfer, B. Jaehne and E.C. Monahan, Eds., AEON Verlag & Studio, Hanau, 529-541.

Frew, N., 1997: The role of organic films in the air-sea gas exchange. In: *The Sea Surface and Global Change*, P.S. Liss and R.A. Duce, Eds., Cambridge University Press, UK, 121-172.

Fröhlich, C., 2000. Observations of Irradiance Variations. *Space Science Reviews* 94, 15-24.

Frouin, R., D.W. Lingner, C. Gautier, K.S. Baker, and R.C. Smith, 1989: A simple analytical formula to compute clear sky total and photosynthetically available solar irradiance at the ocean surface. *J. Geophys. Res.* 94, 9731-9742.

Galvin, C.J., 1972: Wave breaking in shallow water. In: *Waves on Beaches and Resulting Sediment Transport*, R.E. Meyer, Ed., Academic Press, Boston, 413-455.

Garbe, C.S., B. Jähne, and H. Hauβecker, 2002: Measuring the sea surface heat flux and probability distribution of surface renewal events. In: *AGU Monograph Gas Transfer at Water Surfaces*. E.S. Saltzman, M. Donelan, W. Drennan, and R. Wanninkhof, Eds., pp. 109-114.

Garrett C., M. Li, and D. Farmer, 2000: The connection between bubble size spectra and kinetic energy dissipation rates in the upper ocean. *J. Phys. Oceanogr.* 30, 2163-2171.

Garrettson, G.A., 1973: Bubble transport theory with application to the upper ocean. *J. Fluid Mech.* 59, 187-206.

Garwood, Jr., R.W., 1977: An oceanic mixed layer model capable of simulating cyclic states. *J. Phys. Oceanogr.* 7, 455-468.

Garwood, Jr., R.W., and P.C. Gallacher, 1985: Wind direction and equilibrium mixed layer depth: General theory. *J. Phys. Oceanogr.* 15, 1325-1331.

Garwood, Jr., R.W., P. Muller, and P.C. Gallacher, (1985): Wind direction and equilibrium mixed layer depth in the tropical Pacific Ocean. *J. Phys. Oceanogr.* 15, 1332-1338.

Gathman, S. G., 1982: A time-dependent oceanic aerosol profile model. *NRL Rep. 8536, Naval Research Laboratory, Washington, DC*, 35 pp. [NTIS AD-A111148.]

Gautier C., 1978: Some evidence of cool surface water pools associated with mesoscale downdrafts during GATE. *J. Phys. Oceanogr.* 8, 162-166.

Gemmrich, J.R., T.D. Mudge, and V.D. Polonchicko, 1994: On the energy input from wind to surface waves. *J. Phys. Oceanogr.* 24, 2413–2417.

Gemmrich, J.R., and D.M. Farmer, 1999: Observations of the scale and occurrence of breaking surface waves. *J. Phys. Oceanogr.* 29, 2595-2606.

Gemmrich J.R., and D.M. Farmer, 2002: Near-surface turbulence in the presence of breaking waves. Abstract to 2002 Ocean Sciences Meeting, 11-15 February 2002, Honolulu, Hawaii. Published in Supplement to *EOS, Transactions, American Geophysical Union* 83(4), p. OS371.

Gentemann, C.L., C.J. Donlon, A. Stuart-Menteth, and F.J. Wentz, 2003: Diurnal signals in satellite sea surface temperature measurements. *Geophys. Res. Lett.* 30, 10.1029/ 2002GL016291.

Gentemann, C.L., F.J. Wentz, C.A. Mears, and D.K. Smith, 2004: In situ validation of Tropical Rainfall Measuring Mission microwave sea surface temperatures. *J. Geophy. Res.*, 109, C04021, 1-9.

Gerstner, F.J. von, 1802: *Theorie der Wellen*. Abhand. Kön Bömischen Gesel. Wiss., Prague.

Ginzburg, A.I., A.G. Zatsepin, and K.N. Fedorov, 1977: Fine structure of the thermal boundary layer in the water near the air-water interface. Izvestya, *Academy of Sciences, USSR, Atmospheric and Oceanic Physics* 13, 869-875.

Gladyshev, M.I., 1997: Biophysics of the sea surface film of aquatic ecosystems. In: *The Sea Surface and Global Change*, P.S. Liss and R.A. Duce, Eds., Cambridge University Press, UK, 321-338.

Glazman, R.E., and A. Greysukh, 1993: Satellite altimeter measurements of surface wind. *J. Geophys. Res.* 98, 2475-2483.

Godfrey, J.S., R.A. Houze Jr., R.H. Johnson, R. Lukas, J.-L. Redelsperger, A. Sumi, and R.Weller, 1998: Coupled Ocean-Atmosphere Response Experiment (COARE): An interim report. *J. Geophys. Res.* 103(C7), 14,395-14,450.

Goldstein, S., 1931: On the stability of superposed streams of fluids of different densities. *Proc. Roy. Soc. A*, 132, 524–548.

Gong, S.L., L.A. Barrie, and J.-P. Blanchet, 1997: Modeling sea-salt aerosols in the atmosphere: 1, Model development. *J. Geophys. Res.* 102, 3805–3818.

Gordon, H.R., 1997: Atmospheric correction of ocean color imagery in the earth observing system era. *J. Geophys. Res.* 102, 17,081-17,106.

Gordon, H. R., and A. Morel, 1983: Remote assessment of ocean color for interpretation of satellite visible imagery-a review. Lecture Notes on Coastal and Estuarine Studies, Springer-Verlag New York.

Gosnell, R., C.W. Fairall, and P.J. Webster, 1995: The sensible heat of rainfall in the tropical ocean. *J. Geophys. Res.* 100**,** 18,437–18,442.

Gow, A.J., and W.B. Tucker III, 1990: Sea ice. In: *Polar Oceanography*, Academic Press, San Diego et al., 47-122.

Göz, M.F., B. Bunner, M. Sommerfeld, and G. Tryggvason, 2001: Direct numerical simulation of bidisperse bubble swarms. Contribution to the International Conference on Multiphase Flow, New Orleans, May 2001.

Grabowski, W.W., and P.K. Smolarkiewicz, 1999: CRCP: A cloud resolving convection parameterization for modeling the tropical convecting atmosphere. *Physica D* 133, 171(178).

Grachev, A.A., C.W. Fairall, and E.F. Bradley, 1997: Convective profile constants revisited. *Bound. -Lay. Meteorol.* 94, 495-515.

Grachev, A.A., and C.W. Fairall, 2001: Upward momentum transfer in the marine boundary layer. *J. Phys. Oceanogr.* 31, 1698–1711.

Gradshteyn, I. S., and Ryzhik, I.M., 2000: *Tables of Integrals, Series, and Products, 6th ed.* San Diego, CA: Academic Press.

Grassl, H., 1976: The dependence of measured cool skin of the ocean on wind stress and total heat flux. *Bound.-Lay. Meteorol.* 10, 465-474.

Green T., and D.F. Houk, 1979: The removal of organic surface films by rain. *Limnol. Oceanogr* 24, 966–970.

Greenan, B.J.W., N. S. Oakey, and F.W. Dobson, 2001: Estimates of dissipation in the ocean mixed layer using a quasi-horizontal microstructure profiler. *J. Phys. Oceanogr.* 31, 992.

Gregg, M.C., 1975. Oceanic fine and microstructure. *Rev. Geophys. Space Ge.* 13, 586-591 and 635-636.

Gregg, M.C., H. Peters, J.C. Wesson, N.S. Oakey, and T.J. Shay, 1984: Intense measurement of turbulence and shear in the equatorial undercurrent. *Nature* 318, 140-144.

Gregg, M.C., T.B. Sanford, and D.P. Winkel, 2003: Reduced mixing from the breaking of internal waves in the equatorial waters. *Nature* 422, 513-516.

Gregg, M.C., H.E. Seim, and D.B. Percival, 1993: Statistics of shear and turbulent dissipation profiles in random internal wave fields. *J. Phys. Oceanogr*. 23, 1777-1979.

Greenhut, G.K., 1978: Correlations between rainfall and sea surface temperature during GATE. *J. Phys. Oceanogr.* 8, 1135-1138.

Grimshaw, R.H.J., and K.R. Khusnutdinova, 2004: The effect of bubbles on internal waves. *J. Phys. Oceanogr.* 34, 477-489.

Gurvich, A.S., and A.M. Yaglom, 1967: Breakdown of eddies and probability distributions for small-scale turbulence. *Phys. Fluids* 10 (Suppl., Part II), 559-565.

Hagen, J.P., and M. Kurosaka, 1993: Corewise cross-flow transport in hairpin vortices –the "Tornado Effect." *Phys. Fluids A* 5, 3167–3174.

Handler, R.A., T.F. Swean, Jr., R.I. Leghton, and J.D. Swearingen, 1993: Length scales and the energy balance of turbulence near a free surface. *AIAA Journal* 31, 1998-2007.

Hanson, Jr., A.K., and P.I. Donaghay, 1998: Micro- to fine-scale chemical gradients and layers in stratified coastal waters. *Oceanography* 11(1), 10-17.

Hardy, J.T., 1982: The sea-surface microlayer: biology, chemistry and anthropogenic enrichment. *Prog. Oceanogr.* 11, 307-328.

Hardy, J.T., K.A. Hunter, D. Calmet, J.J. Cleary, R.A. Duce, T.L. Forbes, M.L. Gladyshev, G. Harding, J.M. Shenker, P. Tratnyek, and Y. Zaitsev, 1997: Report Group 2--Biological effects of chemical and radiative change in the sea surface. In: *The Sea Surface and Global Change*. Edited by P.S. Liss and R.A. Duce, Cambridge University Press, UK, 35-70.

Hare, J.E., C.W. Fairall, W.R. McGillis, J.B. Edson, B. Ward, and R. Wanninkhof, 2004: Evaluation of the National Oceanic and Atmospheric Administration/Coupled-Ocean Atmospheric Response Experiment (NOAA/COARE) air-sea gas transfer parameterization using GasEx data. *J. Geophys. Res.*, 109, C08S11, doi:10.1029/2003JC001831.

Hasegawa, A., 1985: Self-organization processes in continuous media. *Advan. Phys.* 34, 1-42.

Hasse, L., 1971: The sea surface temperature deviation and the heat flow at the air-sea interface, *Bound.-Lay. Meteorol.* 1, 368-379.

Hinze, J.O., 1955: Fundamentals of the hydrodynamic mechanism of splitting in dispersion process. *A.I.C.H.E. Journal* 1, 289-295.

Hinze, J., 1975: Turbulence. McGraw-Hill, New York, 790 pp.

Hoeber H., 1969: Wind-, Temperatur- und Feuchteprofile in der wassernahen Luftschicht uber dem aquatorialen Atlantik. Sonderdruck aus Meteor. Forschungsergebnisse Reihe B, Heft 3. Berlin, Stuttart: Geburder Borntrager, p. 1.

Hoffmann, K.A. 1989: *Computational Fluid Dynamics for Engineers*. Engineering Education System, Austin, Tex, 567 pp.

Horrocks, L.A., B. Candy, T. Nightingale, R.W. Saunders, A.G. O'Carroll, and A.R. Harris, 2003: Parameterisations of the skin effect and implications for satellite-based measurement of sea-surface temperature. *J. Geophys. Res.* 108, p. 3096.

Houghton, D., 1969: Acapulco'68. *Weather* 24, 2-18.

Houk, D.F., and T. Green, 1976: A note on surface waves due to rain. *J. Geophys. Res.* 81, 4482-4484.

Houze, Jr., R.A., 1989: Observed structure of mesoscale convective systems and implications for large scale heating. *Q. J. Roy. Meteor. Soc.* 115, 425-461.

Houze, R.A., 1993: *Cloud Dynamics*. Academic Press, Boston, 573 pp.

Howard, L. N., 1961: Note on a paper of John Miles. *J. Fluid Mech.* 10**,** 509-512.

Hsiao, M., S. Lichter, and L.G. Quintero, 1988: The critical Weber number for vortex and jet formation for drops impinging on a liquid pool. *Phys. Fluids* 31, 3560-3562.

Hunkins, K., and M.J. Fliegel, 1973: Internal undular surges in Seneca Lake: Natural occurrence of solitons. *J. Geophys. Res*. 78, 539-548.

Hurdy, J.T., 1997: Biological effects of chemicals in the sea-surface microlayer. In: *The Sea Surface and Global Change*, Edited by P.S. Liss and R.A. Duce, Cambridge University Press, UK, 339-370.

Huyer, A., P.M. Kosro, R. Lukas, and P. Hacker, 1997: Upper ocean thermohaline fields near 2°S, 156°E, during the Coupled Ocean-Atmosphere Response Experiment, November 1992 to February 1993. *J. Geophys. Res*. 102, 12,749-12, 784.

Iida, N., Y. Toba, and M. Chaen, 1992: A new expression for the production rate of seawater droplets on the sea surface. *J. Oceanography* 48, 439-460.

Imberger, J., 1985: The diurnal mixed layer. *Limnol. Oceanogr*. 30(4), 737-770.

Intergovernmental Panel on Climate Change (IPCC)**,** Climate Change 2001: *The Scientific Basis, Contribution of Working Group I to the Third Assessment Report of the Intergovernmental Panel on Climate Change*. Cambridge Univ. Press, NY, 2001.

IOCCG, 2000: Remote sensing of ocean color in coastal, and other optically-complex waters. Sathyendranath, S., Ed., Reports of the international ocean-colour coordinating group, no. 3, IOCCG. Published by the International Ocean-Colour Coordinating Group, P.O. Box 1006, Dartmouth, Nova Scotia, B2Y 4A2, Canada, 145 pp.

Ivanoff, A., 1977: Oceanic absorption of solar energy, In: *Modelling and Prediction of the Upper Layers of the Ocean*, E.B. Kraus, Ed., New York, Pergamon, 326 pp.

Jaehne, B., O. Muennich, R. Boesinger, A. Dutzi, W. Huber, and P. Libner**,** 1987: On the parameters influencing air–water gas exchange. *J. Geophys. Res.* 92, 1937-1949.

Jerlov, N.G., 1976. *Marine Optics*. Amsterdam: Elsevier

Jessup, A.T., C.J. Zappa, and H.H. Yeh, 1997: Defining and quantifying microscale wave breaking with infrared imagery. *J. Geophys. Res.* 102(C10), 23,145-23,154.

Jin, Z., T.P. Charlock, and K. Rutledge, 2002: Analysis of the Broadband Solar Radiation and Albedo Over the Ocean Surface at COVE. *J. Atmos. Ocean. Tech.* 19, 1585-1601.

Jo, Y.-H., X.-H. Yan, J. Pan, and W.T. Liu, 2004: Sensible and latent heat flux in the tropical Pacific from satellite multi-sensor data. *Remote Sens. Environ.* 90, 166-177.

Johannessen, O.M., J.A. Johannessen, J.H. Morison, B.A. Farrelly, and E.A.S. Svendsen, 1983: Oceanographic conditions in the marginal ice zone north of Svilbard in early fall 1979 with an emphasis on mesoscale processes, *J. Geophys. Res*. 88, 2755-2769.

Johnson, B., and R. Cooke, 1979: Bubble populations and spectra in coastal waters: A photographic approach, *J. Geophys. Res.* 84, 3761–3766.

Jones, I.S.F., 1985: Turbulence below wind waves. In: *The Ocean Surface-Wave Breaking, Turbulent Mixing and Radio Probing*. Y. Toba and H. Mitsuyasu, Eds., Reidel, 437-442.

Jones, I.S.F., and B.C. Kenney, 1977: The scaling of velocity fluctuations in the surface mixed layer. *J. Geophys. Res.* 82, 1392-1396.

Kamal, J.C., J.C. Wyngaard, Y. Izumi, and O.R. Cote, 1972: Spectral characteristics of surface-layer turbulence, *Q. J. Roy. Meteor. Soc*. 98, 563-589.

Kantha, L.H., and C.A. Clayson, 1994: An improved mixed layer model for geophysical applications. *J. Geophys. Res*. 99, 25,235-25,266.

Kantha, L.H., and C.A. Clayson, 2004: On the effect of surface gravity waves on mixing in an oceanic mixed layer. *Ocean Modelling* 6, 101-124.

Karl, D.M, 1991: RACER: Research on Antarctic Coastal Ecosystem Rates. Preface. *Deep-Sea Res.* 38, v-vii.

Katsaros, K.B., 1976: Effect of precipitation on the eddy exchange in a wind-driven sea. *Dynam. Atmos. Oceans* 1, 99-126.

Katsaros, K.B., 1980: The aqueous thermal boundary layer. *Bound.-Layer Meteorol.* 18, 107-127.

Katsaros, K.B., 1981: Quality of SEASAT SMMR (scanning multichannel microwave radiometer) atmospheric water determination. In: *COSPAR/SCOR/IUCRM Symposium on Oceanography from Space*, Venice, Italy, May 26-30, 1980, *Mar.Sci*. 13, Plenum Press, New York, 691-706.

Katsaros, K.B., 1990: Parameterization schemes and models for estimating the surface radiation budget. G.L. Geernaert and W.J. Plant, Eds., In: *Surface Waves and Fluxes, Vol. II,* Kluwer Academic Publishers, The Netherlands, pp. 339-368.

Katsaros, K.B., and K.J.K. Buettner, 1969: Influence of rainfall on temperature and salinity of the ocean surface. *J. Appl. Meteorol.* 8, 15-18.

Katsaros, K.B., and G. de Leeuw, 1994: Comment on “Sea spray and turbulent air-sea heat fluxes” by Edgar L. Andreas. *J. Geophys. Res.* 99, 14,339-14,343.

Katsaros, K.B., and J. DeCosmo, 1990: Evaporation at high wind speeds, sea surface temperature at low wind speeds: Examples of atmospheric regulation. *Proceedings,*

*Workshop on Modeling the Fate and Influence of Marine Spray,* Marseille, France, June 5-7, 1990, 1-11.

Katsaros, K.B., and A.V. Soloviev, 2004: Vanishing horizontal sea surface temperature gradients at low wind speeds. *Bound.-Layer Meterol.* 112, 381-396.

Katsaros, K.B., A. Fiuza, F. Sousa, and V. Amann, 1983: Surface temperature patterns and air-sea fluxes in the German Bight during MARSEN 1979, Phase 1. *J. Geophys. Res.* 88, 9871-9882.

Katsaros, K.B., W.T. Liu, J.A. Businger, and J.E. Tillman, 1977: Heat transport and thermal structure in the interfacial boundary layer measured in an open tank of water in turbulent free convection. *J. Fluid Mech*. 83, 311-335.

Katsaros, K.B., L.A. McMurdie, R.J. Lind, and J.E. DeVault, 1985: Albedo of a water surface, spectral variation, effects of atmospheric transmittance, sun angle, and wind speed. *J. Geophys. Res.*, 90, 7313-7321.

Katsaros, K.B., A.V. Soloviev, R.H. Weisberg, and M.E. Luther, 2005: Reduced Horizontal Sea Surface Temperature Gradients Under Conditions of Clear Sky and Weak Winds. *Bound.-Layer Meterol.* 116, 175-185.

Kawai, Y., and H. Kawamura, 2002: Evaluation of the diurnal warming of sea surface temperature using satellite-derived marine meteorological data. *J. Oceanography 58*, 805–814.

Keeling, R.F., 1993: On the role of large bubbles in air-sea gas exchange and supersaturation in the ocean. *J. Mar. Res.* 51, 237-271.

Kennan, S.C., and R. Lukas, 1996: Saline intrusions in the intermediate waters north of Oahu, Hawaii. *Deep-Sea Res.* 43(2-3), 215-241.

Kim, H.T., S.J. Kline, and W.C. Reynolds, 1971: The production of turbulence near a smooth wall in a turbulent boundary layer. *J. Fluid Mech.* 50, 133-160.

Kitaigorodskii, S.A., 1962: Application of the theory of similarity to the analysis of wind generated wave motion as a stochastic process. Bulletin of the Academy of Sciences of the USSR, Geophysics Series 73-80 (English Translation).

Kitaigorodskii, S.A., and M.A. Donelan, 1984: Wind-wave effects on gas transfer, In: *Gas Transfer at the Water Surfaces*, W. Brutseart and G.H. Jirka, Eds., Reidel, 147-170.

Kitaigorodskii, S.A., M.A. Donelan, J.L. Lumley, and E.A. Terray, 1983: Wave-turbulence interactions in the upper ocean: Part II. *J. Phys. Oceanogr.* 13, 1988-1999.

Kline, S.J., W.C. Reynolds, F.A. Schraub, and P.W. Runstadler, 1967: The structure of turbulent boundary layers. *J. Fluid Mech*. 30, 741–773.

Knudsen, V.O., R.S. Alford, and J.W. Emling, 1948: Underwater ambient noise. *J. Mar. Res.* 3, 410-429.

Koga, M., 1981: Direct production of droplets from breaking wind-waves-Its observation by a multi-colored overlapping exposure technique. *Tellus* 33, 552-563.

Koga, M,. and Y. Toba, 1981: Droplet distribution and dispersion process on breaking wind waves. *Sci. Rep. Tohoku Univ*., Sr. 5 (Tohoku Geophys. Journal) 28, 1-25.

Kolaini, A.R., P. Dandeault, and A.D. Ruxton, 1995: Passive and active acoustical measurement of laboratory breaking waves. In: *Proceedings of III Int. Meeting on Natural Physical Processes Related to Sea Surface Sound "Sea Surface Sound'94," University of California, Lake Arrowhead, 7-11 March 1994*, edited by M.J. Buckingham and J. R. Potter (World Scientific, Singapore), 229-240.

Kolesnikov, A.G., 1947: Calculation of the diurnal temperature variation of the sea surface. *Doklady Akademii Nauk SSSR* 57(2) (in Russian.).

Kolesnikov, A.G., and A.A. Pivovarov, 1955: Calculation of the diurnal temperature variation according to summary solar radiation and air temperature. *Doklady Akademii Nauk USSR* 102(2) (in Russian).

Kolmogorov, A.N., 1942: Equations of turbulent motion of an incompressible fluid. Izvestia, *Academy of Sciences, USSR; Physics*, 6(1) & (2), 56-58.

Kolmogorov, A.N., 1949: O droblenii kapel v turbulentnom potoke. *Doklady Akademii Nauk USSR* 66(15), 825-828 (in Russian).

Komen, G.J., L. Cavaleri, M. Donelan, K. Hasselmann, S. Hasselmann, and P.A.E.M. Janssen, 1994: *Dynamics and Modelling of Ocean Waves.* Cambridge University Press, 532 pp.

Kopelevich, O.V., S.V. Sheberstov, V.I. Burenkov, M.A. Evdoshenko, and S.V. Ershova, 1998: New data products derived from SeaWIFS ocean color data: examples for the Mediterranean Basin. International Symposium Satellite-based Observation: A Tool for the Study of the Mediterranean Basin, Tunis, 23-27 November, 1998.

Kraus, E.B. and J.A. Businger, 1994: *Atmosphere-Ocean Interaction*. Oxford University Press, 352 pp.

Kraus, E.B., and C. Rooth, 1961: Temperature and steady state vertical heat flux in the ocean surface layer. *Tellus* 13, 231-238.

Kraus, E.B., and J.S. Turner, 1967: A one-dimensional model of the seasonal thermocline. Pt. II The general theory and its consequences. *Tellus* 19, 98-105.

Kraichnan, R.H., 1967: Inertial ranges in two-dimensional turbulence. *Phys. Fluids* 10, 1417-1423.

Kraichnan, R.H., 1975: Statistical dynamics of two-dimensional flow. *J. Fluid Mech*. 67, 155-175.

Kudryavtsev V.N., and G.L. Luchnik, 1979: On thermal state of the cool skin. *Proc. Mar. Hydrophys. Inst*. 3, 105-112.

Kudryavtsev, V.N., and A.V. Soloviev, 1985: On parameterization of cool skin of the ocean. Izvestia*„ Atmospheric and Oceanic Physics* 21(2), 177-183.

Kudryavtsev, V.N., and A.V. Soloviev, 1988: Daytime near-surface current, *Doklady Akademii Nauk SSSR* 303(1), 59-62.

Kudryavtsev, V.N., and A.V. Soloviev, 1990: Slippery near-surface layer of the ocean arising due to daytime solar heating. *J. Phys. Oceanogr.* 20, 617-628.

Kundu, P.K., I.M Cohen, and H.H. Hu, 2004: *Fluid Mechanics*. Elsevier, Amsterdam, 759 pp.

Laevastu, T., 1960: Factors affecting the temperature of the surface layer of the sea. Societas Scientiarum Fennica, Commentatisnes Phisico-Mathematicae, Helsinki 25, N 1.

Lagerloef, G.S.E., C.T. Swift, and D.M. Le Vine, 1995: Sea surface salinity: The next remote sensing challenge. *Oceanography* 8**,** 44–50.

Lamarre, E., and W.K. Melville, 1994: Sound speed measurements near the ocean surface. Instrumentation for the measurement of sound speed near the ocean surface. *J. Acoust. Soc. Amer.,* 96**,** 3605–3616.

Lamarre, E., and W.K. Melville, 1995: Instrumentation for the measurement of sound speed near the ocean surface. *J. Atmos. Ocean. Tech.* 12**,** 317–329.

Landau, L.D., and E.M. Lifshits, 1986: Theoretical Physics, Hydrodynamics Vol. 6, Moscow, Nauka, 736 pp.

Landau, L.D., and E.M. Lifshitz, 1993: *Fluid Mechanics*, 2nd ed., Pergamon Press, New York 593 pp.

Langmuir, I., 1938: Surface motion of water induced by wind. *Science* 87, 119-123.

Large, W.G., G. Danabasoglu, J.C. McWilliams, P.R. Gent, and F.O. Bryan, 2001: Equatorial circulation of a global ocean climate model with anisotropic horizontal viscosity. *J. Phys. Oceanogr*. 31, 518-536.

Large, W.G., J.C. McWilliams, and S.C. Doney, 1994: Oceanic vertical mixing: A review and a model with a nonlocal boundary layer parameterization, *Rev. Geophys.* 32, 363-403.

Large, W.G., and S. Pond, 1981: Open ocean momentum flux measurements in moderate to strong winds. *J. Phys. Oceanogr.* 11, 324-336.

LeBlond, P.H., and L.A. Mysak, 1978. *Waves in the Ocean*, Elsevier, New York, 602 pp.

Leibovich, S., 1977a: On the evolution of the system of wind drift currents and Langmuir circulations in the ocean. Part I. Theory and the averaged current. *J. Fluid Mech.* 79, 715-749.

Leibovich, S., 1977b: Convective instability of stably stratified water in the ocean. *J. Fluid Mech*. 82, 561-585.

Leibovich, S., 1983: The form and dynamics of Langmuir circulations. *Ann. Rev. Fluid Mech*. 15, 391–427.

Leibovich, S., and S.K. Lele, 1982: Thermocline erosion and surface temperature variability due to Langmuir circulations. FDA Rep. #82-07, Sibey School Mech & Aerosp. Eng. Cornell Univ., Ithaca, N.Y.

Leibovich, S., and D. Ulrich, 1972: A note on the growth of small scale Langmuir circulations. *J. Geophys. Res.* 77, 1683-1688.

Leifer, I., and G. de Leeuw, 2001: Bubble measurements in breaking-wave generated bubble plumes during the LUMINY wind-wave experiment. In AGU Monograph *Gas Transfer at Water Surfaces*, E.S. Saltzman, M. Donelan, W. Drennan, and R. Wanninkhof, Eds., 303-309.

Leifer, I., G. de Leeuw, and L.H. Cohen, 2003: Optical measurement of bubbles: System design and application. *J. Atmos. Ocean. Tech.* 20, 1318-1332.

Leifer, I., R.K. Patro, and P. Bowyer, 2000a: A study on the temperature variation of Rise velocity for large clean bubbles. *J. Atmos. Ocean. Tech.* 17, 1392-1402.

Leifer, I., G. de Leeuw, and L.H. Cohen, 2000b: Secondary bubble production from breaking waves: The bubble burst mechanism, *Geophys. Res. Lett. 27*, 4077-4080.

LeMaire, D., P. Sobieski, and A. Guissard, 1999: Full-range sea surface spectrum in nonfully developed state for scattering calculations. *IEEE Trans. Geosci. Remote Sensing* 37, 1038-1051.

Lemon, D.D., D.M. Farmer, and D.R. Watts, 1984: Acoustic measurements of wind speed and precipitation over a continental shelf. *J. Geophys. Res.* 89, 3462-3472.

LeMehaute, B., 1976: *An introduction to hydrodynamics and water wave.* Springer-Verlag, New York, 315 pp.

Le Méhauté, B., and T. Khangaonkar, 1990: Dynamic interaction of intense rain with water waves. *J. Phys. Oceanogr.* 20, 1805–1812.

Lettau, H., 1969: Note on aerodynamic roughness-parameter estimation on the basis of roughness-element description. *J. Appl. Meteorol.* 8, 828-832.

Le Vine, D.M., M. Kao, R.W. Garvine, and T. Sanders, 1998: Remote sensing of ocean salinity: results from the Delaware coastal current experiment. *J. Atmos. Ocean. Tech.* 15, 1478-1484.

Lewis, D.A. and J.F. Davidson, 1982: Bubble splitting in shear flow. *Trans. I.Chem. E.* 60, 283-291.

Lewis, M.R., M.-E. Carr, G.C. Feldman, W. Esaias, and C. McClain, 1990: Influence of penetrating solar radiation on the heat budget of the equatorial Pacific Ocean. *Nature,* 347, 543-545.

Li, M., and C. Garrett, 1997: Mixed-layer deepening due to Langmuir circulation. *J. Phys. Oceanogr.* 27, 121-132.

Lien, R.-C., M.J. McPhaden, and M.C. Gregg, 1996: High-frequency internal waves at 0°, 140°W and their possible relationship to deep-cycle turbulence. *J. Phys. Oceanogr.* 26, 581–600.

Lima-Ochoterena, R., and R. Zenit, 2003: Visualization of the flow around a bubble moving in a low viscosity liquid. *Revista Mexicana De Fisica* 49, 348-352.

Lin, C.C., 1966: *The Theory of Hydrodynamcis Stability*. Cambridge Univ. Press, 155 pp.

Lin, C-L., 2000: Local pressure transport structure in a convective atmospheric boundary layer. *Phys. Fluids* 12, 1112–1128.

Ling, S.C., T.W. Kao, and A.I. Saad, 1980: Microdroplets and transport of moisture from ocean. Proc. ASCE *J. Eng. Mech. Div.* 106, 1327-1339.

Liss, P.S., 1983: Gas transfer, experiments, and geochemical implications. In: *Air-Sea Exchange of Gases and Particles*. P.S. Liss and G.N. Slinn, Eds., Dordrecht, D. Reidel, pp. 241-98.

Liss, P.S., and R.A. Duce, 1997. Preface. In: *The Sea Surface and Global Change*. P.S. Liss and R. A. Duce, Eds., Cambridge University Press, UK, Cambridge.

Liss, P.S., and L. Merlivat, 1986: Air-sea gas exchange rates: introduction and synthesis. In: *The Role of Air-Sea Exchange in Geochemical Cycling*. P.Buat-Menard, Ed., D.Reidel, 113-127.

Liss, P., A.J. Watson, E.J. Bock, B. Jähne, W.E. Asher, N.M. Frew, L. Hasse, G.M. Korenowski, L. Merlivat, L.F. Phillips, P. Schlüssel, and D.K. Woolf, 1997: Report Group 1—Physical processes in the microlayer and the air-sea exchange of trace gases. In: *The Sea Surface and Global Change*, P.S. Liss and R.A. Duce, Eds., Cambridge University Press, UK, 1-34.

Liu, W.T. and J.A. Businger, 1975: Temperature profile in the molecular sublayer near the interface of fluid in turbulent motion. *Geophys. Res. Lett*. 2, 403-404.

Liu, W.T., K.B. Katsaros, and J.A. Businger, 1979: Bulk parameterization of the air-sea exchange of heat and water vapor including the molecular constraints at the interface. *J. Atmos. Sci.* 36, 2052-2062.

Loewen, M.R., and W.K. Melville, 1991a: Microwave backscatter and acoustic radiation from breaking waves. *J. Fluid Mech.* 224, 601-623.

Loewen, M.R., and W.K. Melville, 1991b: A model of the sound generated by breaking waves. *J. Acoust. Soc. Am.* 90, 2075-2080.

Lohmann, U., J. Feichter, J. Penner, and R. Leaitch, 2000: Indirect effect of sulfate and carbonaceous aerosols: A mechanistic treatment. *J. Geophys. Res.* 105, 12,193–12,206.

Loisel, H., and A. Morel, 1998: Light scattering and chlorophyll concentration in case 1 waters: A reexamination. *Limnol. Oceanogr.* 43(5), 847-858.

Lombardo, C.P., and M.C. Gregg, 1989: Similarity scaling of viscous and thermal dissipation in a convecting surface boundary layer. *J. Geophys. Res.* 94, 6273-6284.

Longuet-Higgins, M.S., 1962: Resonant interaction between two trains of gravity waves. *J. Fluid. Mech.* 12, 321–332.

Longuet-Higgins, M.S., 1969: On wave breaking and the equilibrium spectrum of wind-generated waves. *Proc. Roy. Soc*., A310(1501), 151–159.

Longuet-Higgins, M.S., 1992: Capillary rollers and bores, *J. Fluid. Mech.* 240, 659-679.

Longuet-Higgins, M.S., and M.J.H. Fox, 1978: Theory of the almost-highest wave, Part 2, Matching and analytic extension. *J. Fluid Mech.* 85, 769-435.

Longuet-Higgins, M.S., and J.S. Turner, 1974: An “entraining” plume model of a spilling breaker. *J. Fluid Mech.* 63, 1-10.

Lugt, H., and P. Ugincius, 1964: Acoustic rays in an ocean with heat source or thermal mixing zone. *J. Acoust. Soc. America* 36(4), 258-269.

Lukas R., 1990a: Freshwater input to the western equatorial Pacific Ocean and air-sea interaction. In: *Proceedings of the Symposium on Western Tropical Pacific Air-Sea Interactions*, *15-17 November 1988*. China Ocean Press, Beijing, 305-327.

Lukas, R., 1990b: The role of salinity in the dynamics and thermodynamics of the western Pacific warm pool, in preprint, *Proceedings, International TOGA Scientific Conference, WCRP-43, WMO/TD* 379, 73-81.

Lukas R., 1991: The diurnal cycle of sea surface temperature in the western equatorial Pacific. *TOGA Notes*, *January 1991*, No. 2, 1-5.

Lukas, R. and E. Firing, 1984: The geostrophic balance of the Pacific Equatorial Undercurrent. *Deep-Sea Res.* 31, 61–66.

Lukas R., P. Hacker, S. DeCarlo, J. Hummon, F. Santiago-Mandujano, and D. Wright, 2001: Hydrographic observations during the Joint Air-Sea Monsoon Interaction Experimnet (JASMINE) Pilot Study. SOEST data report 5319, University of Hawaii at Manoa, Honolulu, 246 pp.

Lukas, R., and E. Lindstrom, 1991: The mixed layer of the western equatorial Pacific Ocean. *J. Geophys. Res.* C96 (Supplement), 3343-3358.

Lukas, R., P.J. Webster, M. Ji, and A. Leetmaa, 1995: The large-scale context for the TOGA Coupled Ocean-Atmosphere Response Experiment. *Meteorol. Atmos. Phys.* 56, 3-16.

Lumb, F.E., 1964: The influence of cloud on hourly amount of total solar radiation at the sea surface. *Q. J. Roy. Meteor. Soc*. 90, 43-56.

Ly, L.N., and R.W. Garwood, Jr., 2000: Numerical modeling of wave-enhanced turbulence in the oceanic upper layer. *J. Oceanography* 56, 473-483.

Mack, A.P., and D. Hebert. 1997: Internal gravity waves in the upper eastern equatorial Pacific: Observations and numerical solutions. *J. Geophys. Res.*102(9), 21,081-21,100.

Maes, C., J. Picaut, and S. Belamari, 2002: Salinity barrier layer and onset of El Niño in a Pacific coupled model. *Geophys. Res. Lett.* 29(24), 2206, doi:10.1029/2002GL016029.

Makin, V.K., 1998: Air-sea exchange of heat in the presence of wind waves and spray. *J. Geophys. Res.* 103, 1137-1152.

Makin, V.K., and V.N. Kudryavtsev, 1999: Coupled sea surface-atmosphere model. 1. Wind over waves coupling. *J. Geophys. Res.* 104, 7613-7623.

Mammen, T.C., and N. von Bosse, 1990: STEP - a temperature profiler for measuring the oceanic thermal boundary layer at the ocean-air interface, *J. Atmos. Ocean. Tech. 7*, 312-322.

Manton, M.J., 1973: On the attenuation of sea waves by rain. *Geophys. Fluid Dynam.* 5, 249-260.

Marmorino, G.O., and C.L. Trump, 1996: High resolution measurements made across a tidal intrusion front. *J. Geophys. Res.* 101(C11): 25,661-25,674.

Marmorino, G.O., G.B. Smith, and G.J. Lindemann, 2005: Infrared imagery of large-aspect-ratio Langmuir circulation. *Continental Shelf Res.* 25, 1-6.

Marshall, J.S., and W.M. Palmer, 1948: The distribution of raindrops with size. *J. Meteorol.* 5, 165-166

Mårtensson, E.M., E.D. Nilsson, G. de Leeuw, L.H. Cohen, and H.-C. Hansson, 2003: Laboratory simulations and parameterization of the primary marine aerosol production. *J. Geophys. Res.* 108(D9), 4297, doi:10.1029/2002JD002263.

Martinez-Bazan, C., J.L. Montanes, and J.C. Lasheras, 1999: On the breakup of an air bubble injected into fully turbulent flow. Part 2. Size PDF of the resulting daughter bubbles. *J. Fluid Mech.* 401, 183–207.

Mason, M.A. 1952: Some observations of breaking waves. In *Gravity Waves. Natl. Bur. Stand. Circ*. 521, 215-20

Maxworthy T., 1972: The structure and stability of vortex rings. *J. Fluid Mech.* 51, 15-32.

Matsuura, H., 2002: Observed variations of the upper ocean zonal currents in the western equatorial Pacific and their relation to local wind. *J. Geophys. Res.* 107, 3210, doi:10.1029/2000JC000757.

McAlister, E.D., and W. McLeish, 1969: Heat transfer in the top millimeter of the ocean. *J. Geophys. Res.* 74, 3408-3414.

McComas, C.H., and P. Muller, 1981: The dynamic balance of internal waves. *J. Phys. Oceanogr*. 11, 970-986.

McCreary, J.P., 1981: A linear, stratified ocean model of the equatorial undercurrent. *Phil. Trans. Roy. Soc. London*, Ser. A, 298, 603-635.

McCreary, J.P., Jr., K.E. Kohler, R.R. Hood, S. Smith, J. Kindle, A.S. Fischer, and R.A. Weller, 2001: Influences of diurnal and intraseasonal forcing on mixed-layer and biological variability in the Central Arabian Sea. *J. Geophys. Res.* 106. 7139-7155.

McGillis, W. R., et al.: 2004. Air-sea $CO_2$ exchange in the equatorial Pacific, *J. Geophys. Res.* 109*,* C08S02, doi:10.1029/2003JC002256.

McLean, J.W., Y.-C. Ma, D.U. Martin, P.G. Saffman, and H.C. Yuen, 1981: Three-dimensional instability of finite amplitude gravity waves. *Phys. Rev. Lett.* 46, 817-820.

McLeish, W., and G.E. Putland, 1975: Measurements of wind-driven flow profiles in the top millimeter of water. *J. Phys. Oceanogr.* 5, 516-518.

McManus, M.A., A.L. Alldredge, A. Barnard, E. Boss, J. Case, T.J. Cowles, P.L. Donaghay, L. Eisner, D.J. Gifford, C.F. Greenlaw, C. Herren, D.V. Holliday, D. Johnson, S. MacIntyre, D. McGehee, T.R. Osborn, M.J. Perry, R. Pieper, J.E.B. Rines, D.C. Smith, J.M. Sullivan, M.K. Talbot, M.S Twardowski, A. Weidemann, and J.R.V. Zaneveld, 2003: Changes in characteristics, distribution and persistence of thin layers over a 48-hour period. *Marine Ecology Progress Series* 261: 1-19.

McNaughton, K.G., and Y. Brunet, 2002: Townsend's hypothesis, coherent structures and Monin-Obukhov similarity. *Bound.-Layer Meteor.* 102, 161-175.

McNiel C.L., and L. Merlivat, 1996: The warm oceanic surface layer: Implications for $CO_2$ fluxes and surface gas measurements, *Geophys. Res. Lett.* 23**,** 3575-3578.

McPhee, M.G., 1983: Turbulent heat and momentum transfer in the oceanic boundary layer under melting pack ice. *J. Geophys. Res.* 88, 2827-2835.

McPhee, M.G., G.A. Maykut, and J.H. Morison, 1987: Dynamics and thermodynamics of the ice/upper ocean system in the marginal ice zone of the Greenland Sea. *J. Geophys. Res. 92*, 7017–7031.

McPhee, M.G., 1990: Small-scale processes. In: *Polar Oceanography*, W.O. Smith, Jr., Ed., Academic Press, San Diego, 287-334.

McPhee, M.G., and L.H. Kantha, 1989: Generation of internal waves by sea ice. *J. Geophys. Res*. 94, 3287-3302.

McWilliams, J.C., P.P. Sullivan, and C-H. Moeng, 1997: Langmuir turbulence in the ocean. *J. Fluid Mech*. 334, 1-30.

McWilliams, J., 1984: The emergence of isolated coherent vortices in turbulent flow. *J. Fluid Mech.* 146, 2–43.

Medwin, H., 1970: In situ acoustic measurements of bubble populations in coastal ocean waves. *J. Geophys. Res.* 75, 599-611.

Medwin, H., 1974: Acoustic fluctuations due to microbubbles in the near-surface ocean. *J. Acoust. Soc. Am.* 56(4), 1100-1104.

Medwin, H. and M.M. Beaky, 1989: Bubble sources of the Knudsen sea noise spectra. *J. Acoust. Soc. Am.* 86, 1124-1130.

Medwin, H., and C.S. Clay, 1998: *Fundamentals of Acoustical Oceanography*. Academic Press, San Diego, 712 pp.

Medwin, H., and A.C. Daniel, 1990: Acoustical measurements of bubble production by spilling breakers. *J. Acoust. Soc. America* 88, 408-412.

Medwin, H., J.A. Nystuen, P.W. Jacobus, L.H. Ostwald, and D.E. Synder, 1992: The anatomy of underwater rain noise. *J. Acoust. Soc. Amer.* 92, 1613–1623.

Meirink, J.F., 2002: The role of wind waves and sea spray in air–sea interaction. Ph.D. dissertation, Technische Universiteit Delft, 168 pp.

Mellor, G.L., 1996: *Introduction to Physical Oceanography*, Princeton University, Princeton, New Jersey, 260 pp.

Mellor, G.L., M.G. McPhee, and M. Steele, 1986: Ice-seawater turbulent boundary layer interaction with melting or freezing. *J. Phys. Oceanogr*. 16, 1829-1846.

Mellor, G.L., and T. Yamada, 1982: Development of a turbulence closure model for geophysical fluid problems. *Rev. Geophys.* 20, 851-875.

Melville, W.K., 1996: The role of surface-wave breaking in air-sea interaction. *Ann. Rev. Fluid Mech.* 28, 279-321.

Melville, W.K., 1994: Energy dissipation by breaking waves. *J. Phys. Oceanogr.* 24, 2041-2049.

Melville, W.K., and P. Matusov, 2002: Distribution of breaking waves at the ocean surface. *Nature* 417, 58-63.

Melville, W.K., E. Terrill, and L. Ding, 1995: Field measurements of air entrainment by breaking waves. *Proc. of the Third Int. Symp. on Air–Water Gas Transfer.* B. Jahne, Ed., Springer Verlag 285–295.

Merlivat, L, L. Emery, and J. Boutin, 1993: Gas exchange at the air-sea interface. Present status: The case of $CO_2$, paper presented at the *Fourth International Conference on $CO_2$ in the Ocean*, Inst. Natl., des Sci. de l'Univers. Cent. Natl. de Rech. Sci., Carqueiranne, France, Sept. 13-17.

Michell, J. H., 1893: On the highest waves in water. *Philos. Mag., Ser. 5* 365**,** 430–437

Miller, A.J., M.A. Alexander, G.J. Boer, F. Chai, K. Denman, D.J. Erickson III, R. Frouin, A.J. Gabric, E.A. Laws, M.R. Lewis, Z. Liu, R. Murtugudde, S. Nakamoto, D.J. Neilson, J.R. Norris, J.C. Ohlmann, R.I. Perry, N. Schneider, K.M. Shell, and A. Timmermann, 2003: Potential feedbacks between Pacific Ocean ecosystems and interdecadal climate variations., *Bull. Am. Met. Soc.* 84, 617-633, doi: 10.1175/BAMS-84-5-617.

Minnaert, M., 1933: On musical air bubbles and the sound of running water. *Philos. Mag.* 16, 235-248.

Minnett, P.J., R.O. Knuteson, F.A. Best, B.J. Osborne, J.A. Hanafin, and O.B. Brown, 2001: The Marine-Atmosphere Emitted Radiance Interferometer (M-AERI), a high-accuracy, sea-going infrared spectroradiometer. *J. Atmos. Ocean. Tech.* 18, 994-1013.

Mobley, C.D., 1994: *Light and Water: Radiative Transfer in Natural Waters*, Academic Press, San Diego, Calif.

Moeng, C.H., 1984: A large-eddy-simulation model for the study of planetary boundary-layer turbulence. *J. Atmos. Sci*. 41, 2052-2062.

Moffatt, H.K., and A. Tsinober, 1992: Helicity in laminar and turbulent flow. *Ann. Rev. Fluid Mech.* 24, 281-312.

Monahan, E.C., 1993: Occurrence and evolution of acoustically relevant subsurface bubble plumes and their associated, remotely monitorable, surface whitecaps. In: *Natural Physical Sources of Underwater Sound*, B.R. Kerman, Ed., Kluwer Acad., Norwell, Mass., 503-517.

Monahan, E.C., C.W. Fairall, K.L. Davidson, and P.J. Boyle, 1983: Observed inter-relations between 10 m winds, ocean whitecaps and marine aerosols. *Q. J. Roy. Meteor. Soc.* 109, 379-392.

Monahan, E.C., and I. O'Muircheartaigh, 1980: Optimal power-law description of oceanic whitecap coverage dependence on wind speed. *J. Phys. Oceanogr.* 10, 2094-2099.

Monahan, E.C., D.E. Spiel, and K.L. Davidson, 1986: A model of marine aerosol generation via whitecaps and wave disruption. In: *Oceanic Whitecaps and Their Role in Air-Sea Exchange*. E.C. Monahan and G. MacNiocaill, Eds., D. Reidel, 167-174.

Monahan, E.C., and T. Torgersen, 1990: The enhancement of air-sea gas exchange by oceanic whitecapping. In: *Air-Water Mass Transfer*, (eds) S.C. Wilhelms and J.S. Gulliver, (New York: American Society of Civil Engineers), 608-617.

Moncrieff, M.W., S.K. Krueger, D. Gregory, J.-L. Redelsperger, and W.-K. Tao, 1997: GEWEX Cloud System Study (GCSS) Working Group 4: Precipitating convective cloud systems. *Bull. Am. Meteorol. Soc*. 78, 831-845.

Monin, A.S., and V.P. Krasitskii, 1985: Phenomena on the ocean surface. Hydrometeoizdat, Leningrad, 376 pp. (in Russian).

Monin, A.S., and A.M. Yaglom, 1971: *Statistical Fluid Mechanics*, Vol. 1, MIT Press, Cambridge, Mass, 769 pp.

Montgomery, R.B., and E.D. Stroup, 1962: Equatorial waters and currents at 150°W in July-August 1952. *The Johns Hopkins Oceanographic Studies,* Vol. 1. The Johns Hopkins Press, Baltimore. 68 pp.

Moore, D.W., and S.G.H. Philander, 1977: Modeling the equatorial oceanic circulation. In: *The Sea*, Vol. VI, Wiley Interscience, New York, 319-361.

Morel, A., and L. Prieur, 1977: Analysis of variations in ocean color. *Limnol. Oceanogr.* 22, 709-722.

Morel, A., 1980: In-water and remote measurement of ocean color. *Bound.-Lay. Meteorol.* 18, 177-201.

Morrison, J.H., M.G. McPhee, and G.A. Maykut, 1987: Boundary layer, upper ocean, and ice observations in the Greenland Sea marginal ice zone. *J. Geophys. Res*. 92, 6987-7011.

Moum, J.N., and D.R. Caldwell, 1994: Experiment explores the dynamics of the ocean mixing. *EOS, T., Am. Geophys. Un.* 75, 489, 494-495.

Moum, J.N., M.C. Gregg, R.C. Lien, and M.E. Carr, 1995: Comparison of turbulence kinetic energy dissipation rates estimates from two ocean microstructure profilers. *J. Atmos. Ocean. Tech.* 12, 346-366.

Motzfeld, H., 1937: Die turbulente Stromung an welligen Wanden. *Z. Angew. Math. & Mech*. 17, 193-212.

Muench, R.D., 1990: Mesoscale phenomena in the Polar Oceans. In: *Polar Oceanography*, W.O. Smith, Jr., Ed., Academic Press, San Diego, 223-286.

Munk, W., and L. Armi, 2001: Spirals on the sea: A manifestation of upper-ocean stirring. In: *From Stirring to Mixing in a Stratified Ocean, Proceedings 'Aha Huliko'a Hawaiian*

*Winter Workshop. University of Hawaii at Manoa, January 16-19, 2001, SOEST Special Publication*, 81-86.

Murtugudde, R., J. Beauchamp, C.R. McClain, M. Lewis, and A. Busalacchi, 2002: Effects of penetrative radiation on the upper tropical ocean circulation. *J. Climate* 15, 471-487.

Murty, V.S.N., B. Subrahmanyam, M.S.S. Sarma, V. Tilvi, and V. Ramesh Babu, 2002: Estimation of sea surface salinity in the Bay of Bengal using Outgoing Longwave Radiation. *Geophys. Res. Lett.* 29, doi 10.1029/2001GL014424.

Nasmyth, P.W., 1970: Oceanic turbulence. Ph.D. dissertation, University of British Columbia, Vancouver.

Neuwstadt, F.T.M., 1984: The turbulent structure of the stable, nocturnal boundary layer, *J. Atmos. Sci.* 41, 2202–2216.

Nightingale, P.D., G. Malin, C.S. Law, A.J. Watson, P. S. Liss, M.I. Liddicoat, J. Boutin, and R.C. Upstill-Goddard, 2000: In situ evaluation of air-sea gas exchange parameterizations using novel conservative and volatile tracers, *Glob. Biogeochem. Cy.*, 14, 373-387.

Nicolas, G., and I. Prigogine, 1977: *Self-organization in Nonequilibrium Systems: From dissipative structures to order through fluctuations.* New York: Wiley, 491 pp.

Niiler P.P., and E.B. Kraus, 1977: One-dimensional models. In: *Modeling and Prediction of the Upper Layers of the Ocean*, E.B. Kraus, Ed. Pergamon, New York, 143-172.

Nilsson, E.D., Ü. Rannik, E. Swietlicki, C. Leck, P.P. Aalto, J. Zhou, and M. Norman, 2001: Turbulent aerosol fluxes over the Arctic Ocean: 2. Wind-driven sources from the sea. *J. Geophys. Res.* 106, 32,125-32,137.

Novikov, E.A., 1961: The energy spectrum of the turbulent flow in an incompressible fluid. *Dokl. Akad. Nauk SSSR* 139(2).

Nystuen, J.A., 1996: Acoustical rainfall analysis: Rainfall drop size distribution using the underwater sound field. *J. Acoust. Soc. Amer.* 13**,** 74-84.

Nystuen, J.A., 2001: Listening to raindrops from underwater: An acoustic disdrometer. *J. Atmos. Ocean. Tech.* 18, 1640-1657.

Nystuen, J.A., and E. Amitai, 2003: High temporal resolution of extreme rainfall rate variability and the acoustic classification of rainfall. *J. Geophys. Res.* 108, p. 8378, doi:10.1029/2001JD001481.

Nystuen J.A., and H.D. Selsor, 1997: Weather classification using passive acoustic drifters. *J. Atmos. Ocean. Tech.* 14, 656-666.

Nystuen, J.A., M.J. McPhaden, and H.P. Freitag, 2000: Surface measurements of precipitation from an ocean mooring: The acoustic log from the South China Sea. *J. Appl. Meteorol.* 39, 2182–2197.

Oakey, N.H., 1982: Determination of the rate of dissipation of turbulent energy from simultaneous temperature and velocity shear microstructure measurements. *J. Phys. Oceanogr.* 12, 256-271.

Oakey, N.S., 1985: Statistics of mixing parameters in the upper ocean during JASIN phase 2. *J. Phys. Oceanogr.* 15, 1662-1675.

Oakey, N.S., and J.A. Elliott, 1982: Dissipation within surface mixed layer. *J. Phys. Oceanogr.* 12, 175-195.

O'Dowd, C.D., and M.H. Smith, 1993: Physiochemical properties of aerosols over the northeast Atlantic: Evidence for wind-related submicron sea-salt aerosol production. *J. Geophys. Res.* 98, 1137-1149.

O'Dowd, C.D., J.A. Lowe, and M.H. Smith, 1999: Coupling sea-salt and sulphate interactions and its impact on cloud droplet concentration predictions. *Geophys. Res. Lett.* 26, 1311-1314.

Ocampo-Torres, F.J., M.A. Donelan, N. Merzi, and F. Jia, 1994: Laboratory measurements of mass transfer of carbon dioxide and water vapour for smooth and rough flow conditions, *Tellus, Ser. B*, 46, 16–32.

Offen, G.R., and S.J. Kline, 1975: A proposed model of the bursting process in turbulent boundary layers. *J. Fluid Mech.* 70, 209–228.

Oguz, H.N., and A. Prosperetti, 1991: Numerical calculation of the underwater noise of rain. *J. Fluid Mech.* 228, 417-442.

Ohlmann, J. C., D. A. Siegel, and C. Gautier, 1996: Ocean mixed layer radiant heating and solar penetration: A global analysis. *J. Climate* 9, 2265-2280.

Ohlmann, J. C., D. A. Siegel, and C. D. Mobley, 2000a: Ocean Radiant Heating. Part I: Optical Influences. *J. Phys. Oceanogr.* 30, 1833-1848.

Ohlmann, J. C., and D. A. Siegel, 2000b: Ocean Radiant Heating. Part II: parameterizing solar radiation transmission through the upper ocean*J. Phys. Oceanogr.* 30, 1849-1865.

Okuda, K., 1982: Internal flow structure of short wind waves, Part I. The vorticity structure. *J. Oceanogr. Soc. Japan* 38, 28-42.

Olbers, D.J., and K. Herterich, 1979: The spectral energy transfer from surface waves to internal waves. *J. Fluid Mech.* 92, 349-380.

Osborn, T.R., and C.S. Cox, 1972. Oceanic fine structure. *Geophys. Fluid Dyn.* 3, 321-345.

Osborn, T., D.M. Farmer, S. Vagle, S. Thorpe, M. Cure, 1992: Measurements of bubble plumes and turbulence from a submarine. *Atmos. - Ocean* 30, 419-440.

Ostapoff, F., Y. Tarbeyev and S. Worthem, 1973: Heat flux and precipitation estimates from oceanographic observations. *Science* 180, 960–962.

Ozgokmen, T.M., L.I. Piterbarg, A.J. Mariano, E.H. Ryan, 2001: Predictability of drifter trajectories in the tropical Pacific Ocean. *J. Phys. Oceanogr.* 31, 2691-2720.

Paduan, J., and H. Graber, 1997: Introduction to high-frequency radar: Reality and myth. *Oceanography* 10, 36-39.

Patel, V.C., W. Rodi, and G. Scheurer, 1984: Turbulence models for near-wall and low Reynolds number flows. A review. *AIAA Journal*, 23(9), 1306-1319.

Patro, R., I. Leifer, and P. Bower, 2001: Better bubble process modeling: Improved bubble hydrodynamics parameterization. In: AGU Monograph *Gas Transfer at Water Surfaces*, E.S. Saltzman, M. Donelan, W. Drennan, and R. Wanninkhof, Eds., 315-320.

Pattison, M.J., and S.E. Belcher, 1999: Production rates of sea-spray droplets. *J. Geophys. Res.* 104, 18,397-18,407.

Paulson, C.A., and G.S.E. Lagerloef, 1993: Fresh surface lenses caused by heavy rain over the western Pacific warm pool during TOGA COARE. *EOS Trans. AGU* 74, Suppl. to No. 43, p. 125.

Paulson, C.A., and J.J. Simpson, 1981: The temperature difference across the cool skin of the ocean. *J. Geophys. Res.* 86, 11,044-11,054.

Payne, R.E., 1972: Albedo of the sea surface. *J. Atmos. Sci*. 29, 959-970.

Pelinovsky, D.E. and V.I. Shrira, 1995: Collapse transformation for self-focusing solitary waves in boundary-layer type shear flows. *Phys. Lett. A: Math. Gen*. 206, 195-202.

Peng, T.H., W.S. Breocker, G.G. Mathieu, Y.H. Li, and E.A. Bainbrige, 1979: Radon evasion rates in the Atlantic and Pacific Ocean as determined during the GEOSECS program, *J. Geophys. Res*. 84, 2471-2486.

Peng, T.H., T. Takahashi, and W.S. Broecker, 1974: Surface radon measurements in the North Pacific Ocean station PAPA. *J. Geophys. Res*. 79, 1772-1780.

Peters, H., M.C. Gregg, and J.M. Toole, 1988: On the parameterization of equatorial turbulence. *J. Geophys. Res*. 93, 1199-1218.

Petrenko, A.A., J.R.V. Zaneveld, W.S. Pegau, A.H. Barnard, and C.D. Mobley, 1998: Effects of a thin layer on reflectance and remote-sensing reflectance. *Oceanography* 11(1), 48-50.

Phillips, O.M., 1977: *The dynamics of the upper ocean*. Cambridge University Press, 366 pp.

Phillips, O.M., and M.L. Banner, 1974: Wave breaking in the presence of wind drift and swell. *J. Fluid Mech.* 66**,** 625-640.

Phong-Anant, D., R.A. Antonia, A.J. Chamber, and S. Rajagopalan, 1980: Features of the organized motion in the atmospheric surface layer. *J. Geophys. Res.*, 424-432.

Picaut, J., F. Masia, and Y. duPenhoat**,** 1997: An advective-reflective conceptual model for the oscillatory nature of the ENSO. *Science* 277, 663–666.

Pierson, W.J., and L. Moskowitz, 1964: A proposed spectral form for fully-developed wind seas based on the similarity theory of S.A. Kitaigorodsky. *J. Geophys. Res.* 69, 5181-5190.

Pinkel, R., 2000: Internal solitary waves in the warm pool of the western equatorial Pacific. *J. Phys. Oceanogr*. 30, 2906-2926.

Plane, J.M.C., N.V. Blough, M.G. Ehrhardt, K. Waters, R.G. Zepp, and R.G. Zika, 1997: Report Group 3—Photochemistry in the sea-surface microlayer. In: *The Sea Surface and Global Change*. P.S. Liss and R.A. Eds., Duce, Cambridge University Press, UK, 71-92.

Pinkel, R., M. Merrifield, M. McPhaden, J. Picaut, S. Rutledge, D. Siegel, and L. Washburn, 1997: Solitary waves in the western equatorial Pacific Ocean. *Geophys. Res. Lett.* 24, 1603-1616.

Plueddemann, A.J., J.A. Smith, D.M. Farmer, R.A. Weller, W.R. Crawford, R. Pinkel, S. Vital, and A. Gnanadesikan, 1996: Structure and variability of Langmuir circulation during the Surface Waves Processes Program. *J. Geophys. Res.* 101, 3525-3543.

Pollard, R.T., 1977: Observations and theories of Langmuir circulations and their role in near surface mixing. In: *A Voyage of Discovery: George Deacon 70th Anniversary Volume*, M. Angel, Ed., Oxford, Pergamon Press, 696 pp.

Polzin, K., 1996: Statistics of the Richardson Number mixing models and finestructure, *J. Phys. Oceanogr*. 26, 1409-1425.

Poon, Y.-K., S. Tang, and J. Wu, 1992: Interactions between wind and waves. *J. Phys. Oceanogr.* 22, 977-987.

Pope, R.M., and E.S. Fry, 1997: Absorption spectrum (380-700 nm) of pure water. II. Integrating cavity measurements. *Appl. Opt*. 36, 8710-8723.

Powell, M.D., P.J. Vickery, and T.A. Reinhold, 2003: Reduced drag coefficient for high wind speeds in tropical cyclones. *Nature* 422, 279-283.

Prandke, H., A. Stips, 1996: Investigation of Microstructure and Turbulence in Marine and Limnic Waters using the MST Profiler.European Commission, Joint Research Centre, Space Applications Institute, Technical Note No. I.96.87.

Prandtl, L., 1949: Führer Durch die Strömngslehre. 3rd ed., Brawnschweig, F. Vieweg.

Preisendorfer, R.W., 1976: *Hydrologic Optics, Vol I: Introduction*, U.S. Dept of Commerce, Washington, D.C., 1976.

Price, J.F., R.A. Weller, and R. Pinkel, 1986: Diurnal cycling: Observations and models of the upper ocean response to diurnal heating, cooling, and wind mixing. *J. Geophys. Res.* 91, 8411-8427.

Price, J.F., R.A. Weller, and R.R. Schudlich, 1987: Wind-driven ocean currents and Ekman transport. *Science*, 238, 1534-1538.

Price, J.F., T.B. Sanford, and G.Z. Forristall, 1994: Forced stage response to a moving hurricane. *J. Phys. Oceanogr.* 24, 233-260.

Priestly, C.H.B., 1959: *Turbulent Transfer in the Lower Atmosphere*, Univ. of Chicago Press, Chicago, Ill., 130 pp.

Prosperetti, A., 1985: Bubble-related ambient noise in the ocean. *J. Acoust. Soc. Am.* 78, S2.

Prosperetti, A., and H.N. Oguz, 1993: The impact of drops on liquid surfaces and the underwater noise of rain. *Ann. Rev. Fluid Mech.* 25, 577-602.

Pruppacher, H.R., and J.D. Klett, 1978: *Microphysics of clouds and precipitation*. D. Reidel Publishing Company, Dordrecht, Holland, 714 pp.

Pruvost, P., 1972: Contribution à l'étude des échanges radiatifs Atmospère-Ocèan. Calcul des flux dans la mer. Thèse 3ème cycle. Universite de Lille, n 341.

Pumphrey, H.C., and P.A. Elmore, 1990: The entrainment of bubbles by drop impacts. *J. Fluid Mech.* 220, 539-567.

Quilfen, Y, B. Chapron, and D. Vandemark, 2001: The ERS scatterometer wind measurement accuracy: Evidence of seasonal and regional biases. *J. Atmos. Ocean. Tech.* 18(10), 1684-1697.

Rabinovich, S.G., 1995: Measurement Errors: Theory and Practice, *American Institute of Physics*, Woodbury, NY, 279 p.

Randall, D., M. Khairoutdinov, A. Arakawa, and W. Grabowski, 2003: Breaking the cloud parameterization deadlock, *Bull. Amer. Meteor. Soc.* 84(11), 1547-1564.

Rao, K.N., R. Narasima, and M. Badri Narayanan, 1971: The "bursting" phenomenon in a turbulent boundary layer. *J. Fluid Mech.* 48, 339–352.

Raschke, E., 1975: Numerical studies of solar heating of an ocean model. *Deep-Sea Res.* 22, 659-666.

Redelsperger, J.L., P.R.A. Brown, F. Guichard, C. Hoff, M. Kawasima, S. Lang, Th. Montmerle, K. Nakamura, K. Saito, C. Seman, W.K. Tao, and L.J. Donner, 2000: A GCSS model intercomparison for a tropical squall line observed during TOGA-COARE. I: Cloud-resolving models. *Q. J. Roy. Meteor. Soc*. 126, 823-864

Resch, F.R., and G. Afeti, 1992: Sub-micron film drop production by bubbles in seawater. *J. Geophys. Res.* 97, 3679–3683.

Rhines, P.B., 1975: Waves and turbulence on a beta-plane. *J. Fluid Mech.* 69, 417-443.

Richardson, C.L., W.E. Asher, C.J. Zappa, and A.T. Jessup, 2000. Dependence of the controlled flux technique on ambient heat flux for air-water gas transfer. *4th International Symposium on Gas Transfer at Water Surfaces*, Miami Beach, FL, June 2000.

Riley, J.P., and G. Skirrow, 1965. *Chemical Oceanography Vol. I*, Academic Press, London, 712 pp.

Rines, J.E.B., P.L. Donaghay, M.M. Dekshenieks, J.M. Sullivan, and M.S. Twardowski, 2002: Thin layers and camouflage: Hidden *Pseudo-nitzschia* populations in a fjord in the San Juan Islands, Washington, USA. *Marine Ecology Progress Series* 225:123-137.

Robertson, J.E., and A.J. Watson, 1992: Thermal skin effect of the surface ocean and its implications for $CO_2$ uptake. *Nature* 358, 738-740.

Rodriguez, F., and R.J. Mesler, 1988: The penetration of drop-formed vortex rings into pools of liquid. *J. Colloid. Interface Sci.* 121, 121–129.

Roemmich, D., M. Morris, W.R. Young, and J.R. Donguy, 1994: Fresh equatorial jets. *J. Phys. Oceanog*. 24, 540-558.

Roll, H.U., 1965: *Physics of the Marine Atmosphere*. Academic Press, New York, London.

Romanova, N.N., 1984: Long nonlinear waves on layers having large wind velocity gradients. Izvestiya, *Akad. Nauk SSR, Fizika Atmos. I Okeana* 20, 469-475 (Translation: *Izv. Acad. Sci. USSR, Atmosph. Ocean. Phys*. 20, 452-456).

Ruddick, B.R., and J.S. Turner, 1979: The vertical length scale of double-diffusive intrusions. *Deep-Sea Res.* 26(8A), 903-913.

Rudnick, D.L., and J.R. Luyten, 1996: Intensive surveys of the Azores Front 1. Tracers and dynamics. *J. Geophys. Res.* 101**,** 923-940.

Sabines, F.F., 1987: *Remote Sensing Principles and Interpretation, 2nd ed.* W.H. Freeman, New York, NY, 449 pp.

Santiago-Mandujano, F., and E. Firing, 1990: Mixed-layer shear generated by wind stress in the central equatorial Pacific, *J. Phys. Oceanogr*. 20, 1576-1582.

Sandstrom, H., and N.S. Oakey, 1995: Dissipation in internal tides and solitary waves, *J. Phys. Oceanogr.* 25**,** 604-614.

Saunders, P.M., 1967a: Shadowing on the ocean and the existence of the horizon. *J. Geophys. Res*. 72, 4643-4649.

Saunders, P.M., 1967b: The temperature at the ocean-air interface, *J. Atmos. Sci*. 24, 269-273.

Saylor, J.R., K.A. Flack, M.P. Schultz, and G.B. Smith, 2002: The correlation between surface temperature and subsurface velocity during evaporative convection. *Exp. Fluids* 32, 570-579.

Saylor, J.R., and R. A. Handler, 1997: Gas transport across an air/water interface populated with capillary waves. *Physics of Fluids* 9, 2529-2541.

Schlichting, H., 1979: *Boundary-Layer Theory.* McGraw-Hill, New York, 817 pp.

Schlüssel, P., 1996: Satellite remote sensing of evaporation over sea, NATO *ASI Series, I45, Radiation and water in the climate system: Remote measurements.* E. Raschke, Ed., Springer-Verlag, Berlin, 431-459.

Schlüssel, P., 1996: Satellite remote sensing of evaporation over sea, in E. Raschke, Ed. In: *Radiation and water in the climate system: Remote measurements*, NATO ASI Series**,** I 45,Springer Verlag, Berlin, 431-461.

Schlüssel, P., W.J. Emery, H. Grassl, and T.C. Mammen, 1990: On the bulk-skin temperature difference and its impact on satellite remote sensing of the sea surface temperature. *J. Geophys. Res.* 95*,* 13,341-13,356.

Schlüssel, P. and H. Luthardt, 1991: Surface wind speeds over the North Sea from SSM/I observations. *J. Geophys. Res.* 96, 4845-4854.

Schlüssel, P., L. Schanz, and G. Englisch, 1995: Retrieval of latent heat flux and longwave irradiance at the sea surface from SSM/I and AVHRR measurements, *Adv. Space Res.* 16, 107-115.

Schlüssel, P., and A. Soloviev, 2002: Air-sea gas exchange: Cool skin and gas transfer velocity in the North Atlantic Ocean during GasEx-98, *Advances in Space Research* 29(1), 107-110.

Schlüssel, P., A.V. Soloviev, and W.J. Emery, 1997: Cool and freshwater skin of the ocean during rainfall. *Bound.-Layer Meteor.* 95, 82,437-82,472.

Schmidt, W., 1908: Absorption der sonnenstrahlung in wasser, Sitzungsber. Acad. Wiss. Wien 117.

Schneider, E.K., and Z. Zhu, 1998: Sensitivity of the simulated annual cycle of the sea surface temperature in the equatorial Pacific to sunlight penetration. *J. Climate* 11, 1932-1950.

Schoeberlein, H.C., and M.A. Baker, 1996: Status report: Reduction of motion contamination in TOGA COARE velocity measurements. *Technical Report, 13 December 1996*, The Johns Hopkins University, Applied Physics Laboratory, Laurel, MD 20723, 46 p.

Scop, R.A., and N.J. Peters, 1997: Shipboard deployment of a VHF OSCR system for measuring offshore currents. *Oceanography* 34, 80-81.

Shaw, P.T., D.R. Watts, and H.T. Rossby, 1978: On the estimation of oceanic wind speed and stress from ambient noise measurements. *Deep-Sea Res.* 25, 1225-1233.

Shay, L.K., T.M. Cook, H. Peters, A.J. Mariano, R.H. Weisberg, P.E. An, A.V. Soloviev, and M.E. Luther, 2002: Very high-frequency radar mapping of surface currents. *IEEE J. Ocean. Eng.* 27, 155-169.

Shay, L.K., G.J. Goni, and P.G. Black, 2000: Effects of a warm oceanic feature on hurricane Opal. *Mon. Wea. Rev.* 128, 1366-1383.

Shay, T.J., and M.C. Gregg, 1986: Convectively driven turbulent mixing in the upper ocean, *J. Phys. Oceanogr.* 16, 1777-1798.

Shen, L., X. Zhang, D.K.P. Yue, and G.S. Triantafyllou, 1999: The surface layer for free-surface turbulent flows. *J. Fluid Mech.* 386, 167-212.

Shinoda, T., H.H. Hendon, and J.D. Glick, 1998: Mixed layer modeling of intraseasonal sea surface temperature variability in the tropical western Pacific and Indian Ocean. *J. Climate* 11, 2668-2685.

Shinoda, T., and R. Lukas, 1995: Lagrangian mixed layer modeling of the western equatorial Pacific. *J. Geophys. Res.* 100(C2), 2523-2541.

Short, D.A., P.A. Kucera, B.S. Ferrier, J.C. Gerlach, S.A. Rutledge, and O.W. Thiele, 1997: Shipborne radar rainfall patterns within the TOGA/COARE IFA. *Bull. Amer. Meteor. Soc.* 78(12), 2817-2836.

Shrira, V.I., 1989: On the 'sub-surface' waves of the mixed layer of the upper ocean. *Dokl. Akad. Nauk SSSR* 308, 732-736 (*Trans. USSR Acad. Sci., Earth Sci. Sec*. 308, 276-279).

Sieburth, J.M., and P.L. Donaghay, 1993: Planktonic methane production and oxidation within the algal maximum of the pycnocline: seasonal fine scale observation in an anoxic estuarine basin. *Mar. Ecol. Prog. Ser.* 100, 3-15.

Siegel, D.A., and A.F. Michaels, 1996: Quantification of non-algal light attenuation in the Sargasso Sea: Implication for biogeochemistry and remote sensing. *Deep-Sea Res. II* 43, 321-345.

Siegel, D.A., J.C. Ohlmann, L. Washburn, R.R. Bidigare, C.T. Nosse, E. Fields, and Y.M. Zhou, 1995: Solar-radiation, phytoplankton pigments and the radiant heating of the equatorial Pacific warm pool. *J. Geophys. Res.* 100, 4885-4891.

Simpson, J.E., 1987: *Gravity Currents: In the Environment and the Laboratory*. Ellis Horwood Limited, NY, 244 pp.

Simpson, J.E., and P.F. Linden. 1989: Frontogenesis in a fluid with horizontal density gradients. *J. Fluid Mech.* 202, 1-16.

Simpson, J.J., and C.A. Paulson, 1979: Mid-ocean observations of atmospheric radiation. *Q. J. Roy. Meteor. Soc.* 105, 487-502.

Siscoe, G. L., and Z. Levin, 1971: Interaction of water drops with surface waves. *J. Geophys. Res.* 76, 5112.

Skyllingstad, E.D., and D.W. Denbo, 1995: An ocean large-eddy simulation of Langmuir circulations and convection in the surface mixed layer. *J. Geophys. Res.* 100, 8501-8522.

Skyllingstadt, E.D., W.D. Smyth, J.N. Moum, and H. Wijesekera, 1999: Upper ocean turbulence during a westerly wind burst: A comparison of large-eddy simulation results and microstructure measurements. *J. Phys. Oceanog*. 29, 5-28.

Smith, C.R., and J.D.A. Walker, 1997: Sustaining mechanisms of turbulent boundary layers: The role of vortex development and interaction, R.L. Panton, Ed. In: *Self-Sustaining Mechanisms of Wall Turbulence*, Advances in Fluid Mechanics 15, Computational Mechanics Publications, Southampton, pp. 273–308.

Smith, M.H., P.M. Park, and I.E. Consterdine, 1993: Marine aerosol concentrations and estimated fluxes over the sea. *Q. J. R. Meteorol. Soc.* 119, 809-824.

Smith, O.W., and D.M. Nelson, 1985: Phytoplankton bloom produced by a receding ice edge in the Ross Sea: Spatial coherence with density field. *Science* 227, 163-166.

Smith, R.C., and K.S. Baker, 1981. Optical properties of the clearest natural waters (200-800 nm). *Appl. Opt.* 31, 177-184.

Smith, S.D., 1988: Coefficients for sea surface wind stress, heat flux, and wind profiles as a function of wind speed and temperature. *J. Geophys. Res.* 93, 15,467-15,472.

Smyth, W.D., D. Hebert, and J.N. Moum, 1996: Local ocean response to a multiphase westerly wind burst, 1, Dynamic response. *J. Geophys. Res.* 101, 22,495-22,512**.**

Soloviev A.V., 1979: Thin thermal structure of the ocean surface layer in the POLYMODE-77 region. Izvestiya, *Atmospheric and Oceanic Physics* 15, 750-754 (in Russian).

Soloviev A.V., 1982: On vertical structure of a thin surface layer of the ocean under conditions of low wind speed. Izvestiya, *Atmospheric and Oceanic Physics* 18(7), 751-760 (In Russian).

Soloviev, A.V., 1990: Coherent structure at the ocean surface in the convectively unstable conditions. *Nature* 346, 157-160.

Soloviev, A.V., 1992: Small-Scale Structure of the Open Ocean Boundary Layers. Dissertation for Doctor of Physical-Mathematical Sciences Degree, Russian Academy of Sciences, Moscow (in Russian).

Soloviev A.V., and V.A. Bezverkhny, 1990: Coherent structure in the near-surface turbulent boundary layer of the ocean. *Doklady Akademii Nauk SSSR* 312(1), 218-222.

Soloviev, A., and B. Klinger, 2001: Open Ocean Convection. In: *Encyclopedia of Ocean Sciences*, Academic Press, UK, 2015-2022.

Soloviev, A., and R. Lukas, 1996: Observation of spatial variability of diurnal thermocline and rain-formed halocline in the western Pacific warm pool. *J. Phys. Oceanogr*. 26(11), 2529-2538.

Soloviev, A., and R. Lukas, 1997a: Observation of large diurnal warming events in the near-surface layer of the western equatorial Pacific warm pool. *Deep-Sea Res.* 44, Part I, 1055-1076.

Soloviev, A., and R. Lukas, 1997b: Sharp frontal interfaces in the near-surface layer of the ocean in the western equatorial Pacific warm pool. *J. Phys. Oceanogr.* 27(6), 999-1017.

Soloviev, A.V., and R. Lukas, 2003: Observation of wave-enhanced turbulence in the near-surface layer of the ocean during TOGA COARE. *Deep-Sea Res.*, Part I 50, 371-395.

Soloviev, A.V., and P. Schlüssel, 1994: Parameterization of the temperature difference across the cool skin of the ocean and of the air-ocean gas transfer on the basis of modelling surface renewal. *J. Phys. Oceanogr.* 24, 1339-1346.

Soloviev, A.V., and P. Schlüssel, 1996: Evolution of cool skin and direct air-sea gas transfer coefficient during daytime. *Bound.-Layer Meteor.* 77, 45-68.

Soloviev, A., and P. Schlüssel, 1998: Comments on "Air-Sea Gas Transfer: Mechanisms and Parameterizations." *J. Phys. Oceanogr.* 28, 1643-1645.

Soloviev, A., and P. Schlüssel, 2002: A model of the air-sea gas exchange incorporating the physics of the turbulent boundary layer and the properties of the sea surface. In: *AGU Monograph Gas Transfer at Water Surfaces*. E.S. Saltzman, M. Donelan, W. Drennan, and R. Wanninkhof, Eds., pp. 141-146.

Soloviev, A.V., and N.V. Vershinsky, 1982: The vertical structure of the thin surface layer of the ocean under conditions of low wind speed, *Deep-Sea Res.* 29(12A), 1437-1449.

Soloviev, A.V., and A.G. Zatsepin, 1992: Response of density depression pool to wind forcing. Abstract, 24th International Liege Colloquium on Ocean Hydrodynamics: "Sub-Mesoscale Air-Sea Interaction," Liege, Belgium, May 4-8, 1992. *GHER/Model Environment*, 99-100.

Soloviev, A., R. Lukas, and P. Hacker, 2001: An approach to parameterization of the oceanic turbulent boundary layer in the western pacific warm pool. *J. Geophys. Res.* 106, 4421-4435.

Soloviev, A., R. Lukas, and H. Matsuura, 2002: Sharp frontal interfaces in the near-surface layer of the tropical ocean. *J. Marine Systems - Special Issue on Oceanic Fronts* 37(1-3), 47-68.

Soloviev, A.V., N.V. Vershinsky, and V.A. Bezverchnii, 1988: Small-scale turbulence measurements in the thin surface layer of the ocean. *Deep-Sea Res.* 35, 1859-1874.

Soloviev, A., J. Edson, W. McGillis, P. Schlüssel, and R. Wanninkhof, 2001b: Fine thermohaline structure and gas-exchange in the near-surface layer of the ocean during

GasEx-98. In AGU Monograph *Gas Transfer at Water Surfaces*, E.S. Saltzman, M. Donelan, W. Drennan, and R. Wanninkhof, Eds., 181-185.

Soloviev, A., R. Lukas, P. Hacker, M. Baker, H. Schoeberlein, and A. Arjannikov, 1999: A near-surface microstructure sensor system used during TOGA COARE. Part II: Turbulence Measurements. *J. Atmos. Oceanic Tech.* 16, 1598-1618.

Soloviev A.V., R. Lukas, S. DeCarlo, J. Snyder, A. Arjannikov, M. Baker, and D. Khlebnikov, 1995: Small-scale measurements near the ocean-air interface during TOGA-COARE. *Data Report. SOEST-95-05.* University of Hawaii, Honolulu, HI, 257 pp.

Soloviev, A., R. Lukas, S. DeCarlo, J. Snyder, A. Arjannikov, V. Turenko, M. Baker, and D. Khlebnikov, 1998: A near-surface microstructure sensor system used during TOGA-COARE. Part I: Bow measurements. *J. Atmos. Ocean. Tech.* 15, 563-578.

Sorooshian, S., X. Gao, K. Hsu, R.A. Maddox, Y. Hong, H.V. Gupta, and B. Imam, 2002: Diurnal variability of tropical rainfall retrieved from combined GOES and TRMM satellite information. *J. Climate* 15, 983-1001.

Spall, M., and D. Chapman, 1998: On the efficiency of baroclinic eddy heat transport across narrow fronts. *J. Phys. Oceanogr.* 28(11), 2275-2287.

Spangenberg, W.G., and W.R. Rowland, 1961: Convective circulation in water induced by evaporative cooling. *Phys. Fluids* 4, 743-750.

Spiel, D.E., 1997: More on the births of jet drops from bubbles bursting on seawater surfaces. *J. Geophys. Res.* 102, 5815-5821.

Spiel, D.E., 1998: On the birth of film drops from bubbles bursting on seawater surfaces. *J. Geophys. Res.* 103, 24,907-24,918.

Stacey, M.W., 1999: Simulation of the wind-forced near-surface circulation in Knight Inlet: A parameterization of the roughness length. *J. Phys. Oceanogr.* 29, 1363-1367.

Stephen, H., and T. Stephen (eds.), 1964: *Solubilities of Inorganic and Organic Compounds; 2: Ternary Systems, Part I.* Pergamon Press, McMillian Company, NY, 944 p.

Stern, M.E., and J.S. Turner, 1969: Salt fingers and convecting layers. *Deep-Sea Res.* 16, 497-511.

Stevenson, R.E., 1985: Oceanography in orbit. In: *1985 Yearbook and the Future*. *Encyc. Brit*., Chicago, IL, 190-205.

Stevenson, R.E., 1998: Spiraleddies: The discovery that changed the face of the oceans. *21st Century Sci. Technol.* 11, 58-71.

Stevenson, R.E., 1999: A view from space: The discovery of nonlinear waves in the ocean's near surface layer. *21st Century Sci. Technol.*18, 36-47.

Stewart, R.W., and Grant, H.L., 1962: Determination of the rate of dissipation of turbulent energy near the sea surface in the presence of waves. *J. Geophys. Res.* 67, 3177-3180.

Stokes, G.G., 1880: *On the Theory of Oscillatory Waves*, Math. Phys., Paper 1, 314, Cambridge University Press, Cambridge, 197-229.

Stommel, H., 1960: Wind-drift near the equator. *Deep-Sea Res.* 6, part A, 298-302.

Stommel, H., 1993: A conjectural regulating mechanism for determining the thermohaline structure of the oceanic mixed layer. *J. Phys. Oceanogr.* 23(1), 142-148.

Stramski, D., 1994: Gas microbubbles: An assessment of their significance to light scattering in quiescent seas. *Proc. SPIE Ocean Opt.* XII(2258), 704-710.

Stuart-Menteth, A.C., I.S. Robinson, and P.G. Challenor, 2003: A global study of diurnal warming using satellite-derived sea surface temperature, *J. Geophys. Res.* 108(C5), 3155, doi: 10.1029/2002JC001 534.

Stull, R.B., 1988: *An introduction to boundary layer meteorology*, Kluwer Academic Publishers, Dordrecht, Boston, London, 670 pp.

Stull, R.B., and E.B. Kraus, 1987: A transilient model of the upper ocean. *J. Geophys. Res.-Oceans* 92, 10,745-10,755.

Su, M.-Y., 1982: Three-dimensional deep-water waves, Part I, Experimental measurement of skew and symmetric wave patterns. *J. Fluid Mech.* 124, 73-108.

Su, M.-Y., and J. Cartmill, 1995: Effects of salinity on breaking wave generated void fraction and bubble size spectra. In: *Air-Water Gas Transfer*. B. Jaehne and E.C. Monahan, Eds., 305-311.

Su, M.-Y., D. Todoroff, and J. Cartmill, 1994: Laboratory comparisons of acoustic and optical sensors for microbubble measurement. *J. Atmos. Ocean. Tech.* 11**,** 170-181.

Subrahmanyam, B., V.S.N. Murty, R.J. Sharp and J.J. O'Brien, 2005: Air-sea coupling during the tropical cyclones in the Indian Ocean - a case study using satellite observations. *J. Pure Appl. Geophys*. (in press).

Swean, Jr., T.F., R.I. Leighton, R. Handler, and J.D. Swearingen, 1991: Turbulence modeling near the free surface in open channel flow. *AIAA* Paper 91-0613.

Takahashi, T., 2000: Distribution of surface water $pCO_2$ and the net sea-air $CO_2$ flux over the global oceans. Paper presented at the *Ewing Symposium, Lamont Doherty Earth Observatory*, *October 27-28, 2000*.

Takahashi, T., J. Olafsson, J.G. Goddard, D.W. Chapman, and S.C. Sutherland, 1993: Seasonal variations of CO2 and nutrients in the high-latitude surface oceans: a comparative study. *Global Biogeochem. Cy*. 7, 843-878.

Tanahashi, S., H. Kawamura, T. Takahashi, and H. Yusa, 2003: Diurnal variations of sea surface temperature over the wide-ranging ocean using VISSR on board GMS, *J. Geophys. Res.* 108, 3216, doi:10.1029/2002JC001313.

Tandon, A., and C. Garrett, 1995: Geostrophic adjustment and restratification of a mixed layer with horizontal gradients above a stratified layer. *J. Phys. Oceanogr*. 25, 2229-2241.

Tanre, D., M. Herman, P.Y. Deschamps, and A. De Leffe, 1979: Atmospheric modeling for space measurements of ground reflectances, including bidirectional properties. *Appl. Optics* 18, 3587-3594.

Tans P.P., I.Y. Fung, and T. Takahashi, 1990: Observational constraints on the global atmospheric $CO_2$ budget. *Science* 247, 1431-1438.

Taylor, G.I., 1931: Effect of variation in density on the stability of superposed streams of fluid. *P. Roy. Soc. Lon. A* 132, 499-523.

Taylor, G.I., 1938: The spectrum of turbulence. *P. Roy. Soc. Lon. A* 164, 476-490.

Tennekes, H., 1973: The logarithmic wind profile. *J. Atmos. Sci.* 30, 558-567.

Theodorsen, T., 1952: Mechanism of Turbulence. In: *Proceedings of the Second Midwestern Conference on Fluid Mechanic*s, Columbus, Ohio, Ohio State University, pp. 1-18.

Terray, E.A., M.A. Donelan, Y.C. Agrawal, W.M. Drennan, K.K. Kahma, A. J. Williams III, P.A. Hwang, and S.A. Kitaigorodskii, 1996: Estimates of kinetic energy dissipation under breaking waves. *J. Phys. Oceanogr.* 26, 792-807.

Terrill, E.J., and W.K. Melville, 1997: Sound-speed measurement in the surface-wave layer. *J. Acoust. Soc. Am.* 102(5). Part 1, 2607-2625.

Terrill, E.J., and W.K. Melville, 2000: A broadband acoustic technique for measuring bubble size distributions: Laboratory and shallow water measurements. *J. Atmos. Ocean. Tech.* 17, 220-239.

Terrill, E.J., W.K. Melville, and D. Stramski, 2001: Bubble entrainment by breaking waves and their influence on optical scattering in the upper ocean. *J. Geophys. Res.* 106(C8), 16,815-16,823.

Thompson, S.M., and J.S. Turner, 1975: Mixing across an interface due to turbulence generated by an oscillating grid. *J. Fluid Mech*. 67, 349-368.

Thorpe, S.A., 1968: On the shape of progressive internal waves. *Phil. Trans. Roy. Soc. Lon. Ser. A* 263, 563-614.

Thorpe, S.A., 1969: Experiments on the stability of stratified shear flows. *Radio Sci.* 4**,** 1327-1331.

Thorpe, S.A., 1971: Asymmetry of the internal seiche in Loch Ness. *Nature* 231(5301), 306-308.

Thorpe, S.A., 1975: The excitation, dissipation, and interaction of internal waves in the deep ocean. *J. Geophys. Res*. 80, 328-338.

Thorpe, S.A., 1982: On the clouds of bubbles formed by breaking wind-waves in deep water, and their role in air–sea gas transfer. *P. Trans. Roy. Soc. Lon. Ser. A,* 304, 155-210.

Thorpe, S.A., 1985: Small-scale processes in the upper ocean boundary layer. *Nature* 318, 519-522.

Thorpe, S.A., 1986: Bubble clouds: A review of their detection by sonar, of realistic models, and of how may be determined. *Whitecaps and Their Role in Air-Sea Exchange Processes.* E.C. Monahan and G. MacNiocaill, Eds., 57-68, D. Reidel, Norwell, MA.

Thorpe, S.A., 1988: The dynamics of the boundary layers of the deep ocean. *Sci. Prog. Oxf.* 72, 189-206.

Thorpe, S.A., 1992: The break-up of Langmuir circulation and the instability of an array of vortices. *J. Phys. Oceanogr*. 22, 350-360.

Thorpe, S.A., 1995: Dynamical processes at the sea surface. *Prog. Oceanog.* 35, 315-352.

Thorpe, S.A., and A.J. Hall, 1987: Bubble clouds and temperature anomalies in the upper ocean. *Nature* 328, 48-51.

Thorpe, S.A., J.F.E. Jackson, A.J. Hall, and R.G. Lueck, 2003a: Measurements of turbulence in the upper ocean mixing layer using Autosub. *J. Phys. Oceanogr*. 33, 122–145.

Thorpe, S.A., T.R. Osborn, D.M. Farmer, and S. Vagel, 2003b: Bubble clouds and Langmuir circulation: Observations and models. *J. Phys. Oceanogr.* 33, 2013-2031.

Tkalich, P., and E.S. Chan, 2002: Breaking wind waves as a source of ambient noise. *J. Acoust. Soc. Am.* 112(2), 456-563.

TOCS, 1996: Cruise Report K-9709. JAMSTEC, 1997, Yokosuka, Kanagawa, Japan.

Tomczak, M., 1995: Salinity variability in the surface layer of the tropical western Pacific Ocean. *J. Geophys. Res.* 100(C10), 20,499-20,515.

Townsend, A., 1961: Equilibrium layers and wall turbulence. *J. Fluid Mech.* 11, 97-120.

Tsimplis, M., 1992: The effect of rain in calming the sea. *J. Phys. Oceanogr.* 22, 404-412.

Tsimplis, M., and S.A. Thorpe, 1989: Wave damping by rain. *Nature* 342, 893-895.

Turner, J.S., 1973: *Buoyancy Effects in Fluids.* Cambridge Univ. Press, NY.

Ulbrich, C. W., 1983: Natural variations in the analytical form of the raindrop size distribution. *J. Clim. Appl. Meteorol.* 22, 1764-1775.

Umlauf, L., and H. Burchard, 2003: A generic length-scale equation for geophysical turbulence models. *J. Mar. Res*. 61, 235-265.

United States Department of Energy, 1994: Handbook of methods for the analysis of the various parameters of the carbon dioxide system in seawater; version 2.

Vagle, S., and D.M. Farmer, 1992: The measurement of bubble size distributions by acoustical backscatter. *J. Atmos. Ocean. Tech.* 9(5), 630–644.

Vagle, S., and D.M. Farmer, 1998: A Comparison of four methods for bubble size and void fraction measurements. *IEEE J. Ocean Eng.* 23**,** 211–222.

Vagle, S., W.G. Large, and D.M. Farmer, 1990: An evaluation of the WOTAN technique for inferring oceanic wind from underwater sound. *J. Atmos. Ocean. Tech.* 7**,** 576–595.

Vialard, J., and P. Delecluse, 1988a: An OGCM study for the TOGA decade. Part I: Role of salinity in the physics of the western Pacific fresh pool. *J. Phys. Oceanogr.* 28, 1071-1088.

Vialard, J., and P. Delecluse, 1998b: An OGCM study for the TOGA decade. Part II: Barrier-layer formation and variability. *J. Phys. Oceanogr.* 28, 1089-1106.

Van Dyke, M., 1982: *An Album of Fluid Motion.* Parabolic Press, Stanford, CA, 176 pp.

Van Heijst, G.J.F., 1993: Self-Organization of Two-Dimensional Flows. *Nederlands Tijdschrift voor Natuurkunde* 59, 321-325.

Van Heijst, G.J.F., and R.C. Kloosterziel, 1989: Tripolar vortices in a rotating fluid. *Nature* 338(6216), 569-570.

Van Heijst, G.J.F., and J.B. Flór, 1989: Dipole formation and collision in a stratified fluid. *Nature* 340(6230), 212-215.

Van Scoy, K.A., K.P. Morris, J.E. Robertson, and A.J. Watson, 1995: Thermal skin effect and air-sea flux of carbon dioxide: A seasonal, high-resolution estimate. *Global Biogeochem. Cy.* 9, 253-262.

Vershinsky N.V., and A.V. Soloviev, 1977: A profiler for the studies of the ocean surface layer. *Oceanology* 17, 358-363 (in Russian).

Verevochkin, Yu.G., and S.A. Startsev, 2000: Numerical simulation of convection and heat transfer in water absorbing solar radiation. *J Fluid Mech.* 421, 293-305.

Verevochkin, Yu.G., and S.A. Startsev, 2005: Effect of absorption of solar radiation by water of different optical types on convection and heat transfer just under the air-water interface. The case of zero wind speed. *J. Fluid Mech.* 523, 109-120.

Veronis, G., 1960: An approximate theoretical analysis of the equatorial undercurrent. *Deep-Sea Res.* 6, part A, 318-327.

Vialard, J., and P. Delecluse, 1998: An OGCM study for the TOGA decade. Part II: Barrier layer formation and variability. *J. Phys. Oceanogr.* 28(C6), 1089-1106.

Vinayachandran P.N., V.S.N. Murty, and V. Ramesh Babu, 2002: Observations of barrier layer formation in the Bay of Bengal during summer monsoon. *J. Geophys. Res.* 107, doi:10.1029/2001JC000831.

Vladimirov, V.S., 1976: *Equations of mathematical physics*. Nauka, Moscow. (In Russian.)

Volino, R.J., and G.B. Smith, 1999: Use of simultaneous IR temperature measurements and DPIV to investigate thermal plumes in a thick layer cooled from above. *Exp. Fluids* 27, 70-78.

Volkov, Y.A., and A.V. Soloviev, 1986: On vertical thermal structure of near-surface layer of atmosphere above the ocean. Izvestiya: *Atmospheric and Oceanic Physics* 22(9), 899-903.

Volkov Y.A., A.V. Soloviev, V.V. Turenko, V.A. Bezverchnii, N.V. Vershinsky, and F.M.A. Ermolaev, 1989: Investigation of hydrophysical fields structure of the thin surface layer of the ocean from a moving vessel. Izvestiya: *Atmospheric and Oceanic Physics* 25(7), 695-701.

Voronovich, V.V., D.E. Pelenovsky, and V.A. Shrira, 1998a: On internal wave-shear flow resonance in shallow water. *J. Fluid Mech*. 354, 209-237.

Voronovich, A.G., and V.U. Zavorotny, 2001: Theoretical model for scattering of radar signals in $K_u$- and C-bands from a rough sea surface with breaking waves. *Wave. Random Media* 11(3), 247-269.

Voronovich, V.V., V.I. Shrira, and Yu.A. Stepanyants, 1998b: Two-dimensional models for nonlinear vorticity waves in shear flows. *Stud. Appl. Math.* 100, 1-32.

Voropaev, S.I., B.L. Gavrilin, and A.G. Zatsepin, 1981: On the structure of the surface layer of the ocean. Izvestiya: *Akad. Nauk SSSR, Atmospheric and Oceanic Physics* 17, 378-382.

Voropayev, Ya. D. Afanasyev, and I.A. Filippov, 1991: Horizontal jets and vortex dipoles in a stratified fluid. *J. Fluid Mech*. 227, 543-566.

Wadhams, P., 1973: Attenuation of swell by sea ice. *J. Geophys. Res*. 78, 3525-3563.

Wadhams, P., M.A. Lange, and S.F. Ackley, 1987: The ice thickness distribution across the Atlantic sector of the Antarctic Ocean in midwinter. *J. Geophys. Res*. 92, 14,535-14,552.

Waliser, D.E., R.A. Weller, and R.D. Cess, 1999: Comparisons between buoy-observed, satellite-derived, and modeled surface shortwave flux over the subtropical North Atlantic during the Subduction Experiment. *J. Geophys. Res.*104, 31,301-31,320.

Walsh, E.J., R. Pinkel, D.E. Hagan, R.A. Weller, C.W. Fairall, D.P. Rogers, S.P. Burns, and M. Baumgartner, 1998: Coupling of internal waves on the main thermocline to the diurnal surface layer and sea surface temperature during the Tropical Ocean Global Atmosphere Coupled Ocean-Atmosphere Response Experiment. *J. Geophys. Res.* 103, 12,613-12,628.

Wanninkhof, R., 1992: Relationship between wind speed and gas exchange over the ocean. *J. Geophys. Res.* 97, 7373–7382.

Wanninkhof, R., G. Hitchcock, W. Wiseman, G. Vargo, P. Ortner, W. Asher, D. Ho, P. Schlosser, M.-L. Dickson, M. Anderson, R. Masserini, K. Fanning, and J.-Z Zhang., 1997:

Gas Exchange, Dispersion, and Biological Productivity on the West Florida Shelf: Results from a Lagrangian Tracer Study. *Geophys. Res. Let.* 24, 1767-1770.

Wanninkhof, R., and W.R. McGillis., 1999: A cubic relationship between air-sea $CO_2$ exchange and wind speed. *Geophys. Res. Lett.* 26(134), 1889-1892.

Wang, D., W.G. Large, and J.C. McWilliams, 1996: Large-eddy simulation of the equatorial ocean boundary layer: Diurnal cycling, eddy viscosity, and horizontal rotation. *J. Geophys. Res.* 101, 3649-3662.

Wang, Y., J.D. Kepert, and G.J. Holland, 2001: The effect of sea spray evaporation on tropical cyclone boundary-layer structure and intensity. *Mon. Weather Rev.* 129(10), 2481-2500.

Ward, B., and P.J. Minnett, 2001: An autonomous profiler for near surface temperature measurements. *Gas Transfer at Water Surfaces*. M.A. Donelan, W.M. Drennan, E.S. Saltzmann, and R. Wanninkhof, Eds. American Geophysical Union Monograph 127. 167 - 172.

Watson, K.M., B.J. West, and B.I. Cohen, 1976: Coupling of surface and internal gravity waves: A mode coupling model. *J. Fluid Mech*. 77, 185-208.

Webster, P.J., C.A. Clayson, and J.A. Curry, 1996: Clouds, radiation and the diurnal cycle of sea surface temperature in the tropical western Pacific. *Ocean. J. Clim*. 9, 1712-1730.

Webster, P. J., and R. Lukas, 1992: TOGA COARE: The Coupled Ocean-Atmosphere Response Experiment. *Bull. Amer. Met. Soc.* 73, 1377-1416.

Weller, R.A., and S.P. Anderson, 1996: Surface meteorology and air-sea fluxes in the western equatorial Pacific warm pool during the TOGA Coupled Ocean-Atmosphere Response Experiment. *J. Climate* 9, 1959-1992.

Weller, R.A., A.S. Fischer, D.L. Rudnick, C.E. Eriksen, T.D. Dickey, J. Marra, C. Fox, and R. Leben, 2002: Moored observations of upper ocean response to the monsoon in the Arabian Sea during 1994-1995, *Deep-Sea Res. II* 49, 2231-2264.

Weller, R.A., and J.F. Price, 1988: Langmuir circulation within the oceanic mixed layer. *Deep-Sea Res*. 35, 711–747.

Wesson, J.C., and M.C. Gregg, 1994: Mixing in Camarinal Sill in the Strait of Gibraltar. *J. Geophys. Res.* 99, 9847-9878.

Wick, G.A., 1995: *Evaluation of the variability and predictability of the bulk-skin sea surface temperature difference with application to satellite-measured sea surface temperature*. Thesis (Ph.D.), University of Colorado at Boulder. Dissertation Abstracts International, Volume: 56-09, Section: B, page: 4798.

Wick, G.A., W.J. Emery, and P. Schlüssel, 1992: A comprehensive comparison between satellite-measured skin and multichannel sea surface temperature, *J. Geophys. Res.* 97, 5569-5595.

Wick, G.A., W.J. Emery, L.H. Kantha, and P. Schlüssel, 1996: The behavior of bulk-skin sea surface temperature difference under varying wind speed and heat flux. *J. Phys. Oceanogr.* 26, 1969-1988.

Wijesekera, H.W., and T.M. Dillon 1991. Internal waves and mixing in the upper Equatorial Pacific Ocean, *J. Geophys. Res*. 96, 7115-7125.

Wijesekera, H.W., and M.C. Gregg, 1996: Surface layer response to weak winds, westerly bursts, and rain squalls in the western Pacific warm pool. *J. Geophys. Res.* 106(101), 977-997.

Wijesekera, H.W., C.A. Paulson, and A. Huyer, 1999a: The effect of rainfall on the surface layer during a westerly burst in the western equatorial Pacific. *J. Phys. Oceanogr.* 29(4), 612-632.

Wijesekera, H.W., C.A. Paulson, and A. Huyer, 1999b: Spectra and skewness of near-surface turbulent temperature fluctuations forced by surface cooling and wind stress, *Proceeding COARE98, Boulder, Colorado, USA, 7-14 July 1998, World Climate Research Programme, 287-288.*

White, F.M., 1986: *Fluid Mechanics*. McGraw-Hill, NY, 732 pp.

Whitham, G.B., 1974: *Linear and nonlinear waves*. Wiley, NY

Woods, J.D., 1968: An investigation of some physical processes associated with the vertical flow of heat through upper ocean. *Meteorology Magazine* 97(1148), 65-72.

Woods, J.D., 1980a: Diurnal and seasonal variation of convection in the wind-mixed layer of the ocean. *Q. J. Roy. Meteor. Soc.* 106, 379-394.

Woods, J.D., 1980b: The generation of thermohaline fine structure of fronts in the ocean. *Ocean Modeling* 32, 1-4.

Woods, J.D., W. Barkman, 1986a: A Lagrangian mixed layer model of Atlantic 18°C water formation. *Nature* 319, 574-576.

Woods, J.D., and W. Barkmann. 1986b: The response of the upper ocean to solar heating. I: The mixed layer. *Q. J. Roy. Meteor. Soc.* 112**,** 1-42.

Woods, J.D., and V. Strass, 1986: The response of the upper ocean to solar heating. 2. The wind-driven current. *Q. J. Roy. Meteor. Soc.* 112(471), 29-42.

Woolf, D.K., 1993: Bubbles and the air-sea transfer velocity of gases. *Atmos.-Ocean* 31, 517-540.

Woolf, D.K., 1995 Energy dissipation through wave breaking and the air-sea exchange of gases. In: *Air-Water Gas Transfer.* B. Jähne and E.C. Monahan, Eds., AEON Verlag, Hanau, Germany, 185-195.

Woolf, D.K., 1997: Bubbles and their role in air-sea gas exchange. In: *The Sea Surface and Global Change*. P.S. Liss and R.A. Duce, Eds., Cambridge University Press, UK, 173-205.

Woolf, D.K., P.A. Bowyer, and E.C. Monahan, 1987: Discriminating between the film drops and jet drops produced by a simulated whitecap. *J. Geophys. Res.* 92, 5142-5150.

Woolf, D.K., and S.A. Thorpe. 1991: Bubbles and the air-sea exchange of gases in near-saturation conditions. *J. Mar. Res.* 49, 435-466.

Wu, J., 1975: Wind-induced drift current. *J. Fluid Mech.* 68, 49-70.

Wu, J., 1985: On the cool skin of the ocean. *Bound.-Layer Meteorol.* 31, 203-207.

Wu, J., 1992: Bubble flux and marine aerosol spectra under various wind velocities. *J. Geophys. Res.* 97, 2327-2333.

Wu, J., 1993: Production of spume drops by the wind tearing of wave crests: The search for quantification. *J. Geophys. Res.* 98, 18,221-18, 227.

Wu, J., J.J. Murray, and R.J. Lai, 1984: Production and distribution of sea spray. *J. Geophys. Res.* 89**,** 8163–8169.

Wu, J., S.-W. Chung, L.-S. Wen, K.-K. Liu, Y.L. Chen, H.-Y. Chen, and D.M. Karl, 2003: Dissolved inorganic phosphorus, dissolved iron and Trichodesmium in the oligotrophic South China Sea. *Global Biogeochemical Cycles*, 17: 8-1-8-10, doi: 10.1029/2002GB001924.

Wyngaard, J.C., O.R. Cote, and Y. Izumi, 1971: Local free convection similarity, and the budgets of shear stress and heat flux. *J. Atmos. Sci.* 28, 1172-1182.

Yaglom, A.M., 1979: Similarity laws for constant-pressure and pressure-gradient turbulent flows. *Ann. Rev. Fluid Mech.* 11, 505-540.

Yakimov, Y.L., 1959: Why waves are extinguished by rain. Izvestiya: *Sib. Akad. Nauk SSR* 5, 125-126 (in Russian).

Yamazaki, H., and R.G. Lueck, 1990: Why oceanic dissipation rates are not lognormal. *J. Phys. Oceanogr.* 20, 1907-1918.

Yentisch, C.S., 1984: Satellite representation of features of ocean circulation indicated by CZCS colorimetry. In: *Remote Sensing of Shelf Sea Hydrodynamcis*, J.C.J. Nihoul, Ed., Elsevier, Amsterdam, 336-354.

You, Y., 1995: Salinity variability and its role in the barrier-layer formation during TOGA COARE. *J. Phys. Oceanogr.* 25, 2778-2807.

Young, W.R., 1994: The subinertial mixed layer approximation. *J. Phys. Oceanogr*. 24, 1812-1826.

Yuen, H.C., 1977: Nonlinear deep-water waves v. unsteady wavebreaking, *TRW Report No. 3132606013-RV-00.*

Zakharov, V.E. (ed.), 1998: *Nonlinear waves and weak turbulence*. American Mathematical Society. Providence, RI, 197 pp.

Zaitsev, Y.P. 1971: *Marine neustonology* (translated from Russian). National Marine Fisheries Service, NOAA and National Science Foundation, National Technical Information Service, Springfield, Virginia, 207 pp.

Zaitsev, Y., 1997: Neuston of seas and oceans. In: *The Sea Surface and Global Change*. P.S. Liss and R.A. Duce, Eds., Cambridge University Press, UK, 371-382.

Zenk, W., and E.J. Katz, 1975: On the stationarity of temperature spectra at high horizontal wave numbers. *J. Geophys. Res.* 80(27), 3885-3891.

Zhang, G., J. Vivekanandan, E.A. Brandes, R. Meneghini, and T. Kozu, 2003: The Shape–Slope Relation in Observed Gamma Raindrop Size Distributions: Statistical Error or Useful Information? *J. Atmos. Ocean. Tech.* 20, 1106–1119.

Zhang, X., and S. Harrison, 2004: A laboratory observation of the surface temperature and velocity distributions on a wavy and windy air-water interface. *Physics of Fluids* 16, L5-L8.

Zhang, X., M. Lewis, and B. Johnson, 1998: Influence of bubbles on scattering of light in the ocean. *Appl. Opt.* 37, 6525-6536.

Zhang, Y., A.B. Baggeroer, and J.G. Bellingham, 2001: Spectral-feature classification of oceanographic processes using an autonomous underwater vehicle. *IEEE J. Ocean. Eng.* 26, 726-741.

Zhang, Y., and W. Perrie, 2001: Feedback mechanisms for the atmosphere and ocean surface. *Bound.-Layer Meterol.* 100, 321-348.

Zhao, D. and Y. Toba, 2001. Dependence of whitecap coverage on wind and wind-wave properties. *J. Oceanography* 57, 603-616.

Zepp, R.G., T.V. Callaghan, and D.J. Erickson, 1995: Effects of increased solar radiation on biogeochemical cycles. *Ambio* 24, 181-187.

Zilitinkevich, S.S., 1966: Effect of humidity stratification on hydrostatic stability. Izvestiya: *Academy of Sciences, USSR. Atmospheric and Oceanic Physics* 2, 1089-1094.

Zilitinkevich, S.S., and P. Calanca, 2000: An extended similarity-theory for the stably stratified atmospheric surface layer. *Q. J. Roy. Meteorol. Soc.* 126, 1913-1923.

## SUBJECT INDEX

## ATMOSPHERIC AND OCEANOGRAPHIC SCIENCES LIBRARY

1. F.T.M. Nieuwstadt and H. van Dop (eds.): *Atmospheric Turbulence and Air Pollution Modelling.* 1982; rev. ed. 1984
   ISBN 90-277-1365-6; Pb (1984) 90-277-1807-5
2. L.T. Matveev: *Cloud Dynamics.* Translated from Russian. 1984
   ISBN 90-277-1737-0
3. H. Flohn and R. Fantechi (eds.): *The Climate of Europe: Past, Present and Future.* Natural and Man-Induced Climate Changes: A European Perspective. 1984
   ISBN 90-277-1745-1
4. V.E. Zuev, A.A. Zemlyanov, Yu.D. Kopytin, and A.V. Kuzikovskii: *High-Power Laser Radiation in Atmospheric Aerosols.* Nonlinear Optics of Aerodispersed Media. Translated from Russian. 1985 ISBN 90-277-1736-2
5. G. Brasseur and S. Solomon: *Aeronomy of the Middle Atmosphere.* Chemistry and Physics of the Stratosphere and Mesosphere. 1984; rev. ed. 1986
   ISBN (1986) 90-277-2343-5; Pb 90-277-2344-3
6. E.M. Feigelson (ed.): *Radiation in a Cloudy Atmosphere.* Translated from Russian. 1984 ISBN 90-277-1803-2
7. A.S. Monin: *An Introduction to the Theory of Climate.* Translated from Russian. 1986
   ISBN 90-277-1935-7
8. S. Hastenrath: *Climate Dynamics of the Tropics*, Updated Edition from *Climate and Circulation of the Tropics.* 1985; rev. ed. 1991
   ISBN 0-7923-1213-9; Pb 0-7923-1346-1
9. M.I. Budyko: *The Evolution of the Biosphere.* Translated from Russian. 1986 ISBN 90-277-2140-8
10. R.S. Bortkovskii: *Air-Sea Exchange of Heat and Moisture During Storms.* Translated from Russian, rev. ed. 1987 ISBN 90-277-2346-X
11. V.E. Zuev and V.S. Komarov: *Statistical Models of the Temperature and Gaseous Components of the Atmosphere.* Translated from Russian. 1987
    ISBN 90-277-2466-0
12. H. Volland: *Atmospheric Tidal and Planetary Waves.* 1988 ISBN 90-277-2630-2
13. R.B. Stull: *An Introduction to Boundary Layer Meteorology.* 1988
    ISBN 90-277-2768-6; Pb 90-277-2769-4
14. M.E. Berlyand: *Prediction and Regulation of Air Pollution.* Translated from Russian, rev. ed. 1991 ISBN 0-7923-1000-4
15. F. Baer, N.L. Canfield and J.M. Mitchell (eds.): *Climate in Human Perspective.* A tribute to Helmut E. Landsberg (1906-1985). 1991 ISBN 0-7923-1072-1
16. Ding Yihui: *Monsoons over China.* 1994 ISBN 0-7923-1757-2
17. A. Henderson-Sellers and A.-M. Hansen: *Climate Change Atlas*. Greenhouse Simulations from the Model Evaluation Consortium for Climate Assessment. 1995
    ISBN 0-7923-3465-5
18. H.R. Pruppacher and J.D. Klett: *Microphysics of Clouds and Precipitation*, 2nd rev. ed. 1997 ISBN 0-7923-4211-9; Pb 0-7923-4409-X
19. R.L. Kagan: *Averaging of Meteorological Fields*. 1997 ISBN 0-7923-4801-X
20. G.L. Geernaert (ed.): *Air-Sea Exchange: Physics, Chemistry and Dynamics*. 1999
    ISBN 0-7923-5937-2
21. G.L. Hammer, N. Nicholls and C. Mitchell (eds.): *Applications of Seasonal Climate Forecasting in Agricultural and Natural Ecosystems*. 2000 ISBN 0-7923-6270-5

## ATMOSPHERIC AND OCEANOGRAPHIC SCIENCES LIBRARY

22. H.A. Dijkstra: *Nonlinear Physical Oceanography*. A Dynamical Systems Approach to the Large Scale Ocean Circulation and El Niño. 2000 ISBN 0-7923-6522-4
23. Y. Shao: *Physics and Modelling of Wind Erosion*. 2000 ISBN 0-7923-6657-3
24. Yu.Z. Miropol'sky: *Dynamics of Internal Gravity Waves in the Ocean.* Edited by O.D. Shishkina. 2001 ISBN 0-7923-6935-1
25. R. Przybylak: *Variability of Air Temperature and Atmospheric Precipitation during a Period of Instrumental Observations in the Arctic.* 2002 ISBN 1-4020-0952-6
26. R. Przybylak: *The Climate of the Arctic*. 2003 ISBN 1-4020-1134-2
27. S. Raghavan: *Radar Meteorology*. 2003 ISBN 1-4020-1604-2
28. H.A. Dijkstra: *Nonlinear Physical Oceanography*. A Dynamical Systems Approach to the Large Scale Ocean Circulation and El Niño. 2nd Revised and Enlarged Edition. 2005 ISBN 1-4020-2272-7 Pb; 1-4020-2262-X
29. X. Lee, W. Massman and B. Law (eds.): *Handbook of Micrometeorology*. A Guide for Surface Flux Measurement and Analysis. 2004 ISBN 1-4020-2264-6
30. A. Gelencsér: *Carbonaceous Aerosol*. 2005 ISBN 1-4020-2886-5
31. A. Soloviev and R. Lukas: *The Near-Surface Layer of the Ocean*. Structure, Dynamics and Applications. 2006 ISBN 1-4020-4052-0
32. G.P. Brasseur and S. Solomon: *Aeronomy of the Middle Atmosphere*. Chemistry and Physics of the Stratosphere and Mesosphere. 2005 ISBN 1-4020-3284-6; Pb 1-4020-3285-4